ANCHAM

Analytical CHEMISTRY

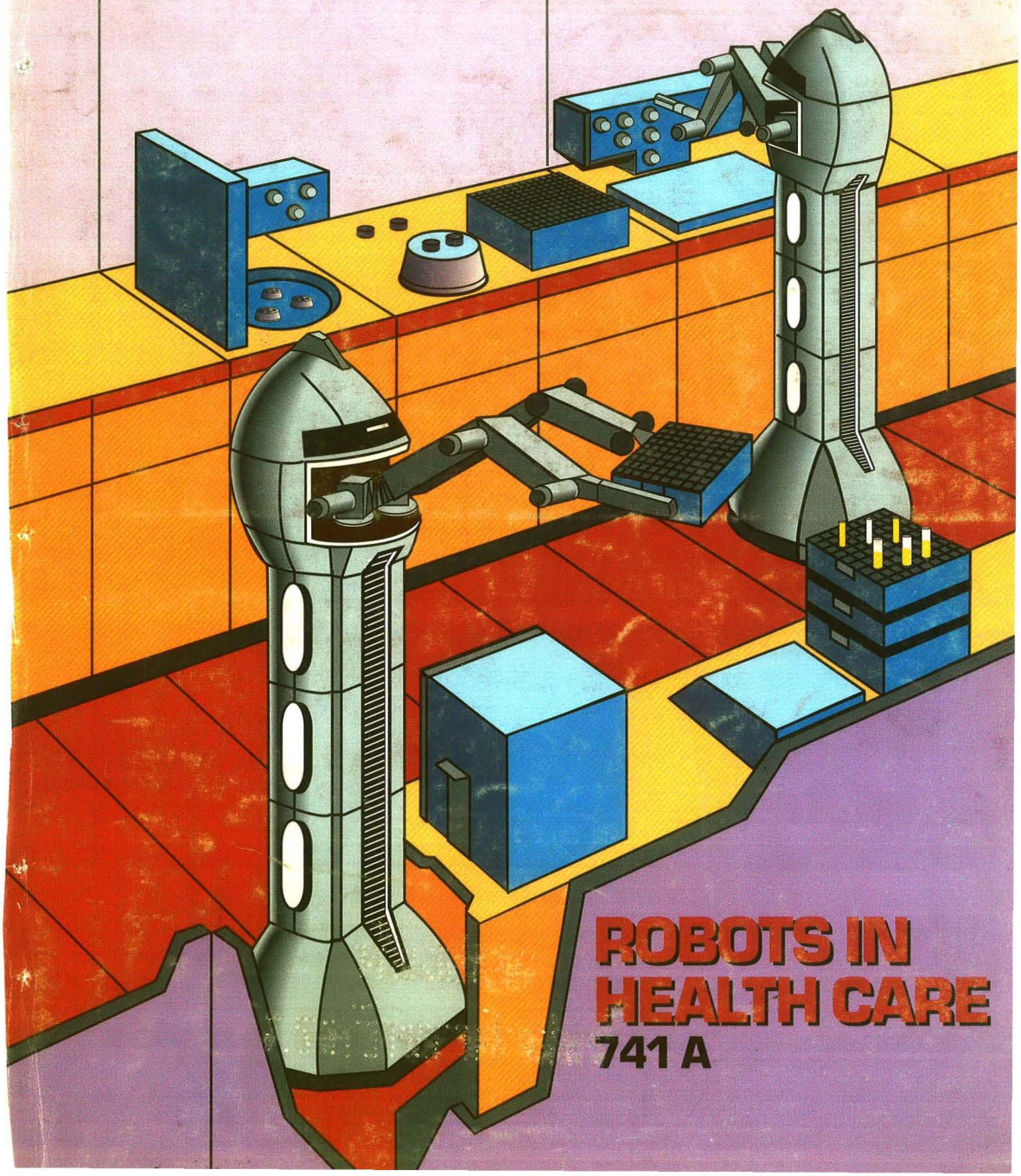

ROBOTS IN HEALTH CARE

741 A

How we made a better HPLC system for QC/QA analysis

We started by eliminating the computer

Our new programmable 307 Pump is at the heart of the system. It controls other system components: an auto-injector, detector and integrator or data analysis system. This system is less expensive than most computer-based QC/QA systems and much easier to operate, too. All the information you need to start a run flashes on the front panel display.

Another key feature of the 307 is that it provides extremely smooth flow rates for repetitive retention times. And flow accuracy is unaffected by pressure changes or by the nature of the liquid.

Then we added an auto-injector that ensures accurate, reproducible results

The Gilson 231/401 Auto-Sampling Injector is another key component in the system. It automates the preparation and injection of up to 120 samples. (A larger capacity unit is available that can handle up to 540 samples.) A built-in rinsing function virtually eliminates cross-contamination due to carry-over. And because the 231/401 loads the sample directly into the injection valve, sample consumption is reduced.

Plus, all these benefits for QC/QA applications

- System requires less than 2 sq. ft. of bench space. Ideal for labs with multiple systems and minimal space.
- Quick system set-up. You can assemble the QC/QA system in 30 minutes or less. All connections are easily accessible.
- Simplifies compliance with GLP guidelines. 307 Pumps have built-in functions for tracking pump head usage.

To learn more about these and other advantages of the Gilson HPLC system for QC/QA analysis, contact your local Gilson representative. Or call us toll-free.

GILSON®

Call 800-445-7661

Gilson Medical Electronics, Inc., Box 27, 3000 W. Beltline Hwy., Middleton, WI 53562 USA, Tel: 608-836-1551, TLX: 26-5478, FAX: 608-831-4451
Gilson Medical Electronics (France) S.A., 72 rue Gambetta, B.P. No. 45, 95400 Villiers-le-Bel, France, Tel: (33) 1 34.29.50.00, TLX: 606682, FAX: (33) 1 34.29.50.80

CIRCLE 50 ON READER SERVICE CARD

How our new automatic AA analyzes mixed runs of samples for up to 8 elements and does it up to 4x faster than our competitors.

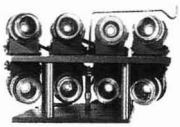

The lamp housing contains 8 hollow cathode lamps in 2 banks of 4 each. That arrangement permits the determination of up to 8 elements without changing lamps.

On each sample, readings are taken for up to 4 elements at once (i.e. one bank of hollow cathode lamps). That enables our AA to perform 4x as many determinations as other AAs.

Theirs

Ours

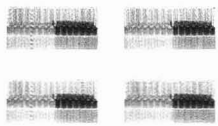

Our new AA comes with the NEC Powermate 286 Plus and ThermoSPEC® software, a package which enables chemists to enter methods, quickly and easily, but also permits personnel with little technical training to run routine analyses.

With computer control and our run specification screen, sets of up to 150 samples may be run in unattended operation and these sets may be mixed, i.e. contain different analytes and call for different standards and dilutions.

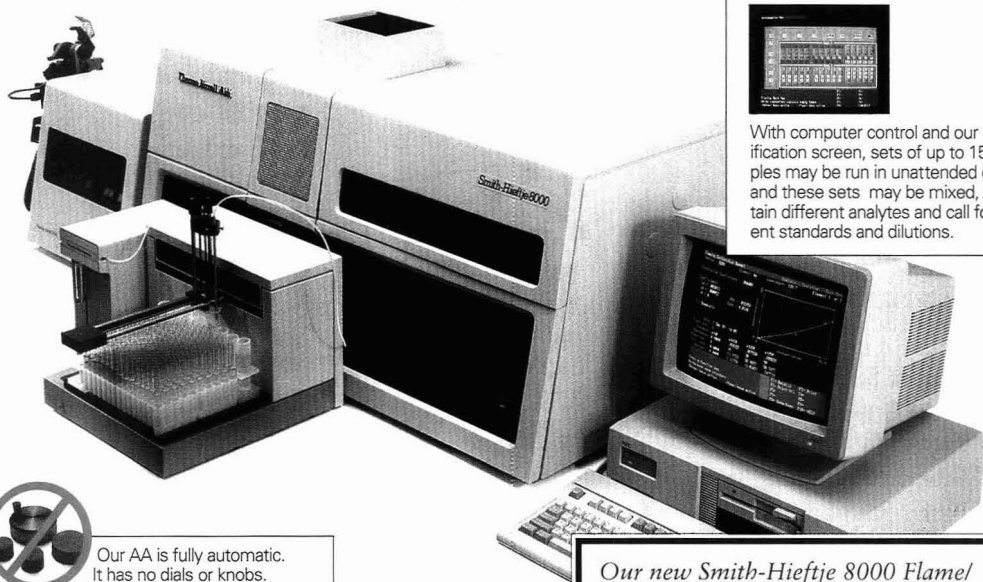

Our AA is fully automatic. It has no dials or knobs. Wavelength and PMT adjustments are made by the instrument and not by you.

In flame or furnace operation, accurate background corrections are made with the patented Smith-Hieftje technique. For furnace, vapor and solid phase matrix interferences are eliminated by our Delay Atomization Cuvette, platform and aerosol sampling device.

Our new Smith-Hieftje 8000 Flame/ Furnace AA spectrophotometer offers the highest productivity by far of any AA on the market today. And that translates into lower per test costs for analytical service laboratories and higher profits for private contract laboratories.

For literature or a demonstration, call (508)520-1880. Or write Thermo Jarrell Ash Corporation, 8E Forge Parkway, Franklin, MA 02038

Thermo Jarrell Ash Corporation

A Division Of Thermo Instrument Systems, Inc.

CIRCLE 138 ON READER SERVICE CARD

Indispensable, Quarterly Reports Edited for Chemists, Information Scientists, and Computer Scientists

Journal of Chemical Information and Computer Sciences

An American Chemical Society Publication

George W.A. Milne, **Editor,**
National Institutes of Health

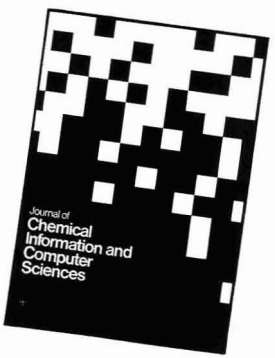

In peer-reviewed research papers and reviews of books and software, this international quarterly journal provides rigorous coverage found nowhere else!

1. Database Search Systems
2. Use of Graph Theory in Chemical Problems
3. Substructure Search Systems
4. Pattern Recognition and Clustering
5. Analysis of Chemical and Physical Data
6. Molecular Modeling
7. Graphics and Natural Language Interfaces
8. Bibliometric and Citation Analysis
9. Synthesis Design and Reactions Databases

Submit your original work!

The review process has been expedited considerably. Many individual scientists have committed to review manuscripts in 2 weeks, and this now permits publication of papers within 15 weeks of receipt! For manuscript guidelines please contact: George W.A. Milne, Building 37, Room 5C28, National Institutes of Health, Bethesda, MD 20892, 301/496-3597.

Join your colleagues the world over!

Associate Editors
Pierre Buffet, *Questel, France*
Reiner Luckenbach, *Beilstein Institute, Germany*
Wendy Warr, *ICI Pharmaceuticals, England*

Book Review Editor
Gary Wiggins, *Indiana University*

Software Editor
Stephen Heller, *U.S.D.A.*

1991 Subscription Information

	U.S.	Canada and Mexico	Europe**	All Other Countries**
ACS Members*				
One year	$ 19	$ 24	$ 28	$ 28
Two years	$ 34	$ 44	$ 52	$ 52
Nonmembers	$129	$134	$138	$138

*Member rates are for personal use only.
**Air service included.

For more information or to subscribe, write:

American Chemical Society
Marketing Communications Department
1155 Sixteenth Street, NW
Washington, DC 20036
1-800-227-5558 (U.S. and Canada) or (202) 872-4363 (in DC and outside the U.S. and Canada)
TLX 440159
FAX 202/872-4615

For nonmember rates in Japan contact Maruzen Co., Ltd.

This publication is available on microfiche, microfilm, and online on CJO on STN International.

JULY 15, 1991
VOLUME 63
NUMBER 14

The Audit Bureau ANCHAM 63(14) 701A–752A/1345–1504 (1991) ISSN 0003-2700

Registered in U.S. Patent and Trademark Office; Copyright 1991 by the American Chemical Society

ANALYTICAL CHEMISTRY (ISSN 0003-2700) is published semimonthly by the American Chemical Society at 1155 16th St., N.W., Washington, DC 20036. Editorial offices are located at the same ACS address (202-872-4570; fax 202-872-4574; Bitnet rmh96@cas; TDD 202-872-8733). Second-class postage paid at Washington, DC, and additional mailing offices. Postmaster: Send address changes to ANALYTICAL CHEMISTRY Member & Subscriber Services, P.O. Box 3337, Columbus, OH 43210.

Claims for missing numbers will not be allowed if loss was due to failure of notice of change of address to be received in the time specified; if claim is dated (a) North America: more than 90 days beyond issue date, (b) all other foreign: more than one year beyond issue date, or if the reason given is "missing from files."

Copyright Permission: An individual may make a single reprographic copy of an article in this publication for personal use. Reprographic copying beyond that permitted by Section 107 or 108 of the U.S. Copyright Law is allowed, provided that the appropriate per-copy fee is paid through the Copyright Clearance Center, Inc., 27 Congress St., Salem, MA 01970. For reprint permission, write Copyright Administrator, Publications Division, ACS, 1155 16th St., N.W., Washington, DC 20036.

Registered names and trademarks, etc., used in this publication, even without specific indication thereof, are not to be considered unprotected by law.

Advertising Management: Centcom, Ltd., 500 Post Rd. East, Westport, CT 06880 (203-226-7131)

1991 subscription rates include air delivery outside the U.S., Canada, and Mexico

	Members	Nonmembers (personal)	Nonmembers (institutional)
U.S.	31	69	289
Canada and Mexico	67	105	325
Europe	112	210	370
Other countries	131	229	389

Nonmembers rates in Japan: Rates above do not apply to nonmember subscribers in Japan, who must enter subscription orders with Maruzen Company Ltd., 3–10. Nihonbashi 2-chrome, Chuo-ku, Tokyo 103, Japan. Tel: (03) 272-7211.

For multi-year and other rates, call toll free 800-227-5558 in the U.S. and Canada; in the Washington, DC, metropolitan area and outside the U.S., call 202-872-4363; fax 202-872-4615.

Subscription orders by phone may be charged to VISA, MasterCard, or American Express. Call toll free 800-333-9511 in the continental U.S.; in the Washington, DC, metropolitan area and outside the continental U.S., call 202-872-8065. Mail orders for new and renewal subscriptions should be sent with payment to American Chemical Society, Department L-0011, Columbus, OH 43268-0011

Subscription service inquiries and changes of address (include both old and new addresses with ZIP code and *recent mailing label*) should be directed to the ACS Columbus address noted above. Please allow six weeks for changes to become effective.

ACS membership information: Lorraine Bowlin (202-872-4567)

Single issues, current year, $13.00 except review issue, $26.00, and LabGuide, $50.00; **back issues and volumes and microform editions** available by single volume or back issue collection. For information or to order, call the number listed for subscription orders by phone; or write the Microform & Back Issues Office at the Washington address.

Analytical® CHEMISTRY

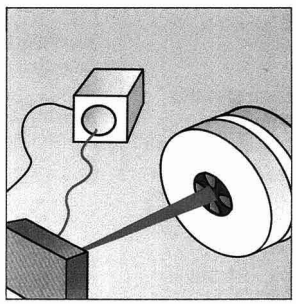

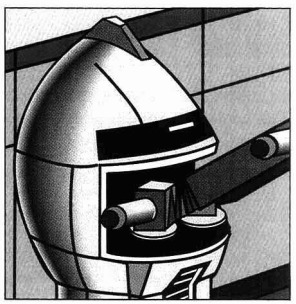

INSTRUMENTATION **715 A**

Microscopic specimens and the nuclear microprobe. MeV ion beams from accelerators can be focused onto sample surfaces and combined with other instrumentation to produce a nuclear microprobe. U.A.S. Tapper and K. G. Malmqvist of the Lund Institute of Technology review the properties of ion beams, discuss the information that can be obtained when they interact with samples, and demonstrate how the nuclear microprobe can be used with a variety of samples

A/C INTERFACE **741 A**

On the cover. **Robots in health care.** Traditionally, health care has been a difficult marketplace for automation because of the complexity of the procedures and the potential risks to human life should an error occur. Robin A. Felder and his colleagues at the University of Virginia Health Sciences Center discuss currently available robots, appropriate clinical laboratory and hospital applications, and impediments to the widespread adoption of this technology in the clinical setting

COVER: Adapted from an original drawing by Don Varner, courtesy of Don Nagy, CCRI.

BRIEFS **706 A**

NEWS **713 A**

Groundwater cleanup process. • Electron microscope reveals **3D atomic structure.** • **Gordon Research Conferences' teaching and research program** initiated

MEETINGS **727 A**

The **1991 joint meeting** of the **Federation of Analytical Chemistry and Spectroscopy Societies and the Pacific Conference** will be held Oct. 6–11 in Anaheim, CA. • 1991 Conferences. • Short courses and workshops. • Call for papers

BOOKS **734 A**

Critical reviews. Recently released books on sensors, MS, proteins, forensics, and QA/QC are reviewed

NEW PRODUCTS & MANUFACTURERS' LITERATURE **738 A**

AUTHOR INDEX **1345**

ห้องสมุดกรมวิทยาศาสตร์บริการ
๒๒ ก.ค. ๒๕๓๔

BRIEFS

Articles

Influence of Column Temperature on the Electrophoretic Behavior of Myoglobin and α-Lactalbumin in High-Performance Capillary Electrophoresis 1346

Open-tube CE of myoglobin yields two peaks corresponding to the Fe^{3+} and Fe^{2+} states with reduction taking place within the column as a function of temperature. A conformational change as a function of column temperature is demonstrated by α-lactalbumin.

Robert S. Rush, Aharon S. Cohen, and Barry L. Karger*, Barnett Institute, Northeastern University, 360 Huntington Avenue, Boston, MA 02115

Preparation and Evaluation of a Bimodal Size-Exclusion Chromatography Column Containing a Mixture of Two Silicas of Different Pore Diameter 1350

A mixed pore-size silica column (80Å and 500Å) provides size-exclusion curves (elution volume vs. log MW) that are linear from 5×10^2 to 2×10^6 MW. Efficiency is virtually pore-size independent.

David M. Northrop, R.P.W. Scott, and Daniel E. Martire*, Chemistry Department, Georgetown University, Washington, DC 20057

Electroosmotic Properties and Peak Broadening in Field-Amplified Capillary Electrophoresis 1354

Equations for the bulk electroosmotic velocity and the peak variance are derived for a CE system in which the capillary column consists of buffers of different concentration but the same composition.

Ring-Ling Chien* and John C. Helmer, Varian Research Center, 611 Hansen Way, Palo Alto, CA 94303

Matrix Elimination in Liquid Chromatography Using Heart-Cut Column Switching Techniques 1362

Accuracy, precision, and the quantitation limit for trace sulfite analysis are 91%, 20% RSD, and 2 ppm, respectively. The advantages include improved chromatography, reduced system abuse, and shorter analysis time.

Steven R. Villaseñor, Mallinckrodt Specialty Chemicals Company, 3600 N. Second Street, St. Louis, MO 63147

Particle Size Distribution by Sedimentation/Steric Field-Flow Fractionation: Development of a Calibration Procedure Based on Density Compensation 1366

By appropriately adjusting rpm to account for particle density, a log (retention time)–log (diameter) calibration plot established using standards becomes applicable to the size determination of sample particles of any density.

J. Calvin Giddings*, Myeong Hee Moon, P. Stephen Williams, and Marcus N. Myers, Field-Flow Fractionation Research Center, Department of Chemistry, University of Utah, Salt Lake City, UT 84112

Nanoliter-Scale Multireflection Cell for Absorption Detection in Capillary Electrophoresis 1372

S/N improvements of up to 40-fold are observed compared with conventional single-pass detection. Theoretical analysis of cell performance using ray tracing for both axial and radial reflections shows good agreement with experimental results.

Tiansong Wang, Joseph H. Aiken, Carmen W. Huie, and Richard A. Hartwick*, Department of Chemistry, State University of New York at Binghamton, Binghamton, NY 13902

Gas Chromatographic Determination of Trace Impurities in High-Purity Nitrogen Using Hydrogen Storage Alloys as a Nitrogen Adsorbent 1376

Two different H storage alloys are combined and used as a N adsorbent for the gas chromatographic determination of trace components such as Ne, Ar, Kr, Xe, and methane in high-purity N.

Hiroshi Ogino*, Yoko Aomura, and Tetsuya Seki, Technical Research Laboratory, Toyo Sanso Company, Ltd., 3-3, Mizuecho, Kawasaki-ku, Kawasaki-shi, Kanagawa 210, Japan

Membrane Technology and Dynamic Response of Ion-Selective Liquid-Membrane Electrodes 1380

The response time of neutral carrier-based ISEs is an essential parameter in membrane technology and depends strongly on the matrix, plasticizers, and constituents of the membranes.

Marin Huser, Peter M. Gehrig, Werner E. Morf, and Wilhelm Simon*, Department of Organic Chemistry, Swiss Federal Institute of Technology (ETH), Universitätsstrasse 16, CH-8092 Zürich, Switzerland and **Ernö Lindner, Judit Jeney, Klára Tóth, and Ernö Pungor*,** Institute for General and Analytical Chemistry, Technical University of Budapest, Gellért tér 4, H-1111 Budapest XI, Hungary

Pulse-Electrolysis Stopped-Flow Method for the Electrospectroscopic Analysis of Short-Lived Intermediates Generated in the Electrooxidation of Triphenylamine 1387

A method using pulse-electrolysis with a column electrode is described and applied to the dimerization reaction of the triphenylamine cation radical.

Munetaka Oyama, Koichi Nozaki, and Satoshi Okazaki*, Department of Chemistry, Faculty of Science, Kyoto University, Kyoto 606, Japan

*Corresponding author

Move Up to Matheson Standards

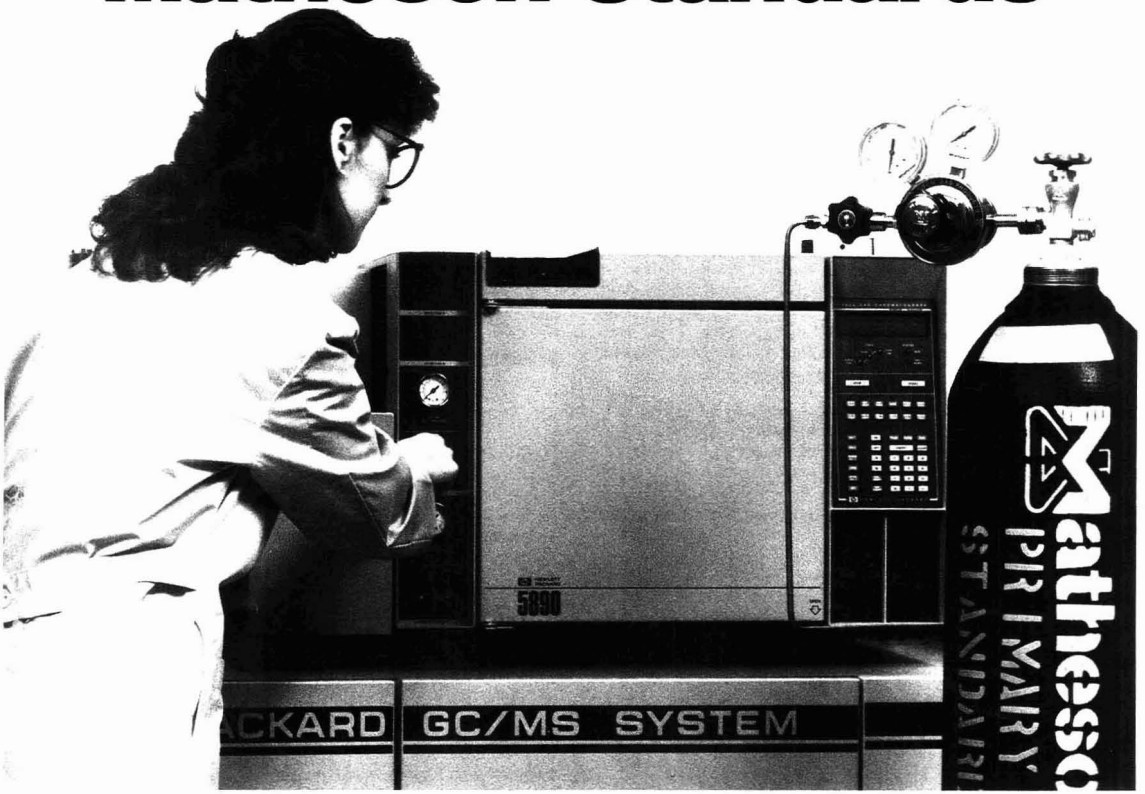

Accurate gas chromatography is dependent upon your technique, your equipment, and your gases. A skilled gas chromatographer can enhance the accuracy of his results by using Matheson products exclusively. Three special products are of utmost importance.

Primary Standard Calibration Mixtures

The heart of your work centers around your calibration standards. Consider Matheson's Primary Standards to improve your results. The accuracy of these mixtures usually exceeds that of most analytical instruments. Matheson Primary Standards are prepared on high load, high sensitivity analytical balances. Each gas component is carefully quality controlled before being weighed into the cylinder. Only weights traceable to the National Bureau of Standards are used. These mixtures give the highest degree of accuracy, precision and confidence. Move up today! Insist on Matheson Primary Standards.

Carrier Gases

The same exacting quality you get in Matheson Primary Standard Calibration Mixtures is also available in Matheson's carrier gases. No slipping in quality control here. Each Matheson UHP, Zero Gas, Ultra Zero Gas, and, of course, Matheson Purity Gas is guaranteed to be exactly what the label says. Nothing more, nothing less. Improve your GC operation today with the right carrier gas from Matheson.

Gas Handling Systems

Don't jeopardize the integrity of your gases with gas handling equipment of inferior quality. Matheson has the right piece of equipment for every job. From regulators that don't outgas impurities, to filters for protecting delicate valves, to flowmeters that measure precisely, Matheson equipment is **the** standard.

When your work requires the best, don't settle for less than Matheson Standards.

From pharmaceuticals to petroleum, from laser technology to aerospace, when only the best will do, do what so many experienced scientists do, move up to Matheson Standards.

For more information, contact Matheson, at (201) 867-4100, or circle the Reader Service Number below.

Matheson®
Gas Products
World Leader in Specialty Gases & Equipment
30 Seaview Drive, Secaucus, NJ 07094

CIRCLE 92 ON READER SERVICE CARD

Direct Examination of the Injection Process in Liquid Chromatographic Separations 1393

Laser-induced fluorescence detection is used to monitor solute zone migration at several points along a packed chromatographic column. The effect of injection solvent composition on the retention and dispersion of solute zones is systematically studied.

Christine E. Evans and Victoria L. McGuffin*, Department of Chemistry, Michigan State University, East Lansing, MI 48824

Theory and Experiment for the Collector–Generator Triple-Band Electrode 1403

The currents obtained at a triple-band electrode are computed using digital simulation in an appropriate conformal map.

Bruno Fosset and Christian Amatore*, Ecole Normale Superieure, Laboratoire de Chimie, 24 Rue Lhomond, 75231 Paris, France and **Joan Bartelt and R. Mark Wightman***, Department of Chemistry, University of North Carolina, Chapel Hill, NC 27599-3290

Peak Resolution in the Determination of Cobalt and Nickel by Differential Pulse and Alternating Current Adsorption Voltammetry 1409

The method permits the simultaneous voltammetric determination of Co and Ni, each in the presence of a large excess of the other. The precision and accuracy are, in most cases, on the order of 5%.

Clinio Locatelli*, Francesco Fagioli, and Tibor Garai, Department of Chemistry, University of Ferrara, Via Luigi Borsari 46, I-44100 Ferrara, Italy

Characterization of the Chemical Architecture of Carbon-Fiber Microelectrodes. 1. Carboxylates 1413

A method to characterize the chemical architecture of the surface of a carbon-fiber microelectrode uses derivatization of carboxyl groups on the carbon surface with a fluorophore followed by imaging with fluorescence microscopy.

Paul Pantano and Werner G. Kuhr*, Department of Chemistry, University of California, Riverside, CA 92521

Composite Multivariate Quality Control Using a System of Univariate, Bivariate, and Multivariate Quality Control Rules 1419

A multivariate quality control system is described that detects bias, trends, and correlation changes. It can reject one or more variables, tolerate missing data, and provide control statistics and graphics.

S. J. Smith*, S. P. Caudill, J. L. Pirkle, and D. L. Ashley, Division of Environmental Health and Laboratory Sciences, Center for Environmental Health and Injury Control, Centers for Disease Control, Public Health Service, U.S. Department of Health and Human Services, Atlanta, GA 30333

Interactive Self-Modeling Mixture Analysis 1425

The method displays intermediate results in the form of spectra, facilitating user interaction. The results of this multivariate data analysis method are comparable with state-of-the-art methods, as shown for Raman spectrometric and FT-IR microscopic data.

Willem Windig* and Jean Guilment, Eastman Kodak Company, Rochester, NY 14652-3712

Synchronous Scan Luminescence Techniques Monitoring Resonance and Nonresonance Fluorescence in Supersonic Jet Spectrometry Applied to Anthracene Derivatives 1433

Two complementary synchronous scan luminescence techniques are applied to a sample containing many PAHs. The components are assigned using the database of 0–0 transitions and the standard spectrum.

Cheng-Huang Lin, Hiroshi Fukii, Totaro Imasaka, and Nobuhiko Ishibashi*, Faculty of Engineering, Kyushu University, Hakozaki, Fukuoka 812, Japan

Kalman Filtering for Data Reduction in Inductively Coupled Plasma Atomic Emission Spectrometry 1441

The filter processes all kinds of background signals and solves the problem of spectral interference. Examples demonstrating the superiority of the filter over the standard three-point background correction procedures are given.

E. H. van Veen* and M.T.C. de Loos-Vollebregt, Laboratory of Analytical Chemistry, Delft University of Technology, de Vries van Heystplantsoen 2, 2628 RZ Delft, The Netherlands

Enhanced Selectivity for Spectrochemical Measurement by Mode Selection in Fully Resonant Nonlinear Mixing 1449

The feasibility of selective mode enhancement is demonstrated using multiresonant nonlinear mixing.

Roger J. Carlson and John C. Wright*, Department of Chemistry, University of Wisconsin—Madison, 1101 University Avenue, Madison, WI 53706

Probe-Mounted Fiber Optic Assembly for Laser Desorption/Ionization Fourier Transform Mass Spectrometry 1452

An interface for LDI/FT-MS based on a fiber optic assembly for transmitting high-power pulsed laser light is useful for general LDI applications and for studying the mechanisms by which such ions are trapped for detection.

Jeremiah D. Hogan, Steven C. Beu, and David A. Laude, Jr.*, Department of Chemistry, The University of Texas at Austin, Austin, TX 78712 and **Vahid Majidi,** Department of Chemistry, University of Kentucky, Lexington, KY 40506

Argon–Xenon Plasma for Alleviating Polyatomic Ion Interferences in Inductively Coupled Plasma Mass Spectrometry 1458

Introduction of Xe into the central channel of the ICP attenuates N_2^+, ClO^+, ArN^+, ArO^+, and other polyatomic ions by 2–3 orders of magnitude. Ion signals can be measured for Si, K, V, Cr, and Fe with little or no background correction.

Fred G. Smith, Daniel R. Wiederin, and R. S. Houk*, Ames Laboratory, U.S. Department of Energy, Department of Chemistry, Iowa State University, Ames, IA 50011

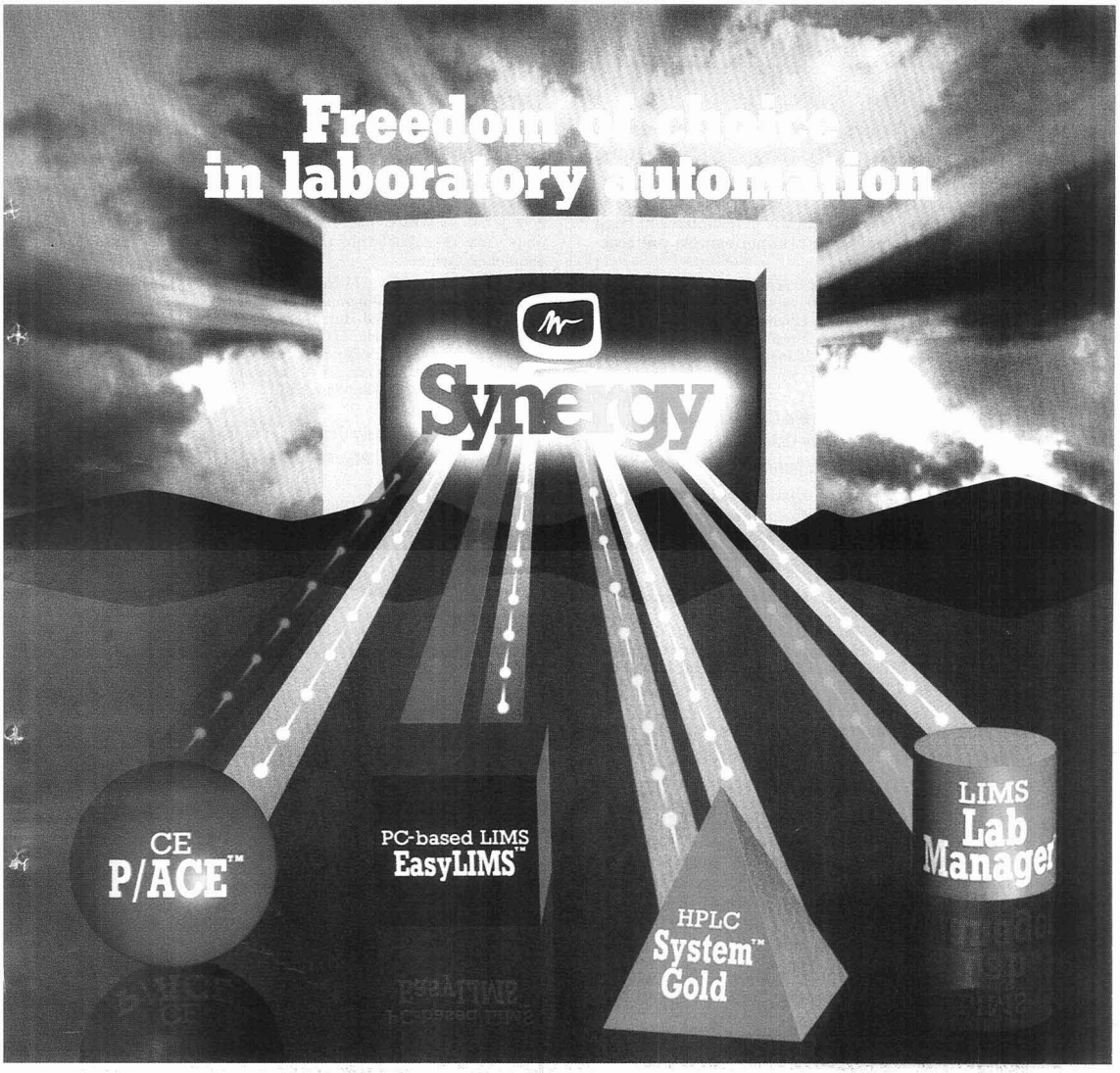

Your productive link to industry-standard computing in separation science

Finally, you're free to automate multiple laboratory operations your way using the most popular hardware and software available. Synergy is a coordinated plan that allows you to connect multiple existing LC's, GC's and other instrumentation to our versatile laboratory information management systems, PC-based EasyLIMS™ or VAX*-based Lab Manager™ LIMS. You can also connect System Gold™ HPLC with P/ACE™ Capillary Electrophoresis—a combination of two complementary techniques with single-point control for advanced LC/CE automation. The synergistic possibilities are endless and the choice is yours.

The results:

- Increased productivity through "paperless" operation of your lab, from sample receipt to sample reporting.
- Dramatic savings from greater sample throughput.
- Enhanced data integrity via automatic transfer of sample results from instruments to LIMS.
- Better GLP/GMP compliance from improved control over data, methods, and reports.
- Improved decision making capabilities with immediate access to sample information.

CIRCLE 14 ON READER SERVICE CARD

Synergy. The coordinated plan that gives you the freedom to use standard computing platforms to create powerful instrument networks. It's our commitment to be your productive link to industry-standard computing in separation science.

For the synergistic details, contact Beckman Instruments, Inc., 2500 Harbor Boulevard, PO Box 3100, Fullerton, CA 92634. (800) 742-2345.

BECKMAN

*VAX is a trademark of Digital Equipment Corporation.

Analysis of Neutral Oligosaccharides by Matrix-Assisted Laser Desorption/Ionization Mass Spectrometry 1463

Molecular weight determination of oligosaccharide compounds and mixtures is reported. Molecular structure is shown to have little influence on the determination. High sensitivity can be achieved with minor sample pretreatment.

Bernd Stahl and Martin Steup, Institut für Botanik, Universität Münster, Schlossgarten 3, D-4400 Münster, Federal Republic of Germany and **Michael Karas* and Franz Hillenkamp,** Institut für Medizinische Physik, Universität Münster, Robert-Koch-Strasse 31, D-4400 Münster, Federal Republic of Germany

Nanoscale Packed-Capillary Liquid Chromatography Coupled with Mass Spectrometry Using a Coaxial Continuous-Flow Fast Atom Bombardment Interface 1467

The nL/min flow rate characteristic of nanoscale (50 or 75 μm i.d.) packed-capillary LC columns facilitates the coupling of LC with MS using a coaxial continuous-flow FAB interface. High-resolution separations are obtained from peptide mixtures and tryptic peptide digests.

M. Arthur Moseley, Leesa J. Deterding, and Kenneth B. Tomer*, Laboratory of Molecular Biophysics, National Institute of Environmental Health Sciences, P.O. Box 12233, Research Triangle Park, NC 27709 and **James W. Jorgenson*,** Department of Chemistry, University of North Carolina, C.B. 3290, Chapel Hill, NC 27514

Tandem Mass Spectrometry of Peptides Using Hybrid and Four-Sector Instruments: A Comparative Study 1473

More structurally informative data at lower limits of analysis are obtained for heavier analytes (M_r > 1000) using high-energy collisionally activated dissociation on the four-sector instrument versus low-energy collisions on the hybrid mass spectrometer. Careful optimization of conditions on the hybrid instrument allows analyses of larger peptides, but the sequence information is incomplete.

Mark F. Bean and Steven A. Carr*, SmithKline Beecham Pharmaceuticals, P.O. Box 1539, King of Prussia, PA 19406 and **Gareth C. Thorne, Marc H. Reilly, and Simon J. Gaskell*,** Center for Experimental Therapeutics, Baylor College of Medicine, Houston, TX 77030

Quaternized Nylon as a Support for Plasma Desorption Mass Spectrometry: Adsorption Mechanisms and Analytical Applications 1482

A cationic surface is prepared for PDMS studies. Adsorption mechanisms for ionic surfactants are discussed and applications for negative ion MS are presented. An affinity separation of ionic surfactants containing hydrophobic alkyl chains from hydrophilic nonionic surfactants in a detergent mixture is also demonstrated.

M. P. Lacey and Thomas Keough*, The Procter & Gamble Company, Miami Valley Laboratories, P.O. Box 398707, Cincinnati, OH 45239-8707

Electrospray Mass Spectrometry: Application of Ion Evaporation Theory to Amino Acids 1488

The difference in the protonated molecule intensities of amino acids obtained by electrospray can be explained by a scheme in which protonated molecules in the liquid phase are extracted into the gas phase after a charged droplet is formed.

Minoru Sakairi*, Central Research Laboratory, Hitachi Ltd., Kokubunji, Tokyo 185, Japan, **Alfred L. Yergey,** National Institute of Child Health and Human Development, National Institutes of Health, Bethesda, MD 20892, and **K. W. Michael Siu, J. C. Yvec Le Blanc, Roger Guevremont, and Shier S. Berman,** Division of Chemistry, National Research Council of Canada, Ottawa, Ontario, Canada K1A 0R9

Evaluation of Inductively Coupled Plasma Mass Spectrometry as an Elemental Detector for Supercritical Fluid Chromatography 1491

An SFC/ICPMS interface is described. Absolute detection limits are obtained for tetrabutyl (0.034 pg) and tetraphenyl (0.047 pg) Sn compounds. The instrument response is linear over 3 orders of magnitude and sample injection reproducibility is < 5% RSD.

Wei-Lung Shen, Nohora P. Vela, Brenda S. Sheppard, and Joseph A. Caruso*, Department of Chemistry, University of Cincinnati, Cincinnati, OH 45221-0172

Correspondence

Signal Enhancement of Elements Due to the Presence of Carbon-Containing Compounds in Inductively Coupled Plasma Mass Spectrometry 1497

Pierre Allain*, Laurent Jaunault, and Yves Mauras, Laboratoire de Pharmacologie, Centre Hospitalier Universitaire, 49033 Angers Cedex, France, **Jean-Michel Mermet,** Laboratoire des Sciences Analytiques, Bat. 308, Université Claude Bernard-Lyon I, 69622 Villeurbanne Cedex, France, and **Thierry Delaporte,** Delsi-Nermag, 98ter, Boulevard Heloise, 95100 Argenteuil, France

Technical Notes

On-Detector Injector for Flow Injection Amperometric Measurements. The Wall-Jet/Thin-Layer Cell 1499

Joseph Wang* and Liang Chen, Department of Chemistry, New Mexico State University, Las Cruces, NM 88003

Application of Scanning Electrochemical Microscopy to Generation/Collection Experiments with High Collection Efficiency 1501

Chongmok Lee, Juhyoun Kwak, and Fred C. Anson*, Arthur Amos Noyes Laboratories, Division of Chemistry and Chemical Engineering, California Institute of Technology, Pasadena, CA 91125

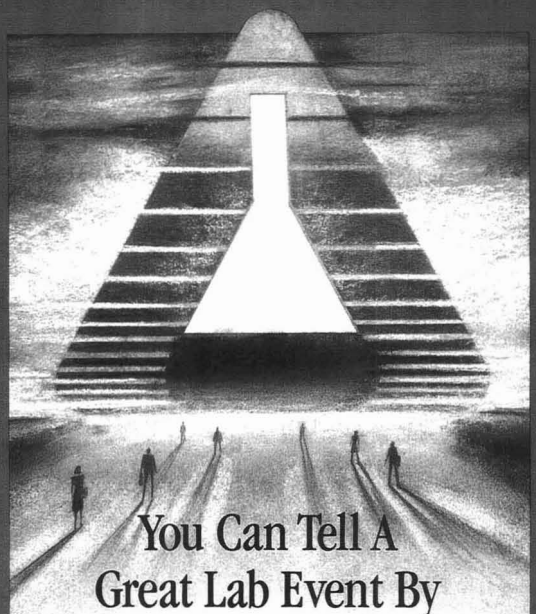

You Can Tell A Great Lab Event By The Companies It Keeps.

ALEX '91. The first lab event designed for all analytical lab professionals.

There's a new lab event on the horizon, and it's shaping up to be the best thing to happen to the industry in a long time. Already, most of the major players have signed on as exhibitors. And the rest will soon be on board.

The conference—25 sessions and four tracks—and the event floor—over one hundred exhibitors—are tied together to bring you new products, new technologies, new solutions, in a way you've never experienced before.

This dynamic new event is generating a rare kind of excitement...gathering incredible momentum. So if you have anything at all to do with a lab, you'll want to know more.

Call 617-449-8938. Or fax 617-449-2674. For exhibitor information only, call 617-449-6600, ext. 4023. Or fax 617-444-0165.

ALEX'91
Analytical Laboratory Equipment Exposition and Conference

©1991 The Interface Group • 300 First Avenue, Needham, MA 02194-2722 U.S.A.
4524FOG2

ALEX '91 • OCTOBER 29–31, 1991
SAN JOSE CONVENTION CENTER • SAN JOSE, CALIFORNIA U.S.A.

CIRCLE 1 ON READER SERVICE CARD

The American Chemical Society Presents
The Premier International Journal for Chemists, Chemical Engineers, and Materials Scientists and Technologists

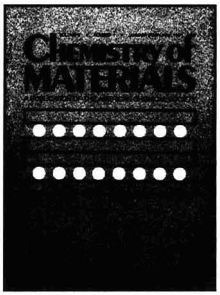

CHEMISTRY of MATERIALS

Editor: Leonard V. Interrante, Rensselaer Polytechnic Institute
Associate Editors: Dennis W. Hess, University of California, Berkeley; Gary E. Wnek, Rensselaer Polytechnic Institute

Indispensable, bimonthly coverage

What are the latest directions in materials chemistry? New materials? Preparation, characterization, and processing science and technology? In bimonthly issues, CHEMISTRY OF MATERIALS provides a valuable, *molecular-level perspective* at the interface of chemistry, chemical engineering, and materials science. Communications and short reviews round out its publication of *original* research.

CHEMISTRY OF MATERIALS examines, in depth:

- Synthesis and investigation of inorganic and organic solid state materials (coverage encompasses studies of molecular precursor routes to nonmolecular, inorganic solids);
- Investigation of polymeric solids and thin films, and their potential application as structural, optical, or electronic materials;
- Preparation and processing, particularly by chemical means, of electronic and optical materials and devices.

A forum for your findings

Guided by a prestigious, international panel of chemists, CHEMISTRY OF MATERIALS delivers a timely turnaround of manuscripts. Interested in submitting your work? Write: Dr. Leonard V. Interrante, Department of Chemistry, Rensselaer Polytechnic Institute, Troy, NY 12180-3590 U.S.A., (518) 276-2644.

Sign up today for peer-reviewed, primary research in materials chemistry

Call Toll Free (U.S. and Canada): 1-800-227-5558
In D.C. and Outside the U.S. and Canada: 202-872-4363
FAX: 202-872-4615
Telex: 440159 ACSPUI or 892582 ACSPUBS
Cable Address: JEICHEM

Or Write:
American Chemical Society
Marketing Communications Dept.
1155 16th Street, N.W.
Washington, D.C. 20036

This publication is available on microfilm, microfiche, and online through CJO on STN international. Member rates are for personal use only. Foreign payment must be made in U.S. currency by international money order, UNESCO coupons, or U.S. bank draft. Orders accepted through your subscription agency. For nonmember rates in Japan, contact Maruzen Co. Ltd. Please allow 45 days for delivery of first issue.

1991 Subscription Rates
Published Bimonthly

	ACS Members		Nonmembers
	One Year	Two Years	One Year
U.S.	$ 49	$ 88	$299
Canada & Mexico	$ 58	$106	$308
Europe*	$ 70	$130	$320
All Other Countries*	$ 72	$134	$322

*Air Service Included.

CHEMISTRY OF MATERIALS ADVISORY BOARD

Editorial Advisory Board

H.R. Allcock, *Penn. State U.*
S. Andersson, *U. Lund, Sweden*
N. Armstrong, *U. Ariz.*
G. Blasse, *U. Utrecht, The Netherlands*
J. Brinker, *Sandia Nat. Labs.*
P. Cassoux, *CNRS, Toulouse, France*
R.E. Cohen, *MIT*
J. Corbett, *Iowa State U.*
J. Crivello, *RPI*
L.R. Dalton, *USCLA*
F.J. Di Salvo, *Cornell U.*
B. Dunn, *UCLA*
A. Ellis, *U. Wisconsin*
R. Elsenbaumer, *Allied-Signal, Inc.*
G.C. Farrington, *U. Penn.*
J.E. Frommer, *IBM*
W. Gladfelter, *U. Minn.*
M. Gratzel, *Institut de Chimie Physique II, Switzerland*
M. Grunze, *U. Heidelberg, Germany*
A. Jacobson, *Exxon*
K. Jensen, *MIT*
E. Kay, *IBM*
K. Kitazawa, *U. Tokyo, Japan*
K. Klabunde, *Kansas State U.*
W. Klemperer, *U. Ill.*
R.S. Langer, *MIT*
L.D. Laude, *U. de l'Etat, Belgium*
J. Livage, *U. Paris VI, France*
T. Marks, *Northwestern U.*
R. Messmer, *GE CRD*
J. Miller, *du Pont*
J. Moore, *RPI*
D. Murphy, *Bell Labs.*
N. Ogata, *Sophia U., Japan*
G.A. Ozin, *U. Toronto, Canada*
T. Pinnavaia, *Mich. State U.*
K. Poeppelmeier, *Northwestern U.*
J. Rouxel, *Inst. des Materiaux, France*
L.D. Schmidt, *U. Minnesota*
L. Schneemeyer, *AT&T Bell Labs.*
D. Seyferth, *MIT*
A. Sleight, *Oregon State U.*
M. Steigerwald, *AT&T Bell Labs.*
G.D. Stucky, *UCSB*
S. Suib, *U. Conn.*
E. Thomas, *MIT*
J.M. Thomas, *Royal Inst. G.B., U.K.*
L. Thompson, *Bell Labs.*
B. Tofield, *Johnson Matthey, U.K.*
S. Veprek, *U. Munchen, W. Germany*
S. Viticoli, *CNR, Rome, Italy*
H.G. von Schnering, *Max-Planck Inst., Germany*
J.H. Weaver, *U. Minn.*
S. Whittingham, *SUNY, Binghamton*
J. Williams, *Argonne Nat. Lab.*
C.G. Willson, *IBM*
A. Wold, *Brown U.*
M. Wrighton, *MIT*
F. Wudl, *UCSB*
P. Zanella, *CNR, Padova, Italy*

Process for Groundwater Cleanup

An environmental process developed at Argonne National Laboratory can help clean up groundwater contaminated since the early days of the atomic era. Renato Chiarizia and E. P. Horwitz have designed a method using liquid membranes to remove uranium and other contaminants from groundwater. Working with K. M. Hodgson of Westinghouse Hanford Co., the scientists developed the liquid membrane process for treating contaminated groundwater at the U.S. Department of Energy site at Hanford, WA, where atomic materials were produced as part of the Manhattan Project during World War II.

The new process uses two liquid membranes working in tandem; one to remove the uranium from the water, and the second to remove the technetium, nitrates, and chromates. A supported liquid membrane is like a porous piece of plastic that is impregnated with an organic solution, says Chiarizia. The organic solution contains a "carrier" that forms a chemical bond with the contaminant, removing it from the groundwater. The carrier then takes the contaminant to a stripping solution where the contaminant is removed and isolated, then the carrier is liberated and returns to the groundwater to pick up more contaminants. The treatment leaves the groundwater clean and reduces the amount of contaminated liquid for disposal by more than 1,000-fold, Chiarizia explained.

The carrier for removing uranium, 2,4,4,-trimethylpentylphosphinic acid (Cyanex 272), reacts selectively with the uranium, leaving behind the calcium and magnesium that should remain in the groundwater. The water-soluble stripping agent is 1-hydroxyethane-1,1-diphosphonic acid (HEDPA). The carrier for removing nitrates, technetium, and chromium is a commercially available long-chain amine, Amberlite LA-2, and the stripping agent is sodium hydroxide.

The process is being considered for routine use at Hanford and will be available to other government sites.

Electron Microscope Reveals 3D Structure

Scientists at Lawrence Berkeley Laboratory (LBL) have obtained the first 3D image of an atomic structure using an electron microscope. Working with Ken Downing, an LBL biophysicist, were LBL physicist Michael O'Keefe, University of California at Berkeley earth scientist Rudy Wenk, and UC visiting materials scientist Hu Meisheng from Nanjing University in China.

The 3D imaging technique evolved because of the limitations of working with biological specimens. One problem with using an electron microscope to observe biological specimens is their sensitivity to radiation damage, allowing biologists to obtain resolutions of only 3–10Å. A result of this sensitivity, says Downing, is that "the resolution in the images isn't good enough to identify real atomic positions." For example, Downing and colleagues at the Medical Research Council in Cambridge, England, have recently determined the structure of a protein in three dimensions, but the resolution was not high enough to see its atomic structure. Because of these limitations, when biologists look at a specimen, they take experimental data from an electron microscope and build a density map—a map of the scattering power of the specimen—in three dimensions to determine the location of its amino acids. Then, they adjust their model—built from a combination of the density map and biochemical information about the amino acid sequence—until the fit with the experimental data is good.

Materials scientists take an opposite approach. They start by proposing a model from the atomic structure and calculate if the image in the microscope matches what the model predicts. They usually obtain only one view of a sample, and atoms may easily be obscured. Often, the images are taken in different focuses; one focus is chosen to match the simulated model without there being a way to check the correctness of the selected focus.

Wenk, who became interested in applying Downing's biological methods to determine the structure of minerals, suggested looking at staurolite, the structure of which was already known by X-ray crystallography. O'Keefe, who had written a computer program used at LBL, entered the information about the crystal sample and the microscope, and a simulated image was produced. In the case of staurolite, the model and the experimental results compared favorably. The computer simulation had predicted that a resolution of 1Å would be required to resolve the atoms in a 2D projection; however, using three dimensions, the atoms were resolved at an even lower resolution of 1.6Å and, in addition, the investigators were able to see the oxygen atoms. Downing says the technique could be applied to materials such as high-temperature superconductors; knowing the position of critical oxygen atoms could enable scientists to build better superconductors and ones that conduct at higher temperatures.

For Your Information

The Board of Trustees of the **Gordon Research Conferences** has approved a program to recognize the unique research contributions made by faculty members at predominantly undergraduate institutions. The **Teaching and Research Program** (TARP) is designed to encourage research-oriented undergraduate faculty to attend future Gordon Research Conferences. The trustees hope that participating faculty will use the information obtained from the conferences in the classroom and that the faculty members will participate regularly in the conferences. It is anticipated that TARP applicants will manage the costs associated with the conferences, although the trustees are prepared to offer modest financial assistance if necessary. For TARP applicant information, contact Richard W. Zuehlke, Assistant to the Director, Gordon Research Center, University of Rhode Island, Kingston, RI 02881-0801 (401-783-4011; fax 401-783-7644).

GET RICH QUICK.

The quick way to enrich trace components in an LC sample is to do it on-line with a Rheodyne column switching valve.

The valve, connected after the injector, lets you concentrate the sample in a pre-column, then elute it onto the analytical column by simply turning the valve handle. You eliminate the task of collecting a batch of enriched sample outside the chromatographic system.

The valve also lets you perform sample cleanup on-line by a similar procedure. You can remove interfering proteins, or polymers, or small molecules present in high concentrations.

Using column switching for enrichment and cleanup is usually faster than batch processing when making repeated analyses. This is especially true when switching is automated under the control of the chromatograph. Indeed, many chromatographs and autosamplers offer automated column switching as an option, using Rheodyne valves for the purpose.

For more information phone your Rheodyne dealer. Or contact Rheodyne, Inc., P.O. Box 996, Cotati, California 94931, U.S.A. Phone (707) 664-9050.

RHEODYNE

CIRCLE 122 ON READER SERVICE CARD

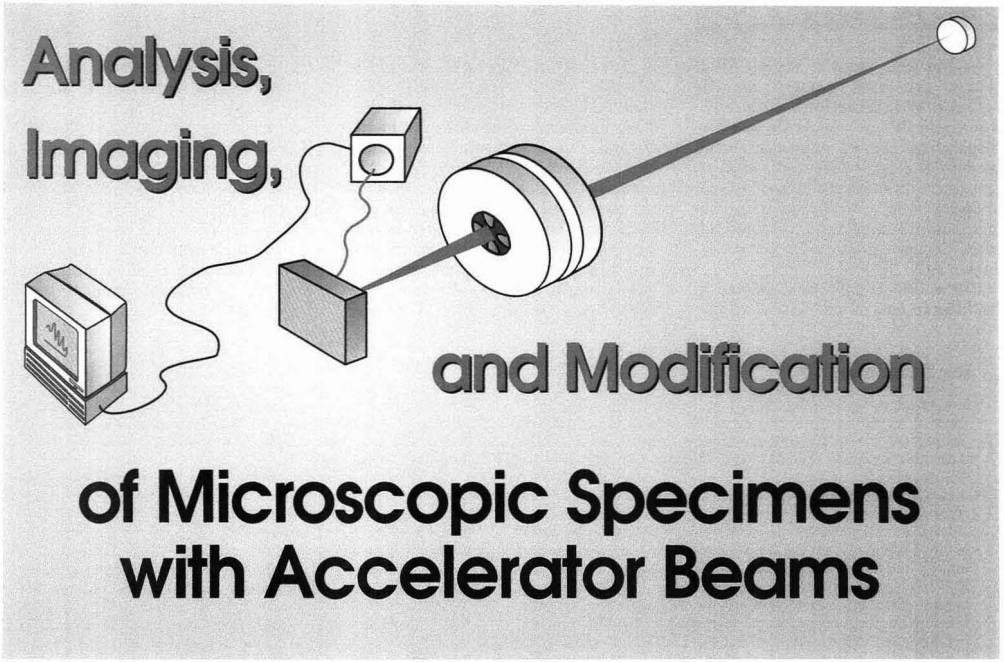

U.A.S. Tapper[1] and K. G. Malmqvist
Department of Nuclear Physics
Lund Institute of Technology
Sölvegatan 14
S-223 62 Lund
Sweden

Traditionally accelerators have been regarded as tools that enable physicists to investigate the inner structure of matter. Although large multinational facilities such as CERN in Switzerland are still used in this manner, many small accelerators are now being used to produce ion beams for other purposes.

Nuclear physicists use accelerators to generate ion species with well-defined energies to irradiate well-characterized targets. This process allows them to test theoretical models of physical concepts and has, over the years, resulted in extensive databases of reaction probabilities and detailed knowledge of many physical processes.

It is also possible to reverse the experimental strategy and characterize unknown materials using well-known, ion-induced atomic and nuclear reactions. If an ion beam from an accelerator is focused onto a sample surface, it can be combined with other instrumentation and used as a microanalytical tool: a nuclear microprobe (*1–3*). Ion beams from accelerators serve the same purpose as other probes in analytical chemistry, such as the electron beam used for X-ray or Auger electron spectroscopy.

Because it can nondestructively quantify trace elements in microscopic specimens, the nuclear microprobe has been used in various fields of science and technology (e.g., medicine, geology, materials science, and archaeology). Another essential capability of a scanning nuclear microprobe is high-resolution transmission microscopy of rather thick specimens.

INSTRUMENTATION

In this INSTRUMENTATION article we will review the properties of MeV ion beams, the types of information they can provide when they interact with samples, and the instrumentation associated with the nuclear microprobe. We will also demonstrate how the nuclear microprobe can characterize, image, and modify a variety of samples ranging from single cells to mineral grains.

MeV ion beams

Ions in the accelerator beam, which can range from protons to heavier ions, decrease their velocity when they interact with matter and produce useful signals for qualitative or quantitative analysis. They can produce visible light, characteristic X-rays, Auger and secondary electrons, photons or charged particles from nuclear reactions, and scattered ions. Any or all of these can be useful in characterizing a specimen. Indeed, the large number of signals containing information about elements, isotopes, and chemistry provide many analytical possibilities for a micrometer/submicrometer analytical probe.

Ions with energy of a few MeV penetrate a few tens of micrometers into solid material and provide a bulk analysis of the surface region by producing signals along its entire path. The analysis is thus surface oriented and differs from an established surface technique such as electron spectroscopy for chemical analysis (ESCA or XPS), which uses an X-ray source for photoexcitation and provides information from only the outermost atomic layers.

[1]Present address: National Accelerator Centre, Cape Town, South Africa.

0003-2700/91/0363-715A/$02.50/0
© 1991 American Chemical Society

As the ions enter a sample their velocity decreases rapidly, primarily because of interactions with electrons, and this process leads to a corresponding energy deposition with increased temperature and radiation damage to the sample. These special properties of ion beam analysis methods are important to remember when designing an analytical procedure.

The wealth of radiation emitted in the interactions of ions with a sample is illustrated in Figure 1. Most of the reaction products carry information about the composition of the sample. Two important techniques are particle-induced X-ray emission (PIXE) and Rutherford backscattering spectroscopy (RBS), both of which provide the elemental content of the sample. PIXE has the highest analytical sensitivity of the ion beam techniques, whereas RBS can be used to measure the elemental distribution with depth—a capability that is important in materials science. PIXE characterizes the elemental content in the sample by detecting X-rays in an energy-dispersive Si(Li) detector. The spectrum obtained consists of the characteristic X-ray peaks superimposed on a continuous background originating from several competing X-ray-producing processes in the sample. A detailed description of various accelerator-based ion beam analysis techniques appears in the box below.

Ion beam analysis

Ion beam analysis (IBA) refers to several analytical techniques, including particle-induced X-ray emission (PIXE), Rutherford backscattering spectroscopy (RBS), elastic recoil detection analysis (ERDA), and nuclear reaction analysis (NRA) (*4, 5*).

A common property of these analytical techniques is that after the incident MeV ion beam enters the target, most of the individual particles penetrate the specimen and roughly retain their incident directions. Gradually the particles lose energy and stop at a characteristic depth for the specific particle in a specific matrix. Part of the energy transferred to the target as the impinging ions decelerate causes various reactions that produce radiation (see Figure 1). The reaction products carry information about the atoms and nuclei in the matrix. By using proper detectors, researchers can acquire this information for element and/or isotope determination. The penetration ranges of the ions are normally a few micrometers to tens of micrometers, resulting in an effectively probed depth of sample that is fairly shallow.

Only a small proportion of the particles will come sufficiently close to the nucleus of a specimen atom to undergo large-angle Rutherford scattering or nuclear reaction and be lost from the beam. The loss of energy, which results from interaction with electrons, is usually described in terms of the stopping power (dE/dx) and may be quoted in terms of energy loss per unit thickness of material traversed. The values depend on the type of ion, its energy, and the matrix composition. The probability for a particular atomic or nuclear interaction is normally expressed as the cross section. Of the four analytical techniques discussed here, the largest cross sections are attained for PIXE, followed by those for RBS and ERDA. NRA normally has significantly smaller cross sections.

The nuclear microprobe can use all of these analytical techniques as well as those based on other signals shown in Figure 1. Because the ion beam may produce many types of radiation, the microprobe irradiation chamber is often equipped with detector systems for simultaneous analysis with several methods. The special characteristics of focused ion beams make special demands on the experimental arrangements because the ion beams carry low currents but high-current densities. In comparison with other microanalytical techniques, ion beam analysis methods are often complementary.

The use of ion beams sometimes makes it possible to determine sample properties not attainable with traditional analytical techniques. Because the information gained is restricted to elements and perhaps isotopes, and because the method cannot provide chemical information, it is somewhat limited. However, the possibility of determining elements with high sensitivity directly in an untreated specimen and (in most situations) nondestructively is very useful. In addition, the IBA methods can be combined with other analytical techniques to provide, for example, high lateral and depth resolution.

Some materials may be sensitive to heat and to radiation-induced damage and hence be unstable under irradiation in vacuum. For several IBA methods it is possible to perform the analysis in air, thereby reducing the heating effects. This can also be done in a nuclear microprobe. In addition to the increased convective cooling, this kind of analysis allows a straightforward and simple analysis of the surface of large and bulky specimens.

PIXE. The principles and design of the nuclear microprobe have much in common with those of the electron microprobe. Just as the main analytical mode of the latter uses characteristic X-ray emission to identify and quantify elements, the nuclear microprobe can use PIXE to carry out elemental analyses. When the incident ions interact with the specimen atoms, electrons are ejected from inner shells. When these vacancies are filled by electrons from higher shells (L, M, etc.), the excess energy is released as an emitted photon (X-ray emission) or, for light elements, is used to eject an electron (Auger emission). For protons and heavier projectiles, the excitation process requires the projectile energy to be much greater than the binding energy to provide appreciable ionization. The cross section peaks when the velocity of the projectile matches that of the electron to be ejected. The X-rays produced are normally detected with an energy-dispersive detector that provides X-ray spectra with characteristic lines superimposed on a continuous background (see Figure 2).

The main limitation of the sensitivity of X-ray techniques is the amount of background underlying the characteristic X-ray lines. The dominant source of background for the electron probe is the bremsstrahlung radiation emitted by the projectiles as they undergo large-angle scattering from target electrons.

Because of the heavy mass of the ions, the background in PIXE at lower X-ray energies is attributed mainly to bremsstrahlung only from secondary electrons ejected by the incident ions. The background in PIXE spectra is 2–3 orders of magnitude lower than that for electrons, thus facilitating trace element analysis (0.1–10 μg/g) in small sample masses. PIXE allows routine analysis of an unknown sample with a precision and accuracy better than 95%.

RBS. Of the various ion beam analysis techniques, RBS is probably the most frequently used because its depth resolution capabilities closely match the specific requirements of solid-state research. Information about the elemental composition of specimens at depths of a few micrometers, which is useful in the electronics industry, can be obtained.

A common arrangement in RBS is for ions with energies of a few MeV to be fired at 90° into the specimen surface and for the energy of the particles scattered through an angle of almost 180° to be measured by a silicon surface barrier detector. The depth resolution is typically a few tens of nanometers, but even better resolution can be obtained by using the ion beam at a grazing incident angle instead of at 90°. In essence the scattering occurs between the nucleus of the incident ion and the nucleus of a particular target atom and is caused by the coulomb repulsion between the charges of the two nuclei involved. The collision in classical RBS is elastic; the projectile retains all of its initial energy except what is lost in making the target nucleus recoil. Not surprisingly,

The nuclear microprobe

The nuclear microprobe resembles the electron microprobe: Protons and electrons, respectively, are focused onto the sample surface and both instruments can be used for imaging and analyzing the sample. In this respect the nuclear microprobe could also have been denoted a proton microscope, but because of its analytical potential, it is normally referred to as a nuclear microprobe. For analytical purposes a lateral resolution of 0.5–1 μm can be obtained, whereas in the imaging mode a 50-nm resolution has been used.

Spectra from the analysis of a tissue sample using an electron and a nuclear microprobe are illustrated in Figure 2. In the low-energy region (0–6 keV) of the X-ray spectrum from the nuclear microprobe (Figure 2b), the background is attributable to secondary electron bremsstrahlung. The X-ray spectrum that results from the use of electron bombardment of the sample (Figure 2a) shows a major difference: the intense bremsstrahlung background extends to energies of ~20 keV. Detection limits for the electron microprobe are on the order of mg/g levels because of this background, which results from increased scattering of the low-mass electrons. The heavier particles used in PIXE are scattered much less, and the detection limits are lower.

Generally the detection limits of this lost energy is greatest when the projectile has a head-on collision with a slightly heavier target nucleus and has its path changed by 180°. The probability or cross section of such scattering through a given angle for this situation, in which the nuclear forces between the projectile and the target may be neglected, is well known.

The energy loss of the impinging ion is specific for each isotope in the specimen, and in an energy spectrum obtained in RBS analysis of a thin target there is a peak from each mass at the energy corresponding to scattering at the particular angle. The areas under the peaks are proportional to the relative concentrations.

In a thick sample the position and shape of the peaks give information on the depth distribution. By varying the velocity (energy) and mass of the projectiles, the analytical sensitivity, the depth resolution, and the spectroscopic separation of neighboring elements can be optimized for the particular analytical situation.

In a typical light matrix (low average atomic number) about 100 μg/g of a heavy element can be quantified. The determination of a light element in a heavy matrix is much less advantageous, and the related ERDA technique is recommended. In classical RBS analysis on fairly well-known samples, high analytical accuracy and precision (better than a few percent) can be obtained.

When RBS is carried out on a specimen with crystalline structure, the phenomenon of channeling must always be considered because it is a potential source of both useful information and errors. Channeling occurs when the crystal is oriented so that the beam enters it close to one of the principal crystallographic planes or axes. The crystal lattice along an ion path allows the ion to be guided along the "channel" between rows of atoms, suffering only gentle prompting from the atoms, so that it loses little energy along its path. The path oscillates from side to side of the channel, staying much too far from the nuclei to suffer RBS, and significantly reduces the stopping power of the material. The effect of axial channeling on the RBS spectrum from a crystal can give information such as interstitial atoms in the lattice and lattice mismatch.

ERDA. ERDA is related to RBS but was introduced more recently. It uses the same elastic scattering between projectile and target nucleus as RBS; however, in this case it is the energy of the recoiling target nucleus that is measured. The kinematics of elastic collisions allow the recoil to occur only in the forward hemisphere, and experience has shown that for useful measurements the projectile should have a higher mass than the target nucleus. Hence, ERDA complements RBS in measuring light elements in matrices of medium or high average atomic number.

If the collision occurs at a certain depth below the specimen surface, then the emitted energy is reduced. Energy is lost as the projectile travels a distance in the specimen before the collision and as the nucleus recoils afterwards. The effect is to give each type of recoiling ion a spectrum in which each energy corresponds to particles coming from a particular depth below the surface. Because of the kinematics in the collision, the particle detector used for the recoiling nucleus is mounted at a grazing angle relative to the incoming ion beam.

The quality of the information provided by ERDA depends crucially on the energy resolution that can be achieved. The depth resolution is 100 nm or more, which is not quite as high as for RBS. This results primarily from the use of a blocking foil that is required to stop the heavy primary ions from reaching the detector. The degraded energy resolution caused by energy straggling in this foil of the particles recoiling from the matrix limits the depth resolution.

A typical analytical situation in which ERDA is a suitable method is hydrogen profiling in materials. This technique has been used extensively in analysis of polymers.

NRA. The vast majority of the individual ions in an MeV ion beam interact with a specimen only by means of their electric charges. However, an interaction sometimes will occur between an incident ion and the nucleus of an atom in the specimen, causing the structure of the nucleus to be altered. It is the detection and identification of a product from such a nuclear reaction that forms the basis of NRA.

The cross section for the occurrence of a nuclear reaction depends in a complicated way on the incident energy and on the internal properties of the particles involved. However, classically, the coulomb barrier prevents a charged projectile from reacting with a specimen nucleus unless its energy is higher than the coulomb barrier. Even if quantum mechanical tunneling provides a small probability to penetrate the barrier, it is clear that when ions of modest energy are used nuclear reactions will take place only with the low-Z elements in the specimen.

This ability to pick out low-Z elements in high-Z matrices is a major feature of NRA. The main difficulty in performing worthwhile NRA with nuclear microprobes is to obtain sufficient signals, in spite of the relatively small cross sections and low beam intensities, to give a respectable level of sensitivity. This places a premium in NRA on detecting the comparatively weak signal as efficiently as possible, and thus detectors that can provide large solid angles are used. The most commonly used projectile for microbeam NRA is the deuteron, which gives useful (d,p) reactions with several very important light elements. Beams of protons, tritium nuclei, ^{3}He, and ^{4}He are also used.

Comparison with other microprobe techniques. Several microanalytical methods are being developed and are available in research facilities or as commercial instruments. Often combined with various techniques for imaging and manipulation, they include the following: laser microprobe, Auger microprobe, electron energy loss spectrometry (EELS), electron microprobe, synchrotron radiation microprobe, and secondary ion mass spectrometry (SIMS).

Some of these techniques, which are based on accelerators (SXRF) or use ions of low energy (SIMS), are not included in this article because we are limiting our presentation to MeV ions and ion accelerators. Other microprobe methods can yield information on valence electrons and hence give chemical information (Auger electron spectroscopy, EELS) and represent examples supporting our general statement that the various microanalytical methods often are genuinely complementary.

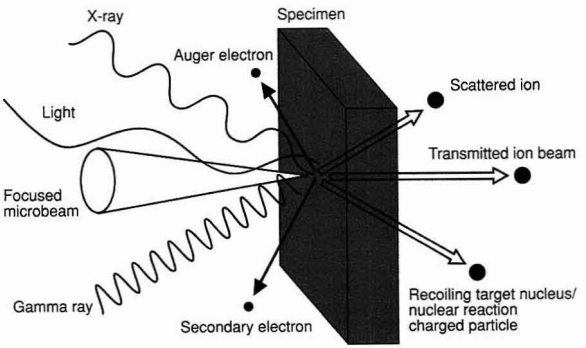

Figure 1. Schematic illustration of the induced radiation processes following the impact of a high-energy ion into solid material.

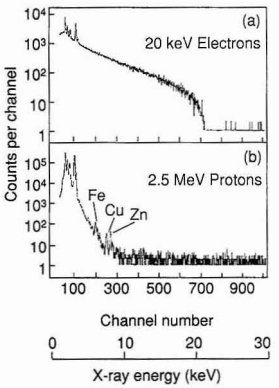

Figure 2. Comparison of X-ray spectra of (a) electron and (b) hydrogen ion (proton) induced X-ray emission from a tissue sample.

The intense background in the upper spectrum is attributable to bremsstrahlung originating from the electron beam. (Courtesy K. Themner, Lund Institute of Technology.)

the nuclear microprobe are 2–3 orders of magnitude better than those of the electron microprobe; thus, more complex instrumentation is used. In addition, PIXE analysis can be performed simultaneously with complementary techniques using the other signals (see Figure 1).

Instrumentation

The vital parts of a nuclear microprobe are an ion source to produce hydrogen ions, an accelerator to accelerate the ions, beam focusing and scanning equipment, a sample chamber, and a data collection system (Figure 3) (*6*). The ion source should give a high, bright emission of ions. The accelerator transfers an image of the illuminating source to the fine collimators in the nuclear microprobe beam line. To use a light optical analogy, the ion beam passing through these collimators forms an object for the microprobe lens system. When focused, the image will fall at the specimen surface. The demagnification factor is normally 10 to 30 ×. The specimen is mounted in a chamber on an *x-y-z*-translator, and the beam probe is scanned across the sample by magnetic or electrostatic fields. The entire beam line must be mounted on a rigid optical table to avoid beam degradation because of vibration.

Complete nuclear microprobe instruments are available for prices comparable to those of sophisticated electron microscopes.

The high spatial resolution obtained in electron microscopy has not been achieved in the nuclear microprobe for two reasons. The sources available for producing hydrogen ions do not give as bright an emission as do field emission electron sources, and the round lenses used in electron microscopy cannot be used because they lack sufficient strength to focus the heavier protons. Instead, quadrupole lenses with more complicated beam optics are required. Extensive work has been done to minimize aberrations in the focusing.

In addition to hydrogen ions and electrons, X-rays from an X-ray tube or a synchrotron radiation source can be used to produce characteristic X-rays in the target (i.e., X-ray fluorescence, XRF, and synchrotron radiation-induced X-ray emission, SRIXE). Microanalysis using the latter technique has been described previously by Jones and Gordon (*7*).

During scanning, large data flows are produced. Detectors in the sample chamber deliver pulses at count rates of kHz, and the pixels (*x*- and *y*-coordinates) corresponding to the event must be stored. This requires a powerful computer-based data acquisition system. Using four detectors with a 1-kHz count rate, we fill 1 Mbyte of memory every 40 s. Part of these data have to be treated online if the analyst is to follow the growth of the spectrum and the map.

This is important because large-area scanning requires hours of irradiation. Data are collected event by event and sorted into pixel spectra (e.g., 256 × 256 spectra). It should then be possible to illustrate any part of the spectrum by the corresponding map and to extract a spectrum from any part of the map.

Spectrum evaluation and calibration procedure

To calculate concentrations of the elements from the spectrum measured, an initial calibration of the experimental apparatus is needed. PIXE is an absolute method in that variables such as reaction probabilities and detection efficiency are known or can be measured accurately. Thus increased analytical precision and accuracy is obtained if the calibration constants are adjusted to fit a series of reference samples, but a relatively accurate analysis can also be obtained without standards.

Computer programs, using linear or nonlinear fitting procedures, determine the areas under the peaks. The corresponding mass of the elements can then be calculated from a calibration library. Normally the precision and accuracy in the mass determination is better than 90–95%. If the analysis is performed against standard samples, the accuracy is limited only by the counting statistics in the spectrum peaks.

Ions scattered from nuclei in the sample (i.e., primarily hydrogen, carbon, nitrogen, and oxygen in organic samples) are detected in an RBS analysis performed simultaneously with the PIXE analysis. From the intensity of the scattering events, the irradiated mass (ng–mg) can be determined. This mass can be used to calculate concentrations from the trace element masses (fg) obtained by PIXE and can be expressed as parts

per million (ppm = fg/ng).

If the determined concentration must be given on an absolute scale that does not rely on a comparison with similar reference samples, no elemental change in the sample volume probed during the proton bombardment is allowed. This is a critical point in the microprobe analysis.

A hydrogen ion with a typical ion energy of 2.5 MeV loses about 150 keV while traversing a 5-μm-thick tissue section. The energy from the beam current is focused in a 1-μm spot and corresponds to a power density of 15 kW/cm^2 assuming a beam current of 1 nA. Fortunately, in practice this is a misleading comparison; the observed sample deterioration is small and shows that the introduced heat is rapidly transferred away from the irradiated spot. In addition, by using a complementary method (e.g., RBS) that monitors the matrix elements during the irradiation, possible element losses can be detected and used for correction in the quantification procedure.

Recent studies have shown that element losses, approximately proportional to the radiation dose, occur during irradiation. The large radiation dose causes a major breakdown in chemical bonds in the probed material, which is probably one reason that element losses are observed. Part of the sample matrix, mainly hydrogen and oxygen, is lost. If one does not compensate for this loss, overestimates of the determined concentrations can be made. Minor increases in trace elements, interpreted as a small shrinkage of the tissue section, have also been found.

Focused beams

Ion beam methods are characterized by their capability to probe small sample masses. This is the basic reason for the use of focused beams; the high sensitivity of PIXE in small sample masses is used. For instance, a focused beam can probe sample masses of 1-μm-thick organic tissue sections at a lateral resolution of 1 μm, giving an analyzed mass of 1 pg (1 μm^3 with a density of 1 g/cm^3). In normal broad-beam PIXE analysis, detection limits down to 0.1 μg/g can be obtained in an organic specimen. However, when one works in the microprobe mode, the ion beam current is typically 100 times lower, corresponding to a factor of 10 worsening of the detection limits for a given analysis time. With detection limits of 1 μg/g, element masses down to 10^{-18} g (corresponding to some thousands of atoms) can be detected, although a few hours are required for analysis. RBS can also be performed with such small sample volumes, but not with the same relative detection limits.

By using a scanning ion beam, it is possible to reveal elemental distributions in small sample structures. The intensity of a spectrum peak then models the intensity displayed at a monitor, and thus the local concentrations can be illustrated. The maps obtained reveal local hot spots of certain elements. The analyst selects the area of interest and probes certain regions to quantify the trace element content. Hence online element maps are often used to guide the analyst. An element map taken during the scanning analysis of a section of brain tissue is shown in Figure 4.

During the development of the nuclear microprobe, workers realized that the orientation of the sample during the analysis was a major problem—sometimes overwhelmingly so. Hence a high-quality sample imaging system is important. Because ion beams normally produce fluorescent light when impinging on targets, the coarse orientation of the sample can be guided by a light microscope connected to the target chamber. Once the area of interest is localized, a scanning analysis can be started. As the structures of interest become smaller, microscopes can no longer assist the analyst because of magnification limitations. Consequently, the beam itself has to be used for imaging, as demonstrated in Figure 4. The resulting element maps of X-ray detector signals sometimes, but not always, give the necessary information.

Recent developments of a technique analogous to scanning transmission electron microscopy (STEM) have resulted in imaging techniques that can better guide the analyst to the target. Figure 5 shows a scanning transmission ion microscopy (STIM) image. High spatial resolution is obtained by stringent collimation of the beam from the ion source. This is possible because STIM measures the energy losses of ions traversing the samples, which means that every beam particle is detected and sorted according to energy. Thus < 1 femtoampere (i.e., 1000 ions/s) is a suitable ion current for STIM, whereas the detection of X-rays requires ion currents close to nanoamperes.

If the accelerator beam is even further collimated, single particles will hit the target and can be used to modify microscopic specimens. An example of an application of the nuclear microprobe in the single-particle mode will be discussed later.

An international mailing list of laboratories with nuclear microprobes can be obtained from the authors.

Microanalysis in air

Although normal nuclear microprobe analysis is performed with the sample mounted on an *x-y-z*-translator inside a vacuum chamber, it is possible to extract the ion beam into air. Thus sensitive specimens that cannot withstand analysis in a vacuum can be examined. This is a unique analytical feature of the nuclear microprobe.

By inserting a thin (10 μm) plastic foil over a small hole at the end of the vacuum tube, the focused ion beam

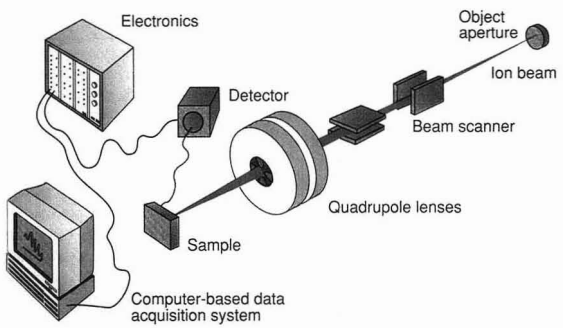

Figure 3. Schematic view of a nuclear microprobe setup.

The high-energy ion beam entering the instrument is produced by an accelerator. (Adapted with permission from Reference 6.)

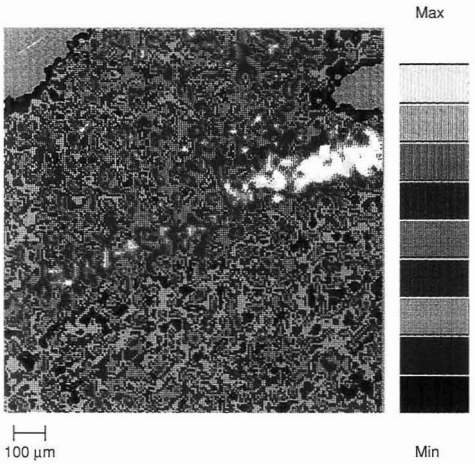

Figure 4. Element maps from a scan of a tissue section.

The scan is fine-tuned to maximize detail; colors indicate arbitrary linear units representing units of element concentration. (Courtesy Jan Pallon, Lund Institute of Technology.)

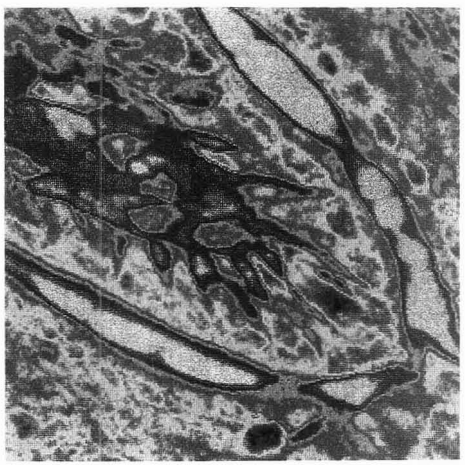

Figure 5. Scanning transmission ion microscopy (STIM) image from an unstained, freeze-dried cryosection of mouse ilium.

The data for the image were collected with a 100-nm beam probe. (Courtesy G. S. Bench, B. J. Kirby, and G.J.F. Legge, University of Melbourne, Australia.)

can traverse the foil without breaking it and strike a sample mounted in air, close to the exit window. Because of the scattering of the ions in the foil and in air, the lateral beam resolution will degrade. It is possible, however, to obtain an effective resolution of ~100 μm.

Scanning nuclear microprobe analysis of large samples (up to hundreds of millimeters) can thus be performed, for instance, mounted on a simple *x-y*-translator. The detection limits in air are slightly higher than those in vacuum, but this technique allows in situ trace element analysis in air with high lateral resolution. An important application is the analysis of sensitive or irreplaceable samples such as paintings and archaeological items.

Trace element determination in single cells

Many types of biomedical tissues have been analyzed with the nuclear microprobe. Trace element determination in biomedical samples is a suitable application of PIXE because high sensitivity is required. The organic part of the sample matrix does not contribute to the characteristic peaks because of the absorption of low-energy X-rays. The best detection limits are obtained in a region of the periodic table (Z = 15–40) where many of the essential elements in human metabolic processes are situated. Probing trace elements inside single cells opens up new possibilities in this field.

Calcium homeostasis disorder in rat brain tissue following ischemia and epileptic seizures has been investigated using the nuclear microprobe (*8*).

Detected (total) calcium concentrations were in the range of 1–50 μmol/g and would have been difficult to quantify using other microprobe techniques. By analyzing tissue sections from brain tissue dissected at intervals after an epileptic seizure, it was possible to observe a net calcium increase in brain regions known to be prone to these attacks. Calcium concentrations in a control region of the brain remained unchanged (Figure 6). The multielement capability of the analyzing method was useful; a simultaneous decrease in the potassium level was also observed.

Increased intracellular copper concentrations in human skin fibroblast cells have been studied in cultured cells from patients suffering from Menkes' disease (*9*), a disease linked with impaired copper metabolism. In comparison with cells taken from a control group, the former showed a sixfold increase in intracellular copper concentrations. Collecting and determining copper in such cells from the skin of a fetus with a high genetic risk could become a clinical application.

Elements known to be toxic to the human body (e.g., the heavy metals lead and mercury) can be determined with low detection limits (1–10 μg/g). In a recent study at our laboratory, it was possible to determine lead distributions in teeth from a monkey fetus after lead exposure. A lead profile along the teeth, with concentrations ranging from a few parts per million and upwards, could be determined. The uptake of lead has also been studied in rat cerebellum following lead nitrate injections. From the microprobe analysis an accumulation in the white matter was detected (*10*).

Another example of the determination of heavy metals in biological systems, shown in Figure 7, is the barium distribution in desmid, a unicellular alga. This genus is known to store $BaSO_4$ microcrystals in vacuoles. The element map shows how the $BaSO_4$ crystals are typically situated at the ends of the desmid. The barium uptake in a 24-h period could be followed by the analysis of the desmids that had grown in a $BaCl_2$ culture (*11*).

Because staining causes severe alterations in the concentrations of elements, a major problem in analyz-

ing biomedical samples is that stained tissue sections cannot be used. This problem has been attacked in several ways: by staining parallel sections, orientation by using nuclear microprobe imaging techniques, or pre-orientation in an electron microscope.

Many attempts have been made to analyze sections from postmortem tissue of Alzheimer patients. The disease is characterized by the occurrence of senile plaques (granulas) in the brain tissue. The plaque core has been reported as having high concentrations of inorganic compounds, especially aluminum. Pathologists, used to characterizing tissue from stained sections under a microscope, cannot definitely identify the status of the plaque and perhaps cannot even observe its presence in unstained sections. Because irradiated areas cannot be stained, it has been suggested that only a part of the (possible) plaque region should be analyzed, leaving the other part for staining and identification.

The electron microprobe community has developed a variety of sample preparation techniques for biomedical specimens. The general rule is that the smaller the structure to be analyzed, the more complicated and difficult the sample preparation.

These techniques have been transferred to the nuclear microprobe, but because PIXE analysis gives lower detection limits than does analysis with the electron microprobe, researchers have not investigated whether in vivo gradients of the trace elements remain unchanged during the sampling, sectioning, and drying of the specimen. This is most likely the case because it is possible to preserve intracellular gradients of very mobile elements such as electrolytes (e.g., calcium and potassium). Nevertheless, more work is required to verify that the preparation methods are adequate.

What is below the mineral surface?

Using the nuclear microprobe for characterizing geological material offers possibilities for localized and quantitative analysis of trace elements. Geological materials are normally complex, heterogeneous structures with mineral grains and inclusions. Chemical characterization of the various compartments has long been important for understanding the basic processes of formation as well as for investigating economical potential of deposits.

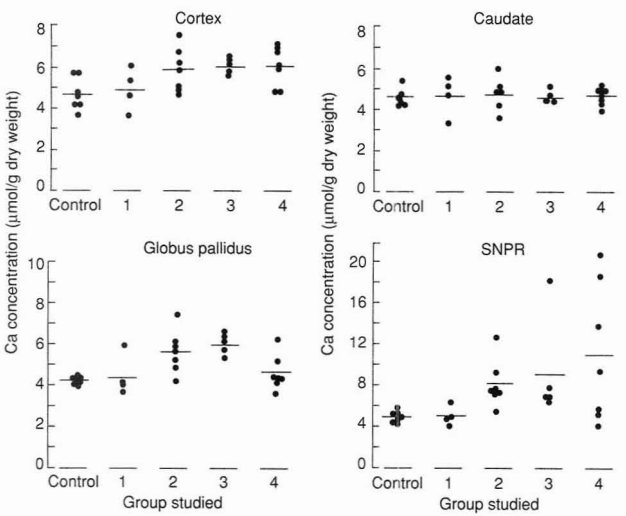

Figure 6. Measured calcium accumulation in four different regions in rat brains, following epileptic seizures.

Regions known to be prone to cell damage (cortex, globus pallidus, substantia nigra pars reticula, or SNPR) show increased calcium concentrations, whereas a control region (caudate) shows moderate or no calcium accumulation. (Adapted with permission from Reference 8.)

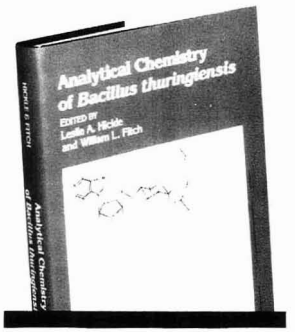

Analytical Chemistry of *Bacillus thuringiensis*

Sure to become the standard reference in the field, this unique text concentrates on describing and using analytical techniques for identifying and quantifying active inclusion proteins and β-exotoxins produced by *Bacillus thuringiensis* (Bt). No other volume brings together in one source all the major analytical techniques—including state-of-the-art immunoassays and chromatographic assays—that researchers in academia and industry have developed to accurately analyze Bt products.

This 13-chapter study covers methods such as reverse-phase HPLC, cyanogen bromide mapping, SDS-PAGE, and multiparameter light scattering. An especially interesting chapter details the expression of toxic proteins in transgenic plants.

Companies developing chemical instrumentation will find this book a rich source of information as will researchers in biological control and analytical and molecular biologists specializing in gene and protein analysis.

CONTENTS

An Overview • Quantification of Active Ingredient Percentage • Quantification of *Bacillus thuringiensis* δ-Endotoxin • Specificity of Insecticidal Crystal Proteins • In Vitro Analysis of δ-Endotoxin Action • Identification of Entomocidal Toxins • Characterization of Parasporal Crystal Toxins • An HPLC Assay for a δ-Endotoxin • Use of SDS—PAGE To Quantify δ-Endotoxins • Immunoassay of Insecticidal Proteins • δ-Endotoxin Production in Inclusion Bodies • Quantification of Insect Control Protein • HPLC Analysis of Two β-Exotoxins

Leslie A. Hickle, *Editor,* Mycogen Corporation
William L. Fitch, *Editor,* Sandoz Crop Protection Corporation

Developed from a symposium sponsored by the Division of Agrochemicals of the American Chemical Society

ACS Symposium Series No. 432
149 pages (1990) Clothbound
ISBN 0-8412-1815-3 LC 90-38800
$34.95

O • R • D • E • R F • R • O • M

American Chemical Society
Distribution Office, Dept. 79
1155 Sixteenth St., N.W.
Washington, DC 20036
or CALL TOLL FREE

800-227-5558
(in Washington, D.C. 872-4363) and use your credit card!

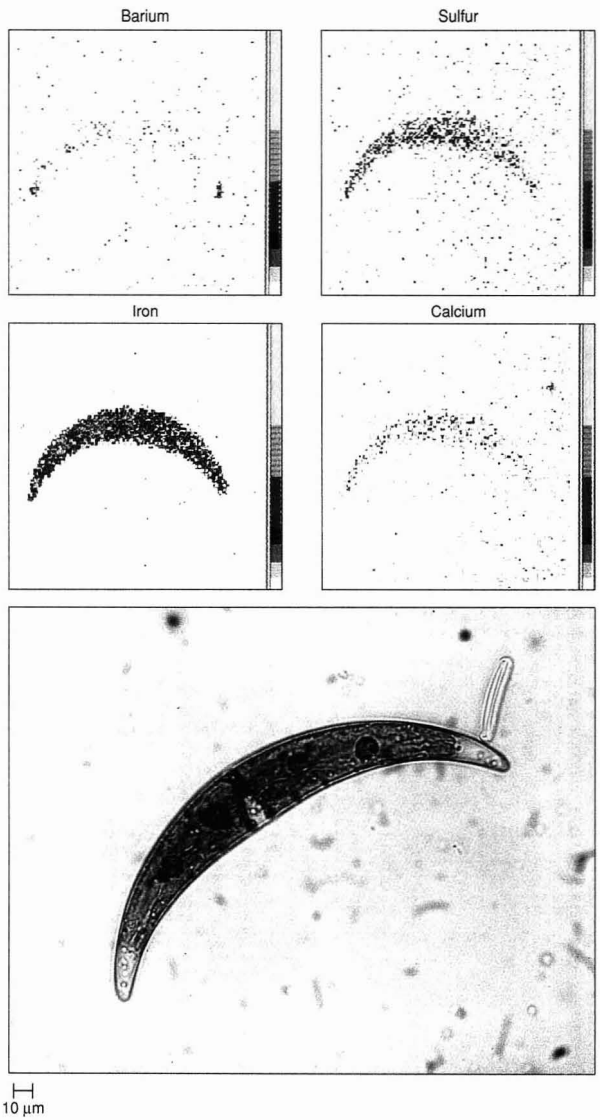

Figure 7. Element distributions in a desmid, a unicellular alga.

This genus is known to store barium sulfate microcrystals, which can be seen at the ends of the desmid as hot spots on the barium map. Colors indicate linear units of element concentrations. (Adapted with permission from Reference 11.)

The standard analytical technique, the electron microprobe, has several limitations; thus, use of the nuclear microprobe in this field has rapidly increased. In many instances, there are significant advantages in using trace elements instead of major elements when constructing models of the genesis of a geological system. The increased use of secondary ion mass spectrometry (SIMS) also results from interest in analyzing trace elements. However, because normal SIMS analysis is of limited use for quantification, there has been a need for a complementary trace element method.

The most obvious sign of the trend for using the nuclear microprobe is the emergence of several facilities dedicated to this type of analysis. In Sydney, Australia, the CSIRO has set up an ion beam analysis laboratory, primarily to serve the mineral industry with analyses for applied geology. In this laboratory several tens of thousands of nuclear microprobe analyses have been performed over the past five years. At the ion beam laboratories in Guelph, Heidelberg, and Los Alamos, all work—including the characterization of extraterrestrial material—has been more or less dedicated to this field. Samples suitable for the nuclear microprobe are similar to the standard type prepared for electron microprobe analysis: ~30-μm-thick polished sections mounted on a backing. Because the nuclear microprobe penetrates deeper than the electron microprobe, the analytical properties are somewhat different. There is a risk of penetrating an underlying region of completely different composition and hence the results of the analysis of such standard samples must be carefully evaluated.

However, this capability to see "below the surface" could also be used in investigating unopened liquid inclusions, which cannot be analyzed with the traditional electron microprobe technique. By using the depth resolution available with RBS analysis, information on the underlying structures can be obtained. Element maps showing images of a specimen "sliced" at various depths are elegant illustrations of what the simultaneous and complementary IBA techniques can achieve.

Several analytical techniques offer suitable methods for the destructive analysis of fluid inclusions. However, because of the uncertainties of using destructive methods, there is a demand for methods that allow analysis of unopened inclusions. The electron microprobe technique normally uses an effective analysis depth of a few micrometers in geological material. Hence, if the inclusions are deeper, electron microprobe analysis is not sufficient.

Two probes that would facilitate nondestructive element analysis in situ are the nuclear microprobe and the synchrotron radiation-based mi-

croprobe (SRIXE). The geometrical dimensions of inclusions are sometimes < 10 μm. Because the attainable lateral resolution of the SRIXE microprobe is fairly poor (>10 μm) and because it also probes the specimen much more deeply, the nuclear microprobe is preferred.

The MeV ions used in nuclear microprobes penetrate through tens of micrometers of material into a liquid inclusion. The X-rays or gamma rays produced when the inclusions are struck can be compared with those from a nearby pure matrix (Figure 8). Knowing the depth from the surface down to the inclusion that can be obtained by RBS analysis, one can correct for the deceleration of the ions and the attenuation of the X-rays.

Grain boundaries

The distribution of elements in mineral grains can be interpreted to facilitate the understanding and modeling of the formation and transformation of the mineral. In such studies, several advantages—especially in the theoretical calculations for various mineral phases—are derived from using trace elements instead of major elements. Garnet xenoliths represent a group of minerals in which the presence of elements preferentially at grain boundaries instead of homogeneously distributed in the bulk could be interpreted as indicative of the liquid phase.

In a study at Oxford by Fraser et al. (*12*), researchers used the scanning nuclear microprobe to analyze different types of garnet iherzolite xenoliths and to determine, in particular, their strontium content. Two types of minerals were investigated; one withstood acid leaching and one did not. Nuclear microprobe analysis confirmed that acid-leachable strontium was concentrated at the grain boundaries, whereas the nonleachable fraction had a homogeneous distribution. In the same manner, it is possible to follow long-term processes of diffusion of elements into mineral phases.

Gold forgeries

Although the materials involved in archaeology and geology are often similar, a major concern in analyzing archaeological artifacts is the nondestructiveness of the analysis. Many objects can never be replaced, and it is therefore necessary to use an analytical method that avoids observable damage to the object. The nuclear microprobe in combination with

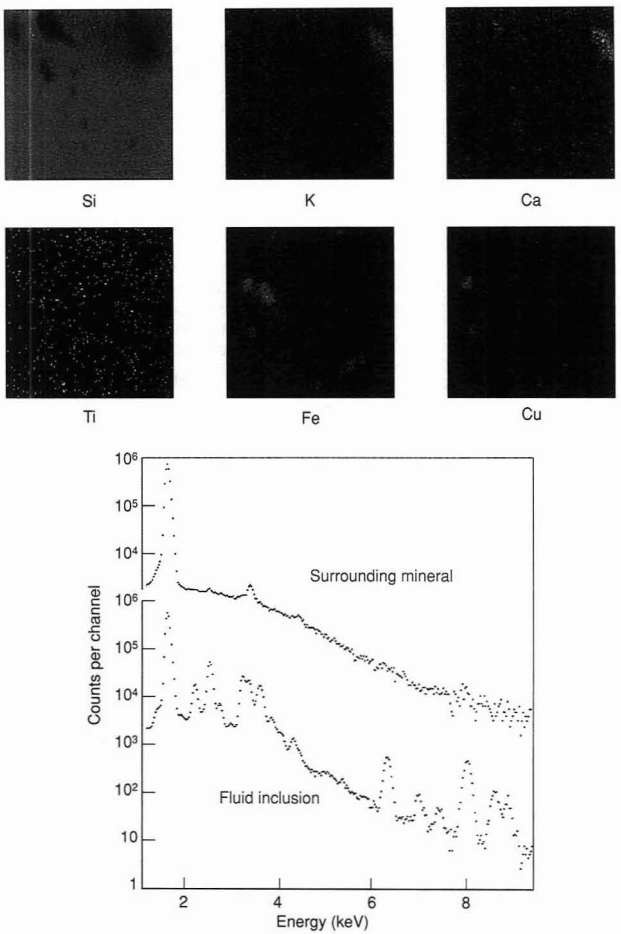

Figure 8. Identification of fluid inclusions situated underneath the surface of a polished mineral section.

The scan shows the site of the inclusion, and the interesting area can be analyzed by the nuclear microprobe. (Courtesy John Campbell, University of Guelph, Canada.)

PIXE fulfills this condition. Unlike XRF, PIXE can easily be used for microprobe analysis of sub-square millimeter regions and for element mapping of larger areas.

In archaeology, interest in and use of microanalysis have increased significantly over the past decade. In the Louvre museum in Paris, an ion beam analysis laboratory has recently been set up for applications in art science and archaeometry and a nuclear microprobe will be installed this year for further analytical capability. Such probes are already used in several other laboratories that specialize in archaeology.

Because nondestructiveness is more important here than in most other applications, there must often be a trade-off in beam size and intensity to avoid damaging an object. Larger probe sizes and lower intensities than in other fields of application are normally used. External beam microprobes are particularly useful in this field.

Metallic objects made of bronze and gold, for instance, are less sensitive than other materials to radiation

damage, whereas for non-noble metals the problems are the presence of patina or thick layers of corrosion. The shallow analytical depth of the nuclear microprobe requires the removal of any such layers to obtain representative results from the bulk material. This may be prohibitive in some cases, but the situation is even worse for most other analytical methods. Because very small areas are sufficient for analysis with the nuclear microprobe, often the damage will be deemed insignificant, even by a conscientious curator.

Several large-scale studies have been performed on copper-based alloys, mainly antique bronzes. In such studies, particular care has to be taken to avoid erroneous analytical data because of surface effects caused by corrosion. Results from the analysis of the patina and the core of an object may show large deviations. On the other hand, the nuclear microprobe makes it possible to characterize bronze objects nondestructively and in much greater detail than previously.

Because noble metals are unaffected by corrosion over long time spans, Demortier and co-workers (*13*) at Namur in Belgium used an external nuclear microprobe to perform systematic investigations of gold jewelry and determine the age and manufacturing processes. Since the nineteenth century, cadmium has been used as an additive to lower the melting point when soldering gold and has been regarded as the signature of a modern object. The Belgian group showed that low concentrations of cadmium could be found also in ancient gold objects. However, the correlation between copper and cadmium is reversed in newly manufactured material. By exploiting the multielemental character of the PIXE method, forgeries of "ancient" gold items can be revealed.

Hidden Greek letters

Paper and related materials are sensitive to radiation damage and to heating effects during the irradiation. However, by using the high lateral resolution of an external nuclear microprobe, it is possible to extract new information on material and printing or writing procedures, identifying faded letters and characterizing inks.

In our laboratory we have used a scanning nuclear microprobe combined with sophisticated multivariate statistical methods to identify faded letters in ancient Greek handwriting on papyrus (*14*). The irradiation was performed in an external microprobe, and the sheet of papyrus was mounted on an *x-y* scanning table.

By moving the specimen during the analysis, we produced two-dimensional element maps. We wanted to identify letters by detecting trace elements from the ink, but this simple approach did not yield good image contrast. After applying chemometric methods and compiling maps of several elements by multivariate statistical methods, we obtained much better contrast in the maps and we were able to identify the letters (see Figure 9).

Nonanalytical use of the nuclear microprobe: irradiation of single cells

Although the nuclear microprobe is used primarily for sample analysis, focused ion beams can be used for other applications. For example, it has been suggested that the nuclear microprobe, using a beam collimated

Tekmar

See us at the Enviracs Show in Washington D.C! Booth 715 & 717

The Tekmar 7000 Headspace Autosampler

- 50 sample capacity
- Interfaces with virtually all GC and GC/MS systems
- Temperature range up to 200°C...

and...

Available with the NEW Moisture Control Module!!

The Tekmar 2000 PLUS

Purge & Trap Dynamic Headspace Concentrator with the new Moisture Control Module™ (MCM™):

- Dramatically reduces the amount of water reaching the GC
- Greatly improves the resolution of early eluting compounds
- Factory installed or installed on an existing 2000

FREE CATALOG

Call Now!

(800) 543-4461

Outside the U.S. and Canada (513) 247-7000 • Telefax (513) 247-7050 • Telex 21-4221
P.O. Box 429576 Cincinnati, Ohio 45242-9576

CIRCLE 136 ON READER SERVICE CARD

Pesticide Processing

The **National Food Laboratory** (NFL) is prepared to assist Agricultural Chemical Company Study Directors with **Raw Agricultural Commodity Processing Studies** for registration or re-registration of Agricultural Chemicals with the U.S. Environmental Protection Agency:

- **Good Laboratory Practice (GLP)** Standards (40 CFR 160) followed
- Pilot **Simulation of Commercial Practices**
- Capabilities oriented toward **Fruit and Vegetable Processing**
- Accomplished **Specialty Projects:** Milk Processing, Coffee Extraction and Drying, etc.

Your questions are welcome. For further information, please call **Robert Marquardt** at (415) 828-1440.

THE NATIONAL FOOD LABORATORY

A Subsidiary of The National Food Processors Association
6363 Clark Ave, Dublin, CA 94568 • (415) 828-1440

CIRCLE 94 ON READER SERVICE CARD

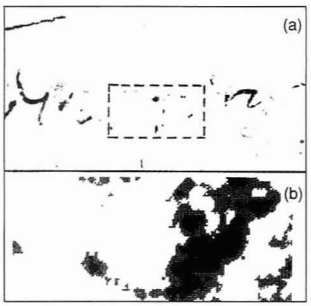

Figure 9. Scan of a Greek letter written on an ancient papyrus.

(a) A portion of the letter examined. (b) After applying chemometric methods to the collected data on element concentrations, researchers identified the faded letter upsilon (written as y). (Courtesy Göran Lövestam, CBNM, and Geel and Eryk Swietlicki, Lund Institute of Technology.)

to transmit only a single ion at a time, can be used to irradiate single cells in vivo (*15*).

A similar project was in fact the first suggested application of the nuclear microprobe. It should be possible to transfer a well-defined radiation dose to the cell in a manner more controlled than in earlier experiments and to monitor the reaction of the cell. To do this, the precision must be sufficient to hit certain compartments in the cell (e.g., the cell nucleus). In the experimental setup the ion beam is bent 90° into a vertical vacuum beam tube and extracted through a thin foil onto cultured cells in a petri dish.

Successful accomplishment of this experiment could lead to a major advance in understanding how the human body reacts to low radiation doses. Current knowledge of the human reaction to radiation is based on the reaction to doses that are orders of magnitude higher than those encountered in our environment and that are extrapolated to lower doses and dose rates.

Accelerators as instruments for the modification and characterization of new materials

The ion beams produced by small accelerators are used in research and industry for manipulating, transforming, and characterizing specific materials. Ion beams could be extremely powerful tools in materials science studies aimed at developing new semiconductor materials or at improving wear resistance in metal alloys in medical applications.

Consequently, accelerators are routine instruments in the research plants of large electronics industries, and special accelerators have been designed for metal hardening. By using nitrogen ions, it is possible to harden the surface of an alloy locally and thus improve its resistance to wear. This is mainly done with large currents and broad beams, but it can also be done with high-resolution microprobes.

The analytical methods most common in materials science are RBS, ERDA, and NRA, all of which allow the determination of depth profiles of elements or isotopes and may be used in a nuclear microprobe. A combination of these techniques has been used for characterizing high-temperature superconductor materials.

Because theoretical explanations of their behavior at low temperatures are uncertain, the special properties of ion beam methods have made important contributions. Similarly, IBA methods may be used for in-depth investigations of the design of new semiconductor structures. The high lateral resolution of the nuclear microprobe could be very useful when designing next-generation electronics circuits. We belong to a consortium working on the development of artificial nanometer structures, and we are aiming for a probe size below 100 nm to allow detailed characterization of the structures (e.g., quantum dots and wells).

Because they can also be used for manipulating and changing material properties, ion beams—mainly low-energy heavy ions—have been used for ion implantation. In the past decade high-energy beams have, for instance, also been used to passivate semiconductor structures at a certain depth. The high lateral resolution of the nuclear microprobe will probably attract a growing interest in this field.

A particularly exciting possibility is to use ions to produce "seed" tracks that function as paths for the etching of canals. This process is used when designing filters in mica. Single ions are used to produce well-defined traces that are subsequently etched. Filters are thus produced with well-defined pore sizes and resistance to heat. If the lateral resolution of the nuclear microprobe were further improved it would be possible to manipulate materials on the atomic scale. We believe that new applications, unforseen by us today, would then be possible.

References

(1) *Principles and Applications of High-Energy Ion Microbeams*; Watt, F.; Grime, G. W., Eds.; Adam Hilger: Bristol, U. K., 1987.
(2) *PIXE—A Novel Technique for Elemental Analysis*; Johansson, S.A.E.; Campbell, J. L., Eds.; Wiley: New York, 1988.
(3) *The Proton Microprobe: Applications in the Biomedical Field*; Vis, R. D., Ed.; CRC Press: Boca Raton, FL, 1985.
(4) Mayer, J. W.; Rimini, E. *Ion Beam Handbook for Materials Analysis*; Academic Press: New York, 1977.
(5) Bird, J. R.; Williams, J. S. *Ion Beams for Materials Analysis*; Academic Press: Sydney, Australia, 1989.
(6) Johansson, S.A.E. *La Recherche* **1990**, *21*, 722.
(7) Jones, K. W.; Gordon, B. M. *Anal. Chem.* **1989**, *61*, 341 A–358 A.
(8) Inamura, K.; Martins, M.; Themner, K.; Tapper, A.; Pallon, J.; Lövestam, G. Malmqvist, K.; Siesjö, B. *Brain Res.* **1990**, *514*, 49.
(9) Allan, G. L.; Camakaris, J.; Legge, G.J.F. *Nucl. Instrum. Methods* **1991**, *B54*, 175.
(10) Lindh, U.; Conradi, N. G.; Sourander, P. *Acta Neuropathol.* **1989**, *79*, 153.
(11) Brook, A. J.; Grime, G. W.; Watt, F. *Nucl. Instrum. Methods* **1988**, *B30*, 372.
(12) Fraser, D. G.; Watt, F.; Grime, G. W.; Takacs, J. *Nature* **1984**, *312*, 352.
(13) Demortier, G.; Decroupet, D.; Mathot, S. *Nucl. Instrum. Methods* **1991**, *B54*, 31.
(14) Lövestam, G.; Swietlicki, E. *Nucl. Instrum. Methods* **1990**, *B45*, 307.
(15) Braby, L. A.; Reece, W. D. *Radiat. Prot. Dosim.* **1990**, *31*, 311.

U.A.S. Tapper (left) received his M.Sc. degree in engineering physics (1985) and his Ph.D. in nuclear physics (1989) from Lund Institute of Technology, University of Lund, Sweden. He has been working as a research associate and as acting associate professor in the department of nuclear physics at the University of Lund. He recently became a researcher at the National Accelerator Centre, Cape Town, South Africa. His research involves development of the nuclear microprobe with emphasis on ion beam optics.

K. G. Malmqvist received his M.Sc. degree in engineering physics (1974) and his Ph.D. in nuclear physics (1981) from Lund Institute of Technology, University of Lund, Sweden. Since 1990 he has been head of the department of nuclear physics at the University of Lund. His research interests include the use of accelerator-based analytical methods (i.e., general ion beam analysis techniques and microanalytical methods). He has been a pioneer in the development of PIXE.

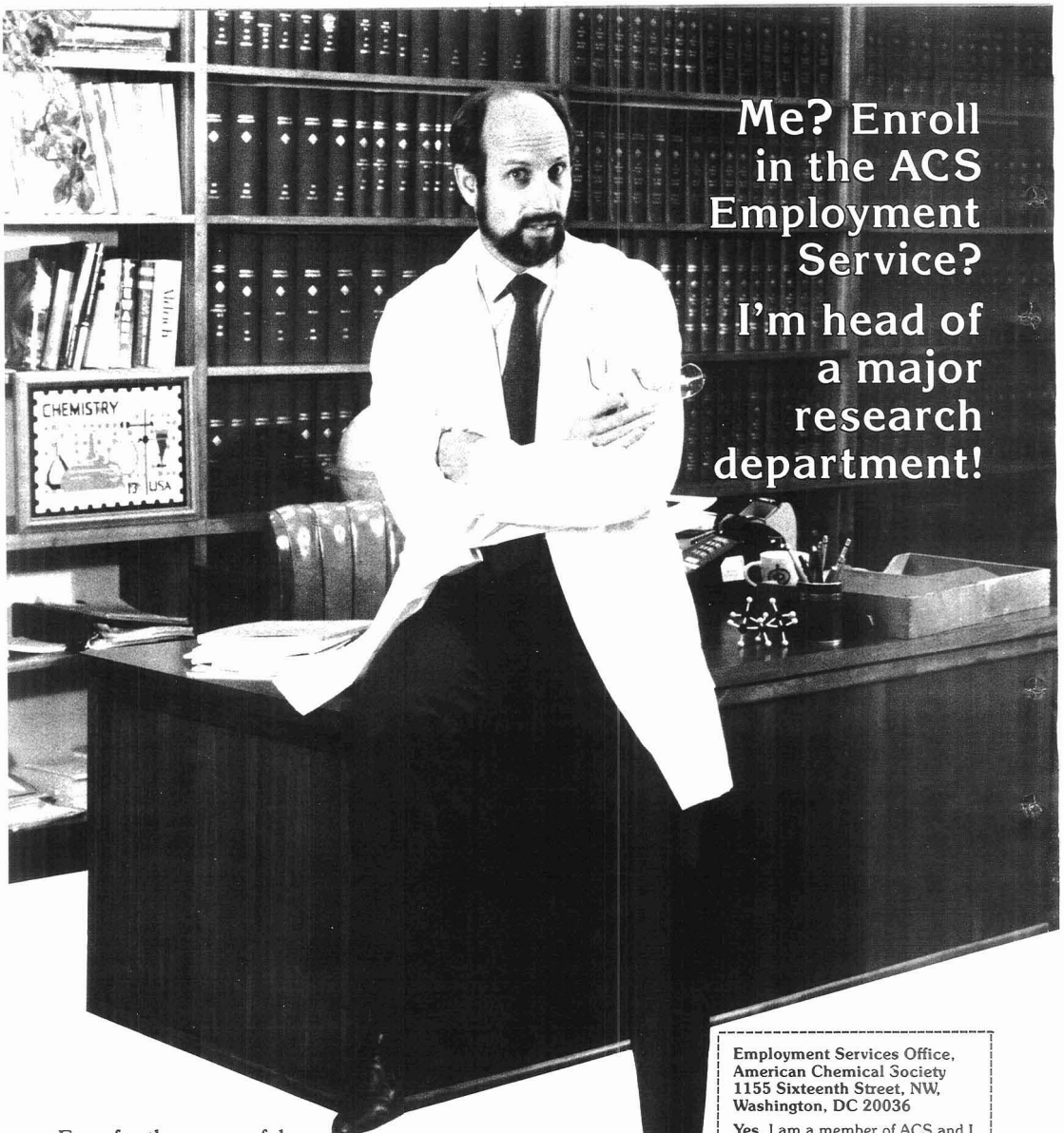

Me? Enroll in the ACS Employment Service? I'm head of a major research department!

Even for the successful chemist or scientist in an allied field, sometimes the best way to get ahead is to make a change.

The ACS Employment Service offers the opportunity to investigate the possibilities discreetly–and at very low cost.

Our Employment Service is free to all ACS members. If you request confidentiality from current employers or other designated organizations there is a nominal charge.

For more information write, use coupon, or CALL TOLL FREE 800-227-5558

Employment Services Office,
American Chemical Society
1155 Sixteenth Street, NW,
Washington, DC 20036

Yes. I am a member of ACS and I would like to learn how the ACS Employment Service can help me advance my career.

Name (please print) _____

Membership # _____

Address _____

_____

City _____

State _____ ZIP _____

1991 FACSS/Pacific Conference Joint Meeting

18th Annual FACSS Conference

30th Annual Pacific Conference

Anaheim, CA
October 6–11, 1991

A combined meeting of the Federation of Analytical Chemistry and Spectroscopy Societies (FACSS) and the Pacific Conference on Chemistry and Spectroscopy will be held Oct. 6–11 at the Disneyland Hotel in Anaheim, CA. FACSS is governed by a board composed of representatives of its member organizations, which include the Division of Analytical Chemistry of the American Chemical Society (ACS), the Association of Analytical Chemists (ANACHEM), the Society for Applied Spectroscopy (SAS), the Chromatography Forum of the Delaware Valley, the Coblentz Society, the Analysis Division of the Instrument Society of America, and the Royal Society of Chemistry (RSC). The Pacific Conference is a regional meeting of the ACS and the SAS. The 1991 conference will be the 27th western regional meeting of the ACS.

More than 1000 research papers and poster presentations in all areas of chemistry are scheduled. The meeting will have a strong analytical component and will feature papers in atomic spectroscopy, biotechnology and clinical chemistry, chemometrics, chromatography, electrochemistry, environmental analysis, IR spectroscopy, lasers, MS, NMR spectroscopy, process analysis, X-ray spectroscopy, and surface analysis. On Saturday, Oct. 5, the 1991 Pacific Conference Teachers' Program will be held. In addition to the technical program, the meeting will feature an instrument exhibit; employment bureau; short courses; workshops; and a series of special events, including a dinner on Wednesday, Oct. 9.

The program will be highlighted by the presentation of several awards. Ben Freiser of Purdue University will receive the ANACHEM award at a special symposium on Wednesday. The FACSS Student Award, the Tomas Hirschfeld Award, and the SAS awards will also be presented.

Also scheduled is a symposium to be held Tuesday morning, Oct. 8, honoring Arnold Beckman in recognition of the 50th anniversary of the Beckman DU spectrometer. The RSC will hold a special analytical division symposium on atomic spectroscopy on Tuesday afternoon. For the first time, the meeting will feature a special computer poster session to be held on Wednesday morning.

ACS is offering 10 short courses in conjunction with the meeting (see p. 730 A). Five SAS short courses—Applied Near-IR Spectroscopy, FT-IR Spectrometry, Plasma Spectrochemical Analysis, Modern Experimental Spectroscopy, and Applications of Industrial IR Spectroscopy—will also be offered. For information on these courses, contact Jo Ann Brown, SAS, P. O. Box 64008, Baltimore, MD 21264 (301-694-8122). Professional Analytical and Consulting Services is also offering short courses. For details, contact Barbara Sherman, PACS, 409 Meade Dr., Coraopolis, PA 15108 (412-457-6576 or 800-369-2587). Additional information and registration forms are available in the preliminary program.

Twelve FACSS-sponsored workshops are scheduled, including a complimentary workshop for undergraduate students entitled "Professional Chemists in Industry." Those interested in preregistering for the workshops should complete the registration form on p. 729 A. If you need additional information, contact Ron Williams, Dept. of Chemistry, Clemson University, Clemson, SC 29634 (803-656-5020).

The employment bureau will be

run by the ACS Oct. 7–9. For information and registration forms, contact John Michael Sophos (202-872-6209 or 800-227-5558, selection 4).

Hotel rooms are available at the Disneyland Hotel, and reservations can be made directly (714-956-6400 or fax 714-956-6582). To receive the special rate, please indicate that you are with the conference. Brea Travel (800-999-1445) is offering special discounts on United and Delta Airlines fares as well as special tour packages.

To preregister, complete the form on the facing page and return it by Sept. 16 to FACSS, P. O. Box 278, Manhattan, KS 66502-0003. For more information, call the FACSS national office (301-846-4797). The list of symposium titles follows; each symposium will comprise approximately eight talks.

Program

MONDAY MORNING

Challenges of Analytical Toxicology

Recent Advances in FT Raman Spectroscopy—I

SFC—I

Novel Methods for Characterization of Ceramics

Electrical Discharges: Characterization and Utilization

Advances in Plasma Spectrometry

Sample Preparation and Digestion

New Techniques in Spectroscopic Imaging

Process FIA—I

NMR Imaging

FTMS and Ion Trap MS—I

Environmental Analysis—I

RIMS—I

MONDAY AFTERNOON

FT-IR

Recent Advances in FT Raman Spectroscopy—II

SFC—II

Novel Methods for Characterization of Ceramics and Other Solids

Analytical Approaches to Ultratrace Analysis in Biological Matrices

Diagnostics and Modeling of Plasma Sources—I

Process FIA—II

ICP: Optical Spectroscopy

FTMS and Ion Trap MS—II

SOAP: Two Decades of Developments

RIMS—II

NMR Studies of Materials Chemistry and Processing

The Graphite Furnace: Fundamentals—I

Novel Approaches in Environmental Monitoring

SERS

TUESDAY MORNING

Symposium Honoring Arnold Beckman: 50th Anniversary of the Beckman DU Spectrometer

Biological Analysis and Bioanalytical Developments

Array Detectors in Molecular Spectroscopy—I

SFC

Novel Methods for Characterization of Electronic Materials

GC

Diagnostics and Modeling of Plasma Sources—II

The Graphite Furnace: Fundamentals—II

Optical Spectroscopy Using Diode Lasers—I

Environmental Analysis—II

NMR Techniques for Analyzing Solutions

Recent Developments in Bioinorganic Chemistry—I

FTMS and Ion Trap MS—III

ESR Techniques and NMR Spectroscopic Investigations

Automation and Process Control

Recent Developments in Main Group Chemistry

Flow-Injection Techniques in Atomic Spectroscopy

TUESDAY AFTERNOON

RSC Analytical Division Symposium: Atomic Spectroscopy

Biological Analysis: New Approaches

Array Detectors in Molecular Spectroscopy—II

Ion Mobility Spectrometry

Novel Methods for Characterization of Catalysts

Signal Processing

GC Detectors

Diagnostics and Modeling of Plasma Sources—III

Graphite Furnace Atomization

Optical Spectroscopy Using Diode Lasers—II

Environmental Analysis—III

Matrix-Assisted Laser Desorption MS

Recent Developments in Bioinorganic Chemistry—II

Recent Developments in Organometallic Chemistry

Poster Session

WEDNESDAY MORNING

ANACHEM Award Symposium: MS and Ion/Molecule Chemistry—I

Bioanalytical Chemistry

Optical Fibers and Other Spectroscopic Developments

Environmental Applications of Chromatography—I

Novel Methods for Characterization of Polymers

Detection Methods in LC

Microcolumn Methods in LC—I

Signal Processing in Spectroscopy—I

ICPMS: Instrumentation and Sample Introduction—I

Recent Developments in Synthetic Organic Chemistry—I

Current Trends in Bioorganic Chemistry—I

Trace Metal Preconcentration Techniques

Nonlinear Optical Studies of Solids and Surfaces

Chemometrics Advances and Applications

Electrochemical Detectors and Sensors

MS

Chemical Speciation

Forensic Chemistry: Applications

Computer Poster Session: Collection and Use of Fundamental Reference Data for Atomic Spectroscopy

WEDNESDAY AFTERNOON

ANACHEM Award Symposium: MS and Ion/Molecule Chemistry—II

Industrial and Pharmaceutical Analysis

Remote Sampling with Vibrational Spectroscopy

Environmental Applications of Chromatography—II

Special Topics in Materials and Surface Analysis

Spectroscopic Techniques in Process Analysis

Microcolumn Methods in LC—II

Signal Processing in Spectroscopy—II

ICPMS: Instrumentation and Sample Introduction—II

Recent Developments in Synthetic Organic Chemistry—II

Current Trends in Bioorganic Chemistry—II

Novel Plasma Devices for Atomic Spectroscopy

Supercomputers That Will Become PCs for Chemical Analysis

REGISTRATION FORM

Federation of Analytical Chemistry & Spectroscopy Societies
Pacific Conference

Last Name (Please print legibly) _____ First Name _____ Middle Initial _____

Affiliation _____

Address _____

City _____ State _____ Zip _____ Country _____ Phone Number _____

Registration Fees

- ☐ 1. Preregistration (Deadline 9/16/91) (check, MC, VISA only) $80
- ☐ 2. Registration at conference (cash, check, MC, VISA) .. $100
- ☐ 3. Single day registration..... $60 for _____ (day)
- ☐ 4. Student, full time $20
- ☐ 5. Workshops (see fees below)..... $___
- ☐ 6. Spouse..... *Complimentary* (Name_____)
- ☐ 7. FACSS Wed. Gala Event..... $45
- ☐ 8. Exhibits Only..... $10
- ☐ 9. Tours (see below)..... $_____

Memberships

- ☐ 1. ACS, Local Section Name _____
- ☐ 2. ACS, Anal. Div.
- ☐ 3. SAS
- ☐ 4. ANACHEM
- ☐ 5. ISA
- ☐ 6. DVCF
- ☐ 7. Coblentz
- ☐ 8. Royal Society of Chemistry

YOUR SCIENTIFIC SPECIALTIES (Enter Letter) ☐☐☐☐☐☐

- A. Spectroscopy-General
- B. Ultraviolet-Visible
- C. Infrared-Raman
- D. Mass Spectroscopy
- E. X-Ray
- F. Emission-AA
- G. Fluorescence
- H. Nuclear Chemistry
- I. Electron Optics
- J. NMR
- K. Solution Chemistry
- L. Electrochemical
- M. Chromatography-Thin Layer
- N. Chromatography-Gas
- O. Chromatography-Liquid
- P. Thermal Analysis
- Q. Computerization
- R. Process Control
- S. Gas Analysis
- T. Other _____

YOUR PRIMARY RESPONSIBILITY (Enter one number) ☐

1. Research
2. Processing/Quality Control
3. Administration
4. Teaching
5. Sales/Marketing
6. Purchasing
7. Service
8. Student
9. Other

Total $_____

- **Make checks payable to FACSS**
- ☐ VISA (13 or 16 numbers)
- ☐ Master Card (16 numbers)

Credit Card Number ☐☐☐☐☐☐☐☐☐☐☐☐☐☐☐☐

Signature _____ ☐☐ MO ☐☐ YR

Printed name as appears on card _____ ➥ expiration date required

FACSS/PACIFIC CONFERENCE WORKSHOPS

- ☐ A. **Sample Preparation** Monday, October 7, Half Day..... $75
- ☐ B. **Chemometrics** Monday, October 7, Full Day $90
- ☐ C. **Lasers in Analysis** Monday, October 7, Half Day..... $75
- ☐ D. **Professional Chemists in Industry** Tuesday, October 8, Full Day ..... Free
- ☐ E. **Near-IR** Tuesday, October 8, Half Day $75
- ☐ F. **Supercritical Fluid Chromatography** Tuesday, October 8, Half Day $75
- ☐ G. **Basic Statistics** Wednesday, October 9, Full Day $90
- ☐ H. **LC/Mass Spectrometry** Wednesday, October 9, Half Day.....$75
- ☐ I. **Optical Standardization** Wednesday, October 10, Half Day.....$75
- ☐ J. **Analytical GC** Thursday, October 10, Full Day.....$90
- ☐ K. **ICPMS** Thursday, October 10, Half Day $75
- ☐ L. **Robotics** Thursday, October 10, Half Day $75

Tours

- ☐ 1. McDonnell Douglas (Space Shuttle) $14
- ☐ 2. Beckman Facilities..... $14
- ☐ 3. Best of Hollywood and Beverly Hills.....$25
- ☐ 4. J. Paul Getty Museum.....$22
- ☐ 5. Orange County Beach Cities.....$26
- ☐ 6. Huntington Library and Gardens.....$40

Deadline for RECEIPT of Preregistration is September 16, 1991. Mail to:

FACSS • P.O. Box 278 • Manhattan, KS 66502–0003

Methods in Instrumentation in Electrochemistry

New Tools for High-Mass Analysis: Electrospray and Matrix-Assisted Laser Desorption—I

Poster Session

THURSDAY MORNING

Proper Sample Handling with Today's IR Instruments—I

Unconventional Vibrational Spectroscopy—I

CE—I

Laboratory Automation Techniques—I

XRF—I

Advances in Solids Elemental Analysis—I

Computer Simulation of Chemical Systems—I

Reactions at Surfaces—I

Laser Ablation ICPMS

Chemical Analysis of Single Cells

Near-IR Techniques in Process Analysis

Physical Electrochemistry

New Tools for High-Mass Analysis: Electrospray and Matrix-Assisted Laser Desorption—II

Laboratory and Modeling Studies of Aerosol Chemistry and Physics

THURSDAY AFTERNOON

Proper Sample Handling with Today's IR Instruments—II

Unconventional Vibrational Spectroscopy—II

CE—II

Laboratory Automation Techniques—II

XRF—II

Advances in Solids Elemental Analysis—II

Computer Simulation of Chemical Systems—II

Reactions at Surfaces—II

Application of ICPMS

Nanoscale Spectrochemistry

Process Control and Application of Near-IR in Quality Control

Spectroelectrochemistry

New Tools for High-Mass Analysis: Electrospray and Laser Desorption

Kinetics and Spectroscopy of Atmospheric Trace Species

Novel Chromatographic Techniques

Poster Session

FRIDAY MORNING

Novel Approaches in the IR and Near-IR Regions

Reversed-Phase HPLC and Ion Pair Chromatography

Laser-Based Spectroscopic Techniques

ICPMS and Glow Discharge MS

Electroanalytical: Biosensors and Modified Electrodes

Physical Chemistry

FT and Optical Spectroscopy

FT-IR Emission Spectroscopy: A New/Old Tool for Spectroscopists

ICP: Instrumentation and Sample Introduction

Molecular Spectroscopy of Thin Films

Environmental Analysis: The Atmosphere

ACS Courses

The following courses are offered in conjunction with the FACSS/Pacific Conference meeting to be held Oct. 6–11 in Anaheim, CA.

■ **Experimental Design for Productivity and Quality in R & D.** Oct. 10–12. Stanley Deming and Stephen Morgan

■ **Atomic Absorption, ICP, and ICPMS.** Oct. 11–12. Marvin Miller and Gordon Wallace

■ **Capillary GC.** Oct. 11–12. Stuart Cram and Milos Novotny

■ **Effective Management of Chemical Analysis Laboratories.** Oct. 11–12. John H. Taylor, Jr., and Mary Routson

■ **Environmental Analytical Chemistry: Air Toxics Monitoring.** Oct. 11–12. William Winberry, R. Rasmussen et al.

■ **Environmental Analytical Chemistry: Water and Waste.** Oct. 11–12. Marcus Cooke et al.

■ **Environmental Law and Regulations.** Oct. 11–12. J. Herbert O'Toole et al.

■ **Mass Spectrometry (GC/MS) in Environmental Analysis.** Oct. 11–12. Philip Epstein and Marcus Cooke

■ **Microwave Sample Preparation: Theory and Methods.** Oct. 11–12. H. M. Kingston and Lois Jassie

■ **Spectroscopic Characterization of Polymers.** Oct. 11–12. Jack Koenig and Bruce Chase

Conferences

■ **44th ACS Summer Symposium on Analytical Chemistry—Characterization of Polymers.** July 28–Aug. 1. Oxford, OH. *Contact: Gilbert E. Pacey, Dept. of Chemistry, Miami University, Oxford, OH 45056 (513-529-2875)*

■ **Meeting of the American Association for Clinical Chemistry.** July 28–Aug. 1. Washington, DC. *Contact: AACC, 2029 K St., N.W., Washington, DC 20006 (202-835-8744)*

■ **14th International EPR Symposium.** July 28–Aug. 1. Denver, CO. *Contact: Gareth Eaton, Dept. of Chemistry, University of Denver, Denver, CO 80208 (303-871-2980)*

■ **33rd Rocky Mountain Conference on Analytical Chemistry.** July 28–Aug. 2. Denver, CO. *Contact: Pat Sulik, Rocky Mountain Instrumental Laboratories, 456 S. Link Lane, Ft. Collins, CO 80524 (303-530-1169)*

■ **22nd Annual Meeting of the Fine Particle Society.** July 29–Aug. 2. San Jose, CA. *Contact: FPS, 505 S. Gary, Suite 47, Tulsa, OK 74104 (918-631-2575)*

■ **Symposium for Innovation in Measurement Science.** Aug. 4–9. Geneva, NY. *Contact: Instrument Society of America, 67 Alexander Dr., P.O. Box 12277, Research Triangle Park, NC 27709 (919-549-8411)*

■ **2nd International Congress on Amino Acids and Analogues.** Aug. 5–9. Vienna, Austria. *Contact: Gert Lubec, University of Vienna, Dept. of Pediatrics, Währinger Gürtel 18, A 1090 Vienna, Austria*

■ **Meeting of the Association of Official Analytical Chemists.** Aug. 12–15. Phoenix, AZ. *Contact: AOAC, 2200 Wilson Blvd., Suite 400, Arlington, VA 22201 (703-522-3032)*

■ **International Conference on Scanning Tunneling Microscopy.** Aug. 12–16. Interlaken, Switzerland. *Contact: C. Gerber, IBM Research Division, Zurich Research Laboratory, Säumwerstrasse 4, CH-8803, Rüschlikon, Switzerland*

■ **33rd Congress of the International Union of Pure and Applied Chemistry.** Aug. 17–22. Budapest, Hungary. *Contact: E. Pungor, Academy of Sciences, H-111 Budapest, Gellert ter 4, Hungary*

■ **Annual Meeting of the Society of Magnetic Resonance in Medicine.** Aug. 17–23. San Francisco, CA. *Contact: Society of Magnetic Resonance in Medicine, 1918 University Ave., Suite 3C, Berkeley, CA 94704*

■ **NATO ASI Conference on Theoretical Advancement in Chromatography and Related Separa-**

tion Techniques. Aug. 18–30. Ferrara, Italy. *Contact: Francesco Dondi, Dept. of Chemistry, University of Ferrara, via L. Borsari, 46, I-44100 Ferrara, Italy*

■ **Inter/Micro-91.** Aug. 19–22. Chicago, IL. *Contact: Nancy Daerr, McCrone Research Institute, 2820 S. Michigan Ave., Chicago, IL 60616 (312-842-7100)*

■ **5th International Conference on Flow Analysis.** Aug. 21–24. Kumamoto, Japan. *Contact: Nobuhiko Ishibashi, Dept. of Applied Analytical Chemistry, Faculty of Engineering, 36, Kyushu University, Hakozaki, Higashiku, Fukuoka 812, Japan*

■ **202nd Annual Meeting of the American Chemical Society.** Aug. 25–30. New York, NY. *Contact: Meetings Dept., ACS, 1155 16th St., N.W., Washington, DC 20036 (202-872-4396)*

■ **IUPAC International Congress on Analytical Sciences.** Aug. 25–31. Makuhari–Messe, Chiba, Japan. *Contact: Japan Society for Analytical Chemistry, 1-26-2, Nishigotanda, Shinagawa, Tokyo 141, Japan*

■ **12th International Mass Spectrometry Conference.** Aug. 26–30. Amsterdam, The Netherlands. *Contact: RAI Organisatie Bureau, Europaplein 12, NL-1078 GZ Amsterdam, The Netherlands*

■ **5th European Symposium on Thermal Analysis and Calorimetry.** Aug. 26–30. Nice, France. *Contact: J. Rouqierol, AFCAT, Thermodynamics and Microcalorimetry Center, 27 rue du 141 eme RIA, 13003 Marseille, France*

■ **4th European Conference on Spectroscopy of Biological Molecules.** Sept. 1–6. York, U.K. *Contact: R. E. Hester, Dept. of Chemistry, University of York, Heslington, York Y01 4DD, U.K.*

■ **8th International Conference on Fourier Transform Spectroscopy.** Sept. 1–6. Lübeck–Travemünde, Germany. *Contact: Gesellschaft Deutscher Chemiker, Abt. Tagungen, P.O. Box 90 04 40, D-6000 Frankfurt 90, Germany*

■ **9th International Bioanalytical Forum—Bioanalysis of Drugs.** Sept. 3–6. Guildford, U.K. *Contact: E. Reid, Guildford Academic Associates, 72 The Chase, Guildford GU2 5UL, U.K.*

■ **3rd Workshop on Chemistry and Fate of Modern Pesticides.** Sept. 4–6. Bilthoven, The Netherlands. *Contact: P. van Zoonen, RIVM, P.O. Box 1, 3720 BA, Bilthoven, The Netherlands*

■ **IMEKO XII—Measurement and Progress.** Sept. 5–10. Beijing, China. *Contact: Secretariat, Chinese Society for Measurement, P.O. Box 1413, Beijing 100013, China*

■ **9th European Congress of Clinical Chemistry.** Sept. 8–14. Cracow, Poland. *Contact: Dept. of Clinical Chemistry, University School of Medicine, ul Kopernika 15, 31-501 Cracow, Poland*

■ **Conference on Advances in Instrumentation and Techniques for Electron and Other Microscopies.** Sept. 10–13. Bristol, U.K. *Contact: Meetings Office, Institute of Physics, 47 Belgrave Square, London SW1X 8QX, U.K.*

■ **Conference on Electrochemical Analysis.** Sept. 11–14. Leipzig, Germany. *Contact: H. Emons, Dept. of Chemistry, Karl-Marx University, Talstrasse 35, Leipzig 7010, Germany*

■ **8th International Conference on Secondary Ion Mass Spectrometry.** Sept. 15–20. Amsterdam, The Netherlands. *Contact: K.T.F. Janssen, Philips Research Laboratories (WY-4), P.O. Box 80.000, NL-5600 JA Eindhoven, The Netherlands*

■ **International Conference on Activation Analysis Applications.** Sept. 16–20. Vienna, Austria. *Contact: Robert Jervis, Dept. of Chemical Engineering and Applied Chemistry, University of Toronto, Toronto, Ontario, Canada*

■ **4th Congress of the Société Française de Chimie.** Strasbourg, France. Sept. 17–20. *Contact: SFC, 250, rue Saint-Jacques, 75005 Paris, France (33 1 43 25 20 78)*

■ **18th International Aerosol Congress.** Sept. 17–20. Hamburg, Germany. *Contact: CPO Hanser Service, P.O. Box 1221, D-2000 Hamburg-Barsbüttel, Germany (49 40 670 60 51 or fax 49 40 670 32 83)*

■ **Conference on Sensors and Their Applications.** Sept. 22–25. Edinburgh, U.K. *Contact: Meetings Office, Institute of Physics, 47 Belgrave Square, London SW1X 8QX, U.K.*

■ **11th International Enzyme Engineering Conference.** Sept. 22–27. Keauhou-Kona, HI. *Contact: Engineering Foundation, 345 E. 47th St., New York, NY 10017 (212-705-7835)*

■ **Production and Purification of Monoclonals.** Sept. 23–25. New Orleans, LA. *Contact: Gail Scho, IBC USA Conferences, 8D Pleasant St., South Natick, MA 01760 (508-650-4700)*

■ **National Symposium on Planar Chromatography: Modern Thin-Layer Chromatography.** Sept. 23–25. Somerset, NJ. *Contact: Janet Cunningham, Barr Enterprises, P.O. Box 279, Walkersville, MD 21793 (301-898-3772)*

■ **2nd Pan American Chemical Congress.** Sept. 24–29. San Juan, Puerto Rico. *Contact: Puerto Rico Chemists Association, Box 11183, Caparra Heights, Puerto Rico 00922*

■ **Biotech USA '91.** Sept. 25–27. Philadelphia, PA. *Contact: Gina Amatruda, CMC, 200 Connecticut Ave., Norwalk, CT 06856-4990 (203-852-0500, ext. 266)*

■ **5th Symposium on Handling of Environmental and Biological Samples in Chromatography.** Sept. 26–27. Baden-Baden, Germany. *Contact: M. Frei-Häusler, Postfach 46, CH-4123 Allschwil 2, Switzerland*

■ **LabQuip World '91.** Oct. 1–3. Philadelphia, PA. *Contact: Expoconsul International, 3 Independence Way, Princeton, NJ 08540 (609-987-9400)*

■ **6th International Conference and Exposition of Sensors and Systems.** Oct. 1–3. Chicago, IL. *Contact: Expocon Management Associates, 7 Cambridge Dr., P.O. Box 1019, Trumbull, CT 06611 (203-374-1411)*

■ **32nd Conference on Analytical Chemistry in Energy Technology.** Oct. 1–3. Gatlinburg, TN. *Contact: W. R. Laing, Oak Ridge National Laboratory, P.O. Box 2008, MS 6127, Oak Ridge, TN 37831 (615-574-4852)*

■ **13th International Symposium on Polynuclear Aromatic Hydrocarbons.** Oct. 1–4. Bordeaux, France. *Contact: Ph. Garrigues, Laboratoire de Photophysique et Photochimie Moléculaire, Université de Bordeaux I, 351, cours de la Libération, F33405 Talence, Cedex, France (33 56 84 63 05)*

■ **4th Annual International Biotechnology Expo and Scientific Conference.** Oct. 6–8. San Francisco, CA. *Contact: Cartlidge & Associates, 3097 Moorpark Ave., Suite 202, San Jose, CA 95128 (408-554-6644)*

■ **International Ion Chromatography Symposium.** Oct. 6–9. Denver, CO. *Contact: Century International, P.O. Box 493, Medfield, MA 02052 (508-359-8777)*

■ **Fall Meeting of the Midwestern Association of Forensic Scientists.** Oct. 6–11. Kansas City, MO. *Contact: Bill Chapin, Johnson County Crime Laboratory, 6000 Lamar, Mission, KS 66202 (913-791-5623)*

■ **Joint Meeting of the Federation of Analytical Chemistry and Spectroscopy Societies (FACSS) and the Pacific Conference on Chemistry and Spectroscopy.** Oct. 6–11. Anaheim, CA. *Contact: FACSS, P.O. Box 278, Manhattan, KS 66502 (301-846-4797)*

■ **Contemporary Topics and the Practice of Chromatography.** Oct. 7–10. Atlanta, GA. *Contact: Bob Held, ASTM, 1916 Race St., Philadelphia, PA 19103 (215-676-5504)*

■ **37th Annual Conference on Bioassay, Analytical, and Environmental Radiochemistry.** Oct.

7–11. Ottawa, Ontario, Canada. *Contact: G. H. Kramer, BRMD, 775 Brookfield Rd., Ottawa, Ontario, Canada*

■ **International GPC Symposium.** Oct. 13–16. San Francisco, CA. *Contact: Carole Wade-Clark, Waters Chromatography Division of Millipore, 34 Maple St., Milford, MA 01757 (508-478-2000)*

■ **Annual Meeting of the American Association of Cereal Chemists.** Oct. 13–17. Seattle, WA. *Contact: AACC, 3340 Pilot Knob Rd., St. Paul, MN 55121 (612-454-7250)*

■ **Symposium on Advanced Control of Chemical Processes.** Oct. 14–16. Toulouse, France. *Contact: ADCHEM '91 Secretariat, LAAS du CNRS, 7, avenue du Colonel Roche, 31077 Toulouse Cedex, France*

■ **3rd International Symposium on ESR Dosimetry and Applications.** Oct. 14–18. Gaithersburg, MD. *Contact: Marc Desrosiers, C214 Radiation Physics Bldg., NIST, Gaithersburg, MD 20899 (301-975-5639)*

■ **2nd Annual Frederick Conference on Capillary Electrophoresis.** Oct. 15–16. Frederick, MD. *Contact: Margaret Fanning, NCI-FCRDC, P.O. Box B, Frederick, MD 21702 (301-846-1089)*

■ **International Congress on Filtration and Separation.** Oct. 15–17. Karlsruhe, Germany. *Contact: Pressaids Ltd., Bridge House, 181 Queen Victoria St., London EC4V 4DN, U.K.*

■ **Toxic Air Pollutants from Mobile Sources.** Oct. 16–18. Detroit, MI. *Contact: Lester Grant, MD 52, Environmental Criteria and Assessment Office, U.S. EPA, Research Triangle Park, NC 27711 (919-541-4173)*

■ **4th Beijing Conference and Exhibition on Instrumental Analysis.** Oct. 18–24. Beijing, China. *Contact: BCEIA, Room 5412, Building No. 4, Xi Yuan Hotel, 100046 Beijing, China*

■ **International Symposium on Laboratory Automation and Robotics.** Oct. 20–23. Boston, MA. *Contact: Christine O'Neil, Zymark Corp., Zymark Center, Hopkinton, MA 01748 (508-435-9500, ext. 2224)*

■ **11th International Symposium on HPLC of Proteins, Peptides, and Polynucleotides.** Oct. 20–23. Washington, DC. *Contact: Janet Cunningham, Barr Enterprises, P.O. Box 279, Walkersville, MD 21793 (301-898-3772)*

■ **7th Symposium on Separation Science and Technology for Energy Applications.** Oct. 20–24. Knoxville, TN. *Contact: J. S. Watson, Oak Ridge National Laboratory, P.O. Box 2008, Oak Ridge, TN 37831 (615-574-6795)*

■ **9th International Conference on Photopolymers.** Oct. 28–30. Ellenville, NY. *Contact: Prabodh Shah, SPE, Mid-Hudson Section, P.O. Box 546, Hopewell Junction, NY 12533*

■ **Annual Meeting of the Instrument Society of America.** Oct. 28–31. Anaheim, CA. *Contact: ISA, 67 Alexander Dr., P.O. Box 12277, Research Triangle Park, NC 27709 (919-549-8411)*

■ **Analytical Laboratory Equipment Exposition and Conference.** Oct. 29–31. San Jose, CA. *Contact: Interface Group, 300 First Ave., Needham, MA 02194 (617-449-6600)*

■ **4th International Conference on Polyimides.** Oct. 30–Nov. 1. Ellenville, NY. *Contact: Prabodh Shah, SPE, Mid-Hudson Section, P.O. Box 546, Hopewell Junction, NY 12533*

■ **Annual Meeting of the Optical Society of America.** Nov. 3–8. San Jose, CA. *Contact: Optical Society of America, 1816 Jefferson Pl., N.W., Washington, DC 20036 (202-223-8130)*

■ **Symposium on Electrochemical Impedance: Analysis and Interpretation.** Nov. 4–5. San Diego, CA. *Contact: John Scully, Sandia National Laboratories, Org. 1834, P.O. Box 5800, Albuquerque, NM 87185 (505-846-8251)*

■ **9th Annual Membrane Technology/Planning Conference.** Nov. 4–6. Newton, MA. *Contact: Business Communications Co., 25 Van Zant St., Norwalk, CT 06855 (203-853-0348)*

■ **Managing Hazardous Air Pollutants: State of the Art.** Nov. 4–6. Washington, DC. *Contact: Lori Adams, Electric Power Research Institute, P.O. Box 10412, Palo Alto, CA 94303-9743 (415-855-8763)*

■ **Tropospheric Ozone and the Environment.** Nov. 5–7. Atlanta, GA. *Contact: Ronald L. Berglund, Union Carbide Corp., 3200 Kanawha Turnpike, South Charleston, WV 25303 (304-747-4985)*

■ **19th Annual Water Quality Technology Conference.** Nov. 10–14. Orlando, FL. *Contact: American Water Works Association, 6666 West Quincy Ave., Denver, CO 80235 (303-794-7711)*

■ **Eastern Analytical Symposium.** Nov. 11–15. Somerset, NJ. *Contact: EAS, P.O. Box 633, Montchanin, DE 19710 (302-453-0785)*

■ **38th Annual Symposium of the American Vacuum Society.** Nov. 11–15. Seattle, WA. *Contact: Marion Churchill, AVS, 335 East 45th St., New York, NY 10017 (212-661-9404)*

■ **KEMIA '91—Finnish Chemical Congress.** Nov. 12–14. Helsinki, Finland. *Contact: Association of Finnish Chemical Societies, Programme Secretary, Eeva Kota-aho, Hietaniemenkatu 2, SF-00100, Helsinki, Finland (358 0 408 022 or fax 358 0 408 780)*

■ **Meeting of the American Association of Pharmaceutical Scientists.** Nov. 17–21. Washington, DC. *Contact: American Assn. of Pharmaceutical Scientists, 601 King St., Alexandria, VA 22314 (703-548-3000)*

■ **22nd International Association of Biological Standardization Congress and Exposition on Characterization and Standardization of Purified Biologicals.** Nov. 18–20. San Francisco, CA. *Contact: Crest International, 940 Emmett Ave., #14, Belmont, CA 94002 (415-595-2704 or fax 415-595-3379)*

■ **Advanced Technology for the Clinical Laboratory and Biotechnology (ATB '91).** Nov. 26–29. Milan, Italy. *Contact: ATB '91 Conference, Via Carlo Farini, 70, 20159 Milan, Italy (39 2 688 0232 3)*

■ **Electrochemical Techniques for Corrosion Measurement.** Dec. 2–4. New Orleans, LA. *Contact: Andy Palus, EG&G Princeton Applied Research, P.O. Box 2565, Princeton, NJ 08543 (609-530-1000)*

■ **Fall Meeting of the Materials Research Society.** Dec. 2–7. Boston, MA. *Contact: MRS, 9800 McKnight Rd., Pittsburgh, PA 15237 (412-367-3003)*

Short Courses and Workshops

■ **HPLC Beginners' Training Course.** Nov. 26–28. Prestbury, Cheshire, U.K. *Contact: N. Rathbone, HPLC Technology, Wellington House, Waterloo St. West, Macclesfield, Cheshire SK11 6PJ, U.K. (44-625-613848)*

For information on the following courses, contact Institute for Professional Education, 2300 Clarendon Blvd., Suite 403, Arlington, VA 22201 (703-527-8700)

■ **Design and Analysis of Experiments.** Aug. 7–9, Sept. 16–18, and Dec. 18–20, Washington, DC

■ **Linear and Nonlinear Regression with Applications.** Aug. 7–9, Oct. 7–9, and Dec. 18–20, Washington, DC

■ **Applied Neural Networks.** Aug. 14–16, Oct. 21–23, and Dec. 16–18, Washington, DC; Sept. 18–20, San Francisco, CA; Nov. 4–6, Chicago, IL

■ **Applied Multivariate Methods Using Popular Statistical Computing Packages.** Sept. 11–13 and Dec. 16–18, Washington, DC; Oct. 23–25, San Francisco, CA

■ **Analysis of Messy Data.** Sept. 16–20 and Dec. 16–20, Washington, DC; Oct. 28–Nov. 1, San Francisco, CA

■ **Applied Statistics.** Sept. 23–25, San Francisco, CA; Oct. 9–11 and Dec. 9–11, Washington, DC

For information on the following courses, contact AOAC, Suite 400, 2200 Wilson Blvd., Arlington, VA 22201 (703-522-3032)

■ **Improving Sampling for Analysis of Food, Drugs, and Agricultural Materials.** Aug. 10–11, Phoenix, AZ; Nov. 4–6, San Diego, CA; Dec. 3–4, Durham, NC

■ **Workshop on Immunoassay.** Aug. 10–11. Phoenix, AZ

■ **Statistics for Methodology Development.** Aug. 15–16, Phoenix, AZ; Nov. 6–8, San Diego, CA; Dec. 3–5, Durham, NC

■ **Quality Assurance for Analytical Labs.** Aug. 15–16, Phoenix, AZ; Nov. 4–5, San Diego, CA; Dec. 2–3, Durham, NC

■ **Laboratory Safety and Compliance.** Aug. 15–16, Phoenix, AZ; Nov. 7–8, San Diego, CA; Dec. 5–6, Durham, NC

For information on the following courses, contact Environmental and Occupational Health Sciences Institute, Centers for Education and Training, UMDNJ/DCHE, 45 Knightsbridge Rd., Brookwood II, Piscataway, NJ 08854 (908-463-5062)

■ **Sampling and Evaluating Airborne Asbestos Dust.** Aug. 12–15, Sept. 16–19, and Oct. 15–18, Piscataway, NJ; Dec. 10–13, Northport, Long Island, NY

■ **Polarized Light Microscopy for Asbestos Identification.** Nov. 18–22, Northport, Long Island, NY

■ **Advanced Asbestos Analysis by Polarized Light Microscopy.** Nov. 25–27, Northport, Long Island, NY

For information on the following courses to be held in Baton Rouge, LA, contact Joyce Ryan, Chroma-Skills, Inc., P.O. Box 98017, #4C, Baton Rouge, LA 70898 (504-766-2634)

■ **Principles of GC.** Sept. 23–25

■ **Operator Troubleshooting.** Sept. 26–27

■ **Capillary GC.** Sept. 30–Oct. 2

■ **Troubleshooting the Capillary System.** Oct. 3–4

Call for Papers

■ **Advanced Technology for the Clinical Laboratory and Biotechnology (ATB '91).** Milan, Italy. Nov. 26–29. Posters are solicited on the following: new analytical concepts and systems, application of advanced analytical approaches to clinical diagnostics, evaluation of new products for the clinical lab, single-cell analysis and cell markers, basic biochemistry, and molecular biology. Abstracts devoted solely to clinical or physiopathological aspects will not be accepted. Request forms from ATB '91, Via C. Farini, 70, 20159 Milan, Italy (39 2 688 0232 3). The deadline for receipt of abstracts is Sept. 15.

■ **Electrochemical Techniques for Corrosion Measurement.** New Orleans, LA. Dec. 2–4. The symposium will cover basic theory, data interpretation, techniques, and field and on-line corrosion measurement. Prospective authors should submit 200-word abstracts no later than Sept. 13 to Andy Palus, EG&G Princeton Applied Research, P.O. Box 2565, Princeton, NJ 08543 (609-530-1000).

Fast, Accurate Refractive Index, and % Solids

Reichert-Jung Auto Abbe and Mark II Refractometers from Leica measure refractive index, % solids and % solids/temperature compensated in any transparent or translucent liquid. Both models feature automatic temperature compensation which eliminates the need for time-consuming manual correction.

High quality optics insure precise, accurate measurements. The Auto Abbe and Mark II require little or no maintenance and are UL and CSA listed.

Auto Abbe Refractometer

The Auto Abbe Refractometer measures automatically at the push of a button. Since results are displayed digitally, potential inaccuracy from hard-to-read shadow lines or ruled scales is eliminated.

Mark II Abbe Refractometer

Designed for durability and reliability in challenging environments, the Mark II Abbe is easy-to-use. Its clear digital display reduces reporting errors and its internal illumination system eliminates the need for external illuminators.

Whatever the application, Leica offers refractometers for fast, accurate results. For more information, write Leica Inc., P.O. Box 123, Buffalo, NY 14240 or call 800-752-5207, ext. 24, 716-891-3000 outside the U.S., or fax 716-891-3080 today.

Leica offers a full line of optical products for industry, the life sciences and education including microscopes and optically-based laboratory instrumentation. Leica brings together Cambridge Instruments, Reichert-Jung and Wild Leitz, renowned names in optical instrumentation.

Leica

CIRCLE 80 ON READER SERVICE CARD

BOOKS

Sensors, MS, Proteins, Forensics, and QA/QC

Sensors in Bioprocess Control. John V. Twork and Alexander M. Yacynych, Eds. 326 pp. Marcel Dekker, 270 Madison Ave., New York, NY 10016. 1990. $115

Reviewed by K. S. Fletcher, Corporate Research, The Foxboro Company, 600 North Bedford St., East Bridgewater, MA 02333

The explosion of research in sensor technology is clearly matched by that in biotechnology and bioprocessing. This book attempts to bring these technologies together and provide a framework to improve bioprocess control through the use of a large and increasing portfolio of new analytical techniques. This multiauthored, 330-page, 12-chapter book is a generally useful overview of this subject, but it is also an uneven collection of reviews; some are strong on teaching, some emphasize new research, and some emphasize commercial equipment. Some redundancy also occurs; for example, nearly every chapter describes the importance of sample handling, even though one chapter is devoted exclusively to this important topic.

The chapters on fiber-optic sensors, thermistor probes, and electrochemical biosensors represent the newest research related to sensors. They are well-written, well-referenced reviews of applications in bioprocess measurement, and they provide excellent discussions of operation principles. A common theme bonds these chapters: the use of biochemical processes coupled to the sensor, which allows light, heat, or the generation of electrochemically observable species to be used for detection.

The difficulty of these applications and their potential for solving measurement selectivity of complex biomolecules are perhaps understated. However, the bioprocess engineer, who already has an understanding of the biochemical processes that these sensors seek to exploit, will find these chapters of significant interest.

The chapter on electrochemical sensors invests considerably more space in the operational aspects of electrochemical devices than in their application; it contains little new material. The chapter on NADH-dependent fluorescence sensors is a well-balanced but cursory overview of techniques for measurement of viable biomass using light launched directly into the medium as well as through fiber optics with immobilized NAD(P)H precursors.

Two chapters on HPLC provide a comprehensive overview of chromatography—its history, operation, system architecture, availability, and

> "... well-written reviews of applications in bioprocess measurement..."

power to solve complex analytical problems—but only one application of bioprocessing is discussed, and brief reference is made to a few others. Solving a biochemical analysis/control problem by using the material in this chapter would pose a significant challenge for the biotechnologist.

The chapters on chemometrics and flow-injection analysis should also be of high value to the biotechnologist—the former from the point of view of adding selectivity to otherwise less than ideal sensors and the latter from the perspective of both accomplishing sampling and using known chemistry to effect automated analyses. The space allotted to chemometrics is insufficient for teaching purposes; one must be either a mathematician working with matrix techniques or a chemometrician to glean much useful information from this chapter.

The chapter "Sensors in Bioprocess Control" provides an excellent overview of process control from the basics to implementation with modern control systems and strategies. The thrust of this chapter is not sensors. However, several examples provide valuable insight into the methodology available for automation and control of bioprocesses.

Sampling, sensors, automated instrumentation and control—all focused on bioprocessing—are found under one cover in this book, and it is highly recommended both for the biotechnologist interested in learning about new sensor technology and the analytical chemist seeking insight into the measurement needs of the biochemistry community.

Treatise on Analytical Chemistry, Vol. 11: Theory and Practice. I. M. Kolthoff, James D. Winefordner, and Maurice Bursey. 311 pp. John Wiley & Sons, 605 Third Ave., New York, NY 10158. 1989. $80

Reviewed by Jeanette Adams, Department of Chemistry, Emory University, Atlanta, GA 30322

This treatise is dedicated to different aspects of gas-phase ion chemistry. The five chapters cover very different topics that range from basic MS to plasma chromatography (PC). The quality of each chapter is as varied as the topics themselves.

Chapter 1, "Mass Spectrometry of Organic and Biological Compounds," is an overview of basic MS that includes detailed discussions of classic inlet systems, ion sources, mass analyzers, and detectors. Some theory and applications also are addressed.

Although Chapter 1 covers the classic techniques in detail, many techniques that were developed in the 1980s and that had appeared by 1987 or 1988—especially regarding MS of biological compounds—are not discussed. Hyphenated techniques of continuous-flow fast atom bombardment MS, supercritical fluid MS, capillary zone electrophoresis/MS, electrospray MS, and matrix-assist-

ed laser desorption MS are not covered. Some basics of quadrupole, sector, and time-of-flight machines are described, but ion trap mass spectrometers are not. Classic detectors are detailed, but the advent of array detectors that significantly reduce detection limits, especially for biomolecules, is not discussed. Metastable ions and collision-induced dissociations (CIDs) are briefly covered, and the Rice–Ramsperger–Kassel (RRK) theory (not the Rice–Ramsperger–Kassel–Marcus/quasi-equilibrium theory, or RRKM/QET) is used to explain unimolecular reactions.

Half of the applications described in Chapter 1 involve interpretation of EI mass spectra; the rest include quantitation of environmental pollutants, MS of some biomolecules, and mixture analysis by MS/MS. The discussion of MS/MS focuses on triple quadrupoles as well as reverse-geometry and three-sector machines. One application of a four-sector mass spectrometer is discussed, although peptide sequencing is not. There are inaccuracies in the basic MS equations and elsewhere that would be misleading to a nonpractitioner.

Chapter 2 covers in depth some specific and exciting areas of research in Fourier transform ion cyclotron resonance (FT-ICR) MS and includes many references from 1988. It is written for the graduate student or expert, and a B. S. chemist might need to consult an introductory review to fully understand the technique. A brief description of basic fundamentals is followed by some of the innovative changes in instrumentation and their underlying principles. These include detailed descriptions of two-section ICR cells, external ion sources, and new ion excitation and ejection techniques.

One problem of ICR, *z*-axis excitation, is discussed in detail in Chapter 2. Applications include recent studies of metal ions and metal ion clusters, carbon clusters, and ion–molecule reactions of metal ions and neutrals; CID of organometallics and studies of ion structure and thermochemistry; and photodissociation of peptide ions, determination of dissociation thresholds, and studies of other physical processes.

Chapter 3 describes the use of rf spark source MS for determining elements at ultratrace levels. Anyone unfamiliar with the technique can gain an understanding and appreciation of both the power and limitations of the methodology. Instrumentation and methods for qualitative and quantitative analysis, including sample preparation and handling, are discussed. Other topics include analyses of metals; thin films and surfaces; and biological, geological, environmental, and forensic samples.

Chapter 4 is a short description of PC, also known as ion mobility spectrometry. The discussion covers the literature through 1976, except for a brief mention of two references published in 1985 (a book and a review of that book). There is no historical background regarding the purpose for the original development of PC, and its impact and use in analytical chemistry are not clearly defined. Thus there is no indication of why one would choose PC over other analytical techniques. The applications section lists compounds that have been studied by PC and respective literature references; one would have to read the previous literature to understand the role of PC in analytical chemistry.

Chapter 5, a thorough description of the fundamentals, methodology, and uses of ion scattering for elemental analysis of surfaces, covers the literature through 1986. This chapter would be useful for any chemist. The mathematics and fundamentals of the technique, which include theories of binary elastic collisions and scattering cross sections, are clearly explained. Effects of atom–atom shadowing, atom motion, and ion neutralization on signal intensity and peak shape are discussed in detail along with experimental apparatus and techniques used in qualitative and quantitative analyses. Applications include determination of in-depth concentration profiles as well as metals on surfaces of conductors, insulators, and catalysts.

Protein Purification: From Molecular Mechanisms to Large-Scale Processes. Michael R. Ladisch, Richard C. Wilson, Chih-duen C. Painton, and Stuart E. Builder, Eds. 280 pp. American Chemical Society, 1155 16th St., N.W., Washington, DC 20036. 1990. $65

Reviewed by Yuan C. Lee, Department of Biology, The Johns Hopkins University, Baltimore, MD 21218

This book is the outcome of a 1988 ACS symposium, "Design of Biochemical Technology." The development of biotechnology based on molecular biology calls for new approaches to the age-old problem of protein purification. This book provides a platform by which to examine some new potentialities.

The range of topics is selective and not expansive. The first three chapters, which address general problems associated with large-scale preparation of proteins, are perhaps the best in the book. Topics include the following: aqueous two-phase systems, hydrophobic interaction chromatography (HIC), radial flow affinity chromatography, metal affinity–recycle extraction, and immunoaffinity chromatography. Some chapters, such as "Site-Specific Proteolysis of Fusion Proteins" and "Chelating Peptide-Immobilized Metal-Ion Affinity Chromatography," apparently are linked to the molecular biology of this problem. The overall focus of the book, however, is more on chemical engineering.

Obviously, large-scale preparation of proteins from a production medium is different from, for example, analysis of minute quantities of enzymes from urine. In the latter case, purity may be attained even at a considerable cost, whereas in the former, economy is the dominant factor. Therefore high-resolution chromatographic methods as commonly practiced in research laboratories may not be suitable for mass production of proteins.

Although many of the contributors recommend nonchromatographic methods, they do not advocate abandoning high resolution. Instead, high resolution is being attempted in different forms, sometimes based on different principles. Although some advice—such as reducing the working volume early in the process—is common wisdom, each case presents different problems and challenges because of the diverse nature of the proteins being mass produced. What is a large scale for one protein may be only a microscale for another. For some proteins, HIC may be very effective, but for others it is of limited value. Because no universal single-step purification is available, making accessible a larger number of different tools would offer greater possibilities for different problems.

It is interesting that although the title professes to deal with "large-scale processes," capillary zone electrophoresis (CZE) is discussed more than once (in conjunction with other electrophoretic forms). However, CZE is inferior even for microscale preparative operations. Despite its newness, inclusion of this topic here is rather questionable.

The book is cleanly produced, although the type size could be larger

for easier reading. The index should have included abbreviations such as HIC and CZE, which are used profusely throughout the text. As an alternative, a unified list of abbreviations would have helped readers. Nonetheless, this is a timely and welcome volume in the emerging field of biotechnology.

Biological Mass Spectrometry. A. L. Burlingame and J. A. McCloskey, Eds. 700 pp. Elsevier Science Publishers, P.O. Box 882, Madison Square Station, New York, NY 10159. 1990. $230

Reviewed by Julie A. Leary, Department of Chemistry, University of California, Berkeley, Berkeley, CA 94720

This book is a compendium of manuscripts (36 chapters) that was presented in August 1989 at the Second International Symposium on Mass Spectrometry in the Health and Life Sciences. The researchers comment on a variety of mass spectral techniques for use in the characterization of proteins, glycoconjugates, nucleic acids, and other biopolymers. Ionization methods include plasma desorption, matrix-assisted laser desorption, electrospray, and fast atom bombardment/liquid SIMS. The mass spectrometer designs that incorporate these techniques are triple quadrupoles, tandem four-sector, Fourier transform, and time-of-flight (TOF) instruments.

The book begins with three strong chapters. Sundqvist covers the basic concepts of sputtering large organic molecules in simple but accurate terms and supplements the text with excellent references. Equally impressive are the chapters by Roepstorff and Hillenkamp who, respectively, cover the applications of plasma desorption and laser desorption TOF to large proteins.

Chapters in the middle portion comment on electrospray in combination with a variety of instruments, array detectors, and strategies for sequencing proteins, glycopeptides, and oligosaccharides, whereas the last few chapters focus on the interaction of MS in the biotechnology and biopharmaceutical arenas. The last chapter, by Cantor, offers an entertaining discourse on the Human Genome Project.

The overall strength of this book lies in the experts who report on their specializations within the field of biological MS. It was refreshing to see that a number of chapters were written by young, bright scientists. However, the overall weakness is that much of the research is now two years old and somewhat outdated. This is unfortunate but can be salvaged by the fact that all of these individuals remain active in their respective areas, and a literature search on the authors provides the reader with the most current research results in the various fields.

The book is well organized and easy to read. At the end of each chapter are actual questions and answers that were parleyed during the symposium. I found these particularly useful because often they were directed at specific experimental details or nuances associated with the research that were not discussed in sufficient detail in the text.

One major criticism, however, is the lack of experimental detail. If the major emphasis was to provide an overview and/or historical account of the various aspects of MS in the area of structural characterization of biological molecules, then I believe this has been accomplished. If, however, the intent was to provide a graduate student or junior researcher with the tools for duplicating or extending these techniques to his or her own research, then it clearly is lacking. The experimental section in some chapters was very sparse and altogether omitted in others. With the exception of this one item, I found the book interesting and fairly informative.

Analytical Methods in Forensic Chemistry. Mat H. Ho, Ed. 440 pp. Prentice Hall Publications, 66 Wood Lane End, Hemel Hempstead, Hertfordshire, HP2 4RG, U.K. 1990. $90

Reviewed by Thomas A. Brettell, New Jersey State Police, P.O. Box 7068, West Trenton, NJ 08628-0068

This book provides an overview of current analytical techniques and future directions of analytical chemistry in forensic science. Certain chapters deal with well-established methods, but most are concerned with analytical methods that have shown substantial progress and that are not found in routine use in the working crime laboratory. The author has focused mostly on modern analytical instrumentation or normal analytical methods concerned with drug or toxicology analysis.

Individual chapters vary substantially in format and discussion; some chapters provide reviews of various techniques on a specific application whereas others discuss a specific technique with wide applications. Most are essentially reprints of research papers that have appeared, and some chapters lack up-to-date references of particular applications.

The first six chapters cover differing aspects of MS such as MS/MS, GC/MS, stable isotope ratio MS, fast atom bombardment MS, and chemical ionization MS, as well as their applications to forensic science.

The next four chapters are devoted to the applications of several spectroscopic methods to the solution of specific forensic problems. Chapter 7 is a compilation of the author's previously published articles on the applications of chiral optical spectroscopy to the detection and quantification of drugs of abuse. It describes in relatively simple terms the concepts of polarimetry, optical rotatory dispersion, and circular dichroism.

Chapter 8 focuses on the potential application of three-dimensional fluorescence in forensic analysis of petroleum-based products, which shows promise for real casework samples.

Chapter 9 discusses the theoretical basis of the radiative energy attention technique and its application to the determination of ethanol in biological fluids.

Chapter 10 describes the specimen preparation and analysis for trace metals by flame and flameless atomic absorption spectrophotometry.

The next 14 chapters deal with chromatographic methods and their applications to various forensic problems, most of which concern the analysis of drugs of abuse and the comparative analysis and profiling of specific types of drugs. Capillary GC and HPLC methods are extensively discussed, and all of Chapter 19 is devoted to the application of gel permeation chromatography as well as the radioimmunological screening, identification, and determination of barbiturates in postmortem blood.

The last five chapters deal with various topics of forensic science such as the latex particle agglutination technique in the immunoassay of therapeutic drugs (Chapter 25), a semiautomated extraction and spotting system for the analysis of drugs in physiological fluids (Chapter 26), the detection of firearm residues by several analytical methods (Chapter 27), a systematic approach to toxicology analysis (Chapter 28), and the potential for and limitations of chemical analysis of physiological evidence (Chapter 29).

In the last few chapters the author

has tried to comprehensively cover most of the analytical techniques applicable to the forensic science laboratory. In this attempt he has omitted several important areas such as pyrolysis GC, microspectrophotometry, FT-IR, the analysis of dyes from fibers, dynamic headspace techniques in the detection of accelerants, and DNA technology. Despite these omissions, the author has provided an excellent text of current analytical methodology with pertinent applications to forensic science. The practicing forensic scientist cannot help but learn new techniques and information to apply to casework samples. Likewise, few analytical chemists would find it difficult not to learn new techniques to apply to forensic science. This book should be on the shelf of every forensic scientist's library.

Handbook of Quality Assurance for the Analytical Chemistry Laboratory. James P. Dux. 203 pp. Van Nostrand Reinhold, 115 Fifth Ave., New York, NY 10003. 1991. $40

Reviewed by Donald F. Gurka, U.S. Environmental Protection Agency, Environmental Systems Laboratory, Quality Assurance Division, 944 East Harmon Ave., Las Vegas, NV 89159

This is a concise beginner's book that covers the basics of establishing, operating, optimizing, and documenting a quality assurance/quality control (QA/QC) program. Topics include definitions, basic statistics and statistical applications, sampling, analytical methods and materials, documentation and organization, setting up and auditing the QA program, and strategies for obtaining laboratory accreditation. Updates to the first edition address computers and laboratory information systems (LIMS).

The style is qualitative; few figures and solved problems appear. But this style is appropriate for a startup laboratory and is directed at managerial personnel concerned with QA/QC oversight roles. The rationale for this is accurately stated as "while the cost of a quality assurance program is often easy to establish with routine accounting and labor allocation procedures, many of the benefits are intangible." Clearly, management must establish QA/QC cost–benefit philosophy, and this book could provide a cornerstone for such thinking.

The strength of the book lies in a detailed exposition of how to establish and monitor the QA/QC program. Example forms and checklists provide an initiation point from which the laboratory can evolve to its own goals. The author's computer mentality is ambivalent, at best; contradictory statements are interspersed throughout the book. For example, on page 12, he states that "computers will eliminate calculation errors, but cannot eliminate errors due to incorrect data input." On page 169, however, he says, "We must always be aware of the problem of deterioration of software quality." Widespread use of optical scanners should enhance the possibility of data transcription errors (i.e., input data are correct but misread). Another glaring error is the statement on page 55 that the chain of custody should start after the sample is received. This is too late to guarantee data defensibility.

These problems do not mar the fact that the book has a very pragmatic approach to daily QA/QC activities. However, it does not provide (as claimed on the jacket) the latest approach to QA/QC systems. Of 17 references for 13 chapters, only two were published after the first edition. A reading list is added at the end to correct this problem, but one-third of these references were previously cited and only the computer-related references can be considered current.

This book is almost perfect for the novice learning about QA/QC. If one already owns the first edition, however, I doubt that it is necessary to purchase the second version.

Books Received

Spectroscopic Properties of Inorganic and Organometallic Compounds, Vol. 23. G. Davidson and E.A.V. Ebsworth, senior reporters. xiv + 495 pp. Royal Society of Chemistry, Distribution Centre, Blackhorse Rd., Herts SG6 1HN, U.K. 1990. $143

This book, a review of the recent literature published up to late 1989, contains more than 5700 references. The eight chapters are " Nuclear Magnetic Resonance Spectroscopy," "Nuclear Quadrupole Resonance Spectroscopy," "Rotational Spectroscopy," "Characteristic Vibrations of Compounds of Main Group Elements," "Vibrational Spectra of Transition-Element Compounds," "Vibrational Spectra of Some Coordinated Ligands," "Mössbauer Spectroscopy," and "Gas-Phase Molecular Structure Determined by Electron Diffraction."

Photon Migration in Tissues. Britton Chance, Ed. x + 195 pp. Plenum Press, 233 Spring St., New York, NY 10013. 1989. $63

This book is the result of a workshop held in April 1988 in Philadelphia. The presentations include optical properties of tissue, adapting fluorescence instrumentation, in vivo near-IR spectroscopy, ultrashort laser pulse tomography, and time-resolved methods. The book contains more than 200 references, with approximately half since 1985. Author and subject indexes are included.

Analytical Chemistry of Silicones. A. Lee Smith, Ed. xxii + 550 pp. John Wiley and Sons, 605 Third Ave., New York, NY 10158. 1991. $125

This is Volume 112 in the series Chemical Analysis: A Series of Monographs on Analytical Chemistry and Its Applications. Topics include trace analysis, surfaces, personal care applications, microscopical characterization, chromatography, NMR, and MS. Approximately half of the 1100 references span the 1980s, with a few as late as 1989. A subject index and an appendix listing physical properties of organosilicon compounds are included.

Introduction to Laboratory Automation. Víctor Cerdá and Guillermon Ramis. xiv + 321 pp. John Wiley & Sons, 605 Third Ave., New York, NY 10158. 1990. $70

This is Volume 110 in the series Chemical Analysis: A Series of Monographs on Analytical Chemistry and Its Applications. The nine chapters are "Automation and Chemistry," "Basic Concepts and Elements of Analog Electronics," "Digital Electronics," "Microprocessors," "Transduction, Signal Conditioning, Data Acquisition, and Control," "Communications," "Instruments and Apparatus for Laboratory Automation," "Automation of Analytical Methods," and "Laboratory Robotics." A bibliography and an index are included.

Chromatographic Analysis of Alkaloids. Milan Popl, Jan Fähnrich, and Vlastimil Tatar. viii + 667 pp. Marcel Dekker, 270 Madison Ave., New York, NY 10016. 1990. $150

The seven chapters are "Classification of Alkaloids," "Properties of Alkaloids Relevant to Chromatography," "Chromatography," "Gas Chromatography," "Liquid Chromatography," "Thin-Layer Chromatography," and "Applications." Of the 1300 references, about half span the 1980s, through 1988. An index is included.

NEW PRODUCTS

Instrumentation

Thermal analysis. Model DSC12E microprocessor-controlled differential scanning calorimeter features isothermal and dynamic operating modes and a temperature range of −40 to 400 °C. An LCD display indicates test parameters including start/end temperatures and heating rate. Mettler **401**

Drug testing. ITS40 Witness System consists of a gas chromatograph/mass spectrometer and software designed for drug-testing laboratories. Full mass spectra are used for drug identification. Finnigan MAT **402**

Nucleic acids. Model 785 vacuum blotter transfers DNA or RNA from an agarose gel onto a solid support membrane. The unit is unaffected by acids and bases commonly used for depurination or denaturation. Bio-Rad Laboratories **403**

Detector. ELSD IIA is an evaporative light-scattering detector designed for HPLC, GPC, and SFC applications. The system operates with a stable, noise-free baseline during a gradient run and accommodates microbore and analytical solvent flow rates. Varex Corp. **404**

Air analysis. Model FP-000A combustible hydrocarbon sensor consists of a matched pair of catalytic sensor beads mounted in a stainless steel housing, a control transmitter circuit, an explosion-proof junction box, and a machine-fitted splash guard. Detcon **405**

Moisture. Span Pac H_2O generates moisture standards in concentrations ranging from 0.1 ppm to > 1000 ppm. The unit, which can be remotely or manually operated, accommodates disposable and refillable permeation tubes. Kin-Tek Laboratories **406**

Chromatography. LC Star 9100 AutoSampler is a microprocessor-based, stand-alone unit for automated HPLC applications. Features include 105-sample capacity and an air-cooled refrigeration option. Varian **407**

GC. ATD 400 thermal desorber, which incorporates an electrically cooled trap and inert flow path, is compatible with any gas chromatograph and all column types. Split points on the cold trap inlet and outlet facilitate independent control of the flow rates during analysis. Perkin Elmer **408**

FT-IR. Model 510 FT-IR spectrometer features a frictionless flex-pivot interferometer design and resolution of 0.8 cm^{-1}. The spectrometer operates with the IBM PC and compatible computers, Apple Macintosh computer systems, and the 620 RISC processor. Nicolet **409**

Diffraction. FPD 900 series powder diffractometers are designed for materials research, geological, and pharmaceutical applications. System configurations include a choice of incident beam monochromators and solid-state energy-dispersive detectors. Philips Electronic Instruments **410**

Software

Image analysis. JAVA version 1.4 is designed for the quantitative analysis of video or digital images. Features include image snapshots, image bit map transforms, enhanced macro facilities, and data worksheet formatting and printing. Jandel Scientific **411**

Curve fitting. Mini-Square is a nonlinear curve fitting and modeling package that provides publication-quality *x-y* plots. Data entered from the keyboard or from a data file can be plotted on the screen, edited, annotated, archived, and reproduced on almost any dot matrix printer. Dynacomp **412**

Manufacturers' Literature

Chromatography. *Waters Column* features articles on high-resolution GPC cleanup of environmental samples and on capillary ion analysis. 16 pp. Waters Chromatography Division of Millipore **413**

CT-1000 constant-temperature bath is designed for kinematic viscosity determinations with glass capillary viscometers. The unit maintains accurate temperature control of ± 0.01 °C within the range of 20–150 °C. Cannon Instrument Co. **414**

Fluorescence. Booklet describes optical filters and coatings for fluorescence instrumentation. Spectrographs of filter sets for specific fluorescent dyes are included. 28 pp. Omega Optical **415**

Newsletter. *Environmental Lab Automation Notes*, Vol. 2, No. 1, features articles on automation of groundwater and wastewater sample analysis and on automated soil extraction systems. 8 pp. Zymark Corp. **416**

IR. Literature describes the design and operational characteristics of IR analytical instruments that use narrow bandpass filters for wavelength discrimination. Applications for liquid and gas stream analysis are discussed. GAC **417**

Companies interested in a listing in this department should send their releases directly to ANALYTICAL CHEMISTRY, Attn: New Products, 1155 16th Street, N.W., Washington, DC 20036.

Food analysis. Application note A-10.4 discusses the quantitative determination of vitamin C in fruit juice by instrumental TLC. Camag **418**

Surface analysis. Brochure highlights the NanoScope atomic force microscope. Information on data analysis and display capabilities is provided. 12 pp. Digital Instruments **419**

pH meters. Bulletin highlights Accumet pH/ion meters. A selection guide provides information on range, accuracy, repeatability, slope control, and special features. 16 pp. Fisher Scientific **420**

Newsletter. *Fei focus* features articles on source–column interactions in the production of submicron electron beams and on imaging time-of-flight SIMS. 8 pp. FEI Co. **421**

Separations. *The Separation Times,* Vol. 5, No. 1, includes articles on the determination of residual solvents in pharmaceutical manufacture and on the conditioning of solid-phase extraction cartridges. 12 pp. J & W Scientific **422**

LC. Brochure describes Superformance columns for biochromatography, which feature high operating pressures, zero dead volume, and a glass cartridge system. EM Separations **423**

Catalogs

HPLC. Catalog includes columns for analytical, preparative, and biochemical applications; affinity adsorbents; column heaters; pumps; detectors; and autosamplers. 368 pp. Rainin Instrument Co. **424**

Chromatography. Catalog features vials, caps, seals, and crimping systems for chromatography autosamplers. An instrument and vial compatibility chart is included. 36 pp. Chromacol **425**

Instrumentation. Catalog includes nitrogen and sulfur analyzers; process and on-line instrumentation; gas chromatographs, detectors, and accessories; and products for sample and data handling. 28 pp. Antek Instruments **426**

Environmental analysis. Catalog features products for laboratory analysis of hazardous waste by EPA methods. Rotary extractors, filtration units, and syringes are included. 20 pp. Associated Design and Manufacturing Co. **427**

For more information on instrumentation and software products, and/or to obtain the free available information on other listed items, please circle the appropriate numbers on one of our Readers' Service Cards.

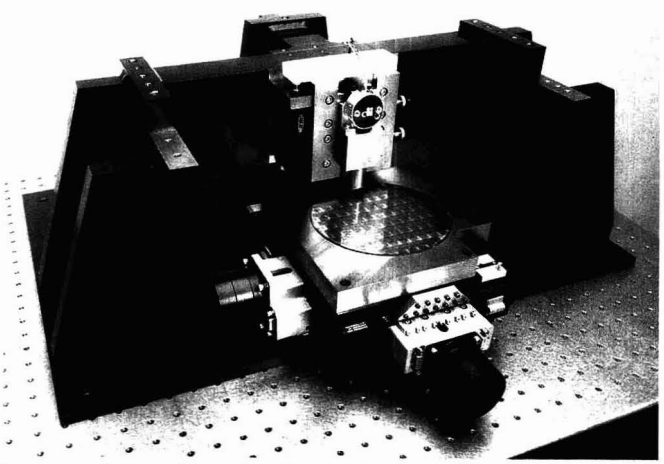

Large-sample scanning probe microscope accommodates samples up to 200 mm in diameter. The *x-y* stage positioning can be controlled manually or automatically and is accurate to within ± 10 μm. Digital Instruments **428**

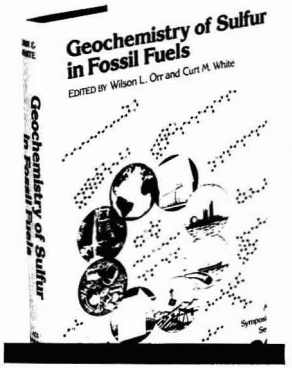

Geochemistry of Sulfur in Fossil Fuels

Sulfur in fossil fuels—how it got there and what form it's in—is the subject of this unique, new volume. It is the first to focus entirely on chemical processes occuring in geological environments.

Thirty-two chapters cover the current state of knowledge and address major advances that have established a new era of understanding at the molecular level in sulfur geochemistry. Various fuel systems are examined, as well as the reasons for their differences and similarities. Major advances made during the last decade by improved analytical methods are emphasized.

The volume begins with an introductory section that presents historical background, addresses environmental consequences of the combustion of fossil fuels, describes microbial metabolism of sulfur compounds, and reviews methods for isolating sulfur compounds. Other sections cover:

- studies of depositional environments
- characterization of sulfur in fossil fuel materials
- molecular structure of sulfur compounds and their geochemical significance
- isotopic studies

A 50-page bibliography compiling references from the individual papers is also included.

Wilson L. Orr, *Editor,* Mobil Research and Development Corporation

Curt M. White, *Editor,* Pittsburgh Energy Technology Center

Developed from a symposium sponsored by the Division of Geochemistry of the American Chemical Society

ACS Symposium Series No. 429
708 pages (1990) Clothbound
ISBN 0-8412-1804-8 LC 90-839
$109.95

O·R·D·E·R F·R·O·M

American Chemical Society
Distribution Office, Dept. 76
1155 Sixteenth St., N.W.
Washington, DC 20036
or CALL TOLL FREE

800-227-5558
(in Washington, D.C. 872-4363) and use your credit card!

An Audiocassette Course from the American Chemical Society

INTERPRETATION OF MASS SPECTRA

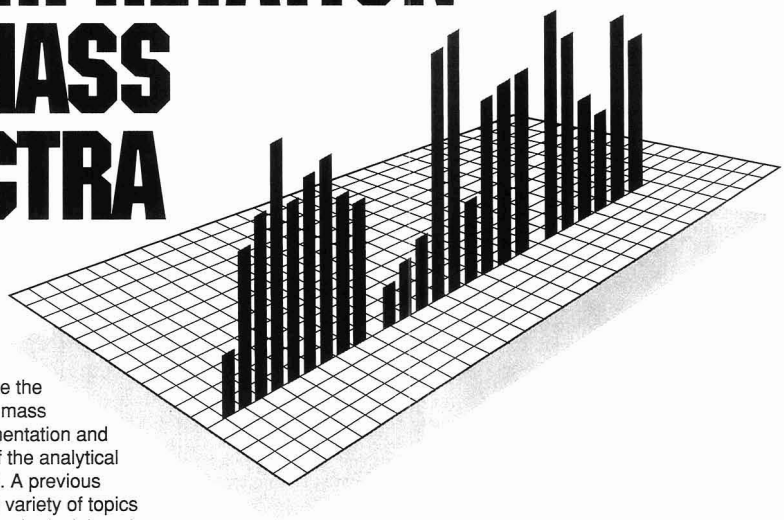

This new audiocassette course teaches you how to make the most effective use of mass spectrometric instrumentation and improve the quality of the analytical information produced. A previous bestseller, it covers a variety of topics — from the fundamental principles of mass spectrometry to newer, electronic forms of ionization and interpretation of the corresponding spectra. It also covers spectra produced by alternative ionization methods as well as additional mass spectrometry techniques that can provide valuable information.

Find out more on MS techniques

With five cassettes and the follow-along workbook, this course reviews the principles of tandem mass spectrometry. It gives you a better understanding of ancillary instrumental techniques — such as library search and accurate mass measurement. Ancillary chemical techniques, including the use of stable isotopes and derivative formation, are also examined.

In addition, this course will give you the know how to interpret spectra derived from alternative ionization techniques and apply mass spectrometry to problems in qualitative or quantitative analysis. You'll become more knowledgeable on how to select the appropriate ionization technique to solve a particular analytical problem.

After completing this course, you'll be able to:

- Use mass spectrometry with other spectroscopic techniques in elucidating chemical structures
- Effectively design experiments to provide a wide range of analytical information
- Improve the quality of analytical information in a wide range of disciplines, e.g., synthesis, structural elucidation, quality control, toxicology, environmental trace analysis
- Provide analytical information for a wide range of compound types
- Give advice on the purchase of mass spectrometric instrumentation

Instructor

John R. Chapman is currently Analytical Systems Manager in the Mass Spectrometry Division of Kratos Analytical. He received his B.S. in chemistry from Imperial College, London, in 1960 and Ph.D. from Oxford University in 1963. After leaving Oxford, he spent three years on the staff of the Medical Research Council. Dr. Chapman is the author of two text books and numerous research publications.

Unit

Five cassettes (5.0 hours playing time) and 200-page manual: $485.00, U.S. & Canada; $582.00, export. Additional manuals: $48.00 each, U.S. & Canada; $58.00, export. (Catalog No. B6)

Order from:

American Chemical Society, Distribution Office, Dept. 23
1155 Sixteenth Street, NW, Washington, DC 20036
or CALL TOLL FREE

1-800-227-5558

(in Washington, DC 872-4363) and use your credit card!
FAX: 202-872-6067

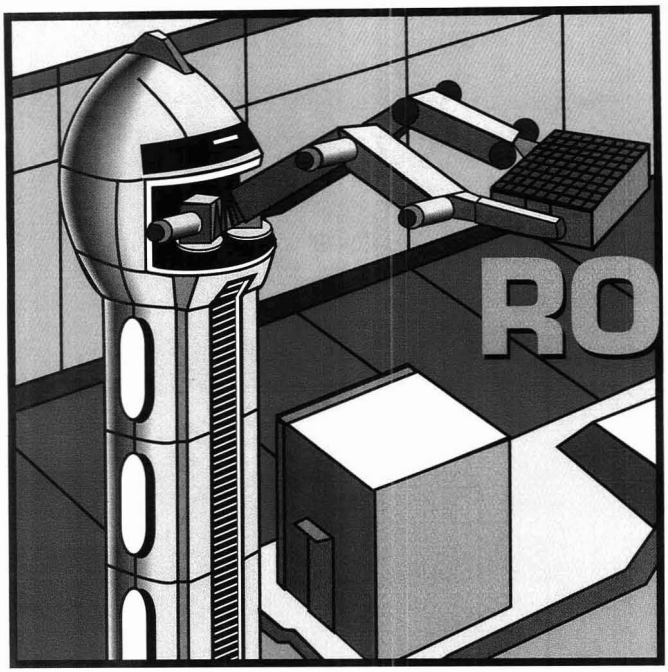

ROBOTS IN HEALTH CARE

Robin A. Felder, James C. Boyd, Keith S. Margrey, William Holman, John Roberts, and John Savory
Department of Pathology
University of Virginia Health Sciences Center
Charlottesville, VA 22908

Application of robotic technology has resulted in dramatic improvements in industrial productivity and quality, and spinoffs of this technology that will have an impact on everyday living are rapidly emerging. Against this backdrop, hospitals across the country are beginning to consider the benefits of robotic automation.

Health care traditionally has been a difficult marketplace for automation because of the complexity of the procedures and the potential risks to human life should an error occur. Nevertheless, exciting medical applications, such as the use of robots as assistants in surgical procedures, have recently been described. Although surgical applications of robots are sensational and attract public attention, there are other areas of the hospital in which robots may have an even more significant impact. They may eliminate mundane chores, reduce the exposure of personnel to communicable diseases, and lower labor costs.

The need for robots

Tertiary care hospitals are prime targets for the introduction of robots. Ever-increasing personnel costs are contributing a major share to rising hospital costs. In clinical laboratories nationwide the cost of labor makes up more than 50% of the cost of each laboratory test, and this figure is rising steadily because higher salaries must be offered to retain existing laboratory technologists and entice young graduates into the field. Skills in areas such as MS, molecular biology, and computer applications are becoming necessary because of the introduction of new techniques and procedures in patient care, making it even harder to find qualified laboratory staff. For example, organ transplantation is now commonplace but brings with it additional needs from support services such as blood banks, tissue typing, biochemical analysis, and even transportation to get the organ from the donor to the patient.

Added to this problem is a decrease in the number of individuals entering non-M.D. health-related professions. For example, the number of medical technology students in the University of Virginia's accredited training program decreased from 23 in 1977 to 10 in 1985, 5 in 1990, and a single applicant for 1991. The vacancy rate for medical technologists was even higher in 1988 than the well-publicized 11.3% vacancy rate for trained nurses (*1*). Health care professionals are thus under pressure to develop novel solutions for stemming the flight of critical personnel from the field while providing better care more efficiently.

Why has the medical industry become an unpopular place to seek employment? Although multiple causes exist, the increasing complexity of the field has driven the more skilled individuals to more lucrative and less demanding fields. The pressures of coping with life-and-death situations as well as demanding schedules (weekends and nights) make hospital laboratory work unattractive. Another important contributing factor is the danger of contracting communicable diseases through patient contact or handling infectious specimens.

Because they are not trained in robotics, health care providers have difficulty perceiving potential appli-

A/C INTERFACE

0003-2700/91/0363-741A/$02.50/0
© 1991 American Chemical Society

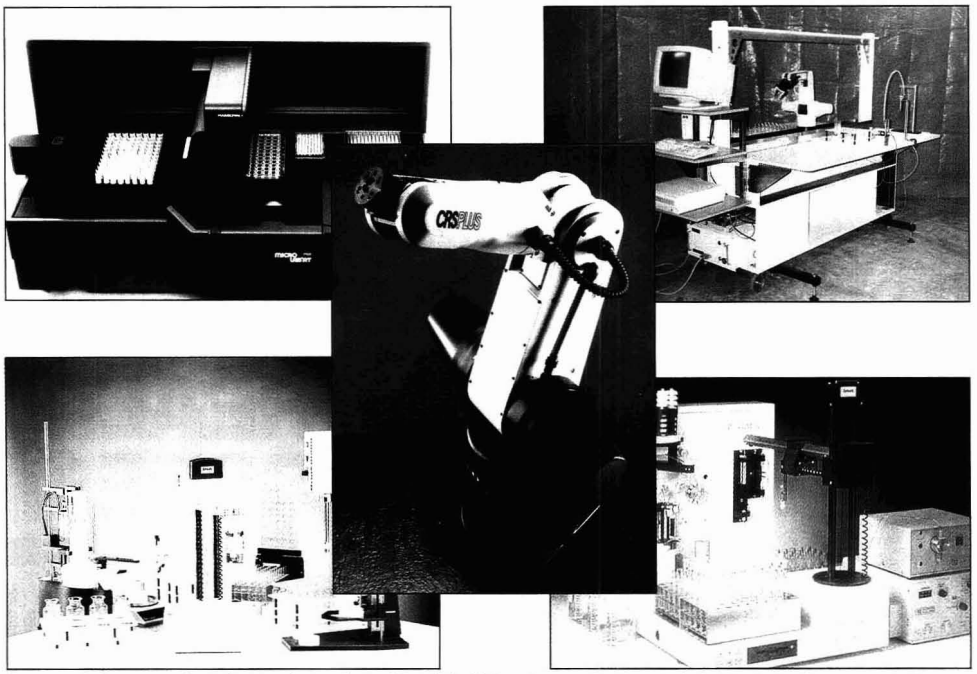

Figure 1. Laboratory robots that can be configured for clinical laboratory applications include (clockwise from upper left) Microlab AT+ (Hamilton Co., Reno, NV), the MAST system robot environment (Automation Design, Greenville, SC), Benchmate and Zymate XP (Zymark, Inc., Hopkinton, MA), and (inset) CRS (Labotics Automation, Inc., Toronto, Canada).

cations for robots, and robotics has been studied in suprisingly few clinical laboratories (*2*). Although current technology has not been tested thoroughly enough to allow unattended use of robots in proximity to patients, existing robots may be useful in many areas of the hospital. For example, the use of robotic automation to improve the safety of medical personnel by reducing their exposure to infectious samples is being investigated. Likewise, there is a high emphasis on improving the efficiency of medical facilities. To date, robots have been applied successfully in operating rooms, in hospital-wide transportation systems, and in hospital clinical laboratories.

Laboratory robots

Robots are available in many different sizes and configurations, ranging from the large industrial variety costing hundreds of thousands of dollars to small teaching robots costing less than $600. Because they are easy to program and cost-effective, robots are an attractive alternative for solving several of the problems currently facing health care planners.

A wide variety of generic laboratory robots are available, as shown in Figure 1. Clinical laboratories can purchase a Cartesian robot that can be configured to pipette liquids into many types of test tube racks or microwell plates. These robots can usually manipulate liquid volumes from as little as 10 μL to as much as 10 mL and are the most popular type for clinical laboratories because medical technologists spend most of their time handling liquids.

Mundane mechanical tasks such as moving disposables around the laboratory bench, centrifuging, or weighing test tubes are better suited to a laboratory robotic arm. These robots can be configured to operate in a cylindrical space (cylindrical robot) or in a complex space (articulating arm). Some articulating robots can achieve 180 in./s when all motors are running at full speed. The robot's speed is slower when moving in a linear path because complex calculations are required to control each joint motor independently. Articulating robots can achieve speeds in excess of 40 in./s when performing linear movements in linear path motions.

Clinical laboratory applications

Although manufacturers of clinical chemistry instruments have built some automation (such as sampling or pipetting) into their devices, they have developed nothing with the reprogrammable versatility of robots. Conversely, manufacturers of robots have developed a few specific applications (such as blood processing and extraction of drugs) that show promise, but nothing that as yet will revolutionize clinical chemistry. Robotics can be used for specimen processing, operation of satellite labs throughout the hospital, and microbiological studies.

Specimen processing. Perhaps the major contribution of robotics in the clinical laboratory will be in the automated processing of specimens. Serum, plasma, urine, and cere-

brospinal fluid samples, for example, must be identified, separated from extracellular fluid, aliquoted, and distributed. These tasks are performed manually and require a large staff, in part because specimens arrive for processing 24 hours a day 7 days a week. (At the University of Virginia Health Sciences Center the receiving and processing staff consists of 20 technicians at an annual cost of $350,000.)

Although automation of this component of the clinical laboratory has been considered a priority for at least 25 years, the complexity of the task is indeed formidable, and complete automation is not yet close to being achieved. Several Japanese companies, however, have introduced automated specimen-processing devices. Hitachi has developed an integrated specimen-processing system that reads bar codes, automatically centrifuges the blood, separates the serum or plasma from the erythrocytes, and stores the specimen until a clinical instrument is ready to perform the analysis. An integrated sample-handling system from International Reagents Corporation (IRC) performs similar specimen processing and also includes a refrigerated station for long-term storage of specimens.

Such automated storage and retrieval systems will reduce the labor-intensive steps of finding and reanalyzing specimens when additional tests are requested. Medical Robotics, Inc., has created a specimen-processing station called the Serumax, which centrifuges specimens, places the serum into a specimen cup for analysis, and creates a separate aliquot for storage. Because this is a closed robotic device, it should reduce the hazard of exposing personnel to virus-contaminated specimens.

A variety of options are becoming available to clinical laboratories interested in automating specimen processing. However, existing systems do not appear to offer much flexibility in handling multiple tube types or the wide variety of containers used for medical specimens. Laboratories may either be designed around the fixed automation inherent in the large integrated Hitachi and IRC systems or incorporate modular workstations such as the Serumax into their existing operations.

Satellite laboratories. A robotically operated satellite laboratory is being investigated at the University of Virginia as an alternative model to the large centralized laboratory facility (*3, 4*). One of the major disadvantages of centralized laboratory facilities is the extended length of time required to obtain analytical results; such long turnaround times can result in compromised patient care, particularly in intensive care units. Traditionally, a costly specimen transportation system has been used to reduce specimen transit time. Recently, however, there has been a trend toward performance of selected laboratory tests using whole blood analyzers located close to the critical-care patient's bedside (*5*). This approach has the advantage of providing an average test turnaround time of only 5 min.

This testing generally has been performed by individuals with minimal training in medical technology, but ancillary testing regulations newly instituted by the Joint Committee for the Association of Hospitals Organization and the College of American Pathologists require a level of quality control comparable to that required by larger laboratories offering similar services. Because most personnel working in intensive care settings have neither the experience nor the desire to perform rigorous quality control, this function will be assumed by trained medical technologists from the clinical laboratory in many centers (*6*), and staffing these satellite whole-blood analysis laboratories with medical technologists will result in much higher costs unless an automated alternative can be developed.

We have developed two such satellite laboratories near critical-care units in the hospital that are staffed entirely by articulating robots (Figure 2). When medical staff enter the room containing the robot they are greeted by a touch-sensitive computer screen (Figure 3); they then enter data such as the patient's hospital identification number and the analyses requested.

After the patient demographics and chemistry profiles are selected and reviewed, the patient's specimen in the original unlabeled syringe is placed in an indexing holding rack through a computer-operated window. The robot, which is a Perkin Elmer Mitsubishi RM 501, retrieves the specimen from the specimen holding rack, decaps it in a proprietary decapper, and introduces it into the analyzers.

After the analysis is complete, the robot recaps the specimen in the capping device and places it in a temporary storage rack. The time required for the medical staff to interact with the robotics laboratory is less than 20 s, after which the robot completes the blood analysis.

Figure 2. The remotely operated robotic critical care laboratory at the University of Virginia consists of a Mitubishi RM-501 robot (Perkin Elmer, Norwalk, CT), which delivers whole-blood specimens to either a Corning 178 blood gas analyzer or a Du Pont electrolyte analyzer.

A custom-designed user interaction station equipped with a touch-sensitive screen interface allows hospital staff to select patient information and analytical tests.

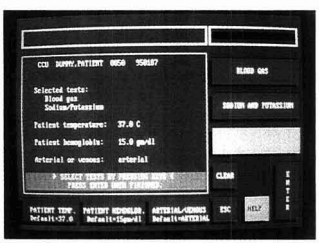

Figure 3. The touch-sensitive screen attached to the front of a standard computer monitor facilitates selection of patients and choice of analytes.

All active entry keys appear in red and all inactive keys in gray.

Results are sent to the main hospital laboratory through a local area network (LAN) coupled to the robot laboratory via optical fibers. In the main laboratory, a trained medical technologist reviews the results of the analysis by observing a computer equipped with a touch-sensitive screen similar to that shown in Figure 3. The technologist may either accept the results if they are within the reference range or repeat the analysis if critical values (those that may indicate a life-threatening condition) are obtained.

If the results are within the limits of normal healthy individuals, the technologist prompts the robot to dis-

card the remainder of the specimen into a hazardous waste container. When critical results are obtained, the robot is asked to repeat the analysis. If the results of the first and second analytical runs agree, the critical result is telephoned to the patient's physician. However, if discrepant results are obtained, a trained engineer must visit the laboratory and resolve the error. The robotic satellite laboratories have been performing clinical specimen analysis for more than six months with only minor errors.

Microbiology. Microbiology has been considered the last place in the clinical laboratory that could benefit from robotic automation. Microbiologic testing involves many pick-and-place operations coupled with the ability of trained technologists to recognize bacterial colonies, and the required visual acuity and manual dexterity are difficult to mimic by robot. However, robots would be useful in reducing the hazards of handling infectious agents, particularly during procedures (such as homogenization or sonication) that produce aerosols.

Investigators have successfully demonstrated that a robot could be programmed to perform the elementary procedure of transferring organisms from agar-containing culture tubes to a fresh tube (*7*). Vision is also beginning to be incorporated; robots can localize, size, and selectively remove colonies for subsequent identification (*8*). Commercial robotic microbiological laboratories, however, are still several years away.

Other hospital applications

Robotic systems are also being developed for use in related areas such as molecular biology laboratories, operating rooms, physicians' offices, and as transportation devices.

Molecular biology. The next major medical frontier is the use of molecular biology for identification and diagnosis of genetic-based diseases. Once an aberrant gene is identified, gene therapy eventually may allow replacement of defective genes. Molecular biologists already are providing many new tests to identify various genetic diseases (e.g., cystic fibrosis and sickle cell anemia), and a rapid expansion in the number and variety of analyses based on genetic markers can be foreseen.

Molecular biology, however, is extremely labor intensive and therefore will require sophisticated automation. DNA synthesizers that allow rapid and accurate production of small (< 250 bases) DNA sequences have been in existence for more than five years (*9*). Although such DNA synthesizers are sophisticated automation, they do not fit the definition of robotic devices because they are dedicated to only one task and cannot be reprogrammed to perform another function.

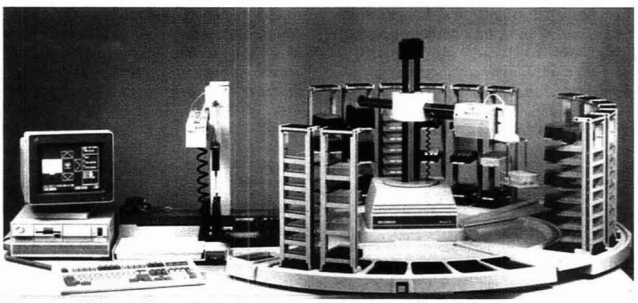

Figure 4. Biomek Cartesian robot, in tandem with a cylindrical robot, can perform a variety of analytical techniques, including DNA testing.

More recently, a Cartesian robot designed for liquid handling has been retrofitted with a custom-designed thermal cycling plate (Figure 4) that allows it to perform the polymerase chain reaction (PCR). PCR allows genetic sequences, which exist in very small quantities in specimens, to be amplified for identification. Many of the manipulations involved in performing DNA tests involve pipetting liquids; therefore, a Cartesian robot dedicated to pipetting can perform most of the steps required.

Surgery. Surgical robots allow more precise, controlled movements than those made by the human hand. Furthermore, the translation of stereotactic coordinate information into movements requires extensive calculations that must be double-checked for accuracy.

Kwoh and co-workers at the Memorial Medical Center in Long Beach, CA, have taken advantage of these robotic capabilities and used a Puma 200 robot to perform brain biopsies (*10*). A computer-aided tomographic (CAT) scanner determined the actual position of the site to be biopsied relative to a stereotactic head clamp. The robot was then directed to move the biopsy needle to the correct site after solving an inverse kinematic problem that located the CAT coordinates of the lesion in the robot's reference frame. A vacuum applied to the needle quickly removed the tissue to be biopsied. By coupling coordinates obtained from the CAT scanner with the movements made by the robot, much less time was required to perform biopsies. Many experiments were conducted on watermelons before human trials were attempted.

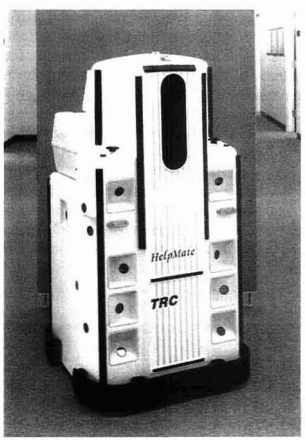

Figure 5. The Helpmate from TRC, Inc. (Danbury, CT).

At Vancouver General Hospital, Andronic Devices Ltd. has developed positioning robots that respond to surgeons' commands to move limbs during arthroscopic and bone surgery. Useful prerobotic versions of these robots are available from Vancouver General Hospital.

Transportation. Robots have also been engineered as hospital transportation devices. W. S. Lob at Transitions Research Corporation (TRC) has described a mobile materials transport robot that is in clinical trials at the Danbury Hospital in Connecticut (*11*). The Helpmate robot navigates the corridors of the hospital, carefully avoiding patients while delivering food trays from the Dietary Department to patient wards (Figure 5).

The engineers at TRC have designed the Helpmate with many layers of safety features. The robot is equipped with a flashing warning light to alert humans of its approach and with turn signals to indicate its next move. Sensors indicating distance (odometry) and proximity (sonar and IR) inform the robot of its position in the hallway and of obstacles that have been placed in its path. Contact bumpers will stop the robot if objects are not detected by the other senses or if there is a sensor failure. Updated versions of the Helpmate include video input; a log polar transform of video array data is used to reduce the microprocessor time necessary to calculate positional data. If all else fails, a highly visible stop switch is accessible to halt a runaway robot.

The Helpmate robot can even ride hospital elevators. To avoid the potential confusion that might result from a robot boarding an elevator full of patients, the robot interacts with the elevator microprocessor to determine if it is empty. Only then will it summon the elevator and ride it.

Nagy and co-workers at the California Computer Research Institute (CCRI) have developed the first dual-armed mobile robot. The CCRI prototype is 5 ft 5 in. high, weighs 180 lbs., and can move at a rate of 1.3–9.4 in./s with a 10-lb. payload (*12*). The CCRI robot can follow a taped path on the floor and dock with recharging sockets, allowing 24-hour-a-day operation (Figure 6). At the University of Virginia we are in the preliminary stages of investigating the use of the CCRI robot for delivery of medical specimens within the laboratory complex and eventual robotic operation of analytical instruments.

Physicians' offices. Robotic technology could also be useful in laboratories peripheral to medical centers. The estimated 100,000 laboratories in physicians' offices in the United States perform ~25% of total laboratory testing. The major incentive for performing laboratory tests in the physician's office is the rapid turnaround. Rapid analysis results in prompt treatment, reduction of patient stress, and fewer repeat office visits (*13*).

The major criticism of testing in the physician's office is inadequate quality control. Regulations recently issued by the Health Care Finance Administration to carry out the Clinical Laboratory Improvement Act of 1988 (CLIA) require each physician's office laboratory to monitor and document quality assurance, proficiency testing, safety, and instrument maintenance. All employees must meet the qualifications set forth by the Department of Health and Human Services and be involved in continuing education programs. Robotics can provide many physicians with on-site laboratory services yet make commercial laboratories or hospitals responsible for monitoring quality, hiring and training qualified personnel, and maintaining instruments.

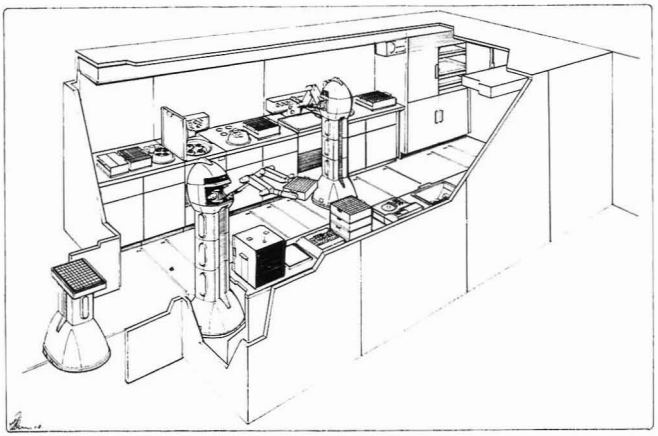

DON VARNER

Figure 6. Mobile two-armed robots perform a variety of laboratory tasks in an artist's vision of a clinical laboratory in the next century.
The robots were developed by Don Nagy at CCRI (Newport Beach, CA).

Acceptance of robots in the health care industry

Health care providers have been cautious in their approach to robotic technology. Much of the delay in using robots in hospitals has resulted from the lack of off-the-shelf systems, the wide variety of electronic and mechanical standards that exist in clinical instrumentation, the shortage of research and development dollars in hospitals, the necessity for manufacturers to have Food and Drug Administration (FDA) approval to sell medical devices, and the combined skills necessary to implement robots in clinical laboratories.

Lack of off-the-shelf systems. Only a handful of companies sell robotic devices for laboratories, and only a few actively market to the clinical laboratory. Of those few, none of the companies have off-the-shelf systems that can perform clinical laboratory tests or process blood specimens. Commercial robotic devices require knowledge of computer programming and electronic interfacing as well as analytical assay design by the end user. Furthermore, the difficulty in designing robotic systems is complicated by the lack of engineers trained in all the disciplines required for clinical laboratories. Zymark, which normally sells turnkey robotic systems for $50,000–$90,000, recently added a line of simple robotic workstations selling for $5,000–$20,000 that should be useful in clinical toxicology and drug-screening laboratories. Their success with the new workstations is being watched very carefully as a barometer of the future of the laboratory robotic industry.

Insufficient standards. One of the major difficulties facing implementors of robotics in health care is the lack of electronic communications, software, or hardware standards in clinical instruments. Many clinical laboratory analyzers, for example, operate as discreet devices with only RS-232C ports for the output of analytical data. Robotic operation of instruments requires an electronic communication standard that allows many of the instrument electronic functions to be accessible to the robot host computer. For example, an analyzer internally programmed to self-calibrate on a predetermined schedule should not initiate a calibration cycle while an irreplaceable medical specimen is being injected into the sampling port.

Standards should also exist for hardware. Many of the injection ports or aspiration needles built into clinical analyzers are simply inacces-

sible to most robotic devices. Thus each site must redesign a separate sample introduction mechanism that is compatible with the instrument hardware. Major differences exist among the instruments used in the laboratory, which makes laboratory systems integration a challenge.

Bar coding, which has been in use in industry for more than a decade, is just beginning to be used in the clinical laboratory. For example, in our laboratory three different analyzers require three different positions for bar code placement on the specimen tube: near the opening of the tube, at the base, and in the middle. This lack of industry standardization requires that either three tubes of blood be drawn from the patient (one for each analyzer) or that three separate aliquots be prepared from the original tube. Needless patient trauma, in the first case, or excessive manual labor and increased chances for error, in the second case, could be avoided if an industry bar code reading standard existed. Fortunately, the National Institute of Standards and Technology has formed a group to study the problems of industrial laboratory standards.

FDA approval. Before a device can be marketed for medical diagnosis, it must be submitted for approval by the FDA, which is responsible for assuring the safety and effectiveness of all medical devices marketed in the United States. In-vitro diagnostic devices intended for the analysis of human specimens for diagnosis and treatment must be approved by the FDA, and robots that are marketed to perform in-vitro diagnostic analyses would require FDA approval. Generating and preparing clinical data for submission to the FDA can be a costly and time-consuming endeavor, and to date laboratory manufacturers in the chemical and pharmaceutical industries have had enough other business that does not require premarket approval. As the industrial marketplace becomes saturated and robot manufacturers turn their attention to the medical marketplace, they will have to learn successful methods for obtaining FDA approval.

Cost. Investment in robotics in the United States lags far behind that of Japan. The Japanese spent $2.5 billion on robotics in 1989 compared with $400 million in the United States (*14*), an over sixfold higher investment in robotic technology. Only three hospitals have actively invested in robotic technology in the United States, and only the Cleveland Clinic Foundation has used the technology for a long enough period to see a return on the investment.

For fixed automation, the responsibility for consistently accurate clinical data lies primarily with the manufacturer that makes the reagents, maintains the hardware, and often provides a quality assurance program. If a manufacturer of an instrument does not deliver on the contracted promise, the analyzer is returned and a replacement from a competing vendor is brought in. However, the guarantee of success inherent with fixed automation is absent when robotic technology is bought by a hospital. Here, the administrator who purchased the robot is ultimately responsible for creating the environment (personnel and facilities) that will use the robot to its greatest advantage.

Hospital administrators have been

If it's LC,

The YMC Catalog provides a comprehensive selection of high performance LC products, including several new chemistries available only from YMC:

- a new line of polymeric gels developed by Mitsubishi Kasei for bio-separations
- new chiral phases for polar to non-polar separations
- 20 different silica and polymer based bonded phases for maximum selectivity
- empty and packed columns from 1.0mm to 200mm diameter plus peripheral support accessories to keep your lab at peak efficiency.

For a copy, just call. For technical assistance, call toll free 800 YMC-6311.

it's in here.

YMC, Inc.

51 Gibraltar Drive
Morris Plains, NJ 07950
201 285-1776
Fax: 201 285-5389
Telex: 3719839 YMC IN UB

CIRCLE 152 ON READER SERVICE CARD

slow to spend scarce health care dollars on a resource that until now has had few demonstrable applications. As more and more applications of robotics are seen in health care, we foresee more hospitals becoming actively involved in developing their own robotic applications.

Personnel. Introduction and maintenance of robots in the health care setting will require the combined skills of administrators, scientists, biomedical engineers, software designers, and clinical systems analysts. Health care scientists must first define the problem that is in need of automation. Systems analysts will decide how the automated technology would fit into the environment for providing health care, and software designers will create a user-friendly system. Many factors must be considered, including location in the health care center, impact on existing computer systems, effect on personnel use and morale and, ultimately, benefits to the patient.

Medical personnel will play a key role in determining the success of the robot. They will be responsible for verifying and ensuring the quality of robot services and for providing the skill to repair mechanical and electronic problems. Currently, very few health care centers possess the combined skills for the deployment of robotics in a timely and efficient manner. However, as more interest develops in the benefits afforded by robots and as more successful robotic systems are deployed, we believe that governmental, industrial, and health care personnel will be encouraged to use robotic automation that will improve the overall effectiveness, safety, and economy of health care.

References

(1) Castleberry, B. M.; Kuby, A. M.; Bryant, B. E. *Laboratory Medicine* **1989**, 437–41.
(2) Newman, A. R. *Anal. Chem.* **1990**, *62*, 1063 A–1065 A.
(3) Felder, R. A.; Boyd, J. C.; Margrey, K. S.; Holman, W.; Savory, J. *Clin. Chem.* **1990**, *36*, 1–10.
(4) Boyd, J. C.; Felder, R. A.; Savory, J.; Margrey, K. S.; Martinez, A.; Vaughn, D. In *Automation and New Technology in the Clinical Laboratory*; Okuda, K., Ed.; Blackwell Scientific Publications: Oxford, England, 1990.
(5) Kost, G. J. *Clin. Chem.* **1989**, *35*, 1232–33.
(6) Hilborne, L. H.; Oye, R. K. *Am. J. Clin. Pathol.* **1990**, *94*, 523–24.
(7) Brewer, D.; Schwartzentruber, K.; Taylor, A. *Appl. Environ. Microbiol.* **1990**, *56*, 819–22.
(8) Godfrey, O. W.; Ford, L. M.; Eaton, T. E. *Appl. Environ. Microbiol.*, in press.
(9) Caruthers, M. H. *Science* **1985**, *230*, 281–85.
(10) Kwoh, Y. S.; Hou, J.; Jonckheere, E. A.; Hayati, S. *IEEE Trans. Biomed. Eng.* **1988**, *35*, 153–60.
(11) Lob, W. S. *Clin. Chem.* **1990**, *36*, 1544–50.
(12) Shigeta, M.; Hirai, J.; Nagy, D. *Proceedings of the 2nd International Workshop on Medical and Health Care Robotics;* Cammell, J. E., Ed.; Newcastle, U.K., 1989, 373–83.
(13) Chesteen, S. A.; Warren, S. E.; Woolley, F. R. *J. Fam. Pract.* **1986**, *23*, 377–82.
(14) Katauskas, T. *R&D* **1990**, *32(6)*, 66–70.

Robin A. Felder, Ph.D. (upper row, second from left), is an associate professor of pathology at the University of Virginia Health Sciences Center and associate director of clinical chemistry and toxicology. He serves as the director of the clinical robots project. Felder received a B.S. degree in chemistry from the College of William and Mary and a Ph.D. in biochemistry from Georgetown University. His long-term plan for the clinical robotics development group is to design robotic systems that improve the quality and cost-effectiveness of health care delivery. In addition, the group plans to provide a facility with knowledgeable engineers and clinical chemists where commercial companies can alpha- or beta-test novel robotics and automation applications.

James C. Boyd, M.D. (upper row, third from left), is an associate professor of pathology and associate director of clinical chemistry and toxicology as well as director of laboratory computer services in the department of pathology. He holds a B.S. degree in applied mathematics from the University of Colorado and an M.D. from Washington University of Medicine. His interests center on computer-assisted interpretation of medical data and the use of artificial intelligence to aid in the integration of clinical laboratory automation.

John Savory, Ph.D. (upper row, far right) is professor of pathology and biochemistry and director of clinical chemistry and toxicology. He received a B.S. degree and a Ph.D. from Durham University (England). He has had a long-term interest in the development and implementation of automation in the clinical laboratory. He is responsible for the implementation and acceptance of robotics in the University Hospital.

Keith S. Margrey (upper row, far left) is the senior engineer of the robotics laboratory. He received a B.S. degree from James Madison University (1974) and a Master of Biomedical Engineering from the University of Virginia (1975). Margrey has worked within the clinical setting for the past 14 years in various support and engineering capacities. For the past six years he has concentrated on applications of automation within the clinical laboratory. His interests and expertise include microcomputer design and fabrication, software design, system communications interfacing, and electronic component design.

William Holman (lower right) is an electrical engineer who has worked in the robotics laboratory since 1989. He holds a B.S. degree from Bridgewater College (1979) and has worked in the clinical chemistry and toxicology laboratories for 10 years as a medical technologist. His interests include software design, automated clinical methods development, systems communications interfacing, database design, and LAN management.

John Roberts (lower left) is an aerospace engineer in the robotics laboratory. He received a B.S. degree in aerospace engineering from Boston University (1987). Before joining the robotics laboratory in 1990, he designed and fabricated electron guns for scientific research. His interests and expertise include mechanical design and implementation, programming, CAD, and electronic design and fabrication.

LABORATORY SERVICE CENTER

4-Aminoantipyrine • Ammonium Purpurate • Bindschedler's Green
2-Bromoethylamine HBr • tert-Butyl Chloride • Cesium Chloride
5-Chlorosalicylaldehyde • 3,5-Dichlorosalicylaldehyde • Esculin
Disodium Succinate • Ethyl Crotonate • Fluorescein • Furoic Acid
Hofmann's Violet • 3-Indolebutyric Acid • Levulinic Acid • Methyl Acetamide
Methyl-tert-Butyl Ether • Methylene Iodide • p-Naphtholbenzein
4-(4-Nitrobenzyl)Pyridine • Oxamide • Potassium & Sodium m-Periodates
Rhodanine • Sodium-4-Hydroxybutyrate • Thioacetamide • Veratraldehyde

Write for our Products List of over 3,000 chemicals

Tel: 516-273-0900 • TOLL FREE: 800-645-5566 Telefax: 516-273-0858 • Telex: 497-4275

EASTERN CHEMICAL
A Division of UNITED–GUARDIAN, INC.
P.O. Box 2500
DEPT. AC
SMITHTOWN, N.Y. 11787

Laboratory Service Center (Equipment, Materials, Services, Instruments for Leasing). Maximum space — 4 inches per advertisement. Column width, 2-3/16″; two column width, 4-9/16″. Artwork accepted. No combination of directory rates with ROP advertising. Rates based on number of inches used within **12** months from first date of first insertion. Per inch: **1″ — $175; 12″ — $170; 24″ — $165; 36″ — $160; 48″ — $155.**

CALL OR WRITE JANE GATENBY

ANALYTICAL CHEMISTRY
500 Post Road East
P.O. Box 231
Westport, CT 06880
203-226-7131/FAX: 203-454-9939

HELP WANTED ADS

ROP display at ROP rates. Rate based on number of insertions within contract year. Cannot be combined for frequency.

Unit	1-TI	6-TI	12-TI
1″ (25 mm)	$200	$180	$170
	24-TI	48-TI	72-TI
	$160	$150	$140

CALL OR WRITE JANE GATENBY

ANALYTICAL CHEMISTRY
500 Post Road East
P.O. Box 231
Westport, CT 06880
203-226-7131
FAX: 203-454-9939

FREE DATA, FAST

To quickly amass data on all of the products you need, consult the Lab Data Service Section on our *Analytical Chemistry* reader reply card insert.

JOURNAL OF CHEMICAL AND ENGINEERING

DATA

Get a World of Precise, Accurate Data.

Don't miss a single issue. Subscribe to JCED today!

Multidisciplinary in nature and international in scope, **Journal of Chemical and Engineering Data** features contributions by distinguished scientists from the world over. Their expert reports represent numerical data bases for private technical information systems, particularly in industry, that will broaden your scientific horizons and improve the quality of your work.

This quarterly journal publishes precise, accurate data on physical, thermodynamic, and transport properties of well-defined material. It also keeps you informed about the latest international standards on symbols, terminology, and units of measurement for reporting data properly.

EDITOR: Kenneth N. Marsh, *Texas A&M University*

Volume 36 (1991) 4 issues per year	ACS Members 1 year	ACS Members 2 years	Nonmembers 1 year
U.S.	$32	$57	$234
Canada & Mexico	$37	$67	$239
Europe*	$41	$75	$243
All Other Countries*	$41	$75	$243

*Air service included.

For more information or to subscribe, contact:
American Chemical Society, Marketing Communications Department, 1155 Sixteenth Street N.W., Washington, D.C. 20036

In a hurry?
Call Toll Free 1-800-227-5558 (U.S. and Canada)
In D.C. and outside the U.S. and Canada: call (202) 872-4363
Fax: (202) 872-4615; **Telex:** 440159 ACSPUI or 892582 ACSPUBS
Cable Address: JEICHEM

Member subscription rates are for personal use only. Subscriptions are based on a calendar year. Foreign payment must be made in U.S. currency, by international money order, UNESCO coupons, or U.S. bank draft, or order through your subscription agency. For nonmember rates in Japan, contact Maruzen Co., Ltd. This publication is available on microfilm, microfiche, and the full text is available online through CJO on STN International.

INDEX TO ADVERTISERS IN THIS ISSUE

CIRCLE INQUIRY NO.	ADVERTISERS	PAGE NO.
1	**ALEX '91** Interface Advertising Associates	711A
14	**Beckman Instruments, Inc.** Techmarketing	709A
50	***Gilson Medical Electronics, Inc.**	IFC
60	***Hewlett-Packard Company** Brooks Communications, Inc.	OBC
80	**Leica Inc.**	733A
92	***Matheson Gas Products** Kenyon Hoag Associates	707A
94	**The National Food Laboratory**	724A
122	**Rheodyne, Inc.** Bonfield Associates	714A
136	***Tekmar**	724A
138	**Thermo Jarrell Ash Corporation** Noon Advertising, Inc.	703A
152	**YMC, Inc.**	746A

Directory section, see page 748A.
** See ad in ACS Laboratory Guide.*
Advertising Management for the American Chemical Society Publications

CENTCOM, LTD

President
James A. Byrne
Executive Vice President
Benjamin W. Jones

Robert L. Voepel, *Vice President*
Joseph P. Stenza, *Production Director*

500 Post Road East
P.O. Box 231
Westport, Connecticut 06880
(Area Code 203) 226-7131
Telex No.643310
FAX: 203-454-9939

ADVERTISING SALES MANAGER
Bruce E. Poorman

ADVERTISING PRODUCTION MANAGER
Jane F. Gatenby

SALES REPRESENTATIVES

Philadelphia, PA . . . CENTCOM, LTD., GSB Building, Suite 405, 1 Belmont Avenue, Bala Cynwyd, Pa. 19004. Telephone: 215-667-9666, FAX: 215-667-9353

New York/New Jersey . . . Dean A. Baldwin, John F. Raftery, CENTCOM, LTD., Schoolhouse Plaza, 720 King Georges Post Road, Fords, NJ 08863, Telephone: 908-738-8200, FAX: 908-738-6128

Westport, CT . . . Edward M. Black, CENTCOM, LTD., 500 Post Road East, P.O. Box 231, Westport, Ct. 06880. Telephone: 203-226-7131, Telex 643310, FAX: 203-454-9939

Cleveland, OH . . . Bruce E. Poorman, CENTCOM, LTD., 325 Front St., Suite 2, Berea, Ohio 44017. Telephone: 216-234-1333, FAX: 216-234-3425

Chicago, IL . . . Michael J. Pak, CENTCOM, LTD., 540 Frontage Rd., Northfield, Ill. 60093. Telephone: 708-441-6383, FAX: 708-441-6382

Houston, TX . . . Michael J. Pak, CENTCOM, LTD. Telephone: 708-441-6383

San Francisco, CA . . . Paul M. Butts, CENTCOM, LTD., Suite 1070, 2672 Bayshore Frontage Road, Mountain View, CA 94043. Telephone: 415-969-4604, FAX: 415-969-2104

Los Angeles, CA . . . Paul M. Butts, CENTCOM, LTD. Telephone: 415-969-4604.

Boston, MA . . . Edward M. Black, CENTCOM, LTD. Telephone: 203-226-7131

Atlanta, GA . . . CENTCOM, LTD. Telephone: 216-234-1333

Denver, CO . . . Paul M. Butts, CENTCOM, LTD. Telephone: 415-969-4604

United Kingdom
Reading, England . . . Malcolm Thiele, Technomedia Ltd., Wood Cottage, Shurlock Row, Reading RG10 OQE, Berkshire, England. Telephone: 0734-343302, Telex #848800, FAX: 0734-343848
Lancashire, England . . . Technomedia Ltd., c/o Meconomics Ltd., Meconomics House, 31 Old Street, Ashton Under Lyne, Lancashire, England. Telephone: 061-308-3025

Continental Europe . . . Andre Jamar, International Communications, Inc., Rue Mallar 1, 4800 Verviers, Belgium. Telephone: (087) 22-53-85, FAX: (087) 23-03-29

Tokyo, Japan . . . Sumio Oka, International Media Representatives Ltd., Room 100, 21 Bldg., 2-2-22 Okusawa, Setagaya-ku, Tokyo 158 Japan. Telephone: 502-0656, Telex #22633, FAX: 5706-7349

Keep track of hundreds — even thousands — of chemicals . . .

NEW! *Chemstock*

Chemical Inventory Database for the Macintosh

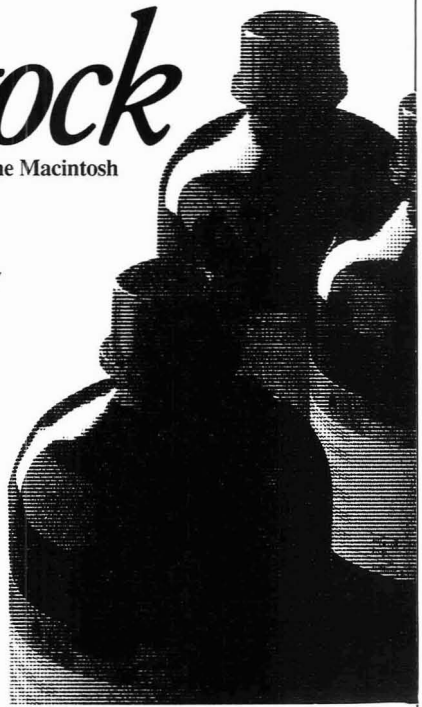

ACS Software
Produced by American Chemical Society

The perfect database for small to mid-sized labs. *ChemStock* is a unique stockroom database that lets you track the chemicals you have on hand. Quickly check quantities, locations, suppliers, and more, using simple standard Macintosh application features.

Searches and sorts the way a chemist would

ChemStock can search and sort by chemical name or formula, quickly reducing a structural formula to its molecular formula for easy searching. And *ChemStock* alphabetizes from a chemist's point of view; gives numbers secondary priority, ignores certain characters, and orders the entries the way a chemist would.

Provides a smooth transition to smarter management

If you are using a general database program, HyperCard, or a spreadsheet to manage inventory, *ChemStock* will import your current files easily. So you can be up and running fast, taking full advantage of *ChemStock's* specialized database management power.

In short, *ChemStock* is chemistry-literate, simple to learn, simple to operate, and a perfect tool for small to mid-sized labs. It's brand new ... and available only from the ACS.

Hardware requirements: Any Macintosh.
Produced by: American Chemical Society
List price: $199
Member price: $149
Academic price: $149

Order today using the coupon below!

Order Form

Send this order form with your payment or purchase order to: American Chemical Society, Distribution Office Dept. 07, PO Box 57136, West End Station, Washington, DC 20037. Call toll-free 1-800-227-5558. In Washington, DC call 202-872-4363. Or fax your order to 202-872-6067.

Yes! Please send me *ChemStock* as indicated below:

Chemstock, ISBN 0-8412-1926-5

- ☐ $199, list price
- ☐ $149, member price
- ☐ $149, academic price

The ACS Guarantee:

If you are unhappy with your purchase or if a program fails to meet your expectations in any way, simply return it within 30 days for a full refund.

Ship to:

Name _____

Address _____

City, State, ZIP _____

Payment Options

☐ Payment enclosed (make checks payable to American Chemical Society).

☐ Purchase order enclosed. P.O. # _____

☐ Charge my ☐ MasterCard/VISA ☐ American Express

Account # _____ Expires _____

Name of cardholder _____

Signature _____

All prices are in U.S. dollars and are valid throughout the U.S. and Canada and are subject to change without notice. Foreign customers, please add 20% to the total order. Canadian and foreign payment must be made in U.S. currency by international money order, UNESCO coupons, or U.S. bank draft. 07

Analytical CHEMISTRY

EDITOR: **ROYCE W. MURRAY**

ASSOCIATE EDITORS: **Catherine C. Fenselau, Georges Guiochon, Walter C. Herlihy, Robert A. Osteryoung, Edward S. Yeung**

Editorial Headquarters
1155 Sixteenth St., N.W.
Washington, DC 20036
Phone: 202-872-4570
Telefax: 202-872-4574
Bitnet: rmh96@cas

Managing Editor: Sharon G. Boots
Assistant Managing Editor: Mary Warner
Senior Editor: Louise Voress
Associate Editor: Grace K. Lee
Assistant Editors: Jane K. Baker, Felicia Wach
Contributing Editor: Marcia Vogel
Director, Operational Support: C. Michael Phillippe
Head, Production Department: Leroy L. Corcoran
Art Director: Alan Kahan
Composition Systems Administrator: Vincent L. Parker
Designers: Peggy Corrigan, Robert Sargent
Production Editors: John W. Laine, Elizabeth Wood
Circulation: David Schulbaum
Editorial Assistant, LabGuide: Joanne Mullican

Journals Dept., Columbus, Ohio
Associate Head: Marianne Brogan
Editorial Office Manager: Mary Scanlan
Journals Editing Manager: Joseph E. Yurvati
Associate Editor: Terri Bailey
Assistant Editor: Stephanie R. Harrell

Advisory Board: Michelle V. Buchanan, M. Bonner Denton, Bernard J. Bulkin, Renaat Gijbels, William S. Hancock, Timothy D. Harris, Thomas L. Isenhour, James W. Jorgenson, Philip D. LaFleur, Alan G. Marshall, John F. Rabolt, Debra R. Rolison, Shigeru Terabe, Michael Thompson, George S. Wilson, Richard N. Zare
Ex Officio: Sam P. Perone

Instrumentation Advisory Panel: Daniel W. Armstrong, Anna Brajter-Toth, Thomas L. Chester, R. Graham Cooks, Jack D. Henion, Sanford P. Markey, Dallas L. Rabenstein, Brenda R. Shaw, Gary W. Small

Published by the
AMERICAN CHEMICAL SOCIETY
1155 16th Street, N.W.
Washington, DC 20036

Publications Division
Director: Robert H. Marks
Journals: Charles R. Bertsch
Special Publications: Randall E. Wedin

Manuscript requirements are published in the January 1, 1991 issue, page 89. Manuscripts for publication (4 copies) should be submitted to ANALYTICAL CHEMISTRY at the ACS Washington address.

The American Chemical Society and its editors assume no responsibility for the statements and opinions advanced by contributors. Views expressed in the editorials are those of the editors and do not necessarily represent the official position of the American Chemical Society.

AUTHOR INDEX

Aiken, J. H., 1372
Allain, P., 1497
Amatore, C., 1403
Anson, F. C., 1501
Aomura, Y., 1376
Ashley, D. L., 1419

Bartelt, J., 1403
Bean, M. F., 1473
Berman, S. S., 1488
Beu, S. C., 1452

Carlson, R. J., 1449
Carr, S. A., 1473
Caruso, J. A., 1491
Caudill, S. P., 1419
Chen, L., 1499
Chien, R.-L., 1354
Cohen, A. S., 1346

Delaporte, T., 1497
de Loos-Vollebregt, M. T. C., 1441
Deterding, L. J., 1467

Evans, C. E., 1393

Fagioli, F., 1409
Fosset, B., 1403
Fukii, H., 1433

Garai, T., 1409
Gaskell, S. J., 1473
Gehrig, P. M., 1380
Giddings, J. C., 1366
Guevremont, R., 1488
Guilment, J., 1425

Hartwick, R. A., 1372
Helmer, J. C., 1354
Hillenkamp, F., 1463
Hogan, J. D., 1452
Houk, R. S., 1458
Huie, C. W., 1372
Huser, M., 1380

Imasaka, T., 1433
Ishibashi, N., 1433

Jaunault, L., 1497
Jeney, J., 1380
Jorgenson, J. W., 1467

Karas, M., 1463
Karger, B. L., 1346
Keough, T., 1482
Kuhr, W. G., 1413
Kwak, J., 1501

Lacey, M. P., 1482
Laude, D. A., Jr., 1452
Le Blanc, J. C. Y., 1488
Lee, C., 1501
Lin, C.-H., 1433
Lindner, E., 1380
Locatelli, C., 1409

Majidi, V., 1452
Martire, D. E., 1350
Mauras, Y., 1497
McGuffin, V. L., 1393
Mermet, J.-M., 1497
Moon, M. H., 1366
Morf, W. E., 1380
Moseley, M. A., 1467
Myers, M. N., 1366

Northrop, D. M., 1350
Nozaki, K., 1387

Ogino, H., 1376
Okazaki, S., 1387
Oyama, M., 1387

Pantano, P., 1413
Pirkle, J. L., 1419
Pungor, E., 1380

Reilly, M. H., 1473
Rush, R. S., 1346

Sakairi, M., 1488
Scott, R. P. W., 1350
Seki, T., 1376
Shen, W.-L., 1491
Sheppard, B. S., 1491
Simon, W., 1380
Siu, K. W. M., 1488
Smith, F. G., 1458
Smith, S. J., 1419
Stahl, B., 1463
Steup, M., 1463

Thorne, G. C., 1473
Tomer, K. B., 1467
Tőth, K., 1380

van Veen, E. H., 1441
Vela, N. P., 1491
Villaseñor, S. R., 1362

Wang, J., 1499
Wang, T., 1372
Wiederin, D. R., 1458
Wightman, R. M., 1403
Williams, P. S., 1366
Windig, W., 1425
Wright, J. C., 1449

Yergey, A. L., 1488

Influence of Column Temperature on the Electrophoretic Behavior of Myoglobin and α-Lactalbumin in High-Performance Capillary Electrophoresis

Robert S. Rush, Aharon S. Cohen, and Barry L. Karger*

Barnett Institute, Northeastern University, 360 Huntington Avenue, Boston, Massachusetts 02115

The influence of column temperature on the electrophoretic behavior of myoglobin and α-lactalbumin in high-performance capillary electrophoresis (HPCE) is presented. The major effect of temperature is to shorten the analysis time by decreasing the viscosity, but specific temperature effects on the protein migration behavior were also observed. Myoglobin, under high field (350 V/cm), was essentially temperature stable from 20 to 45 °C, but at constant current, a second form of myoglobin could be detected at both 214 and 410 nm. The initial form appeared to correspond to the Fe^{3+} and the second to the Fe^{2+} oxidation state of the heme iron. The rate of conversion from Fe^{3+} to the reduced Fe^{2+} in myoglobin, under given electrophoretic conditions, followed first-order kinetics with a rate constant at 30 °C of 304 s^{-1}. A second protein, α-lactalbumin type III, demonstrated a conformational transition that resulted in asymmetric peaks and sigmodial mobility plots versus temperature in the transition region.

INTRODUCTION

High-performance capillary electrophoresis (HPCE) can be viewed as a complementary method to high-performance liquid chromatography (HPLC) for the analysis of peptides and proteins. Temperature can potentially be an important selectivity factor in HPCE as in HPLC. There are at least two aspects of the influence of temperature in HPCE that need to be considered: (1) the impact of temperature on the electrophoretic behavior due to changes in electroosmotic mobility (μ_{eo}) and electrophoretic mobility (μ_{ep}) and (2) the effect of temperature on the structure of the protein, which may undergo thermally induced changes. A corollary of temperature manipulation is the Joule heat generated by the high electric fields. This heat must be actively dissipated; otherwise, the temperature of the buffer will be elevated (*1*).

In this paper, the influence of column temperature on the electrophoretic behavior of two proteins, horse heart myoglobin and bovine α-lactalbumin type III (calcium depleted), has been studied. Myoglobin is stable in the 20–45 °C temperature range and is typical of small globular proteins (*2*). However, in a recent paper sample degradation of myoglobin appeared to occur as the temperature was elevated from 20 to 50 °C (*3*). This anomaly is studied here. As a second example, α-lactalbumin type III is known to have a conformational transition near room temperature (*4*). In addition, conformational alteration of the protein has been studied in depth by chromatography (*5*). Conformational transitions may result in effective charge of hydrodynamic shape changes, or both, and such changes could result in variation in migration time and peak shape of the protein. This paper documents such behavior.

EXPERIMENTAL SECTION

Commercial grade horse heart myoglobin and bovine α-lactalbumin type III (Sigma Chemical Co., St. Louis, MO) were used without further purification. Stock samples were prepared by dissolving the proteins in HPLC grade water at a concentration of 1.0 mg/mL, and aliquots were stored at −20 °C. (For other proteins, maintainence of native conditions may require dilute buffer concentrations in the sample solvent.) Under normal conditions, just prior to electrophoresis, the protein samples were diluted to 0.2 mg/mL in HPLC grade water. The electrophoretic bulk flow marker was 0.02% (v/v) mesityl oxide in water (Aldrich Chemical Co., Milwaukee, WI).

Oxidized myoglobin (ferric) was prepared by bubbling oxygen through the sample for 1 h prior to use. Reduced myoglobin (ferrous) was prepared from the oxidized sample by sodium dithionite (Sigma), and the excess sodium dithionite was removed from the sample by gel filtration on a column of Sephadex G-25 (Pharmacia Fine Chemicals, Piscataway, NJ).

HPCE conditions were as follows: a Beckman P/ACE System 2000 (Beckman Instruments, Palo Alto, CA) was employed throughout the study. Peaks were integrated with Beckman System Gold. The capillary had an effective length of 50 cm and a total length of 57 cm and was operated at defined fields of 250, 350, and 450 V/cm, respectively, unless otherwise specified. The electropherograms were UV monitored on-column at 214 or 410 nm. The buffer was 0.1 M tetrasodium borate, pH 8.3, unless otherwise noted. Samples were pressure injected from vials that were maintained at ambient temperature.

The operation of the electrophoresis system was under computer control. The capillary was first rinsed under high pressure (25 psi) with 0.1 N NaOH for 0.5 min. The capillary was then rinsed under high pressure with electrophoresis buffer for 0.7 min and allowed to equilibrate in the absence of field for 0.5 min. This wash and equilibration step was required for reproducibility (see Table I). Sample injection was conducted under low positive pressure (0.5 psi) for 3 s. Absorbance full scale was set at 0.05 AU. The detector rise time was 0.1 s, and the data collection rate was 5 Hz. Current data were simultaneously collected on data channel B.

The system performance was primarily evaluated by examining the electroosmotic flow at each temperature. Additionally, the influence of temperature on the protein absorbance as well as on the volume injected at each temperature was examined. Each

Table I. Relative Standard Deviation of Migration Time, Peak Area, and Peak Height as a Function of Column Temperature[a]

parameter	myoglobin	α-lactalbumin
	At 20 °C	
migration time	0.35	0.56
peak area	1.49	1.28
peak height	2.17	3.73
	At 35 °C	
migration time	0.09	0.04
peak area	2.31	1.45
peak height	2.35	1.18
	At 50 °C	
migration time	0.25	0.23
peak area	0.09	1.17
peak height	1.21	2.10

[a] Conditions as follows: 350 V/cm in 0.1 M borate buffer, pH 8.3, at the designated temperatures. Each set of experiments was repeated five times.

* To whom correspondence should be addressed.

0003-2700/91/0363-1346$02.50/0 © 1991 American Chemical Society

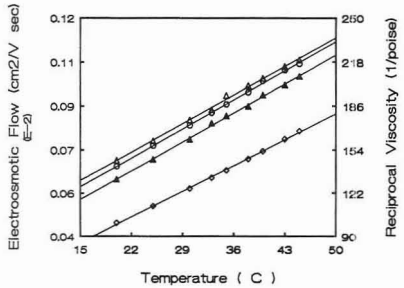

Figure 1. Electroosmostic flow (mesityl oxide) versus temperature for three electric fields: 250 V/cm (open triangles), 350 V/cm (open circles), and 450 V/cm (filled triangles). The reciprocal viscosity of water as a function of temperature is shown as open diamonds (right axis).

HPCE experiment was repeated five times at selected temperatures from which the mean value and the standard deviation were calculated. The number of different temperatures utilized were $N = 9$ for myoglobin and $N = 10$ for α-lactalbumin covering a temperature range from 20 to 45 or 50 °C, respectively.

RESULTS AND DISCUSSION

Influence of Temperature on System Parameters. The electroosmotic flow at various temperatures from 20 to 50 °C at three electric fields, 250, 350, and 450 V/cm, is presented in Figure 1. The operating power range for these experiments was from 0.2 to 1.25 W/m. The plots are parallel and linear for the three fields with correlation coefficients of 0.998, 0.999, and 0.999, respectively. It can be concluded that the resistance is constant at a given temperature and that the temperature regulation is effective under these conditions. While successful as a measure of electroosmotic flow, mesityl oxide was somewhat problematical in this study because of volatility at the elevated temperatures. Other bulk flow markers such as riboflavin may also be employed.

The viscosity of water decreases from 1.00 to 0.55 cP over the temperature range of 20 to 50 °C, i.e., by a factor of 1.82. The electroosmotic flow increased with temperature by a factor of about 1.75 over the same temperature range. Thus, it appears temperature-induced viscosity changes predominately account for the change in electroosmotic flow (μ_{eo}) with temperature (see Figure 1)

$$\mu_{eo} = \epsilon\zeta/4\pi\eta_w \quad (1)$$

where ϵ = dielectric constant, ζ = the zeta potential of the wall, and η_w = the viscosity of the solution in the double layer at the wall (*6*).

Influence of Temperature on Myoglobin Electrophoresis. Figure 2 shows constant field (350 V/cm) electropherograms (corrected for electroosmotic flow) generated for horse heart myoglobin at 214 nm and six column temperatures. The electropherograms demonstrate that, with increasing temperature, the migration, as expected, was faster. A standard curve of integrated area versus concentration of myoglobin was linear with the y intercept nearly at the origin, $r^2 = 0.999$. It was therefore concluded that sample recovery from the capillary was good. Additionally, the integrated peak area with pressurized injection was found to increase with temperature, and the reason for this is discussed later.

As already noted, we previously found sample degradation with temperature increase (*3*); however, those experiments were run at constant current. By this procedure, the myoglobin sample remained in the capillary for roughly the same time as the temperature was varied. On the other hand, the time spent in the column continually decreased with increased temperature at constant field, Figure 2.

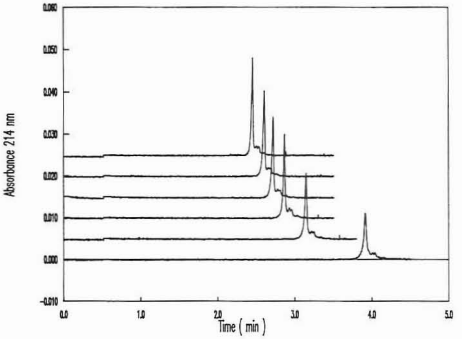

Figure 2. Electropherograms of horse heart myoglobin (0.2 mg/mL) at 20, 30, 35, 40, 45, and 50 °C (ascending direction) at a field of 350 V/cm. Sample was dissolved in water and electrophoresis conducted in 0.1 M tetrasodium borate buffer, pH 8.3, and monitored at 214 nm. The 75-μm (i.d.) capillary had a effective length of 50 cm and a total length of 57 cm. The electropherograms have been corrected for electroosmotic flow. For more details, see Experimental Section.

We reexamined the constant current procedure, and the experiments at various temperatures are shown in Figure 3A (monitored at 214 nm) and Figure 3B (monitored at 410 nm). It can be seen that at 20 °C a single peak was observed, whereas a second slow migrating peak appeared at 30 °C. The second peak grew at the expense of the first at 40 °C, and at 50 °C, essentially only the second peak was observed. The identical pattern seen for 214 and 410 nm strongly suggests, as expected, that a significant conformational change has not occurred. Since the heme group is not covalently attached to the protein molecule, a conformational change typically results in the release of the prosthetic group (*7*, *8*).

Another possible explanation for the behavior in Figure 3 is the reduction of Fe^{3+} to Fe^{2+} metal ion coordinated to the heme group. Physiologically, the iron is in the ferrous form in tissue (*9*). However, exposure to oxygen is known to result in oxidation to the ferric state (*7*).

To test the possibility of the two forms being different oxidation states of iron, freshly prepared myoglobin in water was aerated with oxygen for 1 h. The sample was then electrophoresed at 200 V/cm, on a 50-cm effective length capillary at 35 °C (conditions favorable for observance of the two forms of myoglobin; see Figure 3). A single sharp peak was observed in Figure 4. The oxidized sample was then reduced by the addition of 50 μg of sodium dithionite, and the excess sodium dithionite was removed by passing the reduced sample through a G-25 Sephadex column. The sample was then re-electrophoresed under identical conditions, and a single peak was again seen, but at a longer migration time, Figure 4. Finally, a mixture of four parts oxidized and one part reduced myoglobin was electrophoresed, and two peaks in the appropriate ratio were observed in Figure 4. The results of these experiments confirm that the observed forms of myoglobin represent the two oxidation states of iron, i.e., Fe^{3+} and Fe^{2+}. The faster migrating peak corresponded to the more positive ferric form and the slower moving peak to the ferrous form. This order is expected on the basis of charge differences.

Returning to Figure 3, it is clear that reduction of Fe^{3+} to Fe^{2+} was taking place within the column. The kinetics of conversion from Fe^{3+} to Fe^{2+} were studied by varying the time that myoglobin spent in the column by electric field changes, i.e., the lower the field, the slower the migration time. Figure 5 presents electropherograms for myoglobin at 30 °C in 0.1 M Tris, 0.025 M boric acid, pH 8.6, under electric fields of 100, 150, 200, 300, and 350 V/cm, respectively, and monitored

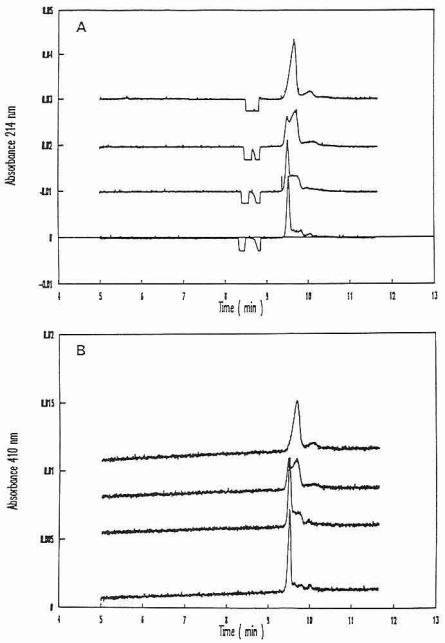

Figure 3. (A) Influence of temperature on the electrophoretic behavior of horse heart myoglobin (0.2 mg/mL) under constant current conditions (9.8 μA) in 0.1 M Tris and 0.025 mM boric acid, pH 8.6. Electrophoresis was conducted at 20, 30, 40, and 50 °C, (ascending direction) at fields of 262, 213, 178, and 153 V/cm, respectively, and monitored at 214 nm. The 75-μm (i.d.) capillary had an effective length of 50 cm and a total length of 57 cm. (B) All conditions as in A except monitored at 410 nm.

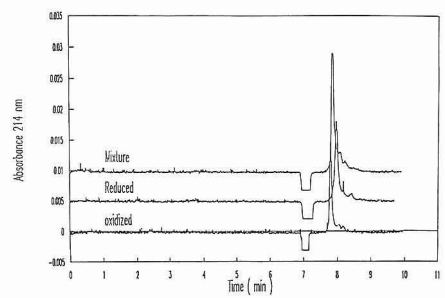

Figure 4. Comparison of the electrophoretic mobility of the ferric (Fe^{3+}) and ferrous (Fe^{2+}) forms of myoglobin. The lower electropherogram is that of the ferric form; the center corresponds with the sodium dithionite reduced ferrous form. The upper is a mixture of four parts ferric and one part ferrous. Electrophoresis buffer conditions were as in Figure 3A; field 200 V/cm, 50-cm effective length, and 35 °C. Details given in text.

at 410 nm. Identical patterns were obtained at 214 nm. The migration time was linear with applied field, $r^2 = 0.969$, and the total integrated area was constant (1.84 ± 0.14). The rate of conversion of peak 1 into the slower moving peak 2 followed first-order kinetics with a rate constant of 304 s^{-1}, $r^2 = 0.973$.

The possibility of applied field influencing the rate constant was studied by varying the column length and maintaining a constant electric field at various temperatures. Over the

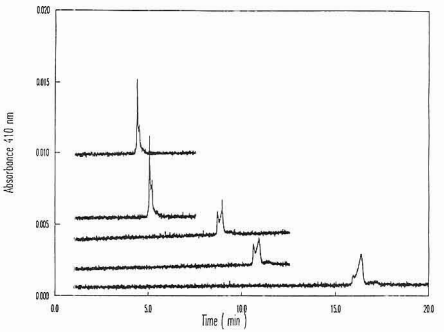

Figure 5. Influence of varying electric field (100, 150, 200, 300, and 350 V/cm, ascending direction) on the behavior of horse heart myoglobin at 30 °C, monitored at 410 nm. Conditions as in Figure 3A.

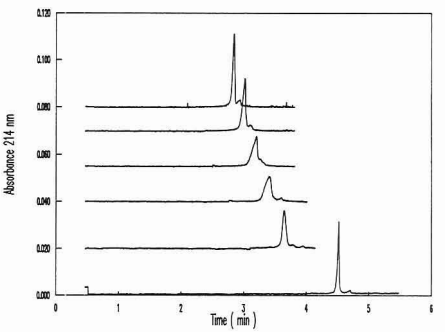

Figure 6. Comparison of the influence of temperature on the electrophoretic behavior of α-lactalbumin (0.2 mg/mL) at 20, 30, 35, 40, 45, and 50 °C (ascending direction) at a field of 350 V/cm. Conditions as in Figure 2.

range studies, field-induced changes appear not to take place because nearly identical profiles were observed at 150 and 200 V/cm using three temperatures (30, 35, and 40 °C) and three effective column lengths (50, 90 and 140 cm) (see Figure 6 for the 200 V/cm profiles). Approximating the rate constant under these conditions produced values in the same order of magnitude.

The mechanism of reduction in the column is interesting to consider. One possibility is a reducing agent impurity in the buffer system. Another possible explanation may be autoreduction, in which an amino acid residue in myoglobin is the reducing agent. Such behavior is known to occur for other heme proteins (*8*). It is interesting that the rate of reduction appeared to be temperature dependent; see Figure 3. Both explanations would be consistent with such behavior.

From the above data, sample handling in the case of myoglobin (as well as other heme proteins) would appear to be a significant consideration in HPCE analysis. Depending on handling and HPCE conditions, a single peak or two peaks may be observed. As in chromatography (*9*), the extent of interconversion of the two forms will be a function of the time spent in the column and the temperature of that column.

Influence of Temperature on α-Lactalbumin. As noted, α-lactalbumin type III (calcium depleted) represents a model protein with which to evaluate temperature-induced conformational changes (*4, 5*). Figure 6 shows electropherograms generated at a constant field of 350 V/cm for α-lactalbumin at 214 nm at six column temperatures. Since the pI of α-

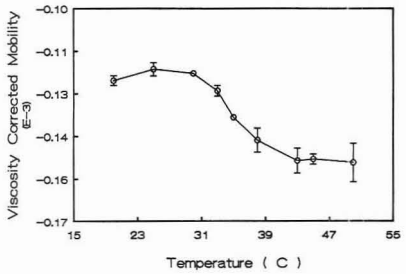

Figure 7. Viscosity-corrected electrophoretic mobility of α-lactalbumin versus temperature at 350 V/cm. Other conditions as in Figure 2.

lactalbumin is 4.2–4.5 (*4*), operation at 8.3 should lead to minimal adsorption of the protein on the column wall. At 20 °C, a single, relatively sharp peak was observed. As the temperature was raised to 30, 35, and 40 °C, the peak broadened substantially, in spite of the fact that migration was faster. Moreover, severe peak distortion was observed at 35 and 40 °C. At 45 and 50 °C, the peak again sharpened. This behavior of α-lactalbumin mimics that found in chromatography where a conformational change was observed (*5*, *10*).

In order to explore the electrophoretic behavior in more detail, we normalized the mobility of the protein to 20 °C in the following manner. First, the mobility of α-lactalbumin (μ_{ep}) was determined from the measured mobility (μ_{app}) as

$$\mu_{ep} = \mu_{app} - \mu_{eo} \quad (2)$$

In this study, the peak maximum was taken as a measure of migration time. The use of the centralized first moment did not significantly change this value. Next, we assumed the major bulk change due to temperature was buffer viscosity. We corrected μ_{ep} at any temperature X to 20 °C by

$$\mu_{ep}^{20°C} = \mu_{ep}^{X°C}(\eta^{20°C}/\eta^{X°C}) \quad (3)$$

where η is the viscosity of water at the given temperature.

A plot of $\mu_{ep}^{20°C}$ versus column temperature at 350 V/cm is shown in Figure 7. The expected sigmodial curve is observed with an approximate transition temperature of 32–33 °C. Intrinsic fluorescence measurements under the same buffer conditions revealed a transition temperature of 31 °C (*11*). The results of Figure 7 are thus consistent with a thermally induced conformational change (*12*). Note that the unfolded state migrated with a faster mobility (more negative) than the folded state. While the unfolded state may be expanded, it is possible that a greater number of negative charges are exposed in this state. Evidently, the enhanced broadening in the transition temperature region, seen in Figure 6, is a consequence of a mixture of two conformational states with different migration times. As in chromatography, distorted peak shapes may reflect a transition region.

Influence of Column Temperature on the Amount Injected. If the column temperature is purposely to be varied to optimize separation, then one must also recognize that the amount injected will be temperature dependent, even if injection conditions remain constant. In this work, pressurized injection was employed, and we will now show the effect of temperature on the volume delivered to the column.

The volume injected can be calculated from the well-known Poiseuille equation

$$V = (\Delta P \pi r^4 t)/(8\eta L) \quad (4)$$

where V is the volume injected, ΔP the pressure difference between the ends of the capillary, r the internal radius of the capillary, t the injection time, η the viscosity of the column buffer at defined temperatures, and L the total length of the capillary. It can be seen that the volume is inversely proportional to the viscosity of the buffer solution, which is highly temperature dependent (≈2%/°C). Figure 8A presents the calculated volume as a function of column temperature from 20 to 45 °C, using the standard conditions for injection and the temperature variation of the viscosity of water. There is almost a 70% increase in the calculated volume injected over the given temperature range.

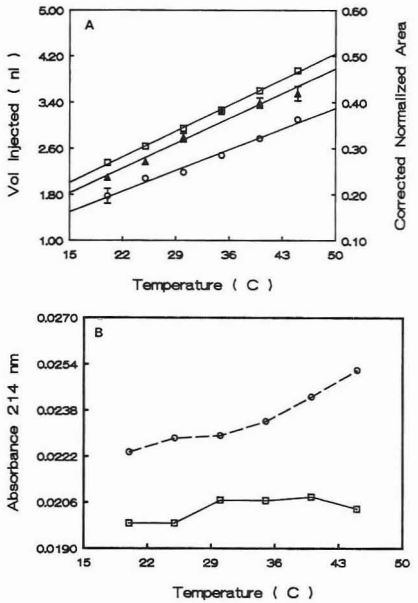

Figure 8. (A) Volume injected (open squares) calculated from the Poiseuille equation as a function of column temperature (left axis). The absorbance corrected normalized integrated area for α-lactalbumin (closed triangles) and for myoglobin (open circles) versus temperature (right axis) (see text for discussion). (B) Absorbance of α-lactalbumin (open circles) and horse heart myoglobin (open squares) against temperature. These measurements were conducted by filling the 75-μm (i.d.) capillary with 0.2 mg/mL protein solutions maintained at ambient temperature. Absorbance readings were taken after 3-min incubation, and the system was rinsed with buffer between readings and calibrated.

We next measured the amount injected of the two proteins, myoglobin and α-lactalbumin, as a function of column temperature. The amount was determined from the integrated peak area after applying two corrections for temperature. First, the peak area was corrected for the change in solute velocity with temperature by dividing the integrated area by the migration time. Second, the change in extinction coefficient with temperature was corrected. Figure 8B presents the absorbance versus temperature data for myoglobin and α-lactalbumin at 214 nm. The absorbance of the protein solutions were determined by filling the capillary with the protein at the designated temperature and reading the absorbance after a 3-min incubation period. Myoglobin absorbance was essentially constant while α-lactalbumin exhibits an increase of about 15%, this latter change being related to the conformational change. The absorbance correction was calculated by multiplying the normalized area by the ratio of the absorbance at 20 °C to that determined at the given temperature.

Returning to Figure 8A, the corrected peak area versus column temperature is presented. It can be seen that α-lact-

albumin followed quite closely to the expected variation in volume with temperature. In the case of myoglobin, there was also reasonable correspondence; however, the slope was slightly lower than the calculated volume change. Nevertheless, the results of Figure 8 clearly show a strong temperature dependence. A corollary of this study is that precision in the amount injected will depend strongly on the column temperature being maintained constant.

Finally, the precision of the measurements with column temperature controlled is shown in Table I. The relative standard deviation in migration time was found to be 0.5% or less, that of the peak area 2.3% or less, and that of peak height 3.8% or less. It is interesting to note that good precision is obtained even at 50 °C. The values in Table I are comparable to those reported by other authors in HPCE (*13*).

CONCLUSIONS

This study has been shown that column temperature can dramatically affect the electrophoretic pattern of proteins in HPCE. Reduction of iron in the heme protein, myoglobin, has been observed. Moreover, this on-column reduction is kinetically controlled, and column temperature affects the rate significantly. Thus, the specific electrophoretic pattern observed will be dependent on sample handling of myoglobin, column temperature, electric field, and column length, among other factors. In addition, we have observed the electrophoretic consequences of a conformational change in α-lactalbumin. In analogy to the behavior in HPLC, the temperature region where both the folded and conformationally altered species simultaneously exist yields an electrophoretic peak that is significantly broadened and somewhat asymmetric.

The results point to the need for good temperature control in order to achieve a reproducible electrophoretic pattern. Moreover, as in HPLC (*5*, *9*, *10*), it must be recognized that broadened or multiple peaks do not necessarily mean that a protein sample is impure. Finally, since other proteins may be far less labile than those studied here, subambient temperature control is a desirable feature of HPCE equipment in the future. Operation at 4 °C is often recommended for protein separations on slab gels as well (*14*).

ACKNOWLEDGMENT

We gratefully acknowledge support by Beckman Instruments, Inc., and the James L. Waters chair in analytical chemistry. We further thank Dr. Shiwen Lin and Dr. Peter Oroszlan for helpful discussions.

LITERATURE CITED

(1) Hjerten, S., *Electrophoresis* **1990**, *11*, 665–690.
(2) Privalov, P. L. *Adv. in Protein Chem.* **1979**, *33*, 167–241.
(3) Nelson, R. J.; Paulus, A.; Cohen, A. S.; Guttman, A.; Karger, B. L. *J. Chromatogr.* **1989**, *480*, 111–127.
(4) Kronman, M. J. *Critical Reviews in Biochemistry & Molecular Biology*; CRC Press: Boca Ratan, FL, 1989; Vol. 24, pp 566–667.
(5) Oroszlan, P.; Blanko, R.; Lu, X.-M., Yarmush, D.; Karger, B. L. *J. Chromatogr.* **1990**, *500*, 481–502.
(6) Terabe, S.; Otsuka, K.; Ando, T. *Anal. Chem.* **1989**, *61*, 251–260.
(7) Rothgeb, T. M.; Gurd, F. N. R. *Methods Enzymol.* **1978**, *52*, 473–486.
(8) Mayo, S. L.; Ellis, W. R., Jr.; Crutchley, R. J.; Gray, H. B. *Science* **1986**, *233*, 948–942.
(9) Lu, X. M.; Benedek, K.; Karger, B. L. *J. Chromatogr.* **1986**, *359*, 19–29.
(10) Wu, S. L.; Benedek, K.; Karger, B. L. *J. Chromatogr.* **1986**, *359*, 3–17.
(11) Oroszlan, P.; Karger, B. L. Unpublished results.
(12) Kim, P. S.; Baldwin, R. L. *Ann. Rev. Biochem.* **1982**, *51*, 459–489.
(13) Moring, S. E.; Colburn, J. C.; Grossman, P. D.; Lauer, H. K. *LC-GC* **1990**, *8*, 34–46.
(14) Chrambach, A. *The Practice of Quantitative Gel Electrophoresis*; VCH: Deerfield Beach, FL, 1985; Chapter 5.

RECEIVED for review December 20, 1990. Accepted March 14, 1991. This is contribution No. 421 from the Barnett Institute of Chemical Analysis and Material Science.

Preparation and Evaluation of a Bimodal Size-Exclusion Chromatography Column Containing a Mixture of Two Silicas of Different Pore Diameter

David M. Northrop, R. P. W. Scott, and Daniel E. Martire*

Chemistry Department, Georgetown University, Washington, D.C. 20057

Size-exclusion results from four different pore-sized silicas were used to select two of these silicas for use in a bimodal size-exclusion column. A mixture of 80- and 500-Å pore-sized silicas provided an exclusion curve of elution volume versus log molecular weight with a linear range from 5×10^2 to 2×10^6 MW. The exclusion properties were retained when a reversed-phase packing was prepared by using the mixed pore-sized silica. Column efficiency was found to be virtually independent of pore size.

INTRODUCTION

Size-exclusion chromatography (SEC) is a liquid chromatographic method that provides molecular weight discrimination of samples. Conditions are chosen such that interactions between the solute and the stationary phase are minimized. As a result, separations occur based on a solute's ability to migrate into and out of the pores of the stationary phase. This is largely determined by the solute's size, specifically the solute's hydrodynamic radius (the molecule and associated solvent) or the radius of gyration for macromolecules (the coiled molecule plus associated and entrained solvent) (*1*), which are related to a solute's molecular weight and shape. Because there is essentially no interaction of solutes with the stationary phase, there is no retention; thus, each solute's elution volume is no greater than the total solvent volume of the column, V_t.

As described by Alhedai et al. (*2*), V_t can be divided into several different regions including contributions from the various parts of the interstitial, V_i, and pore volumes, V_p, where V_t is the sum of V_i and V_p. Nonionic molecules may sample as much of the total solvent volume as their size will permit. As the effective size of a solute increases, it is excluded

0003-2700/91/0363-1350$02.50/0 © 1991 American Chemical Society

from pores that are smaller. If a solute is completely excluded from the pores, it may only sample the accessible interstitial volume. Thus, in SEC, all solutes elute between the accessible interstitial volume and the total solvent volume. Because of this limited range, the analysis is rapid and complete, but this is at the expense of selectivity. It has been shown (*1*) that columns with different pore-size stationary phases provide separations over different molecular weight ranges; thus, it is possible to select a column to provide information about solutes in many different ranges.

SEC has been applied to a variety of separation problems, particularly those involving macromolecules. Polymers with a narrow molecular weight distribution can be separated into narrow bands (*3*), while the characteristic molecular weight distribution curve of broad molecular weight polymers can also be obtained (*4*). SEC of biopolymers has been of particular interest with the development of many procedures for the molecular weight separation of peptides and proteins (*5*).

The narrow molecular weight range that can be separated by a single pore-sized column is one of the limitations of SEC. Ambler et al. (*6*) demonstrated the use of several columns, containing silicas of varying pore sizes, in series to provide a wide range of molecular weight separations. Yau et al. (*7*) found that using a bimodal column set could produce the same result as long as the two columns were picked such that their individual linear exclusion ranges did not overlap. The resulting columns in series provided exclusion over a molecular weight range equal to the combination of both individual ranges. It was also found that the same result could be achieved by manufacturing a single silica particle containing both pore sizes. This was accomplished by layering microspheres of one pore size over a core of microspheres of another pore size. Thus, it is possible to obtain exclusion of solutes over a 4–5-decade molecular weight range by using either two columns in series or a single column containing bimodal pore-sized silica particles.

The purpose of this paper is to describe the characterization of silica packing materials, to be used in SEC, and to describe a simple procedure for the formulation of a single mixed-bed column containing bimodal pore-size silica, using the resulting information. The effect of pore size on efficiency was also studied to determine if mixing silica particles would have any effect on efficiency and, in particular, on the resistance to mass-transfer term. One of the primary reasons for constructing such a column was to study the retention behavior of macromolecules, under reversed-phase conditions, in a system where the exclusion effects were well characterized and where polymers as large as 2×10^6 MW would not be completely excluded. That study is the subject of a subsequent paper.

It should be mentioned that mixed beds of polymer gels have been prepared and utilized in the separation of hydrophilic (*8*) and hydrophobic (*9*) polymers using gel-permeation chromatography (GPC). Columns for this type of work are commercially available. However, silica-based columns are not as expensive as gel columns, they are not as sensitive to solvent changes, they are not as prone to damage if the solvent dries out of the column, and they can, in general, withstand higher operating pressures.

The idea of mixed-bed silicas was suggested in a patent by Kirkland and Yau (U.S. Patent 4160728) and was at one time marketed by Waters Associates, Inc. (Milford, MA), under the trade name μBondagel, E-linear. Specific details as to the procedures for the formulation of these types of columns are not available and, therefore, are presented here.

The effect of pore size on efficiency has been examined by de Vries et al. (*10*) for silica particles and by Copper and Johnson (*11*) for porous glass. However, neither study looked at the specific effect of pore size on the various terms of the van Deemter equation and, in particular, the resistance to the mass-transfer term. Careful characterization of mixed-bed silica columns with respect to efficiency also has not been reported.

Table I. Solutes Used for the SEC Study

solute	MW, g/mol
benzene	78.12
naphthalene	128.19
anthracene	178.24
sodium iodide	149.89
polystyrene (PS)	
PS 517	517
PS 1024	1 024
PS 4000	4 000
PS 9000	9 000
PS 17500	17 500
PS 30740	30 740
PS 50000	50 000
PS 100000	100 000
PS 233000	233 000
PS 390000	390 000
PS 600000	600 000
PS 1800000	1 800 000
PS 2800000	2 800 000
PS 15000000	15 000 000
PS 30000000	30 000 000

EXPERIMENTAL SECTION

Four standard high-performance liquid chromatography (HPLC) columns, 25.0 cm × 0.46 cm, each packed with a different pore-sized (80-, 120-, 300-, and 500-Å average pore diameter) 5-μm particle-size silica, were received from Advanced Separation Technologies, Inc. (ASTEC). All solvents were either HPLC grade or Spectra-analyzed grade from Fisher Scientific (Fair Lawn, NJ). Probe solutes (see Table I) included reagent-grade benzene, naphthalene, anthracene, sodium iodide, and narrow distribution molecular weight standard polystyrenes obtained from Scientific Polymer Products, Inc. (Ontario, NY). 4-(Dimethylamino)pyridine was purchased from Sigma (St. Louis, MO) and *n*-butyldimethylchlorosilane from Petrarch Systems, Inc. (Bristol, PA).

The HPLC system consisted of a Beckman Model 112 pump, a Valco injector with a 0.5-μL internal sample loop, a specially constructed ultraviolet absorbance detector operating at 254 nm with a specially designed 2-μL flow cell, and a constant-temperature circulating bath, which maintained the column temperature at 30.00 ± 0.02 °C throughout the experiments. Elution volumes and flow rates were measured by using a 5.00-mL graduated buret (1 division = 0.01 mL ± 0.001 mL). A Perkin-Elmer Model 56 chart recorder was used for data collection. All solvents were degassed by stirring under vacuum.

Procedures. All experiments described herein were performed in triplicate unless otherwise noted. The size-exclusion properties of each column used in this project were determined by the following procedure. Tetrahydrofuran (THF) was pumped through the column at a flow rate of 0.5 mL/min (the actual flow rate was accurately determined). Injections (0.5 μL) of the polystyrene standards, at approximately 0.05 mg/mL, were made. The retention volume of each solute was measured by using the calibrated buret to collect the effluent.

Efficiency studies were conducted with a 90% THF, 10% H_2O mobile phase with NaI as a pore-excluded marker, to determine the mobile-phase linear velocity, and benzene as the pore probe. Flow rates of 0.1, 0.2, 0.4, 0.8, 1.6, and 3.2 mL/min were used with the linear velocity determined by

$$\bar{u} = L/(V_{ex}/F) \quad (1)$$

where $\bar{u}$ is the linear velocity in cm/s, L is the column length in cm, V_{ex} is the retention volume of the pore-excluded NaI in mL, and F is the volumetric flow rate in mL/s. The efficiency (N = theoretical plates) was determined by

$$N = 4(t_R/w_i)^2 \quad (2)$$

where t_R is the retention time of benzene and w_i is the peak width

Table II. Results of the Total Column Volume Studies

column, Å	V_t, mL	$V_{benzene}$, mL	% diff
80	3.031	2.969	2.09
120	3.207	3.104	3.32
300	3.415	3.363	1.55
500	3.338	3.273	1.99
Mix-NP[a]	3.189	3.158	0.98
Mix-RP[b]	2.999	2.913	2.95

[a] Mix-NP = mixed silica, normal phase. [b] Mix-RP = mixed silica, reversed phase.

at $0.6065h$ where h is the peak height. The height equivalent to a theoretical plate (H) was calculated by

$$H = L/N \tag{3}$$

Values of H and $\bar{u}$ were used to construct plots of H versus $\bar{u}$ and $H\bar{u}$ versus $\bar{u}$, with the latter plot being fitted to a second-order polynomial in order to determine the multipath term, A, the longitudinal diffusion term, B, and the resistance to mass-transfer term, C, according to the van Deemter equation

$$H = A + B/\bar{u} + C\bar{u} \tag{4}$$

or

$$H\bar{u} = A\bar{u} + B + C\bar{u}^2 \tag{4a}$$

Total solvent volume was determined by the small probe solute method and by the column weighing method (2). Benzene was used as the small probe solute and its retention volume measured with neat THF as the mobile phase. The columns were weighed after equilibration with each of four solvents with different densities. The total solvent volume, V_t (mL), was calculated by

$$V_t = (W_1 - W_2)/(d_1 - d_2) \tag{5}$$

where W_1 and W_2 are the weights of the column plus solvents 1 and 2 and d_1 and d_2 are the densities of solvents 1 and 2 in g/mL.

A mixed pore-sized silica was prepared by thorough mixing of 4.80 g of 80-Å pore-sized silica and 5.20 g of 500-Å pore-sized silica. This mixed silica (3.68 g) was reacted following the procedure of Sentell et al. (12) using n-butyldimethylchlorosilane to form a C_4-bonded phase for future reversed-phase studies.

Phase loading was determined as per Sander (13):

$$N_{PL} = 10^6 P_c/S[1200n_c - P_c(M - 1)] \tag{6}$$

where N_{PL} is the surface coverage in μmol/m^2; P_c is the percent carbon, as determined by elemental analysis from Galbraith Laboratories, Inc. (Knoxville, TN); S is the surface area of the silica substrate in m^2/g, as determined by the BET method at ASTEC; n_c is the number of carbons in the bonded phase chain; and M is the molecular weight of the bonded phase chain in g/mol.

Two columns were packed with mixed silica (one normal phase and one reversed phase) by using pentane as a slurry solvent, at 6300 and 9000 psi, respectively, for vertical slurry packing. Each of these columns was examined by using the procedures described above. Exclusion work on the reversed-phase column was done with methylene chloride and THF as the mobile phases so that comparisons to other work could be made.

RESULTS AND DISCUSSION

Molecular weight calibration of the four single pore-sized silica columns was done by measuring the exclusion volume of each of the aromatic and polystyrene solutes listed in Table I. A plot of exclusion volume versus log of molecular weight

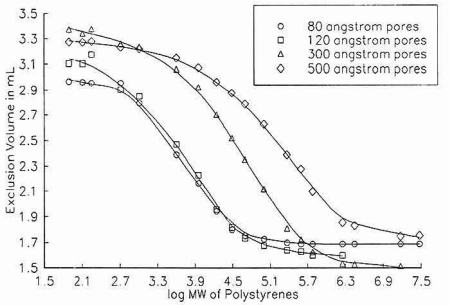

Figure 1. Size-exclusion curves for four different pore-sized silica columns. Conditions: solvent, THF; flow, 0.5 mL/min.; injection of polystyrene solutions, 0.5 μL; detection, 254 nm.

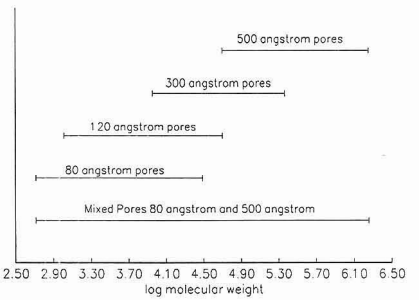

Figure 2. Molecular weight range over which linear size exclusion is provided by different pore-sized silicas. Data extracted from Figure 1 results.

is seen in Figure 1. The log-linear region on each curve is the region where separation based on size-exclusion occurs. Columns with different pore-sized silicas provide exclusion separations over different molecular weight ranges as seen in Figure 2. It is also interesting to note the larger slope of the linear region for the 300-Å column as compared to the other three columns, indicating that the *relative* pore-size distribution for the 300-Å column is skewed more toward the smaller pore diameters. Information from ASTEC indicated that the silica for the 300-Å column was obtained from one source while the silica for the other three columns was obtained from another source.

Total solvent volume and efficiency studies were also conducted on each of these columns. The results of the column weighing and small probe solute procedures are shown in Table II. Note that there is consistently a slightly larger total solvent volume obtained by the weighing method.

The efficiency study results are listed in Table III. The values of F_{opt} were found by

$$F_{opt} = \bar{u}_{opt} V_i/L \tag{7}$$

Table III. Results of the Column Efficiency Studies

column, Å	H_{min}, cm	N_{max}[a]	$\bar{u}_{opt}$, cm/s	A, cm	B, cm^2/s	C, s
80	1.05×10^{-3}	23 800	0.184	2.36×10^{-4}	7.47×10^{-5}	2.21×10^{-3}
120	0.95×10^{-3}	26 300	0.206	3.15×10^{-4}	6.18×10^{-5}	1.45×10^{-3}
300	1.36×10^{-3}	18 300	0.222	2.81×10^{-4}	12.00×10^{-5}	2.44×10^{-3}
500	1.06×10^{-3}	23 600	0.210	4.50×10^{-4}	6.38×10^{-5}	1.45×10^{-3}
Mix-NP	1.15×10^{-3}	21 800	0.181	2.41×10^{-4}	8.21×10^{-5}	2.51×10^{-3}
Mix-RP	1.42×10^{-3}	17 600	0.229	2.11×10^{-4}	13.88×10^{-5}	2.64×10^{-3}

[a] N_{max} = theoretical plates.

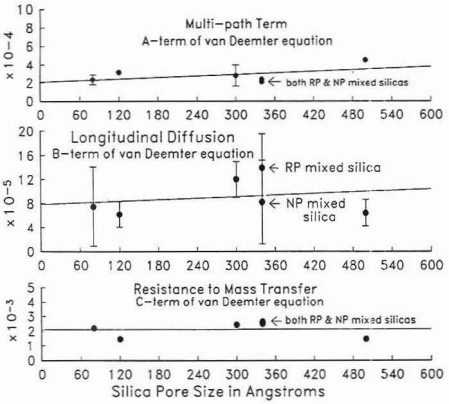

Figure 3. Plot of van Deemter equation constant terms versus average pore diameter. Data extracted from Table III. Error bars are given where significantly larger than data points.

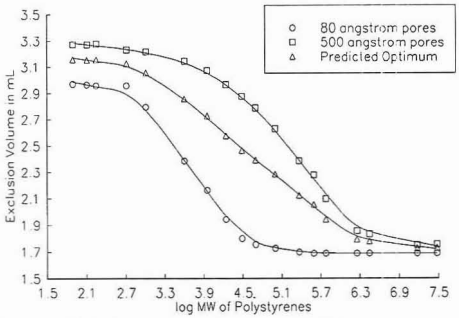

Figure 4. Exclusion results for the 80- and 500-Å pore-sized silicas and the predicted, optimized exclusion curve using 38% of the 80-Å exclusion volumes and 62% of the 500-Å exclusion volumes. Conditions are the same as in Figure 1.

where $\bar{u}_{opt}$ is found by taking the partial derivative of eq 4a and solving for $\bar{u}$, which gives

$$\bar{u}_{opt} = (B/C)^{0.5} \quad (8)$$

Substitution of eq 8 into eq 4 allows one to calculate the minimum plate height, H_{min}, and thus from eq 3 the maximum efficiency, N_{max}.

The purpose of the efficiency study was to determine if changes in pore size had any significant effect on the efficiency or any of the terms in the van Deemter equation. Figure 3 shows plots of the A, B, and C terms, of eq 4 and 4a, versus average pore diameter. The results indicate that these terms are largely independent of pore size. As can be seen, the efficiency data for the mixed-silica columns, which will be discussed later, also follow this trend.

The 80- and 500-Å pore-sized silicas were selected to be used in a mixture based on the nonoverlap of their linear exclusion regions. The optimum exclusion curve was determined by calculating the contributions from each of the silicas by using the lever rule. The result was a mixture in which 38% of the exclusion volume was contributed by the 80-Å silica and 62% by the 500-Å silica. The resulting optimum exclusion volume versus log MW curve demonstrates a linear region from 5×10^2 to 2×10^6 MW as seen in Figure 4. It was found that a limited range of volume percentages around 40:60 would also provide the desired results, giving rise to the idea that an exact

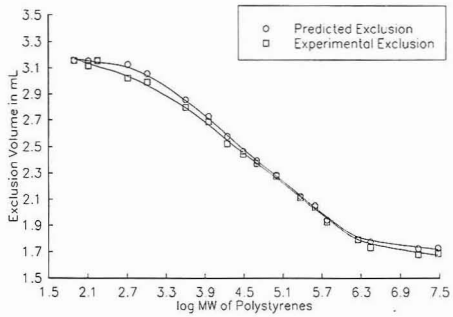

Figure 5. Comparison of the predicted optimized exclusion curve from Figure 4 with exclusion results from the normal-phase mixed-silica column. Conditions are the same as Figure 1.

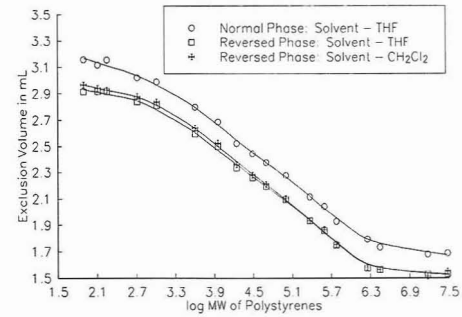

Figure 6. Exclusion results for the normal-phase mixed-silica column using THF as the eluting solvent and exclusion results for the reversed-phase mixed-silica column using THF as the eluting solvent and CH_2Cl_2 as the eluting solvent.

formulation is not critical. The tap densities for the 80- and 500-Å silicas are 0.60 and 0.40 g/mL, respectively. Thus, the weight ratio for the optimum mixture was 48% of the 80-Å silica and 52% of the 500-Å silica. Two mixed-silica columns, one normal phase and one reversed phase, were fabricated as described in the Experimental Section, and these columns were examined for their total solvent volume, efficiency, and exclusion properties. The results of the total solvent volume and efficiency studies are listed in Tables II and III and are similar to those obtained for the single pore-sized silica. Figure 5 shows a comparison of the exclusion results obtained experimentally on the normal-phase, mixed-silica column versus the predicted optimum exclusion curve. The two curves are in close agreement with each other and provide linear exclusion ranges from 5×10^2 to 2×10^6 MW, with correlation coefficients of 0.9971 and 0.9975, respectively.

Since adsorption of biopolymers on silica is a problem, a nonpolar stationary phase was made. Kirkland et al. (*14*) suggested the use of short-chain reversed phases such as the *n*-butyldimethylchlorosilane phase for use in the analysis of biopolymers. Figure 6 shows the SEC results on both the normal-phase column and the reversed-phase column, with the reversed-phase column being examined with two different mobile phases. It is interesting to note that the curves exactly parallel each other, but the reversed-phase curves are shifted to lower exclusion volumes. This suggests that the exclusion volume is lowered by the volume taken up by the added reversed phase. Observations by Vivileechia et al. (*3*), with polymeric organosilane surface modifiers, and Sander et al. (*15*), on monomeric and polymeric C_{18} reversed-phase columns,

support this. The volume of the stationary phase, V_{sp}, can be estimated by

$$V_{sp} = g_{sp}/d_{sp} \quad (9)$$

where d_{sp} is the density of the reversed-phase silane and g_{sp} is the grams of stationary phase, which is determined by

$$g_{sp} = g_p P_c MW_{bp}/MW_c n_c \quad (10)$$

where g_p is the grams of packing used, P_c is the percent carbon, MW_c is the molecular weight of carbon, n_c is the number of carbons in the bonded phase, and MW_{bp} is the molecular weight of the bonded-phase chain. The reversed-phase column was found to have a bonded-phase volume of 0.133 mL by this method. The average volume difference between the exclusion results for the normal-phase and reversed-phase columns, using THF, was 0.185 mL. This would suggest that the addition of the bonded phase may have reduced access to or within some of the pores, since the decrease in the exclusion volume is somewhat larger than would be expected due to the volume taken up by the bonded phase.

CONCLUSION

We have demonstrated in this study that bimodal pore-sized mixtures can be easily prepared from two different pore-sized silicas with the resulting column exhibiting an exclusion volume versus log molecular weight plot with a linear exclusion range that encompasses the linear exclusion ranges of both silicas. By careful selection of the two silicas, a wide range of molecular weights may be examined by SEC in a short period of time. It was also found that efficiency is not significantly affected by pore size, allowing for the combination of various silicas without a loss in efficiency. Finally, the addition of a reversed phase does not alter the exclusion properties of the column other than to decrease uniformly the total solvent volume in the column. However, the volume taken up by the bonded phase is larger than would be predicted, which suggests that some restriction of the pores may be occurring.

In a subsequent paper, the specific retention behavior of polymers on the mixed-silica, reversed-phase column will be considered using various mixed-solvent mobile phases. The exclusion properties and column efficiency of this optimized blend have been carefully evaluated, thus permitting a more definitive examination of retention mechanisms (*16*).

ACKNOWLEDGMENT

We thank Tom Beesley (ASTEC) for providing the normal-phase silica columns and silica for the mixed-, normal-, and reversed-phase columns. We also acknowledge Lane Sander (NIST) for assistance in preparation and packing of the mixed-silica columns.

Registry No. SiO_2, 7631-86-9; PS, 9003-53-6.

LITERATURE CITED

(1) Snyder, L. R.; Kirkland, J. J. *Introduction to Modern Liquid Chromatography*, 2nd ed.; Wiley: New York, 1979.
(2) Alhedai, A.; Martire, D. E.; Scott, R. P. W. *Analyst* **1989**, *114*, 869.
(3) Vivileechia, R. V.; Lightbody, B. G.; Thinot, N. Z.; Quinn, H. M. *J. Chromatogr. Sci.* **1977**, *15*, 434.
(4) Buytenhuys, F. A.; van der Maeden, F. P. B. *J. Chromatogr.* **1978**, *149*, 489.
(5) Welling, G. W.; Welling-Webster, S. In *HPLC of Macromolecules: A Practical Approach*; Janson, J. C., Ryden, L., Eds.; VCH Inc.: New York, 1989.
(6) Ambler, M. R.; Fetters, L. J.; Kester, Y. *J. Appl. Polym. Sci.* **1977**, *21*, 2439.
(7) Yau, W. W.; Ginnard, C. R.; Kirkland, J. J. *J. Chromatogr.* **1978**, *149*, 465.
(8) Kato, Y.; Matsuda, T.; Hashimoto, T. *J. Chromatogr.* **1985**, *332*, 39.
(9) Schultz, H. S.; Alden, P. G.; Ekmanis, J. L. *ACS Symp. Ser.* **1984**, *245*, 145.
(10) de Vries, A. J.; LePage, M.; Beau, R.; Guillemin, C. L. *Anal. Chem.* **1967**, *39*, 935.
(11) Copper, A. R.; Johnson, J. F. *J. Appl. Polym. Sci.* **1971**, *15*, 2293.
(12) Sentell, K. B.; Barnes, K. W.; Dorsey, J. G. *J. Chromatogr.* **1988**, *455*, 95.
(13) Sander, L. C. *CRC Crit. Rev. Anal. Chem.* **1987**, *18*, 299.
(14) Kirkland, J. J.; Glajch, J. L.; Farlee, R. P. *Anal. Chem.* **1989**, *61*, 2.
(15) Sander, L. C.; Glinka, C. J.; Wise, S. A. *Anal. Chem.* **1990**, *62*, 1099.
(16) Alhedai, A.; Boehm, R. E.; Martire, D. E. *Chromatographia* **1990**, *29*, 313 and references cited within.

RECEIVED for review September 17, 1990. Revised manuscript received March 28, 1991. Accepted April 5, 1991. This material is based upon work supported by the National Science Foundation under Grant CHE-8902735.

Electroosmotic Properties and Peak Broadening in Field-Amplified Capillary Electrophoresis

Ring-Ling Chien* and John C. Helmer

Varian Research Center, 611 Hansen Way, Palo Alto, California 94303

Electroosmotic flow in a fused-silica capillary column, partially filled with a buffer of one concentration and containing a second buffer of the same composition but different concentration, is studied. The bulk electroosmotic velocity in this kind of mixed buffer system is derived and shown to be a weighted average of the electroosmotic velocities of the pure buffers. The theory of laminar flow caused by the mismatch between electroosmotic velocities is developed and shown to cause extra peak broadening for samples inside the column. Good agreement with experimental results is found. The length of new buffer introduced by electroinjection can be determined from the variation in electrophoretic current during injection.

INTRODUCTION

High-performance capillary electrophoresis (HPCE) is a major analytical technique for fast and efficient separation of charged species in solutions (*1*). In HPCE, a high voltage is applied across a fused-silica capillary column filled with an electrolytic buffer. Charged species introduced at one end of the column migrate under the influence of the electric field to the other end of the column. The migration velocity of a particular ion species is a combination of the electrophoretic velocity of that species and the bulk electroosmotic velocity of the buffer. Under ideal circumstances, where molecular diffusion is the primary source of zone broadening, the separation efficiency is proportional to the field strength times

0003-2700/91/0363-1354$02.50/0 © 1991 American Chemical Society

the length of the column, i.e., the applied voltage. Separation efficiency up to several million theoretical plates has been reported (*2*, *3*).

One possible way to achieve high field strength with low voltage and reduced heating is to use field-amplified capillary electrophoresis. In field-amplified capillary electrophoresis, the open column is filled with two different concentrations of the same buffer at a given pH. The electric field strength in the region that has lower concentration will be higher because of its higher resistivity.

The amount of the amplified field strength depends on the ratio of the resistivities of the two regions. A sample can be injected into the region of lower buffer concentration and experience an amplified electric field. Unfortunately, there is a peak-broadening mechanism in field-amplified capillary electrophoresis originating from the mismatch of electroosmotic velocities in the two regions. The local electroosmotic velocity in the high-field region is much faster than the local electroosmotic velocity in the low-field region. As a consequence, an electroosmotic pressure and a laminar flow will be generated at the interface between regions with different concentrations and enhance the diffusion of the sample inside the column.

Electroosmotic flow is one of the most interesting properties of HPCE. The electroosmotic force in a capillary column is produced by an electric field and transmitted by the drag of ions acting in a thin sheath of charged fluid adjacent to the silica wall of the column. The origin of the charge in the sheath is an unbalance between positive and negative ions in the bulk solution which balances a fixed charge on the silica wall and generates a zeta potential.

While the electrophoretic velocity of an ion is simply the product of its electrophoretic mobility and the electric field strength acting on it, the analysis of the electroosmotic velocity of the bulk solution is rather complicated. In columns where the electric field strength E and the zeta potential ζ of the wall are constant throughout the column, the bulk electroosmotic velocity can be expressed as $\mu_{eo}E$, where $\mu_{eo} = \epsilon\zeta/4\pi\eta$ is called the electroosmotic mobility and ϵ is the dielectric constant and η is the viscosity in the double layer at the wall. However, in cases where there is a nonconstant distribution in either electric field strength or zeta potential throughout the column, the bulk velocity has to be averaged over the whole column.

A great deal of work has been done to manipulate the electroosmotic flow inside silica capillaries in an effort to increase the resolution in HPCE (*4*–*6*). Generally, resolution is increased when electroosmotic velocity is reduced. However, any technique that produces variations in the electroosmotic velocity along the column is doomed to fail because of peak broadening from laminar flow. Although the mechanism of this "enhanced diffusion" due to laminar flows was recognized before (*7*, *8*), the importance and applications in HPCE have not been elucidated. In addition, although the relationship between electroosmotic mobility and buffer concentration has been investigated by many people (*9*–*11*), the influence of a plug of low-concentration buffer on the average electroosmotic velocity of a column filled with high-concentration buffer is not well understood.

In this report, we develop a simple model to calculate the average electroosmotic velocity and the variances of sample peaks in field-amplified capillary electrophoresis, using a capillary column filled with two different concentrations of the same buffer. Experimental data obtained in this kind of a mixed system are also presented. Good agreement with the predications based on the simple model is observed.

THEORY

Electric Properties and the Concentration Boundary in Field-Amplified Capillary Electrophoresis. In field-amplified capillary electrophoresis, a capillary column of length L is filled with two different concentration buffers of the same electrolyte. Assuming a length xL of the column is filled with concentration 1 and a length $(1 - x)L$ of the column is filled with concentration 2, where $0 \leq x \leq 1$, then the total resistance R of the column will be

$$R = (\rho_1 x + \rho_2(1 - x))\frac{L}{A} \tag{1}$$

where ρ_1 and ρ_2 are the resistivities of buffer 1 and buffer 2, respectively, and A is the cross section of the column.

If one now applies a voltage V across the column, the electric current I will then have the value according to

$$I = \frac{VA}{L(\rho_1 x + \rho_2(1 - x))} \tag{2}$$

This equation can be rearranged and solved for x as

$$x = \frac{(I_2/I) - 1}{(I_2/I_1) - 1} \tag{3}$$

where $I_1 = VA/\rho_1 L$ and $I_2 = VA/\rho_2 L$ are the currents when the column is completely filled with only concentration 1 or 2, respectively. Equation 3 indicates that, if the currents I_1 and I_2 are known, one can calculate and control the filled length x by monitoring the current I of the mixed system.

Since the electric field strength E is simply the product of the current density and the resistivity, the local field strengths E_1 and E_2 in the two regions with different concentrations are given by

$$E_{1,2} = \frac{E_0\rho_{1,2}}{\rho_1 x + \rho_2(1 - x)} \tag{4}$$

where $E_0 = V/L$ is the field strength of a uniform system, whether it is buffer 1 or buffer 2. Equation 4 shows that while the field strength inside the lower resistance region is less than the original uniform field strength, the field strength inside the higher resistance region will be amplified (increased).

While the absolute value of the electric field strength in regions 1 and 2 will depend on x, the ratio between them will remain a constant and only depends on the resistivities

$$E_1/E_2 = \rho_1/\rho_2 \tag{5}$$

In general, the resistivities ρ are inversely proportional to the concentrations C for the same buffer composition. Hence, the ions inside the lower concentration region will experience higher electric field strength and move faster than the ions inside the higher concentration region. Once they pass the concentration boundary, they will experience lower electric field strength and slow down.

If there is no electroosmotic flow, the flux of ions out of the concentration boundary will be exactly equal to the flux toward it. Consequently, this concentration boundary will be stationary, neglecting the effect of diffusion (*12*). In other words, the apparent movement of the concentration boundary in field-amplified capillary electrophoresis comes solely from the electroosmotic flow of the whole bulk solution. This pseudostationary concentration boundary is the major difference between field-amplified capillary electrophoresis and isotachophoresis. In isotachophoresis, where one has different electrolyte solutions in different regions of a single column, the electric fields are inversely proportional to the effective mobilities of the solution inside each region. The boundary is then moving at a constant velocity (*13*).

Electroosmotic Properties in Field-Amplified Capillary Electrophoresis. In the double-layer model, the electroosmotic mobility is proportional to the zeta potential at the silica/water interface. This zeta potential is simply the

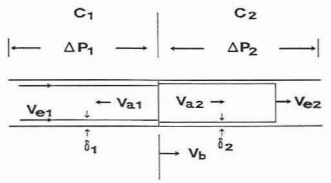

Figure 1. Pressure drops (ΔP_1, ΔP_2) and the laminar flows (V_{a1}, V_{a2}) generated from the mismatch between local electroosmotic velocities (V_{e1}, V_{e2}) and the bulk velocity (V_b) in a column with two different concentrations (C_1 and C_2). δ is the sheath or double-layer thickness.

product of the charge on the interface and the Debye length, which (in a common model) is inversely proportional to the square root of the ionic strength, or the concentration. As the concentration increases, the electroosmotic mobility decreases (*14*). In a column filled with only a single buffer of fixed concentration, the electric field strength is uniformly distributed throughout the column. Consequently, the electroosmotic velocity, which is equal to the electroosmotic mobility times the electric field strength, is also a constant throughout the whole length of the column.

In the case where a concentration boundary exists, the electric field strength will be distributed according to eq 4. In addition, the electroosmotic mobility is also greater in the lower concentration region, which further enhances the difference in the local electroosmotic velocities between two regions. Nevertheless, the amount of compound flow across any plane perpendicular to the column has to be the same according to the continuity principle in a noncompressible fluid. This means that the bulk solution and the concentration boundary are moving at an averaged velocity v_b. The difference in the local electroosmotic velocities and the bulk velocity will generate a hydrostatic pressure across the local regions as shown in Figure 1.

The higher electroosmotic velocity of the input section is then balanced by the hydrostatic pressure, which drives fluid back along the axis of the column, while the fluid in the second section is driven forward along the axis, relative to the lower electroosmotic flow (*15*). A detailed discussioon of this theory of electroosmotic–laminar flow in a column with two buffers is presented in the Appendix.

Physically speaking, the concentration boundary now behaves as a soft wall between two regions of different concentration. If the leading buffer has a slower electroosmotic velocity than the bulk velocity, this soft wall will be pushed forward by the trailing buffer. On the other hand, if the leading buffer has a faster electroosmotic velocity, it then will pull the soft wall along.

In the cases where the resistance to laminar flow is much less than the resistance to electroosmotic flow, we have a simple relation between the bulk velocity v_b and the local electroosmotic velocities in the two buffer region. From eqs A8 and A9 in the Appendix

$$v_b = xv_{e1} + (1 - x)v_{e2} \tag{6}$$

where v_{ej}, j = 1 or 2, are the local electroosmotic velocities. This equation shows that the concentration boundary will move with a weighted average of the electroosmotic velocities.

The local electroosmotic velocity v_{ej} is simply proportional to the local electric field given in eq 4 so that

$$v_{ej} = \frac{v_{eoj}\rho_j}{\rho_1 x + \rho_2(1 - x)} \tag{7}$$

where v_{eoj} is the electroosmotic velocity in a column filled with only a single buffer j of a fixed concentration. Substituting eq 7 into eq 6, we obtain

$$v_b = \frac{\rho_1 x v_{eo1}}{\rho_1 x + \rho_2(1 - x)} + \frac{\rho_2(1 - x)v_{eo2}}{\rho_1 x + \rho_2(1 - x)} \tag{8}$$

Equation 8 shows that the average electroosmotic velocity of the system is not only weighted over the filled lengths of their components but also weighted over their partial resistances. This means that a small plug of low concentration buffer will greatly influence the average bulk electroosmotic velocity of the system.

Laminar Flow and Peak Broadening. The pressure difference caused by the mismatch between local electroosmotic velocity and the bulk velocity will then generate a laminar flow (*16*). The velocity distribution of this laminar flow has a parabolic profile with an average laminar velocity v_a that is exactly equal to the difference between the bulk velocity and the local electroosmotic velocity (see Appendix).

It is well-known that a laminar flow will broaden a narrow band of sample by adding an enhanced diffusivity $D_a = r_0^2 v_a^2/48D$, where r_0 is the radius of the column and D is the normal diffusivity of the sample ions (*17*). The variance of the peak, due to the laminar flow alone after a period of time t, is equal to $2D_a t$ or

$$\sigma_a^2 = \frac{r_0^2 v_a^2 t}{24D} \tag{9}$$

Equation 9 is very similar to the well-known equation in chromatography for peak broadening due to laminar flow. However, the mobile phase in conventional chromatography migrates down the column with the average laminar velocity. One can simply replace $v_a t$ in eq 9 with the column length L. In field-amplified capillary electrophoresis, the sample migrates with a combination of the electrophoretic and the electroosmotic velocity. The migration time and the average laminar velocity are not directly related. As a consequence, the peak variance due to the laminar flow will be proportional to v_a^2. The total variance of a peak in field-amplified capillary electrophoresis is then

$$\sigma^2 = \sigma_{diff}^2 + \sigma_{inj}^2 + \sigma_{int}^2 + \sigma_a^2 \tag{10}$$

where σ_{diff}^2 is the variance due to diffusion, σ_{inj}^2 is the variance due to the injection, and σ_{int}^2 is the variance due to the interactions between the analyte and the walls of the column (*18*).

EXPERIMENTAL SECTION

Apparatus. The experiments in this work were performed by using a home-made CZE systtem similar to that reported by Jorgenson and Lukacs (*2*). Electrophoresis was carried out in a 75-μm-i.d. 365-μm-o.d. fused-silica capillary column (Polymicro Technologies, Phoenix, AZ) that was 75 cm long. Detection was accomplished by on-column absorption using a high-performance liquid chromatography UV detector (JASCO, Tokyo, Japan). The distance from the injection point to the detector was held at 50 cm. The high-voltage power supply (0–30 kV) was purchased from Glassman High Voltage, Inc. (Whitehouse Station, NJ).

In addition to the optical signal, we also monitored the electrophoretic current by measuring the voltage drop across a 10-kΩ resistor in series with the capillary column. Both the optical and electrical signals were then sent to a two-channel analog-to-digital converter board (Varian STAR Integrator, Varian, Palo Alto, CA) in a Compaq 386 computer. Data were collected and analyzed first by the STAR system and converted later to ASCII files for further processing by computer programs written in-house.

Chemical and Electrolytes. To reduce the heating effects, an organic buffer of 2-(*N*-morpholino)ethanesulfonic acid (MES) and histidine (HIS) at pH 6.2 was chosen for our study. A stock solution of 100 mM with respect to both MES and HIS was prepared first and then diluted to concentrations of 50, 25, and 12.5 mM. In the study of the electroosmotic mobility in homogeneous systems, acetone was used as a neutral marker. In the

Table I. Migration Time of the Boundary between Two Concentrations in a Continuous Injection System[a]

injected concn, mM	migration time (min) at concn inside the column			
	12.5 mM	25 mM	50 mM	100 mM
12.5	6.00 (6.00)	6.12 (6.26)	6.46 (6.44)	6.45 (6.40)
25	6.20 (6.26)	6.70 (6.70)	7.04 (7.10)	7.22 (7.15)
50	6.47 (6.44)	7.14 (7.10)	7.83 (7.83)	8.12 (8.11)
100	6.60 (6.40)	7.38 (7.15)	8.16 (8.11)	8.60 (8.60)

[a] The values in the parentheses are from the theoretical calculation based on the migration time of homogeneous systems.

study of peak broadening, samples of 7.31×10^{-4} M PTH–arginine (ARG) and 7.34×10^{-4} M PTH–histidine in distilled water were used. All reagents were purchased from Sigma (St. Louis, MO).

Procedure. Columns were initially filled with one concentration of MES–HIS buffer by using syringe injection. After the column was completely filled with one concentration, electrokinetic injections were then used to introduce the buffer with different concentrations. The amount of injection of the second buffer was monitored and controlled by the electrophoretic current. In the study of peak broadening, a narrow plug of sample consisted of PTH–arginine and PTH–histidine ions was injected by gravity at 3 in. high for 10 s into the column.

RESULTS AND DISCUSSION

Electroosmotic Mobilities in Columns with a Single Buffer. A great deal of work has been done to study the relationship between electroosmotic mobility and buffer concentration in homogeneous capillary electrophoresis (*9–11*). Although the details of the mechanism remain to be elucidated, the flow velocity generally increases with a decrease in buffer concentration according to a double-layer model. We have measured electroosmotic mobilities calculated from the migration time of the neutral marker as a function of concentration for the MES–HIS buffer at pH 6.2. The electroosmotic mobility increases gradually from 4.36×10^{-4} $cm^2/(s\ V)$ at 100 mM to 6.25×10^{-4} $cm^2/(s\ V)$ at 12.5 mM. These values are used to calculate the average electroosmotic velocity in mixed buffer systems.

Electroosmotic Flow in Columns with Two Buffers. Two different methods, continuous injection and fixed length, were used to study the electroosmotic flow in columns filled with two buffers of different concentrations. In continuous injection, the column was first filled with a single buffer of one concentration. We then simply switched the injection end of the column to a buffer of different concentration and filled the column continuously with the new buffer until complete replacement.

Huang et al. have described a method of measuring the electroosmotic flow by monitoring the change in the electrophoresis current when a buffer of different concentration was introduced (*19*). However, as pointed out earlier, a system with mixed concentration buffers will have a different bulk electroosmotic velocity from the single-phase system. The electroosmotic velocity of the bulk solution will change continuously as one injects the new buffer into the system, until reaching the final velocity when the buffer in the column is completely replaced. Only in the case where two concentrations are almost the same, as Huang et al. used in their study, can one use the bulk electroosmotic velocity to calculate the electroosmotic mobility.

The amount of time for a complete replacement of a buffer from one concentration to the other concentration can be calculated from the knowledge of the bulk electroosmotic velocity shown in eq 8. Table I shows the results of the measured and calculated times. The agreement is surprisingly good considering the simplicity of our model. One interesting point shown in Table I is that the relationship between migration times and concentrations is not linear at all. This is especially clear in the case of injecting 12.5 mM buffer into a column filled with a higher concentration buffer. The migration time changes from 6.00 to 6.44 min if the initial buffer concentration inside the column switches from 12.5 to 50 mM. This slowing down of bulk flow is mainly due to the drop of the electroosmotic mobility of the higher concentration buffer. But the migration time then decreases to 6.40 min if the column is initially filled with 100 mM buffer. The reason is that the effect due to the field amplification now overtakes the concentration effect and makes the whole bulk solution move faster.

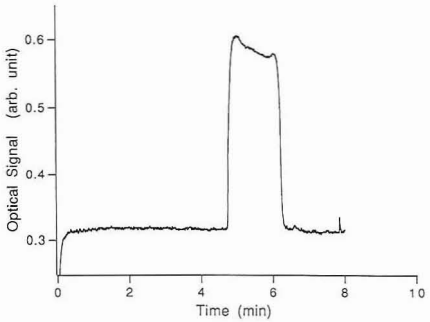

Figure 2. Typical electropherogram resulting from the electroosmotic flow in a column filled with two different concentration buffers. The change in the optical signal is due to the difference in the index of refraction of two buffers. The sharp transition indicates a well-defined concentration boundary.

Table II. Comparison of the Filled Length Calculated from the Difference in Migration Times of Front and Rear Boundaries and the Filled Length Calculated from the Measured Electrophoretic Current[a]

filled buffer, mM	i, μA	x_i	x_w
12.5	20.1	0.118	0.166
	13.0	0.253	0.283
	8.3	0.470	0.477
	4.5	1.000	
25	26.7	0.129	0.131
	21.1	0.254	0.275
	14.3	0.515	0.516
	9.0	1.000	
50	33.3	0.132	0.138
	29.0	0.272	0.287
	24.2	0.522	0.516
	18.2	1.000	

[a] The column was originally filled with 100 mM MES–HIS with a current of 38.3 μA.

In the fixed length system, a fixed length of a buffer with one concentration was injected into a column that originally was filled with another concentration. The length of the filled buffer was controlled by monitoring the change of current according to eq 3. Once the current reached the desired level, the column was switched back to the original buffer. The electroosmotic flow was then started by the application of 25 kV. Figure 2 shows a typical electropherogram, which was taken from the output of the optical detector, of the concentration boundary in the fixed ratio system. A clear and sharp change in the amount of light transmission in the boundary between the two concentrations is due to the change in the index of refraction.

Table II shows the filled lengths calculated from the difference in the migration times between the front and rear boundaries and the results calculated from the electrophoretic

Table III. Migration Times and Electrophoretic Velocities of ARG and HIS Ions in Field-Amplified Capillary Electrophoresis[a]

	t_m, min		v_{ep}, cm/s		v_{ep}/v_{ep}^0		
	ARG	HIS	ARG	HIS	ARG	HIS	E/E_0 (expected)
pure 100 mM	3.974	5.053	0.0734	0.0287	1	1	1
1/2 50 mM	3.518	4.693	0.0956	0.0363	1.310	1.276	1.273
1/2 25 mM	3.006	4.041	0.1138	0.0428	1.558	1.494	1.570
1/2 12.5 mM	2.515	3.398	0.1370	0.0509	1.877	1.776	1.844
1/4 50 mM	3.201	4.414	0.1159	0.0443	1.588[b]	1.547	1.550
1/4 25 mM	2.800	3.742	0.1378	0.0628	1.887[b]	2.201	2.300
1/4 12.5 mM	2.386	3.133	0.1625	0.0792	2.214[b]	2.762	2.888

[a] The column was originally filled with 100 mM MES–HIS buffer, and the samples are injected into the low-concentration region. [b] The ARG ions passed the concentration boundary and moved out of the high-field region.

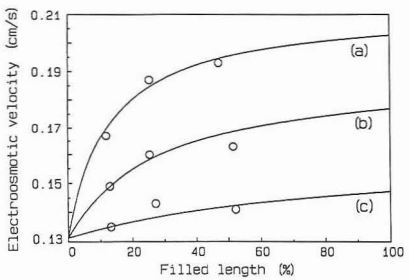

Figure 3. Electroosmotic velocity as a function of filled length. The column was original filled with 100 mM MES–HIS and then injected into a fixed length of different concentrations: (a) 12.5, (b) 25, (c) 50 mM. The solid lines are theoretical curve calculated from eq 8.

current by using eq 3. The two methods are in excellent agreement except for cases where there exists a large disturbance in the concentration boundary caused by high laminar flow.

There are several different methods one can use to obtain the bulk electroosmotic velocity in the fixed length system. We can obtain the bulk velocity from the migration time of the concentration boundary and the length of the column to the detector. Alternatively, we can also obtain the bulk electroosmotic velocity of the mixed system from monitoring of the current. The bulk electroosmotic velocities obtained from the current change and from the optical signal change were in good agreement with each other and with the calculated electroosmotic velocities using eq 8. Figure 3 shows the comparison of the calculated electroosmotic velocities for a column with a 100 mM MES–HIS buffer mixed with lower concentration buffers at various filled lengths. It shows that the lower concentration buffer has a very large influence in the bulk electroosmotic flow even with very short filled length.

Field Amplification in the Low-Concentration Region. The electric field strength in the low-concentration region will be enhanced according to eq 4. To study the field amplification effect, we can inject a narrow band of sample ions into the low-concentration region and measure their electrophoretic velocity. While the bulk electroosmotic velocity is an average of the electroosmotic velocity of the two regions, the electrophoretic velocity of the ions relative to the bulk solution is directly proportional to the local electric field strength.

The sample solution we used contained about 7×10^{-4} M PTH–arginine and PTH–histidine ions. The column, which was originally completely filled with 100 mM MES–HIS, was filled with lower concentration buffer to a specific length. A small amount of sample was injected at the end of the lower concentration region. The column was then switched back into the 100 mM MES–HIS buffer, and the high voltage was turned on to start the electrophoresis.

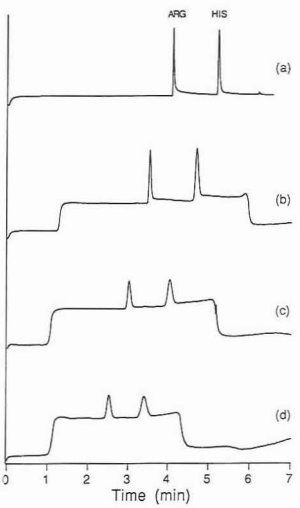

Figure 4. Electropherograms of test samples in a system where one-half of the column was filled with 100 mM MES–HIS and one-half was filled with a lower concentration buffer: (a) 100, (b) 50, (c) 25, (d) 12.5 mM. A narrow band of sample containing PTH–arginine and PTH–histidine ions was injected into the low-concentration region by using gravity injection. The column length is 75 cm, and the separation voltage is 25 kV.

Two different filled lengths, about one-half and one-quarter of the column, of three different lower concentrations were studied. Their electropherograms are shown in Figures 4 and 5. For comparison, electropherograms of the sample injected into the column with pure 100 mM MES–HIS are also shown in Figures 4a and 5a. The results clearly show that the migration times of the sample ions become smaller as the filled concentration gets lower or the filled length gets smaller.

Table III lists the measured migration times of the PTH–arginine and PTH–histidine ions in field-amplified capillary electrophoresis. Using these migration times and the electroosmotic velocities of the mixed system obtained earlier, one can obtain the electrophoretic velocity of PTH–arginine and PTH–histidine ions in field-amplified capillary electrophoresis by using

$$v_{ep} = (L_d/t_m) - v_b \tag{11}$$

where L_d is the column length to the detector and t_m is the migration time of PTH–arginine or PTH–histidine ions. The results are listed in columns 5 and 6 in Table III, respectively. The relative electrophoretic velocity, which is the ratio of

Table IV. Broadening of ARG and HIS Peaks in Field-Amplified Capillary Electrophoresis

	v_b, cm/s	v_{el}, cm/s	v_a, cm/s	σ^2, cm^2		σ_a^2, cm^2	
				ARG	HIS	ARG	HIS
pure 100 mM	0.136	0.136	0.000	0.024	0.029	0.000	0.000
1/2 50 mM	0.141	0.137	0.046	0.129	0.150	0.106	0.123
1/2 25 mM	0.163	0.278	0.115	0.362	0.451	0.330	0.420
1/2 12.5 mM	0.194	0.374	0.180	0.808	1.031	0.770	1.007
1/4 50 mM	0.143	0.228	0.085	0.154	0.389	*a*	0.355
1/4 25 mM	0.160	0.467	0.307	0.238	1.630	*a*	1.602
1/4 12.5 mM	0.187	0.586	0.399	0.305	3.266	*a*	3.237

[a] The ARG ions passed the concentration boundary and moved out of the high-field region.

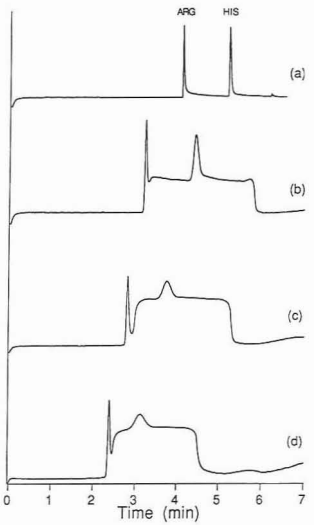

Figure 5. Electropherograms of samples containing PTH-arginine and PTH-histidine ions in a system where three-quarters of the column was filled with 100 mM MES-HIS and one-quarter was filled with a lower concentration buffer: (a) 100, (b) 50, (c) 25, (d) 12.5 mM. The experimental conditions are the same as in Figure 4.

electrophoretic velocity in field-amplified capillary electrophoresis to that in the pure column, represents the field amplification with respect to that under the uniform field strength and is shown in column 7.

The expected field amplification ratio can be calculated from the electric current measurements by using $E_j/E_0 = I_0/I_j$. The results are also listed in the last column of Table III. They generally agree with the results calculated from the electrophoretic velocity data except for cases where the PTH-arginine ions passed the concentration boundary and moved out of the high field region.

Peak Broadening in Field-Amplified Capillary Electrophoresis. Figures 4 and 5 also show that the peak width of sample ions injected in a narrow band become broader as the difference in the concentrations between the two regions increased. In addition, the peak width also becomes broader as the filled length becomes shorter for the same filled concentration. This peak broadening mechanism is the result of the enhanced diffusion caused by the laminar flow inside the column.

The laminar velocity in the sample region is equal to the difference of the local electroosmotic velocity under the amplified field and the bulk electroosmotic velocity. As the filled concentration gets lower or the filled length gets shorter, the electric field in the sample region is amplified to a much larger value than the electric field in the rest of the column. At the same time, the bulk electroosmotic velocity changes only slightly from that of the homogeneous system, i.e., pure 100 mM MES-HIS buffer. As a result, the laminar velocity increases and causes more peak broadening.

The measured bulk electroosmotic velocities of field amplified capillary electrophoresis filled originally with 100 mM HES-HIS buffer are listed in the first column in Table IV. The calculated local electroosmotic velocities using the amplified factor obtained from Table III are listed in the second column. The differences between the two velocities are then listed in the third column.

Also listed in Table IV is the total peak variance converted from the measured full-width half-maximum (FWHM) of PTH-arginine and PTH-histidine peaks by using

$$\sigma = \frac{1}{8 \ln 2}\left(\frac{t_w L_d}{t_m}\right)^2 \qquad (12)$$

where t_w is the FWHM of signal peaks. Assuming there is no laminar flow in a column under uniform electric field strength, we could obtain the variance due only to the laminar flow in field-amplified capillary electrophoresis by subtracting the peak variance obtained from the pure 100 mM buffer system. The results are listed in the last two columns of Table IV. The variance due to the laminar flow shows a good linear relationship with the function $v_a^2 t$ as predicted from eq 9.

CONCLUSIONS

The electroosmotic properties in a capillary column with two regions of different buffer concentration were studied. The ions inside the low conductance region will experience a higher field strength and move faster. However, the boundary between the two concentrations, as well as also the whole bulk solution, moves at a velocity that is the average of the electroosmotic velocity of pure buffers in uniform field weighted over the filled length and the local electric field strength.

The difference between the electroosmotic velocities will generate a back laminar flow and disturb the original plug profile. Samples injected into the field-amplified region will have shorter migration time. However, the broadening mechanism as a result of the laminar flow yields a loss in resolution. The theory and measurement of these effects is in good agreement.

This broadening mechanism will also be a limiting factor for the sample-stacking technique in HPCE. In sample stacking, a large length of sample in a much lower ionic strength buffer is introduced into a column filled with higher ionic strength buffer. The sample ions then migrate very rapidly under the applied electric field until they reach the concentration boundary. Once they pass the boundary, the ions slow down and stack into a much narrower band. The amount of stacking is proportional to the ratio of buffer concentration in the original sample solution to that in the column. The larger the difference in the concentration is, the

narrower the peak will be. However, we have shown in this report that the difference in the concentration of two regions inside the capillary column will build up an electroosmotic pressure and cause extra peak broadening. These two effects, stacking and broadening, work against each other, so that the best condition is somewhere in between the cases of pure water and concentrated buffer for the sample carrier. The studies of the optimization in sample stacking in capillary electrophoresis will be reported elsewhere (*20*).

ACKNOWLEDGMENT

We thank Dean Burgi and Karen Salomon for many helpful discussions pertaining to this work.

APPENDIX. THEORY OF ELECTROOSMOTIC–LAMINAR FLOW IN A COLUMN WITH TWO BUFFERS

Electroosmotic Parameters. The electroosmotic force is produced by an electric field and transmitted by the drag of ions acting in a thin sheath of charged fluid adjacent to the silica wall of a capillary column. If the hydrostatic pressure differential (e.g., due to gravity) across the column is zero, the electrical force is exactly balanced by viscous force in the fluid velocity gradient at the wall, according to Poiseuille's law. The fluid velocity increases from the wall to the inner boundary of the sheath, and the body of the fluid moves in equilibrium with the velocity of this boundary. As the sheath tends to be less than 100 Å thick, the fluid is said to exhibit plug flow in a capillary column; i.e., the fluid velocity is uniform over a 75-μm-diameter column (*14*).

The origin of the charge in the sheath is an unbalance between positive and negative ions, which balances a fixed charge on the silica wall and generates a zeta potential characteristic of the fluid–wall contact. While sheath analysis is complex, the action of the sheath may be characterized by its boundary velocity v_{eo} and an effective sheath thickness δ, such that the force per unit length per unit circumference acting at the sheath boundary is

$$QE_0 = v_{eo}\frac{\eta}{\delta} \tag{A1}$$

where η is the fluid viscosity, Q is the charge per unit area in the sheath, and E_0 is the applied electric field parallel to the wall. The boundary velocity v_{eo}, which is called the electroosmotic velocity, is a measure of the electrical force applied to the sheath. In this analysis, v_{eo} is the velocity of a single, specific buffer in a column of length L with applied voltage V such that $E_0 = V/L$.

Two Buffers. The case of interest is shown in Figure 1, in which the ends of the column are placed in buffers of different ionic strength and resistivity. The column is initially filled with the output buffer. Some time after the potential is applied, we find that the interface between the buffers (it is called the concentration boundary in the main text) is at position xL in the column, where x is measured from the input end.

We consider a system in which the two buffers are only different in concentration and the input section has the higher resistivity. Then the first buffer will have a larger sheath thickness and a higher electroosmotic velocity than the second, $v_{eo1} > v_{eo2}$, eq A1. But the available electroosmotic velocity v_{ej} is proportional to the local electric field given in eq 4 so that

$$v_{ej} = v_{eoj}\frac{E_j}{E_0} \tag{A2}$$

where $j = 1, 2$. These velocities represent the electrical force in each buffer section.

For noncompressible fluids, the net flow of fluid at each cross section is the same. The higher electroosmotic velocity of the input section is then balanced by a hydrostatic pressure that drives fluid in the first section back along the axis of the column, while fluid in the second section is driven forward along the axis, relative to the lower electroosmotic flow. These compensating, pressure-driven flows are laminar flows with a parabolic velocity profile, otherwise known as Poiseuille or *laminar* flow. It follows that the electrical force given parametrically in eq A2 drives the sum of an electroosmotic force and a hydrostatic pressure gradient.

The actual electroosmotic velocity is no longer equal to its pressure-free value, and we call the actual electroosmotic velocities by $v_{s1,2}$. The laminar flow exists inside the moving boundary of the electroosmotic flow and we designate the average laminar velocity with respect to the boundary by $v_{a1,2}$.

The laminar velocities average the parabolic profile such that when multiplied by the capillary cross-sectional area they give the total laminar flow. The pressure gradient that produces v_a can be expressed as a force gradient per unit circumference at the sheath boundary and thereby as an equivalent electroosmotic force given by $Kv_a\eta$, where $K = 4/r_0$ and r_0 is the radius of the capillary (see end). It is this electroosmotic force that drives the pressure gradient. Thus, the force balance stated above is given by

$$v_{ej}\frac{\eta}{\delta_j} = v_{sj}\frac{\eta}{\delta_j} - Kv_{aj}\eta \tag{A3}$$

where $j = 1, 2$. The negative sign comes in because v_{aj} is opposite to the pressure gredient. It is assumed that the two dilute buffers have the same viscosity.

Two more equations govern this system. Since the two ends of the column are at the same pressure, the pressure drops on either side of the buffer interface must be equal. As the pressure drops are proportional to the laminar velocity, we have

$$xv_{a1} + (1 - x)v_{a2} = 0 \tag{A4}$$

Also, as stated above, the net flow of fluid is equal in both sections, and therefore

$$v_{s1} + v_{a1} = v_{s2} + v_{a2} = dx/dt \equiv v_b \tag{A5}$$

where dx/dt is the velocity of the concentration boundary or the bulk velocity of the fluid, v_b. Equations A3–A5 give four equations for v_{s1}, v_{s2}, v_{a1}, and v_{a2}.

To begin the solution, we solve eqs A4 and A5 for v_{a1} and v_{a2}.

$$v_{a1} = -(1 - x)(v_{s1} - v_{s2})$$
$$v_{a2} = x(v_{s1} - v_{s2}) \tag{A6}$$

These are inserted in the laminar terms of eq A3, yielding two simultaneous equations for the actual electroosmotic flows v_{s1} and v_{s2}. These yield the solutions

$$v_{s1} = \frac{(1 + K\delta_2 x)v_{e1} + K\delta_1(1 - x)v_{e2}}{1 + K(\delta_2 x + \delta_1(1 - x))}$$
$$v_{s2} = \frac{K\delta_2 x v_{e1} + (1 + K\delta_1(1 - x))v_{e2}}{1 + K(\delta_2 x + \delta_1(1 - x))} \tag{A7}$$

Then, when eqs A6 are inserted in eq A5, we obtain the differential equation for the movement of the concentration boundary

$$v_b = dx/dt = xv_{s1} + (1 - x)v_{s2} \tag{A8}$$

where v_{sj} is given by eqs A7 and v_{ej} by eqs A2 and eq 4 in the main text.

Under the conditions of this experiment, where $r_0 \gg \delta_j$, we have $K\delta_j \ll 1$ and eqs A7 give

$$v_{s1} \approx v_{e1} \qquad v_{s2} \approx v_{e2} \tag{A9}$$

Essentially, the resistance to laminar flow is much less than the resistance to electroosmotic flow. Only a slight unbalance in the pressure-free electroosmotic flow is required to drive the laminar flow.

The K term will be important in finer capillaries at lower concentrations where the sheath thickness is a significant fraction of the column radius (*14*).

Stability of the Buffer Interface. The derived boundary velocity dx/dt in eq A5 is the average velocity over the cross section of the column. At the interface, the axial velocity as a function of the radius r is discontinuous in the amount

$$\Delta v = (v_{e1} - v_{e2})\left(\frac{2r^2}{r_0^2} - 1\right) \tag{A10}$$

This difference is made up by radical flow representing a circulation of fluid between the wall and the center of the column. Intuitively, this will impose a minimum transition width on the order of the diameter of the column. Otherwise, the flow pattern and the width of the transition will be stable.

Equivalent Sheath Thickness for Laminar Flow. We derive the value of K in eq A3. The velocity of laminar flow $v(r)$ in a tube of radius a filled with fluid of viscosity η with an axial pressure gradient P' is given by

$$v(r) = \frac{P'}{4\eta}(r_0^2 - r^2) \tag{A11}$$

When $v(r)$ is integrated over the cross-sectional area, we get the total flow. The average flow v_a is given by

$$\pi r_0^2 v_a = P'\frac{\pi r_0^4}{8\eta} \tag{A12}$$

The electroosmotic force $Kv_a\eta$ around the circumference of the sheath is equal to the hydrostatic gradient over the column area

$$2\pi r_0(Kv_a\eta) = \pi r_0^2 P' \tag{A13}$$

Eliminating v_a gives $K = 4/r_0$, the inverse of the equivalent sheath thickness.

LITERATURE CITED

(1) Kuhr, W. G. *Anal. Chem.* **1990**, *62*, 403R–414R.
(2) Jorgenson, J. W.; Lukacs, K. D. *Anal. Chem.* **1981**, *53*, 1298–1302.
(3) Karger, B. L.; Cohen, A. S.; Guttman, A. *J. Chromatogr.* **1989**, *492*, 585–614.
(4) Fujiwara, S.; Honda, S. *Anal. Chem.* **1986**, *58*, 1811–1814.
(5) Lauer, H. H.; McManigill, D. *Anal. Chem.* **1986**, *58*, 166–170.
(6) Lee, C. S.; Blanchard, W. C.; Wu, C.-T. *Anal. Chem.* **1990**, *62*, 1550–1552.
(7) Mikkers, F. E. P.; Everaerts, F. M.; Verheggen, Th. P. E. M. *J. Chromatogr.* **1979**, *169*, 1–10.
(8) Roberts, G. O.; Rhodes, P. H.; Snyder, R. S. *J. Chromatogr.* **1989**, *480*, 35–67.
(9) Knox, J. H.; Grant, I. H. *Chromatographia* **1987**, *24*, 135–143.
(10) Tsuda, T. *J. Liq. Chromatogr.* **1989**, *12*, 2501–2514.
(11) VanOrman, B. B.; Liversidge, G. G.; McIntire, G. L.; Olefirowicz, T. M.; Ewing, A. G. *J. Microcol. Sep.* **1990**, *2*, 176–180.
(12) Hjerten, S.; Jerstedt, S.; Tiselius, A. *Anal. Biochem.* **1965**, *11*, 219–223.
(13) Mikkers, F. E. P.; Everaerts1, F. M.; Peek, J. A. F. *J. Chromatogr.* **1979**, *168*, 293–315.
(14) Rice, C. L.; Whitehead, R. *J. Phys. Chem.* **1965**, *11*, 4017–4024.
(15) Wieme, R. J. *Chromatography*; Heftmann, E., Ed.; Reinhold Inc.: New York, 1967; Chapter 10.
(16) Zemansky, M. W. *Heat and Thermodynamics*; McGraw-Hill, Inc.: New York, 1951.
(17) Giddings, J. C. *Dynamics of Chromatography*; Marcel Dekker, Inc.: New York, 1965.
(18) Huang, X.; Coleman, W. F.; Zare, R. N. *J. Chromatogr.* **1989**, *480*, 95–110.
(19) Huang, X.; Gordon, M. J.; Zare, R. N. *Anal. Chem.* **1988**, *60*, 1837–1838.
(20) Burgi, D. S.; Chien, R.-L. Unpublished results.

RECEIVED for review October 19, 1990. Accepted April 5, 1991.

Matrix Elimination in Liquid Chromatography Using Heart-Cut Column Switching Techniques

Steven R. Villaseñor

Mallinckrodt Specialty Chemicals Company, 3600 N. Second Street, St. Louis, Missouri 63147

A generic approach to matrix elimination in liquid chromatography has been developed. A physical rather than chemical means of matrix elimination, i.e., an on-line sample preparation scheme, using column switching techniques, is described herein. The bulk of the sample matrix is diverted to waste and only a "heart-cut" of the chromatogram completely analyzed. The technique has universal applicability, does not suffer the limitations associated with classical matrix elimination, and significantly reduces system abuse. Dramatic improvements in chromatography were realized for sulfite determinations in bulk analgesic formulations. Accuracy, based on spike recovery data, was 91%, precision was within 20% RSD throughout, and the quantitation limit was 2 ppm. It was postulated that the method should be able to accommodate a broad diversity of sample types with little or no matrix interference, since the majority of the matrix has been eliminated from the analysis. Therefore, the method was extended to OTC analgesics, beer, wine, and various food items. The heart-cut technique has also been used in a multidimensional analysis of an organic sample with electrochemical detection and in brine analysis. Advantages realized include superior chromatography, a reduction in system abuse, economic advantages, and greater sample throughput, i.e., shorter analysis time.

INTRODUCTION

Classical matrix elimination in ion chromatography (IC) requires identification of the interference and an appropriate chemical scheme for removal (*1*). Examples include silver ion for chloride removal, barium ion for sulfate removal, and acid–base neutralizations. Although the vehicles used to effect such changes have been improved over the years, e.g., polymeric resin substrates, solid-phase extractors (SPE), and membrane devices (*2*), the basic chemistry has remained unchanged. Similarly, in liquid chromatography (LC), reversed-phase type SPE's are routinely employed to deal with organic interferences. These sample pretreatments frequently become the majority of the analysis time. In addition, the requisite manipulations may result in significant imprecision. Despite these complications, some type of sample treatment is frequently mandated to achieve satisfactory resolution and quantitation of the analyte of interest. Another closely related problem, particularly in IC and to some extent in LC, is column abuse, especially for trace analysis. In some instances, sample pretreatment can be quite effective; however, too often the capacity of the column has been exceeded, and in extreme cases, the capacity has been exceeded by several orders of magnitude. Such excessive column fouling leads to poor peak shape, lower efficiencies, with a corresponding lost in resolution, and shorter column lifetimes. This paper describes a physical, i.e., a mechanical, rather than chemical, approach to matrix elimination. This on-line means of sample preparation is independent of the interference identity or chemistry and substantially reduces system (column and detector) abuse. The sample preparation in the "heart-cut" approach is reduced to "dilute and shoot".

Employing this technique, a touchy, albeit sensitive, method for the determination of sulfite, was transformed into a rugged routine procedure, amenable to a QC lab environment. The generic nature of the heart-cut sulfite method was demonstrated by the variety of samples analyzed: bulk analgesic formulations, OTC analgesics, beer, wine, and various food items (*3*).

A multidimensional heart-cut analysis using electrochemical detection was used to address major matrix interference problems in an organic sample. Economic advantages were also demonstrated for brine analysis as an alternative to silver-ion pretreatment.

EXPERIMENTAL SECTION

Instrumentation. The IC system was a Dionex Model 2020i ion chromatograph equipped with a CDM-I conductivity detector. The detector was interfaced to a Hewlett-Packard Model 3357 lab software operating system on a Model 1000 computer for data reduction. The chromatographic separation was conducted by using a Dionex AS-2 anion-exchange "precolumn" sandwiched between two Dionex high-pressure four-way valves followed by two more AS-2 anion-exchange "separator columns"; see Figure 1. The alternative, multidimensional configuration used a Hamilton PRP-1 reversed-phase column as the precolumn rather than the AS-2 column. Only ports 1–4, the top half of the valves, were used on each valve. Ports 5–8, on the lower half of the valves, were not used; see Figure 2. These particular valves were used because of the high pressures encountered in the generic application of this technique. The eluent used was 1.5 mM sodium carbonate, 1.3 mM sodium bicarbonate, and 0.076% v/v formaldehyde (diluted from Formalin solution) at 1.5 mL/min. An anion micromembrane suppressor was used with 25 mM sulfuric acid regenerant at 3 mL/min.

Experimental details for the other examples are given in the text. The identity of analytes and samples is proprietary.

Safety Note. Formaldehyde is a known carcinogen; therefore, appropriate precautions must be exercised in its handling.

Heart-Cut Column Switching Procedure. Initially, the system is assembled without the separator column in order to determine the heart-cut timing interval. Standards are injected, and the time for the onset of the analyte peak and complete elution of the analyte peak is noted. This time interval is the heart-cut; Figure 3. The entire system is then equilibrated, after reinserting the separator column, and the analysis conducted in a four-step sequence, Figure 2, as follows:

1. Divert initial portion of chromatogram to waste. The sample is injected with valve A closed; eluent flows through the precolumn to valve B, which is opened to waste.

2. Introduce heart-cut to the separator column and detector. At the predetermined time interval, the onset of the heart-cut, valve B is closed to divert the precolumn effluent to the separator column.

3. Bypass the precolumn and detect the analyte. Following the heart-cut interval, when the entire heart-cut has been eluted from the precolumn, valve A is opened to divert the eluent stream to valve B. Valve B is immediately opened to allow eluent from valve A to flow into the separator column, bypassing the precolumn.

4. Reequilibrate the system. After the run is complete, the system is reconfigured as in step 1. The precolumn is now back

0003-2700/91/0363-1362$02.50/0 © 1991 American Chemical Society

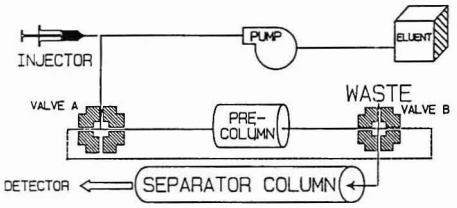

Figure 1. Heart-cut LC configuration.

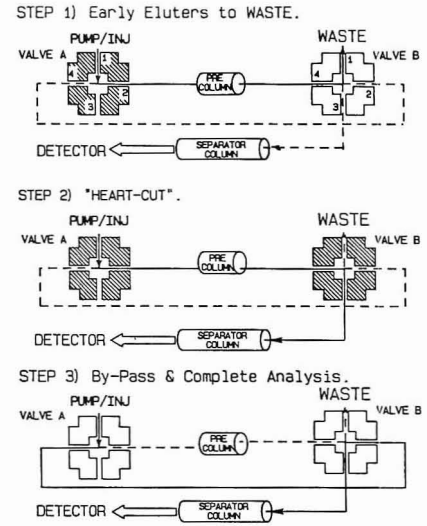

Figure 2. Heart-cut valve configurations.

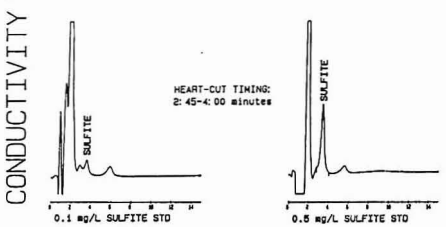

Figure 3. Determination of heart-cut.

on–line and its effluent diverted to waste; i.e., valve A is closed, eluent flows to precolumn, and valve B is opened to waste. Several injections of concentrated eluent, e.g., 10, are made to flush the precolumn of the more strongly retained components, late eluters. Then valve B is closed to put the separator column back in-line, and about half as many injections of concentrated eluent are made to flush the entire system. The system is allowed to equilibrate and the next analysis begun, step 1.

Chemicals. All chemicals were Mallinckrodt AR, and the water was polished (deionized water further purified through a Millipore Milli-Q filtration system).

Sample Preparation. The sample preparation involved weighing 4.00 g of sample into a 100-mL volumetric flask, vigorously mixing with about 95 mL of 0.76% v/v aqueous formaldehyde solution, sonicating 10–15 min, and diluting to volume. A portion of the supernatant was transferred to a centrifuge tube, the tube was centrifuged about 20 min or, time permitting, just allowed to settle, and then the supernatant was filtered through a MSI Cameo II 0.45-μm nylon syringe filter, directly into the IC.

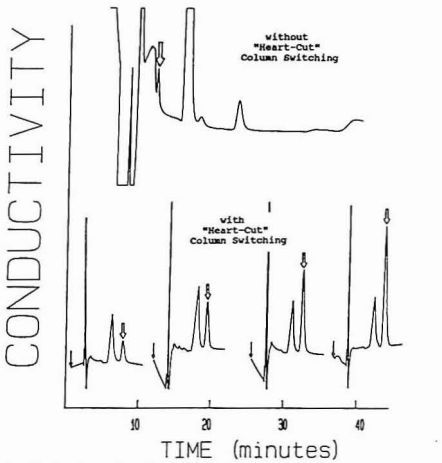

Figure 4. Sulfite in analgesic formulation with and without heart-cut column switching.

Mallinckrodt AR sodium sulfite was the reference material used to prepare solutions for instrument calibration. The suitability of the sodium sulfite for instrument calibration was verified by iodometric assay of sulfite (98.6% Na_2SO_3). Instrument calibration standards at 0.10, 0.25, 0.50, and 0.75 mg/L sulfite were prepared in 0.76% v/v aqueous formaldehyde solution.

RESULTS AND DISCUSSION

The first step in utilizing this technique was to demonstrate its viability. This was achieved with sulfite standards and gradually progressed to samples. No differences were observed for the standards analyzed with and without heart-cut column switching techniques. The heart-cut interval was then fine tuned with spiked samples. On the basis of recoveries, the analyte retention time window, for the precolumn alone, was optimized with respect to starting time and duration. This takes into account any subtle shifts in retention time between standard and sample. The chromatograms, in Figure 4, illustrate the dramatic improvement in chromatography using this technique. Without the heart-cut, the analyte was a small peak on the trailing edge of a large interference peak. The analysis time was 30 min with as much as another 30 min of reequilibration time. This is a typical example of system abuse, the number one offender in LC today (according to the author). With the heart-cut, a baseline-resolved chromatogram was achieved in 10 min. Reequilibration time was also reduced substantially by using ongoing precolumn clean-up techniques, discussed later in the text. Figure 4 also shows heart-cut chromatograms of three spike levels: 5, 10, and 15 ppm. The accuracy, based on spike recovery data, was 91%, the precision was within 20% relative standard deviation (RSD) throughout, and accurate quantitation was achieved down to 2 ppm, Tables I, II, and III. The validation study was conducted with bulk drug items; however, the procedure has also been used for OTC analgesics, Table IV, as well as other pharmaceuticals.

The FDA has established a 10 ppm sulfite-labeling limit for foods and has recommended the same limit for drug items. Hence, a reliable means of analysis, applicable to a variety of sample matrices, would be ideal. The aforementioned method was envisioned as converging on the ideal. In order to put our method to the test, a comparison study was conducted between our method and the Association of Official Analytical Chemists (AOAC) IC method for sulfite analysis in foods (*4*). Our methodology was superior; e.g., the AOAC method could not analyze highly colored foods at all, whereas

Table I. Typical Validation Data of Heart-Cut IC Method for the Determination of Sulfite in Analgesic Formulation A

sample designation	ppm found	recovery, %
Day 1		
analgesic formulation A	3.8	
5 ppm spike	8.6	96
10 ppm spike	13.0	92
15 ppm spike	19.0	101
duplicate sample prep		
Day 2		
analgesic formulation A	5.0	
5 ppm spike	9.2	91
10 ppm spike	14.0	94
15 ppm spike	20.0	102
duplicate sample prep	4.3	
Day 3		
analgesic formulation A	5.8	
5 ppm spike	9.4	86
10 ppm spike	15.0	99
15 ppm spike	20.0	99
duplicate sample prep	4.4	

Table II. Typical Validation Data of Heart-Cut IC Method for the Determination of Sulfite in Analgesic Formulation B

sample designation	ppm found	recovery, %
Day 1		
analgesic formulation B	1.6	
5 ppm spike	6.2	92
10 ppm spike	11.0	94
15 ppm spike	16.0	96
duplicate sample prep		
Day 2		
analgesic formulation B	1.4	
5 ppm spike		
10 ppm spike	11.0	97
15 ppm spike		
duplicate sample prep	1.3	
Day 3		
analgesic formulation B	1.4	
5 ppm spike	6.4	104
10 ppm spike	10.0	88
15 ppm spike	16.0	99
duplicate sample prep	1.0	

Table III. Typical Validation Data of Heart-Cut IC Method for the Determination of Sulfite in Analgesic Formulation C

sample designation	ppm found	recovery, %
Day 1		
analgesic formulation C	<2	
5 ppm spike	4.9	98
10 ppm spike	9.0	90
15 ppm spike	14.0	93
duplicate sample prep	<2	
Day 2		
analgesic formulation C	<2	
5 ppm spike	4.5	90
10 ppm spike	7.2	72
15 ppm spike	11.0	73
duplicate sample prep	<2	
Day 3		
analgesic formulation C	<2	
5 ppm spike	3.7	74
10 ppm spike	7.3	73
15 ppm spike	11.0	73
duplicate sample preparation	<2	

Table IV. Determination of Sulfite in an OTC Analgesic by the Heart-Cut IC Method

sample designation	ppm found	recovery, %
generic aspirin substitute	<2	
5 ppm spike	5.0	101
10 ppm spike	10.0	97
15 ppm spike	14.0	93
duplicate sample prep	<2	

Table V. Determination of Sulfite in Beer by the Heart-Cut IC Method

sample designation	ppm found	recovery, %
Day 1		
beer (av 2.7)	3.0	
5 ppm spike	6.5	75
10 ppm spike	11.0	81
15 ppm spike	15.0	82
duplicate sample prep	2.4	
Day 2		
beer (av 2.3)	2.2	
5 ppm spike	5.6	65
10 ppm spike	10.0	78
15 ppm spike	15.0	82
duplicate sample prep	2.5	
Day 3		
beer (av 2.1)	2.1	
5 ppm spike	5.8	75
10 ppm spike	9.1	70
15 ppm spike	13.0	71
duplicate sample prep	2.0	
PRP-1 Reversed-Phase Precolumn		
beer (av 3.1)	3.4	
5 ppm spike	7.5	88
10 ppm spike	11.0	80
15 ppm spike	15.0	81
duplicate sample preparation	2.9	

no problems were encountered with the heart-cut analysis of a cola soft drink. See ref 3 for a comparison study.

Sulfite determinations in beer were also briefly examined, see Table V. A modest improvement, in recovery, was achieved by substituting a PRP-1 reversed-phase column for the AS-2 ion-exchange precolumn. No significant conclusions can be drawn from such a limited body of data; however, the fact that such a diversity of sample matrices can be investigated with minimal modification of a single method supports the use of the term generic. The methodology described herein would certainly be a good starting point in developing an optimized procedure for the determination of sulfite in beer and represents an alternative to other existing procedures, e.g., ion-exclusion chromatography with pulsed amperometric detection (*5*).

Another example, of the power of this technique, is illustrated in attempts to determine an electrochemically active species in an organic matrix. Initial attempts at a direct analysis, using one and two ion-exclusion columns in series, were unsuccessful, Figure 5. In the former case (one ion-exclusion column), the analyte was completely obscured by the matrix. The latter analyses (two ion-exclusion columns) were made in hopes that, by increasing the number of theoretical plates, the analyte might be resolved from the interfering peak. Even in a sample spiked at more than an order of magnitude greater than the level of interest, the analyte was only marginally discerned. In startling contrast, Figure 5 also shows a multidimensional heart-cut analysis of the same sample. The bulk of the matrix interference is eliminated and the analyte readily quantitated.

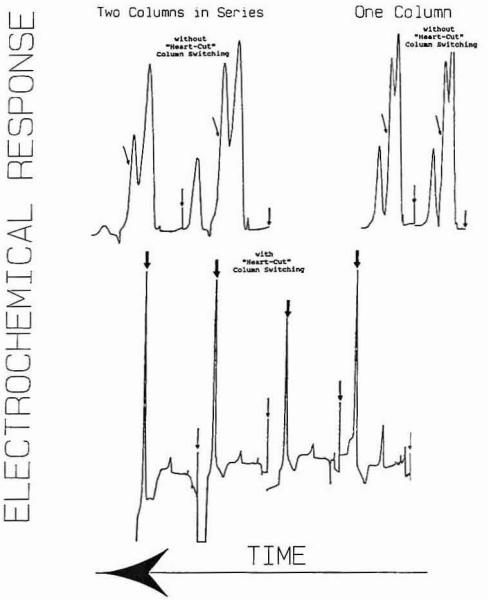

Figure 5. Determination of an electrochemically active species with and without heart-cut column switching.

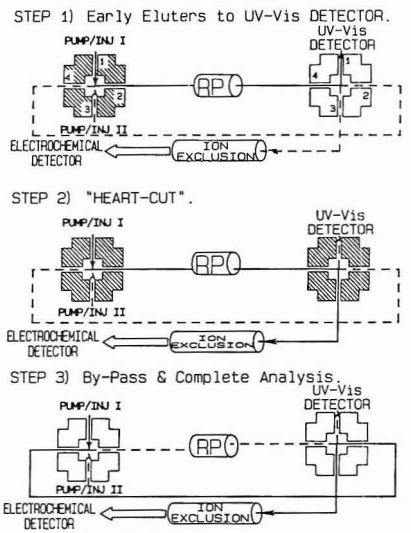

Figure 6. Multidimensional analysis using electrochemical and UV detection.

Electrochemical detector stability is a critical parameter that must be maintained throughout the analysis. In contrast, the conductivity detector is rugged and can withstand considerable abuse. Interruptions in the eluent flow, through an electrochemical detector, *cannot* be tolerated. As a consequence, our basic heart-cut system was modified to include a second pump/injector, Figure 6. A dual-channel instrument facilitates such a modification. In this configuration, eluent flow through the persnickety detector continues unabated throughout the analysis. It should also be noted that the heart-cut technique not only reduces column abuse but also detector abuse since the detector never sees the large portion of the sample matrix that goes to waste.

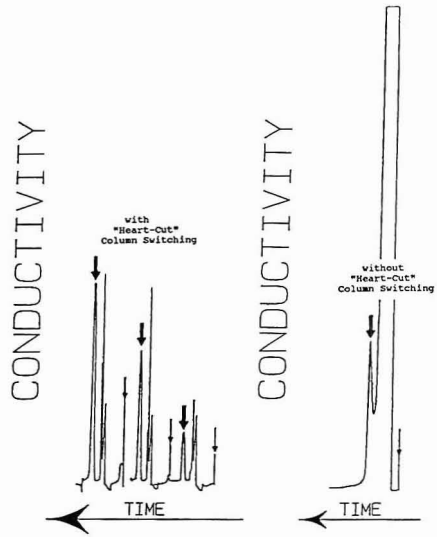

Figure 7. Determination of a preservative in a low sodium salt with and without heart-cut column switching.

A reversed-phase column (Hamilton PRP-1) was used as the precolumn, and an ion-exclusion column (Dionex HPICE-AS1) was used as the separator. The precolumn was used to remove the organic moieties while the less retentive analyte was transferred, in the heart-cut, to the separator column and subsequently detected. Such a multidimensional scheme might be considered an economic approach to mixed bed column chromatography; e.g., Dionex OmniPac columns exhibit both reversed-phase and ion-exchange characteristics. The UV detector was used to monitor the organics flushed from the precolumn.

The additional pump configuration, used in the aforementioned example, also makes possible precolumn clean-up while the analysis is in progress. Such a modification has been used for sulfite analysis to further facilitate sample throughout as well as minimizing detector upsets, discussed earlier in the text.

Figure 7 shows the determination of a preservative in a low sodium salt with and without using the heart-cut technique. The heart-cut analysis shows three injections with increasing preservative content. The intermediate level was also reanalyzed without column switching. Much more accurate quantitation was achieved for the former. Although silver-ion resin sample pretreatment might also yield comparable results, the economic advantages in terms of material and labor make the heart-cut procedure the method of choice.

CONCLUSION

This paper describes a generic approach to on-line LC sample preparation and provides a flexible tool for dealing with matrix interferences. Our heart-cut technique diverts the bulk of the matrix to waste via column switching. Although column switching techniques (*6*) are nothing new, a simple generic approach for routine use rather than sophisticated specific applications is new. A priori, this technique should find considerable application in trace analysis, where routinely more than 99% of the species passed through the system provide absolutely no useful analytical information.

Further applications and a fully automated version of this technology are in progress.

ACKNOWLEDGMENT

I thank my colleagues for reviewing the manuscript: F. E. Brown, D. A. Fay, T. N. Hopper, N. C. Jamieson, G. W. Limpert, and D. L. Tuck. I also thank B. R. Semon for word processor assistance in preparing the manuscript.

Registry No. Sulfite, 14265-45-3.

LITERATURE CITED

(1) Haddad, Paul R. *J. Chromatogr.* **1989**, *482*, 267–278.
(2) Jones, William R.; Jandik, Peter *J. Chromatogr. Sci.* **1989**, *27*, 449–455.
(3) Villaseñor, Steven R. Unpublished results.
(4) Kim, Hie-Joon *J. Assoc. Off. Anal. Chem.* **1990**, *73*, 216–222.
(5) Wagner, Herbert P.; McGarrity, Micheal J. International Ion Chromatography Symposium, San Diego, CA, 1990; *J. Chromatogr.* **1991**, *546*, 119–124 and references cited within. Authors' address: John Labatt Limited, Brewing Research Department, 150 Simcoe St, London, Ontario, Canada N6A 4M3.
(6) Lessard, D.; Nicoll-Griffith, D.; Hill, H. M. *Am. Lab.* **1990**, *22*, 42–48.

RECEIVED for review December 13, 1990. Accepted April 5, 1991. This work was presented at the 1990 International Ion Chromatography Symposium in San Diego, CA. Permission to publish and all funding of this work was granted by Mallinckrodt Specialty Chemicals Company.

Particle Size Distribution by Sedimentation/Steric Field-Flow Fractionation: Development of a Calibration Procedure Based on Density Compensation

J. Calvin Giddings,* Myeong Hee Moon, P. Stephen Williams, and Marcus N. Myers

Field-Flow Fractionation Research Center, Department of Chemistry, University of Utah, Salt Lake City, Utah 84112

Because of the important but mathematically complex role played by hydrodynamic lift forces in sedimentation/steric FFF, applied generally to particles >1 μm in diameter, retention cannot readily be related to particle diameter on the basis of simple theory. Consequently, empirical calibration is needed. Unfortunately, retention is based on particle density as well as size so that a purely size-based calibration (e.g., with polystyrene latex standards) is not generally valid. By examining the balance between driving and lift forces, it is concluded that equal retention will be observed for equal size particles subject to equal driving forces irrespective of particle density. Therefore by adjusting the rotation rate to exactly compensate for density, retention can be brought in line with that of standards, a conclusion verified by microscopy. Linear calibration plots of log (retention time) versus log (diameter) can then be used. This approach is applied to two glass bead samples (5–30 and 5–50 μm) using both a conventional and a pinched inlet channel. The resulting size distribution curves are self consistent and in good agreement with results obtained independently.

Field-flow fractionation (FFF) consists of a great number of operating modes and subtechniques, each having its own unique characteristics and range of applicability (*1–3*). For example, the normal mode of FFF, whether the applied field is sedimentation, thermal, crossflow, or electrical, is applicable to macromolecules and particles up to about 1 μm in diameter, or in special circumstances up to 3 or 4 μm particle size. The dependence of retention on particle size or mass in the normal mode is generally quite predictable, providing the force exerted on the sample particles by the applied field is a calculable quantity (*2*). In the normal mode of sedimentation FFF, for example, the retention time can be calculated with reasonable accuracy from first principles for particles of known size and density (*4*). Thus particle size distributions can be obtained from experimental fractograms (detector response vs time curves) on the basis of theoretical relationships without recourse to the use of calibration standards. (In the normal mode of thermal FFF, some calibration is necessary simply because theoretical relationships do not exist that accurately describe the effective force exerted on polymer molecules or particles by an applied temperature gradient.)

The steric mode of operation of FFF, in contrast to normal FFF, does not yield unknown particle diameters unless subjected to empirical calibration, even if the applied force acting on the particles can be calculated (*5*). The reason calibration is needed is that the relatively large (over 1 μm in diameter) particles subject to steric FFF are substantially influenced by hydrodynamic effects, particularly by hydrodynamic lift forces that tend to drive the particles away from the wall at which they normally accumulate (*3*). By altering the particle–wall distance in the FFF channel, these forces disturb the particle migration rate. While hydrodynamic lift forces have been studied at great length by many investigators (*6–14*), at the present time there are no simple yet general theoretical expressions that predict the magnitude of these forces as a function of particle diameter, shear rate, and the distance of the particle from the accumulation wall. Thus particle retention cannot be directly calculated when lift forces are substantial.

Even though calibration is clearly necessary in steric FFF, a suitable calibration procedure has not been worked out. It is the object of this report to develop such a procedure, particularly for sedimentation/steric FFF.

The first step in carrying out calibration is that of identifying suitable calibration standards. For particle sizing, the best standards (judged in terms of size range, accuracy, and narrowness of distribution) are various latex microspheres or beads. The most frequently used and widely available of these are polystyrene latex beads, which range in size from a few hundredths of a micrometer to many hundred micrometers. Many such samples can be found in the common steric range 1–100 μm.

Our numerous experiments with both steric FFF (unpublished) and the related operating mode of hyperlayer FFF (*15*)

* Corresponding author.

0003-2700/91/0363-1366$02.50/0 © 1991 American Chemical Society

have shown that a plot of log t_r vs log d (where t_r is retention time and d is particle diameter) is approximately linear over a wide diameter range for polystyrene latex spheres. This linear relationship, or linear calibration curve, can easily be made the basis for obtaining particle size distributions from a sedimentation/steric FFF fractogram, *providing* the particles are polystyrene spheres or other particles of the same density.

A major difficulty, unfortunately, arises with this procedure if one attempts to obtain the particle size distribution of particles of a different chemical nature that have a different density. For such particles, the polystyrene calibration curves are no longer applicable because retention time is a function of density as well as size. Thus in some of our early experiments in steric FFF, polystyrene latex beads (density $\rho_p = 1.05$ g/mL) and microporous silica spheres (density $\cong 2.1$ g/mL) of almost identical diameters (5.7 vs 5.6 μm) were observed to have such a major difference in retention times (almost 2-fold) under the same experimental conditions that they could be essentially baseline-resolved (*16*). This result shows clearly that particles of one density cannot be used as calibration standards for particles of another density under the same experimental conditions in sedimentation/steric FFF. Unfortunately, because of the complexities of theory, there is no simple way to extrapolate from one density to another.

Despite the impracticality of directly applying the results obtained for a standard of one density to a sample of another density, we have developed a density compensation procedure that can be utilized to transfer results from a calibration standard to particles of other known densities.

The principles on which this procedure is based are as follows. Particles undergoing steric FFF migration are subject to two opposing forces, the primary (or applied) driving force arising from the application of the field, tending to drive the particles toward the accumulation wall, and hydrodynamic lift forces that act to drive particles away from the accumulation wall. Because of the thinness of the channel, each particle is expected to reach equilibrium rapidly. The equilibrium position will be located a short distance above the accumulation wall, where the two forces exactly balance one another (*3*). We know from previous experiments that if the primary driving force is increased, the particles are driven closer to the accumulation wall, whereas if it is decreased, the particles seek an equilibrium position further from the wall (*3*, *16*). This is confirmed by the fact that the retention time is increased and decreased by these two respective changes. As long as the primary driving force is unchanged and other experimental conditions are the same, the particles will migrate along the channel at a fixed equilibrium height and a fixed velocity. All identical particles migrate at the same velocity and emerge with the same retention time because they are subject to the same primary driving force.

If now we introduce into a sedimentation FFF system a particle of the same size but one that is different in density, it will migrate at a different velocity because the primary driving force, sedimentation, varies with particle density. However, the particle of different density can be made to migrate at the same velocity providing we somehow compensate for the density change in such a way that the primary driving force stays the same. This is accomplished in our procedure by changing the field strength (specifically, the rotation rate) of the centrifuge so that the density change is exactly offset by the rpm change. With such compensation, the primary driving force remains unchanged.

More specifically, the driving force of sedimentation is directly proportional to the density difference $\Delta\rho$ between the particle and its surrounding carrier liquid. This force is also proportional to acceleration G or, equivalently, to rpm^2. Thus when sample particles having a density different from that of the standard particles are used, the calibration curve for the standards can be utilized, providing G for the sample is varied inversely with its $\Delta\rho$, $G = (\text{constant})/\Delta\rho$, with all other conditions including flow velocity remaining the same. (This procedure is based on the reasonable assumption that lift forces are independent of particle density.) Equivalently, this density compensation can be realized if the rotation rate varies as rpm $= (\text{constant})/(\Delta\rho)^{1/2}$. Clearly, the method is applicable only to samples in which all particles have the same density and thus the same $\Delta\rho$.

The calibration procedure based on this density compensation effect thus proceeds as follows. First, a calibration curve relating t_r to d is established using well-characterized standards under appropriate conditions. (The calibration curve may involve a plot of log t_r vs log d, or it may employ any other graphical, analytical, or numerical relationship between t_r and d.) Second, the sample of interest is run with all conditions the same except that G is adjusted according to the relationship $G = (\text{constant})/\Delta\rho$, as explained above. Third, standard procedures and their modifications (see below) can then be used to obtain the particle size distribution.

By compensating for density differences by means of carefully chosen adjustments in field strength or rpm, one can use the most convenient particle size standards regardless of their density. This compensation procedure allows one to bypass the difficulties of the complex theoretical treatments needed (but not yet developed) to relate retention time to particle size and density in steric FFF.

THEORY

The particle size distribution $m(d)$, expressing the relative mass m of particulate matter lying in a unit range of particle diameter d, is obtained from the equation (*17*)

$$m(d) = c(t_r)\left|\frac{dV_r}{dd}\right| \tag{1}$$

where $c(t_r)$ is the corrected (see later) fractogram signal, proportional to the mass concentration c of particulate matter in the channel effluent emerging at retention time t_r, and V_r is the retention volume. Equation 1 can be transformed to

$$m(d) = c(t_r)\frac{dV_r}{dt_r}\left|\frac{dt_r}{dd}\right| = c(t_r)\dot{V}\left|\frac{dt_r}{dd}\right| \tag{2}$$

where $\dot{V}$ represents the flow rate through the channel. The absolute value bars are used because retention times t_r or volume V_r may either increase (normal mode of FFF) or decrease (steric FFF) with d without affecting the validity of the above equations.

Equations 1 and 2 show that the particle size distribution function $m(d)$ can only be obtained from the fractogram response function $c(t_r)$ if the retention time t_r (or, equivalently, the retention volume V_r) is a known function of particle diameter d so that dt_r/dd may be obtained. In normal FFF, as pointed out earlier, this dependency is generally obtained from theory; in steric FFF, the relationship between t_r and d must be obtained by empirical calibration. The precise form of this function is unimportant mathematically, and the way it is obtained is of no significance as long as a valid relationship is known so that dt_r/dd can be obtained.

As noted above, for steric FFF a plot of log t_r vs log d normally yields a straight line. This straight line relationship can be expressed by

$$\log t_r = -S \log d + \log t_{r1} \tag{3}$$

or, if t_r is tabulated as the dimensionless ratio t_r/t° by

$$\log \frac{t_r}{t^\circ} = -S \log d + \log \frac{t_{r1}}{t^\circ} \tag{4}$$

where S, the negative slope of the plot, is equal to the particle

diameter selectivity (sometimes written as S_d), $|\mathrm{d} \log t_r/d \log d|$, t° is the void time, and t_{r1} is a constant equal to the extrapolated value of t_r for particles of unit diameter. These equations can be expressed in the alternate form

$$t_r = t_{r1}/d^S \tag{5}$$

As long as eqs 3–5 are valid, the derivative term in eq 2 becomes

$$\mathrm{d}t_r/\mathrm{d}d = -St_{r1}d^{-(S+1)} \tag{6}$$

When eq 6 is substituted into eq 2, we have

$$m(d) = c(t_r)\dot{V}St_{r1}/d^{S+1} = c(t_r)\dot{V}St_{r1}(t_r/t_{r1})^{(S+1)/S} \tag{7}$$

where the minus sign has disappeared because of the absolute value designation in eq 2. The latter expression of eq 7 can be used directly to obtain $m(d)$ from the fractogram function $c(t_r)$, provided the constants S and t_{r1} are known.

We note that the signal from some detectors used in FFF (particularly detectors, such as ours, that record the level of light scattering) is not only proportional to the mass concentration c of particles per unit volume but also depends on particle size. In this instance, corrections must be applied to obtain the correct distribution function $m(d)$ (see later).

It is inevitable that the acquired $m(d)$ curves will be slightly broadened by band dispersion processes in the channel. However, the variance of our sample peaks is nearly 2 orders of magnitude greater than the variance of latex standard peaks, indicating that the perturbation to $m(d)$ is negligible.

EXPERIMENTAL SECTION

The sedimentation FFF rotor unit, similar to units utilized in previous work (*18*), has the same basic structure as the Model S101 colloid/particle fractionator from FFFractionation, Inc. (Salt Lake City, UT). These systems all have a horizontal spin axis (a vertical spin plane) to prevent larger particles from settling to the edges of the channel during the run due to gravitational sedimentation.

Two different channels were used in this study to verify the generality of the calibration procedure. Channel I is a conventional channel, uniform in cross section from end to end, having a tip-to-tip length L of 92 cm, a breadth b of 2 cm, and a thickness w of 254 μm, equal to the thickness of the Mylar spacer from which the channel was cut. The void volume, measured as the elution volume of a nonretained sodium benzoate peak, is 5.1 mL. Channel II has a more novel pinched inlet design (*19*), in which the first 40% of the channel length is only 127 μm thick as compared to the 254-μm thickness of the remainder of the channel (*20*). This unique structure, designed for stopless flow operation (injection without stopflow), was constructed by using two 127 μm thick sheets of Mylar plastic. The piece having the full channel dimensions, L = 90 cm and b = 2 cm, was cut and removed from one of the sheets. The other sheet was cut in such a way that a "blocking element" was left in place along 36 cm of the inlet end. The blocking element was layered against the inside channel wall, as shown in Figure 1. The void volume of the pinched inlet structure, measured as before, is 3.6 mL.

The standards used for calibration are polystyrene latex beads (Duke Scientific, Palo Alto, CA) with reported diameters of 59.7, 47.9, 29.1, 19.58, 15.0, 9.87, 7.04, 5.002, 3.983, and 2.062 μm (hereafter described as 60, 48, 29, 20, 15, 10, 7, 5, 4, and 2 μm, respectively). Two polydisperse glass bead samples were used to test our calibration procedure for size characterization. A nominal 5–50-μm material from Duke Scientific and a 5–30-μm sample from the National Institute of Standards and Technology (NIST) (SRM 1003) were used. The glass bead samples were treated with a density flotation method to rid them of beads containing bubbles. This density fractionation was achieved by using 1,4-diiodobutane with a density of 2.35 g/mL. The resulting high-density glass bead samples were cleaned with ethyl alcohol and the aqueous carrier several times. Sample volumes of 70–80 μL of well-stirred 35 mg/mL glass bead suspensions were injected for each run. For channel I, the sample was injected directly into the channel inlet by a microsyringe. The carrier flow was then

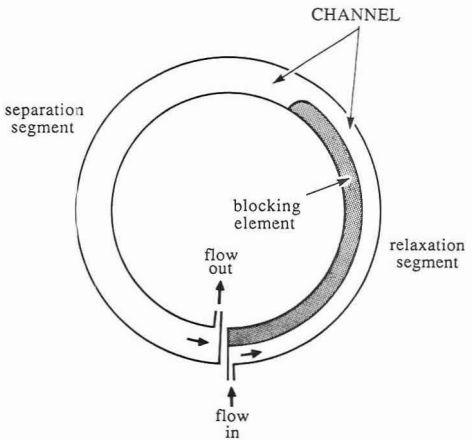

Figure 1. Schematic diagram of structure of pinched inlet channel (channel II) for sedimentation FFF.

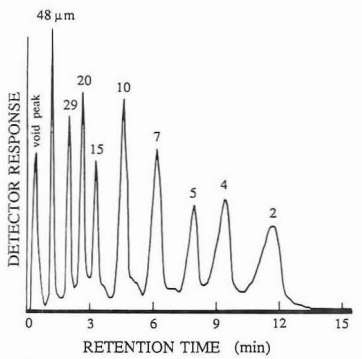

Figure 2. Separation of nine polystyrene latex standards of the indicated diameters in the pinched inlet channel at 800 rpm and $\dot{V}$ = 10.3 mL/min.

interrupted (following the stopflow procedure) and the centrifuge set spinning to achieve sample relaxation. Flow was then resumed. For channel II, whose structure is designed to make the stopflow procedure unnecessary (*19*), the channel was first brought up to its final rotational speed and the sample was introduced into the continuously flowing stream entering through the inlet tubing and seal.

The carrier liquid used for these experiments was doubly distilled water with 0.01% FL-70 detergent (Fisher Scientific Co., Fairlawn, NJ) used for particle stabilization and 0.02% sodium azide used as bactericide. The carrier flow was driven by an FMI Lab pump Model QD-2 (Fluid Meeting, Inc., Oysterbay, NJ).

The eluted sample was monitored at 254 nm by an Altex Model 153 (Beckman Instrument, Fullerton, CA) UV detector. A strip chart recorder from Houston Instrument Corp. (Austin, TX) was used for recording. Particle fractions were collected on a Model FC-80K microfractionator from Gilson Medical Electronics (Middletown, WI). These samples were then examined by microscopy. Calibration curves were established by measuring the retention times of each of a series of latex beads under specified conditions. Retention times can be accurately measured because latex microspheres of different diameters form sharp peaks, as illustrated in Figure 2. This fractogram, obtained by running a sample consisting of a mixture of the nine latex standards of different diameters used in this study in Channel II, illustrates the high resolution that can be achieved in particle size analysis

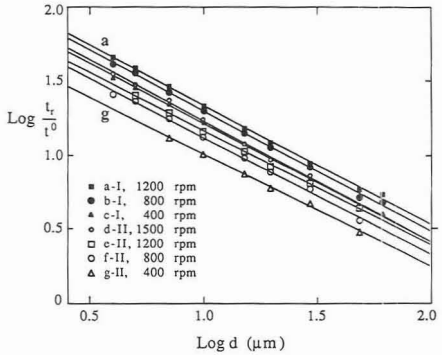

Figure 3. Least-squares linear calibration curves for polystyrene latex standards obtained at a flow rate of 10.3 mL/min. The nine sets of experimental points along the log d axis are obtained for latex microspheres of diameter 4, 5, 7, 10, 15, 20, 29, 48, and 60 μm, respectively. The top three plots (a–c) are for channel I and the four plots below (d–g) apply to channel II. The rpm for each plot is shown in the diagram and in Table I. The slope and intercept parameters are given in Table I.

Table I. Experimental Conditions and Parameters Corresponding to Calibration Plots of Figure 3[a]

plot	channel	rpm	$G\Delta\rho \times 10^{-4}$, g/(cm² s²)	S	t_{r1}/t^0	cc[b]
a	I	1200	1.244	0.813	140.6	0.998
b	I	800	0.553	0.823	132.4	0.998
c	I	400	0.138	0.812	106.4	0.998
d	II	1500	1.943	0.824	113.5	0.998
e	II	1200	1.244	0.780	88.3	0.999
f	II	800	0.553	0.796	82.2	0.998
g	II	400	0.138	0.764	58.9	0.998

[a] All flow rates = 10.3 mL/min. [b] Correlation coefficient for plot.

using sedimentation/steric FFF.

RESULTS AND DISCUSSION

A series of seven calibration plots is shown in Figure 3. The plots correspond to different rotation rates applied to the two different channel systems, as specified in Table I. All runs were made at a flow rate of 10.3 mL/min. The straight lines shown in the figure were obtained by least squares. The slope ($-S$) and intercept (t_{r1}/t^0) are also shown in Table I.

The plots displayed in Figure 3 (and tabulated in Table I) consist only of the linear portions of the logarithmic time–diameter relationship corresponding to fully developed steric FFF. As one proceeds left along any given plot (in the direction of smaller particle diameter), the steric transition region is encountered. As one proceeds into this region, Brownian motion, which dominates the normal operating mode of FFF, plays an increasing role in driving particles away from the accumulation wall. This effect leads to earlier elution than would be expected on the basis of steric effects alone. Therefore, the plots begin to bend downward (toward shorter retention times) upon proceeding through the steric region, eventually passing through a maximum at the steric transition point (see Figure 4). The retention of particles of still smaller diameter is governed largely by normal FFF, but a significant steric influence persists well beyond the transition point.

While the plots of Figure 3 and the theory culminating in eq 7 focus on the straight line portion of the logarithmic plots, the density compensation principle can be extended through the entire steric transition region and, if necessary, into the domain of normal FFF. This is because both steric and normal FFF, other forces being equal, are governed by the magnitude

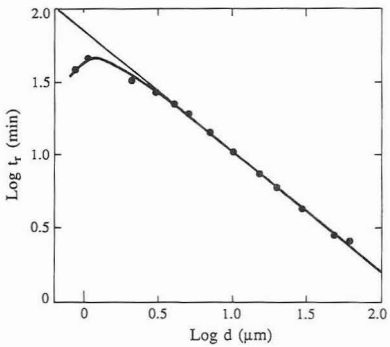

Figure 4. Calibration plot that shows extension of plot a in Figure 3 (channel I) into curved steric transition region for small d.

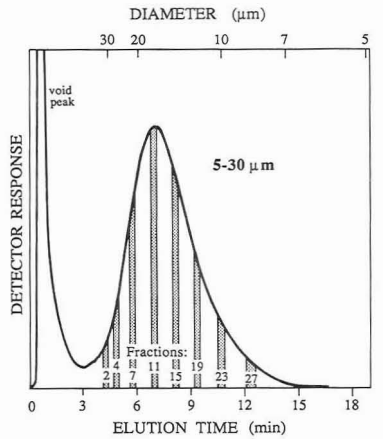

Figure 5. Fractogram of polydisperse 5–30-μm glass bead sample in channel I at 224 rpm, a flow rate of 10.3 mL/min, and a stopflow time of 2 s.

of the primary driving force, which is reduced to a common level by means of the compensation procedure. While particle diameters in normal FFF can be approximately related to retention time by theory, as noted earlier, perturbations caused by steric effects, and even by electrostatic and related forces, can be corrected by density compensation, provided the distributing forces are the same for particles of equal size independent of particle density.

While the validity of eq 7 fails to extend into the steric transition region because eq 3, on which eq 7 is based, no longer applies, the general relationships provided by eqs 1 and 2 are applicable over the entire particle diameter range, including that corresponding to steric FFF, normal FFF, and the transition region. (These equations become momentarily inoperable right at the transition point because dt_r/dd and thus selectivity S equal zero at this point.) It is only necessary to replace eq 3 by a more appropriate relationship to extend eqs 1 and 2 into the transition region and beyond.

Figures 5 and 6 show fractograms of the two polydisperse glass bead samples with nominal diameter ranges of 5–30 and 5–50 μm, respectively. Both fractograms were obtained with the uniform channel, channel I, at a flow rate of 10.3 mL/min and with a stopflow time of 2 s. The 5–30-μm sample, having a density of 2.41 g/mL, was run at a rotation rate of 224 rpm. Under these conditions, the $G\Delta\rho$ value is exactly the same as

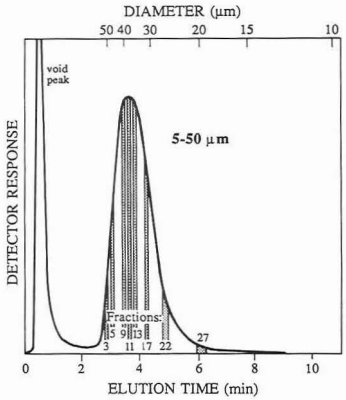

Figure 6. Fractogram of 5–50-μm glass bead sample in channel I at 222 rpm, $\dot{V}$ = 10.3 mL/min, and a stopflow time of 2 s.

that applicable to the polystyrene latex standards represented by line a (1200 rpm) in Figure 3. Since the latter plot fixes a relationship between retention time and particle diameter that under these specific conditions presumably applies to the glass bead sample, a particle diameter scale can be readily applied to Figure 5, as shown along the upper horizontal axis. This scale verifies that most of the glass spheres fall in the range 5–30 μm as specified by the supplier.

The fractogram (Figure 6) of the 5–50-μm sample (density 2.45 g/mL) was obtained at 222 rpm. The $G\Delta\rho$ value here also corresponds very closely to plot a in Figure 3. The diameter scale obtained from the calibration plot is again shown on the upper horizontal axis. Based on this scale, it appears that most of the spheres have diameters from 20–50 μm with only a minor part of the population having a diameter less than 15 μm.

Fractions were collected from the elution stream in both of the above runs in order to examine the bead diameters microscopically and test the validity of our method. More than 30 fractions were collected for each sample, and a detailed microscopic examination was carried out on these. Results are reported here for about one-third of the fractions (Table II). The positions of the reported fractions are shown in the fractograms of Figures 5 and 6 and identified by a fraction number. Table II tabulates the microscopically determined mean diameters (based on a count of from 20 to 30 spheres for each fraction) and compares these to the diameters based on the proposed calibration procedure. The agreement is seen to be excellent, thus confirming in large measure the validity of the density compensation approach to calibration.

The fractionation of glass microspheres according to size is illustrated in Figure 7, which shows micrographs of the original 5–50-μm sample and a number of the fractions collected at positions along the time axis indicated in Figure 6. As expected, the larger particles are eluted in the earlier fractions. Some of these particles show residual bubbles despite the flotation process used in sample preparation.

Given the correctness of the calibration relationship relating retention time to particle diameter as confirmed by the microscopy reported above, we are in a position to convert the fractograms such as those shown in Figures 5 and 6 into particle size distribution (PSD) curves. For this purpose, eq 7 is used along with software developed in-house. This treatment converts the fractogram of Figure 5 into the size distribution curves shown in Figure 8. If the response curve of the fractogram in Figure 5 directly replaces $c(t_r)$ in eq 7,

Table II. Comparison of Glass Bead Diameters of Collected Fractions Based on Calibration Procedure and on Microscopy

fraction	time, min	diameter based on calibration, μm	diameter based on micrograph, μm
	A. Fractions from 5–30-μm Sample (Figure 5)		
2	4.10–4.40	32.6–29.9	32.5 ± 1.7
4	4.70–5.00	27.6–25.5	24.9 ± 3.0
7	5.60–5.90	22.2–20.8	21.0 ± 1.3
11	6.80–7.10	17.5–16.6	17.5 ± 1.1
15	8.00–8.30	14.3–13.7	13.6 ± 1.2
19	9.20–9.50	12.1–11.6	11.7 ± 0.7
23	10.50–10.90	10.3–9.8	9.7 ± 1.1
27	12.10–12.60	8.6–8.2	8.4 ± 0.8
	B. Fractions from 5–50-μm Sample (Figure 6)		
3	2.80–2.90	52.1–49.9	51.9 ± 0.2
5	3.00–3.10	47.9–46.0	47.1 ± 1.8
9	3.40–3.50	41.0–39.6	41.5 ± 2.5
11	3.60–3.70	38.3–37.0	38.4 ± 2.1
13	3.80–3.90	35.8–34.7	36.9 ± 2.6
17	4.20–4.30	31.7–30.7	31.3 ± 1.7
22	4.80–5.00	26.9–25.5	24.9 ± 1.9
27	6.00–6.30	20.4–19.6	18.6 ± 1.4
33	8.30–8.70	13.7–12.9	13.5 ± 0.5

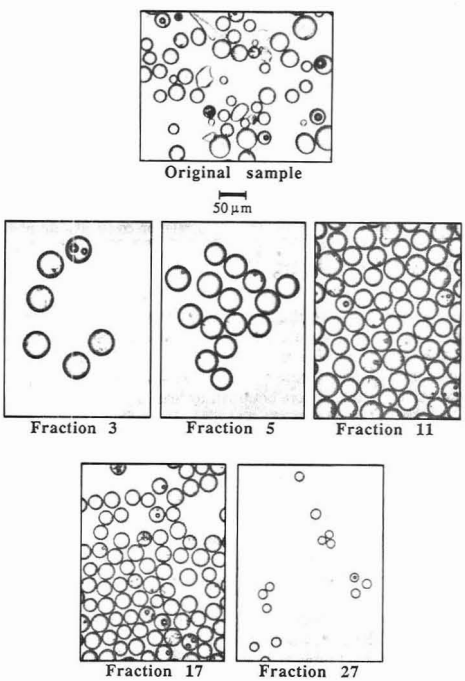

Figure 7. Optical micrographs of original 5–50-μm glass bead sample and of various fractions collected from the eluting stream at the time intervals shown in Figure 6. The detailed results of the microscopic examination of fractions are provided in Table II.

the center PSD curve of Figure 8 emerges. However, as noted earlier, $c(t_r)$ must be corrected if the detector signal, as in our case, depends on particle diameter as well as sample amount. Since the signal from our detector originates in scattered light, it is roughly proportional to the surface area of particles (such

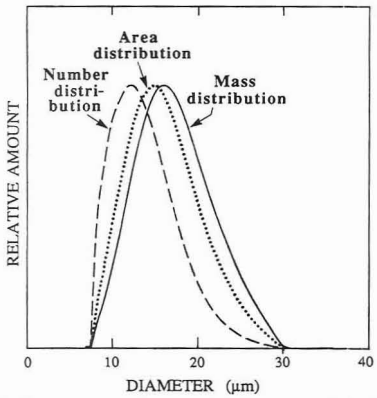

Figure 8. Number, area, and mass distribution curves obtained for the 5–30-μm glass bead sample by using the fractogram shown in Figure 5.

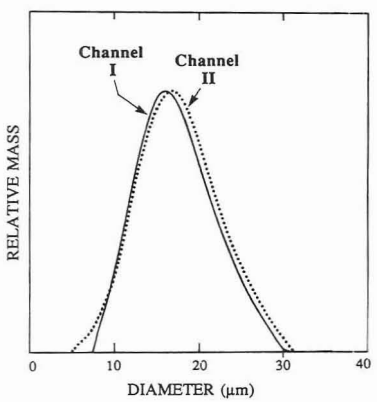

Figure 9. Comparison of mass-based size distribution curves for 5–30-μm glass bead sample (SRM 1003) using channels I (uniform) and II (pinched).

as ours) whose diameters greatly exceed the wavelength (254 nm) of the incident light beam. Thus the uncorrected center curve can be interpreted as a surfce area–weighted size distribution curve. When $c(t_r)$ in eq 7 is obtained by multiplying the signal by particle diameter d, a true mass distribution curve is produced, as shown by the right-hand curve of Figure 8. On the other hand, if the signal is divided by d^2, the number distribution curve shown to the left side of Figure 8 is generated. In subsequent figures we will show only mass-based size distribution curves.

A critical test of our calibration procedure that complements microscopy entails a comparison of particle size distribution (PSD) curves obtained from different channels, such as channels I and II, that differ significantly in structure (uniform versus pinched inlet) and operation (stopflow procedure versus stopless flow injection). Both channels, of course, must be separately calibrated with latex beads, as done here. Once S and t_{r1} are obtained by calibration and G is adjusted for density compensation, the size distribution can be obtained from the observed fractogram by using eq 7.

Figure 9 shows the two PSD curves obtained for the 5–30-μm glass bead sample by using the two different channels I and II. The calibration plots and parameters for these two cases are shown in Figure 3 and Table I as plots a and e for

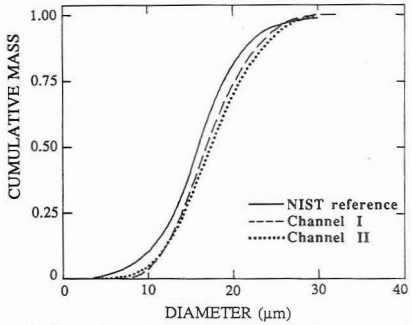

Figure 10. Comparison of cumulative size distribution curves obtained from the two FFF channels and a reference curve obtained from NIST.

the two respective channels. (The input fractogram for the channel I PSD is shown in Figure 5). These two PSD curves are in basic agreement in support of lower and upper cutoff diameters of approximately 5 and 30 μm, respectively, for the sample. They differ by about 1 μm on the diameter of the peak of the distribution, which appears to lie in the vicinity of 15 or 16 μm. Overall, the agreement of the two PSD curves is very good.

The size distribution given by NIST for this standard reference material (SRM 1003) is presented in cumulative form. When the size distribution curves of Figure 9 are converted to cumulative form and plotted against the NIST reference curve, the three close-lying cumulative distributions shown in Figure 10 are obtained. Although the agreement is satisfactory, the NIST reference curve displays diameters from 1 to 2 μm smaller than those obtained from the FFF curves for fixed values of the cumulative mass. (For example, at 50% cumulative mass, the NIST diameter is 15.8 μm while the Channel I diameter is 17.0 μm). This discrepancy, although not major, is not supported by the microscopy results reported in Table II, which show very good overall agreement with the calibration diameters. Some of the difference relative to the NIST curve could be due to the removal of much of the gas-void population, which might shift the PSD of the remaining bead population. However, incomplete removal (as we observe) is probably worse beause the gas inclusions will reduce bead density and lead to early elution, in which case they are counted as larger particles. Clearly, our methodology works imperfectly for particles that are heterogeneous in density like the present glass bead populations.

Some error in the PSD may also be introduced by imperfect sampling techniques since proper sampling is difficult in this size range. However, preliminary experiments involving variations in sampling procedures suggest that the sampling error is <1 μm.

We note that without the density-compensated calibration developed here, the particle diameter at the 50% cumulative point would be shifted from 17.0 to 8.8 μm. The latter value is unacceptably low, demonstrating that density effects must be properly accounted for.

Figure 11 compares the PSD's obtained for the nominal 5–50-μm sample by using channels I and II. The agreement with the reported 5-μm lower limit is not as good as that shown in Figure 8; this may be due to a very small (perhaps negligible) population of 5–10-μm beads, observed microscopically, that are lost in our baseline.

CONCLUSIONS

Although retention in sedimentation/steric FFF is not fully described by theory, particle size distribution curves can be obtained by constructing log t_r versus log d calibration plots

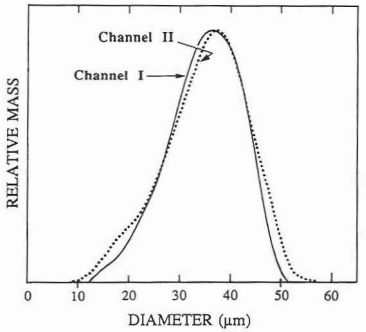

Figure 11. Comparison of mass-based size distribution curves for the 5–50-μm sample obtained from channels I and II.

using polystyrene latex beads and then by changing the rotation rate of the centrifuge to compensate for the density difference between the sample material and the latex calibrant. This procedure is shown to yield good results when tested by (a) microscopy, (b) self-consistency between two different FFF channel structures, and (c) a comparison with an external (NIST) cumulative size distribution curve. Further refinements in this approach should lead to increased speed and accuracy.

GLOSSARY

b	channel breadth
c	mass concentration in effluent
$c(t_r)$	corrected fractogram signal
d	particle diameter
G	acceleration
L	channel length
m	particle mass
$m(d)$	particle size distribution function
S	particle diameter selectivity ($=S_d$)
t°	void time
t_r	retention time
t_{r1}	retention time for particles of unit diameter
$\dot{V}$	flow rate through channel
V_r	retention volume
w	channel thickness

Greek Alphabet

$\Delta\rho$	density difference between particle and carrier
ρ	particle density

LITERATURE CITED

(1) Giddings, J. C. *Anal. Chem.* **1981**, *53*, 1170A–1175A.
(2) Giddings, J. C. *Sep. Sci. Technol.* **1984**, *19*, 831–847.
(3) Giddings, J. C.; Chen, X.; Wahlund, K.-G.; Myers, M. N. *Anal. Chem.* **1987**, *59*, 1957–1962.
(4) Karaiskakis, G.; Myers, M. N.; Caldwell, K. D.; Giddings, J. C. *Anal. Chem.* **1981**, *53*, 1314–1317.
(5) Peterson, R. E., II; Myers, M. N.; Giddings, J. C. *Sep. Sci. Technol.* **1984**, *19*, 307–319.
(6) Segrè, G.; Silberberg, A. *Nature* **1961**, *189*, 209–210.
(7) Segrè, G.; Silberberg, A. *J. Fluid Mech.* **1962**, *14*, 115–135.
(8) Segrè, G.; Silberberg, A. *J. Fluid Mech.* **1962**, *14*, 136–157.
(9) Saffman, P. G. *J. Fluid Mech.* **1965**, *22*, 385–400.
(10) Cox, R. G.; Brenner, H. *Chem. Eng. Sci.* **1968**, *23*, 147–173.
(11) Ho, B. P.; Leal, L. G. *J. Fluid Mech.* **1974**, *65*, 365–400.
(12) Vasseur, P.; Cox, R. G. *J. Fluid Mech.* **1976**, *78*, 385–413.
(13) Cox, R. G.; Hsu, S. K. *Int. J. Multiphase Flow* **1977**, *3*, 201–222.
(14) Leal, L. G. *Annu. Rev. Fluid Mech.* **1980**, *12*, 435–476.
(15) Ratanathanawongs, S. K.; Giddings, J. C. *J. Chromatogr.* **1989**, *467*, 341–356.
(16) Caldwell, K. D.; Nguyen, T. T.; Myers, M. N.; Giddings, J. C. *Sep. Sci. Technol.* **1979**, *14*, 935–946.
(17) Giddings, J. C.; Myers, M. N.; Yang, F. J. F.; Smith, L. K. In *Colloid and Interface Science*; Kerker, M., Ed.; Academic Press: New York, 1976: Vol. IV, pp. 381–398.
(18) Koch, T.; Giddings, J. C. *Anal. Chem.* **1986**, *58*, 994–997.
(19) Giddings, J. C. *Sep. Sci. Technol.* **1989**, *24*, 755–768.
(20) Moon, M. H.; Myers, M. N.; Giddings, J. C. *J. Chromatogr.* **1990**, *517*, 423–433.

RECEIVED for review December 17, 1990. Accepted April 16, 1991. This work was supported by Public Health Service Grant GM10851-33 from the National Institutes of Health.

Nanoliter-Scale Multireflection Cell for Absorption Detection in Capillary Electrophoresis

Tiansong Wang, Joseph H. Aiken, Carmen W. Huie, and Richard A. Hartwick*

Department of Chemistry, State University of New York at Binghamton, Binghamton, New York 13902

A multireflective absorption cell for CZE is fabricated and examined by both static and dynamic measurements. The new cell is characterized by improved sensitivity as compared to conventional single-pass cells, with no increase in cell volume. A 40-fold improvement in sensitivity is obtained when compared to a single-pass cell, with similar noise levels. A concentration detection limit of 6.5 × 10^{-8} M for brilliant green is estimated for the new cell design from static measurements. A theoretical analysis of cell performance using ray tracing for both axial and radial reflections in the new cell shows good agreement with experimental results.

INTRODUCTION

Detection is one of most important and rapidly developing areas in capillary zone electrophoresis (CZE). Various detection principles, such as spectrophotometric, mass spectrometric, electrochemical, and radiometric detection, have been applied to CZE (*1*). Although the sensitivity of UV–visible absorption detection is perhaps the lowest among these detection methods, UV detectors are the most popular detector currently utilized in CZE because of their simplicity and versatility.

Most UV detectors in CZE employ single-pass detection, which was first introduced by Yang for capillary liquid chromatography (*2*). In this design, the light beam travels normal to the capillary axis, crossing the capillary only a single time. According to Beer's law,

$$A = \epsilon bc \qquad (1)$$

where A is the absorbance, ϵ is the molar extinction coefficient of the sample, b is the light path length, and c is the sample concentration. The low sensitivity in single-pass detection is predictable because the path length is limited by the inner diameter of the capillary, typically 50–75 μm. Therefore, even with state of the art detectors, concentration detection limits are rarely lower than ca. 10^{-6} M.

0003-2700/91/0363-1372$02.50/0 © 1991 American Chemical Society

For a given molecule in a particular separation environment, absorption detection limits can be improved by decreasing the noise and/or increasing the path length. Some UV detectors for CZE have noise levels as low as 2×10^{-5} au, resulting in detection limits on the order of ca. 10^{-6} M for a good chromophore. Further reductions in noise levels are possible but remain technically difficult. The other way to improve the detection limit is to increase the effect path length. Rectangular capillaries have been investigated for CZE (*3*). With a 20-fold increase in path length, a 15-fold increase in sensitivity was obtained. A z-shaped absorption cell has been developed for capillary liquid chromatography (*4*). The path length was about 2 cm and sensitivity enhancement was 100–500 times. However, the volume of the z-shaped cell was too large for CZE. Another technology called axial-beam absorption detection has recently been introduced to open tubular capillary liquid chromatography (*5*). The path length in axial-beam detection was estimated to be 1000 times compared to that in single-pass detection, and a 192-fold improvement in detection limit was obtained. However, axial-beam detection requires precise alignment between the capillary and the light source and/or restricts the choice of mobile phase to solutions with refractive indices higher than that of fused silica.

Multireflection of the interrogative light beam with mirrors is a well-known technique to increase effective path length and thus to increase the sensitivity of absorption detection. A multireflection cell was first introduced by White (*6*) in order to analyze low-level gaseous samples by infrared spectroscopy, and multireflection cells (path length 1 to over 100 m) have been a regular accessory for infrared analysis of gas (*7, 8*). To date, however, this technique has not been applied to nanoliter-scale separations such as CZE and micro-LC, despite the obvious needs in both technologies for improved detection sensitivities. In this paper, a successful nanoliter-scale absorption cell based on multireflection from externally mirrored capillaries is reported. The performance of the new cell was evaluated statically and was applied to CZE separations. The basic theory of the new cell is presented by using ray-tracing simulations.

THEORY

The light ray tracing in a capillary can be established by a geometrical optical approach, and some patterns for single-pass detection have been reported (*9–11*). For a multireflection cell, the ray tracing is more complex than that in single-pass cell, since the light path must be traced both radially and axially.

According to geometrical optics (*12*), when a light ray impinges on a reflective surface, reflection will take place and the reflection angle is equal to the incident angle. When a light ray crosses from medium 1 to medium 2, refraction will take place and the refraction angle follows Snell's law:

$$n_1 \sin \theta_1 = n_2 \sin \theta_2 \tag{2}$$

where θ_1 and θ_2 are the incident and the refraction angle and n_1 and n_2 are the refractive index of medium 1 and medium 2, respectively.

There are two situations in the multireflection cell: reflection along the axis of a capillary and reflection along the circumference of a capillary.

Axial Reflection. The ray tracing can be seen from Figure 1. According to eq 2,

$$\theta_2 = \arcsin [(n_1 \sin \theta_1)/n_2] \tag{3}$$

From trigonometry,

$$l_1 = d_1 \tan \theta_2 \tag{4}$$

and

$$\theta_3 = \theta_2 \tag{5}$$

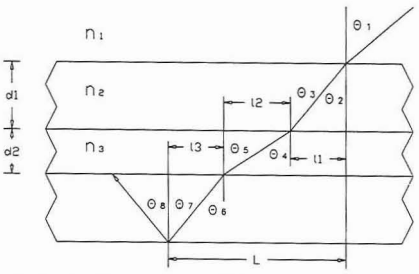

Figure 1. Ray tracing of axial reflection.

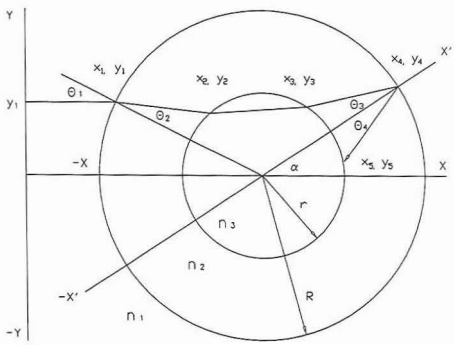

Figure 2. Ray tracing of radial reflection.

Similarly, l_2 and l_3 can be obtained. Then, the total length that the ray traveled is

$$L = l_1 + l_2 + l_3 \tag{6}$$

In the current cell design, the exterior of the capillary is silver mirrored. When the ray strikes the silver coating, it will be reflected with $\theta_8 = \theta_7$ and the tracing will follow the same pattern established above.

After traveling a distance D along the axis of a capillary, the number of reflections of the ray will be

$$N = D/L - 1 \tag{7}$$

N also indicates the increased time in path length. Assume a capillary with 75-μm i.d. × 364-μm o.d., $n_1 = 1.000$, $n_2 = 1.458$, $n_3 = 1.333$(water), and $\theta_1 = 5$; then L will be 0.0222 mm. For a traveling distance of 1 mm, N is equal to 44, that is, 44 time increase in the path length.

Radial Reflection. The ray tracing is shown in Figure 2. The incident ray is assumed to be parallel with the X axis and its position is y_1. According to trigonometry, coordinate x_1 will be

$$x_1 = -(R^2 - y_1^2)^{0.5} \tag{8}$$

Coordinates x_2,y_2, x_3,y_3, and x_4,y_4 can be established by the method in ref 10.

When the ray reflects at point 4, it is obvious that

$$\theta_4 = \theta_3 \tag{9}$$

Therefore, the ray tracings before and after reflection are symmetric along the X',$-X'$ axis, which is rotated by an angle of α with regard to the X, $-X$ axis. The angle α depends on both the incident position (x_1,y_1) of the ray and the refractive indices of each medium.

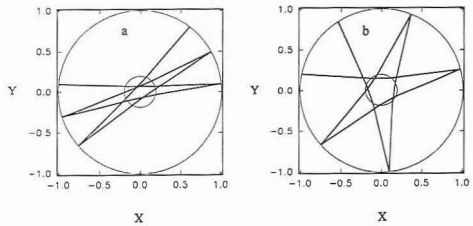

Figure 3. Typical ray tracing after four reflections in a multireflection cell (75-μm i.d. × 364-μm o.d.). (a) Incident position $y_1 = 0.10$; (b) Incident position $y_1 = 0.20$.

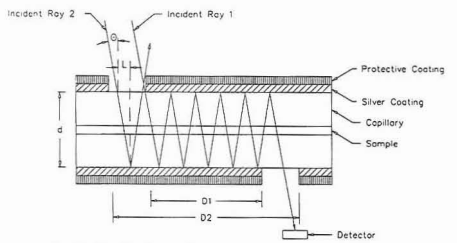

Figure 4. Multireflection cell.

Since the ray tracing is symmetric along the X',$-X'$ axis, further coordinates such as x_5,y_5 can easily be established by mathematic operation. Firsly, convert x_3,y_3 to x_3',y_3' as follows:

$$x_3' = x_3 \cos \alpha + y_3 \sin \alpha \quad (10)$$

$$y_3' = -x_3 \sin \alpha + y_3 \cos \alpha \quad (11)$$

The coordinates x_5',y_5' will be

$$x_5' = x_3' \quad (12)$$

$$y_5' = -y_3' \quad (13)$$

Secondly, convert x_5',y_5' to x_5,y_5 as follows:

$$x_5 = x_5' \cos \alpha - y_5' \sin \alpha \quad (14)$$

$$y_5 = x_5' \sin \alpha + y_5' \cos \alpha \quad (15)$$

Figure 3 presents two typical ray tracings after four reflections in a capillary with 75-μm i.d. and 364-μm o.d., $n_1 = 1.000$, $n_2 = 1.458$, and $n_3 = 1.333$(water) from which the distribution of light along the circumference of the capillary can be seen.

EXPERIMENTAL SECTION

Fabrication of the Cell. A schematic diagram of the multireflection cell is shown in Figure 4. The capillary was made of fused silica with 75-μm i.d. × 364-μm o.d. and 51 cm in length (Polymicro Technologies, Inc., Phoenix, AZ). The capillary also served as the separation column in CZE. An opening of about 1 cm was made on the capillary simply by burning off the polyimide coating of the capillary. Then the silver layer was deposited on the opening by redox reaction of $Ag(NH_3)_2^+$ and glucose (see Reagents subsection). Black paint (Illinois Bronze Paint Co., Lake Zurich, IL) was applied on the silver layer to protect it from physical damage. The light windows made on the cell were separated by distance D_1 and D_2 (0.8 and 1.5 mm, respectively). The cell volume calculated from D_2 was 6.6 nL.

Apparatus. A schematic diagram of the apparatus is shown in Figure 5. A 5-mW He–Ne laser (Model 1105P, Uniphase, Sunnyvale, CA) was used as the light source. The capillary with the multireflection cell was mounted on a conventional cell, which has been described elsewhere (*13*). The conventional cell and a 632.8-nm interference filter (Corion Corp., Holliston, MA) were taped on the window of a photomultiplier tube (R928, Hamamatsu, Somerset, NJ). The entire assembly was then mounted

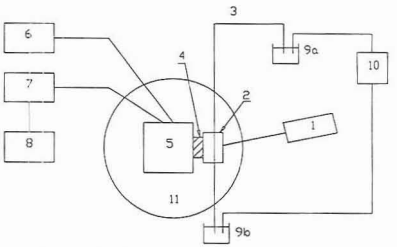

Figure 5. Schematic diagram of apparatus used for multireflection measurements. 1, He–Ne laser; 2, conventional cell; 3, capillary; 4, filter; 5, photomultiplier tube (PMT); 6, PMT high-voltage supply; 7, detection system; 8, recorder; 9a and 9b, buffer reservoir; 10, CZE high-voltage supply; 11, rotary stage.

on a rotary stage, which allowed fine adjustment of incident angle. The photomultiplier tube was operated by a high-voltage supply (2K10, Power Designs Inc., Westbury, NY). The laser beam first passed through the aperture (60 μm × 1.4 mm) of the conventional cell and then struck one of the windows of the multireflection cell. The light intensity exiting the other window was detected by a photomultiplier tube that either was connected to a Keithley 177 digital multimeter (Keithley Instruments, Inc., Cleveland, OH) in static measurement or was recorded by an Oriel 7072 detection system (Oriel Corp., Stratford, CT) and a OmniScribe A5111-5 chart recorder (Houston Instrument, Austin, TX) in CZE running. A PS/MK30P02.5 high-voltage power supply (Glassman High Voltage, Whitehouse Station, NJ) was used for CZE analysis.

Single-pass detection also was conducted by using a conventional cell (*13*) in order to compare the results with the multireflection detection. A similar capillary (75-μm i.d. × 364-μm o.d. and 47 cm in length) was used. The aperture was 60 μm × 0.22 mm and was placed behind the capillary, i.e., a laser beam passed the capillary first and then the aperture.

Evaluation Procedure. The performance of both the multireflection and the conventional cell was examined and compared by static measurement and CZE running. The test compound was brilliant green. In static measurement, the capillary was filled with distilled water and brilliant green–water solution alternately and signal currents were recorded. In CZE running, 0.01 M citrate buffer of pH 4.5 was used and brilliant green was dissolved in the buffer. Bare capillaries were used without special treatment except to wash with 1% NaOH for 20 min. The sample was injected by the siphon method (level difference, 5 cm, 30 s). The running voltage was 15 kV, and the current was 0.03 mA. When necessary, data were converted into absorbance:

$$A = \log (I_0/I) \quad (16)$$

where I_0 and I are currents measured from the reference and the sample solution, respectively.

Reagents. *Silver Deposit. Solution A.* Dissolve 1 g of silver nitrate in 20 mL of distilled water, add concentrated ammonium hydroxide until the solution is clear, then add 20 mL of 4% sodium hydroxide, and use ammonium hydroxide to redissolve all precipitate (**WARNING**: Solution A can generates explosive compounds; do not store solution A over 12 h).

Solution B. Dissolve 0.5 g of glucose in 20 mL of distilled water. The silver deposit reaction will take place when equal amounts of solution A and B are mixed.

Brilliant green was obtained from Aldrich (Milwaukee, WI), ammonium hydroxide from Corco (Fairless Hills, PA), and all other chemicals from Fisher (Fair Lawn, NJ).

RESULTS AND DISCUSSION

Incident Angle. The incident angle θ (see Figure 4) is a critical parameter because it affects the light intensity arriving at the photodetector and controls the number of reflections in the capillary, thus controlling the detection sensitivity. Figure 6 indicates the relationship of output light intensity to incident angle θ. When $\theta \approx 0$, the light intensity is very low (only 10% of the maximal intensity). The output light

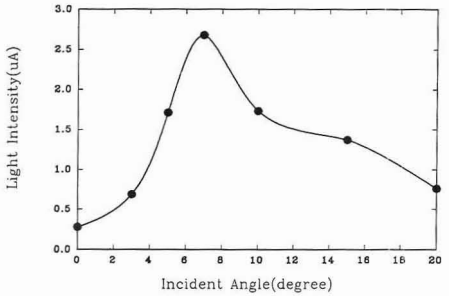

Figure 6. Relationship of incident angle to output light intensity.

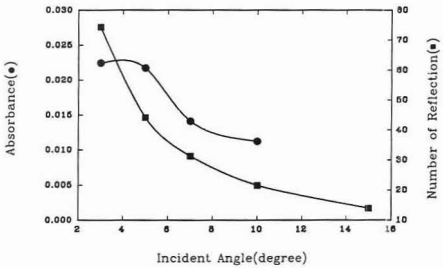

Figure 7. Relationships of incident angle to number of reflection and to absorbance.

intensity quickly increases with increasing θ from 0 to 7°, has a maximum at 7°, and then slowly decreases with increasing θ.

The relationships of θ to the number of reflections and to the sensitivity are shown in Figure 7. In theory, the sensitivity of a multireflection cell is proportional to the number of reflections, and reducing the incident angle will increase the number of reflections. Therefore, decreasing θ will enhance the sensitivity. This appears to be true for θ in the range 5–10°. However, such a relationship does not hold at smaller incident angles. When θ is reduced from 5 to 3°, the calculated number of reflections increases from 44 to 74, which means that the path length will be increased by about 1.7 times. However, the absorbance only increased by 2.8% experimentally, and the loss of light intensity was about 60%. Therefore, an incident angle of 5° was chosen in the following experiments.

Linear Dynamic Range and Detection Limit. The linear dynamic range of the multireflection cell was examined by static measurement with $\theta = 5°$, and the results are shown in Figure 8. The linearity established from Figure 8 is 2 orders of magnitude. In static measurement, noise is about 4.3×10^{-4} au, and the absorbance of 1.1×10^{-7} M brilliant green is 0.0022 au. The calculated detection limit (signal to noise ratio = 3) is 6.5×10^{-8} M. Although brilliant green has a high molar extinction coefficient ($\epsilon = 8.2 \times 10^4$ at 633 nm and pH 5.6), such a detection limit still is very impressive. When applied to actual CZE separations, the calculated concentration limit of detection was increased to 3.0×10^{-7} M (injected concentration) because of band dispersion and increased noise levels.

Comparison with Single-Pass Cell. The performance of the multireflection cell was compared with that of the single-pass cell by both static and dynamic measurements. The results are summarized in Table I, and two electropherograms are presented in Figure 9. It can be seen that the sensitivity of the multireflection cell is over 40 times higher

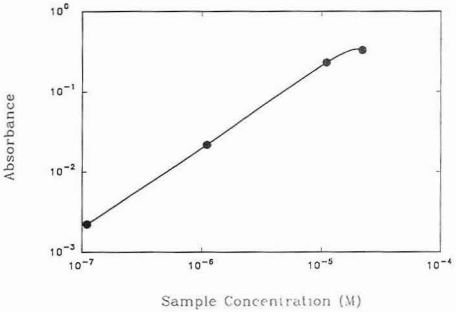

Figure 8. Linear dynamic range of detection with multireflection cell.

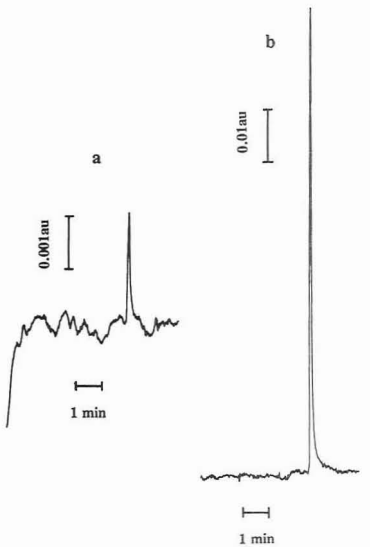

Figure 9. Electrophoregrams of 1.1×10^{-5} M brilliant green. (a) Obtained from single-pass cell; (b) obtained from multireflection cell. See text for conditions.

Table I. Performance Comparison of Multireflection Cell (mc) to Single-Pass Cell (sc)

condition	absorbance[a] mc ($\theta = 5°$)	sc	A_{mc}/A_{sc}
static measurement	0.230	0.0055	41.8
static noise	4×10^{-4}	4×10^{-4}	
CZE measurement	0.0899	0.0022	40.9
CZE noise	8.3×10^{-4}	6.6×10^{-4}	

[a] 1.1×10^{-5} M brilliant green.

than that of the single-pass cell, which is very close to the calculated increase of path length (44 times). Noise levels were similar for both cells.

Cell Design. Literally, the sensitivity of the multireflection cell can be increased further by increasing the distance between the two windows. In practice, however, the distance D_2 will be restricted by loss in separation efficiency. According to previous research (*13*), the distance should not be over 1σ of the peak width, and for a typical peak in CZE, 1σ is about 0.9 mm. Besides the loss in efficiency, longer distance coupled with more reflections also reduces the output light intensity

from the exit window because of the loss in light power during reflection, and at the extreme, the output light intensity will be lower than the detector noise, resulting in no detectable signal. Recently, Werle and Slemr (*14*) have found there is an optimal number of reflections for multireflection cell, and the number depends on the incident light power, the mirror reflectivity, and the modulation method of laser. Therefore, optimization of cell length will be important for different reflective coatings and light sources.

Another important aspect of cell design is the shape and dimensions of the windows. The critical parameters are the axial length and radial width of incident window and the shape of exit window. Although no experiments were conducted, theoretical analysis is very helpful:

(a) In Figure 4, there are two typical incident rays. Ray 1 enters the capillary and ray 2 exits the window after the first reflection. Ideally, all rays between ray 1 and ray 2 should enter the capillary. In order to obtain higher output light intensity from the exit window, the axial length of the incident window should not be smaller than $2L$ (about 0.05–0.1 mm), which allows the maximal amount of light to enter the capillary.

(b) According to the theory of radial reflection, the rays that do not pass the inner diameter of the capillary during the first segment of travel in the capillary (because their incident positions are too far away from the center of the capillary) will never pass the inner diameter in their entire travel and thus have no contribution to sample absorption. Therefore, the radial width of incident window should be equal to or slightly narrower than the inner diameter of a capillary in order to cut off the useless light.

(c) Also from the theory of radial reflection, a ray will rotate an angle after each reflection (Figure 3) with the angle depending on both incident position of the ray and the refractive index of each medium. It is expected that, after many times of reflection, rays will be distributed around the entire circumference of the capillary. Therefore, the exit window should ideally be a ring-shaped window, and a ring-shaped photodetector should be used in order to collect the entire light output.

ACKNOWLEDGMENT

We acknowledge Robin Robinson from the Department of Chemistry, State University of New York at Binghamton, for his assistance in the computer simulations of the ray-tracing studies and Scott Weinberger from Spectra-Physics Analytical Division for his helpful discussions.

LITERATURE CITED

(1) Ewing, A. G.; Wallingford, R. A.; Olefirowicz, T. M. *Anal. Chem.* **1989**, *61*, 292A–303A.
(2) Yang, F. *HRC&CC, J. High Resolut. Chromatogr. Chromatogr.* **1981**, *4*, 83–85.
(3) Tsuda, T.; Sweedler, J. V.; Zare, R. N. *Anal. Chem.* **1990**, *62*, 2149–2152.
(4) Chervet, J. P.; Ursem, M.; Salzmann, J. P.; Vannoort, R. W. *HRC&CC J. High Resolt. Chromatogr. Chromatogr.* **1989**, *12*, 278–281.
(5) Xi, X.; Yeung, E. S. *Anal. Chem.* **1990**, *62*, 1580–1585.
(6) White, J. U. *J. Opt. Soc. Am.* **1942**, *32*, 285–288.
(7) Willard, H. H.; Merritt, L. L., Jr.; Dean, J. A.; Settle, F. A., Jr. *Instrumental Methods of Analysis*, 7th ed.; Wadsworth: Belmont, 1988; p 306.
(8) Kiss-Eross, K. In *Comprehensive Analytical Chemistry*; Svehla, G., Ed.; Elsevier: Amsterdam, 1976; Vol. VI, pp 165–168.
(9) Vindevogel, J.; Schuddinck, G.; Dewaele, C.; Verzele, M. *J. High Resolut. Chromatogr. Chromatogr. Commun.* **1988**, *11*, 317–321.
(10) Synovec, R. E. *Anal. Chem.* **1987**, *59*, 2877–2884.
(11) Bruno, A. E.; Gassmann, E.; Pericles, N.; Anton, K. *Anal. Chem.* **1989**, *61*, 876–883.
(12) Finchman, W. H. A.; Freeman, M. H. *Optics*, 8th ed.; Butterworths: London, 1974; pp 15–21.
(13) Wang, T.; Hartwick, R. A.; Champlin, P. B. *J. Chromatogr.* **1989**, *462*, 147–154.
(14) Werle, P.; Slemr, F. *Appl. Optics* **1991**, *30*, 430–434.

RECEIVED for review January 28, 1991. Accepted April 23, 1991. This research was supported by grants from the Spectra-Physics Analytical Division and from Unilever Research.

Gas Chromatographic Determination of Trace Impurities in High-Purity Nitrogen Using Hydrogen Storage Alloys as a Nitrogen Adsorbent

Hiroshi Ogino,* Yoko Aomura, and Tetsuya Seki

Technical Research Laboratory, Toyo Sanso Company, Ltd., 3-3, Mizue-cho, Kawasaki-ku, Kawasaki-shi, Kanagawa 210, Japan

A combination of two different hydrogen storage alloys was used to assist in the gas chromatographic determination of trace impurities, such as neon, argon, krypton, methane, and xenon, in nitrogen. This system consists of a gas chromatograph combined, in series, with two precolumns filled with Ti/Mn-type and Ca-type hydrogen storage alloys. The former alloy efficiently retains nitrogen at 250 °C and under the pressure of the carrier gas. The latter alloy is used in order to more efficiently adsorb hydrogen, which is released from the former alloy, at ambient temperature. By using a photoionization detector, the detection limits achieved were as follows: 3.7, 0.08, 0.03, 0.04, and 0.09 ppm for Ne, Ar, Kr, CH_4, and Xe, respectively.

*To whom correspondence should be addressed.

INTRODUCTION

High-purity nitrogen used as an inert gas plays an important role in the field of semiconductor manufacture and other high-technology industries. Therefore, impurity analysis is becoming important for the quality control of gases.

In general, for the determination of inherent gas impurities in industrial gases, gas chromatography (GC) has been widely used as the preferred method (*1*). The photoionization detector (PID), which is based on the emission from a direct current discharge in helium gas (*2*), is the universal sensitive detector (*1*, *2*) and has especially high sensitivity for permanent gases. We reported in previous papers (*3–5*) that the PID is suitable for the determination of trace amounts of such gases. However, it has still been hard to separate and accurately determine trace amounts of impurities at less than parts per million levels in nitrogen: the use of a high-sensitivity

0003-2700/91/0363-1376$02.50/0 © 1991 American Chemical Society

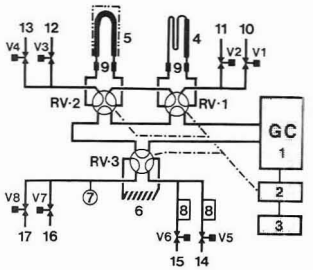

Figure 1. Schematic diagram of the apparatus for the determination of impurities in nitrogen. (1) GC–PID, (2) interface, (3) integrator, (4) second precolumn, (5) first precolumn, (6) sample loop, (7) pressure transducer, (8) mass flow meters, (9) line filters (Nupro, 5 μm), (10) to rotary vacuum pump, (11) hydrogen/helium outlet, (12) hydrogen inlet, (13) helium inlet, (14) sample gas inlet, (15) dilution gas (He/N_2) inlet, (16) sample gas outlet, (17) to rotary vacuum pump.

detector results in a huge nitrogen peak overlapping other peaks that are later eluted. It is necessary to eliminate the nitrogen peak overlap for the determination of trace impurities. To eliminate nitrogen in gases such as helium and argon, a Ti getter is commonly used as a nitrogen adsorbing material. However, this method requires a higher temperature, e.g., over 400 °C, for the complete adsorption of nitrogen. Therefore, if the nitrogen gas contains hydrocarbons such as methane, the Ti getter should cause thermal decomposition of the hydrocarbons. For the last 2 decades, hydrogen storage alloys (HSAs), such as $LaNi_5$, have provided purification and storage techniques for hydrogen gas (*6*, *7*). We have published methods for applying hydrogen storage alloys to gas analysis techniques (*3–5*). This paper describes a new analytical method for determining trace impurities in nitrogen by the use of a photoionization detector (PID) and two different types of hydrogen storage alloys as a nitrogen adsorbent.

EXPERIMENTAL SECTION

Apparatus and Conditions. A schematic diagram of the experimental apparatus is shown in Figure 1. The gas chromatograph with a PID (Hitachi, GC-263-30, Tokyo, Japan) and a GC–MS (Shimadzu, QP-300, Kyoto, Japan) were used in this experiment. This system can be programmed with a computerized integrator (Shimadzu, C-R4A) through an interface and is able to analyze and automatically report its results every 25 min. Two precolumns were installed in series between the gas sampler with a 1.23-mL sample loop and an analytical column. The analytical column packed with a molecular sieve (MS-5A, 60/80 mesh) in a 3-m × 3-mm-i.d. stainless steel tube was used in these experiments. The first precolumn (a 30-cm × $^3/_8$-in.-o.d. U-shaped stainless steel tube) was packed with a Ti/Mn-type HSA (16/60 mesh, 28 g), and the second precolumn (a 12-cm × $^3/_8$-in.-o.d. stainless steel tube) was packed with a Ca-type HSA (16/60 mesh, 7.2 g): the construction of the first precolumn is shown in a previous paper (*4*). Nitrogen was preferentially absorbed by the first precolumn operated at elevated temperature. However, hydrogen was continuously released from the Ti/Mn-type HSA into the carrier gas. Also, when nitrogen was adsorbed with the Ti/Mn-type HSA in the first precolumn, additional hydrogen was released from the Ti/Mn-type HSA in mere trace amounts into the carrier gas (He).

It is necessary to remove such released hydrogen because the background current of the PID significantly increases with the hydrogen and the detector cannot successfully determine the trace amounts of other gases at less than parts per million. On the other hand, the Ca-type HSA in the second precolumn efficiently absorbed hydrogen even at trace levels: this HSA showed much more capacity for hydrogen absorption than that of $LaNi_{4.9}Al_{0.1}$ used in our previous paper. The capacity for hydrogen absorption of the Ca-type HSA was ca. 50 mL, and its amount was enough to completely adsorb a small amount of hydrogen released from the first precolumn. Consequently, a combination of the Ti/Mn-type and Ca-type HSAs was chosen and used to remove nitrogen from sample gas and hydrogen released from the Ti/Mn-type HSA and also during the adsorption of nitrogen with Ti/Mn-type HSA. Operating conditions of the GC-PID, the precolumn, and the GC–MS are given in Table I.

Table I. Operating Conditions of the GC–PID, Precolumns, and GC–MS

GC	
column temp	70 °C
carrier gas	He, 48 mL/min
sample loop	1.23 mL
PID	
discharge gas	He, 38 mL/min
detector temp	100 °C
discharge potential	750 V
discharge current	150 μA
GC–MS	
column temp	70 °C
carrier gas	He, 30 mL/min
GC–MS transfer line temp	150 °C
ion source temp	200 °C
filament current	3.2 mA
electron energy	70 eV
gain	2.5
sample loop	2.00 mL

Materials. The HSAs used in the experiments were purchased from Daido Steel Co., Ltd. (Tokyo, Japan), for $Ti_{0.7}Zr_{0.3}Mn_{0.8}CrCu_{0.2}$ (Ti/Mn-type HSA) and Japan Metals and Chemicals (Tokyo, Japan) for $CaNi_5$ (Ca-type HSA), respectively. Reference gases were prepared by the gravimetric method and were supplied by Toyo Sanso Co., Ltd. A series of experiments, which were done in order to establish the optimum operating conditions for the precolumns and gas chromatograph, were conducted with reference gases having the following compositions: (1) 15.7 ppm Ar and 8.9 ppm CH_4 in N_2; (2) 12.1 ppm Ne, 11.8 ppm Ar, 11.4 ppm Kr, and 12.5 ppm Xe in N_2.

Activation of the HSA. Nitrogen adsorption with the Ti/Mn-type HSA occurred more efficiently at elevated temperature, e.g. >100 °C, and the reaction of the solid alloy with nitrogen gas under the conditions examined in this experiment was irreversible. The hydrogen absorbed at the lower temperature is chemically bound within the hydride crystal lattice, and it is reversibly desorbed from the hydride crystal lattice in the HSA hydride at higher temperature. Both HSAs used required this activation. In this experiment, both HSAs were separately activated: this was the best way to achieve activation. Initially, the HSAs ranging in particle size from 16 to 60 mesh were packed into the stainless steel columns. These precolumns were mounted in the rotary valves, RV-1 and RV-2, evacuated to remove the remaining air inside the tube and/or on their HSAs with a rotary vacuum pump, and then filled and pressurized with high-purity hydrogen (Toyo Sanso, A grade, 99.9999%, v/v) up to 5–6 atm at room temperature after valves V_1, V_2 and V_4 were closed. This condition was held for at least 30 min. Next, valve V_3 was closed and valve V_1 opened to evacuate the precolumn by using a rotary vacuum pump. During its evacuation, the precolumn is heated to 140 °C and allowed to stand for 30 min. The heating unit was then removed from the precolumn so the precolumn temperature could return to ambient. Valve V_1 was then closed and valve V_3 opened. The precolumn was then filled with hydrogen at 5–6 atm of pressure. This condition was maintained for 30 min in order to completely activate the precolumn (HSA). To assure the complete activation of the HSA, the evacuation with the rotary vacuum pump and repressurizing with hydrogen were repeated two or three times. Finally, after valve V_3 was closed and valve V_4 was opened in order to purge the first and/or second precolumn with helium, RV-2 (for the first precolumn) and/or RV-1 (for the second precolumn) was switched back to the analytical position, and then the precolumn was further heated at 250 °C for the Ti/Mn-type HSA and at 180 °C for the Ca-type HSA for 30 min in order to release as much hydrogen as possible from the HSA hydride. If the activated HSAs were filled with nitrogen or hydrogen, the re-

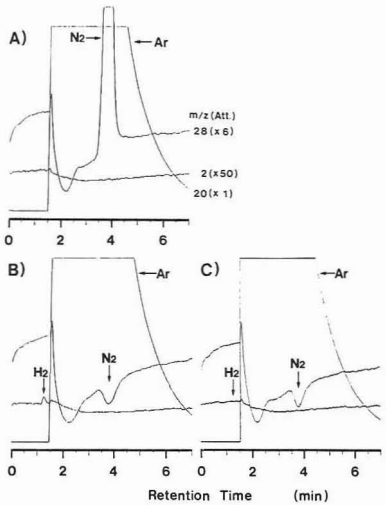

Figure 2. GC–MS selected ion profiles for gas mixture. (A) By ordinary method without any precolumn, (B) obtained from the residual gases passed through the first precolumn (Ti/Mn-type HSA), (C) obtained by the present method using the combination of the first and second precolumn (Ca-type HSA).

generation of the second precolumn (Ca-type HSA) could be actually accomplished by only avacuating it at 140 °C under vacuum, but the first precolumn (Ti/Mn-type HSA) should be replaced with a new precolumn as described later. The activation and regeneration procedures of the Ca-type HSA are almost similar with that already described except for the final temperature. The care during handling, storage, and disposal of these activated HSAs is described in our previous paper (*4*).

RESULTS AND DISCUSSION

Selection of the HSA. In our previous paper (*4*), Mm/Ni-type, La/Ni-type, Lm/Ni-type, and Ti/Mn-type HSAs were evaluated as to whether hydrogen can be completely absorbed by them and whether the resulting residual gases can pass through the precolumn without any losses or contamination: Mm and Lm are mischmetal and lanthanum-rich mischmetal, respectively. All of the examined HSAs showed apparent and reversible hydrogen absorption. However, the Ti/Mn-type HSA showed not only a large capacity for hydrogen absorption at ambient temperature but also the interesting and near perfect adsorption of nitrogen at ambient temperature.

The present investigation was undertaken to see whether the Ti/Mn-type HSA can be utilized as a nitrogen adsorbent for the determination of trace impurities in nitrogen gas by gas chromatography. However, the capacity and efficiency of nitrogen adsorption at ambient temperature were not enough for the repeatable analysis of nitrogen gas samples. Its capacity and efficiency were increased with an increase in heating temperature of the Ti/Mn-type HSA. The first precolumn filled with the Ti/Mn-type HSA was, therefore, set up to heat at 250 °C. As previously described, when the first precolumn (Ti/Mn-type HSA) was used at elevated temperature, a low concentration of hydrogen was continuously released from the Ti/Mn-type HSA and also during nitrogen adsorption.

In order to confirm the absorption capability of nitrogen and hydrogen with the combination of Ti/Mn-type and the Ca-type HSAs, the GC-MS analyses were undertaken with

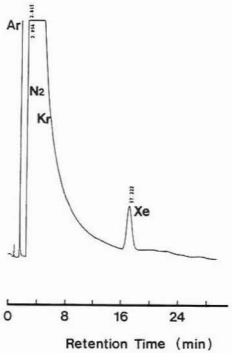

Figure 3. Typical gas chromatograms of Ne (6.5 ppm), Ar (5.9 ppm), and Kr (5.7 ppm), and Xe (6.3 ppm) in nitrogen obtained with the ordinary method.

a standard gas mixture containing 1000 ppm nitrogen in argon. The selected ion monitoring (SIM) profiles obtained from the original standard gas mixture and residual gases passed through the first precolumn, and the combination of the two precolumns is shown in Figure 2.

Figure 2A is the SIM profile of standard gas obtained by the ordinary method (without the precolumn) and shows clearly the peak of nitrogen (retention time: 3.8 min) together with that of argon. However, the result obtained from passing through the first precolumn indicated that the SIM profile did not show the presence of nitrogen, $m/z = 28$, and that the profile of $m/z = 2$ indicated the appearance of hydrogen, which was released due to the reaction of nitrogen with the heated Ti/Mn-type HSA as shown in Figure 2B. On the other hand, if the second precolumn packed with the Ca-type HSA was combined in series with the first precolumn (Ti/Mn-type HSA) as shown in Figure 1, nitrogen and hydrogen peaks could not be observed in the SIM profiles as shown in Figure 2C. This means that nitrogen gas was perfectly absorbed with the first precolumn and a trace amount of hydrogen was also absorbed with the second precolumn: the PID can detect trace amounts of components without any interference of hydrogen released from the first precolumn. Next, in order to determine the capacity of nitrogen adsorption, the sample gas containing 10 ppm Kr and CH_4 in nitrogen was automatically and repeatedly injected at 10-min intervals. The results showed that the first precolumn could adsorb over 680 mL of nitrogen. This means that if a 1.5-mL sample loop is used, analyses of more than 400 samples can be analyzed before a new precolumn is replaced. The capacity of nitrogen adsorption of the Ti/Mn-type HSA, regenerated with the procedure already described, significantly decreased to about $^1/_{10}$th of the original capacity.

Typical Gas Chromatograms. Typical gas chromatograms of the standard gas mixture of Ne, Ar, Kr, and Xe in nitrogen obtained by an ordinary method (without the precolumn) are shown in Figure 3. Gas chromatograms obtained by the present method (with the combination of two precolumns) are shown in Figure 4. The chromatograms show that if the sample containing a large quantity of nitrogen is directly injected into the gas chromatograph without the elimination of nitrogen, it seems impossible to separate and detect trace impurities such as krypton and methane since their component peaks overlap with the huge nitrogen peak and the detection of their components have a large interference due to the huge nitrogen peak. On the other hand, the proposed method provides suitable separation and successful detection of their impurities without interference of nitrogen and hydrogen

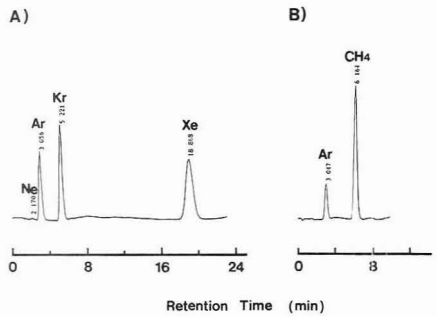

Figure 4. Typical gas chromatograms of gas mixtures: (A) Ne (8.5 ppm), Ar (12.4 ppm), Kr (8.0 ppm), and Xe (8.8 ppm) in N_2; (B) Ar (3.4 ppm) and CH_4 (6.7 ppm) in N_2.

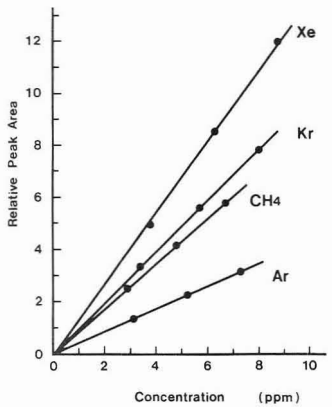

Figure 5. Calibration curves for Ar, Kr, Xe, and CH_4.

because the nitrogen and hydrogen released are completely removed.

Quantitative Features. A series of experiments were conducted in order to obtain the quantitative data for this method. Reference gases were diluted with high-purity nitrogen (guaranteed purity: 99.99995%) by the use of mass flow controllers to give concentrations of Ar, Kr, CH_4, and Xe in the range of ca. 2–9 ppm. The calibration curves obtained were linear in the range of the concentrations examined as shown in Figure 5. The curve of neon was excluded because its sensitivity was too low, and therefore, it was not sufficient to detect neon in the range of 2–9 ppm. The quantitative performance of the system was conducted by repeated injection of 1.60 mL of a nitrogen gas containing Ar (3.5 ppm), Kr (3.4 ppm), CH_4 (6.7 ppm), and Xe (3.8 ppm). The reproducibilities (relative standard deviation, $n = 8$) were 2.1, 0.64, 1.2, and 3.3% for Ar, Kr, CH_4, and Xe, respectively. The detection limits, which were calculated from the minimum

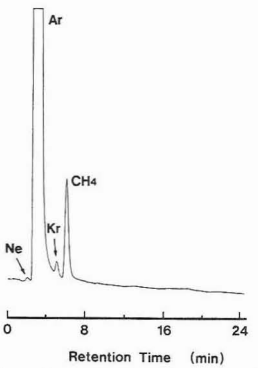

Figure 6. Gas chromatogram for the determination of trace Ne, Ar, Kr, and CH_4 in ambient air: a dry compressed air was used as the sample gas.

peak areas of the integrator detection, were 3.7, 0.08, 0.03, 0.04, and 0.09 ppm for Ne, Ar, Kr, CH_4, and Xe, respectively.

As another application, this method was applied to the gas chromatographic determination of the trace amounts of rare gases and methane in ambient air.

The gas chromatogram obtained is shown in Figure 6. It is obvious that this method can be applied for the determination of trace components, such as Ar, Kr, Xe, and CH_4 not only in nitrogen but also in other gases such as ambient air. In this method, hydrogen, oxygen, carbon monoxide, carbon dioxide, and unsaturated hydrocarbons such as ethylene and acetylene were retained in the precolumn due to their reaction with the hydrogen storage alloy and, therefore, could not be determined.

In conclusion, the combination of different hydrogen storage alloys can be practically applied for the gas chromatographic determination of trace impurities such as rare gases and methane in nitrogen and ambient air. This method can be used in conjunction with gas chromatography–mass spectrometry.

ACKNOWLEDGMENT

We thank M. Mizuno for his valuable comments on hydrogen storage alloys and N. Sakai for his technical assistance with the GC–MS.

LITERATURE CITED

(1) Cowper, C. J.; DeRose, A. J. *The Analysis of Gases by Chromatography*; Pergamon Press Ltd.: Oxford, 1985.
(2) Kawazoe, K.; Kamo, T.; Takata, Y.; Shikama, N. *Bunseki Kagaku* **1985**, *34*, 309–313.
(3) Ogino, H.; Aomura, Y.; Komuro, M.; Kobayashi, T. *Anal. Chem.* **1989**, *61*, 2237–2240.
(4) Ogino, H.; Aomura, Y.; Mizuono, M. *Anal. Chem.* **1990**, *62*, 994–996.
(5) Ogino, H.; Aomura, Y.; Hobo, T. *J. Chromatogr.* **1991**, *541*, 75–81.
(6) Stout, V. L.; Gibbons, M. *J. Appl. Phys.* **1955**, *26*, 1488–1492.
(7) Sandrock, G. D.; Huston, E. L. *CHEMTECH* **1981**, Dec, 754–762.

RECEIVED for review February 2, 1991. Accepted April 24, 1991.

Membrane Technology and Dynamic Response of Ion-Selective Liquid-Membrane Electrodes

Marin Huser, Peter M. Gehrig, Werner E. Morf, and Wilhelm Simon*

Department of Organic Chemistry, Swiss Federal Institute of Technology (ETH), Universitätsstrasse 16, CH-8092 Zürich, Switzerland

Ernö Lindner, Judit Jeney, Klára Tóth, and Ernö Pungor*

Institute for General and Analytical Chemistry, Technical University of Budapest, Gellért tér 4, H-1111 Budapest XI, Hungary

In order to study the parameters affecting the dynamic response behavior of neutral-carrier-based liquid-membrane electrodes, the potential response vs time curves of Na^+-, Ca^{2+}-, and Mg^{2+}-selective electrodes with different membrane compositions were recorded. The effects of the lipophilicity of ionophores and plasticizers, of the presence of incorporated mobile anionic sites and of modifications of the membrane matrix were investigated. The experimental potential–time curves were compared to fitted functions on the basis of theoretical models.

INTRODUCTION

The recent efforts in ion-selective electrode research made a tailored design of highly selective ionophores possible, which resulted in the realization of a large variety of corresponding membrane sensors (*1*, *2*). In spite of the primary importance of the ion–ionophore interactions exploited in these systems, however, selectivity is only one of the crucial parameters determining the whole performance of ionophore-based liquid-membrane electrodes. The ion-selective membranes applied in such macroelectrodes usually consist of about 1 wt % ionophore, 60–65 wt % plasticizer, 30–35 wt % PVC, and a strictly limited amount of lipophilic salt additives like sodium tetraphenylborate (NaTPB) or potassium tetrakis(*p*-chlorophenyl)borate (KT*p*ClBP) (*3*, *4*). Only the appropriate selection of each of these constituents finally guarantees for a highly selective and sensitive electrode that exhibits a stable and reproducible potential response. On the other hand, the specifications required for special applications such as in clinical chemistry can be fulfilled only by a thorough, very careful optimization of the membrane composition, which often involves compromises between competitive influences of components to be made.

The most relevant fields of application of neutral-carrier-based ion-selective electrodes are clinical chemistry and bioelectrochemistry. In both fields the response time of the sensors is of utmost importance when the aim is to achieve a large sample throughput or to follow fast biological processes. On the other hand, there are very stringent requirements concerning the selectivity, sensitivity, potential stability, reproducibility, and lifetime of the sensors (*5*, *6*). To find the best compromise, one should know the exact influence of the different membrane components and of their properties on the response time of the sensor.

In the present work we investigated in more detail the influence of the lipophilicity of the ligand, the lipophilicity of the plasticizer, the presence of lipophilic salt additives in the membrane, and modifications of the membrane matrix on the response time of selected cation-selective neutral-carrier-based PVC membrane electrodes. Similar studies on the response time of potassium sensors with different membrane matrices (PVC or silicone rubber) and with plasticizers of differing polarity were carried out earlier (*7–10*).

To study the effects of lipophilicity of ligand and plasticizer on the dynamic response is, first of all, interesting from a practical point of view, since only sensors based on relatively lipophilic membrane components have practical relevance for clinical routine analysis (*5*). High lipophilicity is even more crucial when minielectrodes, fabricated with modern planar technologies, are concerned (*11*).

However, it is difficult to investigate the dependence of response time on a single parameter. By varying the lipophilicity of the ligand and/or of the plasticizer, not only the extraction properties but also several other decisive parameters of the membrane (e.g. viscosity, ion permeabilities, etc.) are changed. In addition, it was shown earlier that ionophores having the same lipophilicities and only partly differing chemical constitutions may behave completely different in membrane electrodes with respect to slope and selectivity. The observed phenomena were interpreted as the result of kinetic limitations of the carrier-induced ion transfer between aqueous phase and membrane phase (*12*, *13*).

The present studies seem to be important in theoretical respect as well. Therefore, the results on response times of ion sensors were analyzed in the light of theoretical models to get further information concerning the nature of the rate-determining processes.

THEORY

There are a number of different possibilities to compare measured time response curves for ion sensors and to evaluate the relevant results. For practical purposes it is often convenient to characterize the observed potential transients by specifying the time needed to reach 90%, 95%, or 99% of the total potential change due to a given sample activity change. However, characterization of the complete response vs time curve by one single, arbitrarily selected point (e.g. $t_{95\%}$) unavoidably leads to a loss of information or even to erroneous conclusions. For example, the time period after which the final, reliable potential reading can be taken might be underestimated, especially in cases where different sections of the curve are dominated by different rate-controlling processes (*14–16*).

Therefore, the potential transients recorded in the course of the present investigations have not simply been characterized by the respective $t_{90\%}$ data, but they have also been further analyzed by using curve-fitting methods based on theoretical considerations. Equations 1 and 2 have been

$$\Delta E(t) = \Delta E(\infty) + S \log [1 - (1 - a_i^0/a_i)e^{-t/\tau_1}] \quad (1)$$

$$\Delta E(t) = \Delta E(\infty) + S \log [1 - (1 - a_i^0/a_i)(1/(\sqrt{t/\tau_2} + 1))] \quad (2)$$

*To whom correspondence should be addressed.

0003-2700/91/0363-1380$02.50/0 © 1991 American Chemical Society

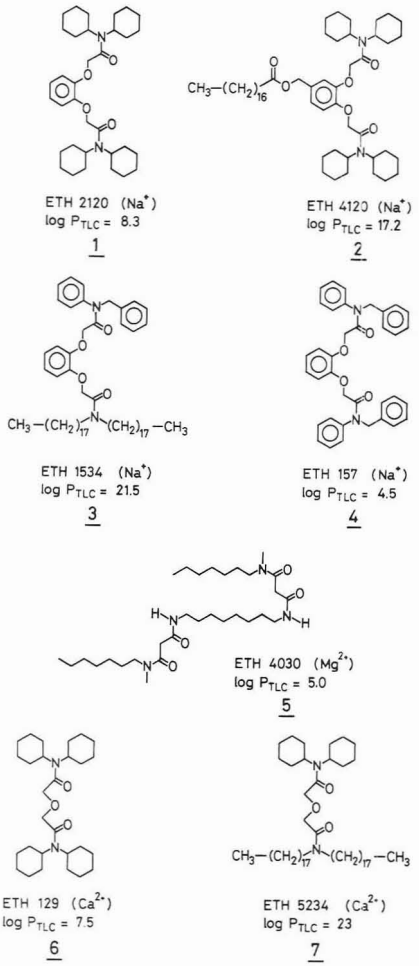

Figure 1. Constitutions and lipophilicity of ionophores discussed.

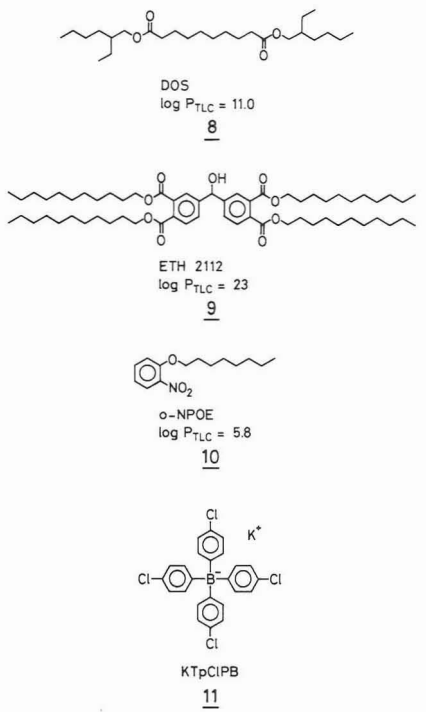

Figure 2. Constitutions and lipophilicity of plasticizers applied and constitution of potassium tetrakis(*p*-chlorophenyl)borate (KT*p*ClPB).

suggested in earlier contributions (*7*, *8*, *14–19*) (for a recent discussion, see ref 20) as approximative descriptions of the dynamic response governed by diffusion/equilibration processes through the stagnant aqueous boundary layer and into the ion-selective membrane, respectively: where $\Delta E(t)$ is the potential change found after the time t, $\Delta E(\infty)$ is the total potential change reached at final steady state, S is the experimentally determined slope of the electrode response function (emf vs log a_i), a_i^0 is the initial activity of the primary ion in the bulk of the sample solution before applying an activity step at $t = 0$, a_i is the new activity value of the primary ion in the bulk of the sample solution after the step change, τ_1 is a time constant (e.g. $\tau_1 = \delta^2/2D$) and its interpretation is dependent on the model assumption used, τ_2 is the time constant for a diffusion process reaching into the membrane phase, t is the period of time after the activity step, δ is the thickness of the aqueous boundary film (Nernstian diffusion layer), D is the mean diffusion coefficient of ions within this boundary layer. The short-time response behavior of the different sensors was generally compared on the basis of eq 1, while the long-time response data were mainly evaluated with eq 2. By the latter relationship, originally, salt extraction and concomitant diffusion processes into the bulk membrane were taken into account (*7*). However, in the light of more recent studies on ionophore-based solvent polymeric membranes (*21*), such systems rather appear to behave as phases with fixed anionic sites, which makes an explanation of bulk diffusion processes within the membrane more problematic (*20*). Nevertheless, a square-root time dependence is often observed in dynamic response measurements on liquid-membrane electrodes as well as on solid-state sensors (*20*, *22*, *23*).

EXPERIMENTAL SECTION

Chemicals. For all experiments, deionized water doubly distilled in Pyrex glass and chemicals of puriss or pa grade were used.

Membranes. The solvent polymeric membranes were prepared according to ref 24 by using 1 wt % carrier, 64–66 wt % plasticizer, and 33 wt % poly(vinyl chloride). All ionophores (see Figure 1) were products of Fluka AG (Buchs, Switzerland) or were synthesized in our laboratories as described in the literature: ETH 2120 (ligand **1**), Fluka 71734; ETH 4120 (**2**) (*25*); ETH 1534 (**3**) (*12*); ETH 157 (**4**), Fluka 71733; ETH 4030 (**5**) (*26*); ETH 129 (**6**), Fluka 21193; ETH 5234 (**7**) (*27*). As plasticizers (see Figure 2), bis(2-ethylhexyl) sebacate (DOS, **8**), Fluka 84818, tetra-*n*-undecyl-3,3′,4,4′-benzhydrol tetracarboxylate (ETH 2112, **9**), Fluka 12103, *o*-nitrophenyl octyl ether (*o*-NPOE, **10**), Fluka 73732, and chloroparaffin (ClP, 60% Cl), Scientific Polymer Products, Inc., New York, were used. As polymeric membrane materials, poly(vinyl chloride) (PVC, high molecular weight, HMW), Fluka 81392, carboxylated PVC (PVC–COOH, with 1.8 wt % COOH groups), Aldrich, 18,955-3, or a vinyl chloride/vinyl alcohol copolymer (PVC–OH, with 3.7 wt % OH groups) (*28*), were selected. The starting material for the preparation of PVC–OH was a copolymer of 82.9 wt % vinyl chloride and 17.1 wt % vinyl acetate prepared

Table I. Summary of Relevant Parameters of Membrane Systems Studied

membrane system											
no.	ionophore[b]	matrix	plastic[b]	amt of KT*p*ClPB,[c] mol %	slope,[a] mV/dec	log K_{ij}^{pot} H^+	Na^+	K^+	Mg^{2+}	Ca^{2+}	R, MΩ
1	1	HMW	8		57.5	−0.8	0	−1.5	−4.2	−3.1	38
2	1	HMW	8	11	56.3	−0.8	0	−1.5	−3.8	−1.6	3.1
3	1	HMW	9		43.6	0.3	0	−0.7	−1.9	−0.1	3800
4	1	PVC–OH	8		58.4	−0.7	0	−1.3	−3.0	−1.7	22
5	1	PVC–OH	8		57.1	−0.5	0	−1.1	−3.5	−0.8	2.2
6	2	HMW	8		57.4	−0.6	0	−1.4	−3.8	−2.8	52
7	2	HMW	8	11	56.1	−0.6	0	−1.3	−3.8	−1.7	4.3
8	3	HMW	8		56.3	−0.1	0	−0.5	−3.6	−2.8	25
9	3	HMW	8	11	57.7	−0.9	0	−0.5	−3.9	−2.4	3.0
10	4	HMW	8		56.6	−1.1	0	−0.4	−3.8	−3.2	60
11	4	HMW	8	11	57.9	−1.4	0	−0.4	−4.0	−2.6	2.2
12	6	HMW	10		27.6	−2.0	−2.5	−2.6	−3.1	0	4.2
13	7	HMW	10		26.7	−0.7	−3.2	−3.5	−3.7	0	8.6
14	7	HMW	10	46	28.5	−3.1	−5.9	−7.5	−4.4	0	0.5
15	5	HMW	chloroparaffin	60	29.0	1.9	−3.7	−3.5	0	0	92 (49)

[a] The slope values listed were determined in an activity range of 10^{-1}–$10^{-3.6}$. [b] The numbers in the column refer to the numbers on Figures 1 and 2. [c] The amount of KT*p*ClPB is relative to the ionophores.

on a small scale (charge 916D) by ICI (Switzerland) AG, Kunststoffwerk, CH-5643 Sins. The poly(vinyl chloride)–poly(vinyl acetate) copolymer (5 g) was dissolved in 100 mL of THF, and during a period of 10 min, the mixture was added dropwise to a solution of 1 wt % NaOH (puriss, Siegfried AG CH-4800 Zofingen) in 30 mL of methanol (MeOH; Fluka, puriss pa) at 50–60 °C. The solution was stirred during 1.5 h at 63 °C, reduced to half of the volume, and then passed through filter paper into 1.5 L of water (25 °C) under stirring. After 10 min, the precipitate was filtered off, suspended in 300 mL of MeOH, and filtered again. The residue was suspended once more in 200 mL of MeOH and poured into 0.8 L of water (25 °C). After the product was filtered and dried (60 °C, vacuum), 1.2 g of product was obtained. The IR spectrum of a membrane cast with 50 mg of PVC–OH in 1.5 mL of THF showed a broad OH signal at 3400 cm^{-1}, the sharp signal at 1732 cm^{-1} due to the CO stretching vibration of the educt being absent. As lipophilic anionic-site additive, potassium tetrakis(*p*-chlorophenyl)borate (KT*p*ClPB, 11), Fluka 60591, was used. The membrane compositions are given in Table I.

emf Measurements. The membranes of about 200-μm thickness were mounted in a Philips IS-560 liquid-membrane electrode body. The active membrane area was 0.126 cm^2. emf values were measured with an Orion Research Model 701 pH meter coupled to an Orion Model 605 manual electrode switch. The external reference electrode was a Radelkis 8201 double-junction Ag/AgCl electrode, with a 1 M potassium chloride or 1 M lithium acetate bridge electrolyte. Selectivity coefficients were determined by the separate solution method (SSM) (*29*) in 10^{-1} M aqueous metal chloride solutions. The activity coefficients used were estimated as described in refs 30 and 31. The measured emf values were corrected for the liquid-junction potentials by using the Henderson formalism (*30*).

Determination of the Internal Resistance of the Cells. The electrical membrane resistances were determined by the voltage divider method using known shunts (*32*). Further details were reported in ref 33.

Determination of Lipophilicities. The lipophilicities of the plasticizers and of the ionophores, log *P*, were determined by thin-layer chromatography (*5b, 34, 35*). The uncertainties in the determined log P_{TLC} values are in the range of ±0.4 up to ±4, depending on the absolute magnitude of data determined.

Response Time Measurements. To determine the dynamic response (voltage vs time-function) of the different electrodes, a switched wall-jet arrangement was used (*36*). The rise time (10%–90%) of the differential electrometer amplifier (Keithley Model 604) with a standard shunt resistance of 10 or 100 MΩ was specified as 5 or 50 ms, respectively. To avoid undesirable and uncontrollable interference by the measuring electronics on the response time functions of membranes with high resistances, the effect of the cell resistance was checked experimentally by increasing this resistance with a standard resistor (of the same order of magnitude) in series to the electrode studied. This procedure allowed the determination of the maximal cell resistance where the rise time of the measuring electronics did practically not affect the response time values. The flow rate was fixed at about 160 mL/min, applying a constant pressure of 0.3 bar on the solution containers.

The standard deviation of the $t_{90\%}$ data as a result of differences in flow rate setting and geometrical differences was found to be ±2 ms at a response time value of 40 ms. However, the membrane to membrane variation of the $t_{90\%}$ data may be considerably larger (in the range ±10–15 ms) as a result of hardly controllable parameters such as ionic impurities in any of the membrane components, changes of membrane properties in time, and differences in the surface geometry of the different electrodes and active surface area of membranes.

All response time measurements were carried out in the presence of a background electrolyte of constant ionic strength in order to minimize effects by streaming potentials and liquid-junction potentials. The choice of this electrolyte was dependent on the selectivity properties of the membrane electrodes. Accordingly, 0.1 M $MgCl_2$ and 0.1 M KCl were used as background electrolytes for measurements with Na^+- and Ca^{2+}-selective electrodes, respectively, and 0.1 M NaCl for Mg^{2+}- and K^+-selective electrodes.

RESULTS AND DISCUSSION

In the course of this work, sodium-, calcium-, and magnesium-selective ionophores of different lipophilicities were incorporated into solvent polymeric membranes prepared with plasticizers of wide ranging lipophilicities. The chemical constitutions of these compounds together with the experimentally determined lipophilicity data ($2.6 \leq \log P_{TLC} \leq 23$) are given in Figures 1 and 2, and the relevant parameters of membrane systems studied are summarized in Table I. On the basis of the results obtained with different ionophores it can be stated that the dynamic characteristics of corresponding membrane electrodes are virtually not influenced by the lipophilicity of the ligands as long as log $P \geq 5$ (see Figure 3 and Table II). The same trends were reported earlier for potassium-selective electrodes on the basis of bis(15-crown-5) and related ionophores (*10, 37*). The moderate slowing-down of the time-response observed for sensors with less lipophilic ionophores can be ascribed to a gradual loss of the relatively water-soluble components from the surface region of the membrane, which may results in a surface layer of low site density and high electrical resistance. No evidence for a relationship between the lipophilicity of the ion carriers and the response time of corresponding ion sensors is found for the calcium-selective systems (Table III). Both Ca^{2+}

Table II. Effect of the Lipophilicity of the Ligand on the $t_{90\%}$ Response Time Data and on the Time Constant of Eq 1 Fitted to the Experimentally Recorded Response Time Curves of the Sodium Sensors

membrane system				params of eq 1[a]		
no.	ionophore	log P_{TLC}	$t_{90\%}$, ms 2 → 3[b]	τ_1, ms 2 → 3[b]	RMSD, mV	$t_{90\%}$, ms 3 → 2[b]
10	ETH 157 (4)	4.5	365	38.2	2.3	82
1	ETH 2120 (1)	8.3	177	12.4	2.1	29
6	ETH 4120 (2)	17.2	202	15.2	2.6	44
8	ETH 1534 (3)	21.5	168	16.9	2.0	59

[a] The curve-fitting procedure was always the same; i.e. 79 data points were taken into consideration (every 20th) from the 1650 collected within 1-s time period. [b] The numbers represent the negative logarithm of solution activities a_i^0 and a_i, while the arrows indicate the direction of the activity step.

Table III. Effect of Lipophilic Salt Additives on the $t_{90\%}$ Response Time Data and on the Time Constant of Eqs 1 and 2 Fitted to the Potential–Time Curves of Different Ca^{2+} Electrodes

membrane system				params of eq 1[a]		params of eq 2[a]		
no.	ionophore	KT*p*ClPB[b]	$t_{90\%}$, ms 4 → 2[c]	τ_1, ms 4 → 2[c]	RMSD, mV	τ_2, ms 4 → 2[c]	RMSD, mV	$t_{90\%}$, ms 2 → 4[c]
13	ETH 5234 (7)	–	48	162	0.21	10.7	0.17	74
14	ETH 5234 (7)	+	23	109	0.25	6.3	0.14	32
12	ETH 129 (6)	–	57					71

[a] The curve-fitting procedure was always the same; i.e. 103 data points were taken into consideration (every 16th) from the 1650 collected within 25-s time period. [b] Membranes denoted with a + sign were prepared with KT*p*ClPB additive. [c] The numbers represent the negative logarithm of solution activities a_i^0 and a_i, while the arrows indicate the direction of the activity step.

Table IV. Comparison of $t_{90\%}$ Response Time Data as Well as of Time Constants of Eq 1 Fitted to the Experimentally Recorded Response Time Curves of Sodium Sensors Based on Ligands of Different Lipophilicity and Containing KT*p*ClPB Additives

membrane system				params of eq 1[a]		
no.	ionophore	log P_{TLC}	$t_{90\%}$, ms 2 → 3[b]	τ_1, ms 2 → 3[b]	RMSD, mV	$t_{90\%}$ ms 3 → 2[b]
11	ETH 157 (4)	4.5	18	4.9	0.49	14
2	ETH 2120 (1)	8.3	24	6.8	0.67	31
7	ETH 4120 (2)	17.2	33	8.4	0.71	30
9	ETH 1534 (3)	21.5	14	4.2	0.23	9

[a] The curve-fitting procedure was always identical; i.e. 79 data points were taken into consideration (every 20th) from the 1650 collected within 1-s time interval. [b] The numbers represent the negative logarithm of solution activities a_i^0 and a_i, while the arrows indicate the direction of the activity step.

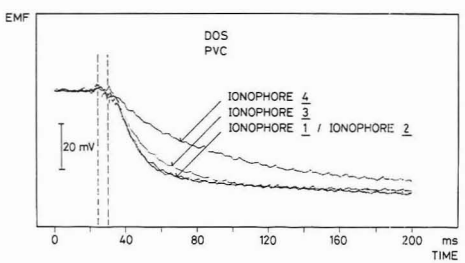

Figure 3. Response time curves of solvent polymeric membrane electrodes with the sodium-selective ionophores **1–4** and DOS (**8**) as membrane solvent. Conditions: concentration step; 10^{-2}–10^{-3} M NaCl; supporting electrolyte; 10^{-1} M $MgCl_2$. The two vertical lines show the start and stop times of the jet switching motion.

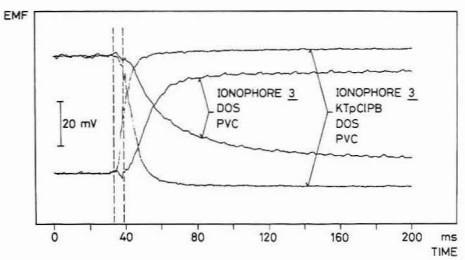

Figure 4. Response time curves of solvent polymeric membrane electrodes with DOS (**8**) as plasticizer and the sodium-selective ionophore **3**. Membranes without additional anionic sites are compared with membranes containing 11 mol % KT*p*ClPB relative to the ionophore. Conditions: concentration steps, 10^{-3}–10^{-2} M NaCl and vice versa; supporting electrolyte, 10^{-1} M $MgCl_2$. The two vertical lines show the start and stop times of the jet switching motion.

ionophores studied dispose of an adequately high lipophilicity and yield membrane electrodes that exhibit a fast and almost identical response.

The incorporation of additional anionic sites (KT*p*ClPB in this work) into conventional neutral-carrier-based PVC membranes generally leads to fast responding electrodes (see Figure 4 and Tables III and IV), and the dynamic behavior is often found to become almost independent of the properties of the ionophore applied (Table IV). The electrodes with KT*p*ClPB additive become so fast that the overall transients are primarily controlled by the time of switching and mixing. Such a favorable effect of lipophilic salt additives in respect to the response time could be confirmed both on the basis of $t_{90\%}$ data and fitted time constants (compare Tables II and IV). Similar results have also been reported earlier (*8*, *37*).

The experimental time response curves were analyzed in more detail by curve-fitting procedures based on the theoretical eqs 1 and 2. The comparison of the results was carried out on the basis of the fitted time constants, of the data obtained for the root mean square deviation (RMSD =

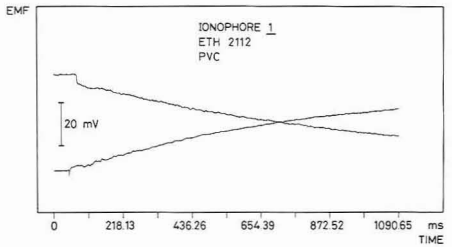

Figure 5. Experimentally recorded potential–time functions of a sodium-selective membrane electrode containing the ionophore **1** and the highly lipophilic plasticizer ETH 2112 (**9**). Conditions: concentration steps, 10^{-3}–10^{-2} M NaCl and vice versa; supporting electrolyte, 10^{-1} M $MgCl_2$.

$[RSS/(n-p)]^{1/2}$, where RSS is the residual sum of squares, n is the number of experimental values taken into consideration, and p is the number of parameters) and of the numerical values found for the curve-fitting parameters (e.g. the slope S of the potential response function).

The model assumptions used for the derivation of eq 1 are probably justified generally for ISE response time measurements under usual conditions. But they might not be valid if the switched wall-jet system is used at high sample flow rate. The switched wall-jet arrangement was developed with the aim to avoid the rate-controlling effect of the diffusion through the aqueous boundary layer in the overall response. Deviations from eq 1 can be attributed to differences between the model assumptions and experimental conditions. But they may indicate that processes other than the diffusion/equilibration through an adhering solution to the electrode surface are rate-determining. In the latter case no or little flow rate dependence is expected and the main goal was achieved. On the contrary a considerable flow rate dependence and a good fit of eq 1 imply that among the rate-determining processes the ion transport through the hydrodynamic boundary layer to the electrode surface is still basically rate determining. In these circumstances small changes in the response time may not be detectable, e.g. in the case of membranes containing KT*p*ClPB.

These studies showed that a dynamic behavior according to the square-root time relationship (eq 2) generally becomes more pronounced in the case of long-term measurements, of sensor systems with poorly lipophilic ligands and when a step from high to low sample activities is followed. In contrast, the response time curves recorded with ionophore-based PVC membranes containing KT*p*ClPB additives are usually in better agreement with the exponential time dependence (eq 1), independently of the lipophilicity of the carrier and of the direction of the activity change (compare RMSD data of Tables II and IV). Very often, however, the experimental curves could be rather well fitted with either of the two equations. Therefore, a clear-cut experimental distinction between the underlying rate-controlling processes (*7*, *8*, *14*–*19*) is not feasible and generally only a qualitative characterization of the curve type is given in this work.

Washing-out of the plasticizer from the solvent polymeric membrane finally results in an increase of the membrane resistance and in a concomitant loss of ion sensitivity (*38*–*40*). For that reason, plastizicers of high lipophilicity have been suggested especially for biomedical applications (*5a*). The compound ETH 2112 was synthesized on the basis of such considerations (*41*). Unfortunately, membrane electrodes prepared with this extremely lipophilic plasticizer showed an unusually high response time (Figure 5) as well as reduced selectivity and sensitivity (Table I). The observed $t_{90\%}$ values

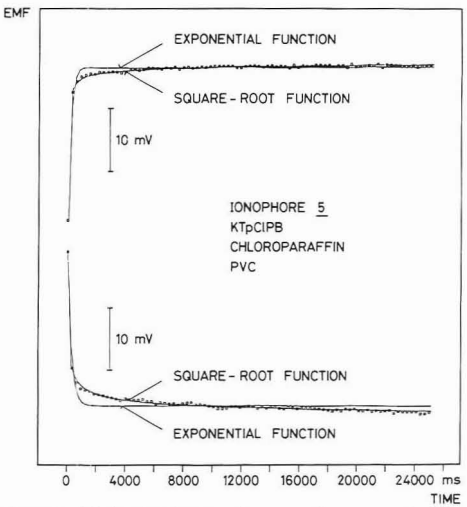

Figure 6. Calculated and measured response time curves of a divalent-ion-selective electrode containing the carrier **5**, 60 mol % KT*p*ClPB relative to the carrier and chloroparaffin as membrane solvent. The curves were fitted on the basis of the exponential function (eq 1) and of the square-root function (eq 2). Conditions: concentration steps, 10^{-3}–10^{-2} M $MgCl_2$ and vice versa; supporting electrolyte, 10^{-1} M NaCl.

are typically in the range of several seconds for this case, i.e. by 1–2 orders of magnitude higher than the values listed in Table II for electrodes containing DOS as plasticizer. Exudation of the plasticizer and formation of a site-free or low site density surface layer of high resistance may be the reason for such a behavior. Unfortunately, the literature about impedance studies of PVC membranes is quite controversial in this respect. Some authors reported on the formation of high-resistance surface films (*9*, *42*, *43*) or on surface-charge-transfer resistances related to slow ion-transfer kinetics (*44*, *45*), while the impedance studies of other authors showed no evidence for surface effects in normal membrane compositions (*46*, *47*); see also ref 48. If the thickness and the resistance of such a layer are large enough, the diffusion of species to the active membrane surface becomes rate-limiting, which finally results in a square-root time dependence of the electrode response (*20*).

On the basis of the divalent-ion-selective ionophore **5**, membrane electrodes suited for water hardness determination, exhibiting a high discrimination of Na^+ and K^+ ions and nearly identical selectivities for Ca^{2+} and Mg^{2+} ions, were realized earlier (*49*) by selecting chloroparaffin (log P_{TLC} = 6.4–10.1) as plasticizer. In the present studies, the response time of this sensor turned out to be considerably longer than that for the Na^+-, K^+-, and Ca^{2+}-selective sensors. The experimentally found $t_{90\%}$ data were 2120 and 600 ms for an activity step of 10^{-2}–10^{-3} M and vice versa, respectively. Furthermore, eq 2 gave an almost perfect fit to the experimental data in both the relatively short-time and the long-time domains (see Figure 6). These results seem to corroborate the previous assumption of a surface layer predominantly formed by the plasticizer. When DOS as plasticizer was replaced with chloroparaffin in fast-responding ion-selective sensors (e.g. bis(crown ether)-based potassium electrode), the rate of response became similarly slow. The incorporation of KT*p*ClPB in such membranes results in some response time decrease as expected, but these values are still considerably larger as compared to those of membranes with DOS.

Table V. Effect of the Membrane Matrix on the $t_{90\%}$ and $t_{95\%}$ Response Time Data and on the Time Constants of Eqs 1 and 2 Fitted to the Potential–Time Curves of HMW- and PVC–OH-Matrix-Based Sodium Sensors

membrane system						params of eq 1[b]		params of eq 2[b]	
no.	ionophore (additive)	matrix	activity step[a]	$t_{90\%}$, ms	$t_{95\%}$, ms	τ_1, ms	RMSD, mV	τ_2, ms	RMSD, mV
1	ETH 2120 (1)	HMW	2 → 3	350	790	89.5	0.57	0.3	0.22
4	ETH 2120 (1)	PVC–OH	2 → 3	898	2890	99	1.24	1.2	0.17
1	ETH 2120 (1)	HMW	3 → 2	30	76	111	0.20	1.8	0.09
4	ETH 2120 (1)	PVC–OH	3 → 2	137	660	169	0.56	18.6	0.16
2	ETH 2120 (1)	HMW	2 → 3	21		6.1	0.41	0.035	1.29
	+ KT*p*ClPB			**35**[c]					
5	ETH 2120 (1)	PVC–OH	2 → 3	46		9.4	1.15	0.23	1.48
	+ KT*p*ClPB			**265**[c]		**35.1**[c]		**5.4**[c]	

[a] The numbers represent the negative logarithm of solution activities a_i^0 and a_i, while the arrows indicate the direction of the activity step. [b] For the curve-fitting procedure, 80 data points at constant time intervals were taken into consideration from the 1650 collected. For the membrane systems without KT*p*ClPB (nos. 1 and 4) and with KT*p*ClPB (no. 2 and 5), time periods of 25 and 1 s, respectively, were evaluated. [c] The experiments were carried out after conditioning the electrodes for 1 day and again after 8 days conditioning. The bold data correspond to the second set of experiments.

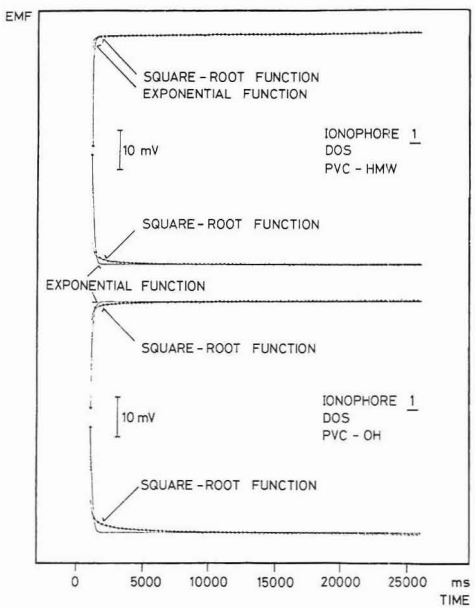

Figure 7. Comparison of calculated and measured response time curves of electrodes with the sodium-selective carrier **1** and DOS (**8**) as plasticizer, which were prepared either from conventional PVC or from hydroxylated PVC (PVC–OH). The curves were fitted on the basis of the exponential function (eq 1) and of the square-root function (eq 2). Conditions: concentration steps, 10^{-3}–10^{-2} M NaCl and vice versa; supporting electrolyte, 10^{-1} M $MgCl_2$.

Membranes with chemically modified PVC copolymer matrices (PVC–COOH, PVC–OH) were introduced in ion-selective sensors primarily in the aim of improving their adhesion on surfaces of electronic semiconductor devices, which is an essential step in the manufacturing of ion-selective field effect transistors (*50*). Although it was shown that in these membranes the predominant part of the fixed ionic sites are in a nondissociated form (*43*, *51*), the corresponding sensors proved to be advantageous in comparison with conventional PVC-membrane-based devices. Thus, the use of the modified polymer matrices leads to a reduction of membrane bulk resistances by a factor of 1.5–5 and to a reduction of membrane surface resistances (*43*), as well as to a reduction of asymmetry potentials caused by protein adsorption onto the membrane after its exposure to blood serum or whole blood (*28*).

However, more detailed investigations revealed that ion-selective electrodes prepared with carboxylated or hydroxylated PVC copolymer membranes generally tend to exhibit a slower response than the conventional PVC counterparts and that the observed time response curves appear to follow a membrane diffusion-controlled transient potential according to eq 2 (Table V and Figure 7). This equation gave a much better fit to the potential–time curves recorded with carboxy or hydroxy PVC based membranes than eq 1. The RMSD data are 2–7 times smaller if eq 2 was fitted to a given set of data points instead of eq 1.

In contrast to the favorable effect of a high density of mobile site additives (e.g. KT*p*ClPB) on the response time found for conventional PVC-based membrane sensors, the speed of response is significantly reduced in the case of these modified polymeric membranes with an increased fixed site density. Even in the presence of a well-defined amount of anionic sites (KT*p*ClPB), electrodes prepared from PVC–OH behave fundamentally different from electrodes prepared from standard PVC (Table V). The response time of standard PVC-based membranes changed only slightly during the experimental time period of 8 days. The incorporation of KT*p*ClPB into PVC–OH-based membranes initially leads to relatively fast responding electrodes, too, but the response time increases considerably with time, and the advantageous effect of KT*p*ClPB becomes less pronounced.

There are some hints that the rate of equilibration is here again limited by diffusion processes reaching into the membrane and may be influenced by the presence of a distinct surface film. Such surface films can generally be formed during membrane preparation (*8*, *9*), by exudation of plasticizer (*42*), by dissolution of active membrane components from the outer membrane region, or by the development of a hydrated layer such as in the case of glass membranes (*52*). In connection with the last possibility, it is worth mentioning that both the carboxylated and the hydroxylated PVC membranes show a remarkably high water uptake during conditioning (*53*).

LITERATURE CITED

(1) Rouilly, M. V.; Badertscher, M.; Pretsch, E.; Suter, G.; Simon, W. *Anal. Chem.* **1988**, *60*, 2013.
(2) Pretsch, E.; Badertscher, M.; Welti, M.; Maruizumi, T.; Morf, W. E.; Simon, W. *Pure Appl. Chem.* **1988**, *60*, 567.
(3) Meier, P. C.; Morf, W. E.; Läubli, M.; Simon, W. *Anal. Chim. Acta* **1984**, *156*, 1.
(4) Pretsch, E.; Wegmann, D.; Ammann, D.; Bezegh, A.; Dinten, O.; Läubli, M. W.; Morf, W. E.; Oesch, U.; Sugahara, K.; Weiss, H.; Simon, W. In *Ion Measurements in Physiology and Medicine*; Kessler, M., et al., Eds.; Springer Verlag: Berlin, Heidelberg, 1985; p 11.
(5) (a) Oesch, U.; Anker, P.; Ammann, D.; Simon, W. In *Ion-Selective Electrodes*; Pungor, E., Ed.; Adadémiai Kiadó: Budapest, 1985; Part 4, p 81. (b) Dinten, O.; Spichiger, U. E.; Chaniotakis, N.; Gehrig, P.; Rusterholz, B.; Morf, W. E.; Simon, W. *Anal. Chem.* **1991**, *63*, 596.
(6) Bührer, T.; Gehrig, P.; Simon, W. *Anal. Sci.* **1988**, *4*, 547.

(7) Morf, W. E.; Lindner, E.; Simon, W. *Anal. Chem.* **1975**, *47*, 1596.
(8) Lindner, E.; Tóth, K.; Pungor, E.; Morf, W. E.; Simon, W. *Anal. Chem.* **1978**, *50*, 1627.
(9) Lindner, E.; Niegreisz, Zs.; Tóth, K.; Pungor, E.; Berube, T. R.; Buck, R. P. *J. Electroanal. Chem. Interfacial Electrochem.* **1989**, *259*, 67.
(10) Tóth, K.; Lindner, E.; Horváth, M.; Jeney, J.; Bitter, I.; Ágai, B.; Meisel, T.; Töke, L. *Anal. Lett.* **1989**, *22*, 1185.
(11) Oesch, U.; Simon, W. *Transducers 87, The 4th International Conference on Solid-State Sensors and Actuators, Digest of Technical Papers*; Institute of Electrical Engineers of Japan, 1-12-1, Yurakucho, Chiyoda-ku, Tokyo, Japan, 1987; p 755.
(12) Oesch, U.; Ammann, D.; Pretsch, E.; Simon, W. *Helv. Chim. Acta* **1979**, *62*, 2073.
(13) Gehrig, P.; Morf, W. E.; Welti, M.; Pretsch, E.; Simon, W. *Helv. Chim. Acta* **1990**, *73*, 203.
(14) Lindner, E.; Tóth, K.; Pungor, E. *Dynamic Characteristics of Ion-Selective Electrodes*; CRC Press Inc.: Boca Raton, FL, 1988.
(15) Lindner, E.; Tóth, K.; Pungor, E. *Anal. Chem.* **1976**, *48*, 1071.
(16) Shatkay, A. *Anal. Chem.* **1976**, *48*, 1039.
(17) Tóth, K.; Gavallér, I.; Pungor, E. *Anal. Chim. Acta* **1971**, *57*, 131.
(18) Markovic, P. L.; Osburn, J. *AIChE J.* **1973**, *19*, 504.
(19) Morf, W. E. *The Principles of Ion-Selective Electrodes and of Membrane Transport*; Akadémiai Kiadó, Elsevier, MIR Publishers: Budapest, Amsterdam and New York, Moscow, 1981, 1981, 1985.
(20) Berube, T. R.; Buck, R. P. *Anal. Lett.* **1989**, *22*, 1221.
(21) Buck, R. P.; Tóth, K.; Gráf, E.; Horvai, G.; Pungor, E. *J. Electroanal. Chem. Interfacial Electrochem.* **1987**, *223*, 51.
(22) Berube, T. R. Response of ion-selective electrodes to step in ion concentrations. Ph.D. Thesis, The University of North Carolina at Chapel Hill, 1989.
(23) Werner, B.; Werner, G.; Lindner, E. Unpublished work.
(24) Craggs, A.; Moody, C. J.; Thomas, J. D. R. *J. Chem. Educ.* **1974**, *51*, 541.
(25) Gehrig, P.; Rusterholz, B.; Simon, W. *Anal. Chim. Acta* **1990**, *233*, 295.
(26) Müller, M.; Rouilly, M.; Rusterholz, B.; Maj-Zurawska, M.; Hu, Z.; Simon, W. *Mikrochim. Acta* **1988**, *3*, 283.
(27) Gehrig, P.; Rusterholz, B.; Simon, W. *Chimia* **1989**, *43*, 377.
(28) Dürselen, L. F. J.; Wegmann, D.; May, K.; Oesch, U.; Simon, W. *Anal. Chem.* **1988**, *60*, 1455.
(29) Guilbaut, G. G.; Durst, R. A.; Frant, M. S.; Freiser, H.; Hansen, E. H.; Light, T. S.; Pungor, E.; Rechnitz, G.; Rice, N. M.; Rohm, T. J.; Simon, W.; Thomas, J. D. R. *Pure Appl. Chem.* **1976**, *48*, 127.
(30) Meier, P. C.; Ammann, D.; Morf, W. E.; Simon, W. In *Medical and Biological Applications of Electrochemical Devices*; Koryta, J., Ed.; Wiley: Chichester, New York, Brisbane, Toronto, 1980; p 13.
(31) Meier, P. C. *Anal. Chim. Acta* **1982**, *136*, 363.
(32) Ammann, D.; Pretsch, E.; Simon, W.; Lindner, E.; Bezegh, A.; Pungor, E. *Anal. Chim. Acta* **1985**, *171*, 119.
(33) Lindner, E.; Tóth, K.; Jeney, J.; Pungor, E.; Buck, R. P.; Kemény, P. In *Ion-Selective Electrodes*; Pungor, E., Ed.; Akadémiai Kiadó: Budapest, 1989; Part 5, p 459.
(34) Simon, W.; Pretsch, E.; Morf, W. E.; Ammann, D.; Oesch, U.; Dinten, O. *Analyst* **1984**, *109*, 207.
(35) Oesch, U.; Brzózka, Z.; Xu, A.; Rusterholz, B.; Suter, G.; Pham, H. V.; Welti, D. H.; Ammann, D.; Pretsch, E.; Simon, W. *Anal. Chem.* **1986**, *58*, 2285.
(36) Lindner, E.; Tóth, K.; Pungor, E.; Berube, T. R.; Buck, R. P. *Anal. Chem.* **1987**, *59*, 2213.
(37) Tóth, K.; Lindner, E.; Jeney, J.; Gráf, E.; Horváth, M.; Pungor, E.; Bitter, I.; Meisel, T.; Ágai, B.; Töke, L.; Buck, R. P.; Kellner, R. In *Ion-Selective Electrodes*; Pungor, E., Ed.; Akadémiai Kiadó: Budapest, 1989; Part 5, p 181.
(38) Oesch, U.; Simon, W. *Helv. Chim. Acta* **1979**, *62*, 754.
(39) Oesch, U.; Simon, W. *Anal. Chem.* **1980**, *52*, 692.
(40) Horvai, G.; Gráf, E.; Tóth, K.; Pungor, E.; Buck, R. P. *Anal. Chem.* **1986**, *58*, 2735.
(41) Oesch, U.; Xu, A.; Brzózka, Z.; Suter, G.; Simon, W. *Chimia* **1986**, *40*, 351.
(42) Tóth, K.; Gráf, E.; Horvai, G.; Pungor, E.; Buck, R. P. *Anal. Chem.* **1986**, *58*, 2741.
(43) Lindner, E.; Gráf, E.; Niegreisz, Zs.; Tóth, K.; Pungor, E.; Buck, R. P. *Anal. Chem.* **1988**, *60*, 295.
(44) Xie, S.-L.; Cammann, K. *J. Electroanal. Chem.* **1987**, *229*, 249.
(45) Xie, S.-L.; Cammann, K. *J. Electroanal. Chem.* **1988**, *245*, 117.
(46) Armstrong, R. D. *Electrochim. Acta* **1987**, *32*, 1549.
(47) Armstrong, R. D.; Nikitas, P. *Electrochim. Acta* **1985**, *30*, 1627.
(48) Horvai, G.; Horváth, V.; Farkas, E.; Pungor, E. In *Ion-Selective Electrodes*; Pungor, E., Ed.; Akadémiai Kiadó: Budapest, 1989; Part 5, p 397.
(49) Maj-Zurawska, M.; Rouilly, M.; Morf, W. E.; Simon, W. *Anal. Chim. Acta* **1989**, *218*, 47.
(50) Satchwill, T.; Harrison, D. J. *J. Electroanal. Chem.* **1986**, *202*, 75.
(51) Ma, S. C.; Chaniotakis, N. A.; Meyerhoff, M. E. *Anal. Chem.* **1988**, *60*, 2293.
(52) Karlberg, B. *J. Electroanal. Chem.* **1973**, *42*, 115.
(53) Tóth, K.; Lindner, E.; Jeney, J.; Pokol, Gy.; Pungor, E. Unpublished work.

RECEIVED for review May 15, 1990. Revised manuscript received March 29, 1991. Accepted April 5, 1991. This work was partly supported by the Swiss National Science Foundation.

Pulse-Electrolysis Stopped-Flow Method for the Electrospectroscopic Analysis of Short-Lived Intermediates Generated in the Electrooxidation of Triphenylamine

Munetaka Oyama, Koichi Nozaki, and Satoshi Okazaki*

Department of Chemistry, Faculty of Science, Kyoto University, Kyoto 606, Japan

A new analytical method was developed for the electrochemical and spectroscopic analyses of short-lived intermediates generated during electrochemical processes. Many-faceted conclusions can be drawn from spectroscopic measurements after pulse electrolysis with a column electrode; e.g. dynamic transformation profiles of absorption spectra correspond to the applied potential. The fundamental characteristics of this method are described in detail. Electrolytic efficiency in the carbon-wool column electrode was evaluated in controlled-potential and controlled-current pulse electrolysis of the tetracyanoquinodimethane anion radical ($TCNQ^{\bullet-}$). In the controlled-potential operation, 0.11 mM $TCNQ^{\bullet-}$ was electrolyzed quantitatively within 200 ms. Up to 2.2 mM, the controlled-current operation permitted quantitative electrolysis with a 50-ms current pulse. Kinetic analysis of the dimerization reaction of the triphenylamine (TPA) cation radical ($TPA^{\bullet+}$) was carried out by this method. The pure solution containing only $TPA^{\bullet+}$ was successfully prepared by pulse electrolysis without any interference by the consecutive reactions. Therefore the absorption coefficient of $TPA^{\bullet+}$ was easily determined and the dimerization rate constant of $TPA^{\bullet+}$ was quite simply analyzed by following the absorbance decay of $TPA^{\bullet+}$. The effect of the parent molecules on the reaction was also clarified by mixing TPA and $TPA^{\bullet+}$ solutions.

INTRODUCTION

In order to analyze the complex chemical reactions of electrogenerated species involved in the electron-transfer process, a novel pulse-electrolysis stopped-flow method was developed and evaluated. There are a number of flow-electrolysis cells for the purpose of electrosynthesis, separation, and analysis (*1*, *2*). We have developed a flow-electrolysis method using a column electrode packed with glassy-carbon grains or carbon fibers (*3*), and utilized it for UV–vis spectrophotometry (*4*, *5*), ESR measurements (*6*, *7*), and the resonance Raman measurements (*8*, *9*) of electrogenerated species. In this electrolysis method, due to the large surface area of the carbon-fiber working electrode versus the sample volume, quantitative electrolysis can be achieved in a very short time (ca. <50 ms).

Evans et al. studied the reaction kinetics of very stable diphenylanthracene cation radicals generated by batchwise electrolysis using the stopped-flow technique (*10*). In this method, however, the objective electrogenerated species are restricted to those that are very stable.

The pulse-electrolysis stopped-flow method has many advantages in that it can be applied not only to the detection and characterization of unstable intermediates whose half-lives are as short as 50 ms but also to the analysis of the reaction kinetics of heterogeneous electrode reactions as homogeneous reactions. This is because the parent molecules are electrolyzed quantitatively in a short time by the pulse electrolysis using a carbon-wool column electrode and the electrolyzed solution is delivered immediately to an optical flow cell by utilizing a stopped-flow technique.

In this study, the pulse-electrolysis stopped-flow method with the carbon-wool column electrode was fundamentally evaluated in detail. As an electrolysis method, both controlled-current and controlled-potential operations can be used. Controlled-potential pulse electrolysis is useful for the characterization of the electrochemical reaction mechanisms, e.g. by observing the absorbance vs applied potential curve by reference to cyclic voltammetry. Controlled-current pulse electrolysis is effective for the quantitative generation of very short-lived species with half-lives as short as 50 ms.

The electrochemical dimerization reaction process of the triphenylamine (TPA) cation radical ($TPA^{\bullet+}$) in acetonitrile (AN) was analyzed by this method. The dimerization reaction mechanism of $TPA^{\bullet+}$ has been studied by electrochemical methods (*11–15*). Nelson et al. studied the chemical oxidation process of TPA with Cu(II) by using a stopped-flow technique (*15*). However, a problem remained in the slow electron exchange between TPA and Cu(II), and moreover the complex mechanisms caused by the oxidant had to be considered.

The pulse-electrolysis stopped-flow apparatus has two operation modes: (1) The time changes in absorption spectra of electrogenerated intermediates can be followed by simply delivering the electrolyzed solution to the optical flow cell (nonmixing mode). (2) The reaction processes of electrogenerated species with various reactants can be observed by mounting a jet-mixer between the electrolysis cell and the optical flow cell (mixing mode). The present method has improved features, in that pure solutions containing only short-lived objective species such as $TPA^{\bullet+}$ can be prepared and that the absorption coefficients of short-lived species can be determined from the absorbance vs applied current plots by using the nonmixing mode. The mixing mode enables not only analysis of reactions with various reactants but also clarification of the effect of parent molecules on the reaction.

EXPERIMENTAL SECTION

Apparatus. Figure 1 shows a cross-sectional view of the cell, which consists of three components: (A) electrolysis cell, (B) jet-mixer, and (C) optical cell. The electrolysis cell, which is suitable for the optical measurement and the stopped-flow operation, was constructed in this work.

Carbon wool having a feltlike structure (CW, Kureha Kagaku Co., Ltd.) was used as the working electrode. Its advantages are that solutions pass through even if it is tightly packed and the solution layer on the surface of electrode becomes thin and homogeneous. Various straight carbon fibers were tested as the electrode materials. However, they were insufficient due to high pressure created in the electrolysis cell and fibers pushed downstream into the optical cell when they were tightly packed.

The carbon wool was packed tightly in a microporous glass diaphragm tube (PGT; 35-mm length × 4-mm i.d.; pore size, 50 Å) to a length of packing over 25 mm. Loose or short packaging (10 mm) caused a decrease in electrolysis efficiency.

Both ends of the column were sealed tightly with O-rings to avoid leakage. The carbon wool was in contact electrically with

0003-2700/91/0363-1387$02.50/0 © 1991 American Chemical Society

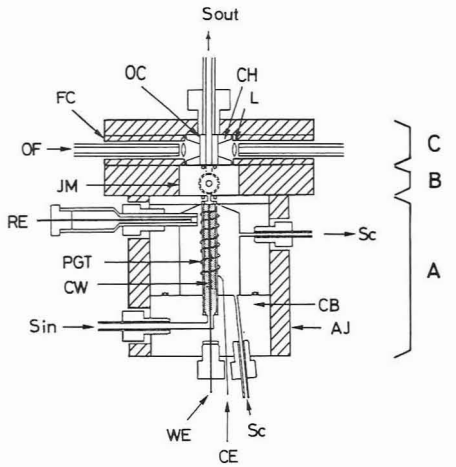

Figure 1. Cross-sectional view of the electrolysis cell and the optical flow-cell: (A) electrolysis cell; (B) jet-mixer; (C) optical cell components. Key: CW, carbon wool working electrode; PGT, porous glass tube; WE, Pt lead to CW; CE, Pt-wire counter electrode; RE, Pt/(I_3^- + I^-) reference electrode; S, sample solution; Sc, counter solution; AJ, aluminum jacket; CB, Difron cell body; JM, double two-jet mixer; OC, optical cell; CH, Macor cell holder; OF, optical fibers; L, focusing lens; FC, optical fiber connector.

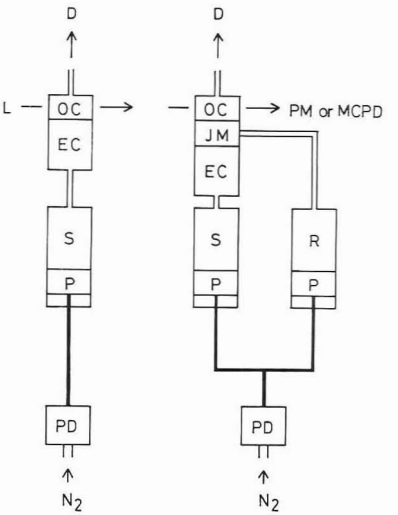

Figure 2. Schematic diagram of pulse electrolysis stopped-flow method: (A) nonmixing mode assembly; (B) mixing mode assembly. Key: PD, piston driver; P, piston; S, sample solution containing parent molecule; R, reactant solution; EC, electrolysis cell; OC, optical cell; D, drain; L, incidental light.

a Pt lead wire (WE, diameter 0.3 mm). Platinum wire (diameter 0.2 mm) wound around the PGT served as a counter electrode (CE). In the case of the controlled-potential electrolysis, the Pt/(I_3^- + I^-) reference electrode (RE) (*16*) was set close to the PGT through a salt bridge with a porous glass tip junction. The AN solution containing 0.1 M tetraethylammonium perchlorate (TEAP) as a supporting electrolyte filled the outer chamber of the PGT as a counter solution (Sc). The body (CB) of the electrolysis cell was made of Difron resin (Daikin Co. Ltd.) and covered with an aluminum jacket (AJ), through which thermostat-regulated water flowed.

A Macor double two-jet mixer (JM) was mounted between the electrolytic cell (A) and the optical cell (C) in the mixing mode assembly. The electrolyzed solution from the electrolysis cell and the reactant solution from the inlet opening perpendicularly to it were mixed once inside the mixer. The premixed solution was separated in two ways, mixed again, and then sent into the optical flow cell. The mixer was covered with an aluminum block to allow thermal conduction with the aluminum jacket of the electrolysis cell for temperature control.

In the optical cell component (C), a cylindrical quartz cell with a 2-mm light path (OC) was mounted in a Macor cell holder (CH). Two optical fibers with focusing lenses (L) were attached perpendicular to the optical cell, which was also covered with an aluminum block. The incident light beam from a halogen lamp (Hamamatsu Photonics; 100 W) was guided to the optical cell through optical fibers. The transmitted light was collected from the opposite side into a spectrophotometer (SP, Unisoku UPS-501) through the optical fibers. Use of the optical fibers permitted the cell assembly to be independent from the piston driver and the spectrophotometer. Therefore, the spectrophotometric measurement was free from the shock caused by the piston drive. Moreover, low-temperature measurement can be carried out by cooling the assembly in a place remote from the light source.

The spectrophotometer is equipped with a photomultiplier (PM; R-2949, Hamamatsu Photonics) and a multichannel photodiode array detector (MCPD; S-2301, Hamamatsu Photonics). The MCPD has 500 channels and covers a 400-nm wavelength region. The time decay curve of absorbance at a fixed wavelength was recorded with the PM. The changes in absorption spectra with time or applied potential were observed by using the MCPD. The time-resolved absorption spectra were obtained successively at the minimum time interval of 35 ms, which was governed by the gate time and the time for clearing the MCPD memory. Although an absorption spectrum was measured with a gate time of 20 ms, the effect of the integration time can be reduced by using a pulse light source such as a Xenon flash lamp. In addition, it is also possible to measure the absorption spectra at millisecond intervals by using the pulse light source and repeating the operation (*17*).

The controlled-potential and controlled-current pulse electrolyses were performed with a PAR Model 173 potentiostat/galvanostat. In the controlled-potential electrolysis, the solution resistance was compensated by a PAR Model 179 module. All measurements were carried out at 25 ± 0.5 °C via a thermostat, Coolnics Model CTR-120.

The system was built around an NEC 9801-VX, 16-bit microcomputer, which controlled the piston drive and electrolysis pulse, as well as performing data acquisition, storage, and real-time display.

Figure 2 shows the schematic diagram of the system operating in two different modes. The nonmixing mode assembly is illustrated in Figure 2A. Immediately after imposing an electrolysis pulse onto the column electrode in the electrolysis cell (EC), the electrolyzed solution (S) was delivered to the optical cell (OC) by a piston (P) driven by nitrogen gas pressure (N_2). The volume of the syringe was controllable between 100 and 400 μL; the volume of the optical cell was 31.4 μL (10-mm length × 2-mm i.d.). The pressure of N_2 gas required to drive the piston was 3–8 kg/cm^2. The measurements of piston drive rate proved that the flow rate was 100–500 mL/min. The dead time between the piston drive and the electrolyzed solution flowing into the optical cell was ca. 15 ms in the nonmixing mode at a pressure of 5 kg/cm^2. A pressure drop and leakage were not observed during measurement with the carbon-wool electrode and a pressure of below 8 kg/cm^2.

The mixing operation mode is illustrated in Figure 2B. In this assembly, the solution containing the parent molecule and the supporting electrolyte was stored in one syringe (S) and the solution containing reactant was stored in the other (R). Immediately after electrolyzing the solution of the parent molecules, both pistons (P) were driven together. The electrolyzed solution was mixed rapidly with the reactant solution in the double two-jet mixer (JM) and delivered into the optical cell (OC).

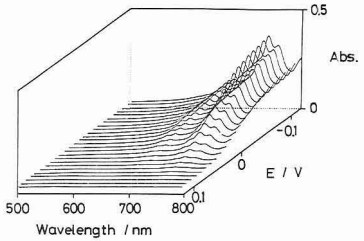

Figure 3. Dynamic transformation profile of $TCNQ^{\bullet-}$ absorption spectra corresponds to the applied potential. Conditions: concentration of TCNQ, 0.1 mM in AN; interval of applied potential, 10 mV.

The conventional cyclic voltammograms (CV) were recorded with a PAR 174 analyzer and the fast scan CV was measured with an apparatus reported previously by the authors (*18*).

Reagents. Acetonitrile (Wako, GR grade) and tetraethylammonium perchlorate (TEAP) were prepared as described previously (*4*). Triphenylamine (TPA; Nacalai Tesque, GR grade) was recrystallized from methanol. Tetraphenylbenzidine (TPB), synthesized through the electrochemical oxidation of TPA and chemical reduction with zinc powder, was purified with a silica-gel column. Tetracyanoquinodimethane (TCNQ; Aldrich) was used without further purification. $TCNQ^{\bullet-}$ solution was prepared by conventional controlled-potential batchwise electrolysis.

RESULTS AND DISCUSSION

1. Cyclic Voltammogram and Dynamic Transformation Profile of the Absorption Spectra in the Electroreduction of TCNQ. The proposed method was evaluated by electroreduction of tetracyanoquinodimethane (TCNQ) to its anion radical ($TCNQ^{\bullet-}$) and compared with cyclic voltammetry.

In the CV of 1 mM TCNQ measured with a glassy-carbon (GC) disk electrode at a scan rate of 0.1 V/s, a reversible one-electron redox process with a redox potential at 0.04 V vs $I_3^- + I^-$ was observed. Figure 3 shows the changes in absorption spectra corresponding to the potential of the column electrode, which was constructed by repeating the measurements under applied stepwise altered potentials. TCNQ was still neutral at an applied potential of around 0.1 V, and showed no absorption in the wavelength range between 500 and 800 nm. By applying the negative potential, green $TCNQ^{\bullet-}$, which has absorption maxima at 677, 740, and 758 nm, was gradually generated. The Nernst plot calculated from Figure 3 indicated that the system involved a one-electron redox process with a redox potential of 0.01 V.

2. Evaluation of Pulse Electrolysis with the Column Electrode. To evaluate the electrolysis efficiency in the proposed method, the efficiency of the oxidation of $TCNQ^{\bullet-}$ to TCNQ was measured. $TCNQ^{\bullet-}$ is stable for several hours in purified AN. The electrolysis efficiency was thus calculated from the absorbance of $TCNQ^{\bullet-}$ before and after electrolysis. The zero level of absorbance was checked before and after measurements by washing out with the solvent AN.

The electrolysis efficiency for the flowing solution has been reported previously (*9*) by using an electrolysis cell of similar dimensions. However, the situation is quite different in the present method, in which electrolysis is performed in a stationary solution.

For the measurement of short-lived species, it is very important to reduce the electrolysis time, i.e. the time from the initiation of electrolysis to the start of the piston drive. The changes in efficiencies corresponding to the electrolysis time are discussed in the following section.

(a) Efficiency in Controlled-Potential Pulse Electrolysis. For the purpose of the characterization of the electrochemical reactions and the selective generation of species,

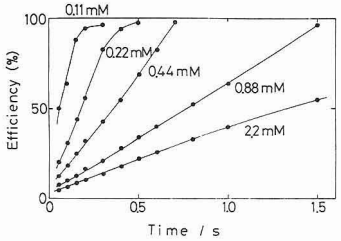

Figure 4. Electrolytic efficiency in the controlled-potential operation. The potential was stepped from −0.2 to +0.2 V.

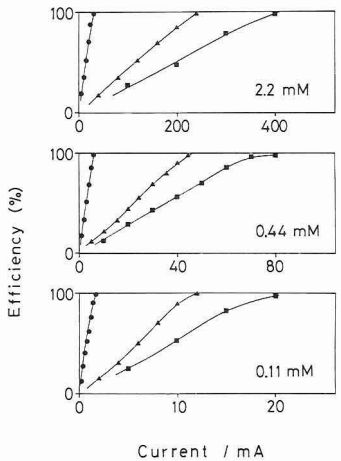

Figure 5. Electrolytic efficiency in the controlled current operation. Electrolysis time: (●) 1 s; (▲) 100 ms; (■) 50 ms.

the controlled-potential operation is advantageous. The efficiency in the potential-step pulse electrolysis of $TCNQ^{\bullet-}$ was determined.

Figure 4 shows the dependence of electrolysis efficiency on the electrolysis time at various concentrations of $TCNQ^{\bullet-}$. The solution containing 0.11 mM $TCNQ^{\bullet-}$ was electrolyzed quantitatively within 200 ms. More electrolysis time was necessary to electrolyze the solution quantitatively when the $TCNQ^{\bullet-}$ concentration was increased. This is probably due to the ohmic potential drop caused by the increase of the current with increasing concentration.

The maximum efficiency was 97–98%, as shown in Figure 4. It was constant even when the oxidation time was increased up to 30 s, which decreased the electrolysis current to zero. Therefore it was concluded that the electrolysis was achieved completely. The value of 97–98% is probably due to the mix of the electrolyzed solution and the solution staying in the optical cell after flowing into the optical cell.

Although the applied potential of Figure 4 was stepped from −0.2 to +0.2 V, the efficiencies varied depending upon the potential according to the Nernst equation described in the previous section.

(b) Efficiency in Constant-Current Electrolysis. If the objective electrochemical reactions are well-characterized, the controlled-current operation is effective as an electrolysis method because the electrolysis is complete instantaneously and can be applied to a low-conducting solution. Figure 5 shows the efficiency of the controlled-current pulse electrolysis of $TCNQ^{\bullet-}$ at different electrolysis times and concentrations. In the concentration range from 0.11 to 2.2 mM, the quan-

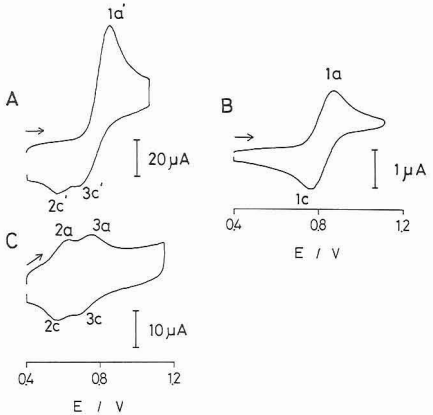

Figure 6. Cyclic voltammograms of TPA and TPB in AN: (A) conventional CV of 1 mM TPA at 0.1 V/s with GC disk electrode (diameter 3.0 mm); (B) fast scan CV of 1 mM TPA at 30 V/s with Pt microelectrode (diameter 30 μm); (C) conventional CV of 0.1 mM TPB at 0.1 V/s with GC disk electrode.

titative electrolysis of $TCNQ^{\bullet-}$ was achieved within 50 ms. Thus, in the controlled-current operation, the solution was quantitatively electrolyzed even at high concentrations up to 2.2 mM with a current pulse of 400 mA × 50 ms.

3. Analysis of the Electrochemical Dimerization Reaction Process of $TPA^{\bullet+}$ in AN. (a) Cyclic Voltammogram and Dynamic Transformation Profiles of the Absorption Spectra in the Electrooxidation Process of $TPA^{\bullet+}$. Figure 6a shows the conventional CV of TPA measured with a GC disk electrode (diameter 3.0 mm). One irreversible oxidation peak (1a′) at 0.85 V, which is attributed to the oxidation of TPA, was observed in the anodic scan. In the reverse cathodic scan, however, two new peaks (2c′, 3c′), which were not attributed to the direct reduction peaks of $TPA^{\bullet+}$, were observed at 0.57 and 0.69 V, respectively. Figure 6B shows the fast scan CV of TPA in AN measured with a Pt microelectrode (diameter 30 μm) and at the scan rate of 30 V/s, in which quasireversible one-electron redox peaks (1a, 1c) were observed at 0.84 and 0.76 V, respectively. Figure 6C shows the conventional CV of the synthetic dimer compound, tetraphenylbenzidine (TPB), measured with the GC disk electrode. Two reversible one-electron redox peaks (2a, 2c and 3a, 3c) were observed at 0.63, 0.57 and 0.74, 0.68 V, respectively. The profiles of these cathodic peaks (2c, 3c) were quite similar to those of Figure 6A (2c′, 3c′).

These CVs are consistent with the pathway that $TPA^{\bullet+}$ dimerizes immediately to produce TPB and that the oxidation potentials of TPB and $TPB^{\bullet+}$ are more negative than that of TPA, as reported previously (*11*). Consequently, the electrooxidation mechanism of TPA is shown as follows:

$$TPA - e^- \rightarrow TPA^{\bullet+} \quad (1)$$

$$2TPA^{\bullet+} \xrightarrow[k_2]{} TPB + 2H^+ \quad (2)$$

$$TPB - e^- \rightarrow TPB^{\bullet+} \quad (3)$$

$$TPB^{\bullet+} - e^- \rightarrow TPB^{2+} \quad (4)$$

Figure 7 shows the change in absorption spectra corresponding to the applied potential of the column electrode in the electrooxidation process of TPB. This figure clearly demonstrates that $TPB^{\bullet+}$, which has an absorption maximum at 480 nm, is generated at potentials around 0.65 V and that TPB^{2+}, which has an absorption maximum at 678 nm, is

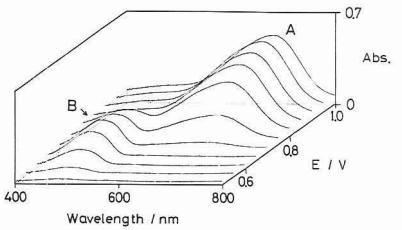

Figure 7. Dynamic transformation profiles of absorption spectra corresponds to the applied potential in the oxidation of TPB: (A) absorption rnaximum of TPB^{2+}; (B) absorption maximum of $TPB^{\bullet+}$. Conditions: concentration of TPB, 0.1 mM; interval of applied potential, 50 mV.

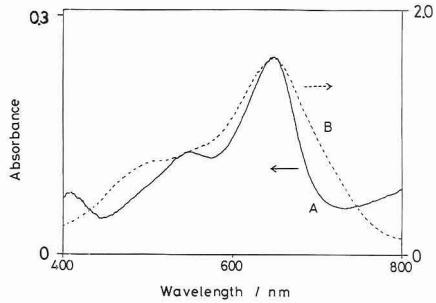

Figure 8. Absorption spectra measured after oxidation of 1.0 mM TPA in AN by controlled-current pulse electrolysis for 50 ms. Applied current: (A) 20 mA; (B) 150 mA. The absorbance scale of spectrum A was expanded to have the same maximum value as spectrum B for the comparison.

generated by applying more positive potentials. These processes coincide with the CV in Figure 6C.

The dynamic transformation profiles of these absorption spectra show not only the species generated but also the potential at which they are produced.

The change in absorption spectra corresponding to the applied potential was also measured by the oxidation of TPA. In this case, however, only mixed absorption spectra of $TPA^{\bullet+}$ and cogenerated TPB^{2+} were observed, as expected from the CV in Figure 6A.

(b) Measurement of the Absorption Spectra of Short-Lived $TPA^{\bullet+}$ in the Course of Electrooxidation of TPA without Interference of Consecutive Chemical Reactions. In the kinetic analysis of $TPA^{\bullet+}$ it is essential to generate only $TPA^{\bullet+}$, but it is very difficult to prepare a pure $TPA^{\bullet+}$ solution by the conventional electrolytic method because TPB^{2+} is also produced at the same potential.

In the present method, however, a pure solution containing only $TPA^{\bullet+}$ was prepared without any interference of the consecutive reactions by using controlled-current pulse electrolysis with a short electrolysis time of 50 ms.

Figure 8 shows the absorption spectra of the electrolyzed solution of TPA at the same pulse amplitude but different current values. Spectrum A was observed under the perturbation with the current pulse of 20 mA for 50 ms, and spectrum B was obtained with the current pulse of 150 mA for 50 ms. As shown in this figure, the spectrum obtained with a low-current pulse of 20 mA differed from that obtained with the high-current pulse of 150 mA.

Judging from the absorption spectra of $TPB^{\bullet+}$ and TPB^{2+} in Figure 7, spectrum B contains the absorption of $TPB^{\bullet+}$ and TPB^{2+}. The consecutive electron-transfer reactions seem to

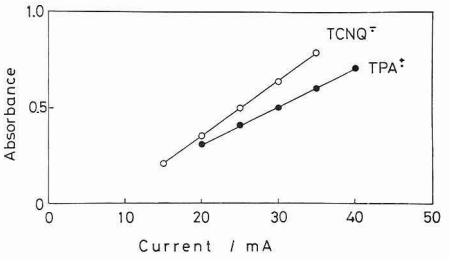

Figure 9. Absorbance vs applied current plots for $TCNQ^{\bullet-}$ and $TPA^{\bullet+}$. Conditions: wavelength, 746 nm for $TCNQ^{\bullet-}$ and 647 nm for $TPA^{\bullet+}$; concentrations of TCNQ and TPA, 1 mM; current pulse, 50 ms.

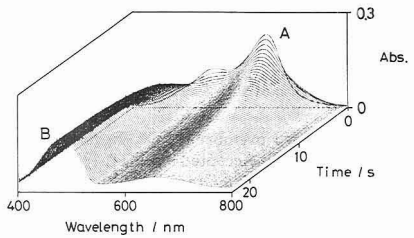

Figure 10. Time-resolved absorption spectra in the course of the electrochemical dimerization reaction of $TPA^{\bullet+}$; (A) absorption maximum of $TPA^{\bullet+}$; (B) absorption maximum of $TPB^{\bullet+}$. Conditions: concentration of TPA, 0.1 mM in AN; current pulse, 20 mA × 50 ms. The time interval of each spectrum was 300 ms. This figure consists of 80 spectra successively measured by the MCPD.

be significant at higher electrolysis current, even within a short period of 50 ms. On the other hand, spectrum A has a sharper absorption maximum at 647 nm and a shoulder at 560 nm, which did not appear in spectrum B. As a result, spectrum A that was obtained with a lower current pulse, i.e. a low concentration of $TPA^{\bullet+}$, can be assigned to the absorption spectrum of pure $TPA^{\bullet+}$.

(c) Determination of the Absorption Coefficient of $TPA^{\bullet+}$. One of the key advantages of this method for the quantitative spectrophotometric analysis of reaction kinetics is that the absorption coefficient of electrogenerated species can be easily determined, provided that a significant reaction does not occur during electrolysis. The absorption coefficient of $TPA^{\bullet+}$ was determined by the absorbance vs applied currents plots for $TCNQ^{\bullet-}$ and $TPA^{\bullet+}$, as shown in Figure 9. As discussed above, a pure $TPA^{\bullet+}$ solution was obtained in the lower concentration range of $TPA^{\bullet+}$. In the current range from 20 to 50 mA, the absorption spectra indicated that the spectral interference of $TPB^{\bullet+}$ and TPB^{2+} with the absorption spectra of $TPA^{\bullet+}$ was almost negligible. Hence the applied current is proportional to the concentration of $TPA^{\bullet+}$. Thereby the increase of the absorbance with the current, i.e. slope of the figure, represents the increase of absorbance with the concentration. On the basis of the linear portion of each slope and by using the molar absorption coefficient of $TCNQ^{\bullet-}$ (1.98×10^4 cm^{-1} M^{-1} at 746 nm) as a standard value, the molar absorption coefficient of $TPA^{\bullet+}$ at 647 nm was estimated as 1.3×10^4 cm^{-1} M^{-1}.

(d) Acquisition of Time-Resolved Absorption Spectra in the Course of the Dimerization Reaction of $TPA^{\bullet+}$. Figure 10 shows the time-resolved absorption spectra in the dimerization reaction of $TPA^{\bullet+}$ observed with a time interval of 300 ms. As shown in these spectra, $TPB^{\bullet+}$ increased with decreasing $TPA^{\bullet+}$. This result indicates that the electron transfer of TPB to $TPB^{\bullet+}$ is very fast. Because the solution stays in the optical cell, the electron transfer is not from the electrode (eq 3) but from $TPA^{\bullet+}$, as shown in eq 5.

Table I. Dependence of k_2 on [TPA]

[TPA]/mM	log ([TPA]/mM)	log (k_2/M^{-1} s^{-1})[a]
0		3.25
0.1	−1.0	3.25
1.0	0	3.42
2.0	0.31	3.57
5.0	0.47	3.60

[a] Averaged values of five runs.

$$TPB + TPA^{\bullet+} \rightarrow TPB^{\bullet+} + TPA \quad (5)$$

TPB^{2+} was barely generated, as shown in Figure 10. Although a small amount of TPB^{2+} was supposed to be produced from the equilibrium between $TPA^{\bullet+}$ and $TPB^{\bullet+}$, the equilibrium constant seemed to be very small, as reported by Debrodt et al. (*14*).

(e) Determination of Dimerization Rate Constant of $TPA^{\bullet+}$. The kinetic analysis of the dimerization reaction of $TPA^{\bullet+}$ given in eq 2 was performed by using the present method. The reaction rate was quite simply analyzed by following the decay of absorbance at 647 nm in Figure 10. As a result of the reaction order analysis (*4*), the log ($-d[TPA^{\bullet+}]/dt$) vs log [$TPA^{\bullet+}$] plots are linear, with a slope of 1.95 (±0.06), which clearly demonstrates that this is a second-order reaction in $TPA^{\bullet+}$ as in eq 6.

$$-d[TPA^{\bullet+}]/dt = k[TPA^{\bullet+}]^2 \quad (6)$$

Once the second-order reaction was determined, the pseudo-second-order rate constant (k) was calculated to be 5.4 (±0.5) × 10^3 M^{-1} s^{-1} from the slopes of the plots of $1/[TPA^{\bullet+}]$ vs time, which were obtained by analyzing the time decay curves. When eqs 2 and 5 are taken into account, k is represented as $3k_2$ by using the rate constant of eq 2. As a result, k_2 was estimated as 1.8 (±0.2) × 10^3 M^{-1} s^{-1}, which was in good agreement with the reported value (*14*).

(f) Effect of [TPA] on the Reaction Mechanism. While this reaction proceeds via the radical–radical coupling mechanism, the radical–substrate coupling mechanism is also significant in the dimerization reactions of aromatic cation radicals (*18*, *19*). Thus, it is necessary to clarify the effect of the parent molecule on the rate law in analyzing the reaction mechanism.

In the present method, this effect can be simply clarified by mixing a solution of $TPA^{\bullet+}$ and TPA in the mixing mode. Table I summarizes the results of the kinetic measurements. The quantitatively electrolyzed 0.1 mM $TPA^{\bullet+}$ solution was mixed with a solution containing neutral TPA, into which 0.1 M TEAP was also added to minimize the changes in the medium caused by mixing the solutions.

Since the reactions proceeded in the second order with respect to [$TPA^{\bullet+}$] in all cases, the pseudo-second-order rate constants were calculated and the effect of [TPA] was revealed. Although a slight increase in k_2 was observed, the dependence of log k_2 on log [TPA] indicates that [TPA] did not participate in the rate law.

CONCLUSION

The method reported here is useful for the characterization of electrogenerated species and the analyses of their reaction kinetics and mechanisms.

Controlled-potential electrolysis, by means of which changes in absorption spectra corresponding to potential can be measured, is useful for the electrospectrochemical characterization of electrochemical reaction processes. On the other hand, once the electrochemical reaction is well-characterized, controlled-current electrolysis with a current pulse as short

as 50 ms is effective for the quantitative generation of very short-lived species, whereas a large iR drop would be expected from the huge applied current.

The absorption spectrum of $TPA^{\bullet+}$ was measured without interference by the consecutive reactions, and the absorption coefficient was determined. Although the determination method is based on the assumption that a significant reaction does not occur during the electrolysis time of 50 ms, the generated TPB is assumed to be less than a few percent of $TPA^{\bullet+}$ on the basis of the homogeneous second-order rate constant. Since absorption spectra of high quality can be measured with a long light path and the absorption coefficient can be determined with high accuracy, this method would be effective for spectroscopical measurement of electrogenerated species in spite of the restriction imposed by the electrolysis time.

By using this stopped-flow method, the decay profiles of short-lived species with half-lives as short as 50 ms would be followed with the nonmixing mode. Furthermore, their very fast and complex reactions with reactants would be analyzed by means of the mixing operation mode.

ACKNOWLEDGMENT

We thank Toshihiko Nagamura of Unisoku Co. Ltd. for his kind support regarding instrumentation.

LITERATURE CITED

(1) Bard, A. J.; Faulkner, L. R. *Electrochemical Method Fundamentals and Applications*; Wiley; New York, 1980; p 398.
(2) Sioda, R. E.; Keating, K. B. In *Electroanalytical Chemistry*; Bard, A. J., Ed.; Dekker: New York, 1982; Vol. 12, p 1.
(3) Okazaki, S. *Rev. Polarogr.* **1968**, *15*, 154.
(4) Oyama, M.; Nozaki, K.; Nagaoka, T.; Okazaki, S. *Bull. Chem. Soc. Jpn.* **1990**, *63*, 33.
(5) Oyama, M.; Nozaki, K.; Okazaki, S. *J. Electroanal. Chem. Interfacial Electrochem.*, in press.
(6) Nagaoka, T.; Okazaki, S.; Fujinaga, T. *J. Electroanal. Chem. Interfacial Electrochem.* **1981**, *127*, 289.
(7) Nozaki, K.; Naito, A.; Ho, T.; Hatano, H.; Okazaki, S. *J. Phys. Chem.* **1989**, *93*, 8304.
(8) Oyama, M.; Nozaki, K.; Okazaki, S. *Bull. Chem. Soc. Jpn.* **1988**, *61*, 4283.
(9) Oyama, M.; Okazaki, S.; Nagamura, T. *Vibr. Spectrosc.*, in press.
(10) Evans, J. F.; Blount, H. N. *J. Org. Chem.* **1976**, *41*, 516; *J. Phys. Chem.* **1976**, *80*, 1011; *J. Am. Chem. Soc.* **1978**, *100*, 4149.
(11) Seo, E. T.; Nelson, R. F.; Fritsch, J. M.; Marcoux, L. S.; Leedy, D. W.; Adams, R. N. *J. Am. Chem. Soc.* **1966**, *88*, 3498.
(12) Nelson, R. F.; Feldberg, S. W. *J. Phys. Chem.* **1969**, *73*, 2623.
(13) Creason, S. C.; Wheeler, J.; Nelson, R. F. *J. Org. Chem.* **1972**, *37*, 4440.
(14) Debrodt, H.; Heusler, K. E. *Z. Phys. Chem.* **1981**, *125*, 35.
(15) Nelson, R. F.; Philp, R. H., Jr. *J. Phys. Chem.* **1979**, *83*, 713.
(16) Coetzee, J. F.; Gardner, C. W., Jr. *Anal. Chem.* **1982**, *54*, 2530.
(17) Oyama, M.; Okazaki, S.; Nagamura, T. *Anal. Chim. Acta* **1991**, *245*, 199.
(18) Nozaki, K.; Oyama, M.; Hatano, H.; Okazaki, S. *J. Electroanal. Chem. Interfacial Electrochem.* **1989**, *270*, 199.
(19) Hammerich, O.; Parker, V. D. *Adv. Phys. Org. Chem.* **1984**, *20*, 55.

RECEIVED for review November 1, 1990. Revised manuscript received April 4, 1991. Accepted April 11, 1991. This work was supported in part by a Grant-in-Aid for Scientific Research from the Ministry of Education, Science, and Culture. M.O. and K.N. thank the Japan Society for the Promotion of Science for financial support.

Direct Examination of the Injection Process in Liquid Chromatographic Separations

Christine E. Evans[1] and Victoria L. McGuffin*

Department of Chemistry, Michigan State University, East Lansing, Michigan 48824

In liquid chromatographic separations, it is necessary for the solute zone to travel from a nonretentive injection valve onto a retentive packed bed. Although it is often assumed that this injection process has little effect on chromatographic performance, experimental evaluation and verification of this important phenomenon have been hindered by the inability to measure fundamental separation parameters directly in the inlet region. With the advent of optically transparent columns and laser-induced fluorescence detection, the direct and accurate measure of the movement and dispersion of solute zones along the column is now feasible. In situ monitoring of the solute zones as they traverse the chromatographic column is accomplished by positioning one detector prior to the packed bed and five detectors directly on the column itself. Upon injection onto the column, a decrease in zone length variance and a concomitant increase in solute concentration are measured as a function of solute capacity factor. Good agreement is seen between experimental measurements and theoretical predictions based on a simple steady-state model of the abrupt change in solute retention in the inlet region. Variation in the injection profile and in the resulting on-column zone profile is also measured as a function of the injection solvent composition. Although solute retention is nearly constant along the column under these conditions, the length variance changes markedly with relatively small changes in the composition of the injection solvent. However, when the injection solvent differs greatly from the mobile phase, changes occur in the zone profile that cannot be predicted on the basis of a simple increase in retention upon injection. These results have important implications in both the routine practice of chromatography, where the composition of the injection solvent is often altered to improve solute resolution, and in the experimental determination of fundamental separation parameters, where the precise control of the zone profile introduced onto the column is essential.

INTRODUCTION

In most theoretical descriptions of the separation process in liquid chromatography, the solute zone is presumed to be present initially on the column as a small, rectangular plug. In practice, however, the solute zone must pass from a nonretentive open tube or injection valve onto a retentive packed bed. This spatial discontinuity in the physical and chemical environment inherent in the injection process may influence both the migration rate and dispersion of the solute zone in the inlet region.

The effect of this discontinuity on chromatographic performance has been much debated for both gas and liquid chromatographic separations (*1–11*). Although the methods of theoretical treatment vary widely, it is generally accepted that the influence of the injection process is dependent on the initial peak profile and the equilibration of solutes between the mobile and stationary phases. Theoretical predictions are further complicated because the solute zone itself may affect the local chemical environment, thus altering the equilibrium conditions in the inlet region (*6*).

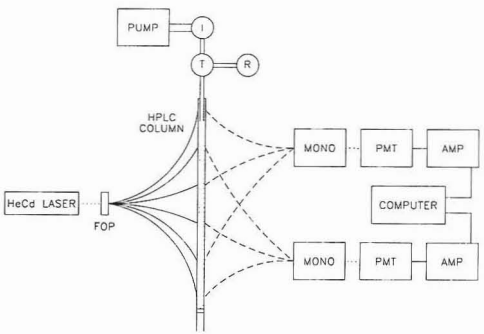

Figure 1. Schematic diagram of on-column fluorescence detection system for microcolumn liquid chromatography: I = injection valve, T = splitting tee, R = restricting capillary, FOP = fiber optic positioner, MONO = monochromator, PMT = photomultiplier tube, AMP = current-to-voltage converter and amplifier.

As the solute enters the column, the front of the zone will be retained by the stationary phase and thus, will travel more slowly than the rear. This abrupt change in velocity results in a decrease in the length variance of the solute zone and a concomitant increase in the local concentration. The shape of the solute profile may be further affected if this increase in concentration is sufficient to extend into the nonlinear region of the equilibrium isotherm (*11*) or if the rate of equilibration is not instantaneous. If the solute profile is altered substantially upon injection or if nonequilibrium conditions persist over a large fraction of the column, the column efficiency as well as the minimum detectable concentration measured at the column outlet may be adversely affected.

In previous investigations, experimental evaluation of the injection process has been limited by the inability to probe the inlet region of a high-efficiency column. With the advent of optically transparent microcolumns, it is now possible to measure the local retention and dispersion of solutes directly on a liquid chromatographic column. In this study, six detectors are positioned sequentially along the column, the first of which is immediately before the packed bed. Utilizing this experimental design, the injection profile may be accurately measured, and the retention and dispersion of solute zones may be directly monitored as a function of distance along the column. By probing the chromatographic column in this manner, the effect of the injection process on chromatographic performance can be determined directly under high-efficiency

* To whom correspondence should be addressed.
[1] Present address: School of Chemical Sciences, University of Illinois, Urbana, IL 61801.

0003-2700/91/0363-1393$02.50/0 © 1991 American Chemical Society

conditions. In addition, the composition of the injection solvent may be systematically varied and the development of the resulting zone profile may be evaluated. Although the influence of the injection solvent has been qualitatively understood and used to practical advantage for many years to improve performance and detectability (*1*, *12*, *13*), this experimental scheme will allow the exact nature of this complex phenomenon to be more fully elucidated. By careful choice and control of experimental parameters, nearly ideal chromatographic conditions may be achieved and the direct comparison of theoretical predictions with experimental measurements will be possible.

EXPERIMENTAL METHODS

Reagents. All organic solvents utilized in this study are high-purity, distilled-in-glass grade (Baxter Healthcare, Burdick & Jackson Division), and water is deionized and doubly distilled (Corning Glass Works, Model MP-3A). Saturated fatty acid standards (Sigma) ranging from n-$C_{10:0}$ to n-$C_{20:0}$ are derivatized with 4-(bromomethyl)-7-methoxycoumarin (Sigma) in acetone as previously described (*14*). Individual fatty acid derivatives are then isolated by using a conventional-scale octadecylsilica column (Applied Biosystems, ODS-224) with methanol as the mobile phase. Resulting fractions are evaporated in a stream of nitrogen at 40 °C and redissolved in acetone. Subsequent dilution is accomplished by reducing an acetone aliquot to dryness and redissolving in the injection solvent of interest at a final concentration of 5×10^{-4} M.

Chromatographic System. A schematic diagram of the chromatographic system is illustrated in Figure 1. A dual-syringe micropump (Applied Biosystems) is utilized to deliver a pure methanol mobile phase onto the column under constant flow conditions. Sample injection is accomplished by splitting a 1.0-μL volume (Valco, Model ECI4W1.) between the microcolumn and a restricting capillary (1:102). An open-tubular fused-silica capillary (0.0050 cm i.d., 25.7-cm length) extends from the injector to 0.1 cm before the packing material to transfer the injected sample zone to the head of the column. Connection in this manner provides minimum band broadening, while simultaneously allowing a detector to be placed immediately prior to the packed bed.

The microcolumn utilized for all studies is fabricated by using a fused-silica capillary (0.020 cm i.d., 43.9-cm length), from which the polyimide coating has been carefully removed to facilitate on-column detection. An acetone slurry of 3-μm octadecylsilica material (Varian, MicroPak SP) is then introduced onto the capillary under moderate pressure (5200 psi). The resulting microcolumn has a plate height (H) of 9.5 μm, a total porosity (ϵ_T) of 0.58, and a flow resistance parameter (ϕ') of 550 under standard test conditions (*15*, *16*). In all chromatographic measurements, the methanol mobile phase is operated at a constant flow rate ($F = 0.78$ μL/min; $u = 0.070$ cm/s) that is slightly greater than the optimum value, resulting in an inlet pressure of approximately 1600 psi.

Detection System. The detection scheme for this study is similar to that described previously (*17*, *18*) and utilizes laser-induced fluorescence to probe solute zones directly on the liquid chromatographic microcolumn. Excitation radiation from a He–Cd laser (Omnichrome, Model 3112-10S) at 325 nm (10 mW) is transmitted to six matched detector blocks using 100 μm i.d. optical fibers (Polymicro Technologies). The first detector is positioned on the 0.0050 cm i.d. open capillary at a distance of 0.4 cm before the head of the column, allowing the measurement of the injection profile immediately prior to the packed bed. The five remaining detectors are positioned on the packed bed at 4.9, 10.4, 15.5, 20.9, and 26.2 cm from the column head and may be used to monitor retention and dispersion processes along the column length. Fluorescence emission is collected in a right-angle, coplanar geometry using larger (500 μm i.d., 0.2 numerical aperture) optical fibers positioned 0.1 cm from the column. In this configuration, the emission fiber acts as the limiting aperture, resulting in a maximum viewed detection volume of 1.8 nL off column and 12 nL on column. The resulting emission is then filtered to minimize scattered and second-order radiation and focused onto the entrance slit of a monochromator (Instruments SA, Model H1061). The emission from the derivatized fatty acids at 420 nm is detected by a photomultiplier tube (Hamamatsu, R1463), and the resulting photocurrent is amplified (100 nA/V, $\tau_{RC} = 0.06$ s) and converted to the digital domain (Data Translation, Model 3405/5716). All data acquisition is performed under computer control (IBM PC-XT) at a rate of 5 Hz with the Forth-based programming language Asyst (Macmillan). This on-column detection scheme yields a linear photocurrent response with concentration that ranges from the detection limit ($\sim 1 \times 10^{-6}$ M) to the solubility limit of the injected solute.

Calculations. As the solute traverses the column, both retention and dispersion are measured at each detector position by using the method of statistical moments (*19*). Although rigorously defined as integrals, practical calculation is performed by finite summation of the fluorescence intensity ($I(t)$) over a minimum of 50 time intervals (dt) equally distributed across the solute zone.

$$M_0 = \sum I(t)\ dt$$

$$M_1 = \sum t\ I(t)\ dt / M_0$$

$$M_2 = \sum (t - M_1)^2\ I(t)\ dt / M_0 \qquad (1)$$

In chromatographic applications, the zeroth moment (M_0) represents the area under the peak, while the first moment (M_1) is the centroid of the peak and is an accurate measure of the solute retention time (t_R). The second moment (M_2), which is normalized to the first and zeroth moments, is equal to the time variance (σ_t^2) of the peak and is a measure of the solute zone dispersion. Unlike most other calculational techniques, statistical moments require no a priori knowledge about the zone profile.

From the statistical moments calculated at each detector position, the capacity factor (k) and plate height (H) may be evaluated at detectors individually or between successive pairs. In the single mode, the capacity factor is determined by using eq 2, where the elution time of a nonretained zone (t_0) is evaluated

$$k = \frac{M_1 - t_0}{t_0} \qquad (2)$$

with a fluorescent decomposition product of the coumarin label that corresponds with the elution time for acetone. For all on-column detector calculations, the transit time between the injector and the head of the column is subtracted from M_1 and from t_0 to omit the delay introduced by the connecting tube. The capacity factor determined by using each detector individually represents the average retention behavior between the point of introduction onto the packed bed and the point of detection. In contrast, dual-mode detection allows the solute retention between detectors to be evaluated by substituting the difference in the first moment (ΔM_1) and the difference in the void time (Δt_0) between detectors for M_1 and t_0 in eq 2. In this manner, the local retention in specific regions along the column may be accurately evaluated. Likewise, determination of the dispersion of solute zones is accomplished in both single and dual modes. In the single mode, the plate height is calculated on the basis of the statistical moments at each detector individually and the distance between the column head and the detector (L).

$$H = \sigma_L^2 / L = M_2 (L/M_1)^2 / L \qquad (3)$$

In the dual mode, the local plate height between detectors is calculated by using eq 3 as well. In this case, however, the difference in the first (ΔM_1) and second (ΔM_2) moments together with the distance (ΔL) between detectors is substituted for their corresponding absolute values (M_1, M_2, and L, respectively). Utilizing this difference method, extracolumn effects are effectively eliminated and the accurate measurement of the local plate height along the column is possible (*17*, *20*).

The single-mode measurements of plate height may, unfortunately, be influenced by extracolumn sources of dispersion. These detrimental contributions to the zone dispersion, which arise from volumetric and temporal sources, are especially important at the short distances of interest in this study. If all sources of variance are independent, the total extracolumn variance, $(\sigma_V^2)_{EX}$, may

Table I. Capacity Factors (k_{INJ}) for Derivatized Fatty Acid Standards as a Function of Solvent Composition

solvent	solutes					
	n-$C_{10:0}$	n-$C_{12:0}$	n-$C_{14:0}$	n-$C_{16:0}$	n-$C_{18:0}$	n-$C_{20:0}$
90% methanol/acetone	0.44	0.68	1.06	1.62	2.48	3.66
95% methanol/acetone	0.47	0.74	1.16	1.80	2.77	4.19
methanol	0.54	0.85	1.34	2.09	3.23	4.95
95% methanol/water	1.20	2.20	3.80	6.80	12.5	21.0
90% methanol/water	2.60	5.10	9.90	19.0	37.0	72.0

be estimated under ideal conditions to be the sum of individual sources (*19*), expressed in the volume domain.

$$(\sigma_V^2)_{EX} = \frac{V_{INJ}^2}{12} + \frac{V_{DET}^2}{12} + F^2\tau_{RC}^2 + \frac{r_{CONN}^2 L_{CONN} F^2}{24 D_M u} \quad (4)$$

In this equation, the contribution from the injection (V_{INJ}) and detection (V_{DET}) volumes is based on an ideal rectangular profile, while the contribution from the detector time constant (τ_{RC}) arises from an exponential decay (*19*). The dispersion occurring within a connecting tube of radius r_{CONN} and length L_{CONN} is assumed to result from a laminar flow profile (*9*, *13*). One method of expressing the magnitude of these extracolumn contributions is the fractional increase (θ^2) in volumetric variance predicted from the column variance, $(\sigma_V^2)_{COL}$, and the known sources of extracolumn variance, $(\sigma_V^2)_{EX}$ (*21*).

$$\theta^2 = (\sigma_V^2)_{EX}/(\sigma_V^2)_{COL} = (\sigma_V^2)_{EX} u^2 / H_{COL}(1 + k_{MP})^2 L F^2 \quad (5)$$

Although not relevant at this point in the discussion, the importance of distinguishing between the solute capacity factor in the mobile phase (k_{MP}) and in the injection solvent (k_{INJ}) will become apparent later. If the column plate height (H_{COL}), solute capacity factor (k_{MP}), and linear velocity (u) are constant along the column, then the fractional increase in the variance (θ^2) is expected to be inversely related to the detector position (L). This relationship is of primary importance in the evaluation of chromatographic efficiency as a function of distance, because the calculated fractional increase is directly related to single-mode measurements of plate height (H_{MEAS}).

$$H_{MEAS} = H_{COL}(1 + \theta^2) \quad (6)$$

Evaluation of θ^2 and the resulting influence on the measured plate height is accomplished by substitution of the experimental values for the injection (V_{INJ}) and detection (V_{DET}) volumes, detector time constant (τ_{RC}), and connecting tubing radius (r_{CONN}) and length (L_{CONN}) into eq 5. The diffusion coefficient (D_M) is estimated from the Wilke–Chang equation (*22*) to be 3×10^{-5} cm^2/s for the n-$C_{10:0}$ fatty acid derivative in methanol. Under the experimental conditions utilized in this study, most of the extracolumn variance is expected to arise from the injection process, with 14% from the injection volume and 62% from the connecting tube. Only 24% of the total extracolumn contribution is predicted from detector sources, with 23% from the viewed volume and less than 1% from the time constant.

Selection of Experimental Conditions. Initial characterization of the inlet region requires the choice of solutes that are both chromatographically and spectroscopically well behaved. Previous investigations in our laboratory indicate that a homologous series of straight chain, saturated fatty acid standards that have been labeled with 4-(bromomethyl)-7-methoxycoumarin meet both requirements (*18*, *20*). This homologous series behaves nearly ideally, exhibiting the theoretically expected semilogarithmic relationship between the capacity factor (k_{MP}) and carbon number (*20*). In addition, the retention behavior of all solutes is independent of concentration in the range examined in this study. The fluorescence characteristics of these model solutes are favorable for use with the He–Cd laser, and the emission intensity measured in the packed bed appears to be independent of solute retention (*18*).

The composition of the mobile phase and injection solvents is also important in determining ideal operating conditions. A pure methanol mobile phase is chosen to eliminate the selective partitioning of individual solvents into the stationary phase that may occur with mixed solvent systems, while providing a reasonable range of solute capacity factors. However, methanol along with premixed solutions of methanol/acetone and methanol/water are utilized as injection solvents. These solvents allow the solute retention in the injection solvent (k_{INJ}) to be systematically varied over a wide range (Table I). Thus, the experimental parameters chosen for this study should allow systematic investigation of the injection process, as well as provide the nearly ideal conditions necessary for direct comparison of experimental measurements with theoretical expectations.

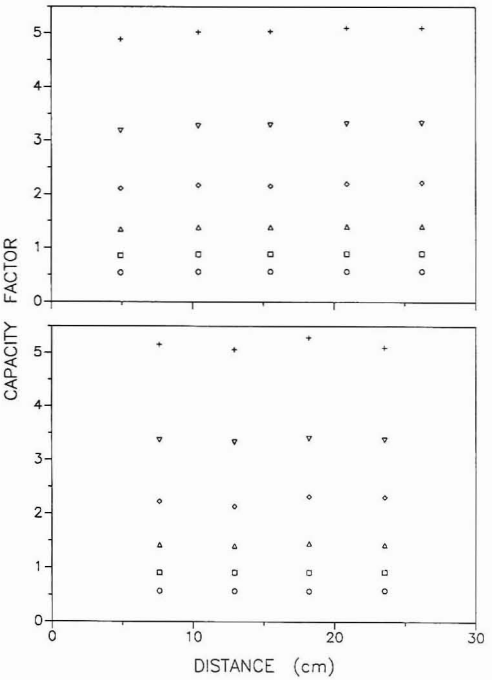

Figure 2. Capacity factor versus distance along the column measured in single (top) and dual (bottom) mode for derivatized fatty acid standards (○) n-$C_{10:0}$, (□) n-$C_{12:0}$, (△) n-$C_{14:0}$, (◇) n-$C_{16:0}$, (▽) n-$C_{18:0}$, and (+) n-$C_{20:0}$. Chromatographic and detection conditions are as described in Experimental Methods.

RESULTS AND DISCUSSION

Retention of Solute Zones. In most theoretical approaches to chromatographic separations, equilibration of the solute zone with the stationary phase is assumed to occur instantaneously. Under chromatographic conditions when this is true, and if solute–solvent and solute–stationary phase interactions are not affected by the local pressure, retention in the inlet region of a liquid chromatographic column is predicted to be constant with distance along the column (*23*). With the present experimental design, it is possible to examine this theoretical prediction by measuring the retention of solutes as they traverse the chromatographic column.

Methanol Injection Solvent. Experimental measurements of capacity factor (k_{MP}) with distance along the column using methanol as the injection solvent are shown in Figure 2 for both single- and dual-mode determinations. The solute capacity factor increases logarithmically with solute chain length,

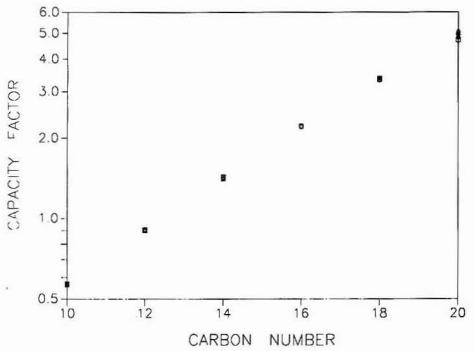

Figure 3. Effect of the injection solvent composition on the single-mode measurements of capacity factor at $L = 26.2$ cm. Injection solvent: (▽) 90% v/v methanol/acetone; (◇) 95% v/v methanol/acetone; (△) methanol; (□) 95% v/v methanol/water; (○) 90% v/v methanol/water.

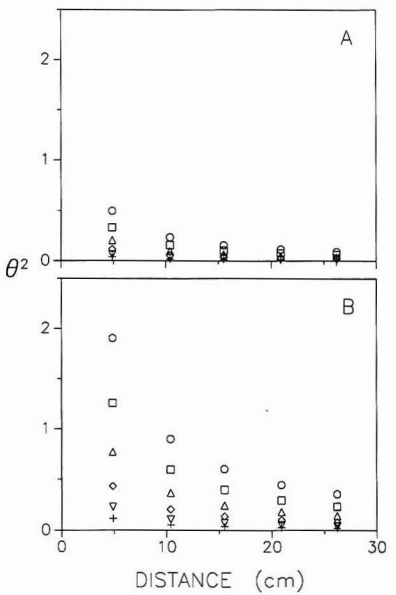

Figure 4. Fractional increase (θ^2) in the column variance caused by extracolumn sources under (A) ideal conditions and for (B) methanol injection solvent. Chromatographic and detection conditions are as described in Experimental Methods, and solutes are as shown in Figure 2.

ranging from 0.54 for n-$C_{10:0}$ to 4.95 for n-$C_{20:0}$ (Table I). Contrary to theoretical predictions, however, capacity factor values measured in the single mode (Figure 2, top) exhibit a small but systematic increase with distance traveled. This increase in k_{MP} of approximately +3.0% in the region from 4.9 to 26.2 cm along the column appears to be independent of carbon number and is statistically significant compared with the average precision of ±0.5% relative standard deviation (rsd). Errors in the determination of t_0 caused by slight retention of the void marker could lead to this positive trend. If so, the local capacity factor measured in the dual mode

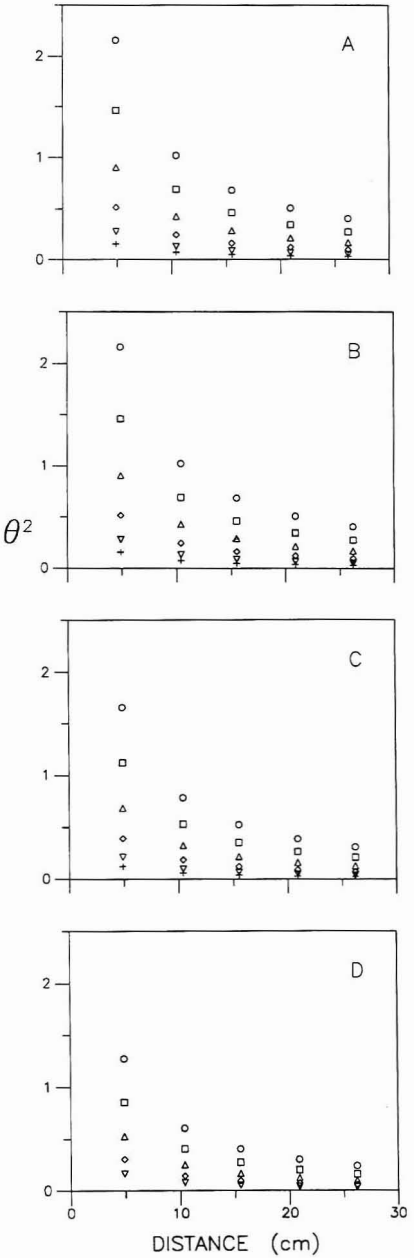

Figure 5. Effect of the injection solvent composition on the fractional increase (θ^2) in the column variance caused by extracolumn sources. Injection solvents: (A) 90% v/v methanol/acetone; (B) 95% v/v methanol/acetone; (C) 95% v/v methanol/water; (D) 90% v/v methanol/water. Chromatographic and detection conditions are as described in Experimental Methods, and solutes are as shown in Figure 2.

would be expected to exhibit the same trend. However, as seen in Figure 2 (bottom), the local capacity factor remains constant with distance for all solutes within the average precision of ±0.6% rsd (with n-$C_{16:0}$ and n-$C_{20:0}$ exhibiting anomalously poor precision at ±4.4% and ±1.5%, respectively). On the basis of these measurements, it is possible that equilibration upon injection is not instantaneous but does occur well before the first detector (L = 4.9 cm). Because of this decreased retention at the column inlet, all solutes exhibit single-mode capacity factor values at the last detector (L = 26.2 cm) that are systematically −0.7% less than local capacity factor values. Thus, a significant proportional error may result if the capacity factor measured at the column exit is presumed to represent the local capacity factor on the column, as is common practice in chromatography.

Other Injection Solvents. In this investigation, the composition of the injection solvent is systematically varied and the retention behavior is, again, evaluated as a function of distance along the column. The mixtures of methanol/acetone and methanol/water (90% and 95% v/v), chosen as the injection solvents for this study, yield a broad range of capacity factors (k_{INJ}) for the derivatized fatty acids (Table I). Even though the retention behavior in the injection solvents varies markedly, no discernable variation is seen in the resulting capacity factors measured on the column. As shown in Figure 3, the retention measured at 26.2 cm along the column is unaffected by the composition of the injection solvent and is in agreement with the theoretically predicted relationship between capacity factor and carbon number. Moreover, single-detector measurements in all injection solvents exhibit the identical increase in capacity factor with distance seen for injections in methanol (Figure 2). Dual-detector measurements are also similar to those performed in methanol and are constant with distance along the column regardless of the injection solvent composition. Thus, the injection solvent has no significant effect, either temporary or persistent, on the retention behavior of the model solutes under these ideal experimental conditions.

Dispersion of Solute Zones. Systematic evaluation of the dispersion or broadening of solute zones is also essential in understanding the factors affecting chromatographic performance. Although the plate height is generally assumed to be constant along the column length, extracolumn and nonequilibrium effects occurring upon injection may lead to unexpected behavior in the column inlet region. To evaluate the effect of the injection process on zone dispersion, the variance and plate height of solute zones with distance along the column are determined from the data set described above. Because the dispersion of solute zones in the inlet region may be a complex phenomenon, it is instructive first to estimate the influence of dispersion arising prior to the column and then to predict the physical and chemical effects of the discrete transition onto the chromatographic column. Finally, single- and dual-mode measurements of the plate height with distance along the column may be evaluated. As in the study of retention, initial investigations focus on the methanol mobile phase as the injection solvent, while later studies explore the effect of the injection solvent composition.

Predicted Effect of Extracolumn Dispersion. Plate height measurements performed at a single detector include dispersion contributions from extracolumn as well as column sources. In experimental determinations, these sources of dispersion arising outside the column may have a substantial influence on the accurate measurement of the column plate height (*24*). Unfortunately, plate height measurements near the column inlet, where the solute zone has traveled only a short distance, may be dominated by extracolumn sources of dispersion. For this reason, it is informative to predict the extracolumn influence expected under the experimental

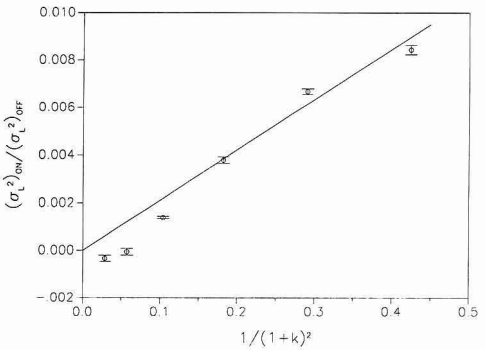

Figure 6. Measured ratio of the length variance on column $(\sigma_L^2)_{ON}$, to that immediately prior to the packed bed, $(\sigma_L^2)_{OFF}$ for methanol injection solvent: (—) theoretical prediction; (O) experimental measurement. Chromatographic and detection conditions are as described in Experimental Methods.

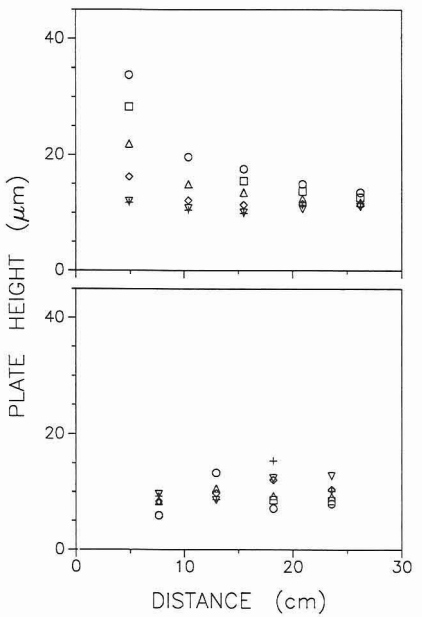

Figure 7. Plate height versus distance along the column for single (top) and dual (bottom) mode determinations. Injection solvent: methanol. Chromatographic and detection conditions are as described in Experimental Methods, and solutes are as shown in Figure 2.

conditions of this study. For clarity, only those sources of dispersion arising outside the column itself will be included in this prediction, and the effect of the transition onto the column will be considered separately. The detrimental influence of extracolumn dispersion may be estimated from the fractional increase in the column variance caused by known extracolumn sources of variance (*21*). Under ideal conditions, the fractional increase in the variance (θ^2) may be described by eqs 4 and 5. The resulting θ^2 values calculated for the experimental conditions in this study are shown in Figure 4A as a function of distance, assuming a column plate height

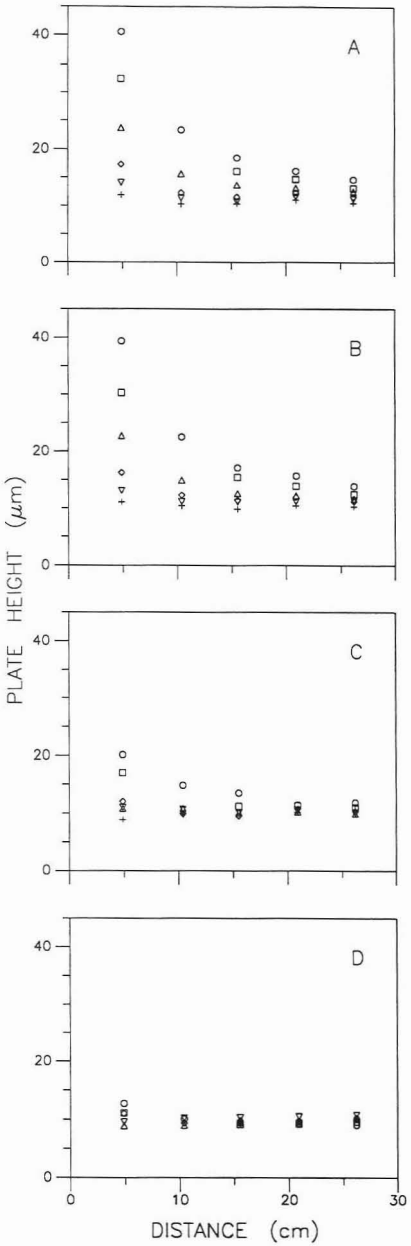

Figure 8. Effect of injection solvent on single-mode measurements of plate height. Injection solvents: (A) 90% v/v methanol/acetone; (B) 95% v/v methanol/acetone; (C) 95% v/v methanol/water; (D) 90% v/v methanol/water. Chromatographic and detection conditions are as described in Experimental Methods, and solutes are as shown in Figure 2.

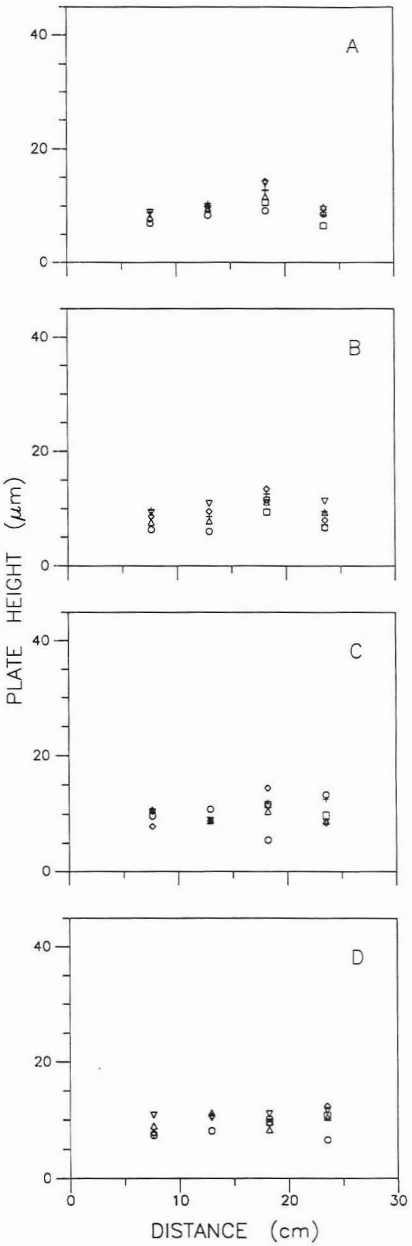

Figure 9. Effect of injection solvent on dual-mode measurements of plate height. Injection solvents: (A) 90% v/v methanol/acetone; (B) 95% v/v methanol/acetone; (C) 95% v/v methanol/water, (D) 90% v/v methanol/water. Chromatographic and detection conditions are as described in Experimental Methods, and solutes are as shown in Figure 2.

(H_{COL}) of 9.5 μm. As expected, the extracolumn influence is greatest at small distances and decreases as the solute zone is further broadened by the column. A substantial decrease in θ^2 is also seen as the solute capacity factor increases, ef-

fectively increasing the volumetric variance contributed by the column. Thus, extracolumn dispersion is predicted to affect not only the magnitude of the measured plate height but also its dependence on distance and capacity factor.

These estimates presuming best-case conditions (eq 4) are often the only indication of the expected magnitude of extracolumn effects. In the present experimental design, a more realistic estimate of θ^2 may be obtained from the variance of the injection profile measured immediately prior to the column. This in situ measurement allows a more accurate determination of the largest sources of extracolumn variance, those contributed by injection and connection processes. Utilizing the methanol mobile phase as the injection solvent, this initial profile is approximately symmetric with an average time variance (σ_t^2) of 4.30 ± 0.32 s^2 (n = 12). As shown in Figure 4B, the θ^2 values calculated from the measured injection/connection variance indicate that the extracolumn variance is substantially greater than first estimated on the basis of ideal injection and hydrodynamic conditions (Figure 4A). In fact, the extracolumn contributions may be as much as twice the column variance measured at the first detector.

In like manner, the dispersion of the solute zone may be evaluated immediately prior to the column as a function of the injection solvent. On the basis of eqs 4 and 5, the influence of solvent composition on this initial zone is expected to be minor, affecting only the solute diffusion coefficient in the connecting tube. However, experimental measurements performed 0.4 cm before the column indicate a systematic change in the variance contributed by injection/connection sources which is opposite to that predicted solely on the basis of the diffusion coefficient in the injection solvent. When 90% and 95% v/v methanol/acetone injection solvents are utilized, the measured time variances are statistically equivalent (4.68 ± 0.16 s^2 (n = 25)) and slightly greater than those measured for methanol injections. In contrast, the measured time variances for 90% and 95% v/v methanol/water injection solvents (2.72 ± 0.22 s^2 (n = 9) and 3.58 ± 0.37 s^2 (n = 12), respectively) are substantially less than for injections in methanol. The fractional increase in the column variance (θ^2) calculated on the basis of these unexpected results is shown in Figure 5. A substantial decrease in θ^2 is seen for the injection solvents containing water, solely due to this systematic decrease in the injection/connection dispersion arising before the solute enters the column. The origin of this decrease in variance remains unclear but may be due to changes in the physical properties of the solvent (viscosity, surface tension, etc.) that influence hydrodynamic flow in the injection valve or in the region near the splitter. Thus, not only is the magnitude of θ^2 substantially greater than expected on the basis of ideal conditions, but also the composition of the injection solvent has a direct influence on the solute zone profile immediately prior to the column. Since neither of these trends is predicted theoretically, evaluation of extracolumn dispersion based on Figure 4A would have greatly underestimated these detrimental effects.

Off- to On-Column Transition. The transition of the solute zone onto the chromatographic column is often assumed to have little effect on the measured plate height. However, in traveling from a nonretentive open tube to a retentive packed bed, the solute zone undergoes an abrupt change in capacity factor. If this transition region alone is considered, the time variances off and on column are expected to remain equal in the absence of additional sources of dispersion. In this case, the relationship between time and length variance may be utilized to relate the length variance immediately prior to the column head ($(\sigma_L^2)_{OFF}$) to the length variance at the beginning of the column ($(\sigma_L^2)_{ON}$). The resulting expression, developed in an analogous manner to the elution of a solute zone from the column exit (*18*), is given by

Table II. Effect of Injection Solvent Composition on the Measured Length Variance Ratio and Plate Height for the n-$C_{10:0}$ Derivative

injection solvent	k_{INJ}	$(\sigma_L^2)_{ON}/(\sigma_L^2)_{OFF}$	plate height, μm[a]
90% methanol/acetone	0.44	0.0100	14.6
95% methanol/acetone	0.47	0.0099	13.9
methanol	0.54	0.0086	13.5
95% methanol/water	1.20	0.0045	11.9
90% methanol/water	2.60	0.0022	9.0

[a] Single-mode measurements at L = 26.2 cm.

$$(\sigma_L^2)_{ON} = (\sigma_L^2)_{OFF}\frac{u_{ON}^2}{u_{OFF}^2}\frac{1}{(1 + k_{INJ})^2} \quad (7)$$

where u_{ON} and u_{OFF} are the mobile-phase linear velocity on and off column, respectively. In this transition, the solute capacity factor in the injection solvent (k_{INJ}) is equal to that in the mobile phase (k_{MP}) when samples are dissolved in the methanol mobile phase. Since the volumetric flow rate is constant in the transition region, the linear velocity expected on column may be written in terms of the tubing radius off and on column (r_{OFF} and r_{ON}, respectively) and the total porosity of the packed bed (ϵ_T). Combining this result with eq 7 yields an expression for the on-column length variance, $(\sigma_L^2)_{ON}$.

$$(\sigma_L^2)_{ON} = (\sigma_L^2)_{OFF}\frac{r_{OFF}^4}{r_{ON}^4}\frac{1}{\epsilon_T^2}\frac{1}{(1 + k_{INJ})^2} \quad (8)$$

In this expression, the terms involving the radius and porosity reflect the physical or structural transition within this region, whereas the term involving the capacity factor reflects the transition in chemical environment. Thus, with knowledge of only a few experimental parameters, the resulting change in the solute zone variance caused by this abrupt transition may be predicted.

Experimental measurement of this phenomenon is accomplished by calculating the ratio of the on-column length variance, extrapolated to zero distance, to that measured off column ($(\sigma_L^2)_{ON}/(\sigma_L^2)_{OFF}$). As shown in Figure 6 for the methanol injection solvent, there is excellent agreement between the measured length variance ratios and those predicted with eq 8. This decrease in the length variance of the solute zone at the column inlet effectively decreases the resulting solute volume injected onto the column as a function of the capacity factor (k_{INJ}), thus reducing the detrimental effects of extracolumn dispersion.

Further studies of the decrease in extracolumn variance are accomplished by altering the composition of the injection solvent. Although the variation in injection solvent has been utilized to advantage by practicing chromatographers for many years, systematic investigations have been limited by the inability to measure the zone profile directly on the column. As seen in eq 8 and later in eq 9, the extracolumn variance is expected to decrease markedly with the solute capacity factor in the injection solvent (k_{INJ}) based on the simple steady-state model. For solutes that are highly retained (large k_{MP}), the influence of the injection solvent is expected to be minor. In contrast, solutes that are only slightly retained (small k_{MP}) are more affected by extracolumn variance and, thus, may benefit greatly from careful choice of injection solvent. Experimental measurement of the length variance ratios for the least retained solute, n-$C_{10:0}$, as a function of injection solvent are shown in Table II. As predicted, when the injection solvent is stronger than the methanol mobile

phase ($k_{INJ} < k_{MP}$), the measured length variance ratio and plate height are both greater than those for the pure methanol injection solvent. Under these conditions, the solute zone is compressed to a lesser extent upon entering the column, and the extracolumn variance caused by the injection is more detrimental. Alternately, when the n-$C_{10:0}$ fatty acid is injected in solvents that are weaker than methanol ($k_{INJ} > k_{MP}$), a substantial decrease in the length variance ratio and measured plate height is clearly seen. Contrary to common misconceptions (*13*), this decrease in the extracolumn variance does not require a large change in injection solvent composition to realize a notable improvement in the measured plate height, even at a distance of 26.2 cm along the column.

On-Column Dispersion Measurements. In most theoretical derivations of dispersion processes in liquid chromatography, plate height is predicted to be independent of distance along the column (*25–27*). As noted above, however, single-mode measurements of plate height are strongly influenced by extracolumn sources of variance and, therefore, are expected to exhibit some dependence on distance. In contrast, dual-mode measurements should be in agreement with theoretical predictions because extracolumn contributions to the variance have been effectively eliminated. In addition to the effect of the injection process itself, the influence of the injection solvent composition on both these measurements may be systematically evaluated.

Prediction of the extracolumn influence on the measured plate height (H_{MEAS}) may be accomplished with eq 4. By assuming that the variance contribution from the injection volume arises from a Gaussian band ($[6\pi r_{OFF}^2(\sigma_L)_{OFF}]^2/36$) rather than the more ideal plug injection ($V_{INJ}^2/12$), the magnitude of the extracolumn influence may be more accurately estimated. If this injection volume resulting from injection/connection dispersion processes is the primary source of extracolumn variance, combining eq 4 with eqs 5 and 6 results in the following expression for the plate height measured at a single detector (H_{MEAS}):

$$H_{MEAS} = H_{COL}\left[1 + \frac{(6\pi r_{OFF}^2(\sigma_L)_{OFF})^2 u_{ON}^2}{36(1 + k_{INJ})^2(1 + k_{MP})^2 L F^2 H_{COL}}\right] \quad (9)$$

On the basis of eq 9, it is clearly expected that the solute capacity factors in the mobile phase (k_{MP}) and in the injection solvent (k_{INJ}) have a substantial influence on the measured plate height. When methanol is employed as the injection solvent, the extracolumn contribution is predicted to be inversely proportional to $(1 + k_{MP})^4$. Moreover, when extracolumn effects are predominant, the measured plate height is expected to depend inversely on the distance traveled (L).

Experimental results of initial studies utilizing methanol as the injection solvent are shown in Figure 7. As expected, extracolumn effects dominate the single-mode measurements (Figure 7, top), leading to the inverse relationship between measured plate height and distance predicted in eqs 5 and 6. However, the detrimental effects of extracolumn variance decrease markedly with capacity factor, as predicted from the $(1 + k_{MP})^{-4}$ dependence (eq 9). Unfortunately, even at a distance of 26.2 cm along the column, the observed dependence of plate height on capacity factor is reversed from that expected if resistance to mass transfer in the mobile phase is limiting solute dispersion. In contrast to the single-mode measurements, however, the dual-mode measurements of local plate height are in good agreement with chromatographic theory (Figure 7, bottom), exhibiting no discernable variation with distance along the column (*28*). In addition, the local plate height measurements exhibit the general capacity factor trend predicted for conditions where mass-transfer processes in the mobile phase are limiting the column plate height.

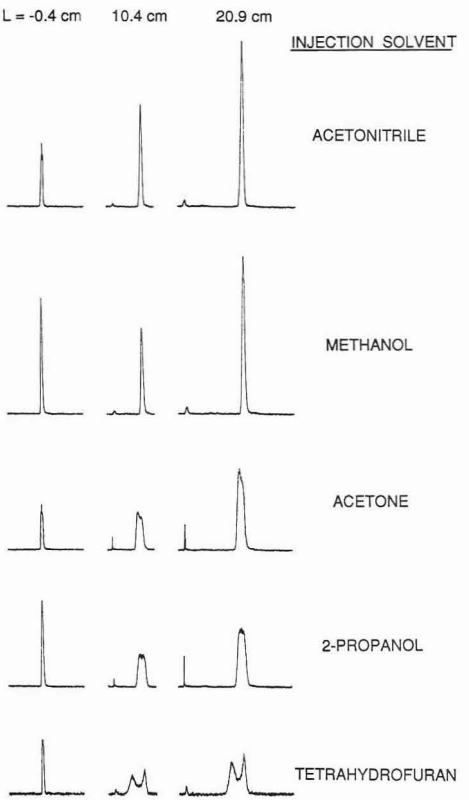

Figure 10. Development of chromatogram of derivatized fatty acid standard, n-$C_{10:0}$, injected in pure organic solvents. Detector positions at 0.4 cm before the column as well as 10.4 and 20.9 cm along the column. Other chromatographic and detection conditions are as described in Experimental Methods.

In further studies, plate height is measured under conditions of varying injection solvent composition. Experimental measurements in the single mode, shown in Figure 8, clearly demonstrate a decrease in plate height with the polarity of the injection solvent. As expected on the basis of eq 9, the effect is most profound for the least retained solutes, resulting in a measured plate height of 40.59 ± 0.12 μm with 90% v/v methanol/acetone and 12.71 ± 1.37 μm with 90% v/v methanol/water for n-$C_{10:0}$ at 4.9 cm along the column. The influence of this decrease in the extracolumn variance on the determination of the true column dispersion becomes apparent for injection in 90% v/v methanol/water (Figure 8D). At short distances, the measured plate height is dominated by the extracolumn variance and decreases with increasing capacity factor. As the distance increases, the column variance becomes predominant and the trend with capacity factor is reversed. Thus, the injection solvent appears to play an important but routinely neglected role in the evaluation of fundamental parameters controlling solute zone dispersion.

In contrast to single-mode measurements of plate height (Figure 8), dual-mode determinations shown in Figure 9 exhibit little change with distance along the column. Moreover, these local plate height measurements show no discernable

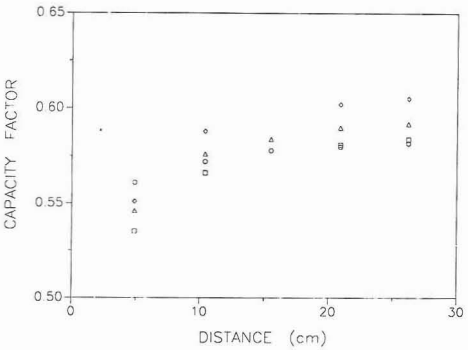

Figure 11. Measured capacity factor versus distance along the column for injection of n-$C_{10:0}$ in pure organic solvents: (◇) 2-propanol; (□) acetone; (○) methanol; (△) acetonitrile. Chromatographic and detection conditions are as described in Experimental Methods.

variation with the injection solvent composition. These results indicate that if the decrease in the length variance does not occur entirely within the transition region, it is certainly completed by a distance of 4.9 cm along the column and is independent of the relatively small changes in solvent composition studied here. In addition, the trend in the local plate height with capacity factor is no longer dominated by extracolumn effects and is in general agreement with predictions based on mobile-phase mass-transfer processes. These preliminary studies indicate that the nonequilibrium condition created by the injection process does not extend a substantial distance onto the column. Surprisingly, this result is also true when small variations in the injection solvent composition are utilized to produce large variations in the capacity factor upon injection.

Both accuracy and precision are important in evaluating the measured and true column plate height. While single-mode measurements are reasonably precise with a standard deviation in the plate height pooled over distance (s_{POOLED}) of ±0.50 μm, extracolumn processes directly affect the measurement accuracy by systematically increasing the measured plate height. In contrast, the dual-mode technique effectively eliminates extracolumn effects and is quite accurate (*17*), but the precision (s_{POOLED} = ±1.1 μm) suffers from the difficulties inherent in any difference measurement. Although these standard deviation values appear to be quite similar, the relative precision of these two techniques differs markedly. The precision of single-mode measurements ranges from approximately ±1.5 to ±4.5% rsd, whereas the dual-mode precision is approximately ±12% rsd. The relative precision of plate height measurements appears to be independent of injection solvent composition. Although these values are well within the expected precision for statistical moment calculations (*29*), further studies will be necessary to determine the exact origin of the variability.

Other Injection Solvents. Until now, this discussion has focused on relatively small changes in the composition of the injection solvent. In practice, however, solvents with physical and chemical properties differing widely from the mobile phase are often utilized to dissolve the solutes of interest. The perturbation upon injection, in this case, is expected to be extreme, and the behavior of the solute zone under these conditions is difficult to predict (*30*, *31*). In these preliminary investigations, the retention and dispersion of a single solute injected in several common organic solvents (acetonitrile, acetone, 2-propanol, and tetrahydrofuran) is evaluated.

As shown in Figure 10, the injection solvent has a clear effect on the solute profile arising on the column, often resulting in anomalous peak shapes. In this figure, the response of the detector positioned 0.4 cm prior to the column is shown together with the response for detectors at 10.4 and 20.9 cm along the column. A single solute (n-$C_{10:0}$) is utilized throughout this study to ensure solubility in all injection solvents. The response shown is well within the linear dynamic range of the detection system, and variations in intensity with injection solvent can be directly compared at a given detector position. However, the measured photocurrent between detectors is not directly comparable due to the difficulties in matching excitation intensities.

Illustration of the detector response in this manner allows direct observation of the chromatographic development as the solute traverses the column. Although only n-$C_{10:0}$ and a small amount of nonretained solute are injected, it is clear that the development of the zone profile varies greatly with the composition of the injection solvent. Injections in methanol and acetonitrile result in well-behaved and symmetric profiles, while zone profiles in the stronger injection solvents exhibit varying degrees of asymmetry. Although exaggeration of any asymmetry in the zone profile present at the first detector is predicted for the strong solvents, the unusual peak shapes seen for injection in 2-propanol and in tetrahydrofuran are not expected. In addition, the zone profile for n-$C_{10:0}$ in acetone and 2-propanol is clearly broadened as expected, while the nonretained zone is sharpened considerably. As in the previous studies, further characterization of these anomalies is accomplished by quantitatively evaluating the retention and dispersion of the zone profiles with distance along the column.

Solute Zone Retention. In contrast to the small changes in solvent composition shown earlier, single-mode measurements of retention are influenced substantially by the injection solvent under these extreme conditions. Not only are the solute retention times affected, as might be expected, but the void time of the nonretained marker is altered as well. Solute injections in acetone exhibit the largest deviation in retention time (M_1) of −1.1% when compared with injections in methanol, while injections in acetonitrile and in 2-propanol show a deviation of only −0.3%. Negative deviations in the void time (t_0) are also measured, with injections in acetone and 2-propanol resulting in variations larger (−1.5%) than those for acetonitrile injections (−1.0%). These factors combine to yield substantial deviations in capacity factor with distance along the column, as shown in Figure 11. While injection in methanol exhibits approximately a +3.0% increase in capacity factor from 4.9 to 26.2 cm along the column, all other solvents produce variations of +8.5% to +9.5%. This apparent increase in nonequilibrium at the entrance to the column is unsurprising in view of the large changes in solvent strength. Injections in tetrahydrofuran have not been included in the above discussion due to the anomalous peak splitting shown in Figure 10.

Solute Zone Dispersion. Initial comparison of the precolumn detector response (Figure 10) reveals a systematic variation in both the intensity and width of solute zones with injection solvent composition. Changes in peak height at this first detector position are difficult to compare directly due to alterations in the variance of the solute zone, coupled with differences in the fluorescence quantum yield with injection solvent. As seen previously, the magnitude of the time variance of the injection profile measured immediately prior to the packed bed is quite solvent specific, with all solvents except tetrahydrofuran exhibiting variance values greater than for methanol injections (4.30 ± 0.32 s^2). Injection in acetonitrile yields a zone variance of 5.58 ± 0.14 s^2, while variance values for injections in both acetone and 2-propanol are the greatest at 6.55 ± 0.15 s^2. This latter result is surprising if hydrodynamic flow upon split injection is the major cause of extracolumn variance, because the viscosity of acetone and

Table III. Effect of Pure Injection Solvents on the Measured Length Variance Ratio and Plate Height for the n-$C_{16:0}$ Derivative

injection solvent	$(\sigma_L^2)_{ON}/(\sigma_L^2)_{OFF}$	plate height, μm[a]
tetrahydrofuran	0.255	255
2-propanol	0.065	59.0
acetone	0.045	44.6
methanol	0.0086	13.5
acetonitrile	0.0068	12.8

[a] Single-mode measurements at L = 26.2 cm.

2-propanol vary substantially (η = 0.36 and 2.4 cP, respectively). These changes in the variance of the injected zone are not presently predictable and are under investigation. Nevertheless, as seen previously, injection solvent composition does indeed have a large effect on the profile of the injected zone and, thus, the plate height measured on the column.

The transition onto the column is also affected by these drastic changes in solvent composition. On- to off-column length variance ratios shown in Table III appear to be in qualitative agreement with eq 8, exhibiting the expected increase with solvent strength. However, the maximum value for the length variance ratio predicted from eq 8 is 0.021 for a nonretained solute (k_{INJ} = 0), which is exceeded when acetone, 2-propanol, and tetrahydrofuran are utilized as injection solvents. Clearly, a discrete change in zone velocity in the transition region does not account for the magnitude of the variance ratios under these extreme conditions.

Rigorous evaluation of this effect will require systematic monitoring of the injection solvent zone as well as the solute zone profiles. It is possible that the profile of the injection solvent is altered markedly upon injection onto the packed bed. Furthermore, these pure injection solvents may modify not only the strength of the mobile phase but also that of the stationary phase. Injection in a solvent with a substantially different composition from the mobile phase may create both mobile- and stationary-phase gradients in the inlet region of the column. In addition, temperature gradients induced by mixing of the pure solvents with the mobile phase may cause large variations in physical properties (e.g., solubility, viscosity, surface tension, diffusion coefficient) across the solute zone profile. Because these effects are not presently predictable, injection in a solvent substantially different from the mobile phase is not recommended. Further investigations will be necessary to understand the complex interactions present upon such drastic changes in injection solvent composition.

CONCLUSIONS

For the well-behaved solutes and the nearly ideal chromatographic conditions explored in this study, nonequilibrium inherent in the injection process does not extend a long distance onto the chromatographic column. However, the length variance of the injected zone is altered substantially upon entering the column as a function of the solute capacity factor. This effect can be used to advantage by choosing an injection solvent that is weaker than the mobile phase, thus concentrating the solute at the column inlet and decreasing extra-column effects. Contrary to common practice, however, only small changes (5–10%) in the composition of the injection solvent are necessary to produce marked improvement in the resulting zone profile. When the injection solvent differs substantially from the mobile phase, deleterious changes in the zone profile may result that are not presently predictable. Further investigations into the dynamic processes present upon injection under these extreme conditions will be necessary to understand this complex process more fully.

This direct method of measuring the movement and dispersion of solute zones has provided a view of the separation process not previously possible. Although applied here to well-behaved solutes and nearly ideal separation conditions, this detection scheme may easily be extended for the systematic investigation of adsorption mechanisms or overload conditions. In addition, this experimental approach is not limited to liquid chromatographic separations but may be adapted for gas and supercritical fluid chromatography as well as capillary electrophoresis.

LITERATURE CITED

(1) Ettre, L. S. In *Sample Introduction in Capillary Gas Chromatography*; Sandra, P., Ed.; Verlag: Heidelberg, 1985; Vol. 1 (see also references cited therein).
(2) deVault, D. *J. Am. Chem. Soc.* **1943**, *65*, 532.
(3) Reilley, C. N.; Hildebrand, G. P.; Ashley, J. W., Jr. *Anal. Chem.* **1962**, *34*, 1198.
(4) Scott, R. P. W. *J. Chromatogr. Sci.* **1971**, *9*, 449.
(5) Snyder, L. R. *J. Chromatogr. Sci.* **1972**, *10*, 187.
(6) Karger, B. L.; Martin, M.; Guiochon, G. *Anal. Chem.* **1974**, *46*, 1640.
(7) Jacob, L.; Guiochon, G. *J. Chromatogr. Sci.* **1975**, *13*, 18.
(8) Conder, J. R. *HRC & CC, J. High Resolut. Chromatogr. Chromatogr. Commun.* **1984**, *7*, 615.
(9) Lovkvist, P.; Jonsson, J. A. *J. Chromatogr.* **1986**, *356*, 1.
(10) Hoffman, N. E.; Rahman, A. *J. Liq. Chromatogr.* **1988**, *11*, 2685.
(11) Dose, E. V.; Guiochon, G. *Anal. Chem.* **1990**, *62*, 1723.
(12) Takeuchi, T.; Ishii, D. *J. Chromatogr.* **1981**, *218*, 199.
(13) Yang, F. J. *J. Chromatogr.* **1982**, *236*, 265.
(14) McGuffin, V. L.; Zare, R. N. *Appl. Spectrosc.* **1985**, *39*, 847.
(15) Bristow, P.; Knox, J. *Chromatographia* **1977**, *10*, 279.
(16) Gluckman, J. C.; Hirose, A.; McGuffin, V. L.; Novotny, M. *Chromatographia* **1983**, *17*, 303.
(17) Evans, C. E.; McGuffin, V. L. *Anal. Chem.* **1988**, *60*, 573.
(18) Evans, C. E.; McGuffin, V. L. *J. Liq. Chromatogr.* **1988**, *11*, 1907.
(19) Sternberg, J. C. *Adv. Chromatogr.* **1966**, *2*, 205.
(20) Evans, C. E.; McGuffin, V. L. *Proc. Int. Symp. Capillary Chromatogr.* **1990**, *11*, 802.
(21) Martin, M.; Eon, C.; Guiochon, G. *J. Chromatogr.* **1975**, *108*, 229.
(22) Wilke, C. R.; Chang, P. *AIChE J.* **1955**, *1*, 264.
(23) Martire, D. E. *J. Chromatogr.* **1989**, *461*, 165.
(24) Huber, J. F. K.; Rizzi, A. *J. Chromatogr.* **1987**, *384*, 337.
(25) Van Deemter, J. J.; Zuiderweg, F. J.; Klinkenberg, A. *Chem. Eng. Sci.* **1956**, *5*, 271.
(26) Giddings, J. C. *Dynamics of Chromatography*; Marcel Dekker, Inc.: New York, 1965; pp 310–312.
(27) Knox, J. H. *J. Chromatogr. Sci.* **1977**, *15*, 352.
(28) Poe, D. P.; Martire, D. E. *J. Chromatogr.* **1990**, *517*, 3.
(29) Chesler, S. N.; Cram, S. P. *Anal. Chem.* **1971**, *43*, 1922.
(30) Tsimidou, M.; Macrae, R. *J. Chromatogr. Sci.* **1985**, *23*, 155.
(31) Khachik, F.; Beecher, G. R.; Vanderslice, J. T.; Furrow, G. *Anal. Chem.* **1988**, *60*, 807.

RECEIVED for review November 2, 1990. Revised manuscript received March 22, 1991. Accepted April 5, 1991. This research was supported by the U.S. Department of Energy, Office of Basic Energy Sciences, Division of Chemical Sciences under Contract No. DE-FG02-89ER14056. Preliminary results were presented at the Pittsburgh Conference on Analytical Chemistry and Applied Spectroscopy, New York, 1990.

Theory and Experiment for the Collector–Generator Triple-Band Electrode

Bruno Fosset and Christian Amatore*

Ecole Normale Superieure, Laboratoire de Chimie, 24 Rue Lhomond, 75231 Paris, France

Joan Bartelt and R. Mark Wightman*

Department of Chemistry, University of North Carolina, Chapel Hill, North Carolina 27599-3290

The currents obtained at a triple-band electrode with a central generator and flanking collectors have been calculated by digital simulation. To determine the current at steady state, a conformal map was used in which space is folded so that the geometry is similar to that of a thin-layer cell with opposing electrodes. This geometry makes the flux lines straighter and thus simplifies rapid, accurate calculations. If flux through the small gap between the collectors in the conformal space is ignored, a condition that is true at steady state, the current is shown to approach that of a thin-layer cell with continuous, opposing electrodes. At infinite times, the collection efficiency will be one and the inverse amplification factor (defined as the current at a single band divided by the generator current) approaches zero. To evaluate the current for experimentally achievable time scales, a different conformal map was used for the simulation. In this case, space was folded on either side of the generator, resulting in a three-sided geometry. Experimental data for the oxidation of ferrocene in acetonitrile are in good agreement with the simulated results. Comparison of the results reported here with prior work on the double- and single-band geometries shows advantages in the present case with respect to the time needed to achieve pseudo steady state.

INTRODUCTION

In previous work, we have examined the faradaic current at the single band and the double band operated in the collector–generator configuration (*1*, *2*). Both of these configurations have many of the advantages that other electrodes of very small dimensions exhibit (*3*). In addition, double-band electrodes used in the collector–generator mode provide information on the electrogenerated products, information not available at single-band microelectrodes operated under quasi-steady-state conditions (*4*, *5*). The usual mode of operation of collector–generator devices is to sweep the generator potential while maintaining the collector at a fixed potential. Voltammograms obtained in this way for a diffusion-limited process are a function of the electrode dimensions and the scan rate. The current at the generator electrode is enhanced by the feedback of electroactive material from the collector. This effect is most apparent at slow scan rates. Similarly, the collector current also increases with decreased scan rate because the diffusion layer of the generator more completely overlaps the region of the collector. Since the potential of the collector remains constant during the experiment, high gain can be used to amplify very small currents. This feature is especially useful when the electrogenerated product is unstable on the electrochemical time scan. As few as 10^5 molecules have been collected in such an experiment (*6*).

* To whom correspondence should be addressed.

The focus of this paper is to present the theory and voltammetric data for triple-band electrodes, in which the outer two bands operate as collectors poised at the same potential and the central band is the generator. We wish to examine the relative merits of the different types of microelectrode arrays because an extended future for these electrodes as electrochemical sensors seem certain, due to their wide applicability and high information content. The theory for interdigitated arrays of bands has been developed by using conformal maps (*7*), and these can be fabricated by microlithographic techniques (*4*, *7–10*). However, the triple band seems particularly attractive, because it is simple to fabricate from metal foils and is capable of a high collection efficiency (*11*).

The theory shown here is based on the use of conformal maps, a procedure we have previously described (*2*). Two conformal maps are used; one that resembles a thin-layer cell is used to arrive at the steady-state currents. A different conformal map is then used for digital simulation of voltammetric data at experimentally achievable time scales. The simulated and experimental results allow a critical comparison to be made between the single-band and the double- and triple-band collector–generator arrays.

THEORY

Conformal Map for the Triple-Band Electrode. The generation of a conformal map for the triple band is shown in Figure 1. In x–y space, the electrode consists of a central generator electrode flanked by two collector electrodes. The generator is of width w_g, and the collectors are both of equal width, w_c. The gaps between the generator and collectors are of equal width, g. Use of the Schwarz–Christoffel transformation allows space to be transformed to a closed box, which is similar to a thin-layer cell. The transformation is accomplished with the following equation with $a = w_g/2$, $b = a + g$, and $c = b + w_c$

$$Z = K\int_0^z 1/((z^2 - a^2)(z^2 - b^2))^{1/2}\,dz \qquad (1)$$

where K is a scaling factor, $Z = \Gamma + j\theta$ is the coordinate in the transformed space, and $z = x + jy$ is the coordinate in x–y space. The positions where space is folded are referred to as the poles of inversion and are at the edges of the generator and the inner edges of the collectors. The width of the generator in the transformed space is

$$w_g^* = K\int_{-a}^{a} 1/((z^2 - a^2)(z^2 - b^2))^{1/2}\,dz \qquad (2)$$

where the superscripted * indicates a dimension in the transformed space. The width of the gap is

$$g^* = K\int_a^b 1/((a^2 - z^2)(z^2 - b^2))^{1/2}\,dz \qquad (3)$$

and the width of the collector is

$$w_c^* = K\int_b^c 1/((z^2 - a^2)(z^2 - b^2))^{1/2}\,dz \qquad (4)$$

0003-2700/91/0363-1403$02.50/0 © 1991 American Chemical Society

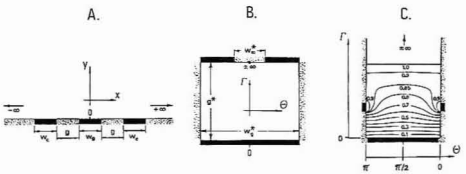

Figure 1. Representation of a triple-band electrode ($w_g = w_c = g$) in the real space (A) or in two different conformal spaces: (B) conformal space for steady-state conditions analogous to a thin-layer cell, (C) conformal space used for the time-dependent simulations. In C are also represented the lines of equal concentration of the electroactive species during a voltammogram at $E_{gen} = E^0 - 10(RT/nF)$, for dimensionless scan rate $p = (g/2)(nFv/RTD)^{1/2} = 0.01$.

Table I. Comparison between the Steady-State Limiting Current at a Triple-Band Electrode Operated in the Collector–Generator Configuration, $(i_{TB})_\infty$, and Thin-Layer Approximation, i_{TL}[a]

		triple band at steady state		
g/w_g[b]	$i_{TL}/nFlDC^0$[c]	w_∞^*/w_g^*	$(i_{TB})_\infty/nFlDC^0$	$C(\pm\infty)/C^0$
0.1	2.407	0.189	2.334	0.778
0.2	2.019	0.231	1.940	0.772
0.3	1.808	0.264	1.721	0.767
0.4	1.667	0.291	1.580	
0.5	1.564	0.314	1.472	0.760
0.8	1.365	0.371	1.266	
1	1.280	0.408	1.178	0.747
2	1.052	0.503	0.942	0.735
5	0.831	0.641	0.713	0.721

[a] Results are shown as a function of the ratio of the gap to generator width with equal widths of the bands ($w_c = w_g$). [b] Real space relative dimensions. [c] Thin-layer cell.

In the conformal space, the triple band resembles a thin-layer cell with the generator on one side and the two collectors on the other side. The bulk of solution is located at the $\pm\infty$ line, which is shown as a point in the two-dimensional representation in Figure 1. The distance between the outer edges of the collectors in the transformed space is

$$w_\infty^* = w_g^* - 2w_c^* \quad (5)$$

Note that the value of w_∞^* depends on the relative gap-to-width ratio in real space.

Solution of the Flux at Steady State. At infinite time, steady-state behavior will be approached and, thus, Fick's second law approaches zero independent of which spatial coordinate system is considered. To approximate the solution for the triple band at steady state, consider the limiting flux when $w_\infty^* = 0$. This cell contains a generator on one surface and a continuous collector on the opposing surface. The collection efficiency of this thin-layer cell is unity at steady state (i.e., the current at the collector and generator will be equal). The dimensionless current (Ψ_{TL}) is

$$\Psi_{TL} = i_{TL}/nFlDC^0 = w_g^*/g^* \quad (6)$$

where l is the length of the electrodes. The ratio w_g^*/g^* is a ratio of elliptical integrals (eqs 2 and 3) and can be evaluated by Simpson's method. The results are given in Table I for different ratios of g/w_g. This solution will be approached by that of the triple band when the ratio of the gap to generator widths is small or the ratio of the collector to generator widths is large.

To account for the steady-state limiting current with finite values of w_∞^*, a finite difference solution for this geometry with $\partial^2C/\partial\Gamma^2 + \partial^2C/\partial\theta^2 = 0$ was developed (Appendix I). The region comprised by w_∞^* includes the $\pm\infty$ line, which normally acts as a sink for products of the generator reaction and as a source of the reactant. This line can be thought of as a small band, and the flux at that band goes to zero at steady state (*1*). Therefore, the current at a triple-band collector–generator assembly at infinite time will be identical with a thin-layer cell of the dimensions in the transformed space, and the collection efficiency also will be unity. The steady-state dimensionless currents for this geometry ($\Psi_g = \Psi_c = (i_{TB})_\infty/nFDlC^0$, where Ψ_c is the sum of the currents at the two collectors) are also given in Table I for various values of w_∞^* with $w_c = w_g$. A comparison of these values with those calculated with eq 6 shows that the approximation is suitable for geometries with small values of g/w_g, since the results are within 3%. The differences increase as g/w_g increases, with a 15% difference at $g/w_g = 5$.

Table II. Generator Current at a Triple-Band Electrode under Steady-State Diffusion Conditions[a]

w_c/w_g	w_∞^*/w_g^*	$(i_{TB})_\infty/nFlDC^0$
0.5	0.530	1.103
1	0.408	1.178
2	0.275	1.232
∞	0	1.280

[a] Function of the ratio of the collection and generator widths with the width of the gap equal to the width of the generator ($g = w_g$).

Similar calculations were also made for the limiting, steady-state flux for the case where $w_c \neq w_g$. The results for three values of w_c/w_g are given in Table II, and it can be seen that, as the ratio increases, the flux approaches that given by eq 6, the last entry. The small variation of the steady-state current over a wide range of w_c/w_g shows that the edge of the collector closest to the generator is the major factor determining the amplitude of the steady-state current.

Response away from Steady State. The steady-state approximation for the triple-band electrode given above was obtained by assuming that $\partial C/\partial\Gamma = 0$ at $\pm\infty$. This is only true in the limit of infinite time, although the flux at this point always will be less than when the collectors are not operating, i.e., when the generator acts as a single band with a flux Ψ_b. To calculate the triple-band case, we note that conservation of fluxes requires that the generator flux must equal the sum of the other fluxes in space. Thus, as steady state is approached in the conformal space, $\Psi_g = \Psi_c + \Psi(\pm\infty,\text{on})$ where $\Psi(\pm\infty,\text{on})$ specifies the dimensionless flux at $\pm\infty$ when the collectors are operating. Because of conservation of flux, the flux at the infinity point for the single band as steady state is approached ($\Psi(\pm\infty,\text{off})$) is equal to Ψ_b, a value that approaches 0. Combination of these two relationships leads to

$$\Psi_c/\Psi_g + [\Psi(\pm\infty,\text{on})/\Psi(\pm\infty,\text{off})](\Psi_b/\Psi_g) = 1$$

We have used this equation in a previous treatment of the double band (*2*).

Evaluation of $\Psi(\pm\infty,\text{on})/\Psi(\pm\infty,\text{off})$ allows examination of the relation between two experimentally measured quantities as steady state is approached: the collection efficiency (Ψ_c/Ψ_g) and the amplification factor (Ψ_g/Ψ_b). By analogous arguments to those made previously (*2*), this ratio is equal to $[1 - C(\pm\infty)/C^0]$ where $C(\pm\infty)$ is the concentration in the conformal map of the triple band near the $\pm\infty$ point, a concentration that differs from C^0 because of the flux that occurs around that point. Values of $C(\pm\infty)/C^0$ at steady state were evaluated from the simulation of the closed box form of the conformal map described in Appendix I. The results of these calculations are given in Table I for the case where $w_c = w_g$. Over the range of g/w_g considered, the value of $1 - C(\pm\infty)/C^0$, and thus $\Psi(\pm\infty,\text{on})/\Psi(\pm\infty,\text{off})$, varies from 0.222 to 0.293. This is unlike the double band where this factor was equal to 0.5, irrespective of dimensions (*2*).

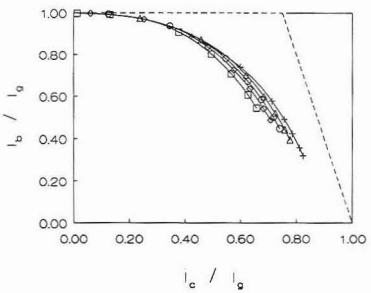

Figure 2. Simulated working curves for the triple-band electrode ($w_g = w_c$) with the inverse amplification factor plotted as a function of the collection efficiency at $E_{gen} = E^0 + 4RT/nF$, for different width-to-gap ratios: $g/w_g = 3$ (□), 2 (◇), 1.5 (○), 1 (△), and 0.5 (+). The limiting behaviors at $i_c/i_g = 0$ or 1 are indicated by the dashed lines (see text for the limit at $i_c/i_g = 1$.

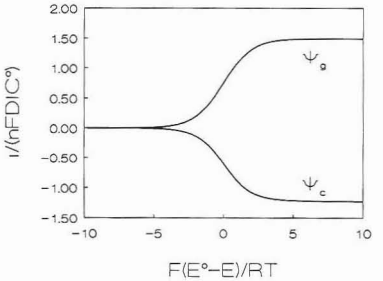

Figure 3. Simulated cyclic voltammograms for a triple-band electrode ($w_g = w_c$; $g = 0.5\ w_g$), for $p = (g/2)(nFv/RTD)^{1/2} = 0.005$.

Thus, a plot of the inverse of the amplification factor versus the collection efficiency will lie between two well-defined limits. At low values of the collection efficiency when there is no feedback, the inverse amplification will be unity. In contrast, at complete steady state, $\Psi_c/\Psi_g = 1$ and $\Psi_b/\Psi_g = 0$. As this limit is approached, that is, near steady state, the slope of the curve will be approximately −4 (i.e., between the ranges of 1/0.222 and 1/0.293 for the ratios of g/w_g considered). The intersection of these two projections limits the range of values that can be obtained (Figure 2). The fact that the limiting slope is greater than with the double band (slope of −2) is simply a reflection of the fact that less flux escapes the triple band.

Conformal Map for Digital Simulation. The closed box is not a convenient topography for digital simulations because of the complexity of expressing the space-dependent diffusion coefficient for this map. Therefore, we have employed the conformal map shown in Figure 1C which yields a three-sided, open box. The transformation is similar to the one used for the double band (*2*), but the poles of inversion are located between the generator and the collector, nearest to the generator. The distance between the two inversion poles is $2d$, which is slightly larger than w_g (see Appendix II). The coordinate system is given by

$$x = d(\cosh \Gamma)(\cos \theta) \quad (7)$$

$$y = d(\sinh \Gamma)(\sin \theta) \quad (8)$$

The spatially dependent diffusion parameter for this map is

$$D^* = D/[2d(\sinh^2 \Gamma + \sin^2 \theta)] \quad (9)$$

The diffusion equation

$$\partial C/\partial t = D^*[\partial^2 C/\partial \theta^2 + \partial^2 C/\partial \Gamma^2] \quad (10)$$

in the conformal space was solved numerically by using the hopscotch algorithm (*12*). Although not shown, the addition of homogeneous kinetic schemes to the diffusion equations is straightforward as was shown for the double band (*2*).

EXPERIMENTAL SECTION

Chemicals. Ferrocene ($FeCp_2$) (Aesar, Johnson-Matthey, Seabrook, NH) was purified by sublimation before use. Solutions of $FeCp_2$ were prepared in acetonitrile (UV grade, Burdick & Jackson, Muskegan, MI) with 0.2 M tetrabutylammonium perchlorate (TBAP). TBAP (Aldrich, Milwaukee, WI) was recrystallized twice from a pentane–ethyl acetate mixture. Solutions were deoxygenated with acetonitrile-saturated nitrogen. The diffusion coefficient for ferrocene in 0.2 M TBAP/CH_3CN is 2.2×10^{-5} cm^2 s^{-1} (*13*).

Electrodes. The triple-band electrodes were prepared by placing one or two layers of mylar film (2-μm thickness, Polaron Instruments, Hatfield, PA) as insulators between three sheets of Pt foil (*11*). The Pt foil was purchased from Aesar in sheets 4 ± 2 μm thick. The electrodes were constructed by applying a small amount of epoxy (Epon 828 with 14% *m*-phenylenediamine, Miller-Stephenson Co., Danbury, CT) first to the bottom glass slide and then between all layers as the electrode assembly proceeds. Pressure was applied during the curing process (150 °C) with a large spring clip to keep the spacing between the Pt foils as small as possible. Electrical connection was made to the back of each foil with silver epoxy (Epo-Tek H2OE, Epoxy Technology, Billerica, MA), and then Torr Seal (Varian Associates, Lexington, MA) was applied as a barrier to solutions. The edge of the assembly was ground smooth with a slurry of 1000-grit carborundum powder on a glass plate. Electrodes were polished with a slurry of 1-μm cerium oxide and fine polished with 0.25-μm diamond paste on a napless cloth (all, Buehler). The surface of the electrode was initially cleaned by sonication in both methanol and water. The surface was cleaned between experiments by wiping with a tissue soaked in acetonitrile.

Electrode lengths were estimated microscopically with a Bausch & Lomb Stereo Zoom microscope. Widths were estimated from photographs obtained with an inverted stage light microscope (Zeiss, Axiovert 35) calibrated with 2-μm divisions. The electrode widths and interelectrode gap widths varied between 4 and 7 μm. It was apparent from these photographs that the bands were misaligned lengthwise by a maximum of 5% in some cases. To correct for this, the values of i_b (single band current) and i_g (generator current) were reduced by a proportional amount (*2*).

Instrumentation. Potential control for the triple-band electrodes was maintained with a bipotentiostat of conventional design. Potential waveforms were generated with a PAR 175 universal programmer (Princeton Applied Research, Princeton, NJ), and voltammograms were recorded on a x–yy' recorder or digital oscilloscope. A conventional three-electrode cell was employed with a large Pt counter electrode and either an SSCE reference electrode or Ag wire quasi-reference electrode.

Simulations. The programs were written in Pascal (Professional Pascal from Metaware, Inc. (Santa Cruz)) and performed on a Compaq 386/20e (clock speed 20 MHz) equipped with a Weitek 1167 numerical coprocessor and on mainframe Gould computers of the Centre de Calcul Recherche of the University Pierre et Marie Curie (Paris, France). Programs are available on request from Christian Amatore.

RESULTS AND DISCUSSION

Evaluation of the Simulation. Figure 3 shows simulated voltammograms for the generator and collector. At this scan rate, the triple band gives a nearly steady-state response at the generator, whereas the collector current slightly increases with time. The accuracy of the simulation was tested by increasing the number of time and space elements over those given in Appendix II, and less than 0.5% change in the results was found. A second test of the program was made in which the collectors were considered as insulators. In this case, the result obtained was identical with that published previously for the single band (*1*). This demonstrates that moving the pole of inversion slightly away from the edge of the generator

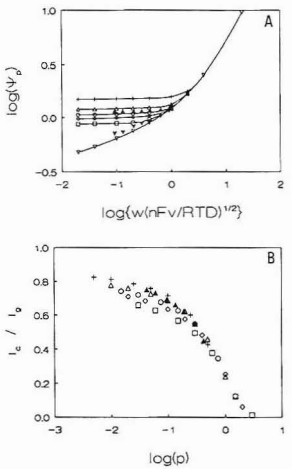

Figure 4. (A) Variations of the dimensionless generator peak current, Ψ_p, as a function of the dimensionless scan rate $(w(nFv/RTD)^{1/2}$ and gap-to width ratio. (B) Collection efficiency as a function of $p = (g/2)(nFv/RTD)^{1/2}$ and gap-to-width ratio. In A and B, theoretical values are indicated by open symbols for $w_c = w_g$ and $g/w_g = 0.5$ (+), 1 (Δ), 1.5 (O), 2 (◇), and 3 (□), and experimental values are indicated by filled symbols (▼) single band; (▲) triple band; $w_g = w_c = 6.9$ μm, $g = 6.4$ μm, 1 = 0.42 cm) for a 1.1 mM $FeCp_2$ solution with 0.2 M TBAP in acetonitrile at 20 °C. Theoretical and experimental collection efficiencies are given at $E_{gen} = E^0 + 4RT/nF$.

does not alter the results. A simulation with equivalent accuracy using a real space coordinate system and a linear grid would need 550 points on the half of the generator used for calculations. The conformal map simulation has a spacing of $2\Delta\Gamma/w_g = 0.0383$ at the outer edge of the generator. This would require that $2\Delta x/w_g = 0.0018$ in real space. The number of points required is the inverse of the latter number.

Approach to Steady State. The simulator was used to evaluate how rapidly steady state is approached. An example set of calculations is shown in Figure 4A and is compared to the scan rate behavior of a single band. At high scan rates, little interaction occurs between the collector and the generator, and the generator current becomes identical with that of the single band. As the scan rate is lowered, the generator current approaches steady-state behavior, and the transition to this behavior depends on the gap size. With small gaps, the diffusion layer of the collector and generator interact more readily, leading to a higher scan rate where the transition occurs. The steady-state value reached is inversely proportional to the gap-to-width ratio in the conformal space and can be approximated by eq 6.

The degree to which true steady-state behavior is attained is shown by the results in Table III. The simulator was used to calculate the currents at a scan rate corresponding to 1 mV s^{-1} for $w_c = w_g = 4$ μm and $D = 2 \times 10^{-5}$ cm^2 s^{-1}). The results were compared to those calculated for true steady-state conditions (Appendix I). The values of the generator currents are within 1% of the steady-state value for small values of g/w_g, but for larger values, greater deviation is seen. These results demonstrate that steady state is achieved more rapidly with small values of g/w_g. Note also that the collection efficiency, which is unity at steady state, approaches this value more slowly for large values of g/w_g.

Effect of Scan Rate. As shown in the Theory section, the relation between the inverse amplification factor and the collection efficiency should fall within the limits given by the solid lines in Figure 2, irrespective of scan rate. The simulator was used to calculate a series of points for different values of p and g/w_g, all with $w_c = w_g$. As seen, the values all lie within the predicted limits. In contrast with the double band, the points do not lie on a single curve, but rather form a family of curves that depend upon the value of g/w_g. For the smallest value of this parameter, the limiting behavior is most closely approached.

Shown in Figure 4B is the collection efficiency as a function of dimensionless scan rate for various values of g/w_g. Again, the curves do not superimpose, a result in direct contrast for that previously shown at the double band (*2*). This is because collection becomes much more efficient at the triple-band electrode as g/w_g becomes small, and the collector–generator assembly acts more like a thin-layer cell. For this reason, the general expression reported elsewhere (*4*) should only be used for electrode assemblies of specific dimensions used in those simulations.

Oxidation of Ferrocene at a Triple Band. The voltammetry of ferrocene in acetonitrile obtained at a triple-band electrode (10 mV s^{-1}) is shown in Figure 5A. Included in the figure are the single-band, generator, and collector voltammograms. The outer collectors were maintained at 0.0 V, while the potential of the central generator was swept. The collection efficiency for this triple band, with the generator scanned at 10 mV s^{-1}, is 0.75. In contrast, the collection efficiency with this electrode operated in the two possible double-band configurations using the central band as the generator was both 0.50 at 10 mV s^{-1}.

Voltammograms obtained with the same electrode when the generator is scanned 100 times faster are shown in Figure

Table III. Approach of Triple-Band Electrode to Steady State with Various Values of g/w_g. Calculations for $w_c = w_g$

g/w_g	dimensionless generator current: steady state	dimensionless generator current: simulated[a]	collection efficiency
0.5	1.472	1.487	0.830
1	1.178	1.203	0.785
2	0.942	0.976	0.720
3	0.832	0.870	0.672

[a] Calculated for $p = 0.01$.

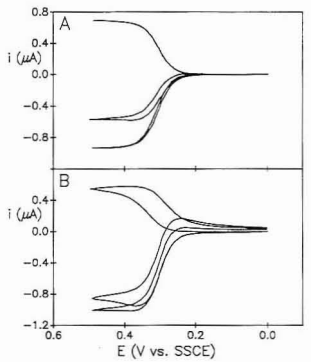

Figure 5. Voltammetry of 1.1 mM $FeCp_2$ with 0.2 M TBAP in acetonitrile at single-band, double-band, and triple-band electrodes. In the triple-band case the central band operates as the generator with the two outer bands as collectors. The central band was used as a single band and as the generator for the double-band case. Electrode length, 0.41 cm; electrode width, 6.9 μm; gap width, 6.4 μm. Scan rates are (A) 0.01 V s^{-1} and (B) 1 V s^{-1}.

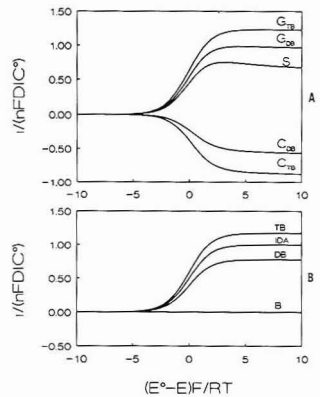

Figure 6. Comparison of the simulated voltammograms at a single (S), double (DB), or triple (TB) band electrode, for $p = 0.1$ (A) or at steady state (B). Simulation conditions: $w_g = w_c = w_b = g$; the generator currents are labeled G, and the collector currents are labeled C in A. In B, the current is also shown for an IDA with electrodes of identical dimensions. Only generator currents are shown because the collection efficiencies are unity.

5B. The collection efficiency of the electrode is decreased to 0.56 at 1 V s^{-1}. Single-band and generator dimensionless peak currents are compared to the simulated values in Figure 4A for data obtained at scan rates from 0.01 to 1 V s^{-1}. Figure 4B compares the collection efficiency obtained in these experiments to the simulation. The agreement with the simulation is seen to be within experimental error.

Comparison between Single-, Double-, and Triple-Band and Interdigitated Array Electrodes. In previous work, we have evaluated the current at a single band and the double band operated in the collector–generator mode (*1*, *2*). The triple-band electrode is advantageous over the double band in that higher collection efficiencies are achieved than with a double band with identical gap size. Another advantage of the triple band is that it approaches steady state more rapidly than the other two types of electrodes. This is illustrated in Figure 6A, where simulated voltammograms are compared at identical scan rates. The current at the single band is clearly not steady state; the triple band has a greater degree of steady-state character than the double band. For the double and triple band, steady state is achieved because of feedback from the collector. The greater feedback that exists at the triple band results in its more rapid approach to steady state. This is directly apparent in the amplification factor, which is found to have greater values at the triple band for fixed values of the collection efficiency (compare Figure 2 with Figure 5 of ref 2). However, in many instances, the double band is the electrode of choice because of the increased experimental difficulty in fabrication of triple bands compared to double bands. Furthermore, although the triple band is a more symmetric structure with respect to the generator, the evaluation of the theory is more complicated and does not lead to concise relationships as were found for the double band (*2*).

Another point of interest is a comparison of these results with the electrochemical response of interdigitated arrays (IDAs). Since the IDAs have been considered under steady-state conditions (*7*), this discussion is limited to conditions where the collection efficiencies are unity for the double-band and triple-band electrodes and IDAs. This is illustrated in Figure 6B, where simulated steady-state voltammograms (limit for $p \rightarrow 0$) are represented for a single band (*1*), a double band (*2*), a triple band (this work), and one element of IDAs (one cathode + one anode) (*7*). For a single band, the steady-state current is zero. The steady-state voltammogram for an IDA was determined by using eq 28 of ref 7 (note that there is a typographical error in eq 21 of the same reference: H is the difference and not the sum of the two potential dependent terms). The larger generator current observed at the triple band in comparison to that observed at one element of an IDA may seem surprising. However, this arises because in each element of an IDA, one generator is associated with one collector (as in the double band) rather than with two collectors (as in the triple band). Moreover, lateral diffusion to the generator is shielded by the other IDA elements. Therefore, an IDA element can be viewed as more similar to a double band than a triple band. However, since there are many generator–collector pairs in an IDA, the total current will be larger for an IDA than for a triple band with elements of identical dimensions.

APPENDIX I

Resolution of the Laplace Equation in the Closed Box: Steady-State Approximation for the Triple Band. The Laplace equation ($\nabla^2 C = 0$) was solved for the closed box with the boundary conditions of $C = 0$ at the generator and $C = C^0$ at the collector with zero flux at the other surfaces, including the $\pm\infty$ line. Because of the symmetry of the system, the calculation was limited to positive values of Γ (corresponding to positive values of x). The zero flux condition was imposed and concentrations calculated with a parabolic approximation of the second derivative. The region where the concentration profiles are most sharply curved is at the outer edges of the collector. Thus, a space grid was chosen that included 85 points across the region $0 < \Gamma < 1.07w_g^*/2$, with 15 more points across the remainder of the collector. A total of 58 points were calculated across the θ axis with 30 of these located adjacent to the collector. The initial concentration profiles were set so that they were linear between $\theta = 0$ (generator surface) and $\theta = g^*$ (collector surface). From these initial profiles, iterations were performed until $|i_g - i_c|/(i_g + i_g) < 10^{-4}$.

APPENDIX II

Diffusion Equations in the Conformal Space Used for Simulations of the Triple-Band Current. To solve for the current at the triple-band electrode, Fick's second law

$$\frac{\partial C_A}{\partial t} = D\left[\frac{\partial^2 C_A}{\partial x^2} + \frac{\partial^2 C_A}{\partial y^2}\right]$$

must be solved. The following boundary conditions define the reversible, diffusion-controlled case where the diffusion coefficients of the reactant (A) and product (B) are equal and where $w_g = w_c = w$:

at $t = 0$

$$y \geq 0, \quad -\infty < x < +\infty; \quad C_A = C^0, \quad C_B = 0$$

at $t > 0$

generator

$$y = 0, \quad -w/2 < x < w/2; \qquad C_A = C^0 \exp[(nF/RT)(E - E^0)]$$

collector

$$y = 0, \quad g + w/2 < x < g + 3w/2; \quad -(g + w/2) < x < -(g + 3w/2); \quad C_A = C^0, \quad C_B = 0$$

insulator

$$y = 0, \quad \text{all remaining values of } x; \quad [\partial C_A/\partial y]_{y=0} = 0$$

Because of symmetry along the y axis, only half of the space needs to be considered. The center of symmetry is at the

center of the generator ($x = 0$). The currents are defined by

$$i_g = 2nFDl\int_0^{w/2}(\partial C_A/\partial y)_{y=0}\,dx \quad \text{generator}$$

$$i_c = 2nFDl\int_{g+w/2}^{g+3w/2}(\partial C_A/\partial y)_{y=0}\,dx \quad \text{collector}$$

The following dimensionless variable and parameters are introduced:

$$a = C_A/C^0; \quad b = C_B/C^0; \quad \tau = t(nFv/RT)$$

$$\alpha = g/w_g, \quad p = (g/2)(nFv/DRT)^{1/2}$$

$$\xi = nF((E - E^0)/RT)$$

In the conformal space, Fick's second law is

$$\partial a/\partial\tau = \beta^2(1/(\sinh^2\Gamma + \sin^2\theta)(\partial^2 a/\partial\Gamma^2 + \partial^2 a/\partial^2\theta))$$

where $\beta = (2g/d)/p$. The term β is introduced because the location of the poles of inversion in the conformal map (d) is different from the edge of the generator. The value of d was selected to be $1.00309w_g/2$ as measured from the center of the generator.

The boundary conditions become

$$\tau = 0; \quad \Gamma > 0, \quad 0 < \theta < \pi/2; \quad a = 1, \quad b = 0$$

$$\tau > 0; \quad \Gamma \to \infty, \quad 0 < \theta < \pi/2; \quad a \to 1, b \to 0$$

generator

$$\Gamma = 0; \quad \cos^{-1}(w/2d) < \theta < \pi/2; \quad b = ae^{\xi}$$

collector

$$\cosh^{-1}((w/2 + g)/d) < \Gamma < \cosh^{-1}((3w/2 + g)/d); \quad \theta = 0; \quad a = 0, \quad b = 1$$

insulator

$$\Gamma = 0, \quad 0 < \theta < \cos^{-1}(w/2d); \quad (\partial a/\partial\Gamma)_{\Gamma=0} = 0;$$
$$0 < \Gamma < \cosh^{-1}((w/2 + g)/d), \quad \theta = 0;$$
$$(\partial a/\partial\theta)_{\theta=0} = 0, \quad \Gamma > \cosh^{-1}((3w/2 + g)/d), \quad \theta = 0; \quad (\partial a/\partial\theta)_{\theta=0} = 0$$

symmetry condition

$$\Gamma > 0; \quad \theta = \pi/2; \quad (\partial a/\partial\theta)_{\theta=\pi/2} = 0$$

The grid employed in the conformal space needs to have a high definition at the poles of inversion to account for curvature in the concentration profiles in these regions. In this work, the θ axis (from $\theta = 0$ (the pole) to $\pi/2$) was divided into 10 equal elements, and the element nearest the pole was subdivided into 10 equally spaced elements, giving a total of 19 points in the θ axis. The edge of the generator is located in the middle of the well-defined region because of the selection of the pole of inversion (d) in the gap. Along the Γ axis, a double scale is also used with 40 equally spaced points across the collector (only one collector needs to be considered, again because of symmetry). Forty grid elements defined the remainder of the axis until the outer bound which was given empirically by $7 - p \ln p$ based on previous results at the single band. The initial dimensionless potential employed was −10 and the final potential +10, and 10 000 iterations were employed.

Registry No. Pt, 7440-06-4; $FeCp_2$, 102-54-5.

LITERATURE CITED

(1) Deakin, M. R.; Wightman, R. M.; Amatore, C. A. *J. Electroanal. Chem.* **1986**, *215*, 49–61.
(2) Fosset, B.; Amatore, C. A.; Bartelt, J. E.; Michael, A. C.; Wightman, R. M. *Anal. Chem.* **1991**, *63*, 306–314.
(3) Wightman, R. M.; Wipf, D. O. *Voltammetry at Microelectrodes*. In *Electroanalytical Chemistry*; Bard, A. J.; Ed.; Marcel Dekker: New York, 1988; Vol. 15, Chapter 3, pp 267–353.
(4) Bard, A. J.; Crayston, J. A.; Kittlesen, G. P.; Varco Shea, T.; Wrighton, M. S. *Anal. Chem.* **1986**, *58*, 2321–2331.
(5) Varco Shea, T.; Bard, A. J. *Anal. Chem.* **1987**, *59*, 2101–2111.
(6) Licht, S.; Cammarata, V.; Wrighton, M. S. *Science* **1989**, *243*, 1176–1178.
(7) Aoki, K.; Morita, M.; Niwa, O.; Tabei, H. *J. Electroanal. Chem.* **1988**, *256*, 269–282.
(8) Chidsey, C. E.; Feldman, B. J.; Lundgren, C.; Murray, R. W. *Anal. Chem.* **1986**, *58*, 601–607.
(9) Sanderson, D. G.; Anderson, L. B. *Anal. Chem.* **1985**, *57*, 2388–2393.
(10) Fosdick, L. E.; Anderson, J. L.; Baginski, T. A.; Jaeger, R. C. *Anal. Chem.* **1986**, *58*, 2750–2756.
(11) Bartelt, J. E.; Deakin, M. R.; Amatore, C. A.; Wightman, R. M. *Anal. Chem.* **1988**, *60*, 2167–2169.
(12) Shoup, D.; Szabo, A. *J. Electroanal. Chem.* **1984**, *160*, 1–17.
(13) Baur, J. E.; Wightman, R. M. *J. Electroanal. Chem.*, in press.

RECEIVED for review November 9, 1990. Accepted March 22, 1991. This research was supported by the National Science Foundation (CHE-8996213) and CNRS (U.A. 1110, "Activation Moleculaire"). Financial support from NATO (International Grants Division) is also acknowledged.

Peak Resolution in the Determination of Cobalt and Nickel by Differential Pulse and Alternating Current Adsorption Voltammetry

Clinio Locatelli,* Francesco Fagioli, and Tibor Garai[1]

Department of Chemistry, University of Ferrara, Via Luigi Borsari 46, I-44100 Ferrara, Italy

The simultaneous determination of cobalt(II) and nickel(II) by differential pulse adsorption voltammetry and fundamental and second harmonic alternating current adsorption voltammetry was compared in the case of very high element concentration ratios. The measurements were carried out in 0.5 M ammonia buffer–1 × 10^{-4} M dimethylglyoxime (DMG) as the supporting electrolyte, employing a semistationary mercury electrode with a drop time of 180–240 s (the long lasting sessile drop mercury electrode) as the working electrode. The accuracy of the analytical procedure was checked by the analysis of the standard reference materials: stainless steel (AISI 321) SRM 121-d and highly alloyed steel (Eurostandard 281-1). The precision, expressed as the relative standard deviation, and the detection limits were also reported for each voltammetric technique. The selectivity of the above-mentioned three techniques was found to increase in the following order: second harmonic alternating current adsorption voltammetry > differential pulse adsorption voltammetry > fundamental harmonic alternating current adsorption voltammetry.

INTRODUCTION

Adsorption voltammetry is an expediting analytical tool for the determination at trace level of quite a large number of elements (*1*), especially those not readily reduced at the mercury electrode (*1–3*).

Apparently, Nangniot (*4*) was the first to suggest the determination of cobalt by the oscillopolarographic measurement of the adsorption of dioxime complexes, mainly the dimethylglyoxime (DMG)–cobalt complex. The reduction of the adsorbed complexes of nickel was studied by polarography (*5*), differential pulse polarography (*6*), differential pulse voltammetry (*7*), and fast linear sweep voltammetry (*8*) on a mercury film electrode (*9*) and a carbon paste electrode (*10, 11*), in addition to a HMDE (*7*) and a DME. These techniques were employed in the analysis of plants (*6, 7*), biological materials (*7–9*), water (*6–10*), coal, fly ash, and others (*9, 11*).

The determination of cobalt in the presence of an excess of nickel (*12*) and zinc (*12–15*) as well as the simultaneous determination of cobalt and nickel (*15–30*) was also reported. The most often used techniques were differential pulse voltammetry (*9*) and linear sweep voltammetry (*16–18*), although cathodic stripping chronopotentiometry (*19, 20*) and square-wave voltammetry (*21*) were also employed.

Triethanolamine (*15, 18*), alcohol (*18*), and citrate (*22*) as well as the application of lower working temperature (*18*) were found to improve the simultaneous determination of cobalt and nickel. The technique was employed for the analysis of biological materials (*15, 16, 20, 22–25*), water (*16, 19–21*), steel (*26*), and PWR coolant (*27, 28*). The application of the method in flow analysis was also reported (*10, 17, 19, 20*).

The determination of cobalt was found to be free from the interference of nickel up to a concentration ratio $c_{Ni}:c_{Co} = 12$ (*14*), while a 250-fold excess of nickel was tolerated in the presence of triethanolamine (*15*). General schemes for the determination of various elements simultaneously to that of cobalt and nickel were also reported (*7, 29, 30*).

Variant opinions were published regarding the mechanism of the reaction of the adsorbed DMG complex. Many authors (*2, 7, 9*) affirmed that the metal is irreversibly reduced at the surface of the mercury electrode while others propose the electroreduction of the ligand (*27*).

In view of the increasing interest in adsorption voltammetry, it was deemed worthwhile to compare the performance of various voltammetric techniques such as differential pulse voltammetry and fundamental and second harmonic alternating current voltammetry, since the latter techniques were seldom used in adsorption voltammetry, although they were found to have definite advantages regarding the selectivity of the analysis (*31–35*). The simultaneous determination of cobalt and nickel, especially in the case of a large excess of one element as compared to the other, was found to be well-suited for this kind of study since the reduction potentials of the DMG complexes of those two elements are very close.

EXPERIMENTAL SECTION

Apparatus. Voltammetric measurements were carried out with an AMEL Model 471 multipolarograph equipped with an AMEL Model 452/T timer and an AMEL Model 291/LF stirrer.

A commerical long-lasting sessile drop mercury electrode (LLSDME) (*36*) with a drop time of 180–240 s was employed as the working electrode, while a saturated calomel electrode and a platinum wire were used as the reference and the auxiliary electrode, respectively.

The voltammetric cell was thermostated at 25.0 ± 0.5 °C. The solutions were deaerated with pure nitrogen for about 20 min prior to the analysis, and nitrogen atmosphere was maintained above the solutions during the experiments. Standard additions were made with Eppendorf micropipettes with disposable plastic tips. The solutions were deaerated for 2 min after each standard addition.

Reagents and Reference Solutions. All solutions were prepared with deionized water. All acids and ammonia were Merck "Suprapure" grade; the other reagents were of analytical-grade purity. Ammonia–ammonium chloride buffer solution (0.5 M) was prepared by mixing an appropriate amount of hydrochloric acid and ammonia solutions. Dimethylglyoxime (DMG) was dissolved in 96% ethanol to obtain a 0.1 M concentration.

Stock solutions of cobalt(II) and nickel(II) were prepared by diluting the respective standard 1000 mg/L BDH solutions. The Teflon voltammetric cell was periodically rinsed with concentrated nitric acid to avoid any contamination. The following standard reference materials were chosen for the analyses: stainless steel (AISI 321) SRM 121-d and highly alloyed steel (Eurostandard 281-1).

Sample Preparation. SRM 121-d (AISI 321) and Eurostandard 281-1 were prepared according to Thomerson and Price

* To whom correspondence should be addressed.
[1] Permanent address: Research Laboratory for Inorganic Chemistry, Hungarian Academy of Sciences, Budaörsi ut 45, H-1112 Budapest, Hungary.

0003-2700/91/0363-1409$02.50/0 © 1991 American Chemical Society

Table I. Experimental Conditions for the Determination of Cobalt(II) and Nickel(II) by Alternating Current Adsorption Voltammetry (ACAV) and Differential Pulse Adsorption Voltammetry (DPAV)[a]

	ACAV	DPAV
E_a, V/SCE	−0.800	−0.800
t_a, s	90 (stirred)	90 (stirred)
t_r, s	30 (unstirred)	30 (unstirred)
dE/dt, mV/s	10	10
f, Hz	100	
ΔE, mV	10	50
ϕ(fundamental harmonic), deg	270 ± 89.1 (Ni) 270 ± 83.2 (Co)	
ϕ(second harmonic), deg	270 ± 63.9 (Ni) 270 ± 60.1 (Co)	
τ, s		0.065
ν, s		0.250
u, rpm	800	800

[a] E_a = adsorption potential; t_a = adsorption time; t_r = rest time between adsorption and start of recording; dE/dt = potential scan rate; f = frequency; ΔE = amplitude of alternating current voltage (ACAV) and pulse (DPAV) superposed; ϕ = demodulation phase angle; τ = pulse duration; ν = pulse repetition; u = stirring rate.

(*37*). Approximately 0.2 g of sample, accurately weighed in a platinum crucible, was dissolved in 1 mL of 37% (m/m) hydrochloric acid, and 1 mL of 69% (m/m) nitric acid was successively added. After the initial reaction had subsided, 2 mL of 60% (m/m) perchloric acid was added, and the solution was evaporated until the sample was fully oxidized and fumes of perchloric acid appeared, allowing to fume for about 5 min. After cooling, the soluble salts were dissolved in about 20 mL of deionized water. The solution was filtered through Whatman No. 541 filter paper and the filtrate diluted to 200 mL with deionized water (the blank tests demonstrated the concentrations of cobalt and nickel to be under the detection limit of the voltammetric techniques employed). Finally, 1 mL of the solution so obtained was diluted to 50 mL with 0.5 M ammonia–ammnonium chloride buffer solution and quantitatively transferred into the voltammetric cell. After addition of 50 μL of the 0.1 M DMG solution (in order to obtain a final concentration equal to 1×10^{-4} M), the analyses were carried out employing differential pulse adsorption voltammetry and fundmental and second harmonic alternating current adsorption voltammetry.

RESULTS AND DISCUSSION

Aqueous Reference Solutions. The experimental conditions of the analysis are listed in Table I. In alternating current voltammetry, the proper adjustment of the phase angle of the faradaic current permits the virtually complete elimination of the capacitive current (*32–34*). Figure 1 shows an example of three typical voltammograms obtained by differential pulse, by fundamental, and by second harmonic alternating current adsorption voltammetry. The voltammograms were recorded in solutions containing an excess of nickel(II) (concentration ratio $c_{Ni}:c_{Co} = 59.4$). Curves 1 indicate the current peaks of nickel(II), while those of cobalt(II) (curves 2) were recorded at increased sensitivity. It is apparent that nickel(II) has a more anodic peak potential than cobalt(II), and the evaluation of the peak current is straightforward in the case of differential pulse and fundamental harmonic alternating current adsorption voltammetry. However, in the case of second harmonic alternating current adsorption voltammetry, the anodic peak of nickel(II) and the cathodic one of cobalt(II) are suitable for evaluation only, while the cathodic peak of nickel(II) and the anodic one of cobalt(II) are subject to mutual interference, since in that potential range the phase angles of the second harmonic alternating current of both elements are approximately equal and consequently the currents due to the electrode reaction of each element are additive (*34*).

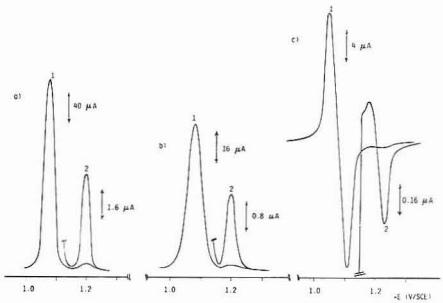

Figure 1. Differential pulse (a), fundamental harmonic alternating current (b), and second harmonic alternating current (c) adsorption voltammograms of a mixture containing Ni(II) (peak 1) and Co(II) (peak 2) in 0.5 M ammonia–ammonium chloride buffer–1×10^{-4} M dimethylglyoxime as the supporting electrolyte. Concentrations: $c_{Ni} = 9.5 \times 10^{-6}$ M; $c_{Co} = 1.6 \times 10^{-7}$ M; $c_{Ni}:c_{Co} = 59.4$. Experimental conditions are given in Table I.

Table II. Analytical Calibration Curves[a]

DPAV[b]	ACAV 1[b]	ACAV 2[b]
$i_{p(Co)} = (0.005 \pm 0.006) + (3.03 \pm 0.02) \times 10^7 c$	$i_{p(Co)} = (0.007 \pm 0.008) + (1.28 \pm 0.07) \times 10^7 c$	$i_{p(Co)} = (0.002 \pm 0.002) + (2.65 \pm 0.05) \times 10^6 c$
$r = 0.9998$	$r = 0.9997$	$r = 0.9995$
$s_r = 3.43\%$	$s_r = 2.93\%$	$s_r = 3.70\%$
DL = 0.66×10^{-9} M[c]	DL = 1.56×10^{-9} M	DL = 7.55×10^{-9} M
$i_{p(Ni)} = (0.002 \pm 0.003) + (2.69 \pm 0.03) \times 10^7 c$	$i_{p(Ni)} = (0.003 \pm 0.003) + (8.03 \pm 0.05) \times 10^6 c$	$i_{p(Ni)} = (0.002 \pm 0.002) + (1.81 \pm 0.02) \times 10^6 c$
$r = 0.9995$	$r = 0.9996$	$r = 0.9993$
$s_r = 4.02\%$	$s_r = 2.52\%$	$s_r = 3.18\%$
DL = 0.74×10^{-9} M	DL = 2.49×10^{-9} M	DL = 1.10×10^{-8} M

[a] The errors correspond to a probability of 95%; i_p = peak current (μA); c = concentration of the electroactive species (M). [b] DPAV = differential pulse adsorption voltammetry; ACAV 1 = fundamental harmonic alternating current adsorption voltammetry; ACAV 2 = second harmonic alternating current adsorption voltammetry. [c] Limit of detection (DL) is expressed according to IUPAC (*38*) and corresponds to a probability of 99%.

The analytical calibration functions of the elements were always determined by using the standard addition method. The data are listed in Tables II and III. The correlation coefficient was excellent for all analytical calibration functions, and the low relative standard deviation (s_r) proved the high precision of the analytical procedure. The corresponding detection limit of each analytical regression function is also reported.

The simultaneous determination of cobalt(II) and nickel(II) was studied in a large range of concentration ratios of the components. The peaks corresponding to each element were well separated in all techniques at low concentration ratios. However, in the case of a large excess in the concentration of one component, an increasing interference was observed in the measurement of the element present in lower concentration. To evaluate the degree of the interference, the peak currents were measured in a wide range of concentration ratios. The data were compared to those calculated by using the analytical calibration function of the individual element (cf. Table II), and the relative errors were calculated for the element present in lower concentration. The errors were plotted in Figure 2 as a function of the concentration ratio of the mixtures. It is apparent in Figure 2 that the selectivity of the measurements increased in the following order: second harmonic alternating current adsorption voltammetry > differ-

Table III. Analysis of the Cobalt(II) and Nickel(II) Mixture by Differential Pulse, Fundamental, and Second Harmonic Alternating Current Adsorption Voltammetry in 0.5 M Ammonia–Ammonium Chloride Buffer–1×10^{-4} M Dimethylglyoxime as the Supporting Electrolyte[a]

	regression functions	r	s_r,[c] %	e,[c] %	DL, M ($K = 3$)[d]
	Analysis of Co(II) in the Presence of Ni(II)[b]				
DPAV					
monovariate	$i_p = (-0.001 \pm 0.002) + (3.13 \pm 0.04) \times 10^7 c$	0.9991	2.8	+3.3	0.64×10^{-9}
bivariate	$i_p = -7.37 \times 10^{-4} + (3.15 \pm 0.02) \times 10^7 c_{Co} + (2.1 \pm 0.2) \times 10^2 c_{Ni}$	0.9990	3.5	+4.0	0.63×10^{-9}
ACAV 1					
monovariate	$i_p = (0.001 \pm 0.002) + (1.21 \pm 0.04) \times 10^7 c$	0.9995	3.7	−5.5	1.65×10^{-9}
bivariate	$i_p = -5.02 \times 10^{-4} + (1.23 \pm 0.07) \times 10^7 c_{Co} + (6.8 \pm 0.8) \times 10^2 c_{Ni}$	0.9990	4.1	−3.9	1.63×10^{-9}
ACAV 2					
monovariate	$i_p = (-0.005 \pm 0.006) + (2.77 \pm 0.07) \times 10^6 c$	0.9997	5.2	+4.5	7.22×10^{-9}
bivariate	$i_p = -2.87 \times 10^{-4} + (2.79 \pm 0.06) \times 10^6 c_{Co} + (1.9 \pm 0.8) \times 10^2 c_{Ni}$	0.9990	4.8	+5.3	7.17×10^{-9}
	Analysis of Ni(II) in the Presence of Co(II)[b]				
DPAV					
monovariate	$i_p = (0.002 \pm 0.003) + (2.62 \pm 0.05) \times 10^7 c$	0.9996	2.0	−2.6	0.76×10^{-9}
bivariate	$i_p = 4.82 \times 10^{-4} + (2.81 \pm 0.05) \times 10^7 c_{Ni} + (1.9 \pm 0.3) \times 10^2 c_{Co}$	0.9997	3.1	+4.5	0.71×10^{-9}
ACAV 1					
monovariate	$i_p = (-0.002 \pm 0.003) + (7.85 \pm 0.08) \times 10^6 c$	0.9994	4.4	−2.2	2.55×10^{-9}
bivariate	$i_p = 3.96 \times 10^{-4} + (8.41 \pm 0.09) \times 10^6 c_{Ni} + (1.3 \pm 0.3) \times 10^2 c_{Co}$	0.9992	4.9	+4.7	2.38×10^{-9}
ACAV 2					
monovariate	$i_p = (0.003 \pm 0.005) + (1.74 \pm 0.04) \times 10^6 c$	0.9990	3.8	−3.9	1.15×10^{-8}
bivariate	$i_p = -3.38 \times 10^{-4} + (1.72 \pm 0.06) \times 10^6 c_{Ni} + (2.0 \pm 0.5) \times 10^2 c_{Co}$	0.9993	4.5	−5.0	1.16×10^{-8}

[a] The errors reported correspond to a probability of 95%. [b] DPAV, ACAV 1, and ACAV 2 (cf. Table II). [c] Mean standard residual deviation (s_r) and relative error (e). [d] Limit of detection (DL) as in Table II.

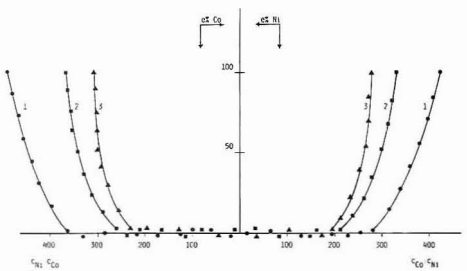

Figure 2. Errors of the analysis as a function of the ratios of the concentration of Ni(II) and Co(II) in the case of second harmonic alternating current (curve 1), differential pulse (curve 2), and fundamental harmonic alternating current (curve 3) adsorption voltammetry.

ential pulse adsorption voltammetry > fundamental harmonic alternating current adsorption voltammetry as the concentration ratios permitting the simultaneous determination of the two elements with a maximum experimental error of 5% were 369:1 > c_{Ni}:c_{Co} > 1:298 for second harmonic alternating current adsorption voltammetry, 265:1 > c_{Ni}:c_{Co} > 1:216 for differential pulse adsorption voltammetry, and 241:1 > C_{Ni}:c_{Co} > 1:203 for fundamental harmonic alternating current adsorption voltammetry. The above-mentioned results concerning the order of selectivity of differential pulse adsorption voltammetry and fundamental harmonic alternating current adsorption voltammetry are in qualitative agreement with data published by Meyer and Neeb (*15*).

Monovariate and bivariate analysis of the experimental data in the above-mentioned concentration ratio ranges permitted a quantitative evaluation of the reciprocal interference in the simultaneous determination of cobalt(II) and nickel(II). The interference of the second element is considered in bivariate analysis and neglected in monovariate analysis. The slopes of the regression functions (cf. Tables II and III) obtained by both the monovariate and bivariate analysis were practically equal to those of the analytical calibration curves, indicating that the reciprocal interference was negligible at a 5% error level. This finding was also confirmed by the negligible value of the interference slope of the bivariate regression functions.

Table IV. Metal Concentrations in the Solutions Obtained by Dissolution of 0.2 g of Standard Material

std material	concn, M	c_{Ni}:c_{Co}
stainless steel (AISI 321) SRM 121-d	$c_{Ni} = 3.81 \times 10^{-5}$ $c_{Co} = 3.39 \times 10^{-7}$	112.4
highly alloyed steel (Eurostandard 281-1)	$c_{Ni} = 3.19 \times 10^{-5}$ $c_{Co} = 7.80 \times 10^{-8}$	409.0

Precision, expressed as the relative standard deviation, accuracy, expressed as the relative error, and the detection limits are also reported in Tables II and III.

It has been shown in earlier communications (*32*, *33*) that the standard addition method permitted the determination of an element even in the presence of an interfering component in an excess beyond the limit of validity of the bivariate regression functions. In such cases, the concentration of the minor constituent is increased by successive standard additions until the concentration ratio of the two components is modified so that an extrapolation of the measured currents permits the evaluation of the concentration of the minor constituent. An example of this kind of analysis is shown in Figure 3. The differential pulse adsorption voltammogram of cobalt(II) is shown in Figure 3a, while in Figure 3b the peak current is plotted vs the concentration of the standard additions of a cobalt(II) solution. When the concentration ratio attained the range of validity of bivariate analysis (i.e., c_{Ni}:c_{Co} < 265), the regression became linear and the concentration of cobalt(II) was determined by extrapolation of the linear portion of the curve. The limit of the linear domain was statistically evaluated with the Student t-test criterion (*39*).

PRACTICAL APPLICATIONS

Cobalt(II) and nickel(II) were determined in the aforementioned standard materials in order to confirm the applicability of the methods. The concentrations of the elements in the solutions obtained by dissolution of 0.2 g of sample are shown in Table IV. The solutions were analyzed under the experimental conditions listed in Table I.

The simultaneous determination of cobalt(II) and nickel(II) in SRM 121-d (AISI 321) was found to be straightforward

Table V. Analytical Functions and Merits of the Analytical Procedure[a]

std materials, elements, and anal. techniques employed[b]	regression functions	r	s_r, %	DL, M (K = 3)[c]
	Stainless Steel (AISI 321) SRM 121-d			
Co				
DPAV	$i_p = (1.09 \pm 0.07) \times 10 + (3.21 \pm 0.06) \times 10^7 c$	0.9989	4.7	0.62×10^{-9}
ACAV 1	$i_p = (4.57 \pm 0.05) + (1.35 \pm 0.03) \times 10^7 c$	0.9990	3.9	1.48×10^{-9}
ACAV 2	$i_p = (0.86 \pm 0.07) + (2.54 \pm 0.08) \times 10^6 c$	0.9988	5.1	7.90×10^{-9}
Ni				
DPAV	$i_p = (9.39 \pm 0.05) \times 10^2 + (2.47 \pm 0.09) \times 10^7 c$	0.9993	4.3	0.81×10^{-9}
ACAV 1	$i_p = (3.20 \pm 0.03) \times 10^2 + (8.41 \pm 0.08) \times 10^6 c$	0.9992	3.9	2.38×10^{-9}
ACAV 2	$i_p = (7.19 \pm 0.04) \times 10 + (1.89 \pm 0.02) \times 10^6 c$	0.9988	5.3	1.06×10^{-8}
	Highly Alloyed Steel (Eurostandard 281-1)			
Co				
DPAV[d]	$i_p = (2.22 \pm 0.07) + (2.85 \pm 0.05) \times 10^7 c$	0.9995	3.3	0.70×10^{-9}
ACAV 1[d]	$i_p = (0.94 \pm 0.04) + (1.20 \pm 0.03) \times 10^7 c$	0.9987	4.9	1.67×10^{-9}
ACAV 2[d]	$i_p = (0.19 \pm 0.04) + (2.43 \pm 0.09) \times 10^6 c$	0.9991	4.1	8.03×10^{-9}
Ni				
DPAV	$i_p = (9.03 \pm 0.09) \times 10^2 + (2.83 \pm 0.06) \times 10^7 c$	0.9996	3.0	0.71×10^{-9}
ACAV 1	$i_p = (2.49 \pm 0.03) \times 10^2 + (7.77 \pm 0.08) \times 10^6 c$	0.9996	3.2	2.57×10^{-9}
ACAV 2	$i_p = (6.13 \pm 0.08) \times 10 + (1.92 \pm 0.05) \times 10^6 c$	0.9994	3.4	1.04×10^{-8}

[a] The errors reported correspond to a probability of 95%. [b] DPAV, ACAV 1, and ACAV 2 (cf. Table II). [c] Limit of detection (DL) as in Table II. [d] Extrapolation of the linear section (cf. the text).

Table VI. Analytical Results

std materials and anal. techniques employed[a]	Co concn, mg/g certified	Co concn, mg/g determined[b]	e, %	s_r, %	Ni concn, mg/g certified	Ni concn, mg/g determined[b]	e, %	s_r, %
		Stainless Steel (AISI 321) SRM 121-d						
DPAV		0.97 ± 0.04	−3.0	2.6		107.2 ± 4.9	−4.0	5.2
ACAV 1	1.00 ± 0.03	0.96 ± 0.06	−4.0	3.6	111.7 ± 2.5	116.3 ± 5.1	−4.1	4.6
ACAV 2		1.04 ± 0.07	+4.0	3.9		115.8 ± 5.3	+3.7	3.3
		Highly Alloyed Steel (Eurostandard 281-1)						
DPAV		0.248 ± 0.021	+7.8	5.0		95.9 ± 4.3	+2.4	4.6
ACAV 1	0.23 ± 0.02	0.255 ± 0.023	+10.9	6.1	93.7 ± 0.5	98.2 ± 3.8	+4.8	4.0
ACAV 2		0.221 ± 0.018	−3.9	3.0		89.0 ± 5.4	−5.0	4.9

[a] DPAV, ACAV 1 and ACAV 2 (cf. Table II). [b] Mean and standard deviation of five independent determinations.

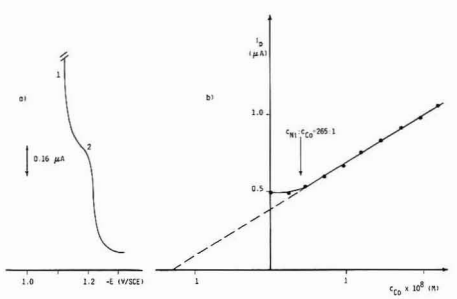

Figure 3. Determination of 1.3×10^{-8} M Co(II) in the presence of 4.1×10^{-6} M Ni(II) (concentration ratio $c_{Ni}:c_{Co} = 315.4$). (a) Differential pulse adsorption voltammogram of the mixture (Ni(II), peak 1; Co(II), peak 2); (b) standard addition of Co(II) (cf. in the text).

since the concentration ratio in the sample solution (i.e., $c_{Ni}:c_{Co} = 112.4$) did not exceed the value of reciprocal interference at 5% error level. Eurostandard 281-1, however, contained a large excess of nickel(II) ($c_{Ni}:c_{Co} = 409.0$), so that determination of cobalt(II) was carried out with the standard addition method shown in Figure 3.

For the voltammetric techniques employed, the linear section of the analytical regression curves was obtained after standard additions of cobalt(II), in order to have concentration ratios $c_{Ni}:c_{Co} < 265$ for differential pulse adsorption voltammetry, $c_{Ni}:c_{Co} < 241$, and $c_{Ni}:c_{Co} < 369$ for fundamental, and second harmonic alternating current adsorption voltammetry, respectively. The successive extrapolation of the linear portion of the curves permitted the determination of cobalt(II). The determination of nickel(II) present in large excess was practically free from interference.

Table V summarizes the analytical calibration functions of the two elements in the sample solutions, while the analytical results are reported in Table VI. It is apparent that the relative errors and the relative standard deviations of the determination of cobalt(II) present in low concentration decreased in the order of increasing selectivity of the techniques, namely, second harmonic alternating current adsorption voltammetry > differential pulse adsorption voltammetry > fundamental harmonic alternating current adsorption voltammetry.

It can be concluded that in adsorption voltammetry, as in polarography (*35*) and in anodic stripping voltammetry (*31–33*), the second harmonic alternating current technique permits us to attain the highest selectivity.

Registry No. Co, 7440-48-4; Ni, 7440-02-0; steel, 12597-69-2.

LITERATURE CITED

(1) Wang, J. *Stripping Analysis*; VCH Publishers Inc.: Deerfield Beach, FL, 1985; Chapters 4, 5.
(2) Van Den Berg, C. M. G. *Analyst* **1989**, *114*, 1527.

(3) Van Den Berg, C. M. G. *Sci. Total Environ.* **1986**, *49*, 89.
(4) Nangniot, P. J. *Electroanal. Chem.* **1967**, *14*, 197.
(5) Crow, D. R.; Rose, M. E. *Electrochim. Acta* **1979**, *24*, 41.
(6) Flora, C. J.; Nieboer, E. *Anal. Chem.* **1980**, *52*, 1013.
(7) Pihlar, B., Valenta, P.; Nürnberg, H. W. *Fresenius' Z. Anal. Chem.* **1981**, *307*, 337.
(8) Kissner, R. *Fresenius' Z. Anal. Chem.* **1988**, *332*, 787.
(9) Braun, H.; Metzger, M. *Fresenius' Z. Anal. Chem.* **1984**, *318*, 321.
(10) Thomsen, K. N.; Kryger, L.; Baldwin, R. P. *Anal. Chem.* **1988**, *60*, 151.
(11) Baldwin, R. P.; Christensen, J. K.; Kryger, L. *Anal. Chem.* **1986**, *58*, 1790.
(12) Bobrowski, A. *Anal. Chem.* **1989**, *61*, 2178.
(13) Emons, H.; Schmidt, Th.; Werner, G. *Anal. Chim. Acta* **1990**, *228*, 55.
(14) Gilbert, M. J. M.; Powell, H. K. J.; Fardy, J. J. *Anal. Chim. Acta* **1988**, *207*, 103.
(15) Meyer, A.; Neeb, R. *Fresenius' Z. Anal. Chem.* **1983**, *315*, 118.
(16) Golimowski, J.; Cendrowska, M. *Chem. Anal. (Warsaw)* **1985**, *30*, 777.
(17) Wahdat, F.; Neeb, R. *Fresenius' Z. Anal. Chem.* **1985**, *320*, 334.
(18) Wahdat, F.; Neeb, R. *Fresenius' Z. Anal. Chem.* **1985**, *322*, 290.
(19) Newton, M. P.; Van Den Berg, C. M. G. *Anal. Chim. Acta* **1987**, *199*, 59.
(20) Eskilsson, H.; Haraldsson, C.; Jagner, D. *Anal. Chim. Acta* **1985**, *175*, 79.
(21) Zhang, H.; Wollast, R.; Vire, J. C.; Patriarche, G. J. *Analyst* **1989**, *114*, 1597.
(22) Chen, H.; Neeb, R. *Fresenius' Z. Anal. Chem.* **1983**, *314*, 657.
(23) Ostapczuk, P.; Stoeppler, M.; Durbeck, H. W. *Fresenius' Z. Anal. Chem.* **1988**, *332*, 662.
(24) Adeloju, S. B.; Bond, A. M.; Briggs, M. H. *Anal. Chim. Acta* **1984**, *164*, 181.
(25) Hasse, S.; Schramel, P. *Mikrochim. Acta* **1983**, *3*, 449.
(26) Weinzierl, J.; Umland, F. *Fresenius' Z. Anal. Chem.* **1982**, *312*, 608.
(27) Torrance, K. *Analyst* **1984**, *109*, 1035.
(28) Torrance, K.; Gatford, C. *Talanta* **1985**, *32*, 273.
(29) Adeloju, S. B.; Bond, A. M.; Briggs, M. H. *Anal. Chem.* **1985**, *57*, 1386.
(30) Ostapczuk, P.; Goedde, M.; Stoeppler, M.; Nürnberg, H. W. *Fresenius' Z. Anal. Chem.* **1984**, *317*, 252.
(31) Garai, T.; Nagy, Z.; Fagioli, F.; Locatelli, C. *Anal. Sci.* **1986**, *2*, 15.
(32) Locatelli, C.; Fagioli, F.; Garai, T.; Bighi, C.; Vecchietti, R. *Anal. Chim. Acta* **1988**, *204*, 189.
(33) Locatelli, C.; Fagioli, F.; Garai, T.; Bighi, C. *Anal. Chem.* **1988**, *60*, 2402.
(34) Bond, A. M. *Modern Polarographic Methods in Analytical Chemistry*; Marcel Dekker Inc.: New York, 1980; Chapter 7.
(35) Garai, T.; Devay, J. *Hung. Sci. Instrum.* **1972**, *25*, 27.
(36) Locatelli, C.; Fagioli, F.; Bighi, C.; Garai, T. *Anal. Lett.* **1984**, *17* (A8), 623.
(37) Thomerson, D. R.; Price, W. J. *Analyst* **1971**, *96*, 825.
(38) IUPAC, Analytical Chemistry Division. *Spectrochim. Acta Part B* **1978**, *33B*, 219.
(39) Liteanu, C.; Popescu, I. C.; Hopirtean, E. *Anal. Chem.* **1976**, *48*, 2010.

RECEIVED for review December 14, 1990. Accepted April 5, 1991.

Characterization of the Chemical Architecture of Carbon-Fiber Microelectrodes. 1. Carboxylates

Paul Pantano and Werner G. Kuhr*

Department of Chemistry, University of California, Riverside, California 92521

A new method to characterize the chemical architecture of a carbon-fiber microelectrode surface is described. Derivatization of carboxyl groups on the carbon surface with a poly(oxyalkalene)diamine (Jeffamine ED-600), followed by biotinylation of the free amine, allowed the attachment of a fluorescein isothiocyanate (FITC) conjugate of ExtrAvidin. The fluorescence observed after excitation at 488 nm was imaged with a fluorescence microscope equipped with a CCD camera, yielding a spatial map of the distribution of modified carboxyl groups on the surface of the carbon fiber with 0.5-μm resolution. Colloidal gold particles (15 nm diameter) coated with ExtrAvidin were used in place of the FITC–ExtrAvidin, and the carbon-fiber surface was imaged with scanning electron microscopy on a submicron scale. This selective information regarding surface-bound functional groups (i.e. carboxylates) has proven invaluable toward the rational design of novel sensors based on surface-modified ultramicroelectrodes.

INTRODUCTION

Covalent modification of carbon electrodes with molecules acting as redox mediators has helped foster ideas as to how these surface-localized compounds participate in heterogeneous electron-transfer processes. For example, modification of carbon electrodes with quinone decreases the overpotential for the oxidation of dihydronicotinamide adenosine diphosphate (NADH) with the subsequent control of the NADH oxidation potential dictated by the surface-bound quinone/hydroquinone couple (*1*). More recently, evidence has appeared that raises questions as to the extent to which these surface functional groups participate in electron transfer. Part of this uncertainty stems from the inherent variability in structure and chemistry in the different forms of carbon. The numerous methods of production and the coresponding differences in lattices and morphology of glassy carbon (gc) and highly ordered pyrolytic graphite (hopg) have been throughly examined owing to their wide range of analytical and industrial usages (*2–5*). Common to both gc and hopg are "edge" and "basal" regions where physical and electrochemical properties are considerably different. Facilitated charge transfer is promoted in the edge plane as dictated by the stacking arrangement of sp^2 carbon orbitals in the lattice, and carbon–oxygen complexes are predominantly found at edge sites of carbon fibers prior to any pretreatment (*6*). Consequently, the edge orientation can show an undesirably high background charging current and can be subject to detrimental memory effects (*7*).

Since anlaytical performance (i.e., sensitivity and response time) is highly dependent on the manner by which the carbon surface is prepared, many methods of activation have been developed to create a higher density of edge orientations (*8, 9*). Mechanical polishing (*10, 11*), electrochemical (*12–18*), radio frequency oxygen plasma (*7, 19, 20*), and microwave plasma methods (*21*), dispersion of metal oxide particles (i.e. alumina) (*23, 23*), and in situ laser (*6, 24–26*) and vacuum heat treatments (*3, 27, 28*) have all been shown to improve heterogeneous electron-transfer rates (k_o) for selected redox couples at carbon electrodes. As such, the differences in activation mechanisms between these treatments has provided the impetus to reevaluate the assignment of the sites of electron transfer at carbon electrodes.

0003-2700/91/0363-1413$02.50/0 © 1991 American Chemical Society

Electrochemical anodization and radio frequency generated oxygen plasmas are especially noted for their ability to increase the density of carboxyl, quinone, phenolic, and other surface oxygen groups on the edge plane of carbon electrodes (*7*, *8*). In conjunction with cleaning the surface (removing chemi- and physisorbed impurities) and roughening the surface (increasing the geometric area of the electrode), the incorporation of surface functionalities was thought to enhance the rate of heterogeneous electron transfer for various redox couples by acting as an interfacial redox mediator (*10*). The growth and removal of an oxide film on the surface of gc electrodes following anodization has been associated by Kepley and Bard to be a function of the electrode's activation and deactivation toward several quinone/hydroquinone redox couples (*18*). Several interpretations have been proposed, most notable are those involving π-bonding orbital interactions (*13*) and the resonance stabilization provided by surface phenolic and carboxyl groups to assist in proton-coupled electron-transfer reactions (*11*, *29*, *30*).

Conversely, the oxygen-depleted surface created by laser and vacuum heat treatments has also been observed to increase k_o by several orders of magnitude for model redox systems such as the one-electron outer-sphere reduction of ferri–ferrocyanide, and the two-electron oxidation of ascorbic acid and dopamine (*20*, *24*, *25*, *27*). Fagan, Hu, and Kuwana have shown that the freshly exposed and unroughened carbon surface obtained after vacuum heat treatment provides a cleaned surface that allows enhanced electrochemical activity. Additionally, the reduced density of surface functional groups resulted in a diminished background charging current. Even though it was suggested that more redox couples need to be evaluated (especially at more positive potentials where surface redox species could participate in mediating electron transfers), these observations question the role of surface functional groups in electron-transfer mechanisms (*27*).

The laser-activated carbon surface is cleaned as well as roughened with visible cracks and defects similar to those observed on carbon surfaces that have been treated electrochemically (*15*). Investigation of these surface defects has been accomplished most elegantly through the use of Raman spectroscopy of gc and hopg electrodes prior to and following activation. Information concerning microcrystallite size and lattice arrangements has lead McCreery and co-workers to correlate the density of edge sites with the growth of the 1360-cm^{-1} Raman vibrational band of the carbon spectra (*31*). Coupled with capacitance and adsorption studies, this spectroscopic marker allowed them to quantitatively correlate increased rates of electron transfer with the density of edge defects created by laser activation of basal plane regions (*26*, *32*, *33*).

Active sites of charge transfer were localized to regions of edge orientation by Engstrom's laboratory, which utilized the imaging capability of optical microscopy to follow the electrogenerated chemiluminescence of luminol (*34–36*). A nonuniform distribution of current density at 250-μm platinum electrodes has been demonstrated with a spatial resolution of 0.3 μm and a 30-ms temporal response (*37*). Recently, the kinetic heterogeneity of hopg was investigated with respect to the potential dependence of the luminol reaction (*38*). The differences in the k_o for luminol oxidation observed between edge and basal territories is extremely convincing evidence to correlate the density of these edge sites with enhanced rates of electron transfer. Unfortunately, the exact chemical nature of these active sites eludes this type of experiment. Since oxides are thought to form along graphitic edges and cracks, the importance of these carbon–oxygen complexes can not be totally ruled out; their presence and activity at low concentrations is still not thoroughly characterized (*39*). Additionally, processes involving surface moieties are also thought to be involved in determining the longevity of electrode activation (*12*).

Many other spectroscopic examinations have been conducted to gain insight into the morphology and makeup of carbon surfaces: Hadamard transform Raman microscopy (*40*), scanning tunneling microscopy (*41*, *42*), scanning electrochemical microscopy (*43*, *44*), scanning electron microscopy (*19*, *20*, *22*, *32*, *45*, *46*), phase-measurement interferometric microscopy (*47*, *48*), ellipsometry (*18*), X-ray diffraction (*18*, *21*), Auger and X-ray photoelectron spectroscopy (XPS) (*7*, *10*, *11*, *27*, *46*). Of particular interest are those that are sensitive enough to analyze the monolayer or submonolayer converage of oxides that can exist across the surface following electrochemical treatments with concentrations typically ranging between 10^{-10} and 10^{-9} mol/cm^2 (*11*, *14*, *15*, *18*, *39*). An extensive investigation has been performed by Procter, Kozlowski, and Sherwood utilizing XPS to quantitatively analyze the increase of carbon–oxygen functionalities on the surface of carbon fibers following various electrochemical treatments (*6*, *16*, *45*, *49*, *50*). Drastic topographical changes accompany the production of surface oxides with the nature of the surface oxide depending upon the potential, the reaction time in solution, and the electrolyte concentration involved in the treatment. A chemical approach to the identification of surface-bound carbonyl groups using XPS was demonstrated by Tougas and Collier (*51*). Reaction of a gc surface with a reagent specific for carbonyl groups (pentafluorophenylhydrazine) introduced both fluorine and nitrogen groups onto the surface, where the XPS analysis of fluorine and nitrogen content was used to estimate carbonyl content. However, it should be noted these analyses are performed under a high vacuum, which solicits questions regarding the loss of functionalized groups from the surface while the sample chamber is pumped down. Moreover, this technique does not have the spatial resolution to map the composition of oxygen along the heterogeneous carbon surface.

The goal of this work is to demonstrate a method that can selectively provide a spatial map of the numerous functional groups on carbon electrode surfaces. The approach was initiated because of this laboratory's need to monitor the development and implementation of covalently bound enzyme-modified ultramicroelectrodes (*52*). While electrochemical methods have proven extremely useful in these characterizations, an independent means of verifying the physical nature of the modified surfaces was necessary. Our search has led us to develop new and interesting methods to characterize the surface properties of modified electrode surfaces. Derivatization of carboxyl groups on the carbon surface with a poly(oxyalkalene)diamine (Jeffamine ED-600), followed by biotinylation of the free amine, allowed the attachment of a fluorescein isothiocyanate (FITC) conjugate of ExtrAvidin. The fluorescence observed after excitation at 488 nm was imaged with a fluorescence microscope equipped with a CCD camera, yielding a spatial map of the distribution of carboxyl groups modified on the surface of the carbon fiber with 0.5-μm resolution. Colloidal gold particles (15 nm diameter) coated with ExtrAvidin were used in place of the FITC–ExtrAvidin, and the carbon fiber surface was imaged with scanning electron microscopy on a submicron scale. This selective information regarding surface-bound functional groups (i.e. carboxylates) was proven invaluable toward the rational design of novel sensors based on surface-modified ultramicroelectrodes.

EXPERIMENTAL SECTION

Chemicals. ExtrAvidin–FITC conjugate, 3-hydroxytyramine (dopamine), and 1-ethyl-3-((dimethylamino)propyl) carbodiimide (Sigma), Epon 828 epoxy (Shell), 1,4-phenylenediamine (Aldrich),

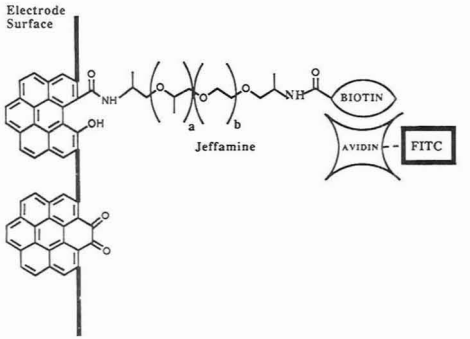

Figure 1. Schematic representation of the derivatization of the carbon surface with a hydrophylic tether (Jeffamine ED-600) which is biotinylated and then coupled to the FITC–ExtrAvidin.

Sulfo-NHS-Biotin (Pierce Chemical), poly(oxyalkylene)diamine (Jeffamine ED-600 and ED-900, Texaco), and Auroprobe EM Streptavidin (15-nm colloidal gold, Janssen Life Sciences) were utilized without further purification. Phosphate buffer (0.15 M NaCl, 0.10 M Na_2HPO_4, pH 7.4) was prepared with water purified by a Milli-Q water purification system (Millipore).

Derivatization. Fabrication of ultramicroelectrodes was performed as described previously (*53*). Briefly, 8-μm carbon fibers (Thornel P-55S) were aspirated into glass capillary tubing (1.2 mm o.d., 0.68 mm i.d., A-M Systems No. 6020). A tapered end was produced after the capillaries were pulled with a Narishige Model PE-2 microelectrode puller, and a seal was achieved by utilizing Epon epoxy with 14% by weight 1,4-phenylenediamine as hardener. Initial activation of the carbon surface was achieved by polishing for 15 min with diamond polish (1 μm, Buehler) followed by sonication of the electrodes in hot toluene for 10 s to remove residual polishing material. Electrochemical treatment consisted of a cyclic potential waveform generated between −0.2 and 2.0 V vs Ag/AgCl at 50 Hz for 3 s. Carboxyl groups on the carbon surface were activated by reaction with 4 mg/mL of the aqueous carbodiimide for 12 h. The electrodes were then dipped into a 0.4 mM buffered solution of Jeffamine ED-600 for 30 min. This attaches the hydrophilic spacer arm to the electrode surface via an amide bond (Figure 1). After the electrodes were rinsed with buffer, they were placed in a 1 mg/mL buffered solution of Sulfo-NHS-Biotin for 5 h to attach the biotin to the free terminal amines of the surface-bound Jeffamines, also through an amide linkage. Following another wash with buffer, the electrodes were dipped into 600 μL of buffered solution containing 100 μL of either FITC–ExtrAvidin or Colloidal Gold Streptavidin for 12–18 h at 4 °C to complete the derivatization. Dopamine-modified electrodes were constructed in a similar manner. After electrochemical pretreatment and activation with the aqueous carbodiimide, the electrodes were dipped in a 5 mg/mL buffered solution of dopamine for various reaction times before a buffer wash and subsequent electrochemical analysis.

Instrumentation. The surfaces of carbon-fiber microelectrodes were characterized spectroscopically with a Raman spectrometer (Dilor XY, Lille, France) equipped with a 100× Olympus BH-2 microprobe attachment and an IBM PS-2 microcomputer for data management. Raman Spectra were obtained by using excitation from the 514.5-nm line of an argon ion laser (Coherent Innova 70) whose power was maintained at 5 mW to minimize surface activation by the laser. A Sony CCTV camera and monitor allowed the laser to be focused down to a 5-μm spot size localized directly on the carbon fiber. The beveled-tip ultramicroelectrodes were positioned face up against a 40× microscope objective, and the scattered light was dispersed through a double monochromator (1800 line grating) before it was collected onto an intensified photodiode array detector. Emission spectra of the FITC–ExtrAvidin modified electrodes were also obtained with the Raman microprobe except that the 488-nm argon ion line was used for excitation and the fluorescence was passed through only one monochromator before detection with a photomultiplier tube.

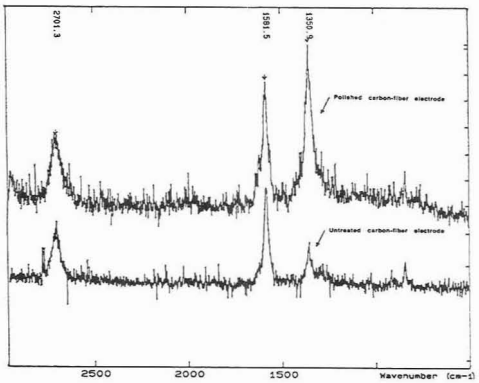

Figure 2. Raman spectra of carbon-fiber microelectrodes taken with an integration time of 10 s. (Number of accumulations of signal and background was 10 each.) Excitation from the 514.5-nm line of an argon ion laser was focused to a 5-μm spot, and the laser power was maintained at 5 mW. The spectra of the polished carbon-fiber electrode (top) shows a considerable growth in the 1351-cm^{-1} band relative to an untreated cut surface of a carbon fiber (bottom).

Fluorescence images of the derivatized carbon surface were obtained from a Carl Zeiss Axioplan microscope equipped with Epiplan Neofluar 40× water immersion lens and a 200-W mercury arc lamp for illumination at 488 nm. A Hamamatsu intensified CCD camera was integrated with a Photonics Argus 10 image enhancement system and a Sony high-resolution color monitor and color video printer to collect all fluorescence longer than 510 nm. Chronocoulometry (−0.4 V to +0.4 V vs Ag/AgCl, τ = 100 ms) and fast-scan cyclic voltammetry (−0.4 V to +0.9 V vs Ag/AgCl, 200 V/s) were performed with a EI-400 potentiostat (Ensman Instruments, Bloomington, IN), where all waveforms were generated and currents acquired via a PC-AT microcomputer (Zenith Data Systems) interfaced by an A/D–D/A interface (Labmaster DMA, Scientific Solutions, Solon, OH). A 100-MHz digital oscilloscope (Nicolet 320) was used to observed all transients, and a Hewlett-Packard ColorPro Plotter was utilized to plot data.

Scanning electron micrographs were obtained with a Phillips 515 LINX AN 1000 electron microscope operated at a voltage of 20.4 kV. Ultramicroelectrodes were mounted on an aluminum stub, and direct electrical contact with the fiber was made with colloidal graphite. The entire assembly was sputter-coated with approximately 10–20 nm of gold to minimize charging.

RESULTS AND DISCUSSION

The freshly cut surface of carbon-fiber microelectrodes was investigated spectroscopically with a Raman microprobe. Thornel carbon fibers resemble glassy carbon in physical characteristics, and the growth of the 1351-cm^{-1} band (*54*) indicates that activation from mechanical polishing indeed produces a distribution of edge-plane defect sites (Figure 2). This Raman mode near 1360 cm^{-1} (referred to as the D band) has been attributed to disorder-induced breakdown of Raman selection rules near graphitic edges (*55*, *56*); hence it has been used as an indicator of microcrystallite size (the 1360/1580 cm^{-1} intensity ratio increasing with decreasing microcrystallite size). A recent investigation by Wang, Alsmeyer, and McCreery has ruled out the possibility that growth of a 1360-cm^{-1} band could occur from the existence of specific vibrations localized at edges (e.g. from oxide or –C═C– grops that are only present at the edge). Since smaller microcrystallites will have greater edge density, they concluded that the chemical composition of the edge as well as the size of the associated crystallite does not influence the frequency of the 1360-cm^{-1} band. Rather it is the presence of the edge that permits scattering by 1360-cm^{-1} band phonons (*56*). Slight

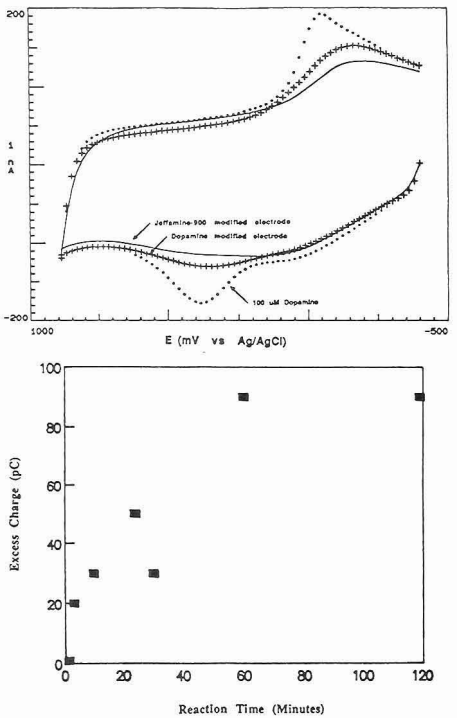

Figure 3. (Top) fast-scan cyclic voltammograms (200 V s^{-1}) of a Jeffamine-modified electrode surface (—), dopamine-modified electrode surface (+++), and the same electrode placed in a 100 μM solution of dopamine (•••). Notice the oxidative and reductive peaks for the surface-bound dopamine correspond at the exact same potential ranges as those seen for the solution-phase dopamine. (Bottom) increase in surface charge for ultramicroelectrodes before and after attachment of dopamine determined by chronocoulometry as a function of reaction time.

growth in the 1582-cm^{-1} band and the 2701-cm^{-1} band (the first overtone of the 1351 cm^{-1} band) can also be observed. The frequency of the 1582-cm^{-1} Raman band has been associated with the magnitude of the stacking dimension (L_c) and indicates the creation of an sp^2-hybridized lattice (*55*). These spectroscopic investigations of the breakdown of the carbon lattice following polishing procedures have been correlated to increased reversibility of electron-transfer kinetics and have been observed following electrochemical and laser treatments as well (*32*). Therefore, oxidative and nonoxidative processes can both promote edge plane density (*39*). Unfortunately, more information relating these edge defects to the distribution of oxygen on the surface cannot be drawn from this Raman spectroscopic approach due to a lack of sensitivity.

A derivatization procedure aimed to highlight the carboxylic acid groups on the carbon surface is presented in Figure 1. After the polished surface of the carbon fiber microelectrode is mildly electrochemically oxidized (−0.2 V to 2.0 V vs Ag/AgCl at 50 Hz for 3 s) to provide a slightly oxygen-enriched surface, a primary amine is covalently bound to the carboxylic acid sites through formation of an amide bond (*57, 58*). A long (approximately 50 Å) (*59, 60*) tether molecule (Jeffamine ED-600) was chosen on the basis that its hydrophilicity would be sufficient to allow further coupling reactions to take place in the aqueous buffer extended away from the hydrophobic

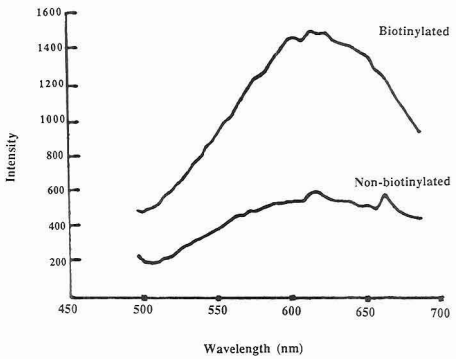

Figure 4. Emission spectra of modified carbon-fiber microelectrodes obtained with a 5-μm spot of 488-nm excited light kept at 5 mW. Spectra are shown for a biotinylated Jeffamine electrode (top) and an unbiotinylated Jeffamine electrode (bottom), both of which were treated with FITC–ExtrAvidin.

carbon surface. A second amide bond is now formed with the other primary amine end of the diamine spacer after treatment with biotin. This facilitates the use of biotin–avidin coupling, where four molecules of biotin can selectively and strongly bind to one molecule of avidin ($K_d = 10^{-15}$ M, which is roughly 2–3 orders of magnitude greater than typical antigen–antibody bonding; *61–65*). The FITC-labeled ExtrAvidin depicted can be interchanged with 15-nm colloidal gold balls coated with streptavidin.

The extent of reaction between the surface-bound carboxylic acids and the primary amine of the tether was assessed by replacing the nonelectroactive Jeffamine with dopamine and performing fast-scan cyclic voltammetry (Figure 3). The surface waves of Jeffamine-modified and dopamine-modified electrodes obtained in a blank solution were compared to a voltammogram taken in a 100 μM buffered solution of dopamine. The correspondence of the oxidative and reductive peaks of the surface-bound dopamine and the dopamine found in solution confirms that it is dopamine that is indeed bound to the electrode surface. A more quantitative assessment was obtained by performing chronocoulometry. To eliminate contributions from all other surface-bound redox couples, chronocoulmetric data were acquired for each electrode before and after the dopamine derivatization reaction. Thus, each electrode served as its own control. A 36 ± 13 pC (n = 6) increase in the charge observed at the carbon surface can thus be attributed to the oxidation of the surface-bound dopamine. This corresponds to one dopamine molecule per 300 $Å^2$ (based on a geometrical surface area of 350 μm^2), similar to the surface coverage found by Tse and Kuwana for macroscopic glassy-carbon electrodes (*1*). This coverage is roughly 10 times greater than the coverage necessary for complete surface coverage with avidin, based on the cross-sectional area of avidin (*66*). The extent of surface coverage can be controlled by varying the length of time the amine is allowed to react with the carbodiimide-activated carboxylate. Maximal coverage, as indicated by reaching a steady-state level, can be obtained in 1 h (Figure 3).

The attachment of FITC–ExtrAvidin to the carbon-fiber surface was also investigated with fluorescence microscopy. Emission spectra obtained from derivatized fibers (Jeffamine–biotin–FITC–ExtrAvidin) and nonbiotinylated controls are shown in Figure 4. A Raman microprobe was used with excitation at 488 nm in air, resulting in FITC fluorescence which had a maximum that was red-shifted ca. 100 nm relative to that observed for FITC in solution. The emission spectrum

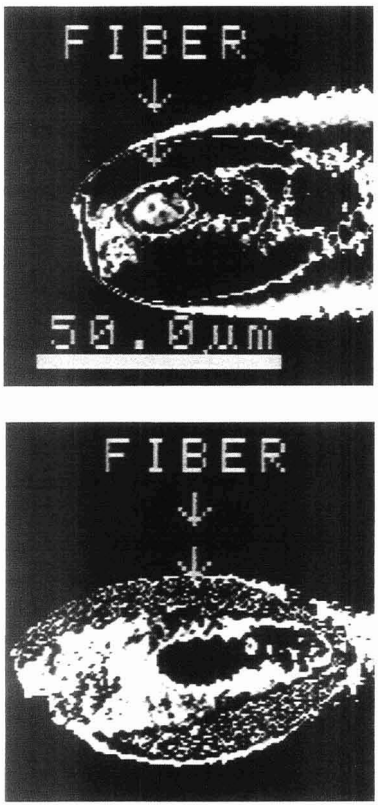

Figure 5. Image of the surface of FITC–ExtrAvidin-modified carbon-fiber microelectrodes obtained with a fluorescence microscope interfaced with a CCD camera. Fluorescence intensity is indicated via a gray scale (highest intensity indicated by white). (Top) a representative image (n = 6) of FITC–ExtrAvidin bound to carboxyl groups on the surface via a Jeffamine–biotin linkage. (Bottom) a control electrode that went through each step of the derivatization except biotinylation, where the dark, oval area in the interior is the carbon fiber surface. Note the absence of nonspecific binding of FITC-ExtrAvidin for the control.

of the FITC-modified carbon-fiber electrode clearly indicates specific biotin–avidin binding, since the intensity is well above that observed for the nonspecific adsorption of FITC–ExtrAvidin demonstrated with the nonbiotinylated control. Even though this experiment shows that the Raman microprobe was sensitive enough to monitor the submonolayer concentration of the immobilized fluorophore, the exact location of these sites could not be determined with this instrument.

The spatial distribution of FITC–ExtrAvidin bound to carboxylates on the surface of a carbon-fiber microelectrode was determined with a fluorescence microscope equipped with a CCD camera. CCD cameras are very sensitive light-gathering devices (*67*), and the small pixel size of the CCD can be used to great advantage when combined with fluorescence microscopy, such that spatial resolution near the diffraction limit of the light used (<0.5 μm) can be obtained (*37*). Since the intensity of the fluorescence emission signal is independent of path length, proportional to the intensity of the excitation source and the concentration of the fluorophore, this technique has the requisite sensitivity to detect a submonolayer coverage of fluorophore. Increased sensitivity was possible since all light

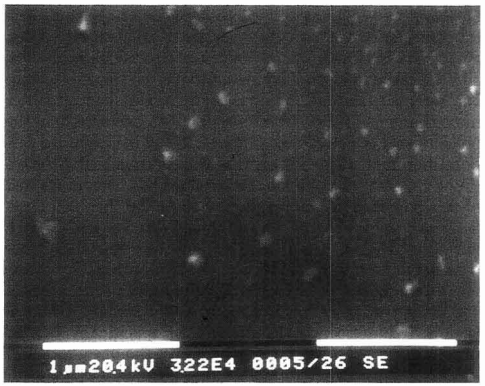

Figure 6. Scanning electron micrograph of colloidal gold particles attached to biotinylated carboxylates on the surface of a carbon-fiber microelectrode. The distribution of ca. 50-nm spots indicates the distribution of streptavidin-coated gold binding sites (via Jeffamine–biotin-derivatized carboxylates on the carbon-fiber surface) on a submicron scale.

longer than the cutoff filter wavelength of 510 nm was passed. A representative image of FITC–ExtrAvidin bound onto the surface of a biotinylated electrode is pictured in the top of Figure 5. The distribution of intensities of fluorescence observed (indicated via a gray scale) reflects the heterogeneity of avidin binding sites on the carbon surface, indicating the distribution of carboxylate residues on the carbon surface. A control electrode, which has gone through each step of the derivatization except the biotinylation (thereby eliminating specific binding sites for avidin) is shown at the bottom of Figure 5. Almost no fluorescence is observed from the carbon surface, indicating the virtual absence of nonspecific binding. These data only show carboxylate residues on the surface that are reactive (i.e., derivatizable), but then, these are the sites of chemical interest. Only those sites on the surface that can react with a species in solution will have an effect on the electrochemical activity of that surface. The spatial resolution obtained in this manner is adequate to image most macroscopic surface features of importance, such as cracks, crevices, and edge boundaries, but cannot generate an image of individual binding sites. This level of resolution may be sufficient to establish a marked correlation between the location of functional groups and electron-transfer properties of those sites.

Higher resolution (on the order of 50 nm) was accomplished through use of Streptavidin-coated colloidal gold and scanning electron microscopy. In this study, the biotinylated carbon-fiber electrode was dipped into a suspension of Streptavidin-coated colloidal gold (15 nm diameter) for 12 h. The SEM image of the electrode was obtained (Figure 6) and a large number of ca. 50-nm wide spots were observed, indicating individual sites of derivatization on the electrode surface. These data indicate the feasibility of SEM as a tool to observe the distribution of avidin binding sites on the surface of the electrode. This provides roughly 1 order of magnitude higher resolution than an optical imaging approach. Scanning tunneling microscopy, atomic force microscopy, or scanning electrochemical microscopy may be able to produce comparable, or better, resolution of surface features marked in this manner. Determination of the chemical architecture of the carbon surface with almost atomic resolution may help to completely identify the composition of electron-transfer sites.

CONCLUSIONS

It is extremely difficult to produce a meaningful relationship

between the structure and microscopic heterogeneous electron-transfer rate of the carbon surface of different electrodes. Differences in cleanliness, the density of functionalized groups, and the carbon morphology are great from surface to surface and sample to sample. Various pretreatments can also alter more than one of the variables thought to participate in the mechanisms of activation. The feasibility of imaging a carbon-fiber microelectrode surface after derivatization with a probe-reagent selective for carboxylates has been presented in this paper. This approach may allow the chemical characterization of many of the functional groups (i.e., $-CO_2H$, $-C{=}O$, $-CH_2OH$, $-CH_3SO_3H$, etc.) on the electrode surface with submicron resolution. The chemical selectivity of the measurement can be altered simply by using probe reagents and/or derivatizing schemes specific for the surface functional groups. Fluorescence visualization of specifically labeled functional groups, when combined with the observation of electrogenerated chemiluminescence of luminol at the same electrode may allow correlation of the chemical architecture of the electrode surface with its electron-transfer properties.

ACKNOWLEDGMENT

The loan of the fluorescence microscope from Max Erb instruments (Burbank, CA) and the donation of Jeffamines from Texaco are gratefully appreciated. We also thank Thomas Hellman Morton for creative discussions, Dan Borchardt for assistance with Raman spectroscopy, Eric Kristensen for the latest revision of his voltammetry solfware, and John Casanko and Marcia Kooda for electron microscopy.

LITERATURE CITED

(1) Tse, D. C.-S.; Kuwana, T. *Anal. Chem.* **1978**, *50*, 1315–1318.
(2) Panzer, R. E.; Elving, P. J. *Electrochim. Acta* **1975**, *20*, 635–647.
(3) Bellby, A. L.; Carlsson, A. J. *Electroanal. Chem. Interfacial Electrochem.* **1988**, *248*, 283–304.
(4) Van der Linden, W. E.; Dieker, J. W. *Anal. Chim. Acta* **1980**, *119*, 1–24.
(5) Kinoshita, K. *Carbon: Electrochemical and Physiochemical Properties*; New York, 1988; p 533.
(6) Kozlowski, C.; Sherwood, P. M. A. *J. Chem. Soc., Faraday Trans.* **1985**, *81*, 2745–2756.
(7) Evans, J. F.; Kuwana, T. *Anal. Chem.* **1979**, *51*, 358–365.
(8) Wightman, R. M.; Deakin, M. R.; Kovach, P. M.; Kuhr, W. G.; Stutts, K. J. *J. Electrochem. Soc.* **1984**, *131*, 1578–1583.
(9) Feng, J. X.; Brazell, M.; Renner, K.; Kasser, R.; Adams, R. N. *Anal. Chem.* **1987**, *59*, 1863–1867.
(10) Hu, I. F.; Karweik, D. H.; Kuwana, T. *J. Electroanal. Chem. Interfacial Electrochem.* **1985**, *188*, 59–72.
(11) Kamau, G. N.; Willis, W. S.; Rusling, J. F. *Anal. Chem.* **1985**, *57*, 545–551.
(12) Noel, M.; Anantharaman, P. N. *Analyst* **1985**, *110*, 1095–1103.
(13) Nagaoka, T.; Yoshino, T. *Anal. Chem.* **1986**, *58*, 1037–1042.
(14) Engstrom, R. A. *Anal. Chem.* **1982**, *54*, 2310–2314.
(15) Kovach, P. M.; Deakin, M. R.; Wightman, R. M. *J. Phys. Chem.* **1986**, *90*, 4612–4617.
(16) Proctor, A.; Sherwood, P. M. A. *Carbon* **1983**, *21*, 53–59.
(17) Wang, J.; Hutchins, L. D. *Anal. Chim. Acta* **1985**, *167*, 325–334.
(18) Kepley, L. J.; Bard, A. J. *Anal. Chem.* **1988**, *60*, 1459–1467.
(19) Miller, C. W.; Karweik, D. H.; Kuwana, T. *Anal. Chem.* **1981**, *53*, 2319–2323.
(20) Evans, J. F.; Kuwana, T. *Anal. Chem.* **1977**, *49*, 1632–1635.
(21) Xie, Y.; Sherwood, P. M. A. *Appl. Spectrosc.* **1990**, *44*, 797–803.
(22) Zak, J.; Kuwana, T. *J. Am. Chem. Soc.* **1982**, *104*, 5514–5515.
(23) Dong, S.; Kuwana, T. *J. Electrochem. Soc.* **1984**, *131*, 813–818.
(24) Poon, M.; McCreery, R. L. *Anal. Chem.* **1986**, *58*, 2745–2750.
(25) Poon, M.; McCreery, R. L.; Engstrom, R. *Anal. Chem.* **1988**, *60*, 1725–1730.
(26) Rice, R. J.; McCreery, R. L. *Anal. Chem.* **1989**, *61*, 1637–1641.
(27) Fagan, D. T.; Hu, I. F.; Kuwana, T. *Anal. Chem.* **1985**, *57*, 2759–2763.
(28) Proctor, A.; Sherwood, P. M. A. *J. Electron Spectrosc. Relat. Phenom.* **1982**, *27*, 39–56.
(29) Cananiss, G. E.; Diamantis, A. A.; Murphy, W. R., Jr.; Linton, R. W.; Meyer, T. J. *J. Am. Chem. Soc.* **1985**, *107*, 1845–1853.
(30) Gunasingham, L.; Fleet, B. *Analyst* **1982**, *107*, 896–902.
(31) Bowling, R.; Packard, R.; McCreery, R. L. *J. Electrochem. Soc.* **1988**, *135*, 1605–1606.
(32) Bowling, R.; Packard, R.; McCreery, R. L. *J. Am. Chem. Soc.* **1989**, *111*, 1217–1223.
(33) Rice, R. J.; Pontikos, N. M.; McCreery, R. L. *J. Am. Chem. Soc.* **1990**, *112*, 4617–4622.
(34) Engstrom, R.; Pharr, C. M.; Koppang, M. D. *J. Electrochem. Soc.* **1987**, *221*, 251–255.
(35) Engstrom, R.; Johnson, K. W.; DesJarlais, S. *Anal. Chem.* **1987**, *59*, 670–673.
(36) Pharr, C. M.; Engstrom, R.; Klancke, J.; Unzelman, P. L. *Electroanalysis* **1990**, *2*, 217–221.
(37) Pharr, C. M.; Engstrom, R. C.; Tople, R. A.; Bee, T. K.; Unzelman, P. L. *J. Electroanal. Chem. Interfacial Electrochem.* **1990**, *278*, 119–128.
(38) Bowling, R. J.; McCreery, R. L.; Pharr, C. M.; Engstrom, R. C. *Anal. Chem.* **1989**, *61*, 2763–2766.
(39) Bowling, R.; Packard, R. T.; McCreery, R. L. *Langmuir* **1989**, *5*, 683–688.
(40) Treado, P. J.; Govil, A.; Morris, M. D.; Strernitzke, K. D.; McCreery, R. L. *Appl. Spectrosc.* **1990**, *44*, 1270–1275.
(41) Chang, H.; Bard, A. J. *J. Am. Chem. Soc.* **1990**, *112*, 4598–4599.
(42) Gerwirth, A. A.; Bard, A. J. *J. Phys. Chem.* **1988**, *92*, 5563–5566.
(43) Engstrom, R. C.; Pharr, C. M. *Anal. Chem.* **1989**, *61*, 1099A–1104A.
(44) Bard, A. J.; Denuault, G.; Lee, C.; Mandler, D.; Wipf, D. O. *Acc. Chem. Res.* **1990**, *23*, 357–363.
(45) Kozlowski, C.; Sherwood, P. M. A. *J. Chem. Soc., Faraday Trans.* **1984**, *80*, 2099–2107.
(46) Petersen, S. L.; Weisshaar, D. E.; Tallman, D. E.; Schulze, R. K.; Evans, J. F.; DesJarlais, S. E.; Engstrom, R. C. *Anal. Chem.* **1988**, *60*, 2385–2392.
(47) White, H. S.; Earl, D. J.; Norton, J. D.; Kragt, H. J. *Anal. Chem.* **1990**, *62*, 1130–1134.
(48) Smith, C. P.; Kennedy, H. L.; Kragt, H. J.; White, H. S.; Biegen, J. F. *Anal. Chem.* **1990**, *62*, 1135–1138.
(49) Proctor, A.; Sherwood, P. M. A. *SIA, Surf. Interface Anal.* **1982**, *4*, 212–219.
(50) Kozlowski, A.; Sherwood, P. M. A. *Carbon* **1986**, *24*, 357–363.
(51) Tougas, T. P.; Collier, W. G. *Anal. Chem.* **1987**, *59*, 2269–2272.
(52) Pantano, P.; Morton, T. H.; Kuhr, W. G. *J. Am. Chem. Soc.* **1991**, *113*, 1832–1833.
(53) Kelly, R. S.; Wightman, R. M. *Anal. Chim. Acta* **1986**, *187*, 79–87.
(54) Rice, R. J.; Allred, C.; McCreery, R. L. *J. Electroanal. Chem. Interfacial Electrochem.* **1989**, *263*, 163–169.
(55) Callstrom, M. R.; Neenan, T. X.; McCreery, R. L.; Alsmeyer, D. C. *J. Am. Chem. Soc.* **1990**, *112*, 4954–4956.
(56) Wang, Y.; Alsmeyer, D. C.; McCreery, R. L. *Chem. Mater.* **1990**, *2*, 557–563.
(57) Rocklin, R. D.; Murray, R. W. *J. Electroanal. Chem. Interfacial Electrochem.* **1979**, *100*, 271–282.
(58) Narasimhan, K.; Wingard, L. B., Jr. *Anal. Chem.* **1986**, *58*, 2984–2987.
(59) Amankwa, L. N.; Scholl, J.; Kuhr, W. G. *Anal. Chem.* **1990**, *62*, 2189–2193.
(60) Nuwayser, L. M.; Simonsick, W. J.; Wilkins, C. L. *J. Am. Soc. Mass Spectrom.* **1990**, *1*, 66–71.
(61) Baeyer, E. A.; Wilchek, M. *Methods Biochem. Anal.* **1980**, *26*, 1–45.
(62) Gunaratna, P. C.; Wilson, G. S. *Anal. Chem.* **1990**, *62*, 402–407.
(63) Luo, S.; Walt, D. R. *Anal. Chem.* **1989**, *61*, 1069–1072.
(64) Ebersole, R. C.; Miller, J. A.; Moran, J. R.; Ward, M. D. *J. Am. Chem. Soc.* **1990**, *112*, 3239–3241.
(65) Wilchek, M., Bayer, E. A., Eds. *Methods in Enzymology*; Academic: San Diego, CA, 1990; Vol. 184, p 746.
(66) Weber, P. C.; Ohlendorf, D. H.; Wendoloski, J. J.; Salemme, F. R. *Science* **1989**, *243*, 85–88.
(67) Epperson, P. M.; Sweedler, J. V.; Bihorn, R. B.; Sims, G. R.; Denton, M. B. *Anal. Chem.* **1988**, *60*, 327A–335A.

RECEIVED for review December 20, 1990. Accepted April 5, 1991. This work was supported, in part, by the National Institutes of Health (Grant GM44112-01A1) and a Presidential Young Investigator Award (W.G.K.) from the National Science Foundation (Grant CHE-8957394). The Dilor XY Raman spectrometer was obtained via a grant from the National Science Foundation to Bryan E. Kohler (Grant CHE-8805482).

Composite Multivariate Quality Control Using a System of Univariate, Bivariate, and Multivariate Quality Control Rules

S. J. Smith,* S. P. Caudill, J. L. Pirkle, and D. L. Ashley

Division of Environmental Health and Laboratory Sciences, Center for Environmental Health and Injury Control, Centers for Disease Control, Public Health Service, U.S. Department of Health and Human Services, Atlanta, Georgia 30333

We propose a composite multivariate quality control (CMQC) system to control simultaneously measured variables. This system is designed to detect unacceptable trends and systematic error in one or more variables, unacceptable random error in one or more variables, and unacceptable changes in the correlation structure in any pair of variables. It is also designed to be tolerant of missing data, to be capable of rejecting as few as one or as many as all variables in a run, and to provide the analyst with control statistics and graphics that logically relate to sources of analytical error. Quality control rules for univariate, multivariate, and correlation conditions are incorporated in the system, as are plots displaying CMQC statistic values and control limits for univariate, multivariate, and correlation parameters. We also discuss advantages of the CMQC over the T^2 and principal component multivariate quality control methods. We demonstrate the CMQC procedure using data from a laboratory process in which 40 variables were measured during 40 characterization runs and 23 runs analyzing unknowns.

INTRODUCTION

By using modern instrumentation, such as gas chromatography or mass spectrometry, analysts can make simultaneous rapid measurement of multiple analytes per specimen. Normally, a quality control (QC) material and several unknown specimens are grouped into a run and analyzed sequentially. Many analytes are measured simultaneously on each specimen in a run. The QC of such measurements presents analysts with special problems due to (1) the difficulty of interpreting one or more control charts for a large number of variables, (2) the intercorrelations inherent in the simultaneous measurements, and (3) the potential for missing values for some variables in any given run.

Tracking large numbers of variables increases the type I error rate. If the variables are statistically independent, the control limits can be adjusted (cf., Bonferroni or Sheffe) but this adjustment reduces the statistical power of the control procedure. Westgard et al. (*1*) have proposed a multirule method for more than one level of a single variable that might be applied to the simultaneous control of several independent variables. Applying multiple, independent control chart rules would not result in the correct type I error rate, however, because of the elliptical nature of the "in-control" region. To address this problem, investigators have proposed multivariate approaches, including the T^2 chart (*2–6*) and principal components (PCs) (*7, 8*).

Analysts using the T^2 or PC methods can take advantage of the correlation of the variables and obtain correct overall type I error rates. Users of the T^2 and PC methods, however, must reliably estimate the correlation matrix; therefore, the number of characterization runs must substantially exceed the number of control variables. If analysts base the correlation matrix estimate on too few characterization runs while using T^2 or PC methods, they tend to reject analytical runs when the observed systematic and random errors are small, but the interrelationships among variables deviate from those predicted from the characterization runs. These methods also require that all data be observed for all variables in every run; such complete data collection becomes increasingly unlikely as the number of variables increases. In addition, if the PC method is used, analysts may have difficulty relating the components conceptually to the variables from which they were estimated. Therefore, the components may be difficult to interpret. Furthermore, neither method allows one to easily relate individual variable values to the multivariate control statistic.

To address these problems encountered in the multivariate control of large numbers of variables, we propose a composite multivariate quality control system that is designed with the following capabilities: (1) can detect unacceptable trends and systematic error in one or more variables; (2) can detect unacceptable random error in one or more variables; (3) can detect unacceptable changes in the correlation structure in any pair of variables; (4) can tolerate missing data; (5) can reject as few as one or as many as all variables in a run; (6) can provide control statistics that logically relate to sources of analytical error.

The control criteria incorporated in the composite multivariate quality control (CMQC) method include univariate, multivariate, and pairwise correlation control statistics. Action and warning rules are specified for each of these statistics.

In addition, we propose a composite univariate QC plot and pairwise correlation plots that allow the user to visually relate individual variable results to multivariate events. We illustrate the CMQC approach by using data from a 40-variable process.

METHODS

Previous multivariate control procedures have been designed to handle the simultaneous control of several related variables, but their use leads to acceptance or rejection of all variables observed in an entire run because one statistic summarizes information for all variables. Thus, these procedures provide no mechanism for rejection of individual variables. This is especially disadvantageous when laboratory resources or samples are limited. Murphy (*9*) has proposed a system of partitioning T^2 to select subsets of out-of-control variables; however, his system was not recommended for more than five variables and would be unfeasible for large numbers of variables. For example, given a 40-variable process, over 800 significance tests are required when using Murphy's method. Therefore, we propose an alternative system that allows analysts to partially reject a run (i.e., as few as one or as many as all variables may be rejected). Because analysts using this approach can identify problems with individual variables, they can take more timely and specific corrective action.

* Corresponding author.

This article not subject to U.S. Copyright. Published 1991 by the American Chemical Society

Table I. Composite Quality Control Rules

Univariate Rules: Reject Measurement(s) for a Single Analyte in a Run

Action Rules

1. Extreme deviation: Reject any single variable outside ± 3 standard deviations during one run.
2. Moderate deviation: Reject any single variable outside ± 2 standard deviations for two consecutive runs (same side of mean).
3. Trend 1: Reject any single variable displaying a consistent trend up or down for seven consecutive runs.
4. Trend 2: Reject any single variable falling on the same side of the mean for 10 consecutive runs.

Multivariate Rules: Reject Measurements for All Analytes in a Run

multivariate control statistic (MCS) = log (sum of squared deviates)/n

Action Rules

1. Extreme deviation: Reject a single run outside the 0.003 probability level.
2. Moderate deviation: Reject two consecutive runs outside the 0.05 probability level.
3. Trend 1: Reject if the statistic increases in value for seven consecutive runs.
4. Trend 2: Reject if the statistic falls above the median for 10 consecutive runs.

Warning Rule

1. Reject a single run outside the 0.05 level.

Correlation Rules: Reject Measurements for a Pair of Analytes in a Run

Control statistic: The probability (PCORR) of the observed results for a pair of analytes is calculated on the basis of the elliptical confidence region for pairwise correlation of the two analytes, which is obtained from the characterization runs.

Action Rules

1. Extreme deviation: Reject any pair of analytes with PCORR values less than 0.003 on at least two consecutive runs.
2. Trend: Reject any pair of analytes with PCORR values that decreases for seven consecutive runs.

Warning Rules

1. Moderate deviation: Reject any pair of analytes with PCORR values less than 0.05 during one run.
2. Trend: Reject any pair of analytes with PCORR values less than 0.5 for 10 consecutive runs.

A summary of the CMQC control rules (Table I) shows the univariate, multivariate, and pairwise correlation warning and action rules. The univariate rules operate on single variables to detect systematic or random errors. The multivariate rules detect systematic and random errors in all of the variables considered together. The pairwise correlation rules supplement the multivariate control rules by providing a test for unacceptable changes in correlation between any two variables.

The process variation for a given analytical system is estimated from a specified number of characterization runs. In the Procedures section, we discuss the number of runs required to characterize an in-control multivariate analytical system; in short, the number depends on the number of variables being simultaneously monitored. Analytical methods used in chemical assays commonly employ standard calibrators, yielding response curves from which concentrations of unknowns are estimated in a series of independent runs. Typically, these methods exhibit among-run variation that greatly exceeds replication error within runs. With these assays, one should use the standard deviation of the run mean concentration for the process variation. This is the approach we use, though the CMQC method is applicable to other methods for computing process variation.

Univariate Control Rules. The proposed CMQC univariate control rules are similar to those commonly used in laboratory quality control. That is, they incorporate two and three standard deviation action limits and tests for runs (Table I). These rules are applied to each variable independently. If any of the four univariate rules are violated for a single variable, the measurements for that variable are not reported for that run.

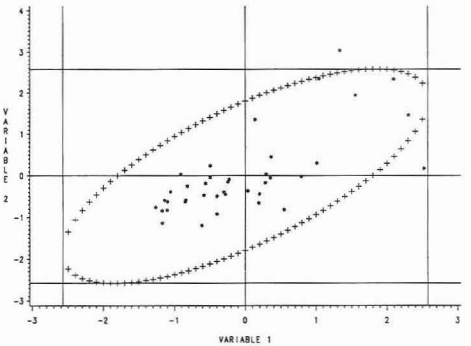

Figure 1. Pairwise correlation plot. An example plot of observed standardized deviates is shown for a pair of variables along with the 95% confidence ellipse determined from the characterization correlations estimate for these two variables.

In the univariate case, the values of the control variable measured in the run's QC sample are compared with control limits estimated from preliminary characterization runs to determine if a run is in control at a given probability level. The successive run values are plotted for visual interpretation of trends and shifts in the results. We found that the most useful way to plot control charts is to use standardized deviates. The standardized deviate for each run equals the control variable result minus the overall mean of the control variable in the characterization runs divided by the standard deviation of the control variable in characterization runs. The control chart is then constructed by using reference lines at ±2 and 3 standard deviations from the mean.

Multivariate Control Rules. We define a new multivariate control statistic (MCS) given by

corrected 24 Dec. 91

$$\text{MCS} = [\log [\sum d^2]]/n \quad \text{for } K = 0$$

$$[\log [\sum d^2 + (K-1)/K]]/n \quad \text{for } 0 < K < n$$

where d_i is the standardized deviate for the ith variable, n is the number of control variables measured in a single run, and K is the number of variables with missing data. The distribution of this statistic is known only for the case of uncorrelated variables, where it is a simple function of χ^2. For correlated variables, the distribution is unknown. We used the log transformation of the sum of squares to induce symmetry in an otherwise right-skewed statistic. The divisor (n) standardizes the statistic for the numbers of deviates, and we used the term $(K-1)/K$ to adjust the statistic for missing measurements. The term $K-1$ is equal to the expected value of the sum of the squared standardized deviates for the K missing results. To estimate critical values for the statistic, we use Monte Carlo simulation.

Pairwise Correlation Rules. We based the pairwise correlation rules on elliptical confidence regions (*10*) determined from correlation estimates from the characterization runs for each pair of standardized deviates (Figure 1). These ellipses are centered at the point (0,0) corresponding to zero deviation from the characterization means for both variables in the pair. The orientation of each ellipse is determined by the degree of correlation between deviate pairs. The length and width of each ellipse is a function of the number of characterization runs used to compute the correlation estimate.

We computed probability (PCORR) values for each pair of deviates for each postcharacterization analytical run on the basis of its distance from and orientation to the (0,0) center of its corresponding characterization ellipse.

Each PCORR value for a pair of analytes should be interpreted as the probability that the observed results for that pair is due to the random variation expected on the basis of the estimated correlation between the two analytes. For example, a PCORR value < 0.003 would indicate a pair of results rarely expected for an analyte pair on the basis of the correlation estimates obtained from the characterization runs. Thus, a pair of results with a PCORR value < 0.003 would be analogous to a single result outside a control limit of 3 on a regular Shewhart quality control chart. We recommend that analysts plot 1 – PCORR values for the current and all previous runs for each pair of variables where the PCORR value on the current run is less than 0.003 or whose PCORR value on the current and most recent runs are both less than 0.05. Analysts should also produce plots when 10 consecutive PCORR values are all less than 0.5 or when they observe 7 consecutive decreasing PCORR values for 1 pair of analytes.

PROCEDURES

Step 1. Specification of Conditions for QC Analysis. The application of CMQC to a specific problem involves a number of preliminary considerations. First, analysts must decide what variables will be monitored, how many runs will be used to characterize the process, and how missing values and incomplete characterization runs will be handled. Potential variables to be monitored include all outcome variables and any other parameters related to these variables. For example, in mass spectrometry, a parameter such as an ion ratio could be included as a control variable. Including such additional parameters, however, can produce an unreasonable number of control variables. Often, separate criteria such as tolerance limits are adequate for monitoring these parameters.

To determine the number of runs needed to properly characterize the process, we had to consider both statistical error and resource constraints. Using Monte Carlo simulation, we investigated error rates for QC means charts as a function of the number of characterization runs used to estimate the variance of the process. We determined the expected probabilities of false rejects and false accepts for 3σ limits (QC means chart) for 10–50 characterization runs. We found that using 10 characterization runs would result in a false rejection rate about 50% larger than expected if the mean and variance of the process were known. We found that using 40 characterization runs would result in only a 20% increase. Thus, by taking 40 characterization runs rather than 10 characterization runs, one can decrease the false acceptance rate by about 40%. These simulations were done for a univariate process; as the number of measured variables in a multivariate process increases, the chances of observing maverick data for one or more variables in the characterization runs increase.

We also simulated a pairwise correlation-based QC process with a 0.997 probability level control limits. We found that using 10 (or even 20) characterization runs yielded false reject rates that were 27 (or 13) times the rate expected, if pairwise correlation was known. Thirty characterization runs would result in almost a 10-fold increase in the false reject rate, and 40 characterization runs would result in a 6–7-fold increase. Increasing from 40 to 50 or more characterization runs had little effect on reducing the false reject rate. The false accept rate with 30 and 40 characterization runs is about 1% and 0.8%, respectively. Thus, the actual number of runs required to adequately characterize a multivariate process will depend upon the impact of the error rates on the control of the process and any constraints imposed by available resources (e.g., cost or time to generate a run, availability of control material, etc.). The sample sizes should be chosen to protect against having too few complete characterization runs (i.e., runs with observations for all variables) and also to protect against unacceptably high false reject and false accept rates.

By using T^2 or PC, one would be restricted to analyzing only those runs of unknowns that include measurements of all variables, whereas by using the CMQC approach one can accommodate runs from which some measurements are missing. The analyst should determine the criteria for excluding runs with an unacceptable number of missing results. For example, one may wish to specify that at least three-fourths of all variables be observed in each reported run and in each characterization run or that certain key variables always be observed in reported runs.

Step 2. Characterization Runs: Determining Estimates of the Quality Control Parameters. Once a set of characterization runs have been generated, decisions must be made about their adequacy and quality. Initially a target mean and standard deviation are obtained for each control variable on all data. Then each variable is standardized separately by subtracting its respective mean and dividing by its respective standard deviation, yielding the standardized deviate.

After standardizing the variables, we recommend that the characterization data be plotted for visual inspection. An individual univariate plot for each variable should be generated. We also recommend the use of a composite univariate plot that allows the easy detection of multivariable trends. In the composite plot (Figure 2; data are discussed in the illustration section), each connected line corresponds to the standardized measurements for a single variable. The horizontal lines correspond to the means of the variables (a value of zero in standardized space). These lines are offset by 6 units to indicate that a point exactly between two lines is 3 standard deviations from its mean. These plots are useful initially in detecting statistically based extreme outliers (e.g., points more than 3.5 standard deviations from the mean), which should be deleted from the characterization data. Variable-by-run matrix displays similar to those in Figures 3 and 4 are useful for summarizing data on the moderate deviations univariate rules.

Next, multivariate control statistic values should be computed and plotted for each of the characterization runs (see Figure 5). By using the composite univariate plot and the MCS plot, checks are made to see if any variables or groups of variables are outside expected limits. Necessary corrections are made and characterization values recomputed.

To evaluate the correlation structure of the characterization data, correlation coefficients should be computed for each pair of standardized deviates. These correlation estimates are then displayed in a histogram as illustrated in Figure 6 or in a matrix format (Figure 7). If any estimate seems to deviate from the majority, the corresponding variable pair is investigated to determine whether the estimate is consistent with the known relationship between the two variables. If errors are detected in the analytical process or data generation procedures, the necessary corrections are made in the characterization data and new means, standard deviations, standardized deviates, and pairwise correlation coefficients are computed. Correlation QC plots similar to the one shown in Figure 8 are then generated for each pair of variables that violate any of the warning or action rules for correlation, and an analysis of the characterization runs is performed by using each of the univariate, multivariate, and pairwise correlation warning and action rules described in Table I.

Step 3. Quality Control Analysis of Unknown Samples. Following the review of the data on a univariate, multivariate, and correlation basis, the working set of char-

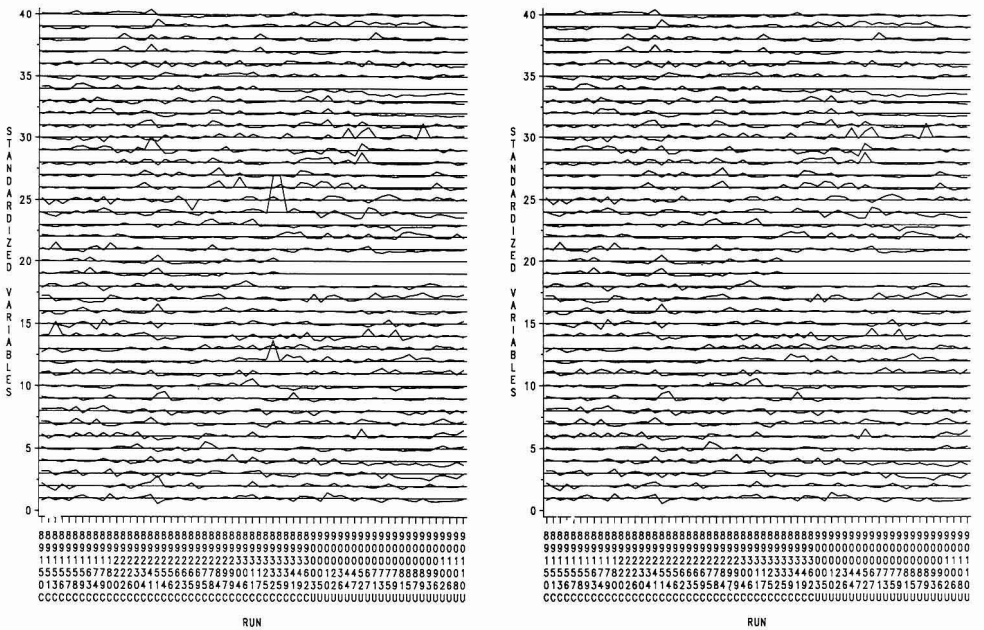

Figure 2. (a, left) Composite univariate plot before statistical outliers in characterization runs were omitted. This composite plot shows the standardized deviates observed by run for each of the 40 volatile compounds before statistical outliers were omitted. The horizontal lines represent the expected zero deviate for each compound. These lines are offset by 6 units, indicating that a point exactly between 2 lines is 3 standard deviations from its respective mean. Each connected line corresponds to the standardized measurements for a single compound. Run numbers within the "C" suffix are characterization runs. Run numbers with the "U" suffix are runs in which unknowns were analyzed. The run number consists of the year "89", followed by the julian date of the run. (b, right) Composite univariate plot after statistical outliers in characterization runs were omitted. A composite plot similar to a is shown. This plot was generated after a 3.5 standard deviation outlier rule had been applied to the observed characterization measurements for each compound.

acterization values is finalized. These data are used to generate estimates of means, standard deviations, standardized deviates, and correlation coefficients for the analysis of future test runs.

ILLUSTRATION

The CMQC method proposed in the preceding section is being applied to a multivariate quality control problem that arose from the Centers for Disease Control's (CDC's) involvement in the Third National Health and Nutrition Examination Survey (NHANES III). The Division of Environmental Health Laboratory Sciences (EHLS) in the Center for Environmental Health and Injury Control (CEHIC) is measuring 40 volatile compounds to be collected from about 1000 people. Mass spectrometry is used to measure these 40 compounds. Because of the complex analytical method and need for a large amount of data reduction by computer, about 2 h is required to process each specimen. The limited volume of whole blood available per unknown sample means that a specimen cannot be reprocessed easily or economically.

Step 1. Specification of Conditions for QC Analysis. We had two sets of 40 runs available to characterize the volatiles analytical method. The first set was run with QC materials at a higher concentration, and the second set was run with materials at a lower concentration. The calibrators for each set consisted of six different preparations. Each calibrator preparation contained from 5 to 9 different compounds, for a total of 40 identical compounds per set. For purposes of illustration, we will discuss the results for the quality control runs in which the high-concentration materials were used. We also will show results for 23 postcharacterization runs.

Step 2. Characterization Runs: Determining Estimates of the Quality Control Parameters. The figures used to illustrate our analysis of the characterization data also include postcharacterization runs that we will discuss in the next section. A composite univariate chart for all runs is shown in Figure 2. In constructing this chart, we applied a preliminary 3.5 standard deviation outlier rule to the characterization data for each compound in order to remove extreme observations. Using this rule, we removed 7 of 1600 potential observations. Though these points are included in the composite plot in Figure 2a, they and any missing observations appear as zero deviations on the respective horizontal lines of the composite plot in Figure 2b. We elucidated the relationship among the compounds included in the same quality control preparation by positioning them together in six different groups on one composite univariate plot. Data are missing for compounds **19** and **20** after run 89332C in the composite plots (Figure 2). This is because, beginning in run 89335C, the analytical standard was changed for these two compounds. The composite plots indicate that some compounds that were included in the same preparations are highly correlated. For example, the plotted points for compounds **19**, **20**, **26–28**, and **31–33**, seem to be almost parallel. These relatively high correlations can be found in Figure 7, where we see a few correlation coefficients approach unity (cf. the point for compounds **19** and **20**).

The values of the multivariate control statistic for characterization and unknowns runs that correspond to Figure 2b

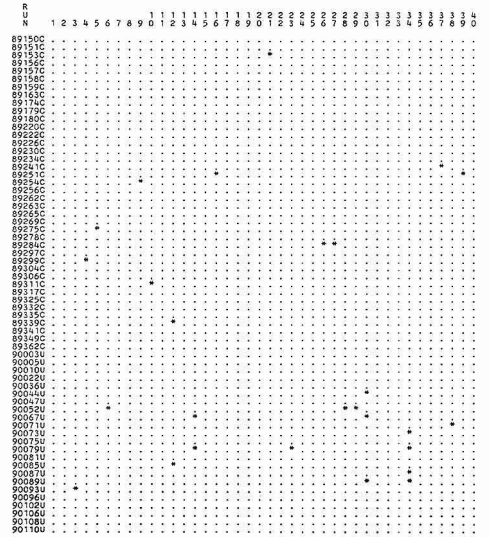

Figure 3. Variable-by-run matrix display of extreme deviations for univariate control rules. This figure shows occurrences of violations of the univariate extreme deviations rules by compound and run for 40 characterization runs and 23 runs analyzing unknowns.

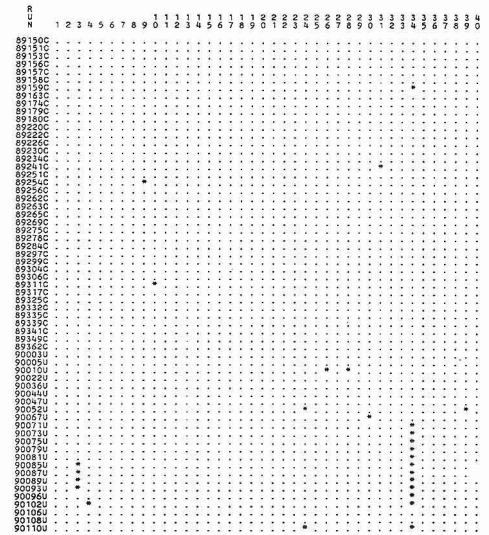

Figure 4. Variable-by-run matrix display of moderate deviations for univariate control rules. This figure shows occurrences of violations of the univariate moderate deviations rules by compound and run for 40 characterization runs and 23 runs analyzing unknowns.

are given in Figure 5. Figure 5 shows that one characterization run (89251C) has values that exceed the 95% probability level control limit (warning rule). When we applied the univariate rules to the characterization runs, we rejected 11 values on the basis of the exctreme deviations rule (Figure 3). We rejected four measurements when we applied the moderate deviations rule (Figure 4). We also identified two of these four by using the extreme deviation rule. The trend 2 rule (10 consecutive runs on one side of the mean) was violated at least

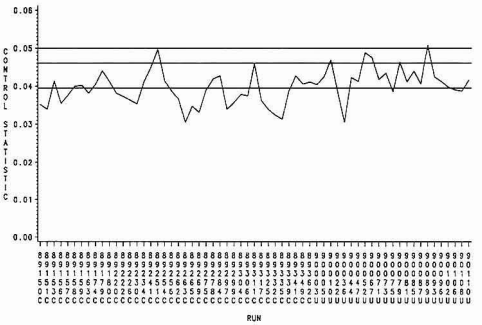

Figure 5. Quality control plot of multivariate control statistic. The values of the multivariate quality control statistic are shown for 40 characterization runs and 23 runs analyzing unknowns. Horizontal lines correspond to the 50th, 95th, and 99th estimated percentiles of the multivariate control statistic. These limits were determined on the basis of simulations by using values of the multivariate control statistic obtained from the 40 characterization runs.

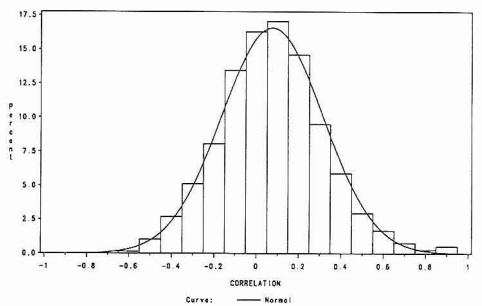

Figure 6. Histogram of pairwise correlations. All pairwise correlations determined from the 40 compounds during 40 characterization runs are included in this histogram.

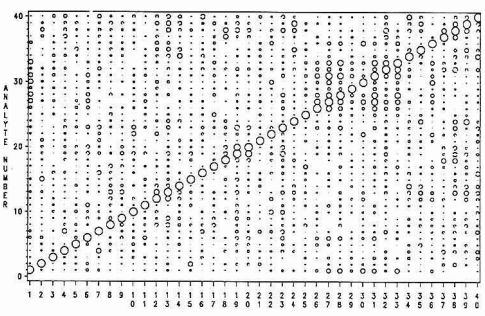

Figure 7. Matrix plot of pairwise correlations. Each pairwise correlation between two compounds is represented by a circle whose area is proportional to the magnitude of the correlation. "Full border" circles represent positive correlations, and "broken border" circles represent negative correlations. Circles on the diagonal represent correlations of plus one. The size of these circles can be used as a reference when other correlations shown on the matrix plot are being evaluated.

once for 12 different compounds. We observed two sets of violations of the trend 2 rule for compound 40; the first set was on the high side of the mean, and the second set was on the low side of the mean.

We generated pairwise correlation QC plots, similar to the one shown in Figure 8, for each pair of compounds for which

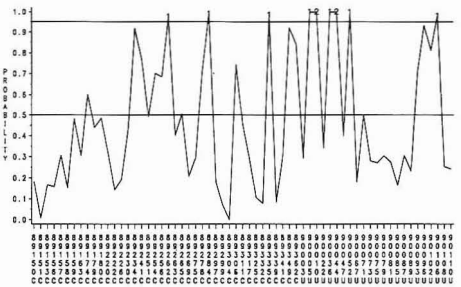

Figure 8. Quality control plot of pairwise correlations. The correlation-based probability values for the standardized deviates of compounds **16** and **38** are shown for 40 characterization runs and 23 runs of unknowns. These probability values represent one minus the probability that the observed pair of deviates behave as expected on the basis of their observed correlation during characterization runs. For example, a probability of 0.99 on the plot indicates that the relationship between the pair of compounds departs significantly in the current run from that observed during characterization. Horizontal lines represent 0.50 and 0.95 probability level control limits. The digit "1" in the plot represents a single out-of-control event. The digit "2" represents out-of-control events in two consecutive runs.

the correlation action rules (Table I) were violated at least once during the 40 characterization runs. The action rules were not violated for any pairs of compounds during the characterization runs. The probability values for compounds **26** and **27** (runs 89150C–89230C) are, with the exception of run 89174C, all below 0.5 (Figure 8). Figure 2b shows that the deviations of compounds **26** and **27** from their respective means were very small during these early characterization runs. Thus, the correlation plots and composite plots used together provide us with useful diagnostic information for the analysis of characterization data.

Step 3. Quality Control Analysis of Unknown Samples. Using the means, standard deviations, standardized deviates, and pairwise correlation estimates obtained from the 40 characterization runs, we next illustrate the CMQC method by analyzing the 23 postcharacterization runs indicated by a U suffix on the run number (Figures 2–8). The composite univariate plots in Figure 2b show that several compounds had results near 3 standard deviations above their respective means. For instance, 5 of the 10 compounds in the LE preparation group (i.e., compounds **26–35**) had extreme results on run 90010U. The values for the multivariate control statistic for the 23 runs analyzing unknowns indicate that runs 90010U, 90052U, and 90079U exceed the 95% probability level control limit and that run 90089U exceeds the 99% control limit. Therefore, run 90089U was rejected on the basis of the extreme deviation rule. In addition, runs 90082U and 90067U were rejected on the basis of the moderate deviation rule. Applying the univariate rules, we rejected one measurement for compound **39** on run 90003U because it exceeded the limits of the extreme deviation rule, and we rejected one additional measurement for compound **26** on run 90010U because it exceeded the limits imposed by the moderate deviation rule.

The extreme deviation action rule for the correlation was violated for the pair of compounds **26** and **27** during consecutive unknowns runs 90005U and 90010U and also during consecutive unknowns runs 90036U and 90044U. These results, presented in Figure 8, also indicate that the warning rules (any pair of deviates with probability values less than 0.05) were violated twice during the 23 runs of unknowns for these 2 compounds. Figure 7 shows that compounds **26** and **27** have a high positive correlation. This positive correlation is also reflected in the composite plot in Figure 2b until unknown run 90005U, at which point compound **26** has an extreme positive shift away from its mean for 2 runs, whereas compound **27** deviates only slightly from its mean during the same 2 runs. The deviation in compound **26** was sufficiently large on these two consecutive runs (i.e., 90005U and 90010U) and on two additional consecutive runs (i.e., 90036U and 90044U) to trigger the extreme deviation correlation action rule.

DISCUSSION

The design of a composite system for the simultaneous control of many variables calls for the consideration of a number of issues, some of which are common to univariate QC, some of which are unique to multivariate QC, and others which relate to problems encountered as the number of control variables increase. The issues common to univariate QC include (1) specification of the size of type I error rates and power of the control rules, (2) determination of the minimal amount of data required for reliable estimates of characterization parameters, and (3) presentation of useful graphical interpretation of the results. The issues unique to multivariate QC include (1) accounting for the correlation structure among the variables and (2) obtaining reliable estimates of multivariate test statistics as a function of the number of variables measured and the correlation structure. Additional considerations addressed by the CMQC method proposed in this report include (1) handling missing observations among different subsets of variables during characterization and unknowns runs, (2) specifying control rules that allow users to accept a run with missing variables, and (3) relating the observed values of multivariate test statistics to the results on the individual variables.

If the number of monitored variables (M) is small ($M < 5$), simple techniques such as Bonferroni adjustments to control limits or the implementation of binomial rules may be useful. These methods, however, do not lead to correct type I error rates and suffer from a loss of power as M increases. Although the type I error rates associated with T^2 (Jackson, Hotelling) and principal components (Jackson, Fisher) are correct for the multivariate case, several problems occur, when analysts apply T^2 or PC to the simultaneous control of many variables.

First, T^2 and PC are applicable only if all variables are observed in each run of unknowns. As the number of measured variables increases, the likelihood of missing data increases rapidly and, for some processes, probably approaches unity. As the demand rises for state-of-the-art measurements that are near detection or quantitation limits, missing data are almost certain in low-concentration QC samples (e.g., only 15 of 40 runs had all measurements in the characterization data presented in the previous section). This missing-data problem makes it difficult to obtain a sufficient number of characterization runs to make precise estimates of the correlation matrix.

Second, analysts using the T^2 and PC procedures reject or accept all variables in entire runs. Although this situation may be tolerable in low-cost experiments when analysts have adequate backup samples and adequate time to reanalyze them, the use of these procedures is not even feasible in many situations. Even when it is feasible, discarding entire runs when only a fraction of the measured variables are invalid causes a duplication of effort and results in the loss of data on otherwise acceptable variables.

Third, analysts have difficulty relating the outcomes of the T^2 and PC multivariate test statistic outcomes to the results observed on the individual control variables. The ability to easily make a connection between the multivariate control statistic pattern and individual variables is very important to analysts because they will not want to repeat runs without adequate justification. They also need to known which var-

iables require attention in order to bring the process under control.

The proposed CMQC method overcomes the three problems pointed out for the T^2 and PC methods. First, it does not require all the variables in a run to be observed. Although the user may set an arbitrary limit on the minimum number of observed variables for a run to be considered useful, the control rules do not impose any limits on missing data. The multivariate control statistic incorporates a correction for missing data, and therefore, its critical values do not require adjustment. Second, the CMQC method allows the users, by independently applying univariate and pairwise control rules, to reject a fraction of the observed variables without discarding the entire run. The rationale for using these rules is that maverick events may affect only a fraction of the measured variables. As we discussed above, we could not place all materials in a single QC preparation; five different QC preparations were required. Thus, using our system analysts could reject any similar maverick measurements associated with the same QC preparation as a group. Third, the CMQC incorporates several unique graphical tools to aid the analyst in interpreting highly dimensional multivariate data. These tools include the composite univariate plot, which allows the user to quickly spot trends, parallelism, and maverick events for all variables. The pariwise correlation control charts are valuable for identifying specific shifts in correlation that could not be detected with only a single-parameter control system like T^2. In addition, the matrix plot is useful for identifying pairs of variables whose correlations are unusual.

In summary, the proposed multivariate control procedure solves several common problems with both univariate and multivariate QC. It also deals with a number of issues that are encountered as the number of control variables increase.

Certain aspects of CMQC are not addressed here. These include (1) the determination of the distribution and critical values for the multivariate statistic as a function of the number of QC variables and the correlation structure; (2) the definition and determination of the multivariate statistical power of the method as a function of the number of QC variables, the correlation structure, and the number of missing variables; and (3) the robustness of the method to missing observations during characterization or analytical runs. Also, a comparison of the MCS statistic results to the T^2 or PC methods would be desirable. The results of simulation analyses on these issues will be presented in a separate paper.

LITERATURE CITED

(1) Westgard, J. O.; Barry, P. L.; Hunt, M. R. *Clin. Chem.* **1981**, *27*, 493–501.
(2) Jackson, J. E. *Ind. Quality Control* **1956**, *12* (7), 4–8.
(3) Hotelling, H. *Multivariate Quality Control, Techniques of Statistical Analysis*; McGraw-Hill: New York, 1947.
(4) Hotelling, H. *Proceedings of the Second Berkeley Symposium in Mathematical Statistics and Probability*; University of California Press: Berkeley, 1950; pp 23–41.
(5) Jackson, J. E.; Morris, H. *J. Am. Stat. Assoc.* **1957**, *52*, 186–199.
(6) Jackson, J. E. *Technometrics* **1959**, *1*, 359–377.
(7) Jackson, J. E.; Mudholkar, G. S. *Technometrics* **1979**, *21*, 341–349.
(8) Fisher, M. T.; Lee, J.; Mara, M. K. *Analyst* **1986**, *3*, 1225–1229.
(9) Murphy, B. J. *The Statistician* **1987**, *36*, 571–583.
(10) Morrison, D. F. *Multivariate Statistical Methods*; McGraw-Hill: New York, 1967; pp 120–121.

RECEIVED for review October 19, 1990. Accepted April 18, 1991.

Interactive Self-Modeling Mixture Analysis

Willem Windig* and Jean Guilment

Eastman Kodak Company, Rochester, New York 14652-3712

In the analytical environment, spectral data resulting from the analysis of samples often represent mixtures. To extract information about pure components often is a major problem, especially when reference spectra are not available. For this type of problem, self-modeling mixture analysis techniques have been developed. Although successful commercial applications have been developed, the application of these techniques to complex data sets requires skilled operators. Furthermore, no general purpose software is available. In order to make self-modeling mixture analysis more accessible, a new method has been developed. For the approach described here, all the intermediate steps can be presented straightforwardly in the form of spectra, and it is possible to direct the procedure by using chemical knowledge of the samples. Examples will be shown of Raman spectroscopic data of a reaction, where spectra of intermediates are extracted, and of FT-IR microscopic data of a polymer laminate, where it will be shown that spectra of layers below the resolution of the FT-IR microscope can be calculated.

INTRODUCTION

Despite the use of hyphenated and/or high-resolution analytical instruments, the resulting spectral data often represent mixtures of several components. Furthermore, reference spectra are not always available to resolve the mixture data by techniques such as least squares or spectral subtraction. For this type of problem, self-modeling mixture analysis techniques have been developed. Generally, the term curve resolution is used for approaches like the one discussed in this paper. We would like to limit the use of the term curve resolution, where the continuous character of the concentration profile, such as the data that result from hyphenated instruments, is used in the algorithm, and use of term self-modeling mixture for algorithms where no such assumptions about the concentration profiles are used. For an excellent review of factor analysis based mixture analysis, see the recent review of Gemperline and Hamilton (*1*, *2*). For a more geometrically oriented explanation, see ref 3. Most of these self-modeling techniques are based on principal component analysis.

Although principal component analysis is currently the state-of-the-art approach for self-modeling curve resolution, its use is mainly limited to the use of the resolution of data of hyphenated techniques, e.g., Hewlett-Packard's Quickres (Infometrix, Inc., 2200 Sixth Ave, Suite 833, Seattle, WA 98121) (*4*), which works with diode-array chromatographic detectors. Quickres is limited to resolving two components, however. Another curve resolution related program is Beckman's peak purity program (Beckman Instruments, Inc., Altex

0003-2700/91/0363-1425$02.50/0 © 1991 American Chemical Society

Division, San Ramon, CA), which determines how may components there are present underneath an HPLC peak. It has to be mentioned that in the area of multivariate calibration factor analysis based techniques such as principal component regression and related techniques such as partial least squares are used successfully on a routine basis.

For more complex data sets, user interaction is required in order to obtain the proper resolution of the data. This is especially true for pure variable based methods, because of their inherent susceptibility to noise (*5*). Furthermore, pure variables may describe unwanted features in the data, such as peak shifts.

The new approach is a pure variable based method (*6*). In spectroscopic terms, a pure variable (e.g., a wavenumber for FT-IR, etc.) is a variable of which the intensity is due to only one of the components of the mixture(s) under consideration. For the data sets discussed in this paper, it is assumed that pure variables are present. In contrast to current methods, the presence of a pure variable will be determined without the use of principal component analysis. It has been shown before that for curve resolution the pure variables can be determined by simple means (*7*). For the new approach described here, all the intermediate steps can be presented in the form of spectra, and it is possible to direct the search procedure for the pure variables, which makes it possible to use the human pattern recognition capabilities to judge and direct the process. Compared to the previously published factor analysis based ISMA technique (interactive self-modeling multivariate analysis) (*5*), this approach is relatively simple to use and therefore will be referred to as the SIMPLISMA approach: simple-to-use interactive self-modeling mixture analysis. The method will be evaluated by comparing it to several published techniques. Furthermore, an example of the resolving of the data obtained by scanning a polymer laminate (X-ray screen) by FT-IR microscopy will be given.

MATERIALS AND METHODS

The first data set results from a study of the formation of silica glasses from solutions of tetraalkoxysilanes by the sol–gel process (*8*). In order to get a better understanding of the process, the time dependence of the sol–gel hydrolysis and condensation of $Si(OCH_3)_4$ (tetramethyl orthosilicate, abbreviated TMOS) in aqueous methanol is studied. The starting material TMOS has a reported Raman shift at 644 cm^{-1}. The products of this reaction are (1) hydrolysis products $Si(OCH_3)_n(OH)_{4-n}$ for which the Raman shifts for n = 3, 2, and 1 are 673, 696, and 726 cm^{-1}, respectively, and (2) condensation products $Si(OSi)_m(OR^*)_3$ for which R* is CH_3 or H. The Raman shifts for m = 1 and 2 are 608 (shoulder at 586) and 525 cm^{-1}, respectively. These products will be indicated as the first and second condensation products.

The results previously obtained by the ISMA approach (*5*) will be a basis for the evaluation of the SIMPLISMA approach. This data set will be referred to as the TMOS data set.

Finally, data obtained by scanning a cross section of an X-ray screen by FT-IR microscopy are shown. It is a study into the feasibility of using self-modeling mixture analysis to obtain information about the different polymer layers of the X-ray screen without a mechanical separation of the screen. The spectra were recorded by using a Digilab IR microscope coupled with an FTS 60 Digilab FT-IR spectrometer. For each spectrum, the observed area was 100 × 120 μm, and the samples were moved with a 10-μm-step XY motorized stage.

THEORY

Determination of the First Pure Variable. The method will be explained by using the mixture data set presented in Table I. A plot of this data set in a three-dimensional axis system is given in Figure 1. The data points lie in a plane, because the sum of the three concentrations is constant, i.e., one, which causes the loss of 1 degree of freedom.

In practice, a mixture data set will consist of hundreds of variables, e.g., m/z values for MS. Assuming a spectral mixture data set with the same composition is given in Table I, the variables will have contributions from one or more of the components. As a result, every variable will be a positive linear combination of the three-component axes. As a consequence, each variable will be bracketed by the three-component axes as presented in Figure 1. If each of these variables is presented by a vector the length of which is limited by the triangular plane, the projection of these variables onto the triangle will result in Figure 2, similar to the triangular three-component mixture plots (*3, 5*). The position of a vector in this triangle gives a direct measure of the contributions of the three components. A variable that has only contributions from one of the components, a so-called pure variable, will coincide with the component axes. The first pure variable can be found by determining the vector with the largest length in the triangular plot. It has to be stressed that the presence of pure components in the data set is not required to obtain this type of result; the only requirement is the presence of pure variables. Since the lengths of the variable vectors in this triangle are determined by their purity, it is possible to plot

Table I. Composition of the Mixtures in Relative Concentrations

	rel comp concns		
mixture no.	A	B	C
1	0.34	0.34	0.32
2	0.44	0.23	0.33
3	0.48	0.25	0.27
4	0.20	0.35	0.45
5	0.21	0.51	0.28
6	0.22	0.54	0.24
7	0.44	0.37	0.19
8	0.17	0.54	0.29
9	0.33	0.05	0.62
10	0.19	0.37	0.44
11	1.00	0.00	0.00
12	0.00	1.00	0.00
13	0.00	0.00	1.00

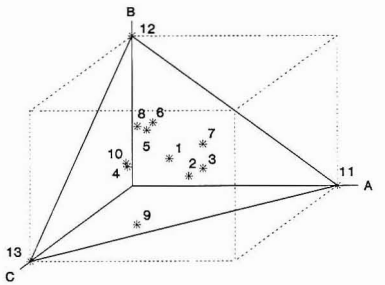

Figure 1. Three-dimensional plot of the data presented in Table I. Due to the fact that the concentrations of the three components add up to one, all the points representing the mixtures lie in a plane.

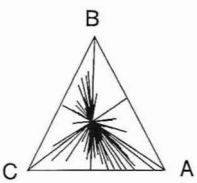

Figure 2. Projection of vectors representing variables (e.g., wavenumbers) for a spectral data set of a three-component mixture such as presented in Table I and Figure 1. Pure variables have a relatively large length.

a spectrum that represents the purity, using the lengths of these vectors for the intensity axis: a variable with a relatively high intensity will be relatively pure; a variable with a low intensity will have contributions from several components. Furthermore, as mentioned above, the variable with the highest intensity is the first pure variable. The presentation of purity values in the form of a spectrum is more directly related to the original data, lends itself better to an interactive approach than the loading type of plots such as shown in Figure 2, and forms the basis for the SIMPLISMA approach. Although the plot shown in Figure 2 is based on principal component analysis, the lengths (purity) of the variable vectors in the triangle can be calculated without the use of principal component analysis, as will be explained below.

The data matrix is represented by **D**, size $v \times c$, where v is the number of variables and c the number of cases (spectra). The length λ_i of a variable i is

$$\lambda_i = ((1/c)\sum_{j=1}^{c}(d_{i,j})^2)^{1/2} \quad (1)$$

The relation between the length, the mean, and the standard deviation is as follows:

$$\lambda_i^2 = \mu_i^2 + \sigma_i^2 \quad (2)$$

where μ_i is the mean of variable i

$$\mu_i = (1/c)\sum_{j=1}^{c} d_{i,j} \quad (3)$$

and σ_i is the standard deviation of variable i

$$\sigma_i = ((1/c)\sum_{j=1}^{c}(d_{i,j} - \mu_i)^2)^{1/2} \quad (4)$$

The vector representation of the relation described by eq 2 is a right triangle with sides σ and μ and hypotenuse λ. Realizing that the mean of the data set lies in the triangle (see Figure 1), it is possible to rationalize the relation between Figure 1 and a right triangle. The vector μ represents the distance between the origin of that particular variable and the triangular plane; the vector λ represents the vector of that variable with length λ. The vector σ now represents the contribution of that variable in the mixture triangle. The value of σ does not represent the purity as presented in Figure 2 though, since every variable vector will have a different length. A proper way to scale the variable vectors is one that limits the length of the vectors by the triangular plane as given in Figure 1. Variables scaled in this fashion will project within the triangle, as in Figure 2. As a consequence, the purity of variable i as represented by a right triangle is defined by

$$p_{i,1} = \sigma_i/\mu_i \quad (5)$$

The second subscript of the purity value p indicates that this is the first purity value. As will be shown below, other purity values will be calculated. The purity value represents $\tan \gamma$, where γ respresents the angle between vectors μ_i and λ_i.

As will be shown later in an example, problems may arise for variables with a low noise range intensity. The value for $p_{i,1}$ may be high due to a value for μ_i approaching zero. In order to correct for this, the purity is redefined by the following adaption of eq 5:

$$p_{i,1} = \sigma_i/(\mu_i + \alpha) \quad (6)$$

If α has a relatively low value with respect to μ_i (i.e., for high values of μ_i), the effect will be negligible, but for low values of μ_i (in the noise range), the effect is that this noise correction term will make the purity value lower, which is exactly what is needed in order to correct for noise. This simple but effective procedure is similar to the one described by Ozeki et al. (*9*).

In practice, all the $p_{i,1}$ values are plotted in the form of a spectrum, the so-called purity spectrum, in which the wavenumber with the highest intensity represents the first pure variable. This visualization of the purity of the variables facilitates the detection of pure variables caused by unwanted features in the data set such as noise, as will be shown later. Because of the scaling procedures involved, problems may arise when one compares the purity spectrum with the original data. In order to establish a link between the original data and the purity spectrum, the standard deviation spectrum appears to be useful, since it has a clear relation with the original data as well as the purity spectrum, as will be shown with examples.

At this point, the relation between the purity value as defined in eq 5 and purity values mentioned in literature need to be established. The Knorr and Futrell (*6*) method and Malinowski's key-set method (*10*, *11*) define the first pure variable as the one with the lowest projection in the first principal component, after scaling the loadings by their lengths. This is equivalent to $\cos \gamma$ in a right triangle. There is also a relation with a method developed by Vandeginste et al., in order to determine the purity of a spectrum (*12*). In this work, the purest ("simplest") spectrum is defined as the one with the smallest area norm ratio. Calculating the mean and length of rows instead of columns of the matrix results in the area and the norm. As a consequence, the area norm ratio is $(\cos \gamma)^{-1}$. Although the cosine and tangent are approximately the same for small angles, it will be clear from the knowledge of these geometrical functions that the tangent will give more distinct purity values.

Summarizing, it is possible to calculate the length of the projection of variable vectors onto the triangular plane, as graphically represented in Figure 2, by applying eq 5. This length equals the purity as defined in eq 5 and as such can be used to determine the first pure variable by selecting the one with the highest length.

Determination of the Next Pure Variables. The problem now is how to determine the second pure variable. Because the pure variables are variables that bracket all the other variables in the configuration illustrated by Figure 1, the next pure variable is the one that is most independent of the first pure variable. It is also important to determine the rank of the data matrix, since the rank is determined by the number of components in the data set. The independence of variables and the rank of a matrix can be determined by a determinant-based function. The use of determinants is also the basis of Malinowski's key-set method (*10*, *11*).

The determinant-based function is calculated as follows. First, the correlation around the origin (COO) (*13*) matrix needs to be calculated. The COO dispersion matrix has been chosen since it gives all the variables an equal contribution in the calculations. If this is not done, the determinant is proportional not only to the independence of the variables but also to the length of the variables. In order to calculate the COO matrix, the data matrix first needs to be scaled by the length.

$$d(\lambda)_{i,j} = d_{i,j}/\lambda_i \quad (7)$$

Again, a problem may arise for variables with very low intensities. In order to give variables with a low intensity and, as a consequence, a low length, the same α is used to correct for low intensity variables in eq 6. As a result, eq 7 is redefined as (see eq 2)

$$d(\lambda)_{i,j} = d_{i,j}/(\mu_i^2 + (\sigma_i + \alpha)^2)^{1/2} \quad (8)$$

The COO matrix now equals

$$\mathbf{C} = (1/c)D(\lambda)D(\lambda)^{\mathrm{T}} \quad (9)$$

As a next step, the following determinant is calculated for variable i:

$$w_{i,2} = \begin{vmatrix} c_{i,i} & c_{i,p_1} \\ c_{p_1,i} & c_{p_1,p_1} \end{vmatrix} \quad (10)$$

The index p_1 represents the index of the first pure variable in the COO matrix.

The use of a value 2 for the second subscript rather than 1 will be explained below. The values of $w_{i,2}$ will be proportional to the same measure as to which variables, i and p_1, are independent. This can be rationalized by knowing that the determinant calculates the surface area of a parallelogram defined by the row (or column) vectors of the elements of **C** given in eq 10. If variables are highly correlated, the angle between the vector representation of these variables will be small, which will result in a small determinant (surface of parallelogram) defined by these vectors, with a minimum value of 0. Variables that don't have any relation with each other have a maximum value of 1, since the diagonal elements of the matrix in eqs 8 and 9 equal 1 (due to the length scaling, if α equals 0). As a consequence, variables highly correlated with the pure variable have a value for $w_{i,2}$ close to 0, while variables that are dissimilar to the pure variable have a high value.

These values of the determinants described above can in principle be used to determine the next pure variable. The determinant does not express the purity, however. For example, a variable that is shared by the three components as illustrated in Figure 1 will have an intermediate value in the determinant calculation, while it will have a minimal value in the purity calculations. Therefore, the determinant spectrum is used as a weight function for the purity spectrum. As a consequence, the elements of the second purity spectrum now become

$$p_{i,2} = (\sigma_i/(\mu_i + \alpha))w_{i,2} \quad (11)$$

The resulting spectrum is called the second purity spectrum. The equation for the determinant in the general case for $i \geq 2$ is as follows:

$$w_{i,j} = \begin{vmatrix} c_{i,i} & c_{i,p_1} & \cdots & c_{i,p_{j-1}} \\ c_{p_1,i} & c_{p_1,p_1} & \cdots & c_{p_1,p_{j-1}} \\ \cdots & \cdots & \cdots & \cdots \\ \cdots & \cdots & \cdots & \cdots \\ c_{p_{j-1},i} & \cdots & \cdots & c_{p_{j-1},p_{j-1}} \end{vmatrix} \quad (12)$$

The index i represents the variable for which the determinant is calculated; the index j indicates that index of the pure variable for which this determinant is calculated. The indices p_n represent the indices of the pure variables determined until now; i.e., p_1 represents the index of the frist pure variable in the COO matrix, p_2 represents the index of the second pure variable in the COO matrix, etc.

In a manner similar to eq 10, the general formulation for the purity spectrum is

$$p_{i,j} = (\sigma_i/(\mu_i + \alpha))w_{i,j} \quad (13)$$

The equation for the standard deviation spectrum is

$$s_{i,j} = \sigma_i w_{i,j} \quad (14)$$

At this point, $w_{i,1}$ needs to be defined. The maximum value for the determinants equals the diagonal elements of the COO matrix. These values can be considered to be the values of the determinant-based weight function before any pure variables have been determined in order to make eq 13 also valid for $j = 1$. With the correction factor α included, the values for $w_{i,1}$ then become

$$w_{i,1} = \lambda_i^2/(\mu_i^2 + (\sigma_i + \alpha)^2) \quad (15)$$

Determination of the Number of Components. At this point, it needs to be discussed how to determine whether the pure variables selected so far account for all the components or if there is more information left. If, for example, two pure variables are representative of the whole mixture system, all other variables in the data set will be linear combinations of the two pure variables, which will result in zero values for the determinant function introduced in eq 12 for the value $j = 3$. As a consequence, the resulting purity and standard deviation spectra, eqs 13 and 14, should also result in zero values. In practice, the value will have a certain positive value due to noise. A possible candidate for determining the rank of the system after determining j pure variables is based on the relative total intensity of the standard deviation spectra, since the standard deviation spectra have the closest relation to the original data, as will be shown with examples.

$$R_{sj} = 100\sum_{i=1}^{v} s_{i,j}/\sum_{i=1}^{v} s_{i,1} \quad (16)$$

This function will have a maximum value of 100, which then is the value before any pure variable has been determined. As a consequence, the values can be considered as relative values with respect to the standard deviation spectrum prior to extracting pure variables. The ratio of the successive values for this function facilitates this process.

$$R_{rj} = R_{sj}/R_{s(j+1)} \quad (17)$$

Since the value of R_{sj} becomes close to 0 after using the proper number of pure variables, the value for this function will be relatively high after determining the proper number of pure variables. At this point, these functions are purely empirical. The total intensities of the spectra as a diagnostic tool make intuitive sense but need to be used in combination with the visual judgement of the purity and standard deviation spectrum. The development of a statistically based function is the subject of the further development of SIMPLISMA. Furthermore, the visual evaluation of the data will be shown to facilitate the determination of the number of components.

Resolution into Spectra and Concentrations. Once the pure variables have been determined, the data set can be resolved into the pure components and their contributions in the original spectra. The data matrix **D** can be expressed as a mixture system by the following equation:

$$\mathbf{D}^T = \mathbf{CP} \quad (18)$$

where $\mathbf{D}^T$ (size $c \times v$) contains mixture spectra in its rows. The matrix **C** (size $c \times n$), where n is the number of pure components, contains the relative amount of the pure components in the mixture spectra in its columns, and **P** (size $n \times v$) contains the (unknown) spectra of the pure components in its rows. For the pure variable approach, the intensities of the pure variables in the spectra in **D** are used in **C**. As a consequence, $\mathbf{D}^T$ and **C** are known, and **P** can be resolved by a least-squares method (*6*).

$$\mathbf{P} = (\mathbf{C}^T\mathbf{C})^{-1}\mathbf{C}^T\mathbf{D}^T \quad (19)$$

Assuming that every component results in the same response in the instrument, concentrations can be calculated based on spectra in **P** that are normalized. This normalization procedure is described by

$$f_i = \sum_{j=1}^{v} p_{i,j} \quad (20)$$

$$\mathbf{Q} = \mathbf{NP} \quad (21)$$

The inverse values of f_i are used for diagonal elements of the matrix N, which then can be used to normalize the spectra in **P**. **Q** (size $n \times v$) contains the normalized spectra. Although the intensities of the pure variables (after correcting for the normalization procedure described above) can be used for the

CORRECTION

corrected 24 Dec. 91

Composite Multivariate Quality Control Using a System of Univariate, Bivariate, and Multivariate Quality Control Rules

S. J. Smith, S. P. Caudill, J. L. Pirkle, and D. L. Ashley (*Anal. Chem.* **1991**, *63*, 1419–1425).

The second equation on p 1420 is incorrect. It should read

$$[\log [\sum d^2 + K]]/n \qquad \text{for } 0 < K < n$$

On lines 10 and 11 directly below the equation, $(K - 1)/K$ and $K - 1$ should both be replaced by K.

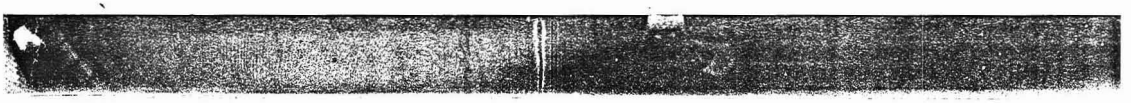

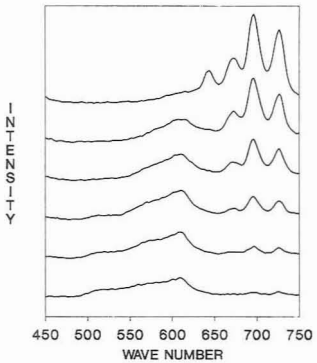

Figure 3. Sample of the TMOS Raman spectra. The time sequence goes from top to bottom.

concentrations, it was decided to obtain the concentrations by a least-squares method, since this results in a noise elimination similar to principal component analysis. Applying the same least-squares approach as described in eq 18, the least-squares approximation for the concentrations is given by

$$\mathbf{A} = (\mathbf{D}^T\mathbf{D})^{-1}\mathbf{D}^T\mathbf{Q}^T \qquad (22)$$

$\mathbf{A}$ (size $c \times n$) now contains the concentrations of the pure components in the mixture spectra.

RESULTS AND DISCUSSION

The technique was extensively evaluated by using data sets described by Ritter et al. (*14*). It appeared that the results were identical, i.e., the pure variables were identical, and the extracted spectra and concentration profiles are identical within round-off errors. Next, the TMOS data set is evaluated in order to compare the SIMPLISMA method with the previously describe factor-analysis-based self-modeling mixture analysis ISMA approach (*5*). A sample of the spectra is given in Figure 3. The first purity spectrum is given in Figure 4A. This spectrum is based on a value of zero for α and thus represents the ratio of the mean and the standard deviations; see eq 6. It will be clear that the similarity of this purity spectrum to the original spectra is limited. Therefore, the standard deviation spectrum is also shown; see Figure 4B, which has a well-defined relation with the purity spectrum. The maximum intensity in the purity spectrum is at 700 cm^{-1}, which therefore is the first pure variable. The intensities of this wavenumber form a smooth curve (not shown), as can be expected from a time-resolved data set, and is accepted as the first pure variable. After eliminating the effect of the first pure variable by using eqs 7–11, the second purity and second standard deviation spectra are the ones given in Figure 4c,d. For the spectroscopist, it will be clear that the first pure variable represents the hydrolysis products, since the three peaks considered to be typical for the hydrolysis products completely disappear after the selection of the first pure variable. Although the determinant-based function (eq 10) may not be easy to understand for a routine user, the effect of the elimination of the component described by the first pure variable makes intuitive sense. The second purity and standard deviation spectra result in the selection of the next pure variable, i.e., 516 cm^{-1}, which is accepted as the second pure variable. The resulting third purity and standard deviation spectra (eqs 12–14, respectively) are given in Figure 4E,F. For the spectroscopist the differences between the second purity/standard deviation spectrum and the third purity/standard deviation spectrum indicate that the second pure variable represented the second condensation product in this reaction. The maximum in the third purity spectrum is at 478 cm^{-1}. The peak that displays this maximum has an odd shape, however. Furthermore, the standard deviation spectrum in Figure 4F shows that this wavenumber is in a

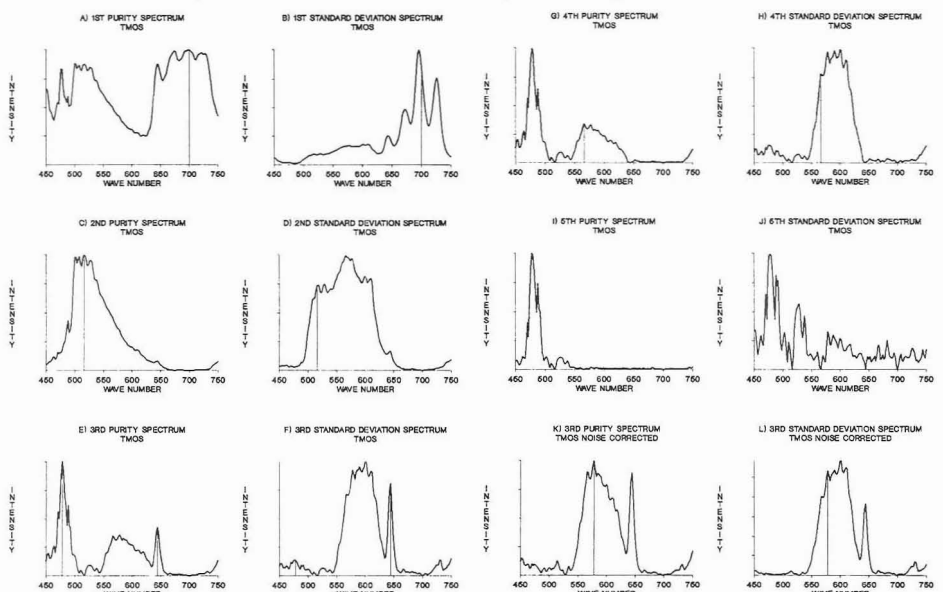

Figure 4. Purity (A, C, E, G, I) and standard deviation (B, D, F, H, J) spectra resulting from the pure variable search by the SIMPLISMA approach with no noise correction. The pure variables are indicated by lines in the spectra. The effect of noise correction for the third purity spectrum is shown in K. The associated standard deviation spectrum is given in L.

Table II. Values of Functions To Determine the Rank of the TMOS Data Set

R_e	R_r	R_e	R_r
100.0000	9.1018	0.0091	97.7223
10.9868	16.8073	0.0001	
0.6737	72.2108		

low-intensity area, which may indicate that this pure variable is caused by noise, which again shows the use of the standard deviation spectrum. A plot of the intensities at 478 cm^{-1} versus time (not shown) shows erratic behavior, while a more or less continuous curve would be expected from a time-resolved reaction. In combination with the low intensity, such erratic behavior is a strong indication that this is a noise peak. It is possible in SIMPLISMA to inactivate the peak around wavenumber 478 cm^{-1} using a cursor, after which the proper pure variable at 644 cm^{-1} is selected, which represents the original starting material TMOS. The fourth purity and standard deviation spectra are given in Figure 4G,H. Comparison with the third and fourth purity/standard deviation spectra shows that the third pure variable represents the starting material TMOS. Ignoring the lower wavenumber range again in the fourth purity spectrum results in the selection of a pure variable selected at 566 cm^{-1}, which represents the first condensation product. After eliminating the effect of this pure variable, the fifth purity spectrum and standard deviation spectrum, Figure 4I,J, clearly consist of only noise, which shows that the process is complete. This is also confirmed by the diagnostic values presented in Table II. It is clear that the visual representation of the SIMPLISMA approach facilitates the determination of the number of components in a data set.

It is now possible to resolve the data set, using the pure variables information. Before this is done, a closer look is taken at the noise problem which interfered with the pure variable search described above. The purity value was high in the region around 478 cm^{-1}, while it was relatively low in the standard deviation spectrum (see Figure 4E,F) from which we can conclude that the mean value of this variable is low. This low mean value is then very likely the cause of the high-purity value. At this point, the use of a noise correction using α seems appropriate. In practice, a value for α of 5% of the maximum of all the mean values appeared to be appropriate. For the TMOS data set, this results in a third purity and standard deviation spectrum as given in Figure 4K,L. Comparison with Figure 4E,F shows that the noise problem is completely eliminated. Due to the intensity changes in the spectra, the third pure variable represents the first condensation product instead of the TMOS. As a consequence, the fourth pure variable will now describe the TMOS component. For the resolution of the data by the eqs 19–22, the pure variables for the noise corrected data set are used, which are slightly different from the ones mentioned above. Although it is possible to eliminate the problematic peak in this case by using an appropriate value for α, as was shown above, for complicated data, a combination of a noise correction by using α and the inactivation proved of certain parts of the spectra appears to be necessary. It is interesting to note that this need for an interactive approach was previously indicated in the papers by Ritter et al. (*14*) and by Knorr and Futrell (*6*). After obtaining the initial results on a mass spectral data set, it was necessary to delete m/z 28 from the original data set, due to an N_2 leak, in order to obtain the proper data analysis results. The spectra and concentration profiles resulting from these pure variables are given in Figures 5 and 6, respectively. Comparison with the results obtained before using the ISMA approach shows a clear similarity.

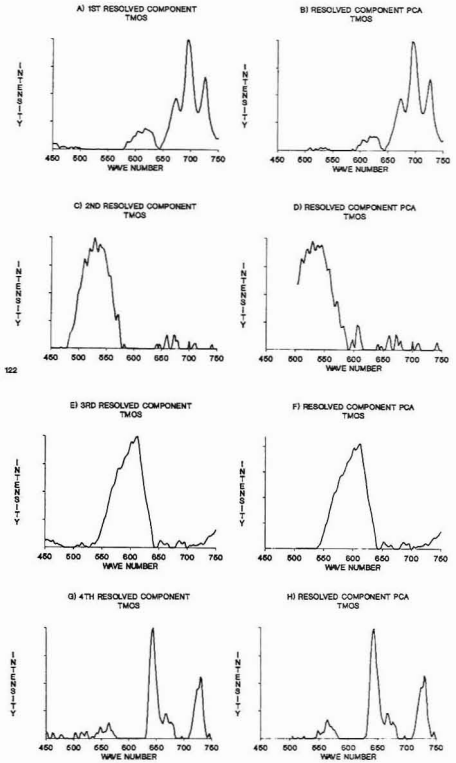

Figure 5. Spectra (A, C, E, G) based on the pure variables as extracted by the SIMPLISMA approach. For comparison, the spectra (B, D, F, H) extracted by the principal component analysis based ISMA approach are given. The results are almost identical.

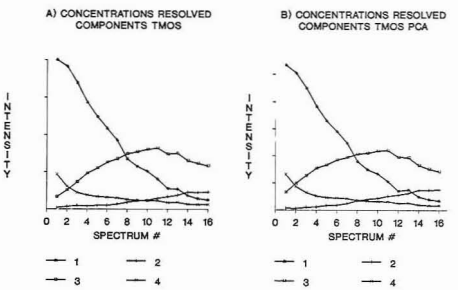

Figure 6. Concentration profiles as extracted by the SIMPLISMA approach (A) and by the ISMA approach (B). No significant differences can be observed.

The final example is the X-ray screen data set. For a schematic of the cross section of the X-ray screen, see Figure 7. The expected profile for the components is also given. Note that the IR spot is larger than several of the layers. The profile of PVC is given rather than of PVA/PVC because it is expected that SIMPLISMA separates the PVA as a separate component, since it is also present in another layer. Since scanning the edges from the screen gives problems in the

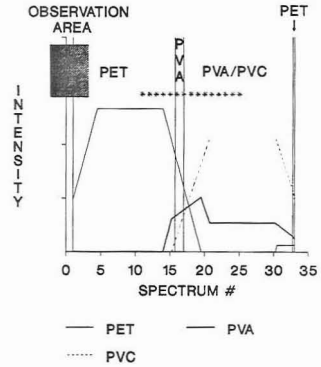

Figure 7. Schematic representation of the X-ray screen together with an estimate of the concentration profiles of the components. The size of the observation area is indicated by a dashed square. The data points used for the analysis are indicated by *.

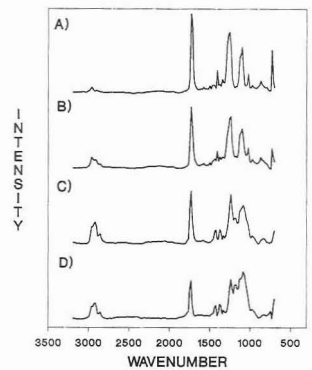

Figure 8. Sample of the obtained spectra of the X-ray screen.

Table III. Values of Functions To Determine the Rank of the X-ray Screen Data Set

R_e	R_r	R_e	R_r
100.0000	4.8269	0.5616	77.6195
20.7172	36.8885	0.0072	

spectra and in order to give a relative high weight to the middle layer, only the range indicated in Figure 7 was scanned. A sample of the obtained spectra is given in Figure 8. For many applications, the standard deviation spectra suffice to resolve the mixture spectra into their components, as will be demonstrated by using this data set. The noise level α is set at 5% of the maximum mean value of all the variables (wavenumbers). The pure-variable selection is indicated in Figure 9. After selecting three pure variables, the diagnostic values indicate that the process may be finished (see Table III), although there are spectrum-like features in Figure 9D. The pure variable indicated in the fourth standard deviation spectrum appears to be in a range of the spectrum that does not contain any information; compare with Figure 8. Furthermore, resolving the mixtures using this fourth pure variable results in spectra with a significant amount of negative intensities. This knowledge is a strong indication that the rank of the data is 3. This example shows that determining the rank of a data set is still problematic, although it is facilitated by the spectral displays. The spectra of the pure components

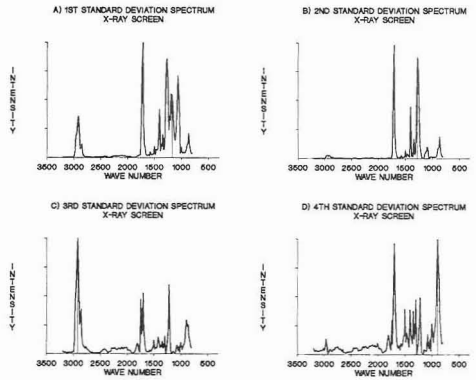

Figure 9. Standard deviation spectra of the X-ray screen data with the pure variables selected indicated by lines.

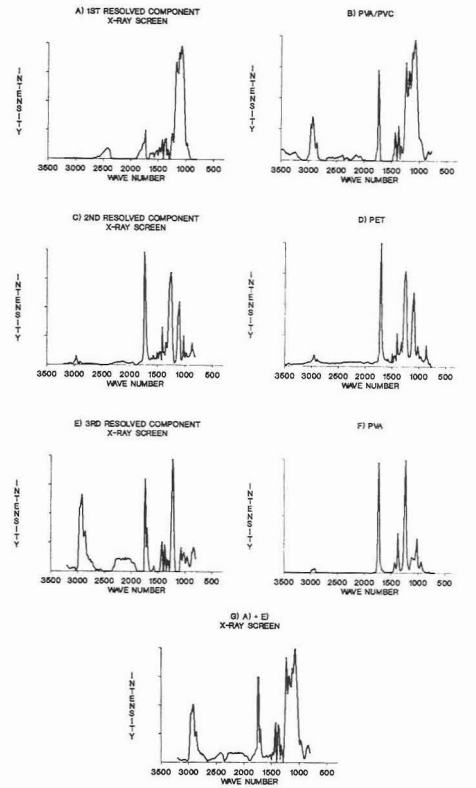

Figure 10. Resolved spectra (A, C, E). The spectra of the mechanically separated layers are given in B, D, and F. The extracted PVC (A) and PVA (E) were combined into a PVA/PVC spectrum presented in G, which has clear similarities with the model spectrum in B.

and the associated concentrations are given in Figure 10 and Figure 11, respectively.

The first extracted spectrum in Figure 10A has similarities with the model spectrum labeled PVA/PVC in Figure 10B. The spectrum in Figure 10B is more complex in nature because of the phosphor in the screen. Furthermore, since PVA

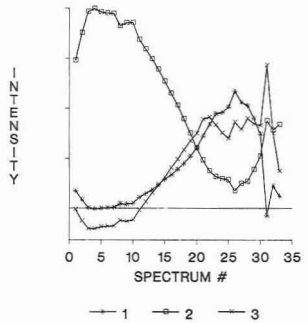

Figure 11. Concentration profiles of the components, as calculated by the SIMPLISMA approach. The pattern labeled 1 refers to the first spectrum in Figure 10, etc. The patterns are clearly similar to the estimated profiles in Figure 7. Especially note the maximum (around spectrum number 20), which is due to the middle PVA layer. The thickness of this layer is clearly below the resolution of the observation area.

is a separate component in the X-ray screen, it is expected that this first extracted spectrum represents PVA/PCV (plus phosphor) minus PVA. In order to demonstrate this, the other extracted components need to be discussed first. The second resolved component in Figure 10C clearly resembles the model spectrum of PET in Figure 10D. This is not so surprising, since PET is present in a pure form within the resolution of the IR spot in the screen. The last resolved component, Figure 10E, has similarities to PVA, Figure 10F. There is a contribution of the methyl group around 2900 cm^{-1}, which is more intense than expected, although PVA is the only source of the methyl group. Possible explanations for this are scattering due to the phosphor and the fact that PVA/PVC is not really a mixture of PVA and PVC, but a copolymer. With this extracted PVA spectrum available, it is now possible to test the hypothesis that the first resolved component "lacks" PVA. The sum of the "PVC" spectrum (Figure 10A) and the PVA spectrum (Figure 10E) results in Figure 10G, which is almost identical with the model spectrum of PVA/PVC in Figure 10B. These results show that self-modeling mixture analysis can give an estimate of the components in a polymer laminate, which have a thickness below the resolution of the FT-IR microscope.

The concentration profiles of the extracted components in Figure 11 include all the spectra. As mentioned above, only some of the spectra were used for the data analysis. It is possible, however, to calculate the least-squares contribution of all the spectra by the proper use of eq 22. Since the edges of the laminate give problems in the spectra, the first few and the last few spectra have to be viewed with caution. One can see that the curves closely match the expected profiles as given in Figure 7. The estimated profiles in Figure 7 are based on the assumption that equal weights of polymers result in equal spectral responses, which is not very likely the case. This is the likely explanation for the differences between the magnitude of the profiles in Figure 4 and Figure 11. It is interesting to note that the PVA concentration has a somewhat jagged behavior in the PVA/PVC layer. The probable cause of this is the presence of the phosphor particles. The negative intensities in the PVA profile are very likely due to negative intensities in the original data set, caused by a less than optimal base-line correction procedure.

CONCLUSION

The results of the SIMPLISMA approach shown above and of several other data sets (not shown) are consistently comparable with the results of the principal component analysis ISMA approach. An advantage of the SIMPLISMA approach is that it displays all the intermediate results in the form of spectra, which gives a "spectroscopic feeling" and makes intuitive sense. This approach makes it also possible to use SIMPLISMA in a responsible way without knowledge of multivariate statistics. On the other hand, since SIMPLISMA is based on multivariate principles, it can be used as an educative tool to introduce people to multivariate techniques.

It has to be stressed that the user interaction with SIMPLISMA does not consist of manipulation of the data: inactivating a certain wavenumber region in the TMOS for a value of zero for α data was appropriate, since it caused a noise problem. Furthermore, the availability of the purity and standard deviation spectra facilitated the determination of the number of components in the data sets, although it may still give rise to problems for complex data sets, as was shown for the X-ray screen data set.

Further developments underway will extend toward the analysis of categorized data, which will be comparable to the resolution of data based on discriminant analysis models, and toward procedures similar to those described by Gemperline (*15*, *16*) and Vandeginste et al. (*17*) to deal with variables that are not pure.

ACKNOWLEDGMENT

Joe L. Lippert is acknowledged for his support of the development of SIMPLISMA and the TMOS project. Charles E. Heckler is acknowledged for discussions. Paul Gemperline (East Carolina University, Greenville, NC) is acknowledged for his comments.

LITERATURE CITED

(1) Gemperline, P. J. *J. Chemom.* **1989**, *3*, 549–568.
(2) Hamilton, J. C.; Gemperline, P. J. *J. Chemom.* **1990**, *4*, 1–13.
(3) Windig, W. *Chemom. Intell. Lab. Syst.* **1988**, *4*, 201–213.
(4) Larivee, R. J. *J. Chemom.* **1989**, *3*, 541–542.
(5) Windig, W.; Lippert, J. L.; Robbins, M. J.; Kresinske, K. R.; Twist, J. P.; Snyder, A. P. *Chemom. Intell. Lab. Syst.* **1990**, *9*, 7–30.
(6) Knorr, F. J.; Futrell, J. H. *Anal. Chem.* **1979**, *51*, 1236–1241.
(7) Windig, W.; Liebman, S. A.; Wasserman, M. B.; Snyder, A. P. *Anal. Chem.* **1988**, *60*, 1503–1509.
(8) Lippert, J. L.; Melpolder, S. B.; Kelts, L. M. *J. Non-Cryst. Solids* **1988**, *104*, 139–147.
(9) Ozeki, T.; Kihara, H.; Hikime, S.; Ikeda, S. *Anal. Sci.* **1987**, *3*, 285–290.
(10) Malinowski, E. R. *Anal. Chim. Acta* **1982**, *134*, 129–137.
(11) Schostack, K. J.; Malinowski, E. R. *Chemom. Intell. Lab. Syst.* **1989**, *6*, 21–29.
(12) Vandeginste, B.; Essers, R.; Bosman, T.; Kateman, G. *Anal. Chem.* **1985**, *57*, 971–985.
(13) Malinowski, E. R.; Howery, D. G. *Factor Analysis in Chemistry*; R. E. Krieger Publishing Company: Malabar, FL, 1989.
(14) Ritter, G. L.; Lowry, S. R.; Isenhour, T. L.; Wilkins, C. L. *Anal. Chem.* **1976**, *48*, 591–595.
(15) Gemperline, P. J. *J. Chem. Inf. Comput. Sci.* **1984**, *34*, 206–212.
(16) Gemperline, P. J. *Anal. Chem.* **1986**, *58*, 2656–2663.
(17) Vandeginste, B. G. M.; Derks, W.; Kateman, G. *Anal. Chim. Acta* **1985**, *173*, 253–264.

RECEIVED for review November 16, 1990. Accepted March 27, 1991.

Synchronous Scan Luminescence Techniques Monitoring Resonance and Nonresonance Fluorescence in Supersonic Jet Spectrometry Applied to Anthracene Derivatives

Cheng-Huang Lin, Hiroshi Fukii, Totaro Imasaka, and Nobuhiko Ishibashi*

Faculty of Engineering, Kyushu University, Hakozaki, Fukuoka 812, Japan

A supersonic jet/fluorescence spectrum is measured either by monitoring fluorescence at $\lambda_{em} = \lambda_{ex}$ (resonant synchronous scan luminescence, R-SSL) or by monitoring total fluorescence but blocking fluorescence at $\lambda_{ex} = \lambda_{em}$ (nonresonant synchronous scan luminescence, N-SSL). The R-SSL technique provides a simple spectrum and is useful for assignment of the chemical species from the database constructed by accumulating the spectral data of 0–0 transitions from the references. On the other hand the N-SSL technique offers a fingerprinting spectrum and is useful for reliable identification with the standard spectrum. A mixture sample containing anthracene, 1-, 2-, and 9-chloro-, 2- and 9-methyl-, and 2-ethylanthracene has been measured. Five compounds are readily identified by R-SSL spectrometry using a database of 0–0 transitions. However, two compounds remain unassigned. These two compounds are identified by careful assignment using the spectral data given by N-SSL spectrometry. The detection limit for anthracene achieved by N-SSL spectrometry is 7×10^{-7} M, which is 2 orders of magnitude better than the value achieved by R-SSL spectrometry. The present method is further applied to solvent-refined coal. Three components, i.e. anthracene and 1- and 2-methylanthracene, are detected in this sample.

Many polycyclic aromatic hydrocarbons (PAHs) are formed both naturally and artificially, and they are emitted into an environment. Some of them are strongly carcinogenic, and their toxicity drastically change with slight modifications in chemical structure. Therefore, a highly selective analytical method is required for assessment of pollution in the environment.

Supersonic jet expansion cools the sample molecule to several kelvin, so that it provides a sharp line structure in the ultraviolet and visible spectra (*1–3*). Supersonic jet (SSJ) spectrometry has great selectivity and allows spectrometric differentiation between molecular species with closely related structures. A combination with chromatography gives additional selectivty; even PAH isomers contained in a real sample can readily be identified (*4*). However, it is difficult to measure an excitation or multiphoton ionization spectrum during the time period that the sample passes through the detector. Therefore, the exciting wavelength should be adjusted to one of the absorption peaks for a specified component prior to the measurement. It prevents practical application of SSJ spectrometry to unknown samples.

Synchronous scan luminescence (SSL) spectrometry has been developed by Lloyd to simplify a fluorescence spectrum (*5*); the excitation and fluorescence wavelengths are synchronously scanned under the optimized separation of these wavelengths. More recently, this spectrometric technique has been applied to SSJ spectrometry (*6*, *7*). It is reported to be useful for further simplification of the SSJ spectrum, giving one or two major peaks for a single component in most cases. It provides us with an effective means for analysis of a mixture sample containing many PAHs. This allows discrimination of a sample molecule from compounds with closely related structures such as isomers, which is sometimes difficult by conventional chromatography/mass spectrometry. The SSJ/SSL spectrum can be measured without prior knowledge of a sample molecule; the excitation and fluorescence wavelengths are adjusted to the same value and are scanned synchronously. Thus this method can be applied to the sample containing an unknown chemical species. This is in contrast to conventional SSL spectrometry, in which the separation between the excitation and fluorescence wavelengths should be optimized depending on the sample molecule measured.

There are, however, several disadvantages in SSJ/SSL spectrometry. The first disadvantage is a large quantity of scattered exciting light; since the monochromator wavelength is scanned by adjusting it exactly to the exciting wavelength. The second disadvantage is poor detectability, especially for a molecule whose pure electronic transition is essentially forbidden and the 0–0 transition peak is negligibly small. In this case, it is difficult even to know whether the component included is not fluorescent or if it is fluorescent but provides a negligibly small signal at the resonance transition. Moreover, only a limited number of spectral lines are observed in the SSJ/SSL spectrum, which sometimes induces an error in the assignment due to an accidental overlap of the spectral line.

In this study we develop a new SSJ/SSL spectrometric technique that has none of the limitations described above; total fluorescence is monitored by blocking fluorescence at $\lambda_{em} = \lambda_{ex}$ (nonresonant synchronous scan luminescence spectrometry, N-SSL). In contrast to conventional resonant synchronous scan luminescence spectrometry (R-SSL), this method is more sensitive and is applicable to the sample whose electronic transition is essentially forbidden but is vibrationally allowed. Furthermore, the sample molecule is more reliably assigned from a fingerprinting pattern observed. A combination of R-SSL and N-SSL (R/N-SSL), in which both spectra are shown in the same graph, provides further information about molecular structure. Therefore, this approach is versatile for reliable assignment of the chemical species in SSJ spectrometry.

We apply this R/N-SSL spectrometry to an artificial mixture containing several anthracene derivatives and also to solvent-refined coal. The chemical species are first assigned from the R-SSL spectrum with a database constructed by accumulating the spectral data of 0–0 transitions for ~320 compounds. The components are further identified from the N-SSL spectrum measured for standard chemicals. Finally, quantitative analysis is performed by N-SSL spectrometry due to its high sensitivity. The analytical advantages and limitations of R/N-SSL spectrometry are further discussed in this work.

EXPERIMENTAL SECTION

Principle. Optical configurations of R- and N-SSL spectrometries are schematically shown in Figure 1. In R-SSL spec-

* To whom correspondence should be addressed.

0003-2700/91/0363-1433$02.50/0 © 1991 American Chemical Society

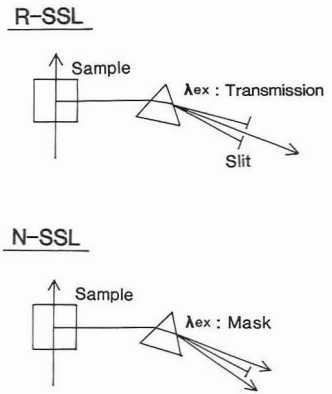

Figure 1. Optial configurations in R-SSL and N-SSL spectrometers.

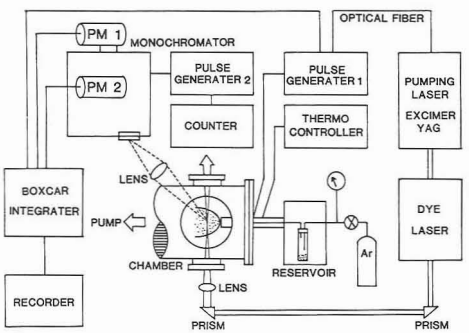

Figure 2. Experimental apparatus for measurements of excitation and R/N-SSL spectra.

trometry, photoemission at $\lambda_{em} = \lambda_{ex}$ is monitored by transmitting it through a slit of a monochromator, whose wavelength is scanned synchronously to the wavelength of the dye laser. Only resonance fluorescence is detected in this scheme. In R-SSL spectrometry, a single component gives one or two major peaks in most cases. Thus R-SSL spectrometry is useful for simplification of the spectrum. However, this is effective only for a molecule giving a strong resonance fluorescence. In contrast to R-SSL spectrometry, total fluorescence except for photoemission at $\lambda_{em} = \lambda_{ex}$ is monitored in N-SSL spectrometry by using an optical mask. This spectrometric technique is more sensitive, due to better efficiencies in fluorescence collection and in scattered-light rejection. This optical configuration has the same advantage as R-SSL spectrometry; the spectrum can be measured without prior knowledge about the spectral properties of the sample since the fluorescence spectrum is always measured by adjusting the monochromator wavelength to the dye laser wavelength.

Apparatus. The experimental apparatus constructed in this study is shown in Figure 2. An excimer-laser-pumped dye laser (Lambda Physik, EMG102MSC, FL2002) or a Nd:YAG-laser-pumped dye laser (Quantel, YG581C-20, TDL50, UVX-2, DCC-3) is used for sample excitation. The pulse width of the laser is ~10 ns, the repetition rate being 20 Hz. The sample is placed in a reservoir, whose temperature is maintained at 50–200 °C to obtain sufficient vapor pressure. For quantitative analysis, the solution sample dissolved in methanol was sprayed from a pinched restrictor continuously into a hot reservoir to vaporize (6). The sample molecule is expanded with a carrier gas of argon into a vacuum from a pulsed supersonic jet nozzle heated ~50 °C above the reservoir temperature. The vacuum chamber is evacuated by a 6-in. pump system (6). In order to obtain a sufficient cooling

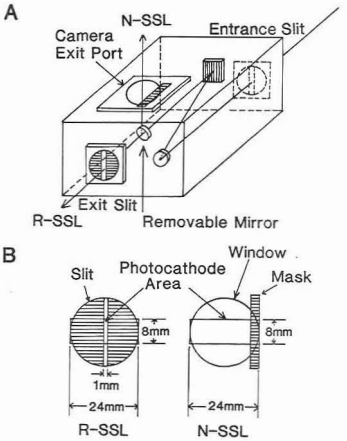

Figure 3. (A) Monochromator for recording R/N-SSL spectra. (B) Relationship between slit of monochromator and photocathode of photomultiplier.

effect, the vacuum chamber was maintained below 3 mTorr. The laser beam is focused by a quartz lens (focal length, 50 cm) into a supersonic jet 10 mm away from the nozzle. Fluorescence is collected by a quartz lens (focal length, 10 cm) onto an entrance slit of a monochromator (Jasco, CT-25CP, 2.1 nm/mm). The slit width was adjusted to 1 mm throughout this experiment. The optical configuration of the fluorescence detection port is shown in Figure 3A. The relationship between the exit port of the monochromator and the photocathode of a photomultiplier (Hamamatsu, R1477) is indicated in Figure 3B. The long axis of the photocathode is adjusted to be perpendicular to the slit of the monochromator for a wide spectral coverage in N-SSL spectrometry. This configuration decreases the sensitivity in R-SSL spectrometry, since the slit height of the monochromator (20 mm) is much larger than the photocathode width of the photomultiplier (8 mm). However, this configuration is used in this study, since it is preferential for a discussion of the sensitivities in these spectrometric methods. The direction of the last mirror is changed to up or down either for N-SSL or R-SSL spectrometry. This allows measurements of both the spectra with a minor change of the experimental conditions. For recording a N-SSL spectrum, an optical mask (width, 3 mm) is placed at $\lambda_{em} = \lambda_{ex}$. The spectral aperture is 2.1 nm for R-SSL spectrometry and 44.1 nm for N-SSL spectrometry. Thus the fluorescence collection efficiency is larger for the latter, and furthermore scattered light is completely blocked by the optical mask. So that, a better sensitivity is given for N-SSL spectrometry. The monochromator wavelength is scanned synchronously to the dye laser wavelength in both cases by a homemade pulse generator, whose pulse rate was adjusted by monitoring it with a frequency counter (NF Circuit Design Block, PC-545A). For a measurement of a conventional excitation spectrum, the monochromator wavelength was fixed to a specified fluorescence peak, and only the exciting (dye laser) wavelength was scanned. In this case the slit width was adjusted to be 1 mm (2.1 nm). The fluorescence signal is measured by a boxcar integrator (Stanford, SR250). The delay time and the gate width were changed, depending on the sample molecule measured.

Reagents. All the anthracene derivatives, biphenyl, 1-methylnaphthalene, and 2-methylnaphthalene were obtained from Tokyo Kasei, naphthalene from Kanto Chemical, and pyrene from Wako Pure Chemical. The laser dyes of BMQ, DCM, and Fluorescein 27 were purchased from Exciton. A carrier gas of argon was supplied from Iwatani.

Preparation of Real Sample. For qualitative analysis, solvent-refined coal produced and refined in Hokkaido, Japan, was placed directly in the reservoir. For quantitative analysis, solvent-refined coal (1 g) was crushed into small particles and was

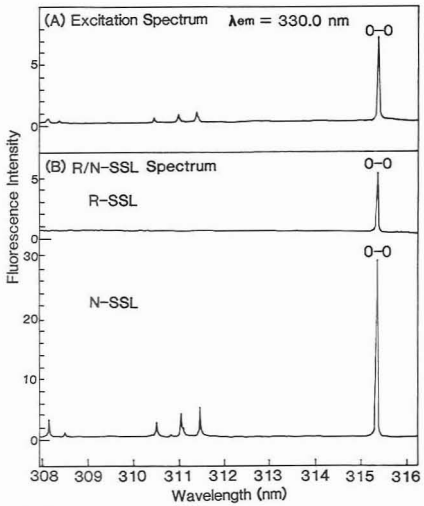

Figure 4. Supersonic jet spectra for 2-methylnaphthalene: delay time, 50 ns; gate width, 500 ns.

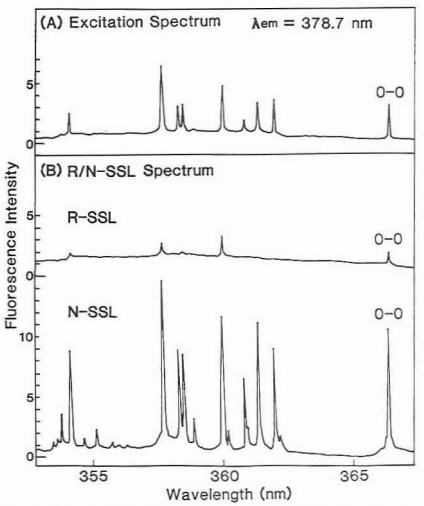

Figure 5. Supersonic jet spectra for pyrene delay time, 200 ns; gate width, 1000 ns.

dissolved in the 250-mL solvent by ultrasonic agitation during 1 h. Benzene was used as a solvent instead of methanol due to a good solubility, since only a small amount could be dissolved in methanol. The residue (0.481 g/1 g of solvent refined coal) was removed by passing the solution sample through a membrane filter (pore size, 1.0 μm).

RESULTS AND DISCUSSION

Group A (Strong 0–0 Transition). Figure 4 shows excitation and R/N-SSL spectra for 2-methylnaphthalene. In the R-SSL spectrum, a single peak is observed at the wavelength of 0–0 transition (315.40 nm). Thus R-SSL spectrometry is useful for simplification of the SSJ spectrum. In the conventional excitation spectrum, the intensity of the spectral line is proportional to the Franck-Condon factor, i.e. the overlap of the wavefunctions for the ground and excited states. This situation is identical with that in the conventional fluorescence spectrum. In the R-SSL spectrum, the spectral line appears only when the molecule is excited to a specified level and emits from this level to the ground state. Therefore, the intensity of the spectral line is proportional to the square of the Franck-Condon factor. Thus small signal peaks observed in the excitation spectrum are reduced further in the fluorescence isolation process, as designated by a "double-filter effect" (*7*). Aromatic hydrocarbons such as 9-methylanthracene, 9-chloroanthracene, and 1,2-dimethylnaphthalene give almost a single peak at 0–0 transition in the R-SSL spectrum and are grouped to this category. These compounds may readily be assigned from the database, in which the wavelengths of the 0–0 transitions have been accumulated for ~320 compounds from the reference values (*8*).

Nonresonant SSL spectrometry gives larger signal peaks, due to a better fluorescence collection efficiency. The fluorescence intensity in the N-SSL spectrum is ~5 times larger than that in the R-SSL spectrum for 2-methylnaphthalene. Furthermore, N-SSL spectrometry provides a lower background signal, since scattered exciting light is completely rejected by an optical mask. The S/N ratio is improved to 3000 for the 0–0 transition peak in N-SSL spectrometry, whereas the value is limited to 150 in R-SSL spectrometry. Thus N-SSL spectrometry is more useful in trace analysis.

Group B (Small Oscillator Strength). Supersonic jet spectra of pyrene are shown in Figure 5. The fluorescence lifetime of the S_1 state was 200–1400 ns depending on the energy level of the excited state, due to a small oscillator strength of the S_0–S_1 transition (*9*). Furthermore, the excited state has small Franck-Condon progressions, so that the fluorescence intensity is rather weak. The fluorescence intensity is much smaller than other compounds such as anthracene derivatives. In this study, the sample was heated to a higher temperature (180 °C) than the melting point (156 °C) to obtain sufficient vapor pressure, whereas the temperature was adjusted to the value slightly below the melting point for other compounds (e.g. 200 °C, mp 216 °C for anthracene). The R-SSL spectrum is more simplified than the conventional excitation spectrum, which seems to be due to mode selectivity in R-SSL spectrometry, i.e. the double-filter effect described above.

The S/N ratio is 10 in the R-SSL spectrum and 60 in the N-SSL spectrum. The scattered light is almost completely rejected even in R-SSL spectrometry by temporal discrimination. Thus the improvement of the S/N ratio by using N-SSL spectrometry is rather small in comparison with Group A (20 times).

The sample molecule may be assigned by using the database, but it should be performed carefully; several peaks are sometimes observed even in the R-SSL spectrum so that three or four peaks remain unassigned. On the other hand the N-SSL spectrum gives many spectral lines, much more than those in the conventional excitation spectrum. Then, identification of the chemical species by N-SSL spectrometry is more reliable because of the fingerprinting pattern observed.

Group C (Forbidden 0–0 Transition). Figure 6 shows excitation and R/N-SSL spectra for 1-methylnaphthalene. The S/N ratios achieved in the R- and N-SSL spectra are 360 and 2800, respectively. The weak signal peak appearing at 314.73 nm corresponds to the 0–0 transition, and a strong peak at 310.64 nm is ascribed to the $\bar{8}_0^1$ transition (*10*). Resonant SSL is useful to simplify the spectrum, even when the 0–0 transition peak is weak; small signal peaks are reduced further in the fluorescence isolation process. A similar result is observed for naphthalene. Only the wavelength of the 0–0 transition has been accumulated in the database (*8*); therefore

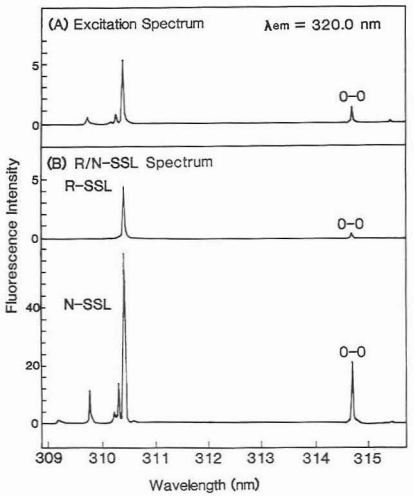

Figure 6. Supersonic jet spectra for 1-methylnaphthalene: delay time, 50 ns; gate width, 500 ns.

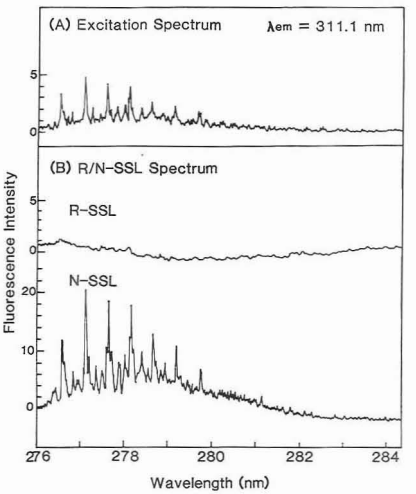

Figure 7. Supersonic jet spectra for biphenyl: delay time, 20 ns; gate time, 100 ns. Only the background signal is observed in the R-SSL spectrum.

it is difficult to identify this group of compounds using the database. So, it might be necessary to reconstruct a database to list the largest peak in the R-SSL spectrum in the future, though experimental measurements are required for many compounds.

Since the 0–0 transition peak in the R-SSL spectrum is relatively weak, this transition is implied to be electronically forbidden and vibrationally allowed. In fact, the electronic transition of naphthalene is known to be forbidden and strong vibronic peaks appear. This is due to the forbidden nature of the S_1–S_0 transition; the first and third excited singlet states have a $^1B_{3u}$ symmetry, and the S_1–S_0 transition moment disappears with configuration interaction (*11*, *12*). Thus R/N-SSL spectrometry is useful to identify whether this molecule is electronically allowed or not. It gives us additional information for assignment of the chemical species.

Group D (Twisted Molecule). Figure 7 shows excitation and R/N-SSL spectra for biphenyl. The R/N-SSL spectrum is quite different from those observed for other aromatic hydrocarbons. The 0–0 transition peak, reported to appear at 283.62 nm (*13*), is not evident in this spectrum. Biphenyl is composed of two benzene rings, which are combined with a C–C single bond. This molecule has different conformation in the ground and excited states; the electronic transition is strongly associated with a torsional motion along the C–C bond, and the equilibrium angles between two benzene rings in the excited and ground states are reported to be 44 and 0°, respectively (*13*). Therefore, the Franck-Condon factor for the 0–0 transition is negligibly small. Thus no appreciable signal appears in the R-SSL spectrum. However, when the molecule is excited to high vibrational levels in the excited state, fluorescence to high vibrational levels in the ground state is obsevable. Thus many sharp lines appear in the N-SSL spectrum.

When no signal is observed in the R-SSL spectrum, it is difficult to judge from the R-SSL spectrum whether a specified component is not included in the sample or if the fluorescence signal is negligibly small due to the small Franck-Condon factor for resonance transition. Information concerned with the energy for the 0–0 transition is difficult to be obtained even by N-SSL spectrometry, but it provides some information, at least a presence of sample. Furthermore, it is useful for identification of the sample molecule from a fingerprinting pattern as described. The S/N ratio was limited to 15 even for the largest peak in the N-SSL spectrum, due to a small Franck-Condon factor.

Analytical Procedure. Resonant and nonresonant SSL spectrometric methods have different characteristics, and the best performance is given when these spectra are presented in the same graph (R/N-SSL). The analytical procedure in this R/N-SSL spectrometry may be suggested, as follows. First, the sample may be measured by N-SSL spectrometry, owing to better sensitivity and nonspecificity. Second, R-SSL spectrometry may be applied in the same spectral region, since it greatly simplifies the spectrum. The sample component might readily be assigned from the database constructed by collecting the wavelengths of the 0–0 transition peaks or the largest peak in the R-SSL spectrum. When no experimental data are available, the database constructed by theoretical calculation of the molecular orbital might give some information in the assignment, though the error in the calculated wavelength of the 0–0 transition peak is reported to be 1–2% (*14*, *15*). Third, some information concerned with molecular structure may be obtained by comparing the R- and N-SSL spectra. For example, if the sample molecule consists of a rigid planar ring, a strong peak corresponding to the 0–0 transition might be observed in both the R- and N-SSL spectra. If no peak is observed in the R-SSL spectrum or if the 0–0 transition peak is negligibly small, the electronic transition might be forbidden or the Franck-Condon factor might be small due to a large conformational change between the excited and ground states. Fourth, the sample molecule may be further identified from a fingerprinting pattern by comparing it with the N-SSL spectra measured for the standard chemicals. Finally, quantitative analysis may be performed on the basis of N-SSL spectrometry because of its high sensitivity.

Mixture Sample. Figure 8 shows the R/N-SSL spectrum for a mixture sample containing seven anthracene derivatives. Only 10 major peaks are observed in the R-SSL spectrum. Spectral simplicity is ascribed to sufficient cooling by supersonic jet expansion and mode selectivity in R-SSL spectrometry. The signal intensity depends on the absorptivity,

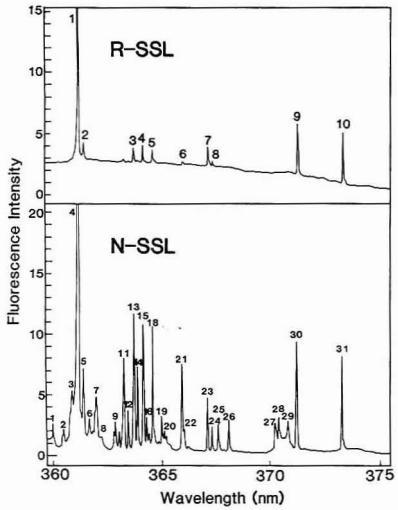

Figure 8. R/N-SSL spectrum for mixture sample containing ~10 mg of each anthracene derivative, i.e. anthracene, 1-, 2-, and 9-chloroanthracene, 2- and 9-methylanthracene, and 2-ethylanthracene.

Table I. Assignment of Signal Peaks Observed in the R- and N-SSL Spectra for the Mixture Sample[a]

	experimental λ, nm			assignment		
	N-SSL		R-SSL	database	R-SSL	N-SSL
1	359.98					A, 2-MA
2	360.47					2-CA, 2-MA
3	360.86					9-MA
4	361.08	1	361.08	A	A, 1-CA	A, 1-CA, 2-CA
5	361.35	2	361.35		2-CA	2-CA
6	361.63					2-MA
7	361.99					1-CA, 9-MA
8	362.17					1-CA
9	362.78					2-CA
10	363.05					1-CA
11	363.18					2-EA, 2-MA
12	363.38					2-EA
13	363.65	3	363.65		2-EA	2-CA, 2-EA
14	363.82					1-CA, 2-EA, 2-MA
15	364.07	4	364.07		2-EA	2-EA
16	364.21					2-MA
17	364.37					1-CA
18	364.50	5	364.50		2EA,2MA	2-EA, 2-MA
19	364.97			2-EA		2-EA
20	365.07			2-MA		2-MA
21	365.90	6	365.90		9-MA	9-MA
22	366.01					9-MA
23	367.09	7	367.09	2-CA	2-CA	2-CA
24	367.31	8	367.31	1-CA	1-CA	1-CA
25	367.60					9-CA
26	368.07					9-CA
27	370.15					9-CA, 9-MA
28	370.40					9-MA
29	370.78					9-MA
30	371.18	9	371.18	9-MA	9-MA	9-MA
31	373.25	10	373.25	9-CA	9-CA	9-CA

[a] Abbreviations: A, anthracene; 2-MA, 2-methylanthracene; 1-CA, 1-chloroanthracene; 9-CA, 9-chloroanthracene; 2-CA, 2-chloroanthracene; 9-MA, 9-methylanthracene; 2-EA, 2-ethylanthracene.

the fluorescence quantum yield, the Franck-Condon factor, and the partial vapor pressure of the sample at the specified temperature (200 °C). In contrast to the R-SSL spectrum, many sharp lines are observed in the N-SSL spectrum. This

Table II. Database of 0–0 Transition for Aromatic Hydrocarbons in the 360–375-nm Region

compd	0–0 transition, nm	ref
anthracene	361.08	16
1-methylanthracene	363.95	17
2-ethylanthracene	364.97[a]	6
2-methylanthracene	365.07	18
2-chloroanthracene	367.09	14
1-chloroanthracene	367.31	14
pyrene	367.44	9
phenyl nitrene	368.42	19
tropolone	370.13	20
9-(3-fluorophenyl)anthracene	370.77	18
2-phenylanthracene	370.80	18
9-(3-methylphenyl)anthracene	371.07	18
9-(4-fluorophenyl)anthracene	371.10	18
9-phenylanthracene	371.14	18
9-methylanthracene	371.18	18
9-(4-methylphenyl)anthracene	371.53	18
pyrazine	372.80	21
9-hexylanthracene	373.03	22
9-chloroanthracene	373.25	9
9-methoxyanthracene	373.40	23
9-bromoanthracene	374.20	24

[a] This signal peak is very weak in the R-SSL spectrum and is neglected in the original paper. However, this peak is rather strong in N-SSL and is tentatively assigned to the 0–0 transition in this work.

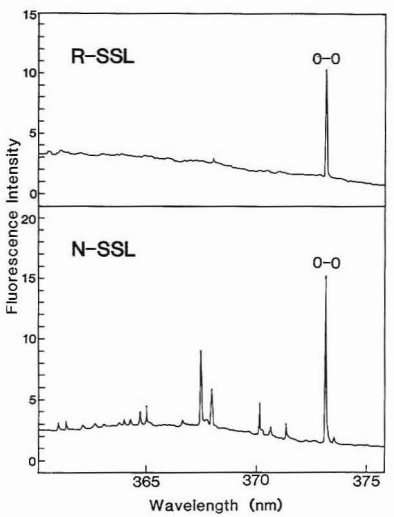

Figure 9. R/N-SSL spectrum for 9-chloroanthracene.

complicated structure is ascribed to a variety of acceptable modes in total fluorescence detection.

Assignment Using Database. The second column of Table I indicates the wavelengths of the peaks observed in the N-SSL spectrum for a mixture sample containing seven PAHs. The peaks observed in the R-SSL spectrum are shown in the fourth column. A part of the database obtained by accumulating the wavelength of the 0–0 transition from references is shown as Table II. Five peaks observed in the R-SSL spectrum, i.e. 1, 7–10, are readily assigned to the 0–0 transitions for five anthracene derivatives from the database. The other five peaks, i.e. 2–6, are due to resonance fluorescence to/from high vibrational levels in the excited stae, and then they are not assigned from the database. The remaining two compounds, i.e. 2-ethylanthracene and 2-methylanthracene,

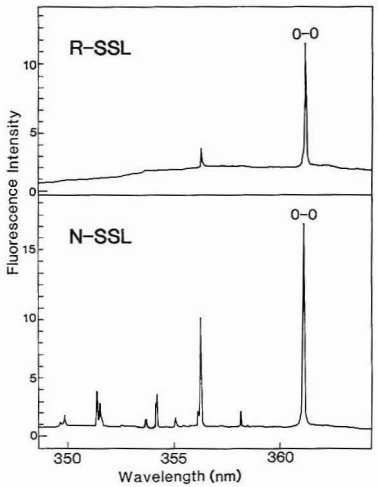

Figure 10. R/N-SSL spectrum for anthracene.

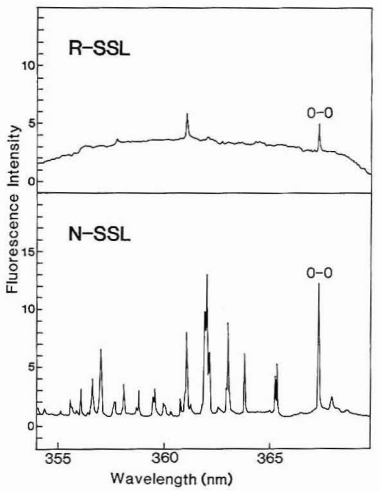

Figure 12. R/N-SSL spectrum for 1-chloroanthracene.

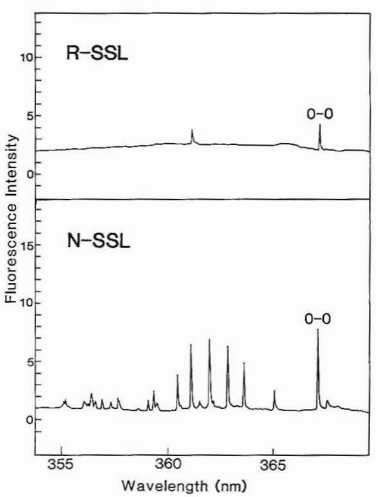

Figure 11. R/N-SSL spectrum for 2-chloroanthracene.

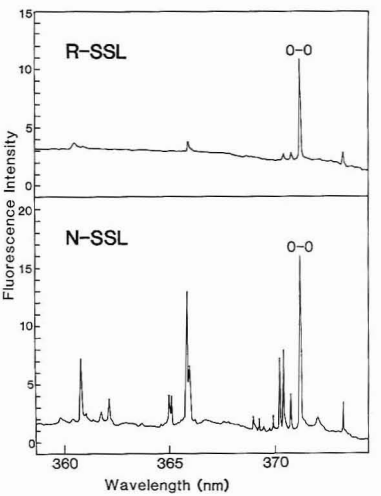

Figure 13. R/N-SSL spectrum for 9-methylanthracene.

are assigned by using the database from the spectral data given by N-SSL spectrometry. These results are summarized in the fifth column of Table I.

Identification with a Standard Spectrum. As shown in Figure 9, only a single peak is observed for 9-chloroanthracene in the R-SSL spectrum (group A). On the other hand, two major peaks are observed for anthracene and 2-chloroanthracene (similar to group B), as shown in Figures 10 and 11. Weaker signal peaks are attributed to resonance fluorescence to/from high vibrational levels in the excited state. Thus peak 2 and a part of peak 1 are attributed to 2-chloroanthracene and 1-chloroanthracene, respectively. This situation is similar to 1-chloroanthracene, as shown in Figure 12; a weak signal peak at 361.08 nm may be possible to assign to the 0–0 transition for anthracene, included as an impurity in the reagent, but the peak observed at 356.03 nm in the spectrum for anthracene is not evident so that this peak is tentatively assigned to 1-chloroanthracene. Peak 6 is also attributed to 9-methylanthracene from the spectrum shown in Figure 13. The R/N-SSL spectra are very complicated for 2-methylanthracene and 2-ethylanthracene (similar to group D), as shown in Figures 14 and 15. This is ascribed to torsional motion with a small vibrational energy or internal rotation giving many isomers along the axis of a C–C single bond between the aromatic ring and the methyl or ethyl group. Thus small peaks 3 and 4 are tentatively assigned to 2-ethylanthracene, and peak 5, to 2-ethylanthracene and 2-methylanthracene (accidental spectral overlap). The results are summarized in the sixth column of Table I.

The above assignments are further confirmed by the standard N-SSL spectra. Possible candidates of the peaks are indicated in the last column of Table I. The assignments

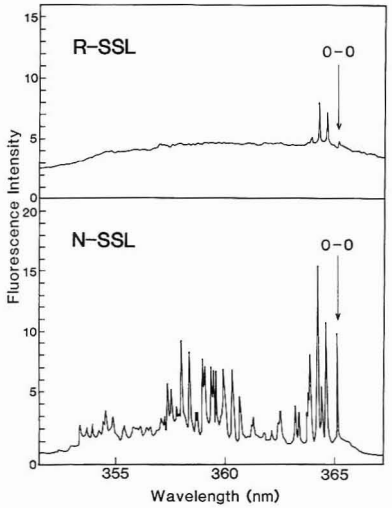

Figure 14. R/N-SSL spectrum for 2-methylanthracene.

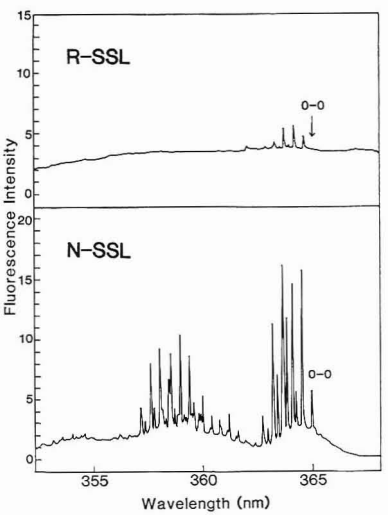

Figure 15. R/N-SSL spectrum for 2-ethylanthracene.

from the R-SSL spectra are readily confirmed. Since there are many spectral lines in the N-SSL spectrum, molecular species are more reliably identified from the fingerprinting pattern observed. However, a few candidates are given for a single peak, and therefore this method is useful only for confirmation of the assignment; it seems to be difficult to assign the chemical species only from the data obtained by N-SSL spectrometry, since it is so complicated, especially in multicomponent analysis.

Detection Limit. A R-SSL spectrum was measured by introducing the solution sample into a hot reservoir to vaporize anthracene continuously for quantitative analysis. The analytical curve was constructed in the $0–10^{-3}$ M range. The S/N ratio was 3 for the sample measured at a concentration of 1×10^{-4} M. The detection limit is similar to the previous value obtained for anthracene (7×10^{-5} M, $S/N = 3$) by R-SSL spectrometry (*6*). A similar analytical curve was constructed by using N-SSL spectrometry in the $0–10^{-3}$ M range, and the detection limit was 7×10^{-7} M. Thus the sensitivity of N-SSL spectrometry is about 2 orders of magnitude better than that of R-SSL spectrometry. It is noted that this detection limit is several times better than that of conventional fluorescence spectrometry monitoring a specific vibrational band (3×10^{-6} M) (*6*). Better sensitivity is ascribed to a higher efficiency in fluorescence collection, since total fluorescence ($\lambda_{em} \neq \lambda_{ex}$, bandpass 44.1 nm) is collected in N-SSL spectrometry.

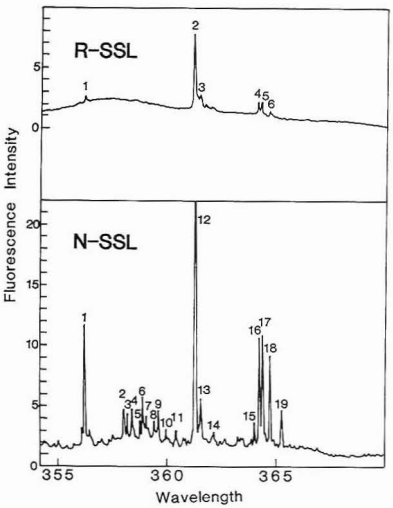

Figure 16. R/N-SSL spectrum for solvent-refined coal.

Table III. Assignment of Signal Peaks Observed in R- and N-SSL Spectra for Solvent-Refined Coal[a]

experimental λ, nm				assignment		
N-SSL		R-SSL		database	R-SSL	N-SSL
1	356.03	1	356.03		A	A
2	357.80					2-MA
3	357.98					A
4	358.17					2-MA
5	358.56					2-MA
6	358.67					?
7	358.83					2-MA
8	359.16					?
9	359.37					?
10	359.76					2-MA
11	360.20					2-MA
12	361.08	2	361.08	A	A	A
13	361.29	3	361.29		?	?
14	361.90					?
15	363.18					2-MA
16	363.95	4	363.95	1-MA	1-MA	1-MA
17	364.07	5	364.07		2-MA	2-MA
18	364.50	6	364.50		2-MA	2-MA
19	365.07			2-MA		2-MA

[a] Abbreviations: A, anthracene; 2-MA, 2-methylanthracene; 1-MA, 1-methylanthracene; ?, unassigned.

Real Sample. Figure 16 shows the R/N-SSL spectrum for solvent-refined coal. The experimental results are summarized in the second and fourth columns of Table III. Apparently, peak 2 in the R-SSL spectrum is assigned to the 0–0 transition for anthracene from the database. Of particular interest is peak 4, which can be assigned to 1-methylanthracene from the database, though this compound is not commercially

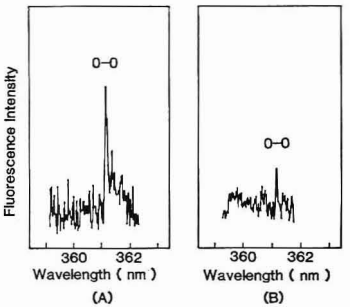

Figure 17. N-SSL spectrum for (A) anthracene (10^{-5} M) and (B) solvent-refined coal. The samples are dissolved in benzene.

available and has not been measured in this study. From the standard spectrum, peak 1 is assigned to resonance fluorescence from the 12^1 level of anthracene. Peaks 5 and 6 are assigned to 2-methylanthracene from the standard R-SSL spectrum. Presences of anthracene and 2-methylanthracene are confirmed further from the N-SSL spectra for the standards. However, several unassigned peaks remain in the R-SSL and N-SSL spectra. They might possibly originate from other anthracene derivatives. Further investigation may be necessary for the assignments, due to lack of spectral data and of the standard chemical.

Quantitative analysis is perfomed for solvent-refined coal by using N-SSL spectrometry, since it is more sensitive than both R-SSL and conventional fluorescence spectrometries. Figure 17A,B shows the N-SSL spectra for anthracene (1×10^{-5} M) and solvent-refined coal in benzene, respectively. In order to avoid errors induced by nonlinearity of signal response, the standard spectrum was measured at anthracene concentrations similar to that of the real sample. The spectral peak for standard anthracene is slightly shaded to longer wavelengths, which is probably due to formation of van der Waals complexes with benzene. No such spectral shade was observed for anthracene dissolved in methanol. This is considered to be due to a strong interaction between π electrons in anthracene and benzene. The signal intensity of the 0–0 transition peak for anthracene in solvent-refined coal is quite small but is evident; the measurement was repeated, and the signal was confirmed to be reproducible. From the intensity ratio of the signal peaks in Figure 17A,B, the concentration of anthracene is determined to be 3×10^{-6} M. The content of anthracne in solvent-refined coal was calculated to be 100 ppm (10^{-4} g of anthracene/1 g of solvent refined coal).

Advantage and Limitation. Resonant SSL spectrometry gives a simple spectrum, and the major peak is mostly assigned from the database of 0–0 transitions, especially for a rigid molecule; there is little configuration change, and the Franck-Condon factor is the largest for the 0–0 transition. This approach is simple and straightforward, since the database is constructed by accumulating the reference data without any experimental work. However, the assignment only from this database is sometimes imperfect, as experienced in this work, for a molecule giving a weak 0–0 transition peak. In this case several components remain unassigned. Moreover, many peaks are observed, especially for a molecule with a low torsional vibrational mode and for a molecule consisting of rotational isomers. In this case several peaks remain unassigned. Thus there are some limitations in assignment of chemical species by using the database of 0–0 transition alone. The database constructed by accumulating the major peaks in the R-SSL spectrum will be more useful, though it requires a lot of experimental work.

There are a limited number of spectral peaks in the R-SSL spectrum, i.e. one or two major peaks for a single component. However, superposition of the signal peak is sometimes unavoidable, as in the cases of anthracene and 1-chloroanthracene or 2-methylanthracene and 2-ethylanthracene. Then, efficient sample cooling and accurate wavelength calibration are essential for reliable assignment. The sensitivity of R-SSL spectrometry is rather poor, which is mainly due to background increase by scattered light of the dye laser. A time-resolved fluorescence spectrometer with a subnanosecond resolution may be useful for background discrimination in determination of anthracene derivatives having rather short fluorescence lifetimes (several nanoseconds).

The N-SSL spectrum consists of more than 30 major peaks for a mixture sample containing seven anthracene derivatives. This approach is more useful for reliable identification. However, the construction of the database is more difficult in N-SSL spectrometry, since more than 10 peaks appear from a single component. Therefore, many spectral parameters should be accumulated for construction of a database. Filing the spectral data and searching the candidates by a computer will be necessary for more reliable assignment in the future.

A combination of R- and N-SSL spectrometries proides us with a sensitive and selective analytical means, due to the spectral simplicity of R-SSL spectrometry and to the high sensitivity of N-SSL spectrometry. This spectrometric method might be applicable not only to anthracene derivatives in solvent-refined coal but also to other PAHs in the environment such as benzo[*a*]pyrene in airborne particulates. Thus R/N-SSL spectrometry may have wide application fields and is useful especially in determination of the sample containing many PAH molecules with closely related structures.

Registry No. Anthracene, 120-12-7; 1-chloroanthracene, 4985-70-0; 2-chloroanthracene, 17135-78-3; 9-chloroanthracene, 716-53-0; 2-methylanthracene, 613-12-7; 9-methylanthracene, 52251-71-5; 1-methylanthracene, 610-48-0.

LITERATURE CITED

(1) Hayes, J. M.; Small, G. J. *Anal. Chem.* **1983**, *55*, 565A.
(2) Johnston, M. V. *Tr AC, Trends Anal. Chem.* **1984**, *3*, 58.
(3) Lubman, D. M. *Anal. Chem.* **1987**, *59*, 31A.
(4) Imasaka, T.; Ishibashi, N. *Prog. Quantum Electron.* **1990**, *14*, 131 (Section 7.5.5, p 222).
(5) Lloyd, J. B. F. *Nature (London)* **1971**, *231*, 64.
(6) Imasaka, T.; Tsukamoto, A.; Ishibashi, N. *Anal. Chem.* **1988**, *60*, 1362.
(7) Imasaka, T.; Maeno, I.; Ishibashi, N. *Analyst* **1990**, *115*, 73.
(8) Ishibashi, N.; Imasaka, T. Report For Grant-in-Aid for Scientific Research from the Ministry of Education of Japan; Project No. 01470065.
(9) Mangle, E. A.; Topp, M. R. *J. Phys. Chem.* **1986**, *90*, 802.
(10) Warren, J. A.; Hayes, J. M.; Small, G. J. *J. Chem. Phys.* **1984**, *80*, 1786.
(11) Dewar, M. J. S.; Longuet-Higgins, H. C. *Proc. Phys. Soc. London, Sect. A* **1954**, *67*, 795.
(12) Jacobson, B. A.; Guest, J. A.; Novak, F. A.; Rice, S. A. *J. Chem. Phys.* **1987**, *87*, 269.
(13) Im, H. S.; Bernstein, E. R. *J. Chem. Phys.* **1988**, *88*, 7337.
(14) Imasaka, T.; Ishibashi, N. *Spectrochim. Acta* **1988**, *43B*, 661.
(15) Imasaka, T.; Sakaki, K.; Ishibashi, N. *Chemom. Intell. Lab. Syst.* **1989**, *6*, 281.
(16) Lambert, W. R.; Felker, P. M.; Syage, J. A.; Zewail, A. H. *J. Chem. Phys.* **1984**, *81*, 2195.
(17) Pepich, B. V.; Callis, J. B.; Burns, D. H.; Gouterman, M. *Anal. Chem.* **1986**, *58*, 2825.
(18) Werest, D. W.; Brearley, A. M.; Gentry, W. R.; Barbara, P. F. *J. Am. Chem. Soc.* **1987**, *109*, 32.
(19) Ozawa, K.; Ishida, T.; Fuke, K.; Kaya, K. *Chem. Phys. Lett.* **1988**, *150*, 249.
(20) Redington, R. L. *J. Chem. Phys.* **1988**, *88*, 627.
(21) Pennor, A.; Amirav, *J. Phys. Chem.* **1988**, *92*, 5079.
(22) Syage, J. A.; Gelker, P. M.; Semmes, D. H.; Adel, F. A.; Zewail, A. H. *J. Chem. Phys.* **1985**, *82*, 2896.
(23) Hirayama, S. *Chem. Phys. Lett.* **1988**, *153*, 112.
(24) Amirav, A.; Horwitz, C.; Jortner, J. *J. Chem. Phys.* **1988**, *88*, 2092.

RECEIVED for review December 17, 1990. Accepted April 1, 1991. This research is supported by Grants-in-Aid for Scientific Research from the Ministry of Education of Japan and by the Kurata Foundation.

Kalman Filtering for Data Reduction in Inductively Coupled Plasma Atomic Emission Spectrometry

E. H. van Veen* and M. T. C. de Loos-Vollebregt

Laboratory of Analytical Chemistry, Delft University of Technology, de Vries van Heystplantsoen 2, 2628 RZ Delft, The Netherlands

In ICP-AES, the analyte signal is superimposed on a background signal. When separating these signals, essentially by manual or automated three-point background correction, there are many instances in which the data reduction fails, e.g., with noisy analyte signals, nonlinear background signals, large and heavily structured background, and spectral interference. On the basis of scans in a fast scanning mode, the Kalman filter approach yields in all cases more accurate and precise results. It does not use a search for peak position or specific background points and processes peak area instead of peak height. It attains, up to 2 orders of magnitude, lower detection limits in the sample solution, for real-world samples. The application of the filter results in 1-pm spectral resolution at 20-pm spectral bandwidth and reduces the need for line selection, high-resolution spectrometers, and chemical separation of analyte and matrix. The improved analytical results obtained with the Kalman filter are due to its capability of noise averaging, of multiple line analysis, and of elimination of the degradation of detection limit caused by line overlap. If line selection is needed, it is done quantitatively. The power of the fully automated approach is illustrated with several applications: the analysis of high-purity uranium and sludge reference material. In every respect, data reduction by Kalman filtering is superior to three-point background correction.

INTRODUCTION

In inductively coupled plasma atomic emission spectrometry (ICP-AES), analyte signals are superimposed on a relatively high background signal. The measured gross signals have to be corrected for this background, which determines the detection limit by its amplitude and noise characteristics. Although many samples from a series may resemble each other, the background level will vary from sample to sample. Therefore, the preparation of one blank and measurement of its signal, followed by subtraction of this value from all the sample signals, is not generally feasible. Since the spectrometer is fixed at the analyte wavelength, this method is called static or on-line background correction.

Common types of background correction are based on two- or three-point, off-line background correction (*1*). As long as analyte signals, originating from elements at the mg/L level in aqueous solution, dominate a smooth continuum background, data reduction by this technique is straightforward. Dependent on the spectrometer used, the top of the analyte signal is found by direct peaking or peak search routines. The one or two background points are selected manually, and measurements are always made at these fixed positions. A drawback is that no information is obtained about the profile of the emission line or about the background shape in the vicinity of the line. Another possibility is the automatic selection of background points from a sample scan, by an algorithm based on the second derivative in the spectral window of the analyte (*2*, *3*). Using the derivative technique, one may select more than two points, allowing for correction for nonlinear continuum background (*2*). When the off-line background exhibits structured interferent emission, the search for background points still seems possible (*3*).

At low analyte signals, when the noise becomes dominant, the results of the search for peak and background points easily are in error. With heavily structured background, the three points may not be found. In the case of overlapping emission lines, the automated algorithms fail. An additional algorithm, like Fourier deconvolution for the instrument function of the spectrometer, may be applied, but this approach is only successful if the peak separation is not less than the bandwidth of the spectrometer (*4*). Interelement correction with direct readers, or dynamic three-point background correction with slew-scan monochromators, is needed, leading to a degradation of detection limits by 1 order of magnitude or even more (*5*). This is caused by optical instability and wavelength positioning errors. In an attempt to remedy the degradation of detection limits, several approaches can be applied, e.g., use of high-resolution (<10-pm) spectrometers or FT-UV interferometers, improvement of wavelength positioning accuracy, chemical separation, line selection, or software based on curve resolution techniques. All these approaches have their drawbacks, and though interferences are partly resolved, data reduction still is based on three-point background correction.

Three-point background correction often is a matter of experience and common sense and needs the identification of a typical sample in order to manually fix the background estimation wavelengths. The strength of the automated algorithms is said to be the independence of analyst expertise, and no identification of a typical sample or a priori spectral knowledge is needed. This means that, by application of such a strategy, an error occurs in cases of overlap so that the analytical result is not correct. It is an illustration of a fundamental problem in ICP-AES: the identification of and correction for spectral interferences. For an unknown sample, one has to examine its composition in a semiquantitative way. On the basis of these results, one examines the spectral windows of the analytes for possible interferents. The window may be 50–200 pm wide, with the analyte emission in its center. Once the spectral characteristics of the sample in the window of the analyte are known, there is no sense in using automated algorithms based on no a priori knowledge. In such cases, no additional information is used when optimizing some parameter, and the approach is leading to a worsening of another parameter. For example, application of the Fourier deconvolution may yield a better resolution, however, at the cost of an increase in noise level, degrading the detection limit.

Taking scans to elucidate the spectral characteristics of the sample, why not use these full scans in automated data reduction instead of trying to select one point for the analyte signal and two points for the background, throwing away the other measured information? Using all the spectral information, which is readily available prior to data reduction, will cost little, and figures of merit like detection limit and accuracy may improve (*6*). Moreover, as discussed below, such an approach would eliminate the direct search or peak search

0003-2700/91/0363-1441$02.50/0 © 1991 American Chemical Society

routines (*7*) and discussions about where and how to select the background points (if we can find useful points at all).

Several multicomponent analysis techniques are described in the literature, which solve essentially the same problem: Given a noisy spectrum which is known (or thought) to be a linear superposition of several separate component spectra, each of which is known from theory or from pure component measurements, determine the maximum likelihood estimates for the component coefficients (concentrations) in the sense of least-squares residual error. In some cases, just one of these components is of interest, although all can be determined.

In two papers (*6*, *8*), we have reported about the potential of Kalman filtering, one of the multicomponent analysis techniques, for automated spectral data reduction in ICP-AES. The first paper deals with the theory of Kalman filtering and its specific implementation for ICP-AES. Illustrations are given based on data from overlapping lines in synthetic solutions. The second paper discusses further studies, especially with respect to line selection as a function of background intensity and to the minimum peak separation required for quantitative resolution of analyte and interfering signals. Although full emphasis was on data from overlapping lines, it was argued that all spectral data reduction (or background correction) in ICP-AES can be based on Kalman filtering.

With multicomponent analysis techniques, an essential requirement is that the wavelength axes in the scans for the pure components and for the samples in the spectral window of the analyte should coincide. For ICP-AES, the optical stability has to be within the order of 0.1 pm. However, due to (mainly temperature) drift, scanning spectrometers do not always meet this requirement. In order to develop a criterion that allows compensation for the optical instability, we explored the so-called innovations sequence (*6*). This sequence is defined in Kalman filtering as the difference between the actual (measured) and filtered (a priori estimated) sample scan. If the models used in filtering are accurate, which means, among others, if all wavelength axes coincide, the sequence shows a white noise band. Based on this fact, the Kalman filter approach eliminates the problem of optical instability. As a consequence, Kalman filtering or any other multicomponent analysis technique may indeed be applied in ICP-AES spectral data reduction. At the same time, since all spectra are accurately positioned with respect to each other, the error in the background determination, as made by dynamic three-point background correction, is virtually zero, thereby improving detection limits.

In the Experimental Section, we will give the basic Kalman filter equations as adapted to ICP-AES and discuss the models used, as well as enough detail with respect to the innovations sequence to make clear the capability of the filter for background correction. Additionally, the way the measurements are done will be discussed. It should be noted that, before application of the filter, one has to know whether there are other components emitting in the spectral window of the analyte and, if so, what their wavelength positions are relative to the analyte emission. By using scanning monochromators and by taking scans to examine the spectral characteristics of the samples, most of the required data are readily available. As far as accurate data are missing, it will appear that it is the innovations sequence again that eases this method development. Therefore, the criterion of a "flat" innovations sequence is the key to the successful application of Kalman filtering.

With this knowledge, the analysis by Kalman filtering is quantitative and is automatically and routinely executed for all types of background. This paper will examine and illustrate the power of the Kalman filter approach by using several sample types. Passing over the data reduction of large signals of single elements on a flat background, we will discuss results for small noisy signals, nonlinear background, heavily structured and large background including spectral interference, and quantitative line selection for trace analysis in samples such as high-purity uranium and the BCR146 standard reference material of sludge.

Table I. Kalman Filter Equations Specified for ICP-AES

system dynamics	$\mathbf{C}(\lambda_k) = \mathbf{I}\mathbf{C}(\lambda_{k-1})$	(1)
measurement model	$x(\lambda_k) = \mathbf{S}^T(\lambda_k)\mathbf{C}(\lambda_k) + v(\lambda_k)$	(2)
state estimate extrapolation	$\mathbf{C}(\lambda_k\|\lambda_{k-1}) = \mathbf{C}(\lambda_{k-1}\|\lambda_{k-1})$	(3)
error covariance extrapolation	$\mathbf{P}(\lambda_k\|\lambda_{k-1}) = \mathbf{P}(\lambda_{k-1}\|\lambda_{k-1})$	(4)
Kalman gain vector	$\mathbf{K}(\lambda_k) = \mathbf{P}(\lambda_k\|\lambda_{k-1})\mathbf{S}(\lambda_k) \times [\mathbf{S}^T(\lambda_k)\mathbf{P}(\lambda_k\|\lambda_{k-1})\mathbf{S}(\lambda_k) + s_z^2]^{-1}$	(5)
state estimate update	$\mathbf{C}(\lambda_k\|\lambda_k) = \mathbf{C}(\lambda_k\|\lambda_{k-1}) + \mathbf{K}(\lambda_k)[x(\lambda_k) - \mathbf{S}^T(\lambda_k)\mathbf{C}(\lambda_k\|\lambda_{k-1})]$	(6)
error covariance update	$\mathbf{P}(\lambda_k\|\lambda_k) = [\mathbf{I} - \mathbf{K}(\lambda_k)\mathbf{S}^T(\lambda_k)]\mathbf{P}(\lambda_k\|\lambda_{k-1})$	(7)
noise assumptions	$s_z^2 = 1$	(8)
initial conditions	$\mathbf{C}(\lambda_0\|\lambda_0) = \mathbf{0}$	(9)
	$\mathbf{P}(\lambda_0\|\lambda_0) = 10000\mathbf{I}$	(10)
innovations sequence	in $(\lambda_k) = [x(\lambda_k) - \mathbf{S}^T(\lambda_k)\mathbf{C}(\lambda_k\|\lambda_{k-1})]/x(\lambda_k)$	(11)
innovations number	$N_{in} = (1/n)\sum_{k=1}^{n}$ in $(\lambda_k)^2$	(12)

EXPERIMENTAL SECTION

Kalman Filter. In Table I, the linear, discrete Kalman filter algorithm is specified for ICP-AES. Since measurements are made over the spectral window of the analyte, the independent variable is the wavelength λ_k. The sample system being studied is modeled by two equations. Equation 1 describes the wavelength dependence of the system and contains the quantities that will be estimated. It takes a trivial form, since the component concentrations in the sample obviously are the same at each wavelength position. As discussed below, always more than one component is present and $\mathbf{C}$ is a vector. $\mathbf{I}$ denotes the identity matrix. Equation 2 relates the concentrations to a measurable quantity. It takes the familiar form relating the concentrations to the measured signal x by the sensitivities $\mathbf{S}$. The superscript T means that $\mathbf{S}$ is a row vector and the scalar v gives the measurement noise present in x. Based on these two equations, the actual filter algorithm for ICP-AES can be specified. Equations 3 and 4 give the optimum a priori estimate $\mathbf{C}$ and its covariance matrix $\mathbf{P}$. Then, the measurement x at λ_k is made, and in eqs 5–7, optimum a posteriori estimates are calculated. Clearly, the filter is recursive and requires initial guesses, given in eqs 9 and 10. With the variance s_z^2 of the measurement noise set to 1 in eq 8, eqs 8–10 guarantee for our equipment that the concentration estimates do not depend on the initial guesses. It should be noted that the ratio between variance and diagonal covariances may be different in other ICP-AES measurement systems.

Placing the value of $x(\lambda_k)$ below the other as a function of k $(=1-n)$, eq 2 can be displayed as the pictograph in Figure 1 to ease the discussion of how to model the measured signal. Let us take, as a rather exhaustive example, one of the most difficult cases of background correction. The left-hand side of Figure 1 shows the measured signal to be the intensity in the sample scan over the window of the analyte. The analyte signal suffers in different degrees from spectral interference (direct line overlap), caused by some other components present in the sample. Furthermore, the unstructured, continuum background may exhibit nonlinear behavior, caused by a line wing due to some component, having its maximum emission outside the spectral window.

From the right-hand side of Figure 1, the sample scan is shown to be a superposition of several separate component sensitivities and continuum background contributions over the spectral window, weighted by the concentrations c and coefficients b. The pure component sensitivities (analyte and interferents) have to be determined experimentally, since modeling with theoretical, Gauss or Voigt, profiles does not lead to quantitation. Pure component scans are measured at approximately the highest concentration level expected in the samples to be analyzed. The intensities are divided by the corresponding concentration values.

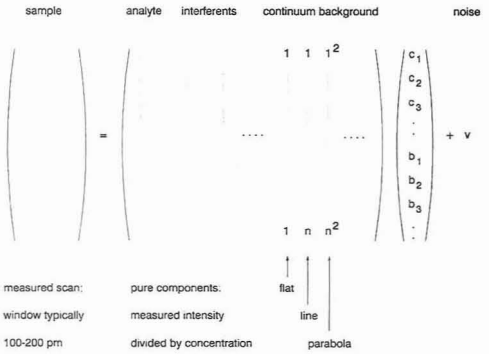

Figure 1. Pictograph of data reduction by Kalman filtering. The concentrations c_i and continuum background coefficients b_i are found in a recursive way; n is the number of data points.

When all the structured emission has been modeled in this experimental way, the "remaining" background can be theoretically modeled. This unstructured, continuum background shows at most a parabolic behavior, caused by a line wing, and can therefore be modeled through the three extra columns in Figure 1. Due to this modeling, the pure component scans do not need correction for their continuum background: when obtaining the pure component sensitivities, the measured total intensity (analyte plus background signal in each data point) is divided by the concentration value. As a consequence, the values of the background coefficients b are biased. However, one is not interested in their exact values.

In instances of a single analyte signal on a flat background, the sensitivity matrix has its smallest dimensions and consists of one pure component (analyte) sensitivity model and one flat continuum background model. The analyte sensitivity model is the calibration and is simply obtained by dividing the total intensity values measured in the calibration scan by the concentration. As usual, with any method, every time the analyte concentrations c_1 are determined, first the calibration is performed. If structured background interferes, one often is not interested in the concentration values c_2, etc., of the interfering components. In this case, only the shape of the model is important. The sensitivity models of the interfering components are determined once and stored in a data base. The next time, the analyte model is calibrated as above and the other models are retrieved from the data base. Filtering the first sample scan from a series of samples, it is best to include all three models for the continuum background. If, after filtering, the background turns out to be constant or linear, the higher order models may be dropped from the matrix to speed up subsequent computations.

Innovations Sequence. The sequence is defined by eq 11 in Table I. It gives the differences between the measured intensities in the sample scan and the a priori estimated intensities, normalized to the measured intensities. If the intensity estimates are accurate, the sequence is a white noise band: we talk about a flat innovations sequence. When calibration is omitted as with the interferents (see above), this does not affect the innovations sequence and the analyte concentration, since only the estimates of the interferent concentrations are accordingly adjusted. If the shape or wavelength position of one or more models is inaccurate, or if some emission is not modeled at all, the analyte concentration estimate is not accurate anymore and the innovations sequence is not flat. How to get the accurate shape is discussed with the experimental modeling in the previous section. In the other cases, we use the criterion of the "flatness" of the innovations sequence. The criterion is based on the innovations number, which is defined by us in eq 12. For a flat sequence, the number is at its minimum. The innovations criterion is used for the following reasons:

1. To position the sample scan at the proper wavelength with respect to the model(s). Given the sensitivity matrix, the sample scan is shifted over the wavelength axis, and for each position, the shifted scan is filtered, followed by the calculation of the innovations number. The minimum number is attained through the technique of successive interval halving. This drift compensation procedure is called by us innovations iteration. For each sample scan, the iteration has to be performed. Shifting scans is use to make quadratic interpolation in between data points.

2. To position the models in the case of structured background at the proper wavelengths. From a solution of the analyte and one interferent, the sample scan is measured; from the two pure component solutions, the models are determined. The models are positioned with respect to each other at some reasonable value of the relative wavelength position. This may be the literature value or the distance measured just now. Through innovations iteration, the minimum innovations number is obtained. Now the models are shifted with respect to each other, and again the number is calculated. The procedure is repeated until the "lowest" minimum innovations number is attained. Here, also, successive interval halving and quadratic interpolation are applied. Instead of the synthetic sample solution, the sample itself may be used; more interferents may be present. This so-called innovations optimization is essential, since the measured distance is affected by drift and since the literature data about relative peak positions usually are insufficiently accurate. With multicomponent analysis, the positions should be known up to 0.1 pm. Moreover, if hyperfine structure is present, the relative position depends on the actual spectrometer used.

At the start of some method development, an accurate knowledge of peak positions is not necessary: it is obtained through the innovations optimization. This part of the computations has to be done only once. The relative position will be stored for future use in the data base together with the interferent model.

3. To flag for unexpected emission. If additional structured background is present or if the continuum background needs an extra model of higher degree, the innovations sequence shows structure (except for line coincidence) or a sloping behavior. Since the innovations number is normalized to the measured intensity, the number should be of the order of the relative standard deviation, which is 0.01 or 1% for the ICP-AES system used by us. If the number is higher than this value, this may be an indication for unmodeled emission. However, it is better to look at the sequence itself. Then, the following rule can be formulated. If values in the sequence do not change sign and all are higher than +0.01 (or − 0.01) over more than the spectral bandwidth (10 data points, see below), a flag for unexpected emission is created, pointing at the region in question.

In the case of structured background, one can try to find out which component is emitting and perform additional measurements. Another approach is the use of a prerecorded scan, e.g., the scan for the analyte. Through the innovations optimization, the peak in this extra scan is accurately located in wavelength with respect to the analyte emission. Since at medium resolution up to about 85% (*8*) of the peak profiles are fully determined by the instrument function of the spectrometer, most of the time quantitation can be obtained in this rather simple way in the presence of unexpected spectral features. It should be noted that this procedure only is necessary in the case of overlapping lines. Otherwise, one just narrows the window in which the spectral data are filtered, without rerunning model or sample scans.

Equipment. The measurements were performed with a Perkin-Elmer Plasma II system equipped with a 1-m Ebert monochromator. In the configuration used for these experiments, the monochromator resolution is medium using a holographic grating with 1800 lines/mm, resulting in a practical spectral bandwidth measured to be about 17 pm (*4*). The spectral window is in the range of 100 pm, the analyte emission showing up in the center of the window. The step size amounts to about 1.5 pm.

Wavelength drift is an important factor to take into account. To compensate for drift during a full analysis, the innovations criterion is applied. In order to minimize drift in one scan, a fast scanning mode is used. The integration time has been chosen between 0.025 and 0.1 s/step. If it happens that the signal-to-noise ratio should be improved, replicate scans are taken. A peak search routine locates the peak maximum; the scans are shifted for coincidence of the maxima and the shifted scans are averaged. At the same time, one can perform the required statistics in the analysis.

Table II. Operating Conditions of the Perkin-Elmer Plasma II ICP Spectrometer

	Cd	B	Co
power, W	1400	1200	1000
obsvn height, mm	15	18	18
nebulizer argon flow, L/min	1.00	1.10	1.19
aux argon flow, L/min	1	1	1
plasma argon flow, L/min	15	15	15
sample uptake rate, mL/min	1	1	1
frequency, MHz	27	27	27
nebulizer	V-groove	V-groove	V-groove

In all experiments, the ICP operating conditions have been optimized for signal-to-background ratio. They are listed in Table II.

The raw, unsmoothed data from the Plasma II system were transferred to a Hewlett-Packard Vectra ES/12 microcomputer system with mathematical coprocessor. Interactive software with graphics support has been written in Turbo Pascal. If a series of measurements can be modeled with the same sensitivity matrix, the calculations in eqs 5 and 7 of Table I need to be done once and the Kalman gain vector is stored. To filter the sample scans, only eq 6 has to be executed. Note that eq 11 is part of eq 6. With the present PC systems, computing time and computer memory are not limiting factors. In all the experiments, the computing time for the fully automated procedure is shorter than the scanning time.

RESULTS AND DISCUSSION

Small, Noisy Signals. A typical sample scan is shown in Figure 2a. It was measured from a 20 μg/L Cd solution in a 90-pm-wide spectral window of Cd II 214.438 nm. Scan times range from 1.5 to 6 s.

The analyte model was determined from a 100 μg/L Cd solution. Obviously, the background is unstructured and flat; therefore, only the constant term was retained in the sensitivity matrix in order to model the continuum background. Application of the Kalman filter yielded the accurate concentration value.

Next, we used the resulting two coefficients (c_1 and b_1) to calculate the analyte and background signals estimated by the filter. From Figure 2a, one can judge the quality of the estimates. It is clear that the filter processes the full scan and, thereby, peak area instead of peak height and performs noise averaging.

Depending on the spectrometer used, conventional data processing is done in either a peak search approach or a direct peaking approach. When applying peak search, at least three points are needed to obtain a good curve fit and therefore a good determination of the peak intensity. More points may be used. However large the scan may be, the data are reduced to only one point for the peak and two for the background, which may be manually selected at fixed positions with respect to the peak. This three-point background correction can also be carried out automatically. A software approach is to smooth first the spectral data. Then, the highest intensity in the scan is determined, and the peak intensity is calculated by fitting a parabola through the highest intensity point and its neighbors. By application of a second-derivative technique, background points are found. A typical result for small, noisy signals is shown in Figure 2b: the peak intensity always is found to be too high and the background too low. Therefore, the net line intensity is too high. Since at small analyte signals the noise in the scan is dominated by the noise of the background signal, and since the peak-to-peak background noise has been measured to be 4.6 times the standard deviation, σ_B, of the background signal, the analyte intensity is up to $4.6\sigma_B$ too high. The effect of this systematic error decreases with higher concentrations. So, by calibration against the 100 μg/L Cd signal, the concentration in the sample is found to be too high. Since the software routines search for maximum and minimum values in the scan, another effect of automated three-point background correction is that always a signal is found, even when no analyte is present. This signal is larger than the signal ($3\sigma_B$) corresponding to the detection limit. Subtraction of the blank value from small analyte signals more or less compensates the too high concentration value, by making the same error twice.

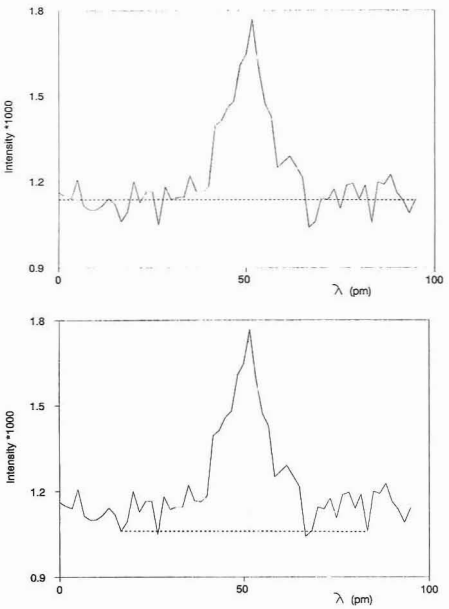

Figure 2. Data reduction of sample scan in the 90-pm-wide spectral window of Cd II 214.438 nm. (–) Sample scan of 20 μg/L Cd; (•••) estimate of analyte signal; (---) estimate of background signal. (a, top) Kalman filtering; (b, bottom) three-point background correction.

Due to the noise-averaging capability of the Kalman filter, the relative standard deviation in the net analyte signal is lower up to a factor of 3 as compared to three-point background correction in the automatic way described above.

Applying the direct peaking approach, the optical system, used in that case, allows for direct access to the top of the line, e.g., by moving the exit slit(s) and/or detector(s) on the Rowland circle. With a refractor quartz plate or via the motion of the entrance slit, (one or) two background points are reached. The points may be at fixed positions with respect to the top or may be found a priori from a scan. Anyhow, one manually selects three points in order to perform a fixed three-point background correction, speaking about "universal" background correction points or "recommended" background compensation regions, thereby introducing possible errors through changing line profile and background shape. Usually, the integration time amounts to 3–10 s/point, resulting in a 9–30-s measurement time. This is about 5 times slower than the measurement time needed for the application of Kalman filtering.

Nonlinear Background. This type of background occurs when the analyte signal is superimposed on the wing of a strong and broad emission line. Significant background changes may be found at wavelengths removed as far as 10 nm from the interfering line center. Figure 3a shows a 100-pm-wide spectral window of Cd II 214.438 nm; the sample

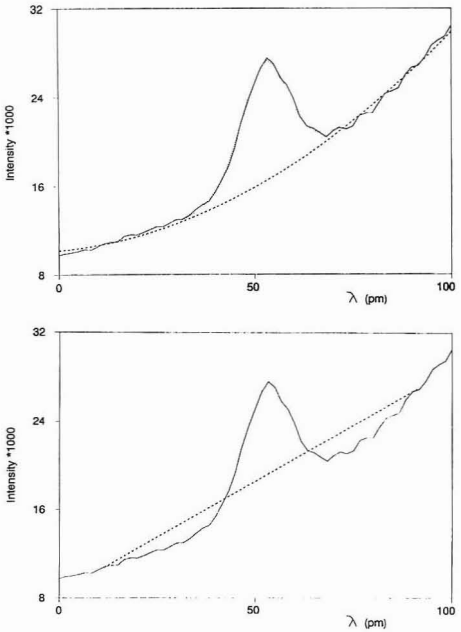

Figure 3. Data reduction of sample scan in the 100-pm-wide spectral window of Cd II 214.438 nm. (—) Sample scan of 500 μg/L Cd in a 9090 mg/L Al solution; (•••) estimate of analyte signal; (- - -) estimate of background signal. (a, top) Kalman filtering; (b, bottom) three-point background correction.

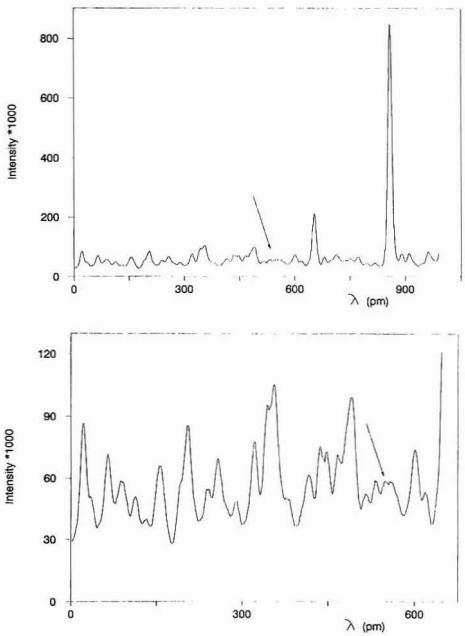

Figure 4. Sample scan of 15 680 mg/L U hydrolysate, spiked with 569 μg/L B. The arrow points at B I 249.773 nm. (a, top) 1000-pm-wide spectral window; (b, bottom) first 600 pm of spectral window in a.

contains 500 μg/L Cd in a 9090 mg/L Al solution. The Al line center is located 100 pm to the right of the Cd line.

The analyte model was determined from a 1 mg/L Cd solution. The background including the aluminum signal is nonlinear but does not show structured emission. So, it was modeled by a parabola for the continuum background in the sensitivity matrix. Application of the Kalman filter yields the accurate Cd concentration value. The quality of the estimates of the analyte and background signals can be judged from Figure 3a.

Modeling the background with a parabola suffices in the present spectral window. If the window is made larger, e.g., 150–200 pm, the innovations sequence shows a sloping behavior and a flag is generated for probably unmodeled emission. Since the aluminum emission is quasi-continuum emission, we prefer to add a fourth polynomial term to the theoretical background model instead of measuring the Al emission. In the latter case, one would have to prepare an Al standard and the rise in scan time is larger than the small rise in computing time. If the spectral window is made quite large (more than 200 pm), the top of the Al emission enters the window and its emission profile has to be measured.

Manual or automated three-point background correction causes systematic errors, since only straight lines can be fitted, whereas the background below the Cd emission has a parabolic shape. If it were always easy to select background points very close to the analyte line, the error would be as small as possible. But a typical selection of points is the one shown in Figure 3b: the error readily amounts to several tens of percents.

A nonlinear fit can be made if more than two background points are selected. This is done by Taylor and Schutyser (2) in their example of Pb in an Al matrix. In their approach, the noise characteristics are of crucial importance and should be determined experimentally and not modeled in an a priori theoretical noise relationship. In a spectral window of 100 sampling points, three to four replicate scans with 0.1–0.5-s integration time per step were needed. Then, in addition to its wider range of applications, Kalman filtering compares favorably with its single scan in a fast scanning mode.

A final possibility is interelement correction or dynamic three-point background correction (5). In a pure Al solution, the ratio is measured of the Al intensity at the analyte wavelength to the Al intensity at another wavelength where the Al signal is known to be free from interference in the sample. The ratio is used in the sample measurements to assess the Al intensity at the analyte wavelength. This approach, which is measured in two separate windows, is quite common in cases of line overlap but takes more time and raises the detection limit (5).

Large and Heavily Structured Background. In Figure 4a, the emission spectrum of a solution of hydrolyzed uranium hexafluoride (UF_6), containing 1.6% U, is displayed in a 1000-pm-wide spectral window of B I 249.773 nm. At first sight, it looks as if one strong line is superimposed on a noisy background. Closer inspection of the first 600 pm of the window in Figure 4b reveals that the "noise" in fact is structured emission from uranium. Note also the high level of the signal: the lowest intensity in the scan has an value of 30 000 units, whereas the reference background signal of the ICP, fed with pure water, amounts to about 1500 units in this wavelength region. This illustrates the main problem with trace analysis in uranium: the huge amount of strong emission lines. Due to the spectral interferences and the rise in background, the detection limits for trace elements in uranium are degraded by 1 or 2 orders of magnitude.

The arrows in Figure 4 point at an emission of 569 μg/L boron, with which the high-purity 15 680 mg/L U hydrolysate has been spiked. The boron contamination of uranium is of

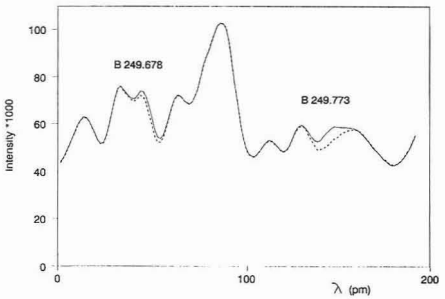

Figure 5. Data reduction of sample scan in the 200-pm-wide spectral window of B I 249.773 nm, including B I 249.678 nm. (—) Sample scan of 15680 mg/L U hydrolysate, spiked with 569 μg/L (---) Kalman filter estimate of background signal.

major importance in the nuclear industry. Because of its large neutron cross section, trace impurities can hinder a fission chain reaction. The ASTM C787 feed specifications for uranium hexafluoride require that the boron value not exceed 1 μg/g U or, in the present case, 16 μg/L boron.

Let us observe more closely the boron emission. Since the boron ground state is split due to spin–orbit coupling, Figure 5 shows apart from the U emission two B emission lines in a 200-pm-wide spectral window. These are the two most prominent lines, and in conventional data processing, inter-element or dynamic three-point background correction is required for both of them. Note that the B emissions are superimposed on sharp edges of U emission and that it is difficult to select a wavelength point at which the signal represents the continuum background signal. Although the detection limit in a pure boron solution is 4.8 μg/L (*9*), in the 1.6% U hydrolysate the detection limit is 505 μg/L and therefore greatly exceeds the ASTM specification. Three-point background correction for such a large and heavily structured background will always fail for trace analysis. This is why methods have been developed to determine trace elements in uranium by using chemical separation, like liquid–liquid extraction, before detection by ICP-AES. Disadvantages are also that some of the trace elements are extracted, the uranium matrix is not fully extracted, and the separation causes contamination, is time consuming, and results in a small sample volume, leaving fair amounts of nuclear waste.

As stated, the Kalman filter approach does not suffer from the dramatic rise in detection limit caused by line overlap. We spiked the high-purity 1.6% U hydrolysate with different amounts of B. Using the B and U pure component models and a flat continuum background, we determined the "Kalman" detection limit according to the procedure described in ref 6. The result is 20 μg/L, which is about the same as the ASTM specification.

This value is unexpectedly low. Certainly, by filtering, the rise in detection limit due to line overlap almost has been eliminated. Then, the Kalman detection limit can be estimated from the background intensity as follows. Since the U emission increases the background level at 249.773 nm from about 1500 in the pure component solution to 52 000 units, the so-called conventional detection limit (*5*) first is calculated to rise by the same amount from 4.8 to 160 μg/L; next, as the result of noise averaging by the filter—say a gain of 2—the conventional limit is expected to reduce to a Kalman detection limit of 80 μg/L. The additional gain from 80 down to 20 μg/L is attributed to the effect of using more than one emission line in the Kalman filter data reduction, viz. two lines of B and about eight lines for U.

Table III. Ratio of Conventional to Kalman Detection Limit as a Function of the Number of Emission Lines in the Spectral Window of the Analyte

analyte–matrix	emission line, nm	no. of lines: analyte	no. of lines: matrix	conventional/Kalman	ref
Zn–Fe	213.856	1	1	1.2	8
Cd–Fe	226.502	1	2	2.3	6
Nd–Pr	401.225	1	2	2.5	6
Si–Cr	251.611	1	3	4.2	8
B–U	249.773	2	8	6.7	this work

In trace analysis with line-rich matrices, already an effect was noticed from the number of matrix emission lines in the spectral window of the analyte (*8*): the extra emission allows an accurate estimate of the matrix emission at the wavelength of the analyte. Thereby, the rise of detection limit due to line overlap virtually has been eliminated, even in the case of nearly coincident emission lines (peak separation less than 3 pm at about 20-pm spectral bandwidth). Here, another effect is observed upon the reduction from conventional to Kalman detection limit. The reduction is not only due to noise averaging, but also due to multiple line analysis. The impact of more emission lines in the spectral window on the detection limit can be seen from Table III. Line-rich matrix elements are notorious for strong interferences, and it is hard to perform trace analysis in the three-point background correction approach. With Kalman filtering, just the opposite is true: the more emission lines, the better chance to resolve a spectral interference and to attain detection limits of the order of the limits for the pure component solutions. As a consequence, there is an advantage in using rather large spectral windows (100–200 pm).

In order to perform routine analysis of uranium, the U models in the spectral windows of the trace elements are determined once and stored in a data base. The model for B or another element should be measured daily for proper calibration, as usual. Together with the continuum background model, the sample scans, directly measured from the matrix solution, can be processed for trace analysis. In a subsequent paper, we will report about the setup of routine analysis by Kalman filter data reduction for about 30 trace elements in uranium that is intended for feed material to a gaseous diffusion plant.

In summary, with Kalman filtering instead of three-point background correction, the B detection limit in the U matrix is reduced from 505 to 20 μg/L: without chemical separation, the ASTM specification and the Kalman detection limit meet each other. This result gives promise for routine trace analysis in line-rich matrices, e.g., in rare-earth elements, refractory alloys, high-purity metals, soils, sediments, or sludges. There will be less need for solid-phase extraction on microcolumns and liquid–liquid extraction or for preconcentration by precipitation and adsorption by using chemically bonded chelating groups.

Line Selection. High-resolution spectrometers can be used to decrease the extent of spectral interferences. Even then, line selection may be required for quite a number of analytes. The determination of Co in soils and sediments gives a clear example of how line selection at high resolution usually is performed (*10*, *11*).

According to a qualitative analysis, the spectral windows of Co are examined for spectral interferences from the major and minor elements found. The most prominent Co line at 238.892 nm is expected to suffer from wing interference due to strong emission of Fe 238.863 nm (see Table IV and refs 12 and 13). The second line at 237.862 nm is subject to overlap from two lines, viz. Fe 237.853 nm and Al 237.841 nm. The

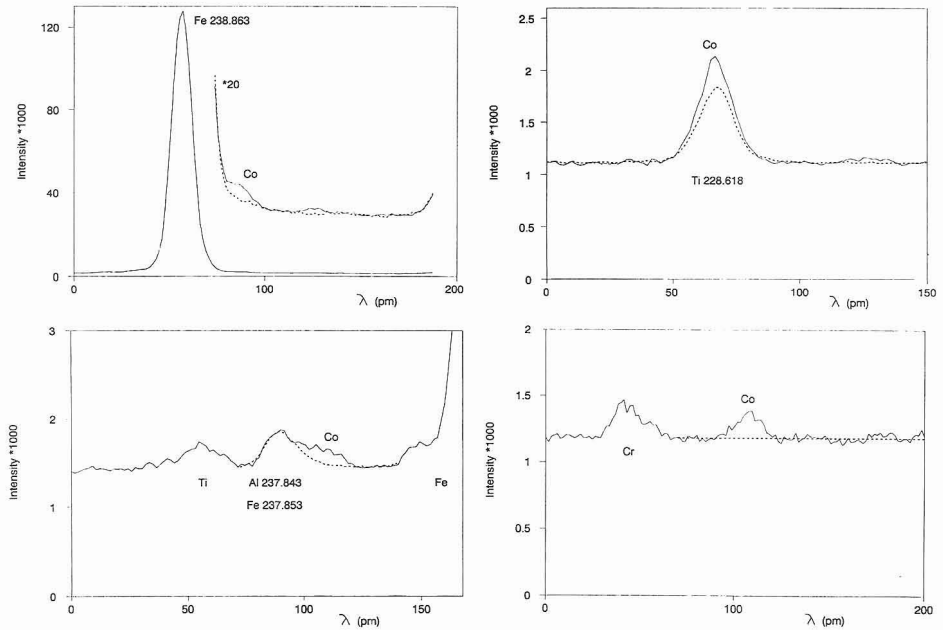

Figure 6. Data reduction of sample spectra at the four most prominent lines of Co. (—) Sample scan of Co in BCR146; (---) Kalman filter estimate of background signal. (a, top left) 200-pm-wide spectral window of Co II 238.892 nm; (b, bottom left) 150-pm-wide spectral window of Co II 237.862 nm; (c, top right) 150-pm-wide spectral window of Co II 228.616 nm; (d, bottom right) 200-pm-wide spectral window of Co II 230.786 nm.

Table IV. First Four Prominent Co Lines for Qualitative Line Selection and Kalman Filter Results for Co in BCR146

wave-length, nm	pure component detection limit, μg/L	interference, nm	Kalman filter results	
			Co concn, μg/g	sd[a]
238.892	6	Fe 238.863	12.1	0.5
237.862	11	Fe 237.853 Al 237.841	11.7	0.9
228.616	12	Ti 228.618	11.8	1.0
230.786	14	none	12.6	1.2
			11.8 certified	0.7

[a] Ten consecutive scans with same sample and sensitivity models.

next Co emission at 228.616 nm cannot be used, since there is almost direct line overlap of Ti 228.618 nm. (This interpretation fails in ref 11, where an emission at 228.624 nm is identified with the Ti 228.618 nm line.) Only the fourth line at 230.786 nm does not suffer from interferences and is suitable for soil and sediment analysis. This practice is called by us qualitative line selection, since the selection is based on whether interfering intensity may be present or not.

In fact, a rigorous, quantitative criterion has to be applied. Such a criterion is the true detection limit, i.e., the limits measured for the various lines in the actual sample solution (*5*). This approach takes some extra time but, unfortunately, has not been applied routinely.

The BCR146 certified reference material is a sewage sludge of industrial origin, produced by the Community Bureau of Reference (Commission of the European Communities). It has been dissolved by us using hydrofluoric acid to obtain the total content of the trace amount of Co, which is certified to be 11.8 ± 0.7 μg/g. In Figure 6, sample scans are displayed in the 150–200-pm-wide spectral windows of the four most prominent Co lines. From the scan around the first line, in Figure 6a at medium resolution (17 pm), it can be seen that the wing interference is not strong. Therefore, it is a bit surprising that with high-resolution spectrometers (*10*) this Co emission has not been used for analysis. This may be a consequence of the qualitative line selection.

The Co, Fe, Al, and Ti models were determined: the continuum background was flat. Through innovations optimization, the Co–Fe peak separation for the most prominent line in Figure 6a is found to be 29.4 pm. For the second line, the Co–Al and Co–Fe separations are 20.7 and 10.5 pm, respectively. In filtering, only the central part of the Co 237.862-nm spectral window has been used (Figure 6b). BCR146 contains a large amount of titanium oxide, so the Co 228.616-nm line is strongly interfered, as can be seen from Figure 6c. Although the Co–Ti peak separation is only 1.5 pm, while using a 17-pm spectral bandwidth, the filter can handle the signals by taking the average of 10 scans, which have been measured at short integration times. In this way, peaks lying 1 pm apart can be discriminated at medium resolution. Matrix matching of the pure component solutions was not necessary. Application of the Kalman filter yields the concentration values, including standard deviations, listed in Table IV. By using automatic three-point background correction for the fourth line, as discussed above with small, noisy signals, a result of 14.9 ± 1.2 μg/g is obtained.

The first conclusion from Table IV is that the concentration value is accurate for all the lines studied. Next, the precision values exactly parallel the detection limits of the four most prominent lines in the pure component solution. By Kalman filtering, the effect of interferents, which raise detection limits in accordance with their intensities for different amounts when

three-point background correction is used, has been eliminated, and line selection is not necessary. It should be noted that line selection does not become superfluous in Kalman filtering. In instances of "significant interference" (*8*, *14*), when the total background signal raises the true detection limit of the first line, by more than a factor of 2 above the true limit of the second line, line selection is necessary. Also, high-resolution monochromators, of course, remain useful, e.g., to recognize or resolve interferences, or to decrease the total background level measured under the analyte line, thereby lowering detection limits.

Finally, the standard deviation in the concentration value is directly related to the Kalman detection limit (*6*), which is a true detection limit (i.e., measured from the actual sample solution and not determined from the hypothetical pure component solution). So, if line selection is required in Kalman filtering, it can be done in a quantitative way: the standard deviation is the rigorous, quantitative criterion for line selection. As usual, in analysis, one measures 4–10 consecutive sample scans. Then, the standard deviation directly results from the calculation of the concentrations by Kalman filtering.

CONCLUSIONS

In ICP-AES analysis, one always should know a priori whether there are other elements emitting in the spectral window of the analyte. Taking scans in order to learn about the spectral characteristics of the sample, it is best to use this information in data reduction or background correction.

In the examples discussed, ranging from "simple" to "desperate" levels of background correction, we have shown that Kalman filtering automatically and quantitatively processes scans that usually are measured with slew-scan monochromators. This data reduction appears to provide several significant advantages over conventional processing of spectral data. The Kalman filter approach including the criterion of the flatness of the innovations sequence corrects the signal accurately for all types of background; uses a fast scanning mode; processes the spectral scan, i.e., peak area instead of peak height; will do with one calibration scan for the analyte and for possible interferent components; may determine simultaneously the concentrations of all components, emitting in the spectral window; optimizes inaccurately known spectral data, such as relative peak positions; uses a data base for the spectral data of the interferents; does not need a search for the peak maximum and the background points; does not need background correction in the pure component scans; flags for unexpected emission, except for exact line coincidence; resolves overlapping signals down to 1-pm peak separation at 20-pm spectral bandwidth; reduces, but not eliminates, the need for line selection, high resolution, or chemical separation of analyte and matrix; performs line selection, if needed, in a quantitative way; allows multiple line analysis; achieves detection limits lower by a factor of 1–3 below the traditional value for the pure component solution, as the natural result of noise averaging over the full spectral window; and does not suffer from the degradation of detection limit due to line overlap.

Taking advantage of the interaction between these several opportunities, Kalman filtering yields precise and accurate results, especially when processing small, noisy analyte signals, nonlinear background signals, or spectrally interfered analyte signals. The approach results in true detection limits (i.e., the limit in the sample solution), which are lower than those attained by three-point background correction.

The use of the innovations sequence is essential, among others to correct for spectral drift. However, the sensitivity matrix equation may be solved by any multicomponent analysis technique. Finally, the approach does not correct for nonspectroscopic matrix effects.

ACKNOWLEDGMENT

We thank A. P. Wassink, from Urenco Nederland Operations B. V., Almelo, The Netherlands, and A. G. Snijders, from Tauw Infra Consult B. V., Deventer, The Netherlands, for the kind supply of samples.

LITERATURE CITED

(1) Boumans, P. W. J. M. *Line Selection and Spectral Interferences, Inductively Coupled Plasma Emission Spectrometry*; Part 1, *Methodology, Instrumentation, and Performance*; Boumans, P. W. J. M., Ed.; Wiley: New York, 1987; Chapter 7, pp 411–417.
(2) Taylor, P.; Schutyser, P. *Spectrochim. Acta* **1986**, *41B*, 81–103.
(3) Salit, M. L.; Collins, J. B. Presented at the Pittsburgh Conference, New York, March 5–9, 1990; Paper 352.
(4) Van Veen, E. H.; Goudzwaard, M. P.; De Loos-Vollebregt, M. T. C.; De Galan, L. *Appl. Spectrosc.* **1989**, *43*, 96–103.
(5) Boumans, P. W. J. M.; Vrakking, J. J. A. M. *Spectrochim. Acta* **1987**, *42B*, 819–840.
(6) Van Veen, E. H.; De Loos-Vollebregt, M. T. C. *Spectrochim. Acta* **1990**, *45B*, 313–328.
(7) Mermet, J. M. Presented at the XXVI Colloquium Spectroscopicum Internationale, Sofia, Bulgaria, July 2–9, 1989; Paper Inv. 27.
(8) Van Veen, E. H.; Oukes, F. J.; De Loos-Vollebregt, M. T. C. *Spectrochim. Acta* **1990**, *45B*, 1109–1120.
(9) Winge, R. K.; Fassel, V. A.; Peterson, V. J.; Floyd, M. A. *Inductively Coupled Plasma-Atomic Emission Spectrometry*; *An Atlas of Spectral Information*; Elsevier: Amsterdam, 1985.
(10) Kanda, Y.; Taira, M. *Anal. Chem. Acta* **1988**, *207*, 269–281.
(11) Schramel, P. *Mikrochim. Acta* **1989**, *3*, 355–364.
(12) McLaren, J. W.; Berman, S. S.; Boyko, V. J.; Russell, D. S. *Anal. Chem.* **1981**, *53*, 1802–1806.
(13) McLaren, J. W.; Berman, S. S. *Spectrochim. Acta* **1985**, *40B*, 217–225.
(14) Boumans, P. W. J. M. *Spectrochim. Acta* **1990**, *45B*, 1121–1138.

RECEIVED for review December 27, 1990. Accepted March 21, 1991. We express our thanks to the Perkin-Elmer Corp., Norwalk, CT 06856, for financial support.

Enhanced Selectivity for Spectrochemical Measurement by Mode Selection in Fully Resonant Nonlinear Mixing

Roger J. Carlson[1] and John C. Wright*

Department of Chemistry, University of Wisconsin—Madison, 1101 University Avenue, Madison, Wisconsin 53706

In this paper, we demonstrate the feasibility of a new family of mode-selective spectroscopies based on multiresonant nonlinear mixing. Three tunable lasers are used for fully resonant four-wave mixing so the output signal depends on the simultaneous contribution from three resonances. Mode selection is accomplished by tuning the lasers to a particular vibrational resonance. Vibrational spectra are obtained by scanning the second resonance. The resulting spectrum shows selective enhancements of all the modes that are related to the mode selected by the first resonance. In this paper, we demonstrate the capabilities of this approach for enhancing features that are very weak in conventional spectroscopies and for separating features that are spectrally overlapped.

INTRODUCTION

Multiresonant nonlinear mixing represents a new frontier for spectroscopy with the promise of high spectral selectivity (*1*). In conventional spectroscopies that are controlled by single optical resonances, a single spectrum must represent a given sample. The spectra for multiresonant mixing spectroscopy can be very different from each other because they depend on a multiplicity of resonances. This multiplicity potentially can provide the experimentalist with great control and selectivity over the measurement.

Multiwave mixing is performed by focusing several lasers into a sample and measuring the output light that occurs at frequency combinations of the input lasers. The light is generated because the electric fields of the lasers induce polarizations in the electron clouds of the sample that are oscillating at the laser frequencies. If the fields are large, there are distortions in the oscillating polarization that have Fourier components at combinations of input frequencies. The light launched by these Fourier components is the signal frequency measured in the experiment. The efficiency of generating the new light is enhanced if there are resonances with energy states of the sample material.

The resonances used for the four-wave mixing experiments reported in this paper are shown in Figure 1. They are identical with a coherent anti-Stokes Raman scattering (CARS) experiment, but the resonances are used for specific purposes. One resonance is used to choose a vibrational mode while a second resonance is established with an excited electronic state. This second resonance can select particular components from a mixture or narrow an inhomogeneous profile. The third resonance is scanned to provide a spectrum. The spectrum contains enhancements for those transitions associated with the mode selected by the first resonance. For molecular samples, the v level is a vibrational state of the ground electronic state, the 0′ level is an excited electronic state, and the v′ level is a vibrational state of the excited electronic state. If states v and v′ correspond to the same vibrational mode or if there is mixing of the two modes, there is an enhancement in the signal that can be quite large. This effect has been used to identify the different vibrational and vibronic features of pentacene-doped benzoic acid (*2*). In this paper, we show how this effect can be used to enhance weak transitions and to resolve peaks that are overlapped.

[1] Present address: The James Franck Institute, 5640 Ellis Ave, Chicago, IL 60637.

THEORY

The efficiency of the four-wave mixing process is controlled by the third-order susceptibility, $\chi^{(3)}$ (*3*). In the third-order perturbation theory, $\chi^{(3)}$ is

$$\chi^{(3)} = \frac{N}{\hbar^3}\left(\frac{n^2+2}{3}\right)^4\left(\sum_{v',0',v,0}\frac{\mu_{00'}\mu_{0'v}\mu_{vv'}\mu_{v'0}}{\delta_{0'0}\delta_{v0}\delta_{v'0}}\right) \quad (1)$$

where

$$\delta_{0'0} = \omega_{0'0} - \Omega_{0'0} - i\Gamma_{0'0}$$
$$\delta_{v0} = \omega_{v0} - \Omega_{0'0} + \Omega_{0'v} - i\Gamma_{v0}$$
$$\delta_{v'0} = \omega_{v'0} - \Omega_{0'0} + \Omega_{0'v} - \Omega_{v'v} - i\Gamma_{v'0}$$

0, 0′, v, and v′ represent the vibrationless ground and excited electronic states and their vibrational and vibronic states, respectively, N is the concentration of chromophores, n is the index of refraction, Ω_{ij} is the laser frequency for the ij resonance, and μ_{ij}, ω_{ij}, and Γ_{ij} are the dipole transition moment, the transition frquency, and the dephasing rate for the i → j transition. The summation occurs over all possible states of the molecule. The intensity of the four-wave mixing is proportional to $|\chi^{(3)}|^2$ and it can become quite large if several terms in the denominator become simultaneously resonant.

The multiple resonances for the four-wave mixing are controlled by the δ_{ij} in the denominator. In the scans reported in this paper, $\delta_{0'0}$ and δ_{v0} are held at constant values while $\delta_{v'0}$ is changed by the scanning. Peaks appear when $\delta_{v'0}$ becomes resonant. This spectrum is related to the absorption spectrum since the linear absorption intensity depends on $|\mu_{v'0}|^2/\delta_{v'0}$. One can show that the relative intensity of lines in the four-wave mixing spectrum scales as the square of the absorption spectrum if there are no specific enhancements from the other resonances (*4*). In this paper, we will be concerned specifically with such enhancements as a means of improving detectability and selectivity.

The key idea is to use one of the resonances to select a specific mode that will be labeled v_s for the mode selected. In order to clarify the discussion, we assume that only the states in resonance are important in the summation of 0, v, and 0′ in eq 1 and that v_s is the mode selected for resonance. We further assume that there are only two excited vibrational states that are important for v′. The first mode will be labeled v_s' and is the same as the mode selected by the ground vibrational state resonance. The second mode is labeled by v_d' and represents all the modes that are different from the selected mode. With this approximation

$$\chi^{(3)} = \frac{N}{\hbar^3}\left(\frac{n^2+2}{3}\right)^4\left(\frac{\mu_{0'0}\mu_{0'v_s}\mu_{v_sv_s'}\mu_{v_s'0}}{\delta_{0'0}\delta_{v_s0}\delta_{v_s'0}} + \frac{\mu_{0'0}\mu_{0'v_s}\mu_{v_sv_d'}\mu_{v_d'0}}{\delta_{0'0}\delta_{v_s0}\delta_{v_d'0}}\right) \quad (2)$$

The first term in $\chi^{(3)}$ has two resonance enhancements that

0003-2700/91/0363-1449$02.50/0 © 1991 American Chemical Society

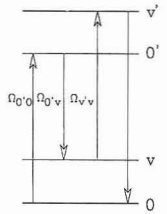

Figure 1. Energy level diagram for four-wave mixing.

are associated with the same mode while the second term has two resonance enhancements that are associated with different modes. If $\delta_{0'0}$ and δ_{v0} are maintained at resonance and a scan over the v' levels is performed by changing $\Omega_{v'v}$, there will be two peaks in the spectrum corresponding to the v' resonance in the two terms of eq 2. If the line widths of v_s' and v_d' are the same, the relative intensities will depend on the ratio $\mu_{v_sv_s'}\mu_{v_s'0}/\mu_{v_sv_d'}\mu_{v_d'0}$. The ratio $\mu_{v_s'0}/\mu_{v_d'0}$ is the same factor that is important in controlling the relative intensities in the absorption spectrum but the ratio $\delta_{v_sv_s'}/\mu_{v_sv_d'}$ is unique to the four-wave mixing experiment. It would be similar to the absorption experiment where state v_s was populated instead of the ground state. The relative size of $\mu_{v_sv_s'}$ and $\mu_{v_sv_d'}$ is controlled by the Franck–Condon overlap between v_s and either v_s' or v_d'. Since v_s and v_s' involve the same mode, there will be a large overlap between them, assuming there aren't large changes in the excited-state structure. The overlap between v_s and v_d' will depend upon how much common character is shared. If the two modes involve motion of common chromophores in the molecule, there could be large overlap. More typically, the modes are isolated or involve motions that are not related to each other, so that $\mu_{v_sv_d'}$ is small while $\mu_{v_sv_s'}$ is large. The effect is a large enhancement of modes with v_s character in the spectrum. For an ideal Franck–Condon system, the enhancement in the relative intensity of the selected peak is $(1 - 2/\Delta^2)^2$ where Δ is the excited-state displacement along the internal coordinate of the selected mode (*4*). For small displacements (e.g., $\Delta = 0.1$), the enhancement could be 4×10^4.

EXPERIMENTAL SECTION

Pentacene-doped benzoic acid crystals (10^{-5} mole fraction) were used as a model system to understand the nonlinear spectroscopy that controls mode selection. This system has become an excellent model for fully resonant four-wave mixing because it is well-understood (*5*). The typical crystal was $5 \times 5 \times 1$ mm and was oriented with a polarized microscope so the polarized pentacene absorption lines were maximized in our experiment. The experiments were performed at 2 K in pumped liquid helium in order to minimize homogeneous broadening of the electronic transitions. An excimer laser was used to pump three tunable dye lasers that were used for $\Omega_{0'0}$, $\Omega_{0'v}$, and $\Omega_{v'v}$ frequencies in the four-wave mixing. The lasers were attenuated so the intensity in the focal region of the sample was typically 0.5, 30, and 1.5 MW/cm^2 for the $\Omega_{0'0}$, $\Omega_{0'v}$, and $\Omega_{v'v}$ lasers, respectively. The typical laser line width was 0.2 cm^{-1}, and the pulse width was 5 ns. The lasers were focused to 50–200 μm into the helium Dewar flask containing the sample. Scans across the v' levels shown in Figure 1 were performed by fixing $\Omega_{0'0}$ and $\Omega_{0'v}$ and scanning $\Omega_{v'v}$. The output signal at $\Omega_{0'0} - \Omega_{0'v} + \Omega_{v'v}$ was spatially isolated with an aperture and spectrally isolated with a double monochromator that was scanned in synchronization with the dye laser. The signal was detected by a photomultiplier and a boxcar averager. Wavelength calibration of the lasers was accomplished with a Fizeau wavemeter. A coplanar phase matching geometry was used with the angles (typically 1–2°) between the beams adjusted to maximize the spatial isolation of the output beam. All of the spectra reported in this paper were recorded with the light polarized along the *c* axis of the crystal.

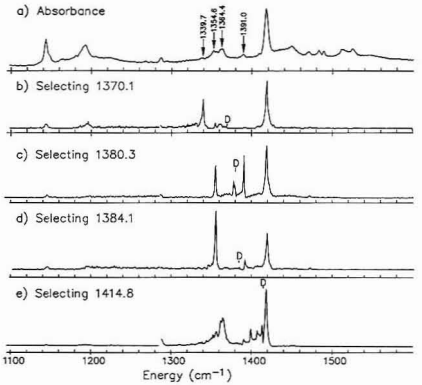

Figure 2. Spectral scans across the vibrational energy states of the excited electronic state of pentacene. The *x* axis is calibrated in terms of the energy difference from the vibrationless excited electronic state at 16 999 cm^{-1}. The top spectrum is a conventional absorption spectrum while the lower four spectra show the four-wave mixing scans over the same region but maintaining resonance with the different ground-state vibrational modes. The energy (in cm^{-1}) is indicated in each scan.

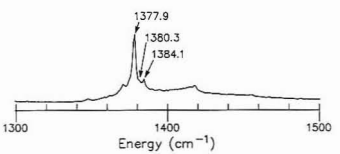

Figure 3. Spectral scan of the fluorescence from pentacene. The *x* axis is calibrated in energy relative to the vibrationless transition between the excited and ground electronic states at 16 999 cm^{-1}.

RESULTS

The absorption spectrum of pentacene-doped benzoic acid is shown in Figure 2a. The *x* axis is calibrated in terms of the excited-state vibrational energy. It is obtained by taking the difference between the absorption energy and the energy of the vibrationless excited electronic state at 16 999 cm^{-1}. Note the very weak lines at 1339.7 and 1391.0 cm^{-1} and the poorly resolved lines at 1354.6 and 1364.4 cm^{-1}.

A series of four-wave mixing scans are shown in Figure 2b–e. For each of these, $\delta_{0'0}$ is set to resonance with the excited electronic state at 16 999 cm^{-1} while δ_{v0} is set to the different vibrational resonances indicated in the figure. The $\delta_{v'0}$ resonance is scanned across the same range as shown in the absorption spectrum. If there are no common modes between the v state selected and the v' states in the spectrum, the relative intensities in Figure 2b–e would scale as the square of the absorption spectrum. The strongest transitions would always be favored by this consideration, and indeed, the 1419-cm^{-1} vibronic transition is seen in all the spectra of Figure 3. (It is strongest when the 1377.9-cm^{-1} vibrational state is selected since it is the same mode as the 1419-cm^{-1} vibronic state.) Despite the presence of this one line, the spectra are generally very different from each other and from the absorption spectrum. There are large selective enhancements of the particular transitions that involve the same mode as that chosen by the constant vibrational resonance.

In Figure 2b, there is a strong enhancement of the very weak transition at 1339.7 cm^{-1} because it corresponds to the same mode as the 1370.1-cm^{-1} vibrational state selected by the δ_{v0} resonance. Note that there is a 30.4-cm^{-1} decrease in the energy of this mode when the electronic state is excited. The

point labeled D in the spectrum corresponds to the 1370.1-cm^{-1} energy of the ground-state mode. An artifact is often observed at this position because it corresponds to the point where $\Omega_{0'0} = \Omega_{v'v}$ in the scan so the detector can observe signal at $2\Omega_{0'0} - \Omega_{0'v}$ and $2\Omega_{v'v} - \Omega_{0'v}$ at the same time as $\Omega_{0'0} - \Omega_{0'v} + \Omega_{v'v}$.

Figure 2d,e shows the separation of the two overlapping lines at 1354.6 and 1364.4 cm^{-1} in the absorption spectrum. In Figure 2d, the selection of the 1384.1-cm^{-1} vibrational mode results in a large enhancement of the 1354.6-cm^{-1} line, while in Figure 2e the selection of the 1414.8-cm^{-1} vibrational mode results in a large enhancement of the 1364.4-cm^{-1} line. The enhancements are so large that there is no visible contribution from the overlapping line. One can also see a line at 1399 cm^{-1} that isn't visible in the absorption spectrum.

Figure 2c shows the enhancement of the weak line at 1391 cm^{-1} when the 1380.3-cm^{-1} vibrational mode is selected, again because they correspond to a common mode that increases by 10.7 cm^{-1} when excited to the higher electronic state. There is also a strong enhancement of the 1354.6-cm^{-1} line, indicating that it is coupled to the 1380.3-cm^{-1} vibration.

Comparison of the spectra in parts c and d of Figure 2 reveals that the line at 1391.0 cm^{-1} is very strongly dependent on the vibrational reasonance. Changing the vibrational resonance from 1380.3 to 1384.1 cm^{-1} eliminates the line. If the 1391.0-cm^{-1} resonance was monitored while the vibrational resonance was scanned, there would clearly be a sharp and strong peak at 1380.3 cm^{-1}. The fluorescence spectrum in Figure 3 shows there is a very weak fluorescence transition that corresponds to the 1380.3-cm^{-1} state. It is buried on the side of the much stronger 1377.9-cm^{-1} state together with the 1384.1-cm^{-1} state. It is clear that mode-selective nonlinear spectroscopy would provide sufficient enhancement to resolve this weak feature in the fluorescence spectrum.

The spectrum in Figure 2e shows selective enhancement for the 1399-cm^{-1} mode in addition to the 1364.4-cm^{-1} mode already discussed. In addition, there are two other weak peaks between the 1399-cm^{-1} and the main 1419-cm^{-1} lines that also appear to be selectively enhanced. These lines are attributed to modes that are coupled to the selected 1414.8-cm^{-1} vibrational mode. The line shape of the 1419-cm^{-1} mode shows destructive interference effects with the nearby resonances. From eq 1, it is clear that all resonance combinations add at the amplitude level so the nonlinear intensity will have cross-terms that can constructively or destructively interfere and alter the line shapes.

CONCLUSIONS

Nonlinear laser methods are very different from traditional spectroscopic methods, and it would be interesting to compare linear and nonlinear methods. Such as comparison, however, is premature because the basic capabilities of the nonlinear methods are not defined. Nonlinear methods are very interesting because they potentially offer some unique advantages. In this work, we have demonstrated a new mode selective capability that can be used for distinguishing overlapped spectral transitions, enhancing weak transitions, and establishing relationships between the vibrational transitions in a molecule. The methods are based on the simultaneous multiple resonances that together control the character of spectra obtained by multiresonant four-wave mixing. Although the capability has been demonstrated for four-wave mixing in a configuration that matches traditional CARS experiments, the ideas and methodology are general and can be potentially applied to any multiresonant nonlinear spectroscopic method. One can except a rapid evolution of these new ideas as research continues.

LITERATURE CITED

(1) Wright, J. C.; Carlson, R. J.; Riebe, M. T.; Steehler, J. K.; Nguyen, D. C.; Lee, S. H.; Price, B. B.; Hurst, G. B. In *Raman Spectroscopy: Sixty Years On: Vibrational Spectra and Structure*; Bist, H. D., Durig, J. R., Sullivan, J. F. Eds.; Elsevier: Amsterdam, 1989; pp 123–158.
(2) Carlson, R. J.; Wright, J. C. *J. Chem. Phys.* **1990**, *92*, 5186–5195.
(3) Shen, Y. R. *Nonlinear Optics*; Wiley: New York, 1984; Chapter 2.
(4) Carlson, R. J.; Nguyen, D. C.; Wright, J. C. *J. Chem. Phys.* **1990**, *92*, 1538–1546.
(5) Decola, P. L.; Andrews, J. R.; Hochstrasser, R. M.; Trommsdorf, H. P. *J. Chem. Phys.* **1980**, *73*, 4695–4697.

RECEIVED for review February 20, 1991. Accepted April 24, 1991. This research was supported by the National Science Foundation under Grant CHE-8903556.

Probe-Mounted Fiber Optic Assembly for Laser Desorption/Ionization Fourier Transform Mass Spectrometry

Jeremiah D. Hogan, Steven C. Beu, and David A. Laude, Jr.*

Department of Chemistry, The University of Texas at Austin, Austin, Texas 78712

Vahid Majidi

Department of Chemistry, University of Kentucky, Lexington, Kentucky 40506

A probe-mounted fiber optic interface for laser desorption/ionization (LDI) Fourier transformation mass spectrometry (FTMS) is demonstrated as an alternative to conventional optical assemblies for mass spectral analysis of nonvolatile and large molecular weight compounds. Among advantages of the fiber optic interface are low cost and ease of alignment and repair. Power densities to 2×10^8 W/cm^2 are obtained at the probe tip for 1064-nm light from a Nd:YAG laser. Results are similar to those obtained with pulsed CO_2 lasers in that cationized molecular species dominate the spectra of peptides, porphyrins, polymers, and polymer additives in the 500–2000-Da range. The effects of sample probe displacement from the trapped-ion cell on LDI/FTMS performance are also evaluated toward an improved understanding of the mechanism by which LDI-generated ions are trapped in the cell. For metal ions such as Au^+, signal intensity is invariant at distances up to 35 cm from the cell. In contrast, potassium-attached organic molecular ions such as gramicidin S, polyethylene glycol 1000, and dilauryl thiodipropionate exhibit a reduction in spectral *S/N* with increasing probe displacement. This is in keeping with a gas-phase mechanism for ion formation in the trapped-ion cell. From a practical perspective, spectral reproducibility and quality are enhanced for both metal and organic samples by positioning the sample probe several centimeters from the cell to minimize spectral distortion due to space charge effects.

The combination of pulsed high-power lasers with Fourier transform mass spectrometry (FTMS) has been successfully applied to a variety of desorption/ionization (LDI), multiphoton/ionization (MPI), and photodissociation (PD) experiments. In particular, following initial demonstrations by Gross (*1*) and Wilkins (*2*), LDI has evolved into a successful and general soft-ionization source for high-mass FTMS analysis of organic molecules and biomolecules. This success is partially attributed to a compatibility of LDI with both the low analyzer pressure and strong magnetic field requirements of high-performance FTMS (*3*). Lasers commonly used for LDI/FTMS are pulsed CO_2 lasers operating at 10.6 μm and Nd:YAG lasers operating at 532 and 1064 cm (*2–14*). Interfaces are constructed from optical components, including windows, mirrors, and lenses, which are compatible with desired laser wavelength and power density and with ultrahigh vacuum. For example, a common CO_2 laser interface employs Zn–Se windows and lenses to steer light from the laser into the vacuum chamber and focus it onto a probe-mounted sample positioned adjacent to and along the center line of the trapped ion cell (*3*). With typical spot sizes of less than 1 mm^2, desired power densities in the 10^8–10^9 W/cm^2 range are easily achieved. A survey of the LDI/FTMS literature indicates that a wide range of chemical compounds are amenable to analysis including peptides to mass 2000 (*4*), porphyrins (*5*), simple sugars and carbohydrates (*6*, *7*), small organic polymers (*8*, *9*), polymer additives (*10*, *11*), nucleosides (*12*), and clinical drugs (*13*), among others. LDI/FTMS performance at high mass can be exceptional as demonstrated by the mass resolution of 60 000 obtained for the mass 5922 ion of a poly(propylene glycol) 4000 ion (*15*).

Despite the successes of LDI/FTMS, present interfaces are not ideal. This is because access to the trapped-ion cell in superconducting magnet systems is restricted and, consequently, optical assemblies are complex and alignment is difficult to achieve and retain. Thus, the first objective of this paper is to introduce a probe-mounted fiber optic assembly, as an alternative to present laser interfaces, that does not suffer from these constraints. Fiber optics previously have been used for laser applications in mass spectrometry with LDI performed in sector (*16*), triple-quadrupole (*17*), and quadrupole ion trap (*18*) mass analyzers and photoionization performed in a quadrupole ion trap (*19*). One disadvantage of the fibers used in this earlier work was that the maximum laser power density of 10^7 W/cm^2 achieved as unfocused output from the fiber would be inadequate to generate desired spectra for many compounds. At least 1 order of magnitude improvement in power density through the fiber would be necessary to reproduce the results obtained with conventional optical designs. However if successful, the higher power fiber optic interface would offer advantages of design simplicity and ease of alignment and repair.

The second objective of the work to be presented is demonstration of the probe-mounted interface in fundamental studies of the mechanism by which ionization and trapping events occur during the LDI/FTMS experiment. An improved understanding of these aspects of the experiment is necessary because progress in FTMS high-mass analysis with not only lasers but also other ionization sources has been frustrated on several fronts: (1) Hunt and co-workers have observed an unexpected reduction in sensitivity and mass resolution in the analysis of organic molecules above a few thousand molecular weight with a liquid secondary-ion mass spectrometry (SIMS) external source FTMS (*20*, *21*); (2) infrared LDI/FTMS fails to generate spectra for peptides beyond mass 2000 (*3*); (3) matrix-assisted ultraviolet LDI/FTMS is to date unsuccessful for the insulin chain-A at mass 2535 and other higher mass proteins (*22*). Spectra can be obtained for the samples and ionization techniques referred to above if time-of-flight (TOF) mass analyzers are substituted for FTMS, so evidently the problem in acquiring LDI/FTMS spectra rests with some aspect of the FTMS experiment. One explanation for the problems just described is that as a consequence of ions being formed outside the FTMS cell in these experiments, the spatial and kinetic energy distribution of the

* To whom correspondence should be addressed.

0003-2700/91/0363-1452$02.50/0 © 1991 American Chemical Society

externally generated ion population is incompatible with the processes by which ions are successfully trapped and detected. For example, externally generated ions must traverse a single trapping electrode and subsequently experience a change in axial kinetic energy with respect to the apparent trapping potential if they are to be retained for detection. Implications of these requirements as they relate to the quality of FTMS spectra, which ultimately are generated, is a subject of interest in the FTMS community (*21*, *23–26*).

The renewed interest in defining the various mechanisms by which LDI occurs can be attributed to recent successes in the field of ultrahigh mass analysis and specifically to the demonstration of matrix-assisted laser desorption (*27*, *28*). Most of these efforts, however, have been the province of TOF mass spectrometry (*29–33*). As will be explained, FTMS is in some ways unsuitable for evaluating the LDI experiment because it behaves as an energy-selective filter in sampling ions. What is known from TOF studies is that a demarcation of laser ionization experiments can be loosely drawn on the basis of laser power density (*29*, *30*). At power densities around 10^5–10^6 W/cm^2, primarily neutral species are desorbed and a secondary-ion source is required to generate ions for analysis. In the region between 10^7 and 10^9 W/cm^2 a transition occurs as increasing numbers of analyte ions result directly from the laser event. Molecular species dominate spectra of large organic molecules. Kinetic energies associated with the organic ions generated in this manner are usually on the order of a few electronvolts (*31*), and it is these ions which are most likely to be detected by FTMS. Possible mechanisms for ionization include thermal evaporation of ions (*1*), ion–molecule reactions in which desorbed neutral species undergo cation attachment or charge exchange (*31*), and ion formation at the surface by a momentum-transfer process (*18*). At still higher power densities, transition to a new ionization regime, termed laser plasma ignition, occurs (*30*). Laser plasma ignition is characterized by extensive fragmentation or atomization of the sample and by product ion kinetic energies in the range of tens to hundreds of electrovolts (*32*, *33*). Distinction between the different regimes based strictly on power density is tenuous, however, as sample, matrix, sample density, wavelength, and pulse duration among other variables are found to influence the threshold and efficiency of ionization. The matrix-assisted UV LDI experiment, in particular, falls outside the generalizations just described. For example, Chait and co-workers find that laser-assisted ultraviolet LDI is most efficient at power densities in the range of 10^5 W/cm^2 (*34*).

Because the laser desorption event can produce such markedly different mass and kinetic energy distributions, it is important to recognize the bias introduced to the spectrum by the mass analyzer selected for detection. FTMS, in particular, is susceptible because the kinetic energy distribution of laser desorbed ions is of the same magnitude as trapping potentials in the trapped-ion cell. Evidence of the difficulty in characterizing the LDI/FTMS experiment is the present inability to explain the observation that while laser desorption occurs outside the trapped-ion cell, large FTMS signals are generated even though trapping potentials are maintained throughout the experiment. Possible explanations that rely upon some aspect of the laser experiment are the occurrence of ion–molecule reactions in the cell and the creation of an electric field by the desorbed ion plasma which acts to shield some ions until the trapping electric fields are penetrated. Alternately, the mechanism by which ions are trapped may be independent of the laser event and instead be another example of a trapping phenomenon observed in numerous external source FTMS experiments in which ions accumulate in the cell. Explanations given for accumulated trapping in FTMS cells include charge-exchange reactions in the cell (*23*), ion–ion or ion–neutral collisional stabilization in the cell (*24*), and the redistribution of z axis kinetic energy into radial energy in inhomogeneous magnetic fields in the cell (*25*, *26*).

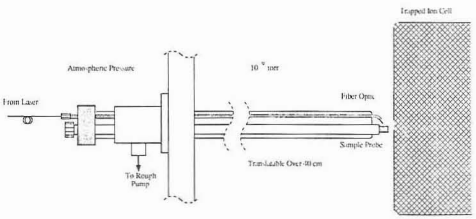

Figure 1. Schematic diagram of the probe-mounted fiber optic interface.

One aspect of the LDI/FTMS experiment that has yet to be fully evaluated, but which should provide insight into the nature of the trapping mechanism, is the spatial orientation of the sample probe with respect to the trapped-ion cell. In most applications the sample probe is positioned in proximity to the cell and usually along the z axis center line of the cell. However, Freiser (*35*) has observed that even when the laser is fired at a sample positioned in the fringing magnetic field, analyte ions are subsequently detected in the cell without focusing or changing the trap plate potentials. Also curious is the observation by Gross (*1*) and Eyler (*36*) of LDI/FTMS spectra for samples positioned several cm from the center line of the cell, near excite and detect plates. Unfortunately, any controlled study of the spatial relationship between the sample and trapped-ion cell is tedious and unreliable with conventional optical assemblies since the vacuum chamber must be vented and the optics repositioned for each new orientation of the sample probe. With no guarantee of reproducibility during translation, such experiments have not been performed. One advantage of the interface to be discussed is that by mounting both the optical fiber and sample on a translatable probe, such measurements are easily accomplished.

In summary, the intentions of this paper are 2-fold: (1) demonstration of the fiber optic/sample probe assembly as an alternative to more traditional optical designs for general application to LDI/FTMS of nonvolatile organic compounds and (2) use of the probe-mounted assembly to evaluate possible mechanisms by which ions are trapped in the FTMS cells.

EXPERIMENTAL SECTION

The FTMS instrument used for the LDI experiments was constructed from components that make up the Nicolet Analytical Instruments FTMS 2000 instrument. It includes a 6-in. bore, 3.0-T superconducting magnet, a 5-in. stainless steel cylindrical vacuum chamber that achieves system base pressures in the low 10^{-9}-Torr range, and a 4.76 cm × 4.76 cm × 9.52 cm elongated stainless steel trapped-ion cell centered in the bore of the magnet. Vacuum system temperatures are continuously maintained at 175 °C. The spectrometer is controlled by software executed on a Nicolet 2000 data station.

The laser used for all desorption studies is a Spectra Physics DCR-11 Nd:YAG laser which for 1064-nm light has an 8–9-ns pulse width and maximum 275-mJ pulse energy. All spectra to be presented were acquired with 1064-nm light. Output from the laser was split by using a 10% reflective lens, with 90% discarded and the remainder focused through a 15 cm focal length lens to a focal point 2 mm in front of the optical fiber. A 2-m length of optical fiber, HIP-P-600 from General Fiber Optics, Inc., specified for high-power applications, was used. It consists of a 600 μm diameter fused-silica core surrounded by a hard plastic optical cladding and a Teflon buffer, which brings the total outer diameter to 1.05 mm. This fiber is capable of transmitting 1064-, 532-, and 355-nm light with sufficient transmission to permit power densities at the sample surface of low-to-mid 10^8 W/cm^2.

The LDI interface shown in Figure 1 integrates the optical fiber and a $^1/_4$-in. sample probe within a hollow 1 m length by $^3/_4$ in. diameter probe assembly. The probe assembly is inserted through a $2^3/_4$ in. gate valve and can be translated along the center line of the vacuum chamber over a 40-cm distance from the edge of the cell to the end of the vacuum chamber, which is in the fringing magnetic field. One end of the optical fiber is mounted in a translatable optical mount and positioned to intercept the path of the laser light. The optical fiber is sheathed in $^1/_{16}$-in. stainless steel tubing sheath that is mounted inside the $^3/_4$-in. probe. The fiber is sealed to vacuum at a $^1/_{16}$-in. Swagelok union with a graphite ferrule. At the high-vacuum end, the $^1/_{16}$-in. tubing is positioned within a few millimeters of the sample surface with the optical fiber protruding from it by about 1 mm. For this work the stainless steel tubing was bent to achieve an incident angle of 45° with respect to the sample surface. The approximate distance between fiber and probe tip was 1 mm. A Gentec Model ED-200 joulemeter was used to calibrate the light energy. For a 9-ns, Q-switched pulse, operating at a 10-Hz repetition rate, light exiting the fiber exhibited an approximately linear calibration covering a range up to 23 mJ. At increased laser energies, dielectric breakdown of air in front of the fiber occurred with consequent reduction in light throughput.

Samples were deposited on a demountable probe tip positioned on the end of a $^1/_4$-in. stainless steel sample probe that was also inserted in the $^3/_4$ in. diameter outer probe. The sample probe was both rotated and translated along the z axis to permit multiple firings over the entire sample surface. Probe tips used for the experiments included a 2 cm length by 6 mm diameter stainless steel cylinder and a similar tip with the end machined to a conical shape at a 45° angle. No difference in LDI spectra was observed for these sample orientations, so the cylinder was used in the present work because of an increased number of laser firings per sample. Organic samples were dissolved in appropriate solvents and deposited dropwise on a spinning probe tip to leave a thin uniform coating. Typically, KBr was either mixed directly with samples in suitable solvents or, alternately, it was burnished on the probe tip. For some experiments the stainless steel tip was plated with gold to obtain Au^+ spectra.

LDI data acquisition commenced with a quench pulse to remove ions from the cell. Termination of the quench event coincided with triggering the laser. After the laser firing a delay of from 500 ms to 5 s (depending on the magnitude of the pressure burst), was inserted to allow system base pressures of about 1×10^{-8} Torr to return. Spectra of organic ions were detected by applying a wide band swept excitation pulse over a 2.6-MHz bandwidth at a sweep rate of 1000 Hz/μs. Broad-band spectra with at least nominal mass resolution were then collected, typically with 32–64K data points acquired over bandwidths ranging from 1000 to 100 kHz. All spectra of organic molecules were acquired from a single laser firing. Ion intensities varied less than 10% from shot to shot, unless otherwise noted. However, 3–5 transients were coadded for translational and laser power studies in which quantitative information was measured. Gold spectra were acquired by applying a 100-μs single frequency excite at the cyclotron frequency of Au^+ followed by broad-band detection. For gold translational studies, 10 transients each resulting from a single laser firing were coadded to generate a single transient. All transients were processed by applying sine bell apodization and a magnitude Fourier transform.

RESULTS AND DISCUSSION

Of initial interest was determination of the general utility of the fiber optic interface for analysis of nonvolatile organic, inorganic, biological, and organometallic materials. The wide applicability of the conventional interface was previously noted, and a similar performance for the fiber optic interface would be desirable. There are, however, several possible complications. Most LDI/FTMS instruments utilize a CO_2 laser capable of higher energies than the Nd:YAG laser, although with 275-mJ maximum pulse energy and spot sizes of less than 0.9 mm^2 necessary power densities for LDI are easily achieved for the Nd:YAG laser. Moreover, the CO_2 laser is not as well suited as the Nd:YAG laser for the fiber optic interface because of its poorer focusing characteristics. A more important restriction to the interface is the damage threshold for the fiber, which limits the pulsed laser energy that can be transported. As originally conceived, the laser light exiting the fiber was to be focused through a lens assembly so that lower laser energies would initially be required. However such an arrangement is difficult to integrate into a probe-mounted interface and detracts from the design simplicity intended with such an interface. Instead, it was decided to evaluate the use of unfocused postfiber light.

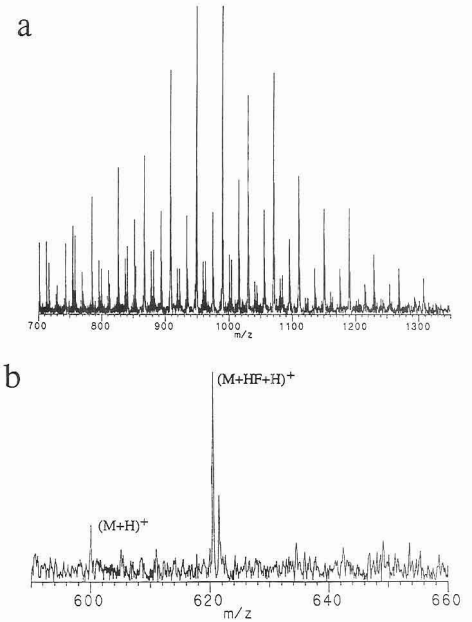

Figure 2. Representative single-shot LDI/FTMS spectra of (a) polyethylene glycol 1000 and (b) sapphyrin (m/z 599).

An important consideration with this design was whether the substantial angular divergence of the light exiting the fiber would result in unacceptably low power densities for ionization. For example, the maximum of 23 mJ of 1064-nm radiation that could be transmitted through the fiber would require a spot size of less than 1 mm^2 to obtain power densities above 10^8 W/cm^2. It was determined that by positioning the 600 μm diameter fiber at a 45° angle with respect to the surface, and within 1 mm of the surface, an elliptical spot size measuring about 0.9 mm^2 was obtained at the sample probe. A nearly linear calibration of laser power ranging from 1×10^7 to 2×10^8 W/cm^2 was then measured for this configuration. This maximum value is 1 order of magnitude higher than that reported with other fiber optic interfaces and approaches acceptable levels for general LDI applications to organic molecules.

LDI/FTMS spectra for a wide range of chemical classes were obtained with the fiber optic interface. These included low molecular weight peptides, polymers, polymer additives, porphyrins, carbon clusters to mass 5000, and metal oxide clusters. Presented in Figure 2 are representative spectra of polyethylene glycol 1000 and sapphyrin (m/z 581), a pentapyrrolic macrocycle (*37*). The PEG 1000 exhibits the expected envelope of potassium-attached $(CH_2CH_2O)_nK^+$ units along with smaller distributions corresponding to Na^+ and H^+ attachment. The sapphyrin spectrum is of interest because it

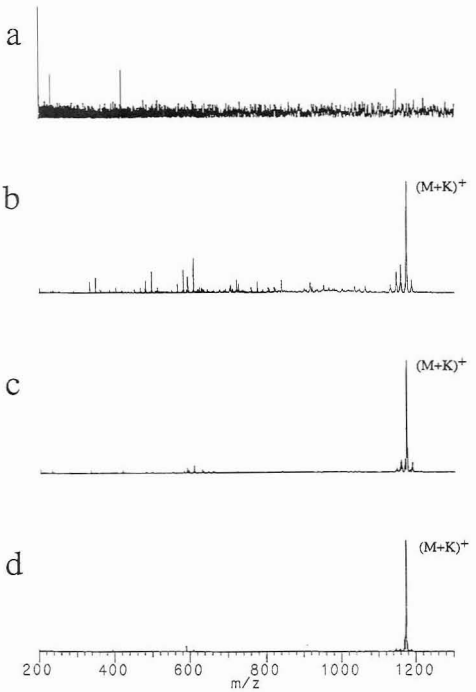

Figure 3. Comparison LDI/FTMS spectra of gramicidin S doped with KBr at laser power densities of (a) 0.7×10^7 W/cm^2, (b) 2.3×10^7 W/cm^2, (c) 5.0×10^7 W/cm^2, and (d) 8.6×10^7 W/cm^2. All spectra were acquired from the 1064-nm line from a Nd:YAG laser focused through the optical fiber.

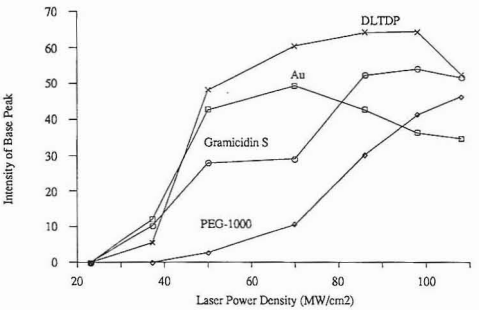

Figure 4. Comparison LDI/FTMS profiles of the signal intensity of the potassium-attached molecular ion for several organic compounds as laser power density through the optical fiber was increased.

was obtained where fast atom bombardment with a double-sector mass spectrometer was unsuccessful in generating a molecular ion; in Figure 2b the encapsulation of F^- in the porphyrin core is distinguished from OH^-, as suggested by the mass difference of 20 corresponding to HF.

The extent of fragmentation as a function of laser power was next examined. A general trend observed for CO_2 lasers is that fragmentation increases with increasing laser power (*3*). However, this was not the case in our initial work with a series of polymer additives (*12*), nor was this trend observed in later experiments in which power density was more carefully controlled. For example, Figure 3 presents comparison spectra of gramicidin S, an 1184 molecular weight cyclic decapeptide, as laser energy transmitted through the fiber is increased. At power densities below 1×10^7 W/cm^2, no ion signal is detected although a visible mark on the probe tip indicates a significant neutral population was desorbed. In the range 1×10^7 to 3×10^7 W/cm^2, the first LDI species are observed and include a significant fraction of fragment ions. At still higher power densities the relative proportion of fragment ions is reduced until, above 5×10^7 W/cm^2, the potassium–attached molecular cation dominates to the extent that even the $(M + Na)^+$ and $(M + H)^+$ species are suppressed. Thus the tendency toward reduced fragmentation at increasing laser power, at least to the limit of power densities for this interface, is supported. Unfortunately, any conclusive evaluation of fragmentation associated with the desorption process is complicated by FTMS detection. For example, it is conceivable that fragment ions continue to be formed at higher laser powers but are not detected because changes in kinetic energy are not conducive to trapping. It is also possible that a discrimination against detection of other ions occurs due to the limited dynamic range in the trapped-ion cell as the $(M + K)^+$ population increases.

One additional trend to be noted from the gramicidin S data in Figure 3 is that the total ion abundance, in the form of molecular species, tends to increase with laser power within the operating range of the fiber. This is confirmed in Figure 4 for other organic molecules where the intensity of the cationized molecular ion is presented as a function of increasing laser power. In general, all exhibit a threshold for ionization of about 2×10^7 W/cm^2, beyond which a sizeable analyte ion populations is detected. The trend toward increasing FTMS signal is typical of all samples to 1×10^8 W/cm^2. Beyond this point reductions in signal intensity for gramicidin S, and dilaurylthiodipropionate (DLTDP, m/z 514.41) are most likely due to the ion population exceeding the space charge limit of the cell. In contrast, PEG 1000 yields high-quality spectra of increasing S/N to the limit of laser power through the fiber. The delayed onset of space charge may be due to the uniform distribution of isomass ion packets throughout the cell, since this would reduce the Coulombic repulsive effects experienced by individual ions.

Translational Studies. One advantage of this fiber optic interface is that it can be used to evaluate the spatial relationship between the desorption/ionization event and subsequent trapping of ions in the cell. This is because once the orientation of the optical fiber with respect to sample is optimized, it can remain fixed as the probe is translated throughout the vacuum chamber. This experiment would be difficult to perform in a reproducible fashion with conventional optics since tedious venting and realignment procedures would be required, with no certainty that desorption characteristics would be retained. The translatable interface can be used to investigate several aspects of the relationship between ion formation and trapping during LDI/FTMS and a few initial experiments are presented here to indicate its capabilities.

To be presented are FTMS signal intensity profiles for gold ions and for several cation-attached organic ions, all acquired with the sample probe positioned at distances of up to 40 cm from the trapped-ion cell. There are important differences between LDI of bare metal and organic materials that should be mentioned to assist in interpretation of the data to be presented. First, the number of metal ions produced in the LDI experiment is much larger than for organic ions under identical laser conditions and is usually in vast excess of the number required to yield high S/N FTMS spectra. Consequently, for most LDI experiments with metals the dynamic range of the trapped-ion cell is exceeded and a nonlinear relationship between desorbed ion population and FTMS signal intensity quickly arises. To minimize this problem, laser

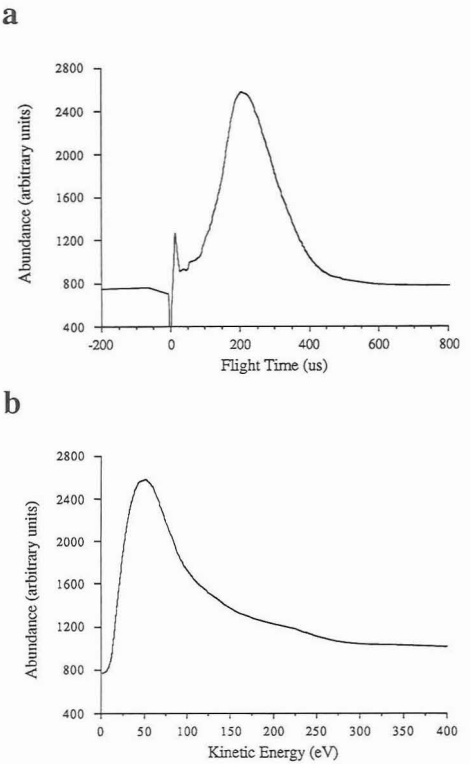

Figure 5. (a) Time of flight and (b) resulting kinetic energy profile for the ion species generated by laser desorption of a gold-plated probe tip. The data are for low-power light from the Nd:YAG 1064-nm line. Data were acquired with a TOF/FTMS instrument with desorption occurring in the fringing magnetic field approximately 1 m from a detector positioned on the opposite side of the magnet.

power densities were reduced to just above the ionization threshold, although at higher trap potentials the linear range of the experiment was still exceeded. A second difference between organic and metal LDI is the mechanism for ion formation. Gold ions are formed by LDI in the dense plasma at the sample surface, while organic ions are formed by cation attachment in the gas phase away from the desorption site. One final difference in the LDI process that is of great importance to the FTMS experiment is the kinetic energy distributions of the desorbed ions. Cation-attached organic ions have kinetic energies of less than 1 eV (*31*), which is compatible with typical FTMS trapping potentials. In contrast, laser-desorbed metal ions exhibit a surprisingly broad kinetic energy distribution extending to hundreds and even thousands of electronvolts (*33*). For example, presented in Figure 5a is a profile of gold ions obtained from TOF detection without postacceleration in a tandem TOF/FTMS instrument (*38*). Laser powers were adjusted to just above the threshold for ionization to minimize the ion population and range of kinetic energies. Still, as the profile in Figure 5b indicates, kinetic energies for Au^+ were distributed around 70 eV and extended to hundreds of electronvolts, values which are not compatible with efficient trapping for FTMS detection.

Presented in Figure 6 are LDI/FTMS profiles of Au^+ signal intensity as a function of increasing distance from the cell for various trapping potentials. In general, signal intensity at the higher trapping potentials is invariant with probe displacement at distances of up to between 30 and 35 cm from the cell. Beyond this region, the FTMS signal intensity falls abruptly as ions encounter a strong initial radial magnetic field and are unlikely to assume appropriate trajectories to overcome the magnetic mirror effect. Even ions that do successfully traverse this region are less likely to be trapped because they incur a greater average axial kinetic energy than ions which are desorbed closer to the cell. There are several explanations for the ability to trap ions that are on average of much higher kinetic energy than are consistent with the applied trapping potentials. One possibility is that some fraction of ions with energies slightly higher than the applied trapping potential penetrate the first electrode and then lose or redistribute axial kinetic energy while in the cell. Alternatively, lower energy ions initially may be shielded from the trapping fields by the desorbed plasma but later experience these fields in the cell as shielding effects in the evolving plasma deteriorate. Neither mechanism must be efficient to generate the abundant FTMS signals that are observed, since with the enormous number of metal ions formed by LDI only a very small fraction would need to possess the appropriate kinetic energies and trajectories to be trapped. Experiments are underway to discern the extent to which either of these effects is occurring.

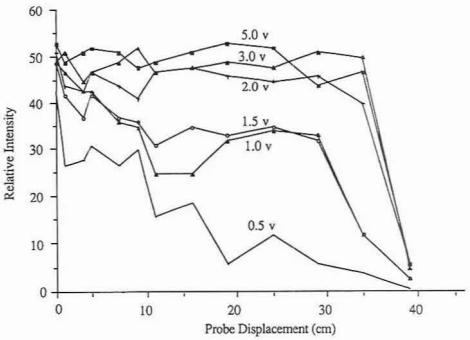

Figure 6. LDI/FTMS signal profiles for Au^+ desorbed from a gold-plated sample probe at increasing displacement from the trapped ion cell and for different trapping potentials. Each datum is the relative peak height from a spectrum consisting of 10 coadded scans. Laser power density was just above the ionization threshold to minimize the number of desorbed ions formed.

An extension of the LDI translational studies to organic molecules doped with KBr was performed. In contrast with the gold ion data, profiles of cation-attached organic molecules in Figure 7 indicate that a continuous reduction in signal intensity occurs as the sample probe is displaced from the trapped-ion cell. Both DLTDP and gramicidin S exhibit a local maximum adjacent to the cell, a depression at 1–3 cm from the cell, a rise to new maxima, and then a gradual erosion of the signal out to 35 cm. PEG exhibits a smoother curve with a maximum at about 5 cm, but the signal disappears at a distance of 25 cm from the cell. The depression observed at distances a few centimeters from the cell in the Figure 7 profiles is not necessarily indicative of reduced $(M + K)^+$ formation in the cell for these probe positions but instead may result from space charge effects. Poor line shapes in the spectra support this contention. These data raise the question of optimum probe position for LDI/FTMS experiments. For the DLTDP and gramicidin S samples it was found that the most reproducible, high-quality spectra were generated with the probe positioned between 5 and 10 cm from the cell. At

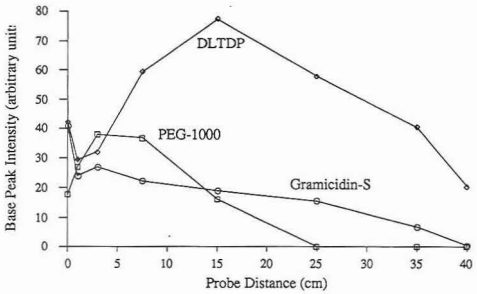

Figure 7. LDI/FTMS signal profiles for the potassium-attached molecular ion of three organic compounds at increasing displacement from the trapped-ion cell. A 1.3-V trapping potential was used. Each datum is the relative peak height from a spectrum consisting of three coadded laser firings, each on fresh sample.

this distance the adverse spectral features such as peak splitting and line broadening were not observed.

Several mechanisms can be suggested to explain the trapping of cation-attached organic ions in the LDI/FTMS experiment, but one in particular, is strongly dependent upon the evolving spatial and kinetic energy characteristics of the laser-desorbed species. From arguments made by Kistemaker for TOF measurements (*31*), ion–molecule reactions between cations in the plasma and intact neutral analyte might be occurring in the cell. The organic ion displacement profiles in Figure 7 do show a strong dependence of the FTMS signal intensity on probe position, which cannot be explained by magnetic mirror effects. Kistemaker's evidence for gas-phase cation attachment is in keeping with these results. For the LDI/FTMS experiment, one feasible explanation is that potassium ions are desorbed with sufficient kinetic energy to overcome the initial trap plate potential, enter the cell where they collide with cooler neutral analyte molecules, and form a cation-attached molecular species that can be trapped. Because probe translation away from the cell would shift the region of maximum overlap for these two velocity distributions, an increasing number of low-energy cation-attached molecular ions would form outside the cell. These cooler ions would not be able to penetrate the trapping fields, and the detected signal would diminish. Work is in progress to verify this mechanism for FTMS trapping of cation-attached organic ions formed by LDI.

LITERATURE CITED

(1) McCreary, D. A.; Ledford, E. B., Jr.; Gross, M. L. *Anal. Chem.* **1982**, *54*, 1435–1431.
(2) Wilkins, C. L; Weil, D. A.; Yang, C. L.; Ijames, C. F. *Anal. Chem.* **1985**, *57*, 520–524.
(3) Nuwaysir, L. M.; Wilkins, C. L. In *Lasers and Spectrometry*; Lubman, D. M., Ed.; Oxford Series on Optical Sciences; Oxford University Press: 1989; Chapter 13.
(4) Wilkins, C. L.; Yang, C. L. C. *Int. J. Mass Spectrom. Ion Processes* **1986**, *72*, 195.
(5) Brown, R. S.; Wilkins, C. L. *Anal. Chem.* **1986**, *58*, 3196–3199.
(6) Coates, M. L.; Wilkins, C. L. *Biomed. Mass Spectrom.* **1985**, *12*, 424.
(7) McCreary, D. A.; Gross, M. L. *Anal. Chim. Acta* **1985**, *178*, 103–116.
(8) Brown, C. E.; Kovacic, P.; Wilke, C. E.; Cody, R. B.; Kinsinger, J. A. *J. Polym. Sci. Polym. Lett. Ed.* **1983**, *23*, 453–463.
(9) Brown, R. B.; Weil, D. A.; Wilkins, C. L. *Macromolecules* **1986**, *19*, 1255–1260.
(10) Asamota, B.; Young, J. R.; Citerin, R. J. *Anal. Chem.* **1990**, *62*, 61–70.
(11) Johlman, C. L.; Wilkins, C. L.; Hogan, J. D.; Donovan, T. L.; Laude, D. A., Jr.; Youseffi, M. J. *Anal. Chem.* **1990**, *62*, 1167–1172.
(12) McCreary, D. A.; Gross, M. L. *Anal. Chim. Acta* **1985**, *178*, 91–103.
(13) Shomo, R. E., II; Marshall, A. G.; Weisenberger, C. R. *Anal. Chem.* **1985**, *57*, 2940–2944.
(14) Watson, C. H.; Baykut, G.; Eyler, J. R. *Anal. Chem.* **1987**, *59*, 1133–1138.
(15) Ijames, C. F.; Wilkins, C. L. *J. Am. Chem. Soc.* **1988**, *110*, 2687–2688.
(16) Emory, W. B.; Wood, K. V.; Cooks, R. G. *Anal. Chem.* **1987**, *57*, 1069–1071.
(17) Cecchetti, W.; Polloni, R.; Maccioni, A. N.; Traldi, P. *Org. Mass Spectrom.* **1986**, *21*, 517–518.
(18) Hand, O. W.; Emory, W. B.; Winger, B. E.; Cooks, R. G. *Int. J. Mass Spectrom. Ion Processes* **1989**, *90*, 97–118.
(19) Louris, J. N.; Brodbelt, J. S.; Cooks, R. G. *Int. J. Spectrom. Ion Processes* **1987**, *75*, 345–352.
(20) Hunt, D. F.; Shabanowitz, J.; Yates, J. R., III; McIver, R. T., Jr.; Hunter, R. L. *Anal. Chem.* **1985**, *57*, 2728–2733.
(21) Hanson, C. D.; Castro, M. E.; Russell, D. H.; Hunt, D. F.; Shabanowitz, J. *FTMS of Large (m/z > 5000) Biomolecules*; ACS Symposium Series No. 359; American Chemical Society: Washington, DC, 1987; pp 100–115.
(22) Hettich, R. L.; Buchanan, M. V. *J. Am. Soc. Mass Spectrom.* **1991**, *2*, 22–28.
(23) Beu, S. C.; Laude, D. A., Jr. *Int. J. Mass Spectrom. Ion Processes* **1990**, *97*, 295–310.
(24) Hunt, D. F.; Shabanowitz, J.; McIver, R. T., Jr.; Hunter, R. L.; Syka, J. E. P. *Anal. Chem.* **1985**, *57*, 765–766.
(25) Kerley, E. L.; Hanson, C. D.; Castro, M. E.; Russell, E. H. *Anal. Chem.* **1989**, *61*, 2528–2534.
(26) Bamber, M.; Wanczek, K. P. Presented at the 37th Annual Conference on Mass Spectrometry and Allied Topics, Miami Beach, FL, 1986.
(27) Karas, M.; Bachmann, D.; Hillenkamp, F. *Anal. Chem.* **1985**, *57*, 2935.
(28) Karas, M.; Bachmann, D.; Bahr, U.; Hillenkamp, F. *Int. J. Mass Spectrom. Ion Processes* **1987**, *78*, 53.
(29) Vertes, A.; Juhasz, P.; Jani, P.; Czytrovszkyp, A. *Int. J. Spectrom. Ion Processes* **1988**, *83*, 45.
(30) Vertes, A.; DeWolf, M.; Juhasz, P.; Gijbels, R. *Anal. Chem.* **1989**, *61*, 1029.
(31) Van der Peyl, G.; Van der Zand, W.; Kistemaker, P. *Int. J. Mass Spectrom. Ion Processes* **1984**, *62*, 51.
(32) Mauney, T.; Adams, F. *Int. J. Mass Spectrom. Ion Processes* **1984**, *59*, 103.
(33) Dinger, R.; Rohr, K.; Weber, H. *J. Phys. D* **1980**, *13*, 2301–2309.
(34) Beavis, R. C.; Chait, B. T. *Rapid Commun. Mass Spectrom.* **1989**, *3*, 233.
(35) Weller, R. R.; Ghaderi, S.; Verburger, O.; Freiser, B. S. Presented at the 36th Annual Conference on Mass Spectrometry and Allied Topics, San Francisco, CA, June 5–10, 1988.
(36) Moini, M.; Eyler, J. R. *J. Chem. Phys.* **1988**, *88*, 5512–5515.
(37) Sessler, J. L.; Cyr, M. J.; Lynch, V.; McGhee, E.; Ibers, J. A. *J. Am. Chem. Soc.* **1990**, *112*, 2810–2813.
(38) Beu, S. C.; Laude, D. A., Jr. *Int. J. Mass Spectrom. Ion Processes* **1991**, *104*, 109–127.

RECEIVED for review November 9, 1990. Accepted April 4, 1991. This work is supported by the Welch Foundation, the Texas Advanced Technology and Research Program, and the National Science Foundation.

Argon–Xenon Plasma for Alleviating Polyatomic Ion Interferences in Inductively Coupled Plasma Mass Spectrometry

Fred G. Smith, Daniel R. Wiederin,[1] and R. S. Houk*

Ames Laboratory, U.S. Department of Energy, Department of Chemistry, Iowa State University, Ames, Iowa 50011

Xenon is added at 10 or 37 mL min^{-1} to the aerosol gas flow of an argon inductively coupled plasma mass spectrometer. Addition of xenon substantially reduces polyatomic ions such as N_2^+, HN_2^+, NO^+, ArH^+, ClO^+, ArC^+, $ClOH^+$, ArN^+, and ArO^+ and facilitates the measurement of ^{28}Si, ^{29}Si, ^{39}K, ^{41}K, ^{51}V, ^{52}Cr, ^{53}Cr, ^{54}Cr, ^{54}Fe, and ^{56}Fe. Isotope ratios are determined with relative standard deviations from 0.6% to 1.6%. Detection limits for the above elements range from 0.3 to 2 $\mu g\ L^{-1}$.

INTRODUCTION

Inductively coupled plasma mass spectrometry (ICPMS) is a sensitive, accurate, and precise method for trace multielemental and isotopic analysis of solutions (*1–4*). However, polyatomic ions arising from argon, water, and mineral acids cause substantial spectral overlap for a number of elements, especially below $m/z = 80$ (*5, 6*).

Techniques for correction or attenuation of these ions are quite varied. The simplest approach is to subtract the background signal from the analyte peak, but this procedure becomes difficult for analyte signals just above the background. The count rates for background ions may also vary with the chemical identity and concentration of the sample matrix. Isotope ratios may be measured for either analyte or interferent to help correct for spectral overlap interferences (*7*), but unobstructed isotopes are not always available. Oxide and hydroxide ions derived from injected water can be reduced by desolvation (*8, 9*) or, in some cases, by introducing the analyte as a hydride (*10*). Electrothermal vaporization (ETV) was used by Gray and co-workers to mitigate ArO^+ and $ArOH^+$ for the determination of iron isotope ratios (*11*). More drastic measures include use of a helium plasma (*12, 13*) to attenuate ions containing argon or a high-resolution mass spectrometer to resolve polyatomic ions and analyte ions of the same nominal mass (*14*).

Several other methods for attenuating polyatomic ions are related to the present work. Rowan and Houk added xenon to a quadrupole collision cell to remove ArO^+ (*15*). Evans and Ebdon introduced an organic solvent or a molecular gas into the central channel of the ICP to reduce $ArCl^+$ and Ar_2^+ for determination of arsenic and selenium (*16*). Lam and Horlick (*17*), Lam and McLaren (*18*), and Lam, McLaren, and Gustavsson (*19*) added N_2 to the outer gas flow of an Ar ICP to attenuate a number of background ions (ArO^+, $ArOH^+$, Ar_2^+, ClO^+, and $ArCl^+$) by 1 order of magnitude. The general characteristics of mixed-gas ICPs were described in a recent review (*20*).

In the present work, small amounts of xenon (10 or 37 mL min^{-1}) are introduced into the central channel of the ICP. The count rates from various polyatomic ions are reduced more extensively than the count rates for analyte ions. The result is improved performance for measurement of several important and otherwise obscured elements (Si, K, V, Cr, and Fe), particularly for isotope ratio determinations.

* Corresponding author.
[1] Present address: Cetac Technologies, Inc., 302 S. 36th St, Omaha, NE 68131.

EXPERIMENTAL SECTION

Instrumentation. The inductively coupled plasma mass spectrometer used was the ELAN Model 250 with upgraded ion optics (Perkin-Elmer SCIEX, Thornhill, Ontario, Canada). The argon in the aerosol gas flow was regulated by a mass flow controller (Model 8200, Matheson Scientific, Secaucus, NJ). The continuous-flow ultrasonic nebulizer was operated at a forward power of 40–45 W (*21, 22*) and a solution uptake rate of 2.0 mL min^{-1}. The wet aerosol was desolvated with a heating chamber (200 °C) and a condenser (0 °C) (*22*). The resulting dry aerosol was transported to the plasma through 0.95 cm i.d. Tygon tubing (~1 m long).

Addition of Xenon. The xenon used was of 99.995% purity (Air Products, Tamagua, PA). The xenon gas flow was controlled with a needle valve. The xenon was conducted through a 1-m length of 0.32 cm i.d. Tygon tubing that was connected to a glass tee attached to the base of the ICP torch. A two-way switching valve was installed ahead of the needle valve so that the xenon flow could be conveniently turned off. This also facilitated measurement of the xenon flow rate with a soapfilm flowmeter (Alltech Model 4074, Deerfield, IL).

Solutions. Analyte solutions were prepared from 1000 mg L^{-1} standards from Fisher Scientific Co. (Fair Lawn, NJ). Ultrex II hydrochloric acid from J. T. Baker (Phillipsburg, NJ) was used to prepare a 1% HCl solution for the ClO^+ interference study. High-purity deionized water (resistance ~ 18 MΩ) was obtained from a Barnstead Nanopure-II system (Newton, MA).

Instrumental Conditions. General instrumental and sampling conditions are given in Table I. Intensities and isotope ratios were measured by peak hopping; spectra were obtained by scanning. A single set of experimental conditions was used for the determination of Si, V, Cr, and Fe. The determination of K required a higher xenon flow rate (37 mL min^{-1}) and a change in the potential of the photon stop. The resolution setting on the mass spectrometer was also increased to yield peaks ~0.5-amu wide at the base. At low resolution a steady signal could not be obtained at $m/z = 41$, perhaps due to overlap from the large Ar^+ peak at $m/z = 40$.

RESULTS AND DISCUSSION

Mass Spectra. Figure 1 presents results for the silicon study. In the blank spectrum (Figure 1A) the polyatomic ions N_2^+ and N_2H^+ are below 200 counts s^{-1}, and NO^+ is under 1000 counts s^{-1} with xenon present. Table II shows the extent of the signal reduction with and without xenon in the ICP. The ions N_2^+ and N_2H^+ are attenuated by approximately a factor of 300, while NO^+ is reduced by a factor of 1400. A 5 mg L^{-1} Si solution gives well-resolved silicon peaks with a sensitivity of 55 000 counts s^{-1} per ppm for $^{28}Si^+$ (Figure 1B). Comparison of the analyte count rates (Table III), to the background count rates (Table II) shows that the ratio of residual background to analyte signal for 1 mg L^{-1} Si is 0.3% for $^{28}Si^+$ and 1.4% for $^{29}Si^+$ when Xe is added. However, the remaining peak from NO^+ is ~30% of the net signal for $^{30}Si^+$. Finally, the back-

0003-2700/91/0363-1458$02.50/0 © 1991 American Chemical Society

Table I. Operating Conditions

ICP torch	Ames Laboratory design (23) outer tube extended 30 mm from middle tube
forward power, kW	1.25[a]
argon flow rates, L min^{-1}:	
outer gas	13
auxiliary gas	0.2[a]
aerosol gas	1.55–1.60[a]
xenon flow rates, mL min^{-1}:	
for Si, V, Cr, Fe	10
for K	37
sampling position, mm	22 from load coil,[a] on center
sampler	copper, 1.1 mm diameter orifice
skimmer	nickel, 0.9 mm diameter orifice
ions lens settings:	
Bessel box barrel, V	+5.4
Bessel box plate lens, V	−11.0
Einzel lenses 1 and 3, V	−19.8
Einzel lens 2, V	−130
Bessel box stop, V	−5.8 for Si, V, Cr, Fe; −4.9 for K
electron multiplier voltage, V	−3400 for Si, V, Cr, Fe; −3000 for K
operating pressures, Torr:	
interface	1
quadrupole chamber	3×10^{-5}
spectral measurements:	sequential monitoring mode
for Si, V, Cr, Fe	low resolution, 10 measurements per peak, measurement time = 1.0 s
for K	high resolution, 20 measurements per peak, measurement time = 0.25 s
all other measurements:	multielement monitoring mode (peak hopping)
for Si, V, Cr, Fe	low resolution, 3 measurements per peak, dwell time = 10 ms, total measurement time = 1.0 s
for K	high resolution, 3 measurements per peak, dwell time = 10 ms, total measurement time = 1.0 s

[a] Typical values for these conditions. There was some variation among experiments conducted on different days.

Table II. Background Count Rates

m/z	ion(s)	Ar only mean,[a] counts s^{-1}	Xe added mean,[a] counts s^{-1}	redn factor
28	N_2^+	50 600	165	300
29	N_2H^+	13 100	40	325
30	NO^+	1.1×10^6	780	1400
40	Ar^+	throttled[b]	14500[c]	
41	ArH^+	throttled[b]	1300[c]	
51	$^{35}ClO^+$	24 000[d]	140	170
52	ArC^+, $^{35}ClOH^+$	8600[d]	670	13
53	$^{37}ClO^+$	7990[d]	45	180
54	ArN^+, $^{37}ClOH^+$	9970[d]	230	45
54	ArN^+	14 100	70	200
56	ArO^+	72 800	430	170
75	$^{40}Ar^{35}Cl^+$	890	7	125
80	$^{40}Ar_2^+$	726 000	200	3600

[a] Mean of 20 measurements. [b] Total count rate above 3.2×10^6 counts s^{-1}; instrument throttled or shutdown. [c] Higher Xe flow rate and resolution were used (see Table I). [d] Count rate obtained during introduction of 1% HCl.

ground from O_2^+ at $m/z = 32$ is of particular note. A large peak ($\sim 1 \times 10^6$ counts s^{-1}) remains even when xenon is added; a determination of sulfur at $m/z = 32$ is not facilitated by addition of xenon.

Results from the potassium study are depicted in Figure 2. Special experimental conditions were used for this element (Table I), notably a higher xenon flow rate and higher resolution. The residual background from ArH^+ at $m/z = 41$ is approximately 1300 counts s^{-1} (Figure 2A). A 10 mg L^{-1} K solution gives a net signal of 14 900 counts s^{-1} at $m/z = 41$ (Figure 2B and Table III). Thus, the ArH^+ peak is still a significant contribution (~9%) to the 10 mg L^{-1} K signal. The small background peak (~200 counts s^{-1}) at $m/z = 39$ in Figure 2A is probably from trace potassium in the water. Since there is little signal at $m/z = 38$ from $^{38}Ar^+$, $^{38}ArH^+$ is not the culprit. The addition of Xe and the use of higher resolution

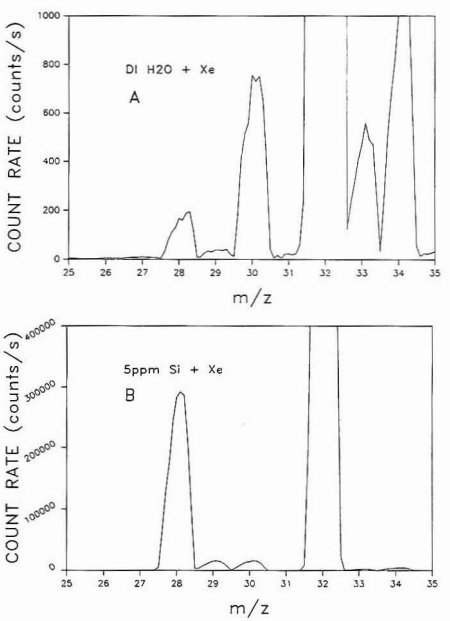

Figure 1. Spectra of (A) deionized water plus 10 mL min^{-1} Xe and (B) 5 mg L^{-1} Si plus 10 mL min^{-1} Xe.

reduce the $^{40}Ar^+$ peak to ~15 000 counts s^{-1}. Thus, the contribution of $^{40}Ar^+$ to the background at $m/z = 39$ or 41 was largely eliminated.

The low level of ClO^+ when xenon is added is shown in Figure 3. The background for 1% HCl plus xenon shows five significant peaks in this region. From Table II the $^{35}ClO^+/^{37}ClO^+$ ratio is about 3/1, as expected from the natural abundances of the two chlorine isotopes. The background at

Table III. Net Analyte Count Rates

ion(s)	Ar only counts s^{-1} per ppm[a]	Xe added counts s^{-1} per ppm[a]	redn factor
$^{28}Si^+$	550 000	55000	10
$^{29}Si^+$	18 600	2870	6
$^{30}Si^+$	throttled[b]	2640	
$^{39}K^+$	510 000	19700[c]	26
$^{41}K^+$	throttled[b]	1490[c]	
$^{51}V^+$	1.5×10^6	207000	7
$^{52}Cr^+$	1.2×10^6	163000	7
$^{53}Cr^+$	129 000	18500	7
$^{54}Cr^+$	32 500	4800	7
$^{54}Fe^+$	139 000	8800	16
$^{56}Fe^+$	2.1×10^6	139000	15
$^{75}As^+$	653 000	890	730
$^{80}Se^+$	528 000	220	2400

[a] Mean of 20 measurements. [b] Total count rate above 3.2×10^6 counts s^{-1}; instrument throttled or shutdown. [c] Higher Xe flow rate and resolution were used (see Table I).

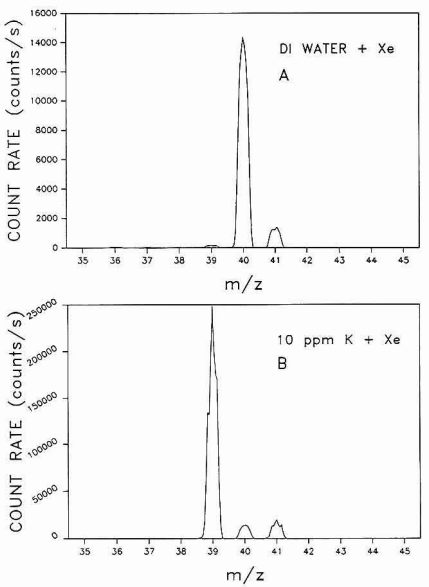

Figure 2. Spectra of (A) deionized water plus 37 mL min^{-1} Xe and (B) 10 mg L^{-1} K plus 37 mL min^{-1} Xe; high resolution.

m/z = 52 is likely a combination of $^{40}Ar^{12}C^+$ and $^{35}ClOH^+$, the former probably arising from carbon-containing impurities in the argon or the solvent. The peak at m/z = 54 is due to both $^{40}Ar^{14}N^+$ and $^{37}ClOH^+$. As shown in Tables II and III, residual backgrounds at m/z = 51–53 are less than 1% of the signals obtained for a solution containing V and Cr, each at 1 mg L^{-1}. However, the background at m/z = 54 is about 5% of the signal from $^{54}Cr^+$. The background at m/z = 53 is reduced by approximately a factor of 180, but that of m/z = 54 drops by only a factor of 45. Nonetheless, signals for the three chromium isotopes drop by only a factor of 7 (Table III) when Xe is added, much less than those of the background peaks. The background ion at m/z = 46 (probably NO_2^+) is also attenuated substantially when Xe is added, although this reduction is hidden by the vertical scale in Figure 3B.

Results for iron are depicted in Figure 4. Addition of Xe attenuates the background ions ArN^+ at m/z = 54 and ArO^+

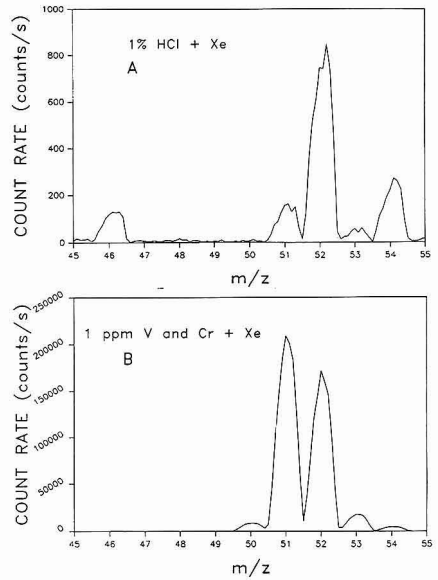

Figure 3. Spectra of (A) 1% HCl plus 10 mL min^{-1} Xe and (B) 1 mg L^{-1} V and Cr in 1% HCl plus 10 mL min^{-1} Xe.

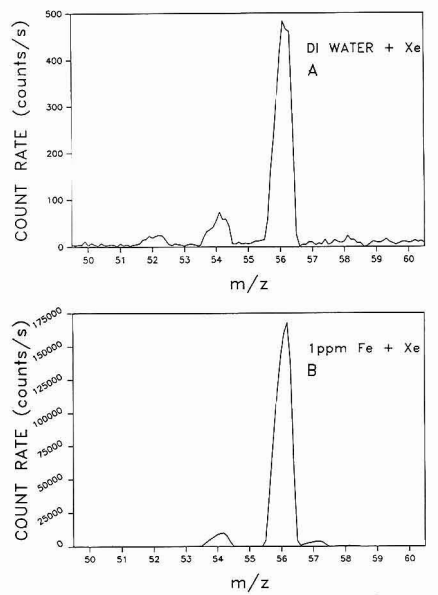

Figure 4. Spectra of (A) deionized water plus 10 mL min^{-1} Xe and (B) 1 mg L^{-1} Fe plus 10 mL min^{-1} Xe.

at m/z = 56 by factors of 200 and 170, respectively, as shown in Table II. In comparison, the $^{54}Fe^+$ signal from a 1 mg L^{-1} solution drops by only a factor of 16. The trend for the $^{56}Fe^+$ signal is similar, but the $^{56}Fe^+$ signal is 2.1×10^6 counts s^{-1} without Xe, and loss of detector gain at this high count rate may preclude a valid comparison (*24*). Figure 4A also shows

Table IV. Isotope Ratio Measurements with Xe Added

soln conc, mg L^{-1}	ratio measd	determined ratio mean	determined ratio RSD, %[a]	accepted ratio (25)
5	$^{28}Si/^{29}Si$	19.10	0.8	19.75
5	$^{28}Si/^{30}Si$	20.82[b]	1.6	29.75
10	$^{39}K/^{41}K$	13.21[b]	1.0	13.86
1	$^{53}Cr/^{52}Cr$	0.1135	0.7	0.1134
1	$^{54}Cr/^{52}Cr$	0.0294	1.4	0.0282
1	$^{56}Fe/^{54}Fe$	15.78	0.6	15.81

[a] Mean and relative standard deviation of 20 measurements. [b] Count rates for $^{30}Si^+$ and $^{41}K^+$ were corrected for contributions from NO^+ and ArH^+.

Table V. Estimated Detection Limits

element	m/z	detn limit, $\mu g\ L^{-1}$
Si	28	0.6
K	39	1
V[a]	51	0.3
Cr[a]	52	2
Fe[a]	56	0.3

[a] In 1% HCl solution.

that addition of xenon eliminates the common background peaks at m/z = 57 and 58, which would facilitate measurement of these minor isotopes of Fe.

Isotope Ratios. The isotope ratios determined when xenon is added are listed in Table IV. The ratios $^{28}Si/^{29}Si$, $^{53}Cr/^{52}Cr$, $^{54}Cr/^{52}Cr$, and $^{56}Fe/^{54}Fe$ agree well with the accepted natural abundance ratios. Thus, isotope ratios could be measured for these elements at ~ppm levels (the usual levels used to obtain good precision) without background correction. However, the ratio $^{28}Si/^{30}Si$ differs markedly from the accepted value. This deviation is likely caused by the substantial NO^+ peak remaining at m/z = 30 relative to the signal from the minor isotope $^{30}Si^+$. Subtraction of the background signal at m/z = 30 does not improve the $^{28}Si/^{30}Si$ ratio very much (20.82 versus the accepted 29.75). Correction for the background at m/z = 41 gives a $^{39}K/^{41}K$ ratio of 13.21, reasonably close to the accepted value of 13.86.

Detection Limits. The detection limits (i.e., the solution concentration necessary to yield a net signal equivalent to 3 times the standard deviation of the background) for the five elements studied are listed in Table V. The major isotope of each element was used. These estimated detection limits are comparable to or slightly better than those observed for these elements if no special steps are taken to attenuate the polyatomic ions by addition of xenon.

Calibration Curves. The linearity of calibration curves for Si, V, Cr, and Fe was tested with the addition of xenon. In each case the major isotope of each element was monitored. For Si, a series of six solutions from 0.01 to 10 mg L^{-1} yielded a calibration curve with a correlation coefficient of 0.9994. Curves from another series of six solutions containing 0.005 to 3 mg L^{-1} V, Cr, and Fe gave correlation coefficients of 0.9985, 0.9989, and 0.9992, respectively.

Effect of Xenon on $ArCl^+$ and Ar_2^+. Further experiments were performed to determine whether added xenon would reduce $ArCl^+$ and Ar_2^+ and facilitate the determination of $^{75}As^+$ and $^{80}Se^+$. Instrumental conditions were matched as closely as possible to those for Si, V, Cr, and Fe, as listed in Table I. A 1% HCl solution was used for background measurements. Figure 5A shows that xenon addition eliminates $ArCl^+$ and reduces Ar_2^+ by a factor of 3600 (Table II) to ~200 counts s^{-1}. However, Figure 5B shows that the nebulization of a 1% HCl solution containing As and Se under the same conditions gives a very low sensitivity: 890 counts s^{-1} per ppm for $^{75}As^+$ and 220 net counts s^{-1} per ppm for $^{80}Se^+$. These signals are approximately 3 orders of magnitude lower than those with argon only (Table III).

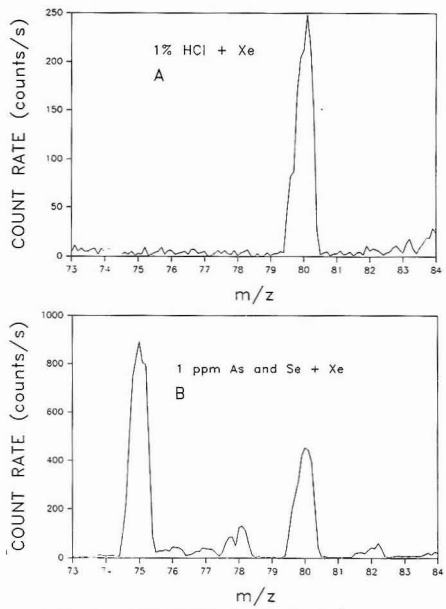

Figure 5. Spectra of (A) 1% HCl plus 10 mL min^{-1} Xe and (B) 1 mg L^{-1} As and Se plus 10 mL min^{-1} Xe.

This observation that the reduction factors for As^+ and Se^+ are much greater than those for other analyte ions leads to a tentative explanation for the effect of added xenon. The first excited state of the neutral xenon atom is 8.31 eV above the ground state; the ionization energy (IE) of xenon is 12.1 eV (26). Both these values are ~3 eV below the corresponding values for Ar, so the addition of small amounts of xenon would be expected to moderate ionization conditions in an Ar ICP. Elements which have IEs below ~8 eV (i.e., the energy corresponding to the first excited state of xenon) remain substantially ionized, which is the case for Si, K, V, Cr, and Fe. Elements which have an IE above ~8 eV such as As (IE = 9.81 eV) and Se (IE = 9.75 eV) are not ionized efficiently with xenon present. Most of the polyatomic species studied in this work have IEs at or above 11 eV (except for NO, 9.27 eV) (27). These more energetic polyatomic ions are attenuated greatly when xenon is added. The fundamental reasons for the effects of xenon on background and analyte peaks are under investigation in our laboratory (28).

Effects of Xe on Plasma Structure and Background. When yttrium is added as a test element, addition of small doses of xenon (10 or 37 mL min^{-1}) causes little visible change in the position of the red initial radiation zone or in the intensity of the blue emission from the normal analytical zone (29). Thus, there is no obvious, drastic change in the characteristics of the ICP when xenon is added.

The background at m/z values devoid of ions is very low (<5 counts s^{-1}) when xenon is added. An example is shown at m/z = 74 in Figure 5A. Without xenon, the background is usually 30 counts s^{-1} for the operating conditions listed in Table I with this particular instrument. With xenon present, Xe^+ was a major background ion, the signal at m/z = 136 (8.9% abundance) being 1.8×10^6 counts s^{-1}. The total count

rate for all Xe^+ peaks was $\sim 2 \times 10^7$ counts s^{-1}. Thus, "matrix" suppression (*30*) caused by Xe^+ is also a likely source of loss of ions (*28*).

The Xe^+ peaks overlap or are adjacent to isotopes of Te, Cs, and Ba, so xenon should not be added when determining these elements. Polyatomic ions containing Xe, such as XeH^+, XeO^+, $XeAr^+$, $NaXe^+$ (from a 100 mg L^{-1} Na solution) or Xe_2^+ were not observed.

Comparison of Xe–Ar ICP with Other Plasmas. A rigorous comparison of the performance of mixed gas Ar–N_2 ICPs (*16–19*) and the He microwave-induced plasma (MIP) (*31*) with that of the Ar–Xe ICP is complicated by several factors. The various investigators employ different nebulizers and desolvation methods, the count rates for analyte and polyatomic ions are sensitive to plasma operating conditions (particularly aerosol gas flow rate), and the criteria chosen for evaluating the potential improvements also differ. For these reasons, the relative merits of these schemes for reducing polyatomic ion interferences will be compared only in general terms and for those operating conditions that yield optimum performance.

Compared to the present work, addition of N_2 to the outer gas does not reduce levels of ArO^+, $ArOH^+$, and ClO^+ as extensively. However, analyte signals remain similar or can even be enhanced if the aerosol gas flow rate is reoptimized after the N_2 is added. Addition of N_2 also attenuates metal oxide ions substantially. The one case that can be compared fairly is that involving $^{56}Fe^+$ and $^{40}Ar^{16}O^+$. With addition of 8–20% N_2 into the outer gas, the background equivalent concentration (BEC) for Fe at $m/z = 56$ is 7 μg L^{-1} without desolvation (*17*) and 0.6 μg L^{-1} with desolvation (*18*). A pneumatic nebulizer was used in both these studies. In the present work, the BEC for Fe at $m/z = 56$ is 3 μg L^{-1}; a more efficient ultrasonic nebulizer with desolvation was used. The background (i.e., the "baseline" under all the peaks) stays about the same when N_2 is added to the outer gas, whereas addition of Xe reduces the background.

Incorporation of N_2 at a very low flow rate (30 mL min^{-1}) into the aerosol gas flow reduces the In^+ signal by a factor of 4. The ratio (In^+ signal)/(polyatomic ion signal) is improved by factors of 2–200 for many species. Unfortunately, the effect of adding N_2 to the aerosol gas on count rates for analyte ions of moderate to high ionization energy is not reported, although the accuracy obtained for As and Se at 100 μg L^{-1} in 1–8% aqueous HCl is improved substantially with N_2 present (*16*). Compared to Xe, modification of the ICP with N_2 is attractive because analyte signals are higher and N_2 is much less expensive. However, polyatomic ions containing N are enhanced when N_2 is added (*16–18*), as expected from the initial ICPMS study with Ar–N_2 plasmas (*32*). Thus, addition of N_2 compromises determination of Si and ^{54}Fe. The Ar–Xe plasma described in the present work is superior for applications involving these ions, particularly for isotope ratio experiments where the sacrifice in Si^+ and Fe^+ signal is not a big problem if sufficient amounts of these elements are available.

Caruso and co-workers have reported the only MS experiments with a He MIP into which the sample is introduced as an aqueous aerosol. N_2^+ and Ar^+ are major ions, and ArN^+ and ArO^+ are still observed. In fact, N_2 is actually added to this plasma to suppress Kr^+ and improve the linear dynamic range. Addition of N_2 enhances the peaks from the usual N-containing ions and also elevates the peak at $m/z = 56$, presumably due to formation of N_4^+ (*31*). Although the concept of a He plasma, either an MIP or an ICP (*33*), for MS is potentially attractive, a viable system for routine analysis of solutions has not yet been demonstrated.

Registry No. ^{28}Si, 14276-58-5; ^{29}Si, 14304-87-1; ^{30}Si, 14092-91-2; ^{41}K, 13965-93-0; ^{51}V, 7440-62-2; ^{52}Cr, 14092-98-9; ^{53}Cr, 13981-78-7; ^{54}Cr, 14304-97-3; ^{54}Fe, 13982-24-6; ^{56}Fe, 14093-02-8; Xe, 7440-63-3; $^{30}Si^+$, 13981-69-6; Si, 7440-21-3; K, 7440-09-7; V, 7440-62-2; Cr, 7440-47-3; Fe, 7439-89-6.

LITERATURE CITED

(1) Houk, R. S.; Fassel, V. A.; Flesch, G. D.; Svec, H. J.; Gray, A. L.; Taylor, C. E. *Anal. Chem.* **1980**, *52*, 2283–2289.
(2) Douglas, D. J.; Houk, R. S. *Prog. Anal. At. Spectrosc.* **1985**, *8*, 1–18.
(3) Houk, R. S. *Anal. Chem.* **1986**, *58*, 97A–105A.
(4) Houk, R. S.; Thompson, J. J. *Mass Spectrom. Rev.* **1988**, *7*, 425–462.
(5) Vaughan, M. A.; Horlick, G. *Appl. Spectrosc.* **1986**, *4*, 434–444.
(6) Tan, S. H.; Horlick, G. *Appl. Spectrosc.* **1986**, *4*, 445–460.
(7) Date, A. R.; Cheung, Y. Y.; Stuart, M. E. *Spectrochim. Acta, Part B* **1987**, *42B*, 3–20.
(8) Hutton, R. C.; Eaton, A. N. *J. Anal. At. Spectrom.* **1987**, *2*, 595–598.
(9) Zhu, G.; Browner, R. F. *J. Anal. At. Spectrom.* **1988**, *3*, 781–789.
(10) Powell, M. J.; Boomer, D. W.; McVicars, R. J. *Anal. Chem.* **1986**, *58*, 2864–2867.
(11) Whittaker, P. G.; Lind, T.; Williams, J. G.; Gray, A. L. *Analyst* **1989**, *114*, 675–678.
(12) Creed, J. T.; Davidson, T. M.; Shen, W. L.; Brown, P. G.; Caruso, J. A. *Spectrochim. Acta, Part B* **1989**, *44B*, 909–924.
(13) Montaser, A.; Chan, S.; Koppenaal, D. *Anal. Chem.* **1987**, *59*, 1240–1242.
(14) Bradshaw, N.; Hall, E. F. H.; Sanderson, N. E. *J. Anal. At. Spectrom.* **1989**, *4*, 801–803.
(15) Rowan, J. T.; Houk, R. S. *Appl. Spectrosc.* **1989**, *6*, 976–980.
(16) Evans, E. H.; Ebdon, L. *J. Anal. At. Spectrom.* **1989**, *4*, 299–300; **1990**, *5*, 425–430.
(17) Lam, J. W. H.; Horlick, G. *Spectrochim. Acta, Part B* **1990**, *45B*, 1313–1325, 1327–1338.
(18) Lam, J. W. H.; McLaren, J. W. *J. Anal. At. Spectrom.* **1990**, *5*, 419–424.
(19) McLaren, J. W.; Lam, J. W.; Gustavsson, A. *Spectrochim. Acta, Part B* **1990**, *45B*, 1091–1094.
(20) Montaser, A.; Van Hoven, R. L. *CRC Crit. Rev. Anal. Chem.* **1987**, *18*, 45–103.
(21) Olson, K. W.; Haas, W. J., Jr.; Fassel, V. A. *Anal. Chem.* **1977**, *49*, 632–637.
(22) Bear, B. R.; Fassel, V. A. *Spectrochim. Acta, Part B* **1986**, *41B*, 1089–1113.
(23) Scott, R. H.; Fassel, V. A.; Kniseley, R. N.; Dixon, D. E. *Anal. Chem.* **1974**, *46*, 75–80.
(24) Kurz, E. A. *Am. Lab.* **1979**, *11*, 67–82.
(25) Weast, R. C., Ed. *CRC Handbook of Chemistry and Physics*; CRC Press, Inc.: Boca Raton, FL, 1985–6; p B-238.
(26) Moore, Charlotte E. *Atomic Energy Levels*; U.S. Government Printing Office: Washington, DC, 1958; Vol. III, p 114.
(27) Rosenstock, H. M.; Draxl, K.; Steiner, B. W.; Herron, J. T. *Journal of Physical and Chemical Reference Data*: *Energetics of Gaseous Ions*; National Bureau of Standards: Washington, DC, 1977; Vol. 6, Supplement No. 1.
(28) Smith, F. G.; Houk, R. S. Unpublished results.
(29) Koirtyohann, S. R.; Jones, J. S.; Yates, D. A. *Anal. Chem.* **1980**, *52*, 1965–1966.
(30) Gillson, G. R.; Douglas, D. J.; Fulford, J. E.; Halligan, K. W.; Tanner, S. D. *Anal. Chem.* **1988**, *60*, 1472–1474.
(31) Creed, J. T.; Davidson, T. M.; Shen, W.-L.; Brown, P. G.; Caruso, J. A. *Spectrochim. Acta, Part B* **1989**, *44B*, 909–924.
(32) Houk, R. S.; Montaser, A.; Fassel, V. A. *Appl. Spectrosc.* **1983**, *37*, 425–438.
(33) Montaser, A.; Chan, S.-K.; Kopenaal, D. W. *Anal. Chem.* **1987**, *59*, 1240–1242.

RECEIVED for review December 10, 1990. Accepted April 18, 1991. The Ames Laboratory is operated by Iowa State University for the U.S. Department of Energy under Contract No. W-7405-ENG-82. This research was supported by the Office of Basic Energy Sciences.

Analysis of Neutral Oligosaccharides by Matrix-Assisted Laser Desorption/Ionization Mass Spectrometry

Bernd Stahl and Martin Steup

Institut für Botanik, Universität Münster, Schlossgarten 3, D-4400 Münster, Federal Republic of Germany

Michael Karas* and Franz Hillenkamp

Institut für Medizinische Physik, Universität Münster, Robert-Koch-Strasse 31, D-4400 Münster, Federal Republic of Germany

Matrix-assisted laser desorption ionization mass spectrometry (LDI-MS) was used for mass determination of neutral nonderivatized oligosaccharides and mixtures thereof. Dihydroxybenzoic acid or caffeic acid served as matrix. A nitrogen laser (λ = 337 nm, τ = 5 ns) was used for ion desorption. For comparison oligoglucans were analyzed by both high-performance and thin-layer chromatography. With LDI-MS glucan species were generally detected as monosodium and monopotassium carbohydrate adduct ions. Addition of lithium chloride to the analyte resulted in the formation of an additional monolithium glucan adduct ion. No fragmentation of the analyte was observed. LDI-MS as described here was also applied to analyze oligofructans, mannose-containing oligosaccharides and glycolipids. LDI-MS has the advantages of being able to resolve complex carbohydrate mixtures, of high sensitivity and simplicity of analyte preparation; sample pretreatment, such as desalting is usually not required for LDI-MS.

INTRODUCTION

Oligosaccharides represent a heterogeneous group of biologically important compounds, either as free carbohydrates or as constituents of glycoconjugates. Free oligosaccharides occur as intermediates or end products of the cellular carbon metabolism. In plants they play an important role in carbon fluxes within the cells and in the entire organism (*1*, *2*). Oligosaccharides covalently bound to non-glycan constituents (such as proteins), are involved in a variety of biological functions (*3–5*).

Both free and bound oligosaccharides can occur as mixtures of oligomers that differ in features, such as degree of polymerization, monomer composition, and the type(s) of intersugar linkage(s).

Therefore, biochemical analysis of oligosaccharides often requires both the resolution of complex carbohydrate mixtures and the characterization of the individual oligomer type. Oligosaccharide mixtures can be separated by a variety of established methods, among which are gel filtration (*6*, *7*), thin-layer chromatography (*8–10*), and high-performance liquid chromatography (*11*, *12*). These techniques are of limited use in accurate mass determination. Oligosaccharides having the same degree of polymerization but differing in molecular shape (e.g. linear or cyclic molecules) often possess different chromatographic characteristics. Thus a correlation between retention time and size of an oligosaccharide holds only within a homologeous series of oligomers. The use of structurally identical molecular weight (MW) standards is essential. Therefore, molecular weight determinations of compounds of unknown structure and of mixtures thereof are difficult to perform.

Mass spectrometric techniques such as fast atom bombardment have been applied both for molecular weight determination and analysis of glycans up to a MW of 3500 (*13–17*). However, for neutral underivatized oligosaccharides FAB exhibits a low ion yield and thus sensitivity (1–50 nmol of sample required (*17*)). Derivatization is typically used to either enhance surface activity or introduce preferred sites for (de)protonation.

In this communication results of matrix-assisted UV laser desorption/ionization mass spectrometry (LDI-MS) of native neutral homoglycans are presented.

The method, recently developed by some of the authors, has until now mainly been used for molecular weight determination of proteins up to masses of ca. 350 000 Da (*18–22*).

As shown in this report, LDI-MS is also a powerful tool for the determination of molecular masses and size distribution of oligosaccharides. In a first experiment a linear and a cyclic α–glucan, maltoheptaose and cycloheptaose, respectively, were analyzed separately and as a mixture. LDI-MS has then been used for analysis and mass determination of commercial maltodextrins and dextrans. Finally, the technique has been applied to the evaluation of the kinetics of an enzymatic polymerization reaction. For this purpose, glucosyl transfer from glucose 1-phosphate to a primer, catalyzed by glucan phosphorylase (E.C.2.4.1.1.), was chosen.

EXPERIMENTAL SECTION

LDI-MS. The mass spectrometer used was a reflector type time of flight (TOF) microprobe instrument (LAMMA 1000) with a nitrogen laser (Laser Science Inc.) of 337-nm wavelength and 5-ns pulse width. The apparatus has been described in detail elsewhere (*23*). The laser beam was focused onto the sample at an angle of 45° to the surface normal. Typical spot sizes range from 10–30 μm, with irradiances at the sample surface of 10^6–10^7 W/cm^2. Ions were accelerated to an energy of 3 keV before entering the TOF mass spectrometer. At the detector ions were postaccelerated to a maximum kinetic energy of up to 20 keV for more efficient detection by a secondary electron multiplier (EMI 9643). The analogue signals were recorded with a transient digitizer (LeCroy 9400) with 10 or 20 ns/channel resolution and then transferred to a PC.

All spectra shown are accumulations of 10–60 single spectra. Measurements typically take 10–15 min, including sample preparation.

Analyte Preparation for Mass Spectrometric Investigation. 2,5-Dihydroxybenzoic acid was used as matrix except when stated otherwise. It was dissolved to a concentration of 10 g/L in a 10% (v/v) ethanol–water solution. Analytes (0.1–1 g/L) were prepared in doubly distilled water and then diluted with an appropriate volume of the matrix solution (typically 1:4 to 1:10, v/v). Aliquots of the resulting mixture (1 μL or less) were placed on a piece of silver plate. The solvent was removed in a gentle stream of air and the solid sample/matrix mixture was then transferred into the vacuum chamber of the mass spectrometer. In some experiments dihydroxybenzoic acid was replaced by derivatives of cinnamic acid (e.g. caffeic or ferulic acid). In these

0003-2700/91/0363-1463$02.50/0 © 1991 American Chemical Society

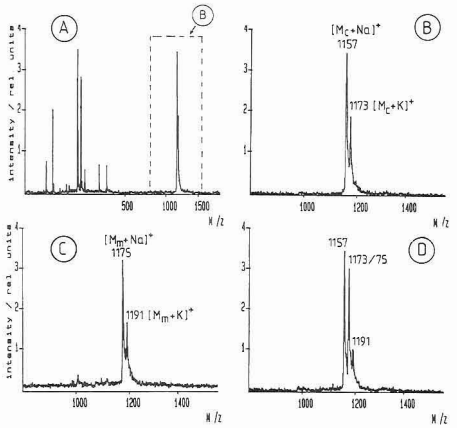

Figure 1. Matrix LDI mass spectra of cycloheptaose (A, B), maltoheptaose (C), and an equimolar mixture of both heptaoses (D): (A) complete spectrum; (B–D) expanded analyte ion mass region; index "c" and "m" for cycloheptaose and maltoheptaose, respectively. Conditions: matrix, dihydroxybenzoic acid; sample, 50 ng of heptaose (A–C), 100 ng (D). The spectra are averages of 10 single spectra each.

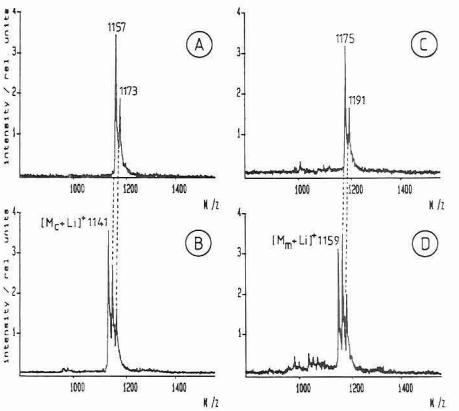

Figure 2. Matrix LDI spectra of cycloheptaose (A, B) and maltoheptaose (C, D): (A, C) lithium-free sample; (B, D) sample in 0.16 mM LiCl. Conditions: matrix, dihydroxybencoic acid. The spectra are averages of 20 spectra; index "c" and "m" for cycloheptaose and maltoheptaose, respectively.

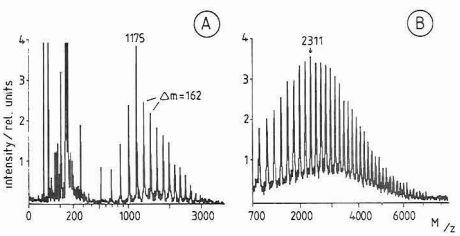

Figure 3. Matrix LDI spectrum of maltodextrins (A) and dextrans (B). The various oligoglucan species differ in mass by 162 Da as indicated in the figure. Conditions: matrix, dihydroxybencoic acid; sample 100 ng (A), 200 ng (B). The spectra are averages of 20 (A) and 60 (B) single spectra. A mass of 2311 Da is equivalent to a DP of 14 glucoses.

cases, the matrix solution was prepared by dissolving one of these derivatives in a 50% (v/v) ethanol–water solution to a final concentration of 10 g/L, with the addition of 0.1% (v/v) of trifluoroacetic acid.

HPLC. Two different HPLC methods were used. Equal flow rates (1 mL/min) and sample volumes (50 μL) have been used in both cases. A HPX-87 (Bio-Rad) column with a refractive index detector was used for the analysis of cycloheptaose, maltoheptaose, and their mixture (1 mg/mL each). The column had been equilibrated with degassed water prior to measurement. The chromatography was performed at 85 °C. HPLC analysis of the products of the enzymatic reaction was carried out at room temperature with a CarboPac PA1 (Dionex) anion-exchange column and a pulsed amperometry detector (*24*). The carbohydrates have been eluted with a linear gradient of 0–0.5 M NaOAc in 0.15 M NaOH.

TLC. For thin-layer chromatography, silica gel plates (Polygram SIL, Macherey and Nagel, Düren, FRG) were used. Chromatograms were developed twice, using a mixture of *n*-butanol, 2-propanol, and water (7:8:5, v/v/v) as solvents. Following chromatography the samples were detected by the procedure described by Bounias (*25*).

Oligosaccharides. Maltoheptaose and cycloheptaose were purchased from Boehringer (Product No. 691828) and Sigma (C 4767), respectively. The maltodextrin mixture was a commercial dextrin preparation (Serva 18716) from which high molecular weight compounds had been removed by ethanol precipitation (75% final concentration, see ref 26). Dextrans were purchased from Fluka (31417 dextran 5000).

Enzymatic Polymerization. The reaction mixture (2.5 mL) contained 50 mM Mes–NaOH (pH 6.48), 20 mM glucose 1-phosphate, 5 mM maltoheptaose, and 45 μg of glucan phosphorylase, purified from pea cotyledons. This phosphorylase isozyme represents a type II enzyme (for details see ref 2). The enzyme was purified to apparent homogeneity as described elsewhere (*27*). The reaction was initiated by adding the enzyme to the reaction mixture. At time intervals, an aliquot of the mixture was taken out of the reaction vial and heated for 2 min in a boiling water bath. Denatured protein was pelleted (5 min at 5000 g), and the supernatant was stored frozen (–20 °C) or analyzed immediately.

RESULTS

With matrix-assisted UV laser desorption ionization mass spectrometry, analysis of oligosaccharides can be performed without noticeable fragmentation of the analyte. In the spectra obtained, all signals in the low-mass range (below 500 Da) exclusively represent ions of the matrix and are observed also in the absence of the analyte. Figure 1A,B show the LDI mass spectrum of cycloheptaose. The analyte was detected as a monosodium (m/z 1157) and a monopotassium (m/z 1173) cation. Comparably intense signals were observed when a linear oligoglucan, maltoheptaose, was analyzed. Again, monosodium and monopotassium cations at m/z 1175 and 1191 are seen (Figure 1C). In a LDI spectrum of an equimolar mixture of the linear and the cyclic heptaose (Figure 1D), the sodium adduct ion of cycloheptaose and the potassium adduct ion of maltoheptaose are clearly resolved, whereas the two other ion species (K^+ of cycloheptaose and Na^+ of maltoheptaose), which differ in mass by only 2 Da, are not resolved under the experimental conditions used. Figure 2 shows the effect of lithium chloride addition to maltoheptaose or cycloheptaose. Under these conditions a third molecular ion peak was observed that represents the monolithium oligosaccharide adduct (Figure 2B,D).

In another series of experiments, a complex mixture of maltodextrins (α-1,4-linked oligoglucans; Figure 3A) and dextrans (α-1,6-linked oligoglucans; Figure 3B) were analyzed by LDI-MS. For both analytes two series of monosodium and monopotassium oligoglucan ions are observed. The masses of the maltodextrins range from 500 to 3500 Da equivalent

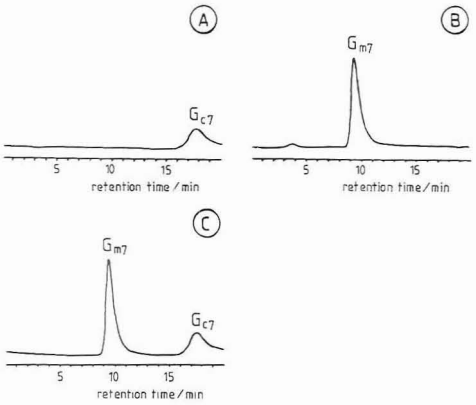

Figure 4. HPLC analysis of glucans with a HPX-87 column and refractive index detection: (A) cycloheptaose (G_{c7}; 20 μg); (B) maltoheptaose (G_{m7}; 20 μg); (C) equimolar mixture of cycloheptaose and maltoheptaose (20 μg each).

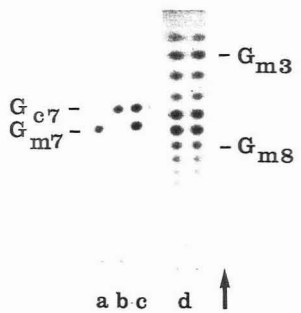

Figure 5. Thin-layer chromatography: (lane a) maltoheptaose (5 μg; G_{m7}); (lane b) cycloheptaose (5 μg; G_{c7}); (lane c) a mixture of both heptaoses (each 5 μg); (lanes d) maltodextrin sample (50 μg). (G_{m8} = maltooctaose; G_{m3} = maltotriose). The arrow marks the migration direction.

to a degree of polymerization (DP) of up to 22. For dextrans, masses up to 7000 Da were observed equivalent to a DP of up to 43. Similar signals were obtained by using caffeic acid as the matrix. The presence of lithium chloride led to the formation of additional lithium adduct ions as expected (data not shown).

For control and comparison, some of the various oligosaccharide samples were analyzed by standard chromatographic procedures. In HPLC (HPX-87; Bio-Rad), maltoheptaose and cycloheptaose were clearly resolved, with the retention time of the cyclic oligosaccharide being longer than that of the linear glucan (Figure 4A–C). In thin-layer chromatography, cycloheptaose had a higher mobility than maltoheptaose. Its R_f value was between those of maltopentaose and maltohexaose (Figure 5 lanes a–c). When the maltodextrin mixture (see Figure 3A) was analyzed by TLC, compounds with a DP of up to 12 were resolved (Figure 5 lanes d).

In a further experiment, LDI-MS was applied for the analysis of products of an enzymatic polymerization reaction. A pea type II glucan phosphorylase was incubated at room temperature with glucose 1-phosphate and maltoheptaose as primer. The enzymatic reaction resulted in the formation of an increasingly complex maltodextrin pattern (Figure 6A–F).

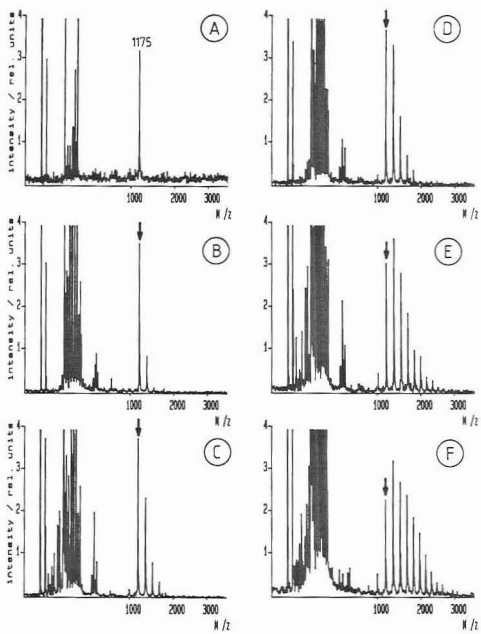

Figure 6. LDI-MS product analysis of enzymatic glucan elongation. Conditions: matrix, dihydroxybencoic acid; sample before (A) and immediately after enzyme addition (B); (C–F) 5-, 10-, 30-, 60-min reaction period. The arrow marks maltoheptaose, the original primer.

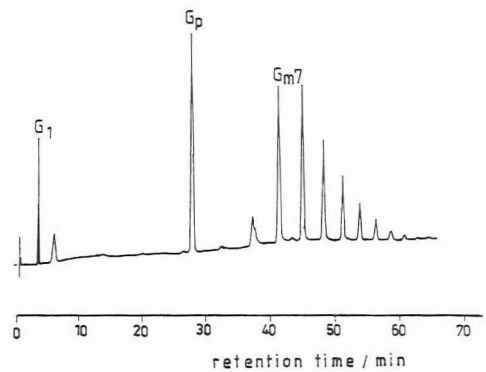

Figure 7. HPLC product analysis of enzymatic elongation with a CarboPac PA1 column and pulsed amperometric detection. The sample was taken after 30-min incubation time with the enzyme. (G_1 = glucose; G_p = glucose 1-phosphate; G_{m7} = maltoheptaose as primer).

Depending upon the reaction time, the size distribution of the oligoglucans was shifted toward the higher molecular weight region. After 60 min, molecular ions up to 2800 Da were obtained. At the same time, maltodextrines with a degree of polymerization lower than that of maltoheptaose were formed. This effect, which is due to phosphorolysis occurring simultaneously with the polymerization reaction, has been previously observed in similar experiments in which TLC was applied for the product analysis (2).

For comparison, the reaction products after 30 min incubation time were analyzed by HPLC using a CarboPac PA1

(Dionex) column and pulsed amperometric detection (Figure 7). A signal pattern of oligosaccharides comparable to that of the mass spectrum is obtained (see Figure 6E).

DISCUSSION

In this paper matrix-assisted LDI-MS has been used to determine distribution and masses of neutral nonderivatized oligosaccharides. Both α-1,4- and α-1,6-linked glucans served as analytes. Each glucan species was detected as both a monosodium and monopotassium molecular adduct ion. Protonated molecules were not observed. Fragmentation of the analyte did not occur to any noticeable extent. Cleavage of intersugar bonds would show an additional series of ions, shifted by a mass difference of 17 Da relative to the unfragmented oligosaccharide. In addition to α-1,4- or α-1,6-linked glucans, LDI-MS has also been successfully applied to mass determination of nonglucose oligomers, such as mannose oligomers and *N*-acetylated oligosaccharides (data not shown). Likewise, native and permethylated glycolipids up to 10 000 Da have also been analyzed by LDI-MS (*28*). The experimental conditions were essentially the same as described here. Thus, it appears that the technique described here can be applied to a wide range of oligo/polysaccharides and glycoconjugates (such as glycoproteins and glycolipids).

Compared to standard procedures of carbohydrate analysis, matrix-assisted LDI-MS has distinct advantages such as a short measuring time (typically 10–15 min) and a direct access to molecular masses. Mass determination is not affected by other molecular properties, such as axil ratio, which strongly affects chromatographic analysis. When equal amounts of cyclic or linear glucans were analyzed for both compounds, approximately the same signal intensities were observed. This indicates that distinct structural features of both analytes do not affect the desorption/ionization process. Likewise, within the range of masses considered here no mass-dependent discrimination was observed.

When the products of an enzymatic polymerization reaction were analyzed, a time-dependent shift of the oligoglucan spectrum toward the high molecular weight region was found.

For comparison, the same products were analyzed by a high-resolution HPLC technique (Figure 7). With both HPLC and LDI-MS essentially the same size distribution was observed (Figure 6E). The reliability of the technique described here was further demonstrated by experiments in which equimolar mixtures of defined mannose oligomers were analyzed and no mass-dependent discrimination was found (data not shown). Thus, it appears that LDI-MS of neutral carbohydrates allows for an semiquantitative analysis of complex oligomer mixtures. It is expected to be especially useful if mixtures of branched and unbranched oligo/polysaccharides are to be analyzed. These features make LDI-MS a very useful supplementary tool for chromatographic techniques. LDI-MS as described here is a very sensitive method. In a preliminary test a total amount of 1 ng (ca. 1 pmol) of maltoheptaose was used for preparation and successfully analyzed. It is expected that a systematic evaluation of the optimal analyte to matrix ratio and minimum sample volume needed will lead to a still further increase of sensitivity, as has been observed for other classes of biomolecules. The application of the technique described here to naturally occurring mixtures of oligosaccharides is in progress.

ACKNOWLEDGMENT

We are indebted to Dr. Yi Yang for the HPLC analysis of the heptaoses and Dionex GmbH (Idstein, FRG) for the HPLC analysis of the enzymatically formed glucan products.

LITERATURE CITED

(1) Kandler, O.; Hopf, H. *The Biochemistry of Plants*; Preiss, J., Ed.; Academic Press: New York, 1980; Vol. 3, pp 221–270.
(2) Steup, M. *The Biochemistry of Plants*; Preiss, J., Ed.; Academic Press: New York, 1988; Vol. 14, pp 255–296.
(3) Lechner, J.; Wieland, F. *Annu. Rev. Biochem.* **1989**, *58*, 173–194.
(4) Rademacher, T. W.; Parekh, R. B.; Dwek, R. A. *Annu. Rev. Biochem.* **1988**, *57*, 785–838.
(5) Kaushal, G. P.; Szumilo, T.; Elbein, A. D. *The Biochemistry of Plants*; Preiss, J., Ed.; Academic Press: New York, 1988; Vol. 14, pp 421–463.
(6) John, M.; Schmidt, J.; Wandrey, C.; Sahm, H. *J. Chromatogr.* **1982**, *247*, 281–288.
(7) Natowicz, M.; Baenziger, J. U. *Anal. Biochem.* **1980**, *105*, 159–164.
(8) Honda, S. *Anal. Biochem.* **1984**, *140*, 1–47.
(9) Würsch, P.; Roulet, P. H. *J. Chromatogr.* **1982**, *244*, 177–182.
(10) Nurok, D.; Zlatkis, A. *Carbohydr. Res.* **1980**, *81*, 167–172
(11) Cheetham, N. W. H.; Teng, G. *J. Chromatogr.* **1984**, *336*, 161–172.
(12) Voragen, A. G. J.; Schols, H. A.; Searle-van Leeuwen, M. F.; Beldman, G.; Rombouts, F. M. *J. Chromatogr.* **1986**, *370*, 113–120.
(13) Egge, H.; Peter-Katalinic, J. *Mass Spectrom. Rev.* **1987**, *6*, 331–393.
(14) Dell, A.; Morris, H. R.; Egge, H.; Von Nicolai, H.; Strecker, G. *Carbohydr. Res.* **1983**, *115*, 41–52.
(15) Dell, A.; Ballou, C. E. *Carbohydr. Res.* **1983**, *120*, 95–111.
(16) Dell, A. *Methods in Enzymology*; McCloskey, J. A., Ed.; Academic Press: San Diego, 1990; Vol. 193, pp 647–660.
(17) Poulter, L.; Burlingame, A. L. *Methods in Enzymology*; McCloskey, J. A., Ed.; Academic Press: San Diego, 1990; Vol. 193, pp 661–689.
(18) Karas, M.; Bachmann, D.; Bahr, U.; Hillenkamp, F. *Int. J. Mass Spectrom. Ion Processes* **1987**, *78*, 53–68.
(19) Karas, M.; Bahr, U.; Hillenkamp, F. *Int. J. Mass Spectrom. Ion Processes* **1989**, *92*, 231–241.
(20) Karas, M.; Bahr, U.; Ingendoh, A.; Hillenkamp, F. *Angew. Chem., Int. Ed. Engl.* **1989**, *28*, 760–61.
(21) Karas, M.; Ingendoh, A.; Bahr, U.; Hillenkamp, F. *Biomed. Environ. Mass Spectrom.* **1989**, *18*, 841–843.
(22) Beavis, R. C.; Chait, B. T. *Rapid Commun. Mass Spectrom.* **1989**, *3*, 436–439.
(23) Feigl, P.; Schueler, B.; Hillenkamp, F. *Int. J. Mass Spectrom. Ion Phys.* **1983**, *47*, 15–16.
(24) Weiss, J. *Ionenchromatographie*; VCH Verlagsgesellschaft: Weinheim, FRG, in press.
(25) Bounias, M. *Anal. Biochem.* **1980**, *106*, 291–295.
(26) Steup, M. *Methods in Plant Biochemistry*; Lea, P. J., Ed.; Academic Press: New York, 1990; Vol. 3, 103–128.
(27) Conrads, J.; Van Berkel, J.; Schächtele, C.; Steup, M. *Biochem. Biophys. Acta* **1986**, *882*, 452–463.
(28) Egge, H.; Peter-Katalinic, J.; Karas, M.; Stahl, B. *Pure Appl. Chem.*, in press.

RECEIVED for review December 14, 1990. Accepted April 15, 1991. Financial support of the Deutsche Forschungsgemeinschaft and the Bundesministerium für Forschung und Technologie is gratefully acknowledged.

Nanoscale Packed-Capillary Liquid Chromatography Coupled with Mass Spectrometry Using a Coaxial Continuous-Flow Fast Atom Bombardment Interface

M. Arthur Moseley,[1] Leesa J. Deterding, and Kenneth B. Tomer*

Laboratory of Molecular Biophysics, National Institute of Environmental Health Sciences, P.O. Box 12233, Research Triangle Park, North Carolina 27709

James W. Jorgenson*

Department of Chemistry, University of North Carolina, C.B. 3290, Chapel Hill, North Carolina 27514

Nanoscale packed-capillary liquid chromatography (LC) columns have been coupled with mass spectrometry (MS) using a coaxial continuous-flow fast atom bombardment interface. The combined system has been applied to the analysis of mixtures of peptides, including synthetic mixtures of bioactive peptides and tryptic digests of proteins. Nanoscale packed-capillary columns offer two principal advantages for LC/MS analysis—high chromatographic separation efficiencies and low mobile-phase flow rates. The high separation efficiencies facilitate the separation of complex mixtures, and the low mobile-phase flow rates reduce problems with coupling the LC effluent with the high-vacuum, high-voltage environment of sector MS ion sources. The columns used in this work were 50- or 75-μm i.d., 1–2 m long, packed with 10-μm C18 particles, using mobile-phase flow rates of 50–350 nL/min.

Separation science methodologies have greatly benefitted from the trend toward miniaturization. The best example of this is the well-known advantages of capillary gas chromatography over conventional packed-column gas chromatography (GC). Smaller inner diameter gas chromatography columns yield significantly better separation efficiencies, yield shorter analysis times, and greatly facilitate the coupling of GC with mass spectrometry.

Similar advantages are found in liquid chromatography when miniaturization of the columns occurs. As with GC, the highest separation efficiencies are obtained with open tubular liquid chromatography (OTLC) columns, which have the stationary phase coated onto the wall of the column. Due to the much higher viscosity of liquids as compared to gases and the resultant increase in resistance to mass transfer in liquid mobile phases compared with gas mobile phases, the optimum OTLC column inner diameter is significantly smaller than the optimum GC column inner diameter. Theory predicts (*1*) that the optimum OTLC column inner diameter, over a range of analysis times and pressures, will be 1.5–3 μm. This very small optimum OTLC column inner diameter results in a small column wall surface area and, therefore, a small amount of stationary phase. This results in a low capacity factor, which reduces the dynamic range of the amount of analytes that can be injected onto the column before overloading occurs.

Nanoscale packed-capillary LC columns offer a solution to this capacity problem due to the high surface area to volume ratio of columns packed with porous silica particles. This improves the analysis of polar analytes due to an increased capacity factor and also permits the injection of large volumes of dilute aqueous sample onto reversed-phase columns, with focusing of the analytes onto the front of the stationary-phase packing. Also, the columns can be fabricated from commerically available packing materials, offering a wide selection of stationary-phase chemistry.

A number of research groups have successfully produced packed capillary columns with inner diameters between 150 and 350 μm (*2–8*). While such columns will typically have minimum reduced plate heights equivalent to conventional LC columns, flow dispersion (eddy diffusion) and/or resistance to mass transfer tends to be more significant than is found with conventional LC columns (*9*). This has been attributed to the increased contribution of the "wall effect", where the column wall influences the structure of the packing bed, decreasing the particle density and, thus, reducing mobile-phase flow resistance. In LC columns, there are two discreet regions of packing bed structure, a less densely packed region at the wall of the column, extending approximately 5 particle diameters from the column wall, and a more densely packed region in the remainder of the column bed in the center of the column. Eddy dispersion will increase as the wall effect region increases in its percentage contribution to the total bed volume (*10*). In capillary LC columns with 350–150-μm i.d. packed with 5-μm particles, a high percentage (≈5–25%) of the packing bed structure will be influenced by the wall effect.

In 1988, Karlsson and Novotny reported an evaluation of packed-capillary columns with inner diameters as low as 44 μm (*11*) where it was found that such columns showed an improvement in separation efficiency over the 150–350-μm-i.d. columns. The packing bed structure in columns with this inner diameter would be expected to be homogeneous, with the entire column bed being influenced by the wall effect.

Kennedy and Jorgenson (*12*) performed a comprehensive study on the effect of column diameter on column performance and found that packed capillary LC columns with a column inner diameter to particle size ratio of <10:1 offered several significant advantages. This study evaluated columns with 50–20-μm inner diameters packed with 5-μm C18 particles and found column performance, in terms of minimum reduced plate height, improved with decreasing column inner diameter. Statistical analysis revealed that the improved performance is a result of decreased flow dispersion and a decrease in resistance to mass transfer in the mobile phase. This was attributed to a more uniform packing bed density, because the entire packing bed will be wall effected. Furthermore, the smaller id packed capillary LC columns yield additional improvements in separation efficiency due to more effective trans column (radial) diffusional relaxation of retention and mobile phase flow inhomogeneities.

Packed capillary LC columns with column inner diameter to particle size ratios of <10:1 (with particle sizes ≤ 10 μm)

* Authors to whom correspondence should be sent.
[1] Also at the Department of Chemistry, University of North Carolina.

0003-2700/91/0363-1467$02.50/0 © 1991 American Chemical Society

have mobile-phase flow rates in the low nanoliter/minute range, as well as injection and detection volumes of a few nanoliters. Because of the nanoliter scale of the mobile-phase flow rates, injection volumes, and detection volumes, these columns are described as nanoscale packed-capillary LC columns. Nanoscale packed-capillary LC columns have been shown to have high separation efficiency and to be suitable for the analysis of nanoliter scale samples, including the analysis of the contents of single cells (*13–16*). The detection systems typically used with these nanoscale LC columns are single graphite fiber electrochemical detectors (*13–20*) and laser-induced fluorescence detectors (*20–22*), both offering exceptional sensitivity (attomoles) but limited qualitative information regarding analyte structure.

In order to obtain qualitative information from analytes separated by nanoscale LC, we have interfaced these columns with mass spectrometry. Fast atom bombardment (FAB), introduced in 1981 by Barber et al. (*23*), provides a powerful desorption/ionization source for the mass spectrometric analysis of polar, nonvolatile, and/or thermally labile analytes. The coupling of FAB with flowing liquid streams by Ito et al. (Frit-FAB/MS) (*24*) and Caprioli et al. (continuous-flow FAB/MS) (*25*) has provided a very useful interface between LC and FAB/MS (*26–32*). The success of these LC/continuous-flow FAB/MS interfaces led us to investigate the coupling of nanoscale LC columns with continuous-flow FAB.

Nanoscale LC columns place rigid requirements on the design of an LC/MS interface due to their very low mobile-phase flow rates and detection volumes. The previously reported LC/CF-FAB/MS interfaces were designed to operate with larger packed LC columns (4.6–0.22-mm i.d.), with mobile-phase flow rates (delivered to the mass spectrometer) of 3–10 μL/min. In these systems, the matrix (typically glycerol) needed for the FAB process was introduced either in the mobile phase and analyte solutions or was added postcolumn into the LC effluent by using a mixing tee. These approaches are not compatible with our nanoscale LC separation systems because the flow rate of the FAB matrix required for a stable FAB ion beam is greater than the total mobile-phase flow rates from nanoscale packed columns. Postcolumn introduction of the FAB matrix into the LC effluent using a mixing tee is problematic due to the relative magnitudes of the two liquid streams, leading to severe chromatographic peak broadening.

For these reasons, we designed an interface that uses a coaxial flow of the nanoscale packed-capillary LC effluent and FAB matrix in two separate fused silica capillary columns (*33*). In this interface, chromatographic band broadening is minimized because the mixing of the matrix and the nanoscale LC effluent takes place only at/on the FAB probe tip. This allows the composition and flow rate of the LC mobile phase to be optimized for the separation of the sample components and the composition and flow rate of the FAB matrix to be independently optimized for analyte detection. While this coaxial interface was specifically designed for use with nanoscale LC systems, when modified for use with packed capillaries with inner diameters of 320 μm, it has been found to offer higher separation efficiencies (by up to a factor of 4) and lower limits of detection compared with precolumn addition of the FAB matrix to the LC mobile-phase reservoirs (*34*). We have previously reported some preliminary results on the coupling of nanoscale packed-capillary LC with CF-FAB for both MS (*35*) and MS/MS (*36*) analysis of mixtures of synthetic peptides. In this paper, we extend this application to more complex mixtures of synthetic peptides and to the analysis of tryptic digests of proteins.

EXPERIMENTAL SECTION

Nanoscale Packed-Capillary LC Columns. The nanoscale packed-capillary LC columns used in this work were prepared by a modification of the method of Kennedy and Jorgenson (*12*). Fused-silica capillary columns (Polymicro Technologies, Phoenix, AZ) with inner diameters of 50 to 75 μm were cut into 2.5-m lengths. Approximately 0.5 cm of the polyimide coating was burned off the outlet end of the column. The column was then rinsed with 2-propanol and dried with a stream of helium. A frit was constructed on the outlet end by tapping the outlet end into a vial containing 5-μm spherical silica particles until a 100–200-μm length of the column was filled. The particles were scintered into place by using a microtorch. Prior to packing the columns with stationary phase, the frits were pressure tested to ≈100 bar pressure with 2-propanol. A slurry of 30:1 (milliliters:grams) *n*-hexane and 10-μm porous spherical C18 particles, either AQ-C18 (YMC Corp., Morris Plains, NJ) or Hypersil C18 (Shandon, Astmoor, England), was prepared and sonicated for approximately 5 min. The slurry was then loaded into a stainless steel slurry packing reservoir fabricated in house. The slurry reservior was fabricated from a stainless steel cylinder, 3.5 cm tall and 7 cm in diameter, into which a 3-mL volume cavity was drilled. The slurry reservoir was mounted onto a magnetic stirrer, and a Teflon-coated stirbar was placed in the reservoir. The lid of this vessel contained two inlet ports with $^1/_{16}$-in. fittings, and the fused silica column was mounted into one fitting by using vespel ferrules (Alltech, Deerfield, IL), while the other fitting was connected to a syringe pump (μLC-500, Isco, Inc., Lincoln, NE) by using stainless steel tubing. The syringe pump, operated in the constant-pressure mode, was initially taken to 5 bar, and the pressure was increased stepwise to 275 bar over approximately 30 min. A stereomicroscope was used to monitor the progress of the column packing.

The AQ-C18 stationary phase was decidedly easier to pack, giving fewer problems with column plugging and column bed void regions. The manufacturer developed this phase specifically to provide high-resolution separations in high-percentage aqueous mobile phases through the use of a proprietary polar end-capping reagent. This stationary phase exhibits high retention of water-soluble compounds, and these retention characteristics were exploited in this work in the LC preconcentration experiments.

Coaxial Continuous-Flow FAB Probe. The FAB probe used in this work was fabricated in house and has been described previously (*33*). The inner diameter of the hole in the stainless steel FAB probe tip was carefully matched to the outer diameter of the sheath capillary column to prevent backflow of the column effluent into the probe tip. This has been found to be necessary to minimize both peak broadening and to minimize ion source pressure fluctuations. The FAB matrix was pumped through the sheath capillary (160-μm i.d., 350-μm o.d.) by using a syringe pump (Model μLC-500, Isco, Inc.). Previous work has found 25% glycerol in water to be the preferred FAB matrix solution for the analysis of peptides as positive ions (*35*). This solution was pumped through the sheath capillary column at a flow rate of approximately 300–400 nL/min. An in-line 0.5-μm frit filter (Supelco Inc., Bellefonte, PA) was used to filter the FAB matrix from the syringe pump to prevent pump seal particulates from entering the interface. In order to provide adequate back pressure for regulation of the syringe pump flow, a 25-μm × 3-m fused-silica capillary column was used to connect the in-line filter on the syringe pump with the coaxial tee.

Chromatographic System. The chromatographic injections and solvent delivery were accomplished by using a system developed for use with OTLC (*37*) and modified for use with conventional LC gradient pumps (*38*). By using this injection system, subnanoliter injections can be made with minimal band broadening from the injector. An alternative sample introduction system that was used in this work uses a stainless steel pressure vessel (*38*). A microvial of sample solution was placed into the vessel, and the LC capillary column was inserted through the lid of the vessel into the vial of sample solution. The vessel was then pressurized with helium gas to "inject" the sample solution onto the column. After injection, the column was removed from the injection vessel and reinserted into the gradient LC system. Note that the pressure vessel can be used as a mobile-phase pump for isocratic analysis by simply replacing the sample vial with a vial of mobile phase and pressurizing the vessel to yield the desired mobile-phase flow rate. The pressure vessel was designed to withstand in excess of 650-bar pressure; however, the desired

mobile-phase flow rates can be attained at pressures of ≤170 bar, even when the 2-m nanoscale LC columns were used at 5 times their optimum mobile-phase velocity.

Gradients were formed and delivered by using a pair of Waters 6000A pumps and a Waters 660 gradient controller (Milford, MA). Linear gradients of acetonitrile–water or methanol–water were used for the chromatographic separations, and each mobile-phase reservoir contained 0.1% trifluoroacetic acid (TFA) as an ion-pairing reagent for the peptides. Acetonitrile–water mixtures were preferred due to their lower viscosity compared to methanol–water mixtures.

Mass Spectrometer. A VG ZAB-4F mass spectrometer (Altrincham, England) was used for this work. This instrument has been previously described in detail (*39*). The mass spectrometer is of B_1E_1–E_2B_2 geometry and is equipped with an Ion Tech fast atom bombardment gun. Xenon was used as the FAB gas (8 kV at 1 mA). Analyte ions were accelerated to 8 kV. The MS work utilized only the first two sectors (B_1E_1) of the instrument, and ions were detected in the third field-free region with a photomultiplier tube detector. The magnet was scanned exponentially at a rate of 7 s/decade over a mass range from, typically, 20 Da above to 20 Da below the mass of the molecular ion species being studied. The MS/MS analyses utilized the first two sectors to focus the parent ions into the collision cell in the third field-free region where collisions with helium gas (50% parent ion beam attenuation) induced dissociation to daughter ions. The daughter ions were analyzed by using a linked scan at constant B_2/E_2, with detection of daughter ions in the fifth field-free region with a photomultiplier tube detector. Data analysis was accomplished with a VG 11-250 data system. Supplementary data analysis was performed by using a Sun 3/60 workstation (Mountain View, CA) using Kratos (Ramsey, NJ) Mach 3 software. The results of the nanoscale LC/MS analysis have been output as single ion chromatograms of the protonated molecular ions.

Chemicals. All peptides and the glycerol were obtained from Sigma (St. Louis, MO) and were used as delivered. All solutions were prepared by using 18-MΩ water (Milli-Q System, Millipore Corp., Bedford, MA). Acetonitrile (HPLC grade) was obtained from Fisher Scientific (Fairlawn, NJ). Trifluoroacetic acid (sequencing grade) was acquired from Pierce (Rockford, IL). All solutions, both samples and mobile phases, were filtered (0.45 μm) immediately prior to use.

Tryptic Digestion of Proteins. TPCK-treated trypsin (Worthington Biochemicals Corp., Freehold, NJ) solutions were prepared at a concentration of 1 mg/mL in 0.1 mM HCl. Proteins were dissolved in 0.1 M ammonium bicarbonate (adjusted to pH 8.5 by using ammonium hydroxide) to give concentrations of 10^{-4} M. Digestions were performed by using an enzyme:substrate ratio of 1:100 (w:w) at 37 °C for 1 h. Enzymatic digestion was stopped either by the addition of trifluoroacetic acid to give a final concentration of 0.2% trifluoroacetic acid (v:v) (cytochrome C) or by freeze-drying (glucagon and bovine growth hormone releasing factor).

RESULTS AND DISCUSSION

Nanoscale LC Column Preparation. The initial experiments addressed the use of 10-μm C18 particles packed into 50-μm-i.d. fused-silica columns. The minimum length of the column is determined by the geometry of the ZAB-4F mass spectrometer ion source and the coaxial continuous-flow FAB probe, which together requires a column at least 90 cm long, rather than by chromatographic considerations. Furthermore, the installation and removal of the probe from the ion source is greatly facilitated if the LC column is longer than 150 cm. For non mass spectrometric applications, typical nanoscale reversed-phase LC columns range from 25 to 50 cm in length and are packed with 5-μm particles due to their higher separation efficiency as compared to 10-μm particles. A consideration of the flow resistance parameter equation (*40*) reveals that the pressure drop across a packed column is inversely proportional to the square of the particle diameter. The use, therefore, of 5-μm particles rather than 10-μm particles will lead to a 4-fold increase in mobile-phase pressure drop across the column. While the flow resistance of nanoscale columns has been found to be lower than conventional columns (*12*), the mobile-phase pressure required for *relatively* quick (≤2–3 h) gradient analysis using 2-m-long nanoscale LC columns packed with 5-μm particles was determined to be in excess of that available from our gradient pumps. Therefore, 10-μm particles have been used in this work.

While the optimization of LC column performance is often discussed in terms of mobile-phase flow rate, the appropriate parameter is, of course, mobile-phase linear velocity. Calculations based upon the optimum reduced linear velocity parameters (*12*) show that the optimum linear velocity using 10-μm particles in nanoscale LC columns should be approximately 0.042 cm/s, and thus, the optimum dead time for a 2-m-long column should be 79 min. While this linear velocity should give optimum separation efficiency, it leads to prohibitively long analysis times and an excessively large amount of data when using a mass spectrometer as the chromatographic detector. Because the column length is longer than necessary for the analytical separations of interest to this project and the optimum analysis time is longer than is desired, a trade-off of theoretical plates for analysis time can be made by operating the columns at mobile-phase linear velocities higher than optimum. Based on the reduced parameters (*12*), a 2-m-long column packed with 10-μm particles should be able to generate 115 000 plates. When the same column is used with a mobile-phase linear velocity 5 times the optimum, 66 000 plates should be obtained, but the dead time of the column has been reduced from 79 to 16 min, thus giving a 5-fold reduction in analysis time.

The ease of packing nanoscale columns has been found to be directly proportional to the ratio of the column inner diameter to particle size. Kennedy found that, when this ratio was <5:1, packing columns 35 cm long was considerably more difficult than when the ratio was >5:1 and that, although the fabrication of 200-cm-long 50-μm-i.d. columns packed with 10-μm particles was difficult, with care, such columns can be fabricated. The packing of 75-μm-i.d. columns with 10-μm-i.d. particles was considerably more facile, and these columns can readily be fabricated in 3–4 h. The ratio of the column inner diameter to particle size outer diameter is 7.5:1. While the flow rate for the 75-μm-i.d. columns is a factor of 2.4 higher than that from 50-μm-i.d. columns (with identical mobile-phase linear velocity), the total mobile-phase flow rates, even when using 5 times the optimum linear mobile-phase velocity, is less than 500 nL/min. Thus, even when this mobile-phase flow is added to the 300–400 nL/min flow of the FAB matrix solution, the total liquid flow delivered to the mass spectrometer ion source is less than 1 μL/min, a value well within the pumping capacity of the standard diffusion pump system on the ZAB-4F ion source. For these reasons, 75-μm-i.d. columns have been used for the majority of this work. It should be noted that the cost of materials of each column is less than $10.00; thus, these packed capillary columns can be fabricated in house for a very small fraction of the cost of commerically available 320-μm-i.d. capillary columns.

Preconcentration LC Experiments. Mass spectrometrists are often required to analyze samples that are characteristically of a low volume, low concentration, and/or contaminated with salts. These problems can be minimized through the use of nanoscale packed-capillary LC columns. When a simple separation of the organic component(s) from the salts that may be present in the sample is desired, a very short column bed (1–2 cm) may be used. By using the sample introduction vessel, sample volumes as low as 5 μL can be analyzed. The column, mounted in the FAB probe but outside the mass spectrometer, is first equilibrated with water, containing 0.1% trifluoroacetic acid (for peptide analysis). The

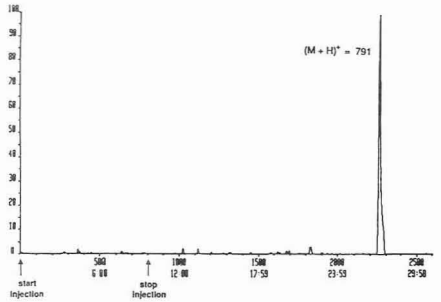

Figure 1. Preconcentration LC/MS analysis of a dilute solution (0.1 pmol/μL) of β-casomorphin. Ten microliters of solution was injected onto the column over 10 min, followed by isocratic elution using 40% acetonitrile in water (0.1% TFA) at 0.5 μL/min.

sample solution is then introduced onto the column with the sample volume adjusted as necessary to compensate for analyte concentration. Sample volumes in excess of 50–100 μL may be used, if required, because the organic analytes will be retained on the AQ-C18 stationary phase. Next, the column is flushed with the aqueous mobile phase to purge inorganic salts from the column. After wiping the tip clean with water to remove any salts on the tip, the probe is inserted into the mass spectrometer. Data acquisition is started, and the organic components are eluted in a narrow peak by using either isocratic elution (e.g., 40 or 80% acetonitrile in water) or a sharp gradient profile (e.g., 0 to 80% acetonitrile in water over 5 min). A gradient profile is preferred, particularly for unknown samples, due to the retention characteristics of peptides in the stationary phase. If, however, the elution characteristics of the peptide sample are known, isocratic elution is preferred due to its ease of use.

An example of the use of the preconcentration nanoscale LC columns is given in Figure 1. In this experiment, a 50-μm-i.d. column was packed with 2 cm of 10-μm AQC-18 in the detector end of the column. A 10-min-long injection of 0.1 pmol/μL β-casomorphin in 0.1% TFA/water at a flow rate of ≈ 1 μL/min was made. By using 40% acetonitrile in water (0.1% TFA), the peptide was eluted from the column in a sharp chromatographic peak with a high signal to noise ratio (from a 10-min injection of a dilute sample).

Nanoscale LC/MS Analysis of Synthetic Peptide Mixtures. Two mixtures of synthetic bioactive peptides were analyzed—a mixture of neuropeptides and a mixture of angiotensin-related peptides. Both separations used a 2-m-long, 75-μm-i.d. column fully packed with 10-μm particles. Seven peptides were included in the neuropeptide mixture: proctolin, Lys-bradykinin, bradykinin, α-melanocyte stimulating hormone, neurotensin, substance P, and substance P free acid. The neuropeptides were analyzed under gradient conditions of 0% (10-min hold) and then stepped to 10%, with a linear gradient from 10 to 50% acetonitrile in water over 120 min (0.1% TFA in both mobile-phase reservoirs). Equimolar amounts of 10 pmol of each neuropeptide were injected. Good chromatographic peak shape was obseved for all compounds when the abundance of the protonated molecular ions was plotted in the form of single ion chromatograms (Figure 2). All peptides were separated within a total analysis time of 90 min. The elution window was from 55 to 90 min, indicating that, if the gradient had started at higher than 10%, the analysis could have been completed within 1 h.

The separation efficiency of the nanoscale LC column was determined from an isocratic analysis of proctolin (10-pmol injected) using 25% acetonitrile in water (0.1% TFA). The

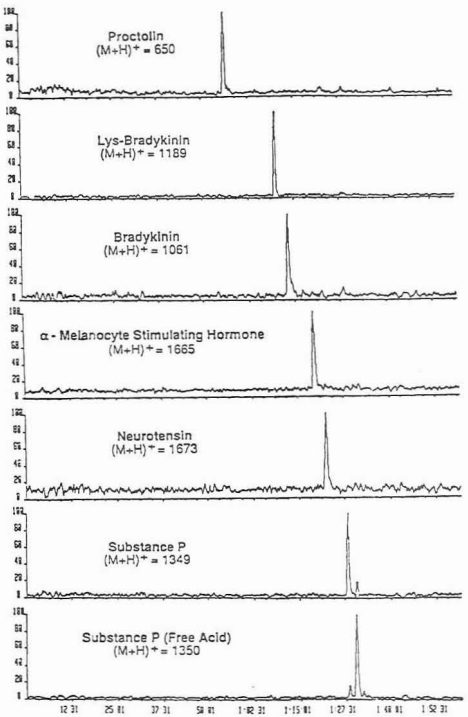

Figure 2. Nanoscale LC/MS analysis of a mixture of seven neuropeptides. Ten picomoles of each peptide were injected onto the column, with gradient elution conditions of 0% (10-min hold), stepped to 10%, followed by a linear gradient to 50% acetonitrile in water (0.1% TFA) over 120 min.

separation efficiency, as measured by the peak width at half-height, was 59 000 theoretical plates. This compares favorably with the theoretical calculations based upon the reduced parameters of Kennedy and Jorgenson (*12*), which predicts 66 000 plates for a 2-m-long column packed with 10-μm particles operated at 5 times the optimum linear velocity.

The mixture of angiotensin-related peptides comprised five components—the tetradecapeptide angiotensinogen 1–14, angiotensin III, angiotensin II, Sar^1-Gly^8-angiotensin II, and Val^5-angiotensin II. These peptides are structurally quite similar, and this mixture was expected to present a challenging separation. The gradient used for this analysis was 0% (10 min), stepped to 25%, followed by a linear gradient to 30% acetonitrile in water (0.1% TFA) over 120 min. The two forms of angiotensin II and the angiotensinogen were separated (Figure 3), while angiotensin II and angiotensin III were found to coelute under these conditions. It is interesting to note that the two peptides, angiotensin II and Val^5-angiotensin II, identical except for the substitution of a valine for an isoleucine (both uncharged, nonpolar amino acids), were separated in time by $\approx$11 min. This contrasts with the coelution of angiotensin II and angiotensin III, which differ by the addition of aspartic acid, a negatively charged amino acid. Apparently, the increased hydrophilicity due to the acidic side chain of aspartic acid compensates for the expected increase in retention time due to the addition of an amino acid.

Nanoscale LC/MS Analysis of Tryptic Digests of

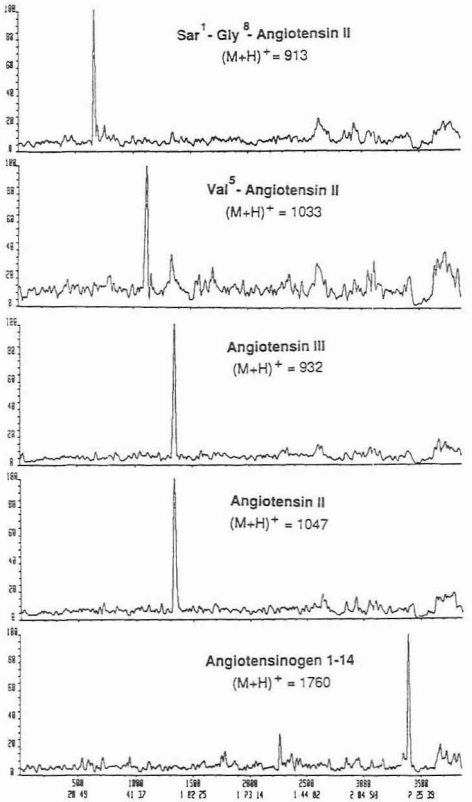

Figure 3. Nanoscale LC/MS analysis of a mixture of five angiotensin-related peptides (10 pmol per component) using gradient analysis conditions of 0% (10 min), stepped to 25%, followed by a linear gradient to 30% acetonitrile in water (0.1% TFA) over 120 min.

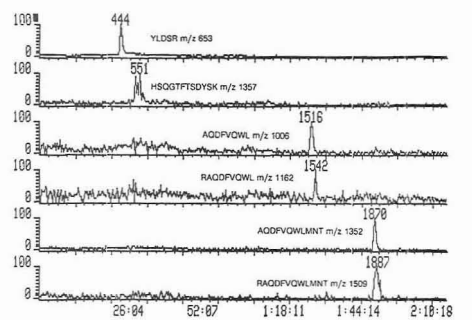

Figure 4. Nanoscale LC/MS analysis of a tryptic digest of glucagon. An injection corresponding to approximately 45 pmol of the undigested protein was made (1 mg total protein was digested). The mobile phase gradient was 0–70% acetonitrile in water (0.1% TFA) over 120 min.

Proteins. The analyses of the tryptic digests of glucagon, bovine growth hormone releasing factor, and horse heart cytochrome C were performed. For the glucagon (MW = 3482) digest analysis, an injection corresponding to approximately 45 pmol of the undigested protein was made. The mobile-phase gradient was 0–70% acetonitrile in water (0.1% TFA) over 120 min. All the expected tryptic fragments were found

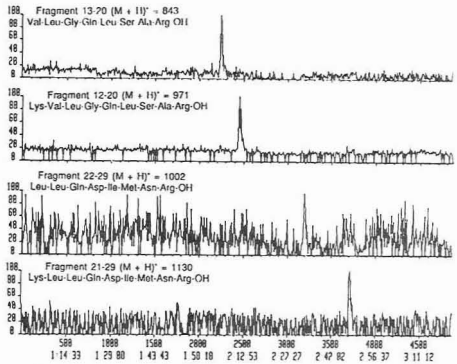

Figure 5. Nanoscale LC/MS analysis of a tryptic digest of bovine growth hormone releasing factor (1–44) using an injection volume corresponding to approximately 0.8 pmol of undigested protein, with a mobile-phase gradient of 0–70% acetonitrile in water (0.1% TFA) over 120 min.

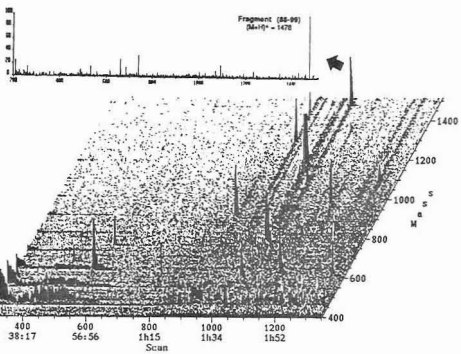

Figure 6. Isometric plot of the nanoscale LC/MS analysis of a tryptic digest of horse heart cytochrome C. A relatively large injection was made, corresponding to approximately 96 pmol of the undigested protein (1 mg of protein digested). The gradient used for this analysis was 0% (10 min), stepped to 15%, and then linearly programmed to 35% acetonitrile in water (0.1 TFA) over 120 min. The background subtracted mass spectrum of one component, peptide 88–99, m/z 1478, is shown in the inset.

(Figure 4), except for the tryptic fragment, yielding only a single arginine, which was below the mass spectral scan range used for this experiment. Acceptable peak shape was obtained for all fragments except for the fragment at m/z 1357, which was excessively wide and comprised of a series of spikes. This was attributed to a short-term instability of the ion beam from the FAB probe as the glycerol clusters also were "spiking" during the elution of this fragment.

Growth hormone releasing factor (bovine 1–44, MW = 5107) was analyzed by using an injection corresponding to approximately 0.8 pmol of undigested protein, and a mobile-phase gradient identical with that used in the analysis of the glucagon digest. At this low level, only four of the nine expected tryptic peptides were observed (Figure 5). Good chromatographic peak shape was obtained, with acceptable signal to noise ratios for these four fragments.

The analysis of a larger protein, cytochrome C (horse heart, MW = 12384), was performed to generate a larger number of tryptic fragments, in order to present a more challenging analysis. To ensure detection of as many fragments as possible, a relatively large injection of digest was made, corre-

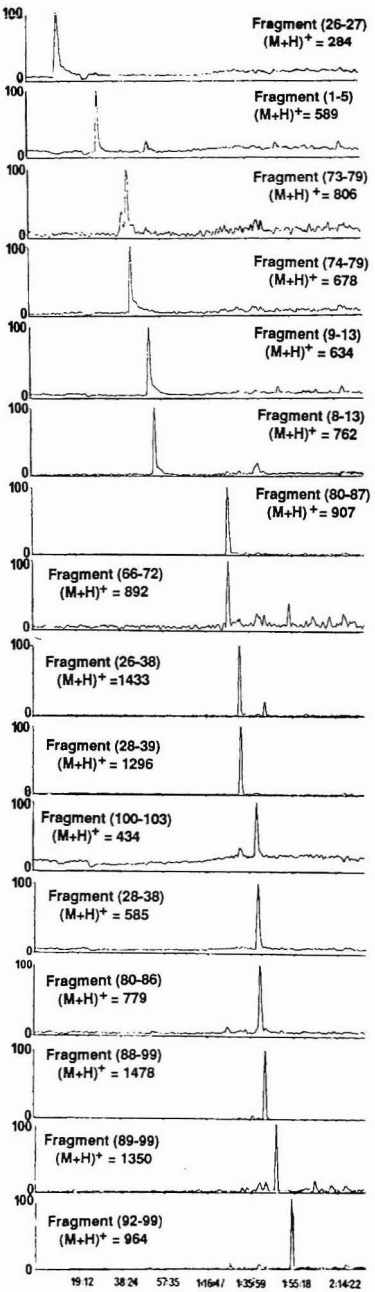

Figure 7. Single ion chromatograms of 16 tryptic fragments extracted from the isometric plot in Figure 6.

sponding to an injection of approximately 96 pmol of the undigested protein (75% of the original protein was undigested, however). The gradient used for this analysis was 0% (10 min), stepped to 15%, and then linearly programmed to 35% acetonitrile in water (0.1% TFA) over 120 min. Because the matrix background ions dominate the total ion chromatogram, an isometric plot is used to visualize the results (Figure 6). Over 40 chromatographic peaks were found in the analysis, 22 of which have been assigned as tryptic fragments, including tryptic fragments resulting from incomplete digestion. The inset in Figure 6 shows a typical mass spectrum (background subtracted) of one of the components, fragment 88–99, m/z 1478. Sixteen of the most abundant chromatographic peaks have been assigned as tryptic fragments (Figure 7). Good chromatographic peak shape was obtained, and while several of the single ion chromatogram peaks overlapped to some degree, all but two of the mass spectra show only one analyte.

CONCLUSIONS

Nanoscale packed-capillary LC columns have been shown to be useful for high-resolution separations of peptide mixtures. These nanoscale LC columns, which offer chromatographic advantages over commercially available "microcapillary" LC columns, can be easily and inexpensively prepared in house. Columns prepared in this manner have been found to be stable indefinitely if careful attention to filtering of sample solutions and mobile phases is shown.

The coaxial continuous-flow FAB probe permits the coupling of these nanoscale columns with FAB/MS with minor loss in chromatographic separation efficiency, which has been attributed to the independent delivery of the LC effluent and the FAB matrix directly to the FAB probe tip. The low mobile-phase flow rates of these columns facilitate their coupling with the high-vacuum environment of mass spectrometer ion sources. The total volumetric flow rate of the LC column and the FAB matrix solution was less than 1 μL/min, a flow rate easily tolerated by the standard diffusion vacuum pumps of the ion source.

LITERATURE CITED

(1) Jorgenson, J. W.; Guthrie, E. J. *J. Chromatogr.* **1983**, *255*, 335.
(2) Yang, F. J. *J. Chromatogr.* **1982**, *236*, 265.
(3) Yang, F. J. *HRC&CC, J. High Resolut. Chromatogr. Chromatogr.* **1986**, *9*, 848.
(4) Takeuchi, T.; Ishii, D. *J. Chromatogr.* **1982**, *238*, 409.
(5) Gluckman, J. C.; Hirose, A.; McGuffin, V. L.; Novotny, M. *Chromatographia* **1983**, *17*, 303.
(6) McGuffin, V. L.; Novotny, M. *J. Chromatogr.* **1983**, *255*, 381.
(7) DeWeerdt, M.; Dewaele, C.; Verzele, M. *HRC&CC, J. High. Resolut. Chromatogr. Chromatogr.* **1987**, *10*, 553.
(8) Hoffmann, S.; Blomberg, L. *Chromatographia* **1987**, *24*, 416.
(9) Borra, C.; Soon, M. H.; Novotny, M. *J. Chromatogr.* **1987**, *385*, 75.
(10) Kennedy, R. T.; Jorgenson, J. W. *Anal. Chem.* **1989**, *61*, 1128.
(11) Karlsson, K. E.; Novotny, M. *Anal. Chem.* **1988**, *60*, 1662.
(12) Kennedy, R. T.; Jorgenson, J. W. *Anal. Chem.* **1989**, *61*, 1128.
(13) Jorgenson, J. W.; Rose, D. J.; Kennedy, R. T. *Am. Lab.* **1988**, *20*, 32.
(14) Kennedy, R. T.; Jorgenson, J. W. *Anal. Chem.* **1989**, *61*, 436.
(15) Oates, M. D.; Jorgenson, J. W. *Anal. Chem.* **1989**, *61*, 432.
(16) Kennedy, R. T.; Oates, M. D.; Cooper, B. R.; Nickerson, B.; Jorgenson, J. W. *Science* **1989**, *246*, 57.
(17) White, J. G.; St. Claire, R. L., III; Jorgenson, J. W. *Anal. Chem.* **1986**, *58*, 293.
(18) Knecht, L. A.; Guthrie, E. J.; Jorgenson, J. W. *Anal. Chem.* **1984**, *56*, 479.
(19) St. Claire, R. L.; Jorgenson, J. W. *J. Chromatogr. Sci.* **1985**, *23*, 186.
(20) Oates, M. D.; Jorgenson, J. W. *Anal. Chem.* **1989**, *61*, 1977.
(21) Guthrie, E. J.; Jorgenson, J. W.; Dluzneski, P. R. *J. Chromatogr. Sci.* **1984**, *22*, 171.
(22) Dluzneski, P. R.; Jorgenson, J. W. *HRC&CC, J. High Resolut. Chromatogr. Chromatogr.* **1988**, *11*, 332.
(23) Barber, M.; Bordoli, R. S.; Sedgwick, R. D.; Tyler, A. N. *J. Chem. Soc., Chem. Commun.* **1981**, 325.
(24) Ito, Y.; Takeuchi, T.; Ishii, D.; Goto, M. *J. Chromatogr.* **1985**, *346*, 161.
(25) Caprioli, R. M.; Fan, T.; Cottrell, J. S. *Anal. Chem.* **1986**, *58*, 294.
(26) Caprioli, R. M.; DaGue, B. B.; Wilson, K. *J. Chromatogr.* **1988**, *26*, 640.
(27) Chen, K. H.; Cotter, R. J. *Rapid Commun. Mass Spectrom.* **1988**, *2*, 237.
(28) Lisek, C. A.; Bailey, J. E.; Benson, L. M.; Yaksh, T. L.; Jardine, I. *Rapid Commun. Mass Spectrom.* **1989**, *3*, 43.
(29) Vekey, K.; Edwards, D.; Zerilli, L. F. *J. Chromatogr.* **1989**, *488*, 73.
(30) Ashcroft, A. E. *Org. Mass Spectrom.* **1987**, *22*, 754.
(31) Games, D. E.; Pleasance, S.; Ramsey, E. D.; McDowall, M. A. *Biomed. Environ. Mass Spectrom.* **1988**, *15*, 179.

(32) Hutchinson, D. W.; Woolfitt, A. R.; Ashcroft, A. E. *Org. Mass Spectrom.* **1987**, *22*, 304.
(33) deWit, J. S. M.; Deterding, L. J.; Moseley, M. A.; Tomer, K. B.; Jorgenson, J. W. *Rapid Commun. Mass Spectrom.* **1988**, *2*, 100.
(34) Pleasance, S.; Thibault, P.; Moseley, M. A.; Deterding, L. J.; Tomer, K. B.; Jorgenson, J. W. *J. Am. Soc. Mass Spectrom.* **1990**, *1*, 312.
(35) Moseley, M. A.; Deterding, L.; Tomer, K.; Kennedy, R. T.; Bragg, N. L.; Jorgenson, J. W. *Anal. Chem.* **1989**, *61*, 1577.
(36) Deterding, L. J.; Moseley, M. A.; Tomer, K. B.; Jorgenson, J. W. *Anal. Chem.* **1989**, *61*, 2504.
(37) Jorgenson, J. W.; Guthrie, E. J. *J. Chromatogr.* **1983**, *255*, 335.
(38) Caprioli, R. T.; Tomer, K. B. In *Continuous Flow Fast Atom Bombardment Mass Spectrometry*; Caprioli, R. M., Ed.; Wiley & Sons: New York, 1990; p 93.
(39) Cole, R. B.; Guenat, C. R.; Gaskell, S. J. *Anal. Chem.* **1987**, *59*, 1139.
(40) Knox, J. H. *J. Chromatogr. Sci.* **1980**, *18*, 453.

RECEIVED for review December 20, 1990. Accepted April 23, 1991.

Tandem Mass Spectrometry of Peptides Using Hybrid and Four-Sector Instruments: A Comparative Study

Mark F. Bean and Steven A. Carr*

SmithKline Beecham Pharmaceuticals, P.O. Box 1539, King of Prussia, Pennsylvania 19406

Gareth C. Thorne,[1] Marc H. Reilly,[2] and Simon J. Gaskell*

Center for Experimental Therapeutics, Baylor College of Medicine, Houston, Texas 77030

Product-ion spectra produced by high- and low-energy collisionally activated dissociation (CAD) of $[M + H]^+$ ions of a series of peptides (M_r 550–2500) have been compared on four-sector and hybrid tandem mass spectrometers, respectively. The fast atom bombardment product-ion spectra obtained for the smallest peptide analyzed (methionine–enkephalin) were remarkably similar, but substantial differences in fragmentation were observed for the heavier analytes. For peptides with $M_r > 1000$, more complete sequence information was obtained from high-energy CAD on the four-sector instrument. Nevertheless, low-energy CAD on the hybrid mass spectrometer was able to produce partial sequence information even for the largest of the peptides compared. *Limits of analysis*, defined as the least quantities of analyte for which product-ion spectra of essentially uncompromised quality could be obtained, were similar (ca. 15 pmol) for small peptides, but lower limits were achieved for larger peptides ($M_r > 1000$) with the four-sector instrument. High-energy CAD spectra were found to be highly reproducible, with qualitatively similar spectra obtained over a wide range of operating conditions. In contrast, it was necessary to carefully control collision gas pressures and collision energies in order to obtain good reproducible data for low-energy CAD. Experimental procedures for obtaining reproducible spectra with good sensitivity for peptides on the hybrid instrument are presented.

INTRODUCTION

Tandem mass spectrometry is now a well-established technique for obtaining detailed structural information of peptides (*1–4*). A variety of tandem mass spectrometer configurations have been described that are capable of at least unit resolution of both precursor and product ions and that reduce the detection of artifact peaks. The majority of analytical applications have been performed on one of three types of instruments: (a) four-sector mass spectrometers of BEEB (*4–6*) or EBEB (*7*) design with a collision cell located between the second and third sectors (E = electric; B = magnetic); (b) triple quadrupoles consisting of two quadrupole mass filters (Q) and a central rf-only quadrupole (q) used as a collision chamber (*8*); and (c) hybrids of EBqQ (*9*) or BEqQ (*10*) design in which q generally acts as the collision cell.

The most important distinctions between the tandem MS instrument types concern the experimental conditions governing dissociations of precursor ions. The yield of product ions in tandem MS experiments is increased beyond that of unimolecular decay by activation of precursor ions, most often through collision with a neutral gas. Collision energy can be controlled on each type of instrument but with rather different implications. Tandem double-focusing mass spectrometers focus and analyze high-kinetic-energy (10-keV) precursor ions. Collision energy is varied by grounding or electrostatically floating the collision cell and reaccelerating the ions after the cell (allowing the 5- or 10-keV collisions used in this study). Ion residence times in the field-free region between the mass spectrometers are short. In the hybrid configuration, there is a mismatch of ion velocities and beam profiles between the analyzers so that the precursor ions must be decelerated from 6 or 8 keV to less than 500 eV (but generally less than 100 eV) and the beam reshaped before entering the floated q collision region in order to allow for product-ion analysis in Q. Thus, in hybrid instruments as in triple quadrupoles, precursor ions have low kinetic energies and their residence time in the quadrupole collision chamber is correspondingly long (tens to hundreds of microseconds).

The collision energy in the laboratory frame of reference (E_{lab}) is defined by the kinetic energy of the precursor ion and is thus markedly greater for the four-sector instrument than for the triple-quadrupole or hybrid instruments (*11*). In reality, the average energy deposited is somewhat less than predicted by Newtonian mechanics, and the proportion of the center-of-mass collision energy (E_{cm}) actually converted to internal energy of the precursor ion is not readily determined. Scattering of the residual precursor ions and the product ions is an unavoidable consequence of the collision process. These factors have manifold implications with respect to low- and high-energy collision phenomena, and their discussion is be-

* Authors to whom correspondence should be addressed.
[1] Present address: VG Analytical Ltd., Floats Rd, Wythenshawe, Greater Manchester M23 9LE, U.K.
[2] Present address: VG Instruments, 32 Commerce Center, Cherry Hill Drive, Danvers, MA 01923.

0003-2700/91/0363-1473$02.50/0 © 1991 American Chemical Society

yond the scope of the present work. The interested reader is referred to the detailed studies of Boyd et al. (*12–14*) and Derrick et al. (*15–18*) in addition to the two older reviews (*19, 20*) for futher discussions of the fundamental processes involved in collisional activation experiments.

The analytical utility of FAB ionization coupled with tandem MS on four-sector instruments for structural analysis of naturally occurring and protein-derived peptides is now well-established (*3, 4, 21–36*). In all of these studies, peptides were activated by high-energy collisions with the target gas. Hunt and co-workers have demonstrated that low-energy collisions in a triple-quadrupole mass analyzer can also be useful for peptide sequence analysis of biologically derived samples (*1, 37–42*). Greatly increased ion transmission in the triple quadrupole has been achieved by passing the entire ion cluster related to the selected precursor $(M + H)^+$ (up to a 10-Da-wide mass window) through Q1 (*1*), although this can result in uncertainty in the assigned masses. With the exception of a few recent reports (*43–45*), studies of peptides by tandem MS on hybrid instruments have involved commercially available model compounds rather than naturally occurring peptides or peptides derived from proteins (*13, 46–48*).

From a practical standpoint, it is important to determine the analytical implications of the use of high- and low-energy collision regimes on tandem instruments. In the present study, we have assessed the relative merits of a four-sector (BEEB) and a hybrid (BEqQ) instrument for one specific application: namely, the generation of structurally informative product-ion spectra by collisional activation of $(M + H)^+$ ions of peptides. Specifically, we compare the two instrument types with regard to (a) their ability to reproducibly provide analytically useful tandem mass spectra, (b) the differences in the structural information present in the respective product-ion mass spectra, and (c) the relative sensitivities of the tandem MS analyses. The latter was assessed by determining the minimum amount of sample for which a product-ion spectrum could be recorded with essentially the same analytically useful structural information obtainable from unlimited sample. We refer to this measurement as our *limit of analysis*.

A preliminary report of the current study including nonpeptide samples has been previously presented (*49*). Poulter and Taylor recently published a study describing the low- and high-energy CAD spectra of peptides (*45*) in which they noted that arginine positioned at either end of a peptide had a detrimental effect on the ability to obtain product-ion spectra on the hybrid instrument. They observed mostly b- and y-series ions on the hybrid mass spectrometer, although a-type ions could be detected below mass 200. They also corroborated our initial suggestion (*49*) of a practical upper mass limit of about 1000 Da for peptides. No comparative data were shown, however, apparently because the higher mass, low-energy CAD spectra showed no useful fragmentation. Another recent study, also reporting analyses of peptides by tandem MS using four-sector and hybrid instruments (*50*), confirmed earlier conclusions and determined that the limitations of the hybrid instrument were caused by inferior CAD efficiency rather than poor ion transmission with respect to the four-sector mass spectrometers. Although comparative spectra were presented, quantitative considerations were not addressed. This report extends the number of peptide comparisons in terms of composition and mass range and makes quantitative comparisons for the low-energy and high-energy CAD spectra. Optimized conditions for recording limit-of-analysis spectra on both instruments are presented.

EXPERIMENTAL SECTION

Chemicals. Rubidium iodide was obtained from Alfa Products, Danvers, MA. Cesium iodide (99.9%), anhydrous lithium iodide, potassium chloride (99+%), dithioerythritol (99+%), dithiothreitol (99%), 2-hydroxyethyl disulfide (2,2′-dithiodiethanol), and 3-nitrobenzyl alcohol were obtained from Aldrich Chemical Co., Inc., Milwaukee, WI. Sodium iodide and trifluoroacetic acid were purchased from J. T. Baker Chemical Co., Phillipsburgh, NJ. Monothioglycerol (98%) was bought from Sigma Chemical Co., St. Louis, MO. Human adrenocorticotropic hormone fragment 18-39 (ACTH clip peptide 18-39), substance P, and renin substrate tetradecapeptide (porcine angiotensinogen) were purchased from Peninsula Labs, Belmont CA. Substance P fragment 2-11 was bought from Sigma. Methionine–enkephalin was obtained from Vega Biochemicals, Tucson, AZ. Angiotensin III and a synthetic tetradecapeptide (AEGETTTFTALTEK) were synthesized and HPLC purified in-house at SmithKline Beecham Pharmaceuticals. Additional samples of substance P, methionine–enkephalin, and angiotensin III were obtained from Sigma. All materials were used without further purification.

Four-Sector Tandem Mass Spectrometry. Four-sector tandem MS experiments were conducted on a VG ZAB-SE 4F (BEEB) mass spectrometer (VG Analytical Ltd., Manchester, U.K.) operated at 10-kV ion acceleration and equipped with a high-voltage (35-kV) cesium ion gun (*51*), standard FAB/continuous-flow FAB source on the first mass spectrometer (MS-1), and standard electron multiplier detectors. The magnetic (B) and electric (E) fields of MS-1 were fixed to pass the selected precursor ion, and the MS-1 slits were adjusted for unit mass resolution (50% valley definition); the resolution of MS-2 was set between 700 and 1000. MS-2 was calibrated by using a second ion source and a xenon FAB gun located before the collision cell between MS-1 and MS-2. The calibration sample consisted of a mixture of potassium chloride with lithium, sodium, and cesium iodides in ethanol/tap water (1/5). We have found that traces of rubidium, iron, chromium, and aluminum can be detected in the ion beam (either as contaminants of the calibration salts, of the water, or of the stainless steel probe surface) and that these have been useful in bridging the mass gap between K^+ (m/z 39) and Cs^+ (m/z 133), thus obviating the addition of rubidium iodide. This is desirable because rubidium isotopes can complicate mass assignment of the calibrant ion peaks. The time-to-mass conversion table resulting from calibration of a conventional exponential down magnet scan of MS-2 is used by the data system to calculate the B_2 and E_2 field link-time point and the scan functions for the magnet and the y-focus lens located in front of the collector slit; this function is automatically downloaded into the scan-control hardware. Any analyte of mass falling within the calibration range may be analyzed by tandem MS with the single calibration although the scan function must be recalculated for each analyte of different mass. A typical calibration from m/z 2300 to 6 provided acceptable mass assignments for 6 weeks to 6 months. The criteria for acceptability were assignments within 0.5 Da as long as the direction of error was consistent throughout the spectrum. The selected precursor ions were collisionally activated by introducing helium into the collision cell located between MS-1 and MS-2 at a pressure sufficient to reduce beam intensity by 75%. By grounding or electrically floating the collision cell to 5 kV, collisions energies of 10 or 5 keV were chosen. Product-ion spectra are acquired in MS-2 by link scanning of E_2 and B_2. B_2 is scanned exponentially down (25 s/decade) to the field calculated to pass the precursor ion, at which point the E_2 and B_2 field references are linked to maintain a constant B_2/E_2 scan ratio. All data were arrayed in multichannel acquisition of peak profile data with 15–30 raw data samples (channels) per peak. Typically 6–12 scans were summed by using a VG 11-250J data system to acquire and process all data. Raw time–intensity data were twice smoothed through a number of points corresponding to one-third of the peak width prior to centroiding and mass conversion.

Initial experiments were aimed at producing the best spectrum without regard to sample concentration. The experimental variants were collision cell voltage (grounded or 5 kV) and sample matrix (thioglycerol, a 3/1 mixture of dithiothreitol/dithioerythritol in methanol, an 8/3/1 mixture of 3-nitrobenzyl alcohol/dithioerythritol/dithiothreitol in methanol with 1% trifluoroacetic acid, and 2-hydroxy disulfide).

Subsequent experiments sought to establish lower limits of analysis. For these experiments, each acquisition consumed

10–10 000 pmol of sample dissolved in 2 μL of solvent. The 2-μL peptide solution was placed on the FAB probe tip with a borosilicate glass micropipette, and the solvents were evaporated under vacuum in the probe lock of the mass spectrometer. Approximately 1 μL of thioglycerol matrix was added prior to analysis by FABMS. After several scans, the parent ion beam signal diminished; at this time, data acquisition was temporarily halted, the probe withdrawn, the glass micropipette rinsed onto the probe, dried, and a further 1 μL of matrix added, and data acquisition resumed. A new micropipette was used for each analysis. Measurements made at the lower limit of analysis were replicated with freshly weighed and diluted samples.

Hybrid Tandem Mass Spectrometry. Low-energy CAD analyses were performed on a VG ZAB SEQ hybrid mass spectrometer (VG Analytical Ltd.) operated at an accelerating voltage of 8 kV and unmodified in all respects relevant to the present analyses. The instrument is equipped with a conventional FAB gun generating xenon atoms with energies of 8 keV. Similar sensitivities were observed with a conventional FAB source and with a source designed for conventional or continuous-flow sample introduction. For the analyses reported here, sample introduction was via a conventional FAB probe. The liquid matrix used was a mixture (1:1 by volume) of thioglycerol and 2-hydroxyethyl disulfide. The primary FAB beam was xenon atoms with energies of 8 keV. Parent-ion beam resolution was at least unity (50% valley definition). The quadrupole mass analyzer was operated at 1–2-Da resolution, except for analyses of higher mass analytes, for which the product-ion resolution was degraded. Sample-specific details are provided in the figure legends. Argon was used as the collision gas in the rf-only quadrupole collision cell at pressures of $(1.5–4) \times 10^{-4}$ mbar (as estimated from the recorded analyzer pressure and the known conductance from the collision region). The collision energy (laboratory frame of reference) was 14–27 eV. The parent ions were selected by mass spectrometry hardware, and the quadrupole was scanned under control of the VG 11/250J data system. The scan control includes ramping of the float potential of the quadrupole mass filter (Q) to optimize transmission of product ions of differing mass. Acquisition of daughter-ion signals was via the data system in a multichannel analyzer mode. Scans were of 10–60-s duration, and 6–20 scans were accumulated; details are given in the figure legends. Mass assignments of the daughter-ion spectra were made following centroid calculations and were based on a simple two-point linear calibration of the quadrupole mass scale.

RESULTS AND DISCUSSION

This report is specifically focused on a comparison of the quality of structural data and the reproducibility of obtaining data with limited sample by product-ion scanning using high-energy CAD on a four-sector instrument and low-energy CAD on a hybrid instrument. The relative ease of operation of the two instruments is also compared. The samples chosen included small peptides that yield strong molecular ion signals in FAB (methionine-enkephalin, angiotensin III, substance P, and substance P fragment 2-11), a variety of large peptides (renin substrate, ACTH clip 18-39 peptide), and a tetradecapeptide representative of a tryptic fragment derived from a protein digest.

Relative Ease of Operation and Reproducibility of Data for Hybrid and Four-Sector Instruments. The mode of tandem MS operation on the four-sector instrument is conducive to obtaining highly reproducible results. The collision energy (in the laboratory frame of reference) is precisely defined by the potential difference between the ion source (10 kV) and the collision cell (ground or 5 kV in the analyses reported here). Electrostatically floating the collision cell improves the transmission of low-mass product ions with only a slight reduction of overall dissociation fragment yields. In addition, product-ion resolution improves due to a decrease in the fractional energy spread. The gas pressure in the collision region can be reproducibly set by attenuation of any precursor ion signal. However, pressure settings are not critical since qualitatively similar spectra are obtained over a wide range of parent-ion attenuations (e.g., 25–75% attenuated (*52*)). Calibration of product-ion spectra is straightforward and is described in detail in the Experimental Section.

In contrast, establishing reproducible conditions for tandem MS analysis using the hybrid instrument requires greater attention to experimental detail. The collision energy is again determined by the potential difference between the ion source and the collision region; in this instance, the quadrupole collision region floats to within 10–50 V (in the analyses described in this report) of the source potential. Careful calibration of this potential is required; the procedure, however, is complete in less than 1 min.

Because of the narrow window of ion kinetic energies optimally analyzed in the quadrupole (*10*), it is necessary to ramp its potential with mass. This ramp is achieved by maximizing the signals corresponding to the precursor ion and a fragment representing a low mass relative to the precursor. For this purpose, the analyte itself may be used or a standard compound such a substance P fragment 2-11 (see below). Again, the apparent complexity of the optimization process belies the ease of its experimental implementation, which requires 5–10 min for completion.

Adjustment of gas pressure on the basis of attenuation of precursor-ion signal (following the technique appropriate to the four-sector instrument) is prone to error on the hybrid instrument. This is attributable to the known variation in precursor-ion transmission through an rf-only quadrupole with small changes in collision energy and is associated with the periodicity of transmission as a function of ion kinetic energy (*53*). Experience has suggested that satisfactory reproducibility of collision conditions may be achieved by adjustment of gas pressure as recorded in the analyzer housing to a predetermined value. Optimal collision gas pressures and collision energies may be determined for individual analytes but may, in practice, be closely predicted from the molecular mass of the analyte and previous experience of similar compound types. Thus, for example, satisfactory CAD analyses of low-mass peptides are generally achieved with an indicated gas pressure of $(1.5–2) \times 10^{-6}$ mbar argon (translating to an estimated pressure of $(2.7–3.6) \times 10^{-4}$ mbar in the collision quadrupole) and a collision energy of 20–30 eV. Optimal results with larger peptides have been achieved with a collision gas pressure of $(0.5–1) \times 10^{-6}$ mbar ($(0.9–1.8) \times 10^{-4}$ mbar in q) and a collision energy of 15–20 eV. A higher gas pressure generates an excessive yield of low-mass fragments from higher mass (>800-Da) peptides. The apparent anomaly of a lower optimal collision energy for higher mass peptides is rationalized in terms of the desirability of longer collision-region residence times achieved with low collision energies, thus favoring observation of the products of low-energy dissociation processes (including unimolecular decay). It has been found to be good practice in the Baylor laboratory to establish appropriate collision conditions by reference to data obtained with frequently analyzed samples. A single analysis of a known sample also permits the simple two-point calibration of the linear quadrupole mass scale.

Qualitative Comparisons of Product-Ion Spectra. Product-ion spectra comparing the two instrument configurations are shown in the figures with annotations for peptide fragmentations following the nomenclature of Johnson and Biemann (*3*, *31*), which is substantially modified from an earlier nomenclature still in use (*54*). In addition to lower case *abcd* for fragments retaining the N-terminal amino acid and *vwxyz* for fragments retaining the C-terminus, upper case amino acid single letter codes are used to designate single amino acid immonium ions and side-chain losses. "Internal" peptide fragments with acylium ion structures are indicated by partial sequences in single-letter code. Observed cleavages

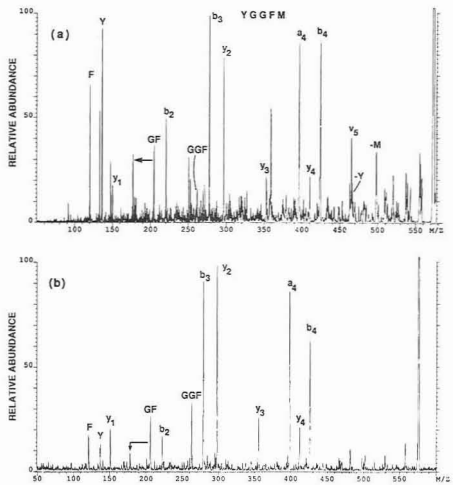

Figure 1. Methionine–enkephalin ((M + H)$^+$, m/z 574.2) product-ion spectra. Arrows from internal fragments indicate 28–Da losses (CO). (a) 10 pmol; high-energy CAD on the four-sector instrument (thioglycerol matrix; collision cell at ground potential; 75% attenuation of precursor ion beam). (b) 17 pmol; low-energy CAD on the hybrid instrument (thioglycerol/2-hydroxyethyl disulfide (1/1) matrix; 25-eV collision energy; estimated collision gas pressure, 2.7 × 10^{-4} mbar; 10 s/scan; 20 scans; product-ion resolution, 1.5 Da).

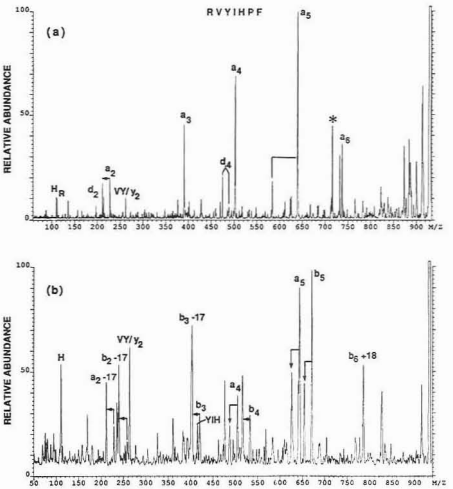

Figure 2. Angiotensin III ((M + H)$^+$, m/z 931.5) product-ion spectra. An asterisk indicates a matrix-related fragment ion; arrows indicate 17-Da losses (NH_3); connecting line from a_5 indicates a_{n-1} side-chain cleavage (see text). (a) 15 pmol; high-energy CAD on the four-sector instrument (refer to Figure 1a for conditions). (b) 32 pmol; low-energy CAD on the hybrid instrument (thioglycerol/2-hydroxyethyl disulfide (1/1) matrix; 26-eV collision energy; estimated collision gas pressure, 2.7 × 10^{-4} mbar; 10 s/scan; 20 scans; product-ion resolution, 1.5).

of peptides and the proposed mechanisms of fragmentation involved have been reviewed for high-energy (*3*, *31*) and low-energy CAD (*1*, *47*).

All spectra are smoothed and plotted in continuum rather than bar chart format by a VAX-based VG Opus data system with the exception of the high-energy CAD spectra of renin substrate and the ACTH clip peptide, which could not be processed due to limitations imposed by software incompatibility. The continuum format has the compelling advantage that the quality of the data is more readily apparent. Labeled masses represent calculated values throughout the paper; observed masses were, in general, within 0.3 Da of calculated. The figures illustrate spectra obtained at or near levels corresponding to the limit of detection on the hybrid instrument so that informative peaks may be approaching the noise level. Obviously the signal-to-noise ratio for spectra from both instruments improves greatly as the sample loading is increased. Moreover, product ions due to fragmentation of matrix-related ions of the same mass as the selected precursor (discussed under limits of analysis below) are not observed at higher loadings.

Methionine–Enkephalin. The smallest peptide included in the present study was methionine–enkephalin (M_r 573.2). Figure 1 can be profitably compared with previously published CAD spectra acquired under high- or low-energy regimes on a variety of instruments (low-energy: (M + H)$^+$ (*47*, *55*); metal-cationized precursor (*47*)) (high energy: (M + H)$^+$ (*56–58*); metal-cationized precursor (*56*, *59*, *60*)). The high- and low-energy CAD spectra of methionine–enkephalin are remarkably similar, each exhibiting fragments from both termini sufficient to reveal the entire sequence. This behavior is expected for peptides lacking a strongly basic terminal residue such as arginine, which can serve to localize positive charge and direct fragmentation. The same internal fragments (*1*, *3*, *31*, *46*) are also observed in each spectrum. Immonium ions from single aromatic amino acids are prominent in both spectra, albeit unusually intense in the high-energy data.

Angiotensin III. In contrast to the observations with methionine–enkephalin, the low- and high-energy CAD product-ion spectra recorded for angiotensin III are substantially different. The high-energy data (Figure 2a) reveal a simple pattern of a-series cleavages with accompanying β-γ cleavage of the a_n side chain to give d_n ions. The latter are useful in distinguishing amino acid isomers (e.g., Leu vs Ile) and isobars (Leu vs hydroxyproline). For example, the peaks corresponding to a 14-Da loss (more prominent in spectra recorded at the 50-pmol level) and a 28-Da loss from a_4 allow unequivocal identification of the position-4 amino acid as isoleucine rather than the isobaric leucine (*61*, *62*). Cleavage of the entire a_{n-1} side chain (*31*, *61*), although less frequent, is sometimes observed in cases where the a_n side chain is small or aromatic. One such fragment is readily discerned at m/z 585.2. The spectrum as a whole is a good example of charge localization of an N-terminal arginine, which under high-energy CAD conditions drives remote-site fragmentations in a defined pattern along the whole molecule. The relative order of the first two amino acids cannot be deduced from the data.

The low-energy CAD product-ion spectrum (Figure 2b) is substantially more complex than the high-energy CAD spectrum (the data from the hybrid mass spectometer may be compared to previously published spectra from the same instrument (*47*, *63*)). Again, intense N-terminal ions dominate, consisting in this case of a- and b-series ions along with "satellites" 17 Da lower due to loss of ammonia from the N-terminal arginine. In addition, the C-terminal fragment y_2 (isobaric with a VY internal) is prominent. Side-chain fragmentations to give the d series are not detected in the low-energy CAD spectra in keeping with previous observations suggesting a high-energy requirement for such cleavages (*13*, *64*). Despite the absence of a_6 or b_6 ions, the requisite sequence information is carried by an ion attributed the structure b_6

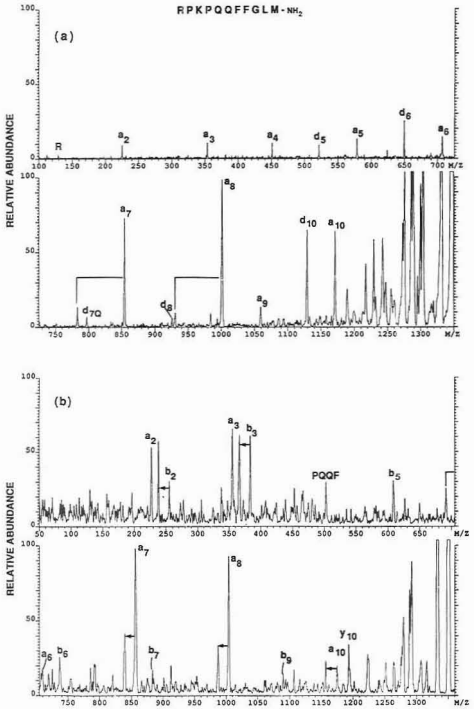

Figure 3. Substance P ($(M + H)^+$, m/z 1347.7) product-ion spectra. (a) 100 pmol; high-energy CAD on the four-sector instrument (refer to Figure 1a for conditions). Connecting lines indicate a_{n-1} side-chain cleavages (see text). The peak labeled "d_{7q}" represents an a_γ-type acylium ion with β–γ cleavage of the Gln (residue 6) side chain (*31*). (b) 370 pmol; low-energy CAD on the hybrid instrument (thioglycerol/2-hydroxyethyl disulfide (1/1) matrix; 27-eV collision energy; estimated collision gas pressure, 2.7×10^{-4} mbar; 30 s/scan; 7 scans; product ion resolution, 3 Da). Arrows indicate 17-Da losses (NH_3).

+ 1 + OH but labeled "b_6 + 18" in the figure for simplicity. This rearrangement, representing loss of C-terminal amino acid residue but with retention of the C-terminal hydroxyl group, has recently been studied in detail in the Baylor laboratory (*47*, *65*). A b_5 + 18 ion is also observed. The mechanism of formation of ions of this type appears to be analogous to the fragmentation of alkali metal-cationized peptides reported by several laboratories (*66*, *67*) and examined in detail by Gross and co-workers on a three-sector instrument of EBE configuration under high-energy CAD and metastable decomposition conditions (*56*). The corresponding rearrangements are not, however, observed in the high-energy CAD spectrum of the $(M + H)^+$. As in the case with the high-energy data, the order of the first two amino acids cannot be determined.

Substance P. Figure 3 shows a comparison of product-ion spectra for substance P, another peptide containing an N-terminal arginine residue; in this case, the C-terminus is amidated. A great number of spectral comparisons can be made for this frequently used model neuropeptide for high-energy CAD (*31*, *45*, *49*, *68–72*) as well as for low-energy CAD (*49*, *73*). The major features of the high-energy dissociation spectrum (Figure 3a) are the prominent and simple series of N-terminal ions, a_{2-10}, together with d-series ions providing confirmation of amino acid sequence. No internal or C-terminal fragments are observed.

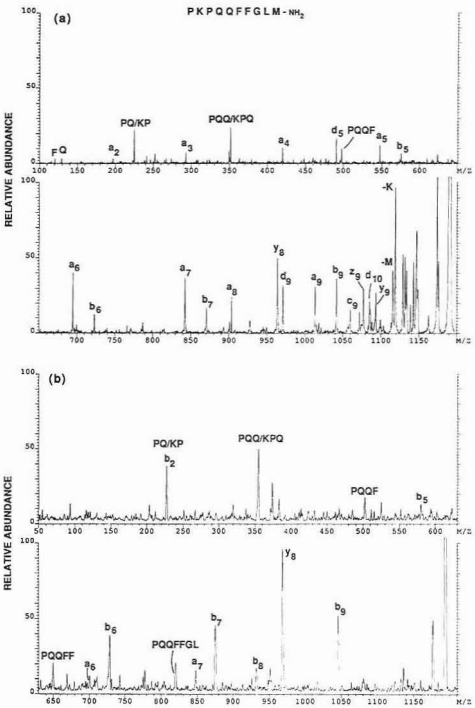

Figure 4. Des-Arg^1-substance P, fragment 2-11 ($(M + H)^+$, m/z 1191.6 product-ion spectra. (a) 100 pmol; high-energy CAD on the four-sector instrument (refer to Figure 1a for conditions). (b) 85 pmol; low-energy CAD on the hybrid instrument (thioglycerol/2-hydroxyethyl disulfide (1/1) matrix; 25-eV collision energy; estimated collision gas pressure, 2.7×10^{-4} mbar; 30 s/scan; 10 scans; product ion resolution, 2 Da).

The spectrum from the hybrid instrument (Figure 3b) is considerably more complex, due largely to the arginine ammonia losses observed for almost every peak. A partial series of N-terminal ions can be identified. Two examples of internal fragments (PKP and PQQF) are seen in the low-energy CAD spectrum. Several peaks at high mass (m/z 1200–1300) are reproducible but not readily explained. The limit of analysis is estimated to be more than an order of magnitude better on the four-sector instrument than on the hybrid mass spectrometer (see Table I and discussion below).

Des-Arg^1-Substance P. Compared to substance P, the des-Arg^1-analogue (substance P fragment 2-11) provides a substantially more satisfactory result on the hybrid instrument but a more complex spectrum on the four-sector instrument. The simplicity of the hybrid spectrum may be attributed, at least in part, to the absence of the previously noted satellite ions due to ammonia loss from arginine; this simplicity of fragmentation is also reflected in the improved limit of analysis (Table I). Results can be compared with previous publications (high energy, ref 60; low energy, ref 46). The low-energy CAD spectrum (Figure 4b) includes a prominent, albeit incomplete, b series together with a single abundant C-terminal ion (y_8). The N-terminal fragment ion series for the first amino acid are often not detected in either high- or low-energy CAD spectra of peptides (*3*, *74*). The internal PQ, PQQ, PQQF, PQQFF, and PQQFFGL acylium ions constitute the clearest and most structurally informative series in the spectrum. The striking abundance of these internal fragments in the low-

Table I. Approximate Limits of Analysis

peptide	four sector, pmol	hybid,[a] pmol
methionine–enkephalin	10	15 (a)
angiotensin III	15	32 (a)
substance P fragment 2-11	85	85 (a)
substance P	15	370 (b)
tetradecapeptide	250	1500 (c)

[a] Product ion resolution = (a) 1.5 Da; (b) 3 Da; (c) 2 Da.

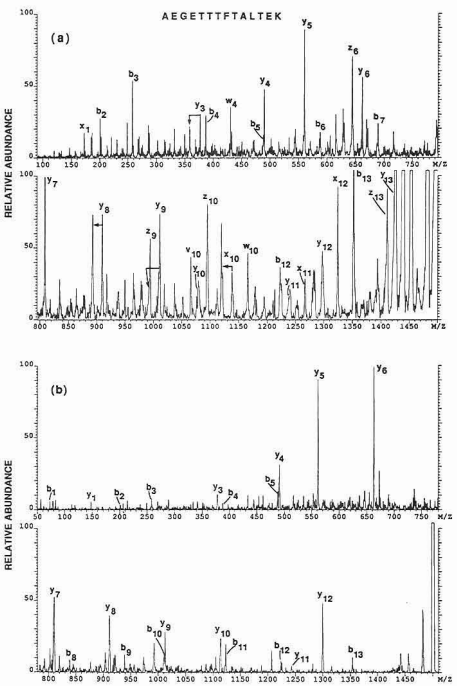

Figure 5. Tetradecapeptide ((M + H)$^+$, m/z 1498.7) product-ion spectra. (a) 1 nmol; high-energy CAD on the four-sector instrument (refer to Figure 1a for conditions). Arrows from y_n ions indicate 18-Da losses (H_2O). (b) 1.5 nmol; low-energy CAD on hybrid instrument (thioglycerol/2-hydroxyethyl disulfide (1/1) matrix; 16 eV collision energy; estimated collision gas pressure, 1.8 × 10^{-4} mbar; 15 s/scan; 12 scans; product ion resolution, 2 Da).

energy collision spectra of peptides was first noted by Hunt et al. (*1*). The a series, although present, is relatively weak. Substance P fragment 2-11 is used in the Baylor laboratory as a routine test analyte to assure satisfactory tandem MS performance.

In contrast to the low-energy data, the high-energy product-ion spectrum of substance P fragment 2-11 (Figure 4a) is somewhat more complex than the corresponding spectrum of substance P (Figure 3a) due to the absence of the charge-localizing N-terminal Arg. N-Terminal fragments still dominate due to the charge-directing influence of the Lys at position 2 in the peptide, but in addition to the a- and d-ion series, other N-terminal ions such as the b and c series, as well as some C-terminal fragments in the y and z series, are now observed. Internal fragments are also significantly more abundant in this spectrum than in that of full-length substance P, although these ions are less intense than in the low-energy data.

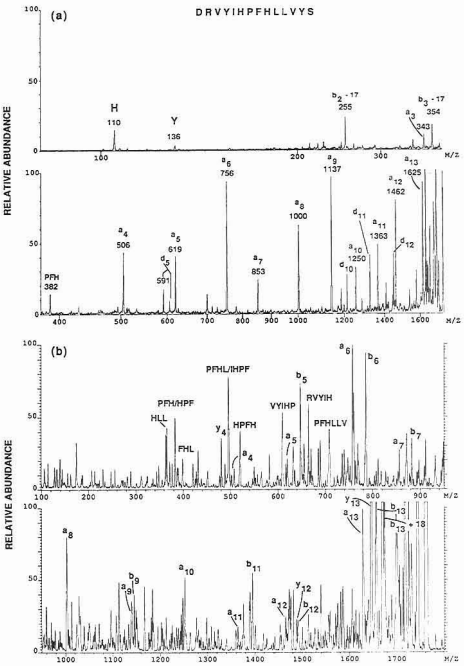

Figure 6. Renin substrate peptide ((M + H)$^+$, m/z 1758.9) product-ion spectra. (a) 1 nmol; high-energy CAD on the four-sector instrument (refer to Figure 1a for conditions). (b) 5.7 nmol; low-energy CAD on the hybrid instrument (thioglycerol/2-hydroxyethyl disulfide matrix; 14-eV collision energy; estimated collision gas pressure, 1.2 × 10^{-4} mbar; 45 s/scan; 9 scans; product ion resolution, 2Da).

Tryptic-Like Tetradecapeptide. Figure 5 shows a comparison of data obtained for a tetradecapeptide with a basic C-terminal residue; it is therefore representative of the type of peptide expected from tryptic digests and typical of the kind of problem encountered in protein sequencing. The high-energy CAD product-ion spectrum (Figure 5a) is quite complex, containing extensive structural detail in the form of both b- and y-series ions, together with members of x, v, and w series derived by additional side-chain cleavages (*31*). These fragments define the sequence of residues 3-14 of the peptide; the relative order of the first two amino acids cannot be determined from the data. Neutral loss of water noted for many of the C-terminal ions in this spectrum is typical for Thr- or Ser-containing peptides.

The low-energy CAD product-ion spectrum (Figure 5b) is substantially less satisfactory, although a nearly complete set of b and y ions can be observed to confirm the known sequence. A chief problem with the data is the inability to distinguish many of the unidentified low-intensity peaks from the structurally interpretable signals of similar intensity. This would cause difficulties in attempting to elucidate the structure of a peptide of unknown sequence.

Renin Substrate 1-14 and ACTH 18-39. The apparent trend to an increasing advantage to high-energy CAD on the four-sector instrument as the analyte molecular mass increases is further substantiated by the data obtained for the two final peptide examples. Figure 6 and 7 show product-ion spectra recorded for a renin substrate peptide (M_r 1757.9) and an ACTH clip peptide (M_r 2464.2). For comparison with other

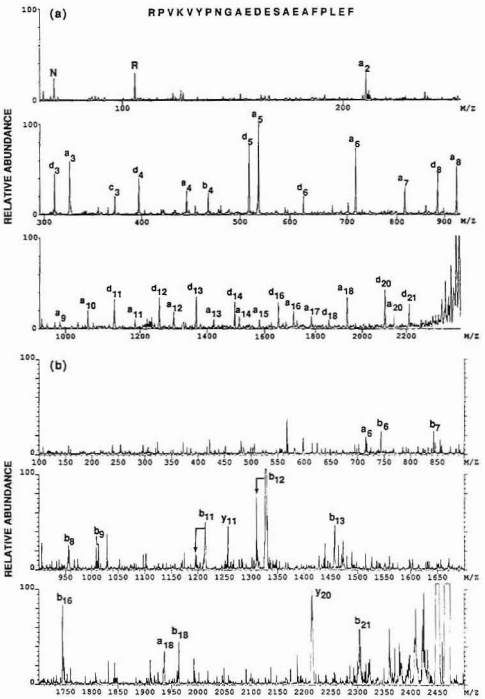

Figure 7. ACTH, fragment 18-39 ($(M + H)^+$, m/z 2465.2) product-ion spectra. Arrows indicate 17-Da losses (NH_3). (a) High-energy CAD on the four-sector instrument (collision cell at 5 kV). (b) Low-energy CAD on the hybrid instrument (thioglycerol/2-hydroxyethyl disulfide (1/1) matrix; 14-eV collision energy; estimated collision gas pressure, 1.3 × 10^{-4} mbar; 60 s/scan; 6 scans; product ion resolution, 4 Da).

four-sector data, refer to refs 64 and 75 and refs 2, 3, and 75, respectively; low-energy collision data from a triple quadrupole for ACTH clip peptide have been reported (*73*). The four-sector data are impressive with respect to the clarity of the sequence information and define the sequence of all but the first two amino acids.

The low-energy CAD spectra obtained with the hybrid instrument include the expected a and b ions accompanied by ammonia-loss satellites. Prominent internal fragments are also observed in the renin spectrum. The data for both peptides are of some utility for confirming the known structures but are not of sufficient quality to be helpful if the analyses were of true unknowns.

Limits of Analysis. We have defined the limit of analysis as the smallest quantity of analyte for which product-ion spectra with essentially uncompromised structural information content (relative to spectra recorded with unlimited sample) can be obtained. Comparison of the limits of analysis for the two tandem instrument configurations follows the expected trends (Table I). Although this definition is necessarily imprecise, an impression of the quality of data that this criterion represents may be obtained from Figures 1 and 2, which show spectra obtained at the limits of analysis on both instruments. The established limits were similar for low mass peptides, but spectral clarity was still excellent for the tetradecapeptide (M_r 1496.7) at 250 pmol on the four-sector instrument, whereas the corresponding hybrid instrument spectrum was less satisfactory and required 1500 pmol. It should be noted that the use of a cesium ion gun on the four-sector instrument rather than a xenon atom gun has little influence on precursor ion beam intensity for peptides with masses under 2000 Da (*76*).

Table II. Comparison of Determinants of Product-Ion Spectral Intensity during Tandem Mass Spectrometry of Angiotensin III ($(M + H)^+$, m/z 931.5)

	four sector, %	hybrid, %
transmission of precursor ion through MS-2 (no collision gas)[a]	60	27
transmission of precursor following introduction of collision gas[a]	15	6.7
intensity of principal product[a]	0.1[b]	0.1[c]

[a] Transmission of ions through MS-1 (identical on both instruments) is defined as 100%. [b] Intense side-chain losses were ignored as products. [c] Transmissions of precursor and product ions are independently optimized with respect to collision energy.

The limit of analysis in tandem MS is influenced by many factors, including the precursor ion beam intensity and matrix interference, ion transmission through each sector of the instrument, the resolution (slit) settings, the nature, density, and target thickness of the collision gas, the residence time in the collision cell, the collision energy, the yield of product ions, and the detection efficiency. Some of the factors related to collision energy and residence time in the cell have been discussed in a previous study using the BEqQ hybrid instrument (*46*). In the present work, a direct comparison of ion transmissions was made between the four-sector and hybrid instrument configurations during analyses of the nonapeptide, angiotensin III. The results are shown in Table II. The numbers are necessarily approximate but give an indication of the general relative position of the two instruments. For this example, with M_r 930.5, the cumulative attenuation factor is similar on the two instruments. However, it is apparent that, without any collision gas present, the overall transmission at this mass is notably less on the hybrid than on the four-sector instrument. Furthermore, transmission through the quadrupoles decreases markedly with increasing mass so that an advantage to the four-sector configuration is expected to become increasingly apparent as the mass of the analyte increases. This advantage is quite independent of any decrease in dissociation efficiency due to a decrease in E_{cm} with increasing precursor mass. Dissociation efficiency is, of course, strongly compound dependent. These trends are clearly illustrated by the high- and low-energy CAD product-ion spectra presented here for peptides of increasing mass as well as in the limits of analysis.

A further point regarding the purity of the precursor ion beam warrants discussion. Although both instruments in this study are capable of very high-resolution selection of precursor ions from a mixture, in practice, unit resolution of the monoisotopic ion is both sufficient and desirable to optimize sensitivity. As a consequence, spectra recorded at the limit of analysis contain a few ions attributable to losses of glycerol, thioglycerol, etc., from matrix-related precursor ions isobaric with the peptide $[M + H]^+$. We found that matrix product ions are particularly pronounced when using 3-nitrobenzyl alcohol as a matrix on the four-sector instrument with the cesium ion gun. Although the signal is desirably long-lasting with this matrix, the limit of analysis for angiotensin III on the four-sector instrument was only 200 pmol vs 15 pmol when thioglycerol was used as the matrix. Matrix interference in tandem MS has been studied by Falick et al. (*77*). With recent progress in the coupling of liquid chromatographs with FABMS, the problem of matrix interference may be reduced.

CONCLUSIONS

The comparative study reported here has sought to provide an objective assessment of the relative merits of a four-sector

mass spectrometer (with high-energy CAD) and a hybrid instrument (with low-energy CAD) for the structural characterization of peptides. The study has focused specifically on the use of product-ion scanning; other scanning modes in tandem MS such as selected reaction monitoring, constant neutral loss, and precursor-ion analyses have not been considered (for examples of the uses of these scanning modes on the hybrid mass spectrometer see refs 47 and 78). These scan modes are either difficult or impossible to implement on the tandem magnetic instrument, being hampered by electronic or software complexity.

It is clear for the examples in this study that extensive structural information can be obtained from both instruments for peptides up to 1000 Da in mass. The four-sector mass spectrometer can probably produce good data from the great majority of peptides in this range, while the hybrid instrument is more sensitive to composition (especially terminal arginines) and mass (the best data being produced for smaller peptides). Above 1000 Da, sequence data obtained by using low-energy CAD on the hybrid instrument was of poorer quality (though of some use for substantiating proposed or known sequences), whereas complete sequence information was obtained for a peptide of M_r 2464.2 by using the four-sector instrument. It has been shown previously that useful, albeit incomplete, structural information for peptides up to ca. M_r 4000 could be obtained on this four-sector mass spectrometer (*52*). The evident advantage of high-energy CAD at higher mass is consistent with previous reports (*49*, *50*). Nevertheless, the low-energy CAD spectrum for the tryptic-like tetradecapeptide (M_r 1497.8) is quite informative, and it is obvious that, with careful attention to the optimization of conditions, the mass range for tandem mass spectrometry on the hybrid instruments may be higher than previously reported (*45*, *49*, *50*). Similar limits of analyses were observed on the two tandem instruments for peptides with masses up to approximately 1000 Da, but superior sensitivity was obtained for larger peptides by using the four-sector instrument. Implementation of more advanced detection methods such as array detectors has already been shown to greatly improve signal-to-noise ratios obtainable on the four-sector instruments (*70*, *75*, *79*). In this regard, if the 2 orders of magnitude improved sensitivity reported previously for substance P with an array detector (*70*) translates into 2 orders of magnitude lower limits of analysis, then excellent CAD spectra at an impressive 150-fmol level may be feasible, although this has yet to be demonstrated. Such detectors cannot be implemented on hybrid or triple quadrupole mass spectrometers. With regard to the relative utility of the two instruments for protein-sequencing applications, it is rewarding to compare the data obtained from the tryptic-like tetradecapeptide. The high-energy collision spectrum is more easily interpreted and required only one-sixth the sample needed on the hybrid instrument.

Notable differences of fragmentation paths were observed under the two collisional activation regimes. Internal fragments were generally more prominent in the low-energy CAD spectra, in keeping with the findings of Alexander et al. (*50*). These internal fragments yielded good sequence information in at least one instance. Charge localization on the N-terminus results in a- and d-series fragments in the high-energy regime but a- and b-series fragments for low-energy collisions. Similar tendency toward side-chain cleavages (v and w series) can be observed in high-energy CAD data for peptides with charge localization on the C-terminus (*3*). Such cleavages are not only useful for confirmation of amino acid residues but are essential for distinguishing isobaric amino acid residues such as Leu/Ile (*62*, *63*) or α-/β-Asp (*80*). This type of distinction is not possible under the low-energy collision regimes used for the present analyses. Side-chain fragmentations of the w type have, however, been observed at low abundance by using a hybrid instrument with collision energies in excess of 200 eV (*13*). High-energy collisions also produce compositional information more reliably in terms of single amino acid immonium ions or side-chain losses from the $(M + H)^+$ (*13*).

Finally, it is also apparent that the high-energy CAD spectra of peptides are more reproducible than those acquired under low-energy CAD. Comparison of the previously published high-energy CAD spectra for substance P on instruments of different configurations (BEEB or EBEB) from three different manufacturers (*31*, *45*, *49*, *68–72*) reveals that these are very similar both in terms of the observed ions and their relative abundances. Therefore, spectral library searches on high-energy CAD data should in theory be relatively simple. More importantly, algorithms for computer interpretation of the data have already been developed (*81–84*). In a limited study, Alexander et al. demonstrated superior success of computer interpretation of high-energy compared to low-energy CAD data for peptides with $M_r > 900$ (*50*). It should be noted that the substance P spectrum obtained under the optimized instrument conditions presented here shows substantially different relative abundances compared with one obtained previously on the hybrid instrument (*49*). However, it is remarkably similar to one recently obtained on a triple quadrupole (*73*). Obtaining the same reproducibility under low-energy CAD regimes is inherently more complex because the product-ion spectra vary more with collision energy and target gas pressure.

ACKNOWLEDGMENT

M. Bean and S. Carr gratefully acknowledge the excellent technical assistance of Richard Vickers of VG Analytical Ltd. during early stages of this study. The work at Baylor benefitted from the technical assistance of Ralph Orkiszewski. A preprint of a submitted paper describing an analogous comparison of high- and low-energy collisions of peptides on hybrid and four-sector instruments was kindly furnished by R. K. Boyd and K. L. Rinehart (*50*).

LITERATURE CITED

(1) Hunt, D. F.; Yates, J. R., III; Shabanowitz, J.; Winston, S.; Hauer, C. R.; *Proc. Natl. Acad. Sci. U.S.A.* **1986**, *83*, 6233–6237.
(2) Biemann, K.; Martin, S. A. *Mass Spectrom. Rev.* **1987**, *6*, 1–76.
(3) Biemann, K. *Biomed. Environ. Mass Spectrom.* **1988**, *16*, 99–111.
(4) Carr, S. A.; Hemling, M. E.; Roberts, G. D. In *Macromolecular Sequencing and Synthesis; Selected Methods and Applications*; Schlesinger, D. H., Ed.; Alan R. Liss: New York, 1988; pp 83–99.
(5) Hass, J. R.; Green, B. N.; Bateman, R. H.; Bott, P. A. 32nd Annual Conference on Mass Spectrometry and Allied Topics, San Antonio TX, May 27–June 1, 1984; pp 380–381.
(6) Boyd, R. K.; Bott, P. A.; Harvan, D. J.; Hass, J. R. *Int. J. Mass Spectrom. Ion Proc.* **1986**, *69*, 251–263.
(7) Sato, K.; Asada, T.; Ishihara, M.; Kunihiro, F.; Kammei, Y.; Kubota, E.; Costello, C. E.; Martin, S. A.; Scoble, H. A.; Biemann, K. *Anal. Chem.* **1987**, *59*, 1652–1659.
(8) Yost, R. A.; Enke, C. G. *J. Am. Chem. Soc.* **1978**, *100*, 2274–2275.
(9) Bateman, R. H.; Green, B. N.; Smith, D. C. 30th Annual Conference on Mass Spectrometry and Allied Topics, Honolulu, HI, June 6–11, 1982; pp 516–517.
(10) Schoen, A. E.; Amy, J. W.; Ciupek, J. D.; Cooks, R. G.; Dobberstein, P.; Jung, G. *Int. J. Mass. Spectrom. Ion Proc.* **1985**, *65*, 125–140.
(11) Gaskell, S. J. In *Mass Spectrometry in Biomedical Research*; Gaskell, S. J., Ed.; Wiley: New York, 1986; pp 137–147.
(12) Boyd, R. K.; Harvan, D. J.; Hass, J. R. *Int. J. Mass Spectrom. Ion Proc.* **1985**, *65*, 273–286.
(13) Alexander, A. J.; Thibault, P.; Boyd, R. K. *Rapid Commun. Mass Spectrom.* **1989**, *3*, 30–34.
(14) Alexander, A. J.; Boyd, R. K. *Int. J. Mass Spectrom. Ion Proc.* **1989**, *90*, 211–240.
(15) Neumann, G. M.; Sheil, M. M.; Derrick, P. J. *Z. Naturforsch.* **1984**, *39A*, 584–592.
(16) Gilbert, R. G.; Sheil, M. M.; Derrick, P. J. *Org. Mass Spectrom.* **1985**, *20*, 430–431.
(17) Rumpf, B. A.; Allison, C. E.; Derrick, P. J. *Org. Mass Spectrom.* **1986**, *21*, 295–303.
(18) Sheil, M. M.; Derrick, P. J. *Org. Mass Spectrom.* **1988**, *23*, 429–435.
(19) Dawson, P. H.; Douglas, D. J. In *Tandem Mass Spectrometry*; McLafferty, F. W., Ed.; Wiley: New York, 1983; pp 125–148.
(20) Todd, P. J.; McLafferty, F. W. In *Tandem Mass Spectrometry*; McLafferty, F. W., Ed.; Wiley: New York, 1983; pp 149–174.

(21) Crabb, J. W.; Armes, L. G.; Carr, S. A.; Johnson, C. M.; Roberts, G. D.; Bordoli, R. S.; McKeehan, W. L. *Biochemistry* **1986**, *25*, 4988–4993.
(22) Johnson, R. S.; Biemann, K. *Biochemistry* **1987**, *26*, 1209–1214.
(23) Biemann, K.; Scoble, H. A. *Science* **1987**, *237*, 992–998.
(24) Mathews, W. R.; Johnson, R. S.; Cornwell, K. L.; Johnson, T. C.; Buchanan, B. B.; Biemann, K. *J. Biol. Chem.* **1987**, *262*, 7537–7545.
(25) Johnson, T. C.; Yee, B. C.; Carlson, D. E.; Buchanan, B. B.; Johnson, R. S.; Mathews, W. R.; Biemann, K. *J. Bacteriol.* **1988**, *170*, 2406–2408.
(26) Johnson, R. S.; Mathews, W. R.; Biemann, K.; Hopper, S. *J. Biol. Chem.* **1988**, *263*, 9589–9597.
(27) Gibson, B. W.; Yu, Z.; Aberth, W.; Burlingame, A. L.; Bass, N. M. *J. Biol. Chem.* **1988**, *263*, 4182–4185.
(28) Anderegg, R. J.; Carr, S. A.; Huang, I. Y.; Hiipakka, R. A.; Chang, C.; Liao, S. *Biochemistry* **1988**, *27*, 4214–4221.
(29) DeWolf, W. E., Jr.; Carr, S. A.; Varrichio, A.; Goodhart, P. J.; Mentzer, M. A.; Roberts, G. D.; Southan, C.; Dolle, R. E.; Kruse, L. I. *Biochemistry* **1988**, *27*, 9093–9101.
(30) Anderegg, R. J.; Betz, R.; Carr, S. A.; Crabb, J. W.; Duntze, W. *J. Biol. Chem.* **1988**, *263*, 18236–18240.
(31) Johnson, R. S.; Martin, S. A.; Biemann, K. *Int. J. Mass Spectrom. Ion Proc.* **1988**, *86*, 137–154.
(32) Carr, S. A.; Roberts, G. D.; Hemling, M. E. In *Mass Spectrometry of Biological Materials*; McEwen, C. N., Larsen, B. S., Eds.; Marcel Dekker, Inc.: New York, 1990; pp 87–136.
(33) Crabb, J. W.; Johnson, C. M.; Carr, S. A.; Armes, L. G.; Saari, J. C. *J. Biol. Chem.* **1988**, *263*, 18678–18687.
(34) Houtz, R. L.; Stults, J. T.; Mulligan, R. M.; Tolbert, N. E. *Proc. Nat. Acad. Sci. U.S.A.* **1989**, *86*, 1855–1859.
(35) Hassell, A. M.; Johanson, K. O.; Goodhart, P.; Young, P. R.; Holskin, B. P.; Carr, S. A.; Roberts, G. D.; Simon, P. L.; Chen, M.-J.; Lewis, M. *J. Biol. Chem.* **1989**, *264*, 4948–4952.
(36) Carr, S. A. *Adv. Drug Delivery Rev.* **1990**, *4*, 113–147.
(37) Steffens, J. C.; Hunt, D. F.; Williams, B. G. *J. Biol. Chem.* **1986**, *261*, 13879–13882.
(38) LeVine, H., III; Hunt, D. F.; Zhu, N.-Z.; Shabanowitz, J. *Biochem. Biophys. Res. Commun.* **1987**, *148*, 1104–1109.
(39) Hunt, D. F.; Yates, J. R., III; Shabanowitz, J.; Zhu, N.-Z.; Zirino, T.; Averill, B. A.; Daurat-Larroque, S. T.; Shewale, J. G.; Roberts, R. M.; Brew, K. *Biochem. Biophys. Res. Commun.* **1987**, *144*, 1154–1160.
(40) Michel, H.; Hunt, D. F.; Shabanowitz, J.; Bennett, J. *J. Biol. Chem.* **1988**, *263*, 1123–1130.
(41) Krishnamurthy, T.; Szafraniec, L.; Hunt, D. F.; Shabanowitz, J.; Yates, J. R., III; Hauer, C. R.; Carmichael, W. W.; Skulberg, O.; Codd, G. A.; Missler, S. *Proc. Natl. Acad. Sci. U.S.A.* **1989**, *86*, 770–774.
(42) Hunt, D. H.; Yates, J. R., III; Shabanowitz, J.; Bruns, M. E.; Bruns, D. E. *J. Biol. Chem.* **1989**, *264*, 6580–6586.
(43) Gaskell, S. J.; Reilly, M. H.; Porter, C. J. *Rapid Commun. Mass Spectrom.* **1988**, *2*, 142–145.
(44) Schaffer, M. H.; Noyes, B. E.; Slaughter, C. A.; Thorne, G. C.; Gaskell, S. J. *Biochem. J.* **1990**, *269*, 315–320.
(45) Poulter, L.; Taylor, L. C. E. *Int. J. Mass Spectrom. Ion Proc.* **1989**, *91*, 183–197.
(46) Gaskell, S. J.; Reilly, M. H. *Rapid Commun. Mass Spectrom.* **1988**, *2*, 188–191.
(47) Thorne, G. C.; Gaskell, S. J. *Rapid Commun. Mass Spectrom.* **1989**, *3*, 217–221.
(48) Baeten, W.; Claereboudt, J.; Van den Heuvel, N.; Claeys, M. *Biomed. Environ. Mass Spectrom.* **1989**, *18*, 727–732.
(49) Gaskell, S. J.; Reilly, M. H.; Carr, S. A.; Bean, M.; Vickers, R. Proceedings of the 36th ASMS Conference on Mass Spectrometry and Allied Topics, San Francisco, CA, June 5–10, 1988; pp 111–112.
(50) Alexander, A. J.; Thibault, P.; Boyd, R. K.; Curtis, J. M.; Rinehart, K. L. *Int. J. Mass. Spectrom. Ion Proc.* **1990**, *98*, 107–134.
(51) Barber, M.; Green, B. N. *Rapid Commun. Mass Spectrom.* **1987**, *1*, 80–83.
(52) Carr, S.; Green, B. N.; Hemling, M. E.; Roberts, G. D.; Anderegg, R. J.; Vickers, R. 35th ASMS Conference on Mass Spectrometry and Allied Topics, Denver, CO, May 24–29, 1987; pp 830–831.
(53) Alexander, A. J.; Dyer, E. W.; Boyd, R. K. *Rapid Commun. Mass Spectrom.* **1989**, *3*, 364–372.
(54) Roepstorff, P.; Fohlman, J. *Biomed. Mass Spectrom.* **1984**, *11*, 601.
(55) Jankowski, K.; Gaudin, D.; Virelizier, H.; Rolando, C.; Tabet, J.-C.; Pare, J. R. J. *Spectrosc. Int. J.* **1985**, *4*, 231.
(56) Grese, R. P.; Cerny, R. L.; Gross, M. L. *J. Am. Chem. Soc.* **1989**, *111*, 2835–2842.
(57) Neumann, G. M.; Derrick, P. J. *Org. Mass. Spectrom.* **1988**, *19*, 165.
(58) Taylor, L. C. E.; Hazelby, D.; Wakefield, C. *Int. J. Mass Spectrom. Ion Phys.* **1983**, *46*, 407–410.
(59) Cerny, R. L.; Gross, M. L. 35th ASMS Conference on Mass Spectrometry and Allied Topics, Denver, CO, May 24–29, 1987; pp 82–83.
(60) Guenat, C.; Dino, J., Jr.; Tomer, K. B. 35th ASMS Conference on Mass Spectrometry and Allied Topics, Denver, CO, May 24–29, 1987; pp 554–555.
(61) Stults, J. T.; Watson, J. T. *Biomed. Environ. Mass Spectrom.* **1987**, *14*, 583–586.
(62) Johnson, R. S.; Martin, S. A.; Biemann, K.; Stults, J. T.; Watson, J. T. *Anal. Chem.* **1987**, *59*, 2621–2625.
(63) Gaskell, S. J.; Haroldsen, P. E.; Reilly, M. H. *Biomed. Environ. Mass Spectrom.* **1988**, *16*, 31–33.
(64) Martin, S. A.; Johnson, R. S.; Costello, C. E.; Biemann, K. In *Analysis of Peptides and Proteins*; McNeal, C. J., Ed.; Wiley: Chichester, England, 1988; pp 135–150.
(65) Thorne, G. C.; Ballard, K. D.; Gaskell, S. J. *J. Am. Soc. Mass Spectrom.* **1990**, *1*, 249–257.
(66) Renner, D.; Spiteller, G. *Biomed. Environ. Mass Spectrom.* **1988**, *15*, 75–77.
(67) Tang, X.; Ens, W.; Standing, K. G.; Westmore, J. B. *Anal. Chem.* **1988**, *60*, 1791–1799.
(68) Scoble, H. A.; Martin, S. A.; Biemann, K. *Biochem. J.* **1987**, *245*, 621–622.
(69) Martin, S. A.; Biemann, K. *Int. J. Mass Spectrom. Ion. Proc.* **1987**, *78*, 213–228.
(70) Hill, J. A.; Martin, S. A.; Biller, J. E.; Biemann, K. *Biomed. Environ. Mass Spectrom.* **1988**, *17*, 147–151.
(71) Burlingame, A. L. Proceedings of the 36th ASMS Conference on Mass Spectrometry and Allied Topics, San Francisco, CA, June 5–10, 1988; pp 727–728.
(72) Aschcroft, A. E.; Buchanan, R. A. C.; Elliott, G. J.; Evans, S.; Milton, D. J.; Wright, B.; Walls, F. C. Proceedings of the 36th ASMS Conference on Mass Spectrometry and Allied Topics, San Francisco, CA, June 5–10, 1988; pp 1156–1157.
(73) McCormack, A. L.; Hunt, D. F.; Shabanowitz, J.; Zhu, N.-Z.; Griffin, P. R. Proceedings of the 37th ASMS Conference on Mass Spectrometry and Allied Topics, Miami Beach, FL, May 21–26, 1989; pp 899–900.
(74) Hunt, D. H.; Shabanowitz, J.; Yates, J. R.; Griffin, P. R.; Zhu, N. Z. In *Mass Spectrometry of Biological Materials*; McEwen, C. N., Larsen, B. S., Eds.; Marcel Dekker, Inc.: New York, 1990; pp 169–195.
(75) Hill, J. A.; Biller, J. E.; Martin, S. A.; Biemann, K.; Yoshidome, K.; Sato, K. *Int. J. Mass Spectrom. Ion Proc.* **1989**, *92*, 211–230.
(76) Carr, S. A.; Vickers, R.; Roberts, G. D. Unpublished results.
(77) Falick, A. M.; Medzihradsky, K. F.; Walls, F. C. *Rapid Commun. Mass Spectrom.* **1990**, *4*, 318–322.
(78) Gaskell, S. J.; Reilly, M. H. *Rapid Commun. Mass Spectrom.* **1988**, *2*, 139–142.
(79) Cottrell, J. S.; Evans, S. *Anal. Chem.* **1987**, *59*, 1990–1995.
(80) Carr, S. A.; Bean, M. F.; Hemling, M. E.; Roberts, G. D. In *Biological Mass Spectrometry*; Burlingame, A. L., Ed.; Elsevier: Amsterdam, The Netherlands, 1990.
(81) Hamm, C. W.; Wilson, W. E.; Harvan, D. J.; *Comput. Appl. Biosci.* **1986**, *2*, 115–122.
(82) Scoble, H. A.; Biller, J. E.; Biemann, K. *Fresenius' Z. Anal. Chem.* **1987**, *327*, 239–245.
(83) Johnson, R. S.; Biemann, K. Biomed. *Environ. Mass Spectrom.* **1989**, *18*, 945–957.
(84) Zidarov, D.; Thibault, P.; Evans, M. J.; Bertrand, M. *Biomed. Environ. Mass Spectrom.* **1990**, *19*, 13–26.

RECEIVED for review January 15, 1991. Accepted April 18, 1991. The VG ZAB SEQ hybrid mass spectrometer at Baylor College of Medicine was purchased by the Howard Hughes Medical Institute. Work at Baylor was supported by the National Institutes of Health (GM 34120 and AI 29916) and by a generous gift from the Burroughs Wellcome Company.

Quaternized Nylon as a Support for Plasma Desorption Mass Spectrometry: Adsorption Mechanisms and Analytical Applications

M. P. Lacey and Thomas Keough*

The Procter & Gamble Company, Miami Valley Laboratories, P.O. Box 398707, Cincinnati, Ohio 45239-8707

A novel quaternized Nylon surface has been prepared to aid the study of analyte adsorption and desorption to and from the solid supports used in plasma desorption mass spectrometry. At low ionic surfactant coverage onto an oppositely charged surface, binding occurs by an ion-exchange mechanism that is largely independent of alkyl chain length. At higher surface coverage, the longer chain homologues are preferentially adsorbed due to hydrophobic forces. The nature of the adsorption interaction can be varied in PDMS, simply by changing the sign of the charge on the solid support. This capability has important analytical implications that will be discussed. The quaternized Nylon surface has not proven to be useful for the characterization of peptides or proteins. However, for negative-ion studies with various other classes of compounds, it provides 10–100 times higher sensitivity than obtained from nitrocellulose surfaces. Finally, an affinity separation of ionic surfactants containing hydrophobic alkyl chains, from a mixture also containing hydrophilic nonionic surfactants, is also demonstrated.

INTRODUCTION

Sample preparation plays a critical role in plasma desorption mass spectrometry (PDMS). Initially, thin films of nonvolatile analytes were prepared by an electrospray technique (*1*). Subsequently, Macfarlane and co-workers (*2*) proposed the idea of selectively binding an analyte from solution onto a thin solid support suitable for PDMS analysis. This idea was demonstrated by binding polarizable cations from aqueous solution onto a cation-exchange surface (*2*). In the ensuing search for improved substrates for PDMS applications, several other supports were developed including polyethylene terephthalate (Mylar) and polypropylene (*3*), Mylar impregnated with hydrophobic cationic surfactants (*4, 5*), nitrocellulose (*6, 7*), silicon (*8*), Nylon, octadecane and polybrene (*9*), and anthroic acid (*10*). Alternatively, mixing analytes with suitable small-molecule matrices such as glutathione (*11*) and sucrose octaacetate (*12*) have also been demonstrated to be useful PDMS sample preparation approaches. Several reviews of PDMS sample preparation techniques have been published recently (*5, 7, 13*).

Nitrocellulose, electrosprayed over aluminized Mylar, is currently the support of choice for the characterization of peptides, proteins and other polar biological molecules (*6, 7*). This surface, which is negatively charged when exposed to aqueous media, offers several benefits relative to the initial PDMS sample preparation techniques. They include simple sample preparation, easy removal of alkali-metal salts that hinder the desorption process, sensitivity enhancement of 2 orders of magnitude, and improved peak shape, which increases the practical mass resolution achieved in the PDMS experiment.

We sought to develop a complementary positively charged surface possessing some of the analytical attributes of the negatively charged nitrocellulose surface. We prepared a positively charged surface by electrospraying Nytran, quaternized Nylon-66, onto aluminized Mylar. We then studied the binding of cationic and anionic surfactants, from aqueous solution, to both Nytran and nitrocellulose. The mechanism of surfactant binding onto oppositely charged surfaces is dependent upon bulk solution concentration. Binding occurs by ion exchange (*14–16*), a process that is largely independent of alkyl chain length, below about 10^{-4} M. Adsorption driven by hydrophobic interactions (*14–16*), a chain length dependent process, becomes important with bulk concentrations above ca. 10^{-4} M. Of course, surfactant ion exchange does not occur with surfaces of like charge.

Nytran has not proven analytically useful for the characterization of peptides and proteins by PDMS. However, it appears to be more generally useful for negative-ion PDMS studies than nitrocellulose. Negative-ion response for various compound classes such as anionic surfactants, triglycerides, phospholipids, and cholesterol esters is enhanced 10- to 100-fold from Nytran, relative to the response observed from nitrocellulose. This is particularly useful for the characterization of "real" samples, such as isolates from biological matrices, where the complementary information from positive- and negative-ion spectra is often needed for analyte identification. Furthermore, we have demonstrated that Nytran is useful as an affinity surface, to selectively bind both cationic and anionic surfactants containing hydrophobic alkyl chains from detergent formulations also containing hydrophilic nonionic surfactants (neodols).

EXPERIMENTAL SECTION

Reagents. The analytes were obtained from various commercial sources and were used without additional purification. The homologous series of alkyltrimethylammonium chlorides had stated purities >95%. However, these materials, which were not specifically dried, probably contain variable amounts of water since they are hygroscopic.

Instrumentation. All mass spectra were obtained on a Bio-Ion 20 (Applied Biosystems Sweden AB, Uppsala, Sweden) PD mass spectrometer that has been previously described (*17–19*). Mass calibration was accomplished by using H^+ and Na^+ as reference ions.

Surface Preparation. A portion of a Nytran membrane (0.45-μm pore size, Schleicher & Schuell, Inc., Keene, NH) was dissolved in concentrated, reagent grade formic acid (88%, J. T. Baker Chemical Co., Phillipsburg, NJ) overnight at ambient temperature. The insoluble portion of the membrane was discarded and the formic acid solution concentrated to dryness. The residue was reconstituted in formic acid at a concentration of 10–12 mg/mL prior to electrospraying onto aluminized Mylar sample foils (Applied Biosystems Sweden AB, Uppsala, Sweden). The resulting Nytran foils were considerably less uniform in appearance than commercial (Applied Biosystems Sweden AB) electrosprayed nitrocellulose foils, because of the difficulty in electrospraying formic acid. However, the foil surface was readily covered. Typical Al-containing background ions, from the aluminized Mylar surface, were absent from the PD mass spectra of Nytran-covered foils. Furthermore, an infrared reflection absorption spectrum (Digilab SPS 40, Cambridge, MA) of the Nytran-covered foil was virtually identical with one obtained from

0003-2700/91/0363-1482$02.50/0 © 1991 American Chemical Society

Table I. Summary of Positive- and Negative-Ion PD Mass Spectra of CsI Obtained from Nitrocellulose and Nytran Substrates

substrate	measd intens[a] Cs^+	I^-	I^-/Cs^+
nitrocellulose	6130	89	0.02
Nytran	456	1071	2.35

[a] Number of ions detected after integrating for 2 000 000 primary events.

analysis of the original membrane.

Sample Preparation. The Nytran surface charge was verified by positive- and negative-ion PDMS analyses of CsI. Separate nitrocellulose and Nytran foils were loaded with 10-μL portions of a 10^{-2} M solution of aqueous CsI. After 10 min the excess solution was blown off the foil, which was then washed with deionized water prior to analysis. Positive- and negative-ion PD mass spectra were obtained for 2 000 000 primary events with ion-accelerating voltages of ±12 kV.

Ionic binding mechanisms to nitrocellulose and Nytran were investigated by analysis of an approximately equimolar (10^{-6} M) mixture of C_8- to C_{18}-trimethylammonium chlorides (C_8- to C_{18}TMAC's). For these studies, 10 μL of a solution containing about 10 pmol/μL of each surfactant was loaded onto the surfaces and allowed to equilibrate for 10 min. The excess solutions were blown off the foils, which were then washed with deionized water prior to analysis.

We analyzed CsI from a nitrocellulose foil after the surface had been completely covered with C_{18}TMAC. This was done to demonstrate that surface charge reversal occurred after loading C_{18}TMAC. For this experiment we loaded 10 μL of a 10^{-3} M aqueous C_{18}TMAC solution onto nitrocellulose. After equilibration, the excess solution was blown off and the foil was water washed. On top of this modified foil was loaded 10 μL of a 10^{-2} M solution of CsI. Again, after equilibration, the foil was water-washed prior to analysis by positive- and negative-ion PDMS (±12 kV). Spectra were integrated for 2 000 000 primary events.

RESULTS AND DISCUSSION

Verification of Surface Charge. Following Macfarlane and co-workers (*3*), we chose CsI as an analyte to probe the electrostatic component of the adsorption interaction. It is ideal for this purpose, since it is composed of a cation and anion having comparable charges, sizes, and polarizabilities. Therefore, cation and anion binding can be investigated simultaneously with ions having very similar properties (*3*). The positive- and negative-ion PD mass spectra are summarized in Table I. The nitrocellulose-coated foil exhibits a Cs^+ cation that is more than 10 times larger than that observed from the Nytran-covered foil. On the other hand, the I^- signal from the Nytran-covered foil is substantially greater than that observed from the nitrocellulose-coated foil. The measured intensity ratio of I^-/Cs^+ was 0.02 from nitrocellulose and 2.35 from Nytran. Clearly, the Nytran surface contains positively charged binding sites while nitrocellulose contains negatively charged surface sites.

Ionic Surfactant Binding Mechanisms. Binding of ionic surfactants from aqueous solution onto surfaces with strongly charged sites may occur by a variety of mechanisms including ion exchange, ion pairing, hydrogen bonding, and hydrophobic adsorption (*14*, *15*). At low bulk concentration of surfactant, binding is thought to occur mainly by exchanging surfactant ions for the counterions orginally associated with the surface. A dramatic increase in surfactant binding is observed at higher bulk concentrations, as a result of hydrophobic interactions. After complete surface coverage has been achieved, the original charge on the surface may actually be reversed. This results because the surfactant molecules, adsorbed by hydrophobic interactions involving their alkyl chains, have their charged head groups pointed up from the surface toward the aqueous medium.

At low bulk concentrations, surfactant binding to an oppositely charged surface occurs by an ion-exchange mechanism. In this regime, the number of moles of surfactant adsorbed per unit area will be largely controlled by the number of surface binding sites and the size of the hydrophilic group and will be independent of alkyl chain length. In the specific case of alkanesulfonates adsorbed onto alumina (pH = 7.2), for example, the adsorption of nonassociated sulfonate ions results in an isotherm characterized by a single straight line that is independent of alkyl chain length (*16*). Similarly, the PD mass spectrum obtained from analysis of an approximately equimolar mixture of C_8- to C_{18}TMAC's, loaded onto a negatively charged nitrocellulose surface, shows comparable response for each homologue (Figure 1a). This spectrum is completely consistent with our expectations based on analyte binding through an ion-exchange mechanism. When this same mixture is loaded onto the Nytran surface, surfactant binding by ion exchange is eliminated because the surfactant head group and the surface binding sites are both positively charged. Adsorption might still occur, but by hydrophobic interactions. Under these circumstances, the surface concentration of the surfactant should be strongly dependent upon alkyl chain length because of the increased change in free energy associated with removal of the longer chains from solution, and because of the increased van der Waals attraction with increasing chain length (*14*, *15*). Furthermore, the hydrophobic binding energy of short-chain homologues may not be large enough to offset the electrostatic repulsion between the head groups of the analyte and the surface. Results obtained from analysis of the equimolar alkyl–TMAC mixture, conducted on the Nytran surface, are given in Figure 1b. Considerable discrimination against the short-chain homologues is evident. Only C_{16}- and C_{18}TMAC's are observed above background.

At higher bulk concentrations, we expect increased surfactant adsorption to the solid surface. Furthermore, the longer chain homologues should be preferentially adsorbed (*14–16*). The results of the PDMS analyses of several equimolar mixtures of C_{12}- and C_{16}TMAC, adsorbed onto nitrocellulose, are summarized in Figure 2. The observed ratios of molecular cations are reasonably constant and approximately unity at bulk concentrations below 10^{-4} M. At higher bulk concentration the observed response for the C_{16} homologue increases dramatically relative to that of the C_{12} homologue. The large increase in the slope of the curve marks the end of the ion-exchange regime and the onset of surfactant adsorption by hydrophobic binding. The same trends were observed from the analyses of several equimolar mixtures of C_9- and C_{14}-alkylbenzene sulfonates adsorbed onto positively charged Nytran.

After complete coverage of the surface, we expect the original surface charge to be reversed to that of the polar head group of the adsorbed surfactant. After coverage with a cationic surfactant, the surface charge of nitrocellulose should be reversed from negative to positive. Under these conditions, we expect greatly enhanced adsorption of I^- relative to Cs^+ in the analysis of CsI. Indeed, the measured ratio of I^-/Cs^+ increased to 0.42, which is more than 20 times larger than the I^-/Cs^+ ratio obtained when CsI was analyzed from an untreated nitrocellulose foil (see Table I).

Analytical Implications of the Surfactant Adsorption Mechanisms. Both the static-FABMS and PDMS methods detect molecules that have been adsorbed to surfaces (Figure 3). In the case of FAB, analytes adsorbed to the surface of a liquid are sampled. In PDMS, analytes that have been adsorbed to a solid surface are subsequently sampled. Analyte surface activity differences, which are strongly dependent upon

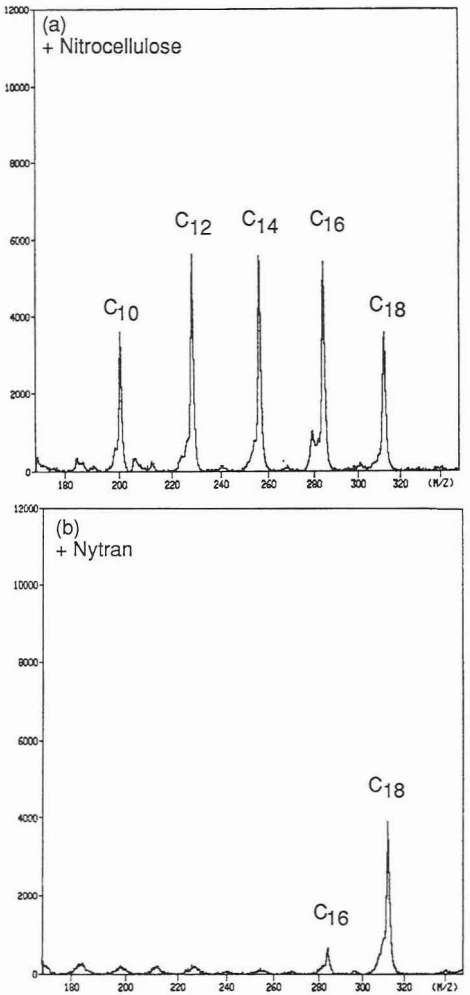

Figure 1. Positive-ion PD mass spectra of an approximately equimolar mixture of alkyl–TMACs bound to (a) nitrocellulose and (b) Nytran surfaces. The *x* axis corresponds to mass/charge ratio, while the *y* axis corresponds to intensity.

alkyl chain lengths for a series of homologous surfactants, often exhibit prominent effects on relative response in static-FABMS (*20–22*). From a practical standpoint, this leads to the selective detection of the more surface-active components in mixtures and precludes the use of homologues as internal standards for quantitative FABMS applications (*23*). Quantitative applications of static-FAB typically require the availability of stable isotopic internal standards. Furthermore, it may be difficult to obtain accurate quantitative surfactant homologue distributions by static-FABMS unless several stable isotopic internal standards, chosen to bracket the distribution, are used for calibration (*24*).

The relative insensitivity of PDMS response to alkyl chain length, at least at bulk concentrations within the ion-exchange regime, suggests that PDMS might provide semiquantitative

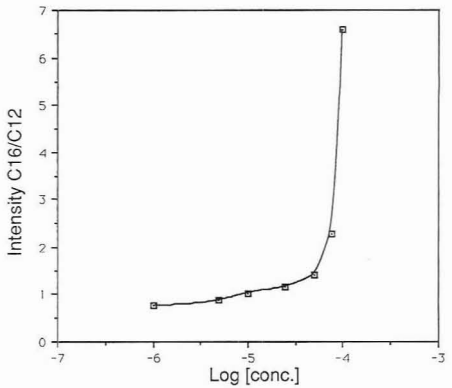

Figure 2. Observed PD mass spectral intensity ratio from equimolar mixtures of C_{16}TMAC and C_{12}TMAC, as a function of bulk solution concentration.

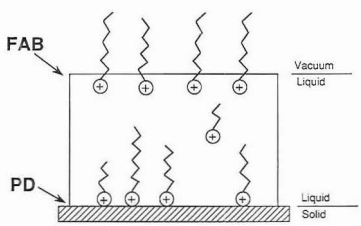

Figure 3. Schematic illustrating the different surfaces that are sampled in static-FABMS and PDMS.

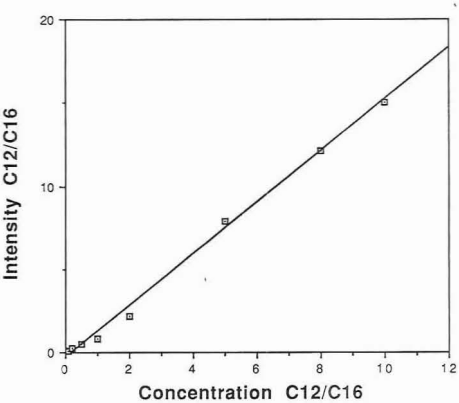

Figure 4. Observed PD mass spectral intensity ratio of C_{12}TMAC/C_{16}TMAC as a function of the bulk solution concentration ratio of these cationic surfactants.

homologue distributions without the use of internal standards and that homologues might generally serve as calibration standards for quantitative PDMS studies. The feasibility of quantitative PDMS using a chemical internal standard has already been demonstrated. Jungclas and co-workers (*12*) have quantitated the cytotoxic drug etoposide from the serum of cancer patients using teniposide as a internal standard. In the present study, the calibration curve shown in Figure 4 was constructed by using C_{16}TMAC as an internal standard for

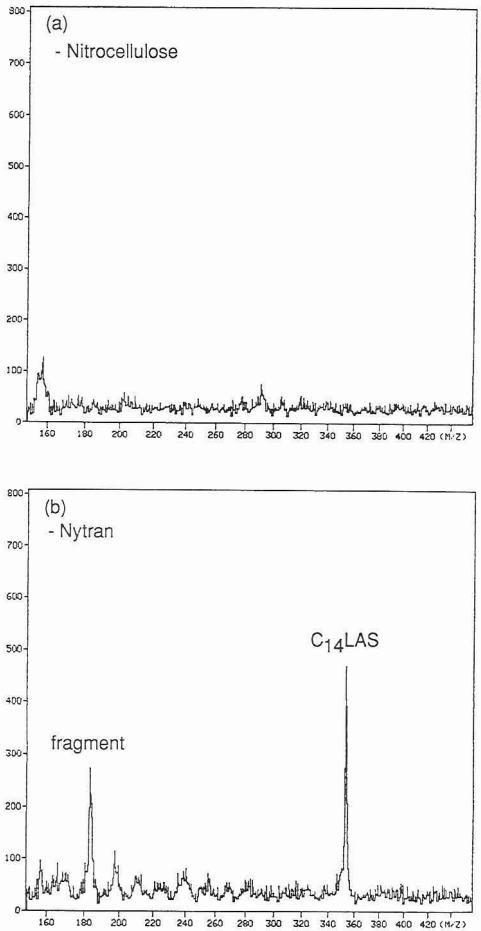

Figure 5. Negative-ion PD mass spectra of 50 pmols of LAS bound to (a) nitrocellulose and (b) Nytran surfaces. The *x* axis corresponds to mass/charge ratio, while the *y* axis corresponds to intensity.

C_{12}TMAC. Linear response was observed for 2 orders of magnitude variation in concentration of C_{12}TMAC.

Comparison of Nytran and Nitrocellulose for Selected Analytical Applications. Negative-Ion Mass Spectra. The Nytran surface is completely ineffective for the PDMS characterization of peptides and small proteins such as synthetic pentapeptides, insulin, and lysozyme. Positive-ion PD mass spectra can be routinely obtained on 10 pmol of insulin from the nitrocellulose surface. However, no response was observed from 100 pmol of insulin loaded onto a Nytran foil. Positively charged Nylon membranes have a higher protein-binding capacity than nitrocellulose (*25*), so the peptides and proteins may simply bind so tightly that subsequent desorption of the intact molecular ions is highly unfavorable.

The negative-ion PD mass spectra obtained after loading 50 pmols of sodium tetradecylbenzenesulfonate (C_{14}LAS) onto nitrocellulose and Nytran are compared in Figure 5. The spectrum obtained from nitrocellulose (Figure 5a) shows no response for the molecular anion at m/z 353. The corresponding spectrum obtained from the Nytran foil (Figure 5b) shows an abundant molecular anion as well as an expected fragment ion at m/z 183. Molecular anions of LAS have been readily detected to the 1.5-pmol level (signal to noise ratio >5) from the Nytran surface. Incidentally, aluminized Mylar is another surface that offers improved negative-ion sensitivity relative to nitrocellulose. Unfortunately, its background spectrum, which is dominated by Al_2O_3 cluster ions below m/z 1000, is so intense that it strongly interferes with analyses of low levels of analytes in this molecular weight range. Ion-pairing C_{14}LAS with hydrophobic counterions such as tetrabutylammonium cations enhances its negative-ion PDMS response off the nitrocellulose surface, an effect similar to that previously noted in static FABMS (*21*). Ion-pairing has no effect on the LAS response when the analysis was conducted from the Nytran surface.

Phospholipids are an important class of nonvolatile and thermally labile molecules that are amenable to other desorption mass spectrometry techniques such as field desorption (*26*) and static-FABMS (*27, 28*). This class of compounds can also be readily analyzed by PDMS and we have obtained both positive- and negative-ion spectra from 100 pmol of phosphatidylcholine loaded onto both nitrocellulose and Nytran (data not shown). The positive-ion spectra are virtually identical for the two surfaces, both showing comparably abundant MH^+ ions at m/z 790. However, the negative-ion spectra were quite different. The spectrum obtained from the nitrocellulose surface showed no signals above background in the m/z 200–1000 range. The spectrum from the Nytran surface showed, in addition to a weak $(M - CH_3)^-$ molecular anion, a prominent $C_{17}H_{35}CO_2^-$ fragment ion that defines the fatty acid composition of the molecule. The negative-ion data are essential for defining the fatty acid composition of phospholipids, and in the case of static-FABMS, negative-ion detection is considered to be the method of choice for structural characterization (*27*).

The negative-ion sensitivity enhancements observed when ionic compounds are analyzed off Nytran, rather than nitrocellulose, are also observed for nonpolar, nonionic species such as triglycerides and sterol esters. The negative-ion PD mass spectrum obtained from 100 pmol of 1,2-dipalmitoyl-3-myristoylglycerol, evaporated from benzene/hexane (30/70) onto Nytran, showed relatively strong signals for both $C_{13}H_{27}CO_2^-$ and $C_{15}H_{31}CO_2^-$. The corresponding spectrum from the nitrocellulose surface showed no response for the expected RCO_2^- fragment ions and provided no direct confirmation of the fatty acid composition of the analyte. Similar results were obtained from sterol esters. The positive- and negative-ion spectra obtained after 5 nmol of cholesterol palmitate, loaded onto nitrocellulose and Nytran foils, are given in Figure 6. The positive-ion spectrum from nitrocellulose exhibits a weak MH^+ molecular ion and is dominated by the $(\text{cholesterol} - OH)^+$ fragment ion, which confirms the sterol part of the molecule. Confirmation of the fatty acid is not obtained from the negative-ion spectrum. The positive-ion spectrum obtained from the Nytran surface is similar to that obtained from nitrocellulose. However, the negative-ion spectrum exhibits an intense $C_{15}H_{31}CO_2^-$ fragment ion, confirming the identity of the fatty acid.

The need for complementary positive- and negative-ion mass spectra becomes particularly apparent in the analyses of samples isolated from biological matrices. During the course of this work, we analyzed a series of HPLC isolates from the sterol ester fraction obtained from hamster feces. The positive-ion mass spectra were dominated by $(\text{sterol} - OH)^+$ ions. However, molecular weight confirmation was sometimes difficult because the HPLC isolates were often not single compounds and the spectra exhibited a number of potential molecular ions in the 500–800 range. The corresponding negative-ion spectra, obtained from the Nytran surface, ov-

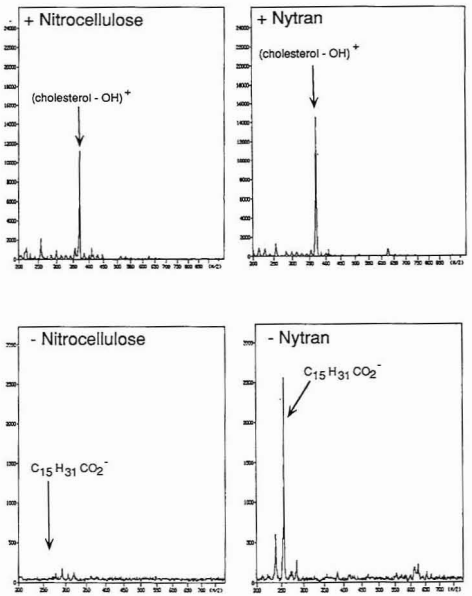

Figure 6. Positive (+) and negative (–) ion PD mass spectra of 5 nmols of cholesterol palmitate from nitrocellulose and Nytran surfaces. The *x* axis corresponds to mass/charge ratio, while the *y* axis corresponds to intensity.

ercame this problem because they were dominated by RCO_2^- fragment ions. Combination of the two pieces of complementary data allowed identification of the sterol esters contained in each of the HPLC isolates.

Electron transfer to the surface provides one possible explanation for the poor negative-ion sensitivity obtained from the nitrocellulose support (*29*). Electron transfer from analyte anions to the electronegative surface nitrate groups, according to eq 1, would result in analyte ion neutralization and sen-

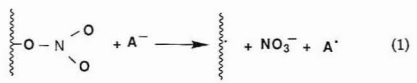

(1)

sitivity loss. Several studies with Nytran, aluminized Mylar and nitrocellulose foils revealed that analyte negative-ion response was consistently lower for analyses carried out on nitrocellulose than for those analyses carried out on either aluminized mylar or Nytran. These results suggest the involvement of the nitrate groups in the process leading to reduced negative-ion sensitivity. Furthermore, in accordance with eq 1, an abundant NO_3^- anion is observed in the negative-ion PD mass spectra obtained from nitrocellulose-coated sample foils.

Selective Adsorption of Hydrophobic Surfactants from Complex Mixtures. The Nytran surface has been shown to adsorb both anionic surfactants (Figure 5) and cationic surfactants having a hydrophobic alkyl chain (Figure 1b). Hydrophilic nonionic surfactants apparently do not strongly adsorb from aqueous solution, and this fact can be used to analytical advantage in the characterization of commercial surfactant formulations. The point is illustrated in Figure 7 by comparison of the PDMS results obtained from an artificial detergent formulation containing cationic (ditallowdimethylammonium chloride, DTDMAC), anionic

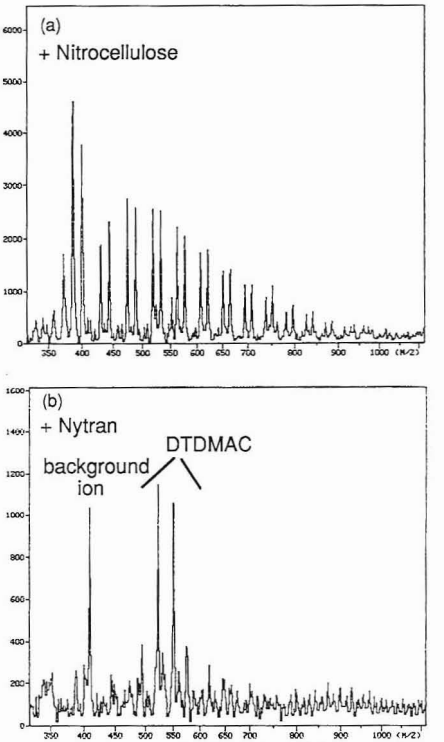

Figure 7. Positive-ion mass spectra of an artificial detergent formulation bound to (a) nitrocellulose and (b) Nytran surfaces. The *x* axis corresponds to mass/charge ratio, while the *y* axis corresponds to intensity.

(LAS), and nonionic (neodol) surfactants. The positive-ion spectrum obtained from the nitrocellulose surface exhibits cationized ($M^- + 2Na^+$) LAS as the most abundant ions (m/z 371, 385, 399). The mass range from 400 to 900 Da is dominated by cationized neodols. The cationic surfactant (molecular cations at m/z 494, 522, 550) is largely obscured by the strong response from the nonionics. The corresponding positive-ion spectrum from Nytran shows no response for LAS because small positively charged ions like Na^+, needed for cationization, do not adsorb to this surface and are not available for ionization. The neodols are not detected either. We see no evidence for the MH^+ molecular ions that dominate neodol's PD mass spectrum obtained from the nitrocellulose surface when Na^+ has been washed off the foil. Obviously, this hydrophilic nonionic surfactant does not adsorb to the Nytran surface from aqueous solution. The only ions observed in the positive-ion spectrum are the DTDMAC molecular cations, except for a common background ion at m/z 408. Of course, the LAS molecular anions were readily detected in the negative-ion spectrum obtained from this Nytran foil. This particular example illustrates the use of the PDMS sample foil to provide a crude "affinity" chromatographic separation of the hydrophobic ionic surfactants from the hydrophilic nonionics.

CONCLUSIONS

A novel quaternized Nylon substrate has been prepared and evaluated for plasma desorption mass spectrometry. This

substrate has been quite useful for studying adsorption mechanisms of ionic surfactants onto charged surfaces. Furthermore, it has also been shown to provide 10–100 times better negative-ion response than is obtained from nitrocellulose surfaces for several classes of compounds. Finally, it has proven effective as an "affinity surface", allowing the separation of anionic and hydrophobic cationic surfactants from mixtures also containing hydrophilic nonionic surfactants.

Nytran foils are more difficult to prepare than conventional nitrocellulose foils and much less uniform in appearance. Whether the additional foil preparation effort (relative to nitrocellulose) is justified depends entirely on the analytical problem at hand. It should also be noted that other cation- and anion-exchange surfaces, such as Mylar and polypropylene (*3*) or Mylar impregnated with cationic surfactants (*4*, *5*), might also exhibit some of the beneficial attributes of Nytran that have been outlined in this paper. These other surfaces were not specifically investigated here. In the case of Mylar impregnated with a cationic surfactant, one should anticipate a significant positive-ion background response (potential interference) due to detection of the parent cationic surfactant and a number of structurally significant fragment ions.

ACKNOWLEDGMENT

We thank Gloria Story and Curtis Marcott for obtaining the infrared reflection absorption spectra from the nytran membrane and the nytran-covered sample foil. We also thank Ron Jandacek, Tony Steimle and Alan McDowell for providing the HPLC isolates of the sterol ester fraction from hamster feces. Finally, we thank Phil Brode and Robert Laughlin for critically reviewing the manuscript prior to submission.

LITERATURE CITED

(1) McNeal, C. J.; Macfarlane, R. D.; Thurston, E. L. *Anal. Chem.* **1979**, *51*, 2036–2039.
(2) Jordan, E. A.; Macfarlane, R. D.; Martin, C. R.; McNeal, C. J. *Int. J. Mass Spectrom. Ion Processes* **1983**, *53*, 345–348.
(3) Macfarlane, R. D.; McNeal, C. J.; Martin, C. R. *Anal. Chem.* **1986**, *58*, 1091–1097.
(4) McNeal, C. J.; Macfarlane, R. D. *J. Am. Chem. Soc.* **1986**, *108*, 2132–2139.
(5) McNeal, C. J. In *Mass Spectrometry of Large Non-Volatile Molecules for Marine Organic Chemistry*; Hilf, E. R., Tuszynski, W., Eds.; World Scientific Publishing Co.: Singapore, 1990; pp 51–60.
(6) Jonsson, G. P.; Hedin, A. B.; Hakansson, P. L.; Sundqvist, B. U. R.; Save, B. G. S.; Nielsen, P. F.; Roepstorff, P.; Johansson, K. E.; Kamensky, I.; Lindberg, M. S. L. *Anal. Chem.* **1986**, *58*, 1084–1087.
(7) Roepstorff, P. *Acc. Chem. Res.* **1989**, *22*, 421–427.
(8) Save, G.; Hakansson, P.; Sundqvist, B. U. R.; Jonsson, U.; Olofsson, G.; Malmquist, M. *Anal. Chem.* **1987**, *59*, 2059–2063.
(9) Roepstorff, P. In *Mass Spectrometry of Large Non-Volatile Molecules for Marine Organic Chemistry*; Hilf, E. R., Tuszynski, W., Eds.; World Scientific Publishing Co.: Singapore, 1990; pp 23–32.
(10) Wolf, B.; Macfarlane, R. D. Presented at the 38th Annual Conference on Mass Spectrometry and Allied Topics, Tuscon, AZ, June 3–8, 1990.
(11) Alai, M.; Demirev, P.; Fenselau, C.; Cotter, R. J. *Anal. Chem.* **1986**, *58*, 1303–1307.
(12) Jungclas, H.; Fritsch, H. W.; Kohl, P.; Schmidt, L. In *Mass Spectrometry of Large Non-Volatile Molecules for Marine Organic Chemistry*; Hilf, E. R., Tuszynski, W., Eds.; World Scientific Publishing Co.: Singapore, 1990; pp 96–102.
(13) Cotter, R. J. *Anal. Chem.* **1988**, *60*, 781A–793A.
(14) Rosen, M. J. *J. Am. Oil Chem. Soc.* **1975**, *52*, 431–435.
(15) Rosen, M. J. *Surfactants and Interfacial Phenomena*; John Wiley and Sons: New York, 1978; pp 26–55.
(16) Wakamatsu, T.; Feurstenau, D. W. In Advances in Chemistry Series No. 79; Weber, W. J., Matijevis, E., Eds.; American Chemical Society: Washington, DC, 1968; pp 161–172.
(17) Lacey, M. P.; Keough, T. *Rapid Commun. Mass Spectrom.* **1989**, *3*, 323–328.
(18) Takigiku, R.; Keough, T.; Lacey, M. P.; Schneider, R. E. *Rapid Commun. Mass Spectrom.* **1990**, *4*, 24–29.
(19) Loo, J. A.; Edmonds, C. E.; Smith, R. D.; Lacey, M. P.; Keough, T. *Biomed. Environ. Mass Spectrom.* **1990**, *19*, 286–294.
(20) Ligon, W. V.; Dorn, S. B. *Int. J. Mass Spectrom. Ion Processes* **1984**, *57*, 75–90.
(21) Ligon, W. V.; Dorn, S. B.. *Int. J. Mass Spectrom. Ion Processes* **1984**, *61*, 113–122.
(22) Lacey, M. P.; Keough, T. *Rapid Commun. Mass Spectrom.* **1989**, *3*, 46–50.
(23) Simms, J. R.; Keough, T.; Ward, S. R.; Moore, B. L.; Bandurraga, M. M. *Anal. Chem.* **1988**, *60*, 2613–2620.
(24) Wernery, J. D.; Peake, D. A. *Rapid Commun. Mass Spectrom.* **1989**, *3*, 369–399.
(25) Bio-Rad Laboratories, Product Bulletin 1080, 1983; pp 1–12.
(26) Keough, T.; DeStefano, A. J. *Anal. Chem.* **1981**, *53*, 25–29.
(27) Munster, H.; Stein, J.; Budzikiewicz, H. *Biomed. Environ. Mass Spectrom.* **1986**, *13*, 423–427.
(28) Weintrab, S. T. In *Mass Spectrometry of Biological Materials*; McEwen, C. N., Larsen, B. S., Eds.; Marcel Dekker, Inc.: New York, 1990; pp 257–286.
(29) Nord, R. F.; Macfarlane, R. D. Presented at the 37th Annual Conference on Mass Spectrometry and Allied Topics, Miami Beach, FL, May 21–26, 1989.

RECEIVED for review February 5, 1991. Accepted April 18, 1991.

Electrospray Mass Spectrometry: Application of Ion Evaporation Theory to Amino Acids

Minoru Sakairi*

Central Research Laboratory, Hitachi Ltd., Kokubunji, Tokyo 185, Japan

Alfred L. Yergey

National Institute of Child Health and Human Development, National Institutes of Health, Bethesda, Maryland 20892

K. W. Michael Siu, J. C. Yvec Le Blanc, Roger Guevremont, and Shier S. Berman

Division of Chemistry, National Research Council of Canada, Ottawa, Ontario, Canada K1A 0R9

We describe the result of applying the ion evaporation theory to a series of amino acids. The very good correlation (r = 0.98) of the natural logarithms of protonated molecule intensities observed by electrospray with the difference between the hydration free energies of molecules and the gas-phase binding free energies of molecules and protons in amino acids is consistent with the ion evaporation model. It seems that the difference in the protonated molecule intensities of amino acids obtained by electrospray can be explained by a scheme in which protonated molecules in the liquid phase are extracted into the gas phase after a charged droplet is formed.

INTRODUCTION

Electrospray mass spectrometry has received much attention during the last few years. The unique feature of this method is its ability to generate multiply charged ions from proteins, peptides, and nucleotides and to detect them with high sensitivity by quadrupole mass spectrometers (*1–3*).

Numerous investigations about the ionization mechanism of electrospray have been reported (*4–8*). One possibility to quantitatively discuss the ionization mechanism is the ion evaporation theory proposed by Iribarne and Thomson (*9, 10*). They reported in this theory that solvated ions were extracted into the gas phase from a charged droplet produced by electrospray. Since they investigated only alkali-metal ions, we have tried to apply the theory to organic compounds. However, the solvation free-energy data of solvated ions of organic compounds are not available. Therefore, we assumed that ions of organic compounds were directly desorbed from a charged droplet to simplify the calculation. In this paper, we report the result of applying the ion evaporation theory to a series of amino acids.

EXPERIMENTAL SECTION

The details of the electrospray mass spectrometric system have already been described (*8*). The electrospray probe used consisted of an approximately 1-in. stainless steel tube with 100-μm i.d. attached by epoxy glue to a 4-in. × $^1/_{16}$-in.-o.d. stainless steel tube. The probe tip was positioned approximately 15 mm from a sample aperture and was typically biased to 3 kV with respect to ground. Sample solutions were continuously infused with a syringe pump (Harvard Apparatus, Model 22) at a typical flow rate of 0.5 μL/min. The flow rate fluctuation of the syringe pump was less than 2%.

We selected amino acids with nonpolar side chains (alanine, isoleucine, leucine, phenylalanine, tryptophan, and valine) and amino acids with uncharged polar side chains (asparagine, glutamine, glycine, serine, threonine, and tyrosine) from 20 amino acids. The other essential amino acids were passed over for lack of data of reliable solvation free energies or binding free energies (cysteine, methionine, proline, aspartic acid, glutamic acid, arginine, lysine, and hystidine).

The protonated molecule intensities of the amino acids were measured by continuously flowing amino acid solutions (10^{-5} M concentration prepared in deionized, distilled water acidified with 0.1% formic acid (pH 2.9)) at a flow rate of 0.5 μL/min. The experiments were performed at room temperature (298 K) under atmospheric pressure (1.01×10^5 Pa). Ten replicate analyses were performed. All amino acids were purchased from Sigma Chemical Co. (St. Louis, MO).

CALCULATION

As detailed by Iribarne and Thomson (*9, 10*), ion evaporation may be regarded as a reverse process of placing a gas-phase ion in solution. According to this ion evaporation mechanism, we considered a simple scheme for detecting protonated molecules of amino acids. Here, we assumed that protonated molecules of amino acids were directly desorbed from a charged droplet produced by electrospray, although solvated ions were considered to be extracted in the ion evaporation theory. This is because we cannot estimate the solvation free energies of solvated protonated molecules of amino acids.

In this case, the number of detected ions per unit time with a mass spectrometer (I) may be simply expressed as follows:

$$I \propto N_0 b_1 b_2 T_1 T_2 \qquad (1)$$

where N_0 is the number of sample molecules introduced into the ion source of the mass spectrometer per unit time, b_1 is the efficiency of producing protonated molecules in the liquid phase (the ratio of the concentration of protonated molecules in the liquid phase (C_1) to the concentration of sample molecules introduced into the ion source (C_0)), b_2 is the efficiency of extracting protonated molecules from the liquid phase into the gas phase (the ratio of the concentration of protonated molecules extracted into the gas phase (C_2) to the concentration of protonated molecules in the liquid phase (C_1)), T_1 is the transmission efficiency of protonated molecules in the ion source, and T_2 is the transmission efficiency of protonated molecules in the mass spectrometer.

The reaction of protonation of molecules in the liquid phase is expressed as

$$M + SH^+ \rightarrow MH^+ + S$$

where M and S represent sample and solvent molecules, respectively. If the liquid-phase binding free energies associated with the reactions $M + H^+ \rightarrow MH^+$ and $S + H^+ \rightarrow SH^+$ are expressed as ΔG_{BL} and ΔG_{BS}, respectively, b_1 may be given as follows, using the concentrations of solvated protons (C_P) and solvent molecules (C_S):

$$b_1 = C_1/C_0 = (C_P/C_S) \exp(-(\Delta G_{BL} - \Delta G_{BS})/RT) \qquad (2)$$

0003-2700/91/0363-1488$02.50/0 © 1991 American Chemical Society

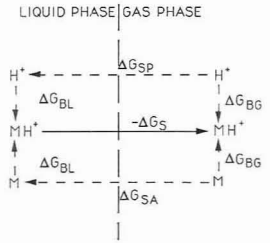

Figure 1. Energy cycle for calculating the difference between the hydration free energy of a protonated molecule and the liquid-phase binding free energy of a molecule and a proton. ΔG_S, hydration free energy of a protonated molecule; ΔG_{BL}, liquid-phase binding free energy of a molecule and a proton; ΔG_{BG}, gas-phase binding free energy of a molecule and a proton; ΔG_{SA}, hydration free energy of a molecule; ΔG_{SP}, hydration free energy of a proton.

where R is the gas constant and T is the absolute temperature. While using the total solvation free energy of bringing a protonated molecule from infinity into a charged droplet (ΔG_{TS}) (*9*, *10*), b_2 may be expressed as

$$b_2 = C_2/C_1 = \exp(-(-\Delta G_{TS})/RT) \quad (3)$$

According to the ion evaporation theory, ΔG_{TS} is given by

$$\Delta G_{TS} = \Delta G_S + \Delta G_E \quad (4)$$

where ΔG_S is the solvation free energy of a protonated molecule and ΔG_E is the electrostatic contribution of bringing the protonated molecule from infinity into a charged droplet (*9*, *10*). From eqs 1–4, we can finally obtain

$$I \propto N_0(C_P/C_S)\exp(-(-\Delta G_S + \Delta G_{BL} - \Delta G_{BS} - \Delta G_E)/RT)T_1T_2 \quad (5)$$

If C_P and C_S are much higher than C_0, they can be considered to be constants. The experimental conditions described above satisfy this condition. Further, under identical experimental conditions, it is reasonable to consider that ΔG_{BS}, ΔG_E, T_1, and T_2 are constants for all of the protonated molecules of the amino acids. Therefore, if N_0 is constant,

$$\ln I \propto \Delta G_S - \Delta G_{BL} \quad (6)$$

where ln I is the natural logarithm of I.

However, we cannot directly determine the values of $\Delta G_S - \Delta G_{BL}$ because of the difficulty in accounting for solvation effects on charged species in the liquid phase. Therefore, we replaced the parameter of $\Delta G_S - \Delta G_{BL}$ with the alternative thermodynamic cycle parameters of the gas-phase binding free energy of an amino acid molecule and a proton (ΔG_{BG}) and the solvation free energies of an amino acid molecule (ΔG_{SA}) and a proton (ΔG_{SP}). Since the last three parameters can be determined experimentally or by calculation, Figure 1 should lead to a determination of $\Delta G_S - \Delta G_{BL}$

$$\Delta G_S - \Delta G_{BL} = -\Delta G_{BG} + \Delta G_{SA} + \Delta G_{SP} \quad (7)$$

Since the electrospray is operated at room temperature under atmospheric pressure, we can adopt data at standard conditions. The data of the gas-phase binding free energies of amino acid molecules (M) and protons (H^+) associated with the reaction $M + H^+ \rightarrow MH^+$ at standard condition (ΔG_{BG}) can be taken from the compilation of published data (*11*). The standard solvation free energy of an amino acid molecule (ΔG_{SA}) was estimated as follows.

Since solvation free energies are additive (*12*, *13*), the solvation free energy of an amino acid molecule ($RCH_2(NH_2)COOH$) is expressed as (*14*)

$$\Delta G_{SA} \sim \Delta G_S(RH) + \Delta G_S(glycine) \quad (8)$$

Table I. Gas-Phase Binding Free Energies Associated with the Reaction $M + H^+ \rightarrow MH^+$ (ΔG_{BG}), Hydration Free Energies of Amino Acid Molecules [$\Delta G_S(RH)$], and the Values of $-\Delta G_{BG} + \Delta G_S(RH)$[a]

amino acids	ΔG_{BG}, kJ/mol	contributions of side chains to $\Delta G_S(RH)$, kJ/mol	diff, kJ/mol
isoleucine	−883.8	9.7	893.5
leucine	−880.5	8.7	889.2
tryptophan	−911	−24.75	886.3
phenylalanine	−888.9	−3.77	885.1
valine	−875.9	8.18	884.3
alanine	−865	8.37	873.4
tyrosine	−898.1	−25.67	872.4
glycine	−853.3	0	853.3
threonine	−882.6	−20.98	861.6
serine	−875	−21.4	853.6
asparagine	−887.6	−40.63	847
glutamine	−881.7	−39.41	842.3

[a] The gas-phase binding free energies and the hydration free energies are taken from refs 11 and 15, respectively.

where $\Delta G_S(RH)$ and $\Delta G_S(glycine)$ are the solvation free energies of the compound corresponding to the amino acid side chain and glycine, respectively. In these solvation free energies, $\Delta G(RH)$ can be referred to as the published thermodynamic data (*15*, *16*). The compounds corresponding to the side chains of the amino acids that we chose are methane (alanine), isobutane (isoleucine), butane (leucine), methylbenzene (phenylalanine), 3-methylindole (tryptophan), propane (valine), acetamide (asparagine), propionamide (glutamine), methanol (serine), ethanol (threonine), and 4-methylphenol (tyrosine).

From eqs 6–8

$$\ln I \propto -\Delta G_{BG} + \Delta G_S(RH) + \Delta G_S(glycine) + \Delta G_{SP} \quad (9)$$

is obtained. Since the last two terms are common to all of the amino acids, the difference in the values of $-\Delta G_{BG} + \Delta G_S(RH) + \Delta G_S(glycine) + \Delta G_{SP}$ is directly reflected by the difference in the values of $-\Delta G_{BG} + \Delta G_S(RH)$. Therefore, eq 9 is finally simplified to

$$\ln I \propto -\Delta G_{BG} + \Delta G_S(RH) \quad (10)$$

If the argument here is right, a good correlation between ln I and $-\Delta G_{BG} + \Delta G_S(RH)$ should be observed.

RESULTS AND DISCUSSION

Although the electrospray generally works better with solutions containing methanol, none was used in this study for simplicity in data interpretation. In this case, the solvation free energy simply became the hydration free energy. Table I shows the gas-phase binding free energies associated with the reaction $M + H^+ \rightarrow MH^+$ (ΔG_{BG}), the hydration free energies of the compounds corresponding to the amino acid side chains, [$\Delta G_S(RH)$], and the values of $-\Delta G_{BG} + \Delta G_S(RH)$.

Figure 2 shows the plot between the values of $-\Delta G_{BG} + \Delta G_S(RH)$ and the natural logarithms of the protonated molecule intensities, in arbitrary units, obtained by electrospray (ln I) in the amino acids. The correlation coefficient was calculated to be 0.98. In this case, mass discrimination was minimal and was simply ignored, because the peaks of all 12 amino acids occurred over a relatively narrow mass range. The range indicated on each data point represents the standard deviation of the mean of 10 measurements.

Judging from the high correlation coefficient, it is apparent that there is a strong relationship between the values of $-\Delta G_{BG} + \Delta G_S(RH)$ and ln I in the amino acids. This result apparently proves the validity of eq 6. In other words, the protonated molecule intensities of the amino acids by electrospray can be predicted by the values of $-\Delta G_{BG} + \Delta G_S(RH)$. For

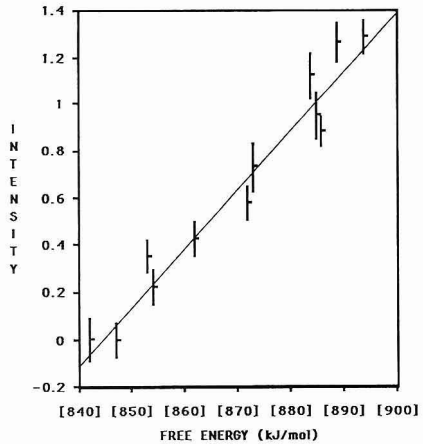

Figure 2. Plot of $-\Delta G_{BG} + \Delta G_S(RH)$ versus ln I (ΔG_{BG}, gas-phase binding free energies of molecules and protons; $\Delta G_S(RH)$, hydration free energies of molecules; ln I, natural logarithm of the protonated molecule intensities of the amino acids) (r = 0.98).

comparison, we also evaluated the correlation coefficient between the values of $-\Delta G_{BG}$ and ln I and the correlation coefficient between the values of $\Delta G_S(RH)$ and ln I. These were calculated to be 0.12 and 0.78, respectively. These values clearly show that it is important to consider both physical parameters of the gas-phase binding free energy (ΔG_{BG}) and the solvation free energy ($\Delta G_S(RH)$) for interpreting the difference in the protonated molecule intensities of the amino acids.

On the other hand, the argument here has a problem that a predicted intensity ratio of protonated molecules between two amino acids with eq 10 is much higher than an observed one. For example, although the predicted intensity ratio of leucine to aspargagine is about 2.5×10^7 with eq 10, the observed one is only 3.5. Now we have considered that this gap is derived from the overestimation of the hydration free-energy difference in the amino acids. We assumed that protonated molecules were directly desorbed from a charged droplet. However, hydrated protonated molecules must be really desorbed since water attachement to ions results in the hydration free-energy reduction of the ions, as pointed out in alkali-metal ions by Iribarne and Thomson (*9*, *10*). Unfortunately, however, we cannot estimate how many water molecules are attached to the protonated molecules of the amino acids when such ions are desorbed from a charged droplet. Even if we can estimate the number of the water molecules attached, we don't have a method to calculate the hydration free-energy reduction resulting from water molecule attachment. To the contrary, if we can have such data, we may perfectly succeed in explaining the difference in the protonated molecule intensities of the amino acids.

Registry No. Alanine, 56-41-7; isoleucine, 73-32-5; leucine, 61-90-5; phenylalanine, 63-91-2; tryptophan, 73-22-3; valine, 72-18-4; asparagine, 70-47-3; glutamine, 56-85-9; glycine, 56-40-6; serine, 56-45-1; threonine, 72-19-5; tyrosine, 60-18-4.

LITERATURE CITED

(1) Yamashita, M.; Fenn, J. B. *J. Phys. Chem.* **1984**, *88*, 4451.
(2) Yamashita, M.; Fenn, J. B. *J. Phys. Chem.* **1984**, *88*, 4471.
(3) Whitehouse, C. M.; Dreyer, R. N.; Yamashita, M.; Fenn, J. B. *Anal. Chem.* **1985**, *57*, 675.
(4) Vestal, M. L. Proceedings of the 37th ASMS Conference on Mass Spectrometry and Allied Topics, Miami Beach, FL, 1989; p 41.
(5) Smith, R. D.; Udseth, H. R.; Loo, J. A.; Edmonds, C. G.; Barinaga, C. J. Proceedings of the 37th ASMS Conference on Mass Spectrometry and Allied Topics, Miami Beach, FL, 1989; p 391.
(6) Fenn, J. B.; Mann, M.; Meng, C. K.; Wong, S. F.; Whitehouse, C. M. *Mass Spectrom. Rev.* **1990**, *9*, 37.
(7) Schmelzeisen-Redeker, G.; Bütfering, L.; Röllgen, F. W. *Int. J. Mass Spectrom. Ion Proc.* **1989**, *90*, 139.
(8) Siu, K. W. M.; Gardner, G. J.; Berman, S. S. *Org. Mass Spectrom.* **1989**, *24*, 931.
(9) Iribarne, J. V.; Thomson, B. A. *J. Chem. Phys.* **1976**, *64*, 2287.
(10) Thomson, B. A.; Iribarne, J. V. *J. Chem. Phys.* **1979**, *71*, 4451.
(11) Lias, S. G.; Liebman, J. F.; Levin, R. D. *J. Phys. Chem. Ref. Data* **1984**, *13*, 695.
(12) Kauzmann, W. *Adv. Protein Chem.* **1959**, *14*, 1.
(13) Nozaki, Y.; Tanford, C. *J. Biol. Chem.* **1971**, *246*, 2211.
(14) Ooi, T.; Oobatake, M.; Nemethy, G.; Scheraga, H. A. *Proc. Natl. Acad. Sci. U.S.A.* **1987**, *84*, 3086.
(15) Cabani, S.; Gianni, P.; Mollica, V.; Lepori, L. *J. Solution Chem.* **1981**, *10*, 563.
(16) Wolfenden, R.; Andersson, L.; Cullis, P. M.; Southgate, C. C. B. *Biochemistry*, **1981**, *20*, 849.

RECEIVED for review March 4, 1991. Accepted April 18, 1991.

Evaluation of Inductively Coupled Plasma Mass Spectrometry as an Elemental Detector for Supercritical Fluid Chromatography

Wei-Lung Shen,[1] Nohora P. Vela, Brenda S. Sheppard, and Joseph A. Caruso*

Department of Chemistry, University of Cincinnati, Cincinnati, Ohio 45221-0172

Supercritical fluid chromatography coupled with inductively coupled plasma mass spectrometry shows high potential for the determination at ultratrace levels of organometallic compounds of environmental interest. In this study the determination of organotin compounds at ultratrace levels is demonstrated. In this work a supercritical fluid chromatography/inductively coupled plasma mass spectrometry (SFC/ICPMS) interface was developed. Separation of tetraalkyltin compounds shows detection levels in the subpicogram range (0.034 pg for tetrabutyltin; 0.047 pg for tetraphenyltin). The linear ranges are over 3 orders magnitude (1–1000 pg). The reproducibility of sample injections are better than 5% RSD.

INTRODUCTION

In the past decade, the potential benefits of supercritical fluid chromatography (SFC) as an alternative chromatographic technique to liquid or gas chromatography have been demonstrated (*1–3*). Separations of metal-containing compounds with supercritical fluids have been the subject of numerous investigations (*4, 5*). Several element-selective optical detectors, such as the microwave-induced plasma (MIP) (*6–8*), radio frequency plasma (*9*), inductively coupled plasmas (ICP) (*10–12*), and others, have been studied as element-selective detectors for SFC using optical emission. However, the need remains for a more sensitive, element-selective detector for SFC. Among several possible element-selective detection techniques, inductively coupled plasma mass spectrometry (ICPMS) appears to offer a new and attractive approach. ICPMS has advantages of low detection limits, isotope determination capabilities, potential for isotope dilution analysis, and the capability for multielement analysis (*13–17*). These advantages make SFC/ICPMS potentially a selective and highly sensitive chromatographic detection technique for many elements in the periodic table.

Organotin compounds are used as thermal stabilizers, catalysts, biocides, and antifouling agents (*18, 19*). These compounds are well-known as toxic pollutants to aquatic organisms and mammals, even at low concentration. Additionally, the toxicity of these compounds depends on their chemical form, so speciation information is necessary.

A variety of analytical techniques have been developed for speciating organotin compounds. Among them, GC (*20, 21*) and HPLC with ultraviolet detection (*22–26*) are listed in the literature. Recently, organotin compounds have been speciated and detected by GC/MIPMS (*27*) and HPLC/ICPMS, (*28, 29*). However, high background signals were observed in both cases.

SFC has the advantage over GC of being able to accommodate thermally labile, nonvolatile and high molecular weight compounds. Similar to GC, SFC also provides gaseous sample introduction to the plasma. In this way, SFC also eliminates the disadvantage of solution nebulization (such as from HPLC) that results in low (usually 5% or less) analyte transport efficiency into the plasma.

This is the first study using SFC/ICPMS to separate and detect organotin compounds. Since SFC can be used to analyze thermally labile compounds and because the toxic nature of some organotin compounds in the environment, organotin compounds are good demonstration candidates to test and evaluate ICPMS for SFC detection. In this preliminary study, developing the SFC/ICPMS interface and determining background spectral features with SFC/ICPMS, plus the effects of varying some SFC parameters, are investigated. Detection limits, linear dynamic ranges, and reproducibility for the organotin compounds studied are presented and discussed.

EXPERIMENTAL SECTION

(a) Supercritical Fluid Chromatography. A number of papers have described and reviewed considerations for SFC instrumentation (*1–3, 30–34*). The overall system diagram of SFC/ICPMS used in this study is shown in Figure 1. The supercritical fluid chromatography system included a Hewlett-Packard 5890 Series II gas chromatographic oven (Hewlett-Packard, Avondale, PA) and a Lee Scientific supercritical pump Series 600 (Lee Scientific, Salt Lake City, UT) controlled by an XT clone computer that was used to deliver the supercritical fluid. Liquid CO_2 used was Bone Dry grade (99.8% purity, Linde Specialty Gases, Union Carbide Corp., Somerset, NJ). A SB-Octyl-50 capillary column and a frit restrictor (50 μm i.d.), with a linear flow of 1.5 cm/s, were purchased from Lee Scientific. This capillary column was 50 μm i.d., 195 μm o.d., and 2.5 m in length, and was coated with a 0.25 μm film thickness. Injection into the capillary column was achieved by using a VICI valve (Valco Co., Houston, TX) with a 0.2-μL sample loop. Time split techniques were used for sample introduction. A computer program existing in the SFC controller is used to select injection time. The amount of analyte injected into the column was calculated by using column dimensions, initial pressure, and linear flow of the mobile phase. The amount of sample injected was 10 nL (0.075-s injector duration). The VICI valve was controlled by a pneumatic controller that was activated by helium gas at 90 psi back-pressure.

(b) SFC/ICPMS Interface. The SFC/ICPMS interface is shown in Figure 2. A $^1/_8$-in. copper tube was inserted into the injector tube of the ICP torch to heat the restrictor (~200 °C). A three-way $^1/_8$-in. Swagelok union was used to introduce heated argon makeup gas from the bottom, and from the other end, the restrictor was inserted. The rear side of this three-way Swagelok union was stepped down to $^1/_{16}$-in. i.d. with a $^1/_8$-$^1/_{16}$-in. reducing Swagelok union. The frit restrictor was inserted and positioned flush with the exit of the inserted copper tube and the $^1/_{16}$-in. end was sealed with a graphite ferrule to fix the position of the frit restrictor. The whole interface was wrapped with $^1/_4$-in. heating tape (Glas-Col, Terre Haute, IN) and insulated with glass fiber materials (Fisher, Fairlawn, NJ). The heated transfer line was constructed from $^1/_{16}$ in. o.d. stainless steel tubing wrapped with a high-temperature heating cord (Glas-Col, Terre Haute, IN), and a thermocouple was placed at the center of the transfer line to monitor the temperature with a laboratory-built control unit. A variable transformer was used to control the power supplied to the heating cord to maintain constant transfer line temperature. The SFC column was inserted completely through the transfer

[1] Union Carbide Research Center, Charleston, WV.

0003-2700/91/0363-1491$02.50/0 © 1991 American Chemical Society

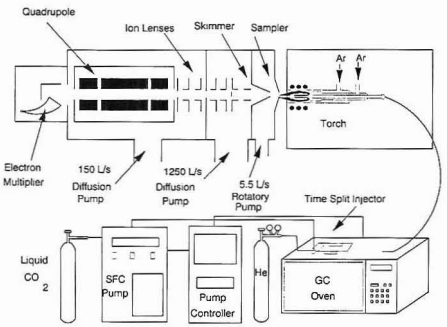

Figure 1. SFC/ICPMS system diagram.

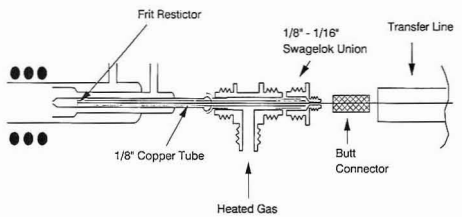

Figure 2. SFC/ICPMS interface.

Table I. SFC/ICPMS Operating Conditions

ICP Conditions	
Ar coolant flow	15 L/min
Ar aux flow	1.5 L/min
forward power	1.35 kW
reflected power	<5 W
Mass Spectrometry	
lenses	tuned on Ar_2^+ (80)
1st stage pressure	2.2 mbar
2nd stage pressure	$<1 \times 10^{-4}$ mbar
3rd stage pressure	$(2.7–3.2) \times 10^{-6}$ mbar
SFC Conditions	
injection vol	10 nL
oven temp	75 °C
transfer line temp	75 °C
restrictor temp	~200 °C
Optimal Pressure Program	
init pressure	100 atm
hold time	1 min
ramp pressure	80 atm/min
final pressure	200 atm

line and connected with the restrictor by a butt connector. In order to avoid destroying the ceramic frit restrictor, the temperature of the interface was maintained at approximately 200 °C. If the temperature of the frit restrictor was too low, a spike signal background was observed because of analyte condensation. Since the column was inserted through the transfer line, this temperature was maintained at 75 °C, the same temperature of the GC oven, in order to minimize temperature effects and condensation of organotin compounds.

(c) Mass Spectrometry. The mass spectrometer used in this work was a VG PlasmaQuad equipped with time-resolved acquisition (TRA) software (VG Elemental, Winsford, Cheshire, U.K.). As shown in Figure 1, the nebulizer was removed and replaced with the SFC interface. No other modifications were made. The typical operating conditions of the ICPMS are listed in Table I.

(d) Reagents. Tetramethyltin (TMT), tetrabutyltin (TBT), tetraphenyltin (TPT), tributyltin acetate (TBTA), dibutyltin

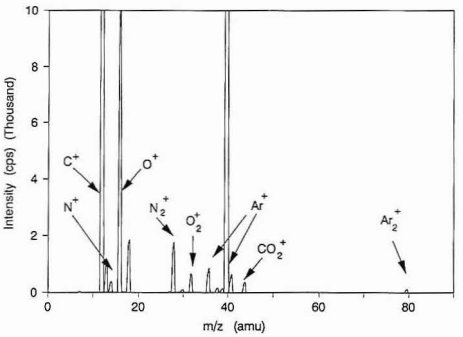

Figure 3. Overall SFC/ICPMS background scan. (The electron multiplier voltage was reduced.)

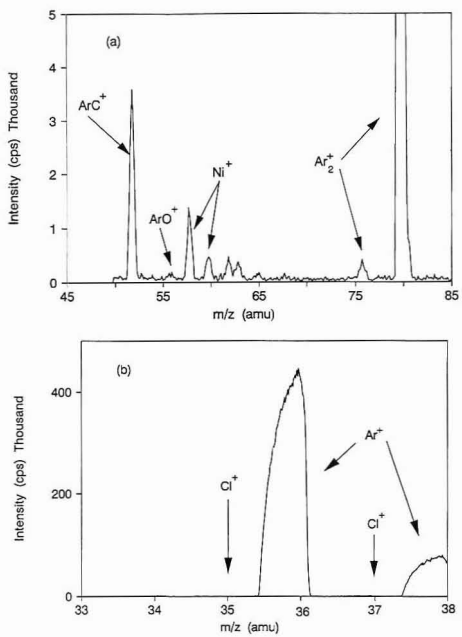

Figure 4. SFC/ICPMS background scan (normal electron multiplier voltage): (a, top) scan region from *m/z* 45–85; (b, bottom) *m/z* 33–38.

diacetate (DBTDA) [$(CH_3)_4Sn$, $(C_4H_9)_4Sn$, $(C_6H_5)_4Sn$, $(C_4H_9)_3SnOOCCH_3$, and $(C_4H_9)_2Sn(OOCCH_3)_2$, respectively] were obtained from Alfa Products (Ward Hill, MA) with stated purities of 97%, 97%, 100%, 97%, and 100%, respectively. Solvents used for standard preparation were HPLC grade hexane and toluene (Fisher, Fairlawn, NJ). Stock solutions (1000 ppm) of TMT, TBT, TBTA, and DBTDA were prepared in hexane. TPT stock solution was prepared in toluene. A series of standards (from 100 ppb to 100 ppm) were then prepared from these 1000 ppm stock solutions by dilution with hexane.

RESULTS AND DISCUSSION

(1) Background Spectral Features of Argon ICPMS with SF Carbon Dioxide Eluent. To assess the limitations for ICPMS detectability, it is important to recognize the isobaric interferences in the background mass spectrum.

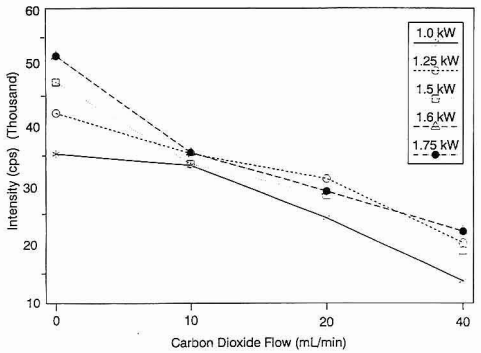

Figure 5. Effects of carbon dioxide flows and power levels on Sn signal at m/z 120.

Figures 3 and 4 show different regions of the background spectra with supercritical fluid eluent at reduced and normal electron multiplier voltages (1800 and 2600 V, respectively). The background spectra for SFC/ICPMS are much simpler than those associated with solution nebulization. In Figure 3, at reduced electron multiplier voltage, the major background species shown are $^{12}C^+$, $^{13}C^+$, $^{14}N^+$, $^{16}O^+$, $H_2{}^{16}O^+$, $^{23}Na^+$, $^{14}N_2{}^+$, $^{14}N^{16}O^+$, $^{16}O_2{}^+$, $^{36}Ar^+$, $^{38}Ar^+$, $^{23}Na^{16}O^+$, $^{40}Ar^+$, $^{40}ArH^+$, $^{12}C^{16}O_2{}^+$, and $^{40}Ar_2{}^+$. In Figure 4a, at normal multiplier voltages (higher gain), an additional species shown is $^{12}C^{40}Ar^+$. However, the background signal at m/z = 56 is lower than that with solution nebulization. This observation indicates that there is potential for Fe determination. Figure 4b shows the expected high background signal at m/z = 36 and 38 due to argon isotopes. This figure also demonstrates a reduction in the background at m/z = 35 and 37 compared to the signal observed with direct solution nebulization. According to this result, there is the possibility for organochlorine determination using a dry plasma and carbon dioxide in the mobile phase. The signal above mass 80 showed no additional isobaric interference and was at background levels of 20–30 counts/s (cps).

(2) Effects of CO_2 on Sn Signal. The effect of CO_2 on the Sn analyte signal was studied by solution nebulization of 100 ppb Sn in a 1% HNO_3 solution. CO_2 was introduced as the auxiliary flow to the ICP torch. As shown in Figure 5, the Sn signal, at m/z = 120, decreases with increasing CO_2 flow rate and increases with ICP forward power. However, the losses due to increased amount of CO_2 are not recovered by increasing the power. The sampler was coated with carbon after running 10 mL/min of CO_2 for about 10 min. When the power was higher than 1.5 kW, there was arcing between the sampler and the plasma. The plasma dimensions were decreased as the CO_2 flow rate increased, and the tail of plasma showed a violet-green color from carbon emission. Since the capillary SFC eluent is usually at a flow less than 1 mL/min of CO_2, the effects of CO_2 are minimal and thus ICP normal operating conditions (1.35 kW and 16 L/min of Ar + CO_2 total flow rate) were used.

(3) SFC Chromatograms. After the background spectral features and effects of CO_2 on Sn signal were studied, a 100-pg mixture of TBT, TPT, TBTA, and DBTDA was used to determine SFC operating conditions. As shown in Figure 6a, only TBT and TPT are separated under initial conditions. TBTA and DBTDA were lost in the broadened peak shown just above background signal. This is probably caused by the nonpolar mobile phase. The mobile phase does not have enough solvent strength to efficiently partition and elute TBTA and DBTDA. This suggests that a modifier (such as methanol) to increase the solvent strength is needed for TBTA

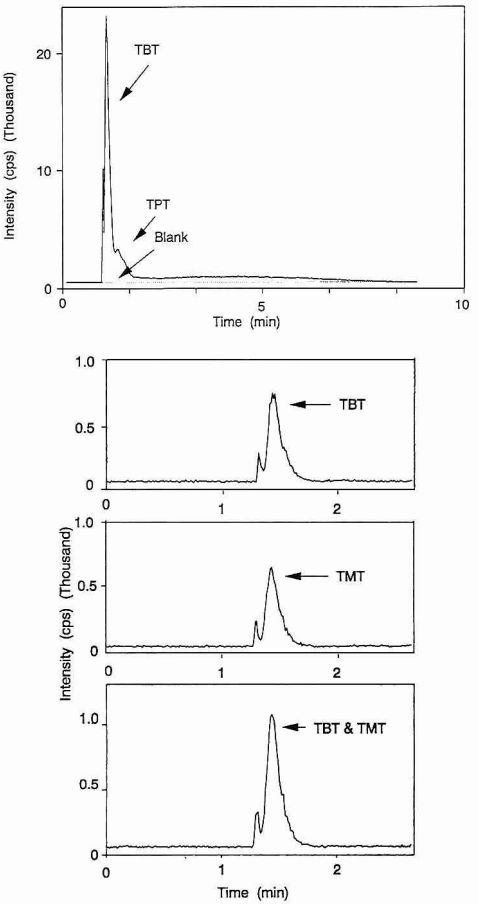

Figure 6. SFC/ICPMS chromatogram of organotin compounds (top to bottom): (a) tetrabutyltin, tetraphenyltin, and blank signal; (b) tetrabutyltin; (c) tetramethyltin; (d) mixture of tetrabutyltin and tetramethyltin.

and DBTDA elution. Earlier studies in this laboratory have shown excellent separation of tetra- and trialkyltins using a DB1701 stationary phase in GC studies (27). Figure 6b shows chromatograms of separate injections of TBT, TMT, and their mixture at 10 pg each. No separation was shown between these two organotin compounds. This indicates minimal interaction of these two compounds with the stationary phase. Since both TMT and TBT are nonpolar compounds with similar structures, a longer column or alternative stationary phase could potentially separate these two compounds. Therefore, TBT and TPT were chosen to study the effects of varying SFC parameters. Modifiers to increase solvent strength thereby separating TBTA and DBTDA as well as alternative column stationary phases to separate TMT and TBT are currently under investigation.

(*a*) *Effects of Isobaric Pressure in SFC.* Separate dependence on isobaric pressure conditions were studied by using a mix of 10 pg of tetrabutyltin and tetraphenyltin. The chromatograms for isobaric pressures of 80, 100, 125, and 150 atm are shown in Figure 7. At isobaric pressures below 100 atm, the TBT peaks were broadened and the TPT peaks were

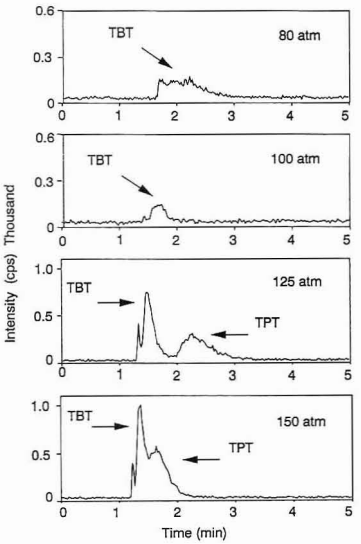

Figure 7. Separation of TBT and TPT at different isobaric pressures (top to bottom): (a) 80 atm; (b) 100 atm; (c) 125 atm; (d) 150 atm.

lost in the background or were not eluted. A high-pressure program was needed to clean the column before the next run. With the pressure at 125 atm, the TBT and TPT peaks were more well-defined, but the TPT peak was still broad. At a pressure of 150 atm, both peaks were much sharper but were not resolved. Clearly, the solvent strength (density or pressure program) in SFC plays an important role in this separation. In general, the solvent strength is increased with increasing density of the supercritical fluid. Related with this are the solubility properties and the viscosity of the mobile phase. The results obtained in this section indicate that it is not possible to get a good separation between TBT and TPT at constant pressure, so different pressure programs were evaluated.

(*b*) *Pressure Ramp.* A mixture of 10 pg of TBT and TPT was injected into the SFC system with the pressure program initially 100 atm and pressure ramp varied from 20 to 100 atm/min with a final pressure of 200 atm. Figure 8 clearly demonstrates the effect of the variation in the mobile-phase strength (density and solubility properties) when different ramps were used. As shown in Figure 8, the faster the pressure is ramped, the sharper the peaks and the shorter the retention time, but at the same time resolution is degraded. In order to recover resolution and at the same time maintain sharp peaks, a new set of chromatograms were run. In this case a hold time in the pressure program is introduced.

(*c*) *Hold Time in Pressure Program.* TBT and TPT (10 pg of each) were injected into the SFC system by using this program: initial pressure 100 atm with a hold time varying from 1 to 2 min, followed by a pressure ramp of 80 atm/min and final pressure of 200 atm. As shown in Figure 9, better separation was achieved as the initial hold time was increased. The TBT peak height decreased with a hold time increase. The TPT peak height started to decrease at an initial hold time longer than 1.5 min. At a 1-min hold time, the TBT peak height was larger than the TPT peak height. At a 1.5-min hold time, the TBT peak height was about equal to the TPT peak height. At a 2-min hold time, the TBT peak height was smaller than the TPT peak height. Again, this demonstrates

Table II. Analytical Figures of Merit for Organotins Using SFC/ICPMS

	tetra-butyltin	tetra-phenyltin
reproducibility, % (10-pg peak area)	1.52	3.97
absolute detn limit, pg [10 nL (100 ppb)]	0.035	0.043
linear range (1–1000 pg) (100 ppb to 100 ppm)	3	3
slope (log–log)	0.9938	1.0201
corrln coeff	0.99998	0.9999

Table III. Comparison of Absolute Detection Limits of Organotin Compounds (as Sn)

	detector	def	detn limit, pg	ref
SFC	ICPMS	3σ	0.035–0.043	this work
GC	MIPMS	(standard torch) 3σ	1–4	27
		(Ta injector) 3σ	0.09–0.35	27
HPLC	ICPMS	3σ	400–1000	28
	ICPMS	3σ	27–126	27
GC	mass spectrometer		200	35
	electron capture	2σ	31–85	36
	MIPAES	2σ	6.1	37
HPLC	AES	3σ	200–1700 ng	28

that the density program (or pressure program) has important consequences for the tin separation in SFC because of its effects on analyte interaction between the mobile and stationary phases. Simultaneously, it is necessary to consider that an increase in the hold time at a certain pressure (or density) also allows higher diffusion to occur and peak broadening is observed.

The chromatogram shown at the top of Figure 9 corresponds to the conditions listed in Table I and constitutes the best conditions found in this preliminary study. This chromatogram shows base line resolution and the peak width for TBT and TPT are about 30 s, similar to those observed in gas chromatography. However, additional investigation is necessary in order to separate TMT and TBT and to elute successfully TBTA and DBTDA.

(*d*) *Mobile Phase and Temperature Programming.* In this initial study only density programming was utilized, although the capability for mobile phase and temperature programming is available.

(4) Reproducibility and Analytical Figures of Merit. Six replicate 10-pg TBT and TPT mixtures were injected. The peak area precision of injections for TBT and TPT were 1.52% and 3.97%, respectively. The detection limits and linear ranges of TBT and TPT are listed in Table II. Calculation of absolute detection limits is based on 3 times the standard deviation of background for five replicate 1-pg injections (100 ppb concentration, 10 nL). The absolute detection limits for TBT and TPT are 0.035 and 0.043 pg, respectively. The linear ranges are over 3 orders of magnitude (100 ppb to 100 ppm or 1 pg to 1 ng). To show the detectability with SFC/ICPMS, Figure 10 gives a chromatogram of a 1-pg mixture of TBT and TPT. Comparative detection limits with other techniques reported in the literature are listed in Table III. The absolute detection limits are lower than HPLC/ICPMS (*28*, *29*). In part this is because of the increased sample transport efficiency with SFC. Also, gaseous samples are more efficiently ionized in plasmas. The absolute detection limits of Sn compounds are also lower in comparison with GC/MIPMS (*27*).

(5) Time-Resolved Acquisition (TRA) Scan for Isotope Determination. One of the potential attractive features of

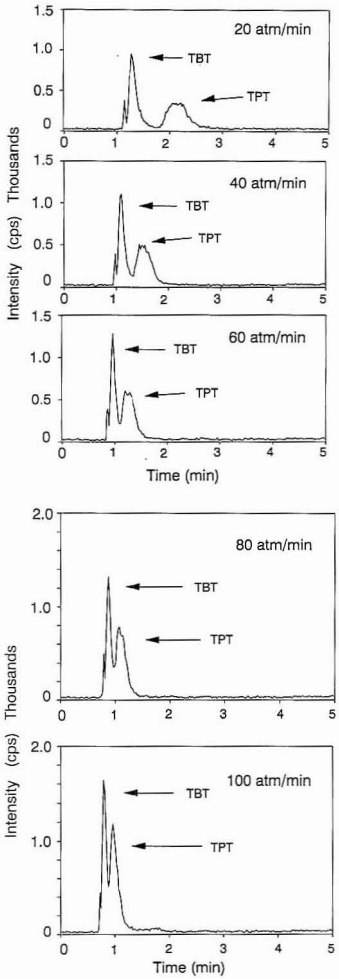

Figure 8. Effects of different pressure ramps on separation (top to bottom): (a) 20 atm/min; (b) 40 atm/min; (c) 60 atm/min; (d) 80 atm/min; (e) 100 atm/min. For these runs initial and final pressures were 100 and 200 atm, respectively.

ICPMS is the possibility of multielement chromatograms by monitoring different masses for each element in a sample plus different isotopes of the same element. Figure 11 shows a TRA scan of 100 pg of TBT and TPT. The determination at different isotope masses is based upon three continuous runs, which are listed in Figure 11. The experimental isotope ratios of 120 to 118 and 120 to 116 are 1.34 and 2.27, respectively. The actual isotope ratios are 1.37 and 2.32, respectively. The errors from the actual were 2.6% and 1.9%, respectively, demonstrating the potential for multielement chromatograms and isotope ratio information available at ultratrace levels with SFC/ICPMS.

CONCLUSIONS

Supercritical fluid chromatography/inductively coupled plasma mass spectrometry provides a new alternative for ultratrace organometallic analysis. This first study coupling these excellent techniques demonstrates the separation and

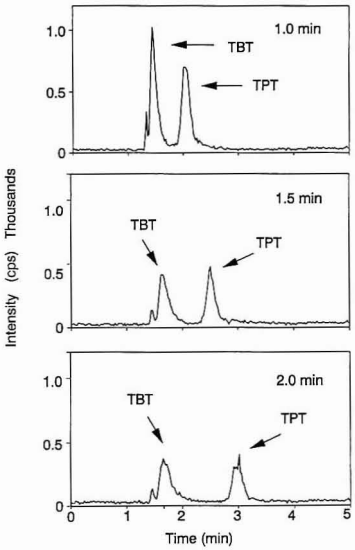

Figure 9. Effects of different hold times at an initial pressure of 100 atm, followed by a ramp of 80 atm/min until it reaches a final pressure of 200 atm (top to bottom): (a) 1 min; (b) 1.5 min; (c) 2 min.

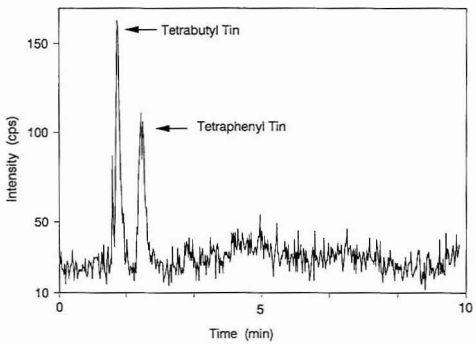

Figure 10. SFC/ICPMS chromatogram for a 1-pg injection of tetrabutyltin and tetraphenyltin.

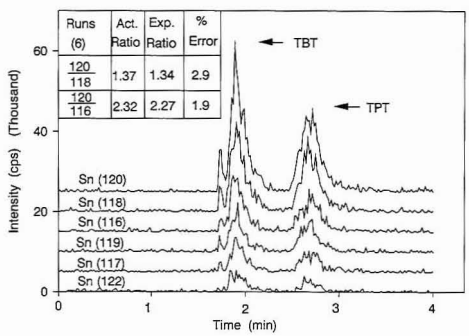

Figure 11. Time-resolved acquisition (TRA) scan of SFC chromatograms at different Sn isotopes, illustrating the ability to do multimass monitoring for mass-selective chromatograms for a single injection.

detection of organotin compounds. The absolute detection limits obtained by SFC/ICPMS are at the subpicogram level with linear ranges over 3 orders of magnitude. At the present time, TBTA, DBTDA, and TMT have not been determined because of insufficient solvent strength to elute these two compounds or strong interaction with the stationary phase. However, this can be improved by increasing the solvent strength, adding the modifier to increase the solvent polarity, and using an alternative stationary phase or a longer column. At its current stage, the SFC parameters and the ICPMS operating conditions have not been totally optimized. More optimization of SFC is needed through temperature programming, pressure programming, modifiers and/or alternative stationary phases. This new approach shows high potential for simultaneously determining complex mixtures of organometallic pollutants (such as As, Pb, Sn, Hg) and non-metal compounds (including halogenated organic compounds such as pesticides) at ultratrace levels.

ACKNOWLEDGMENT

We thank Ms. Lisa Mika for helping with the initial SFC system installation.

Registry No. TBT, 1461-25-2; TPT, 595-90-4.

LITERATURE CITED

(1) Lipsky, S. R.; Duffy, M. L. *LC-GC* **1986**, *4*, 898–906.
(2) Davies, I. L.; Raynor, M. W.; Kithinji, J. P.; Bartle, K. D.; Williams, P. T.; Andrews, G. E. *Anal. Chem.* **1988**, *60*, 683A–702A.
(3) White, C. M.; Houck, R. K. *HRC & CC, J. High Resolut. Chromatogr. Chromatogr. Commun.* **1986**, *9*, 3–16.
(4) Ashraf-Khorassani, M.; Hellgeth, J. W.; Taylor, L. T. *Anal. Chem.* **1987**, *59*, 2077–2081.
(5) Smith, R. D.; Yonker, C. R.; Fulton, J. L.; Tingey, J. M. *J. Supercrit. Fluids* **1988**, *1*, 7–14.
(6) Luffer, D. R.; Galante, L. J.; David, P. A.; Novotny, M.; Hieftje, G. M. *Anal. Chem.* **1988**, *60*, 1365–1369.
(7) Galante, L. J.; Selby, M.; Luffer, D. R.; Hieftje; G. M.; Novotny, M. *Anal. Chem.* **1988**, *60*, 1370–1376.
(8) Motley, C. B.; Ashraf-Khorassani, M.; Long, G. L. *Appl. Spectrosc.* **1989**, *43*, 737–741.
(9) Skelton, R. J.; Farnsworth, P. B., Jr.; Markides, K. E.; Lee, M. L. *Anal. Chem.* **1989**, *61*, 1815–1821.
(10) Fujimoto, C.; Yoshida, H.; Jinno, K. *J. Chromatogr.* **1987**, *411*, 213–220.
(11) Olesik, J. W.; Olesik, S. V. *Anal. Chem.* **1987**, *59*, 796–799.
(12) Li, S. F. Y. *At. Spectrosc.* **1989**, *10*, 66–67.
(13) Hieftje, G. M.; Vickers, G. H. *Anal. Chim. Acta* **1989**, *216*, 1–24.
(14) Douglas, D. J.; Houk, R. S. *Prog. Anal. At. Spectrosc.* **1985**, *8*, 1–18.
(15) Houk, R. S.; Thompson, J. J. *Mass Spectrom. Rev.* **1988**, *7* (4), 425–461.
(16) Houk, R. S. *Anal. Chem.* **1986**, *58*, 97A–105A.
(17) Date, A. R.; Gray, A. L. *Spectrochim. Acta, Part B* **1983**, *38*, 29–37.
(18) Blair, W. R.; Olson, G. J.; Brinckman, F. E.; Paule, R. C.; Becker, D. A. *An International Butyltin Measurement, Methods, Intercomparison, Sample Preparation and Results of Analysis*; U.S. Department of Commerce: Gaithersburg, MD, 1986.
(19) Thompson, J. A. J.; Sheffer, G. M.; Pierce, R. C.; Chau, Y. K.; Cooney, J. J.; Cullen, W. R.; Maguire, R. J. *Organotin Compounds in the Aquatic Environment: Scientific Criteria for Assessing Effects on Environmental Quality*; National Research Council: Ottawa, Canada, 1985.
(20) Chau, Y. K.; Wong, P. T. S.; Bengert, G. A. *Anal. Chem.* **1982**, *54*, 246–249.
(21) Muller, M. D. *Anal. Chem.* **1987**, *59*, 617–623.
(22) Kenis, P.; Zirino, A. *Anal. Chim. Acta* **1983**, *149*, 157–166.
(23) Arakawa, Y.; Wada, O.; Manabe, M. *Anal. Chem.* **1983**, *55*, 1901–1904.
(24) Langseth, W. *Talanta* **1984**, *31*, 975–978.
(25) Yu, T.-H.; Arakawa, Y. *J. Chromatogr.* **1983**, *258*, 189–194.
(26) Jewett, K. L.; Brinckman, F. E. *J. Chromatogr. Sci.* **1981**, *19*, 583–593.
(27) Suyani, H.; Creed, J. T.; Caruso, J. A.; Satzger, R. D. *J. Anal. At. Spectrom.* **1989**, *4*, 777–782.
(28) Suyani, H.; Creed, J. T.; Davidson, T.; Caruso, J. A. *J. Chromatogr. Sci.* **1989**, *27*, 139–143.
(29) Suyani, H.; Heitkemper, D.; Creed, J. T.; Caruso, J. A. *Appl. Spectrosc.* **1989**, *43*, 962–967.
(30) Koehler, J.; Rose, A.; Schomburg, G. *HRC & CC, J. High Resolut. Chromatogr. Chromatogr. Commun.* **1988**, *11* (2), 191–197.
(31) Guthrie, E. J.; Schwartz, H. E. *J. Chromatogr. Sci.* **1986**, *24*, 236–241.
(32) Bally, R. W.; Cramers, C. A. *HRC & CC, J. High Resolut. Chromatogr. Chromatogr. Commun.* **1986**, *9* (11), 626–632.
(33) Porter, N. L.; Richter, B. E.; Bornhop, D. J.; Later, D. W.; Beyerlein, F. H. *HRC & CC, J. High Resolut. Chromatogr. Chromatogr. Commun.* **1987**, *10*, 477–478.
(34) Schwartz, H. E.; Barthel, P. J.; Moring, S. E. *HRC & CC, J. High Resolut. Chromatogr. Chromatogr. Commun.* **1987**, *10* (12), 668–669.
(35) Mainema, H. A.; Burger-Wirsma, T.; Versluis-de Haan, J. D.; Gevers, E. C. *Environ. Sci. Technol.* **1978**, *12*, 288–293.
(36) Hattory, Y.; Korbayashi, A.; Takemoto, S.; Takami, K.; Juge, Y., Sugimac, A. Nakamoto, M. *J. Chromatogr.* **1984**, *259*, 315–341.
(37) Estes, S. A.; Uden, P. C.; Barnes, R. M. *Anal. Chem.* **1981**, *53*, 1829–1837.

RECEIVED for review December 19, 1990. Accepted April 25, 1991. We are grateful to the National Institute of Environmental Health Sciences for providing research support through Grants ES-03221 and ES-04908. We are also grateful to the NIH-BRS shared Instrument Program for providing the VG PlasmaQuad through Grant S10RR02714. VG Elemental and Lee Scientific are credited for providing partial instrumentation support.

CORRESPONDENCE

Signal Enhancement of Elements Due to the Presence of Carbon-Containing Compounds in Inductively Coupled Plasma Mass Spectrometry

Sir: The use of an inductively coupled plasma (ICP) as an ionization source for mass spectrometry (MS) has gained general acceptance. The advantages of ICPMS are well-known: low limits of detection and quasi simultaneous multielement determination with the possibility of measuring isotopic abundance. The main limitation is the observation of isobaric interferences, mostly due to the formation of molecular compounds (*1*), in particular, oxides (*2*). The mass of the matrix has also been reported (*3*) as a possible source of analyte interferences, probably caused by ion transport in the mass spectrometer.

We surmised the possible role of organic compounds as signal enhancers for some elements during analysis of biological samples by ICPMS. In this work, we will report some preliminary investigations on this enhancement effect using glycerol and glucose as the organic matrix. The results will be compared to those previously published for optical spectrometry.

EXPERIMENTAL SECTION

The system has been described in detail in a previous work (*4*). It consisted of a 56-MHz tuned line ICP generator and a modified Nermag R 1010 C mass spectrometer. A Meinhard nebulizer associated with a double-pass spray chamber was used. The operating parameters were power of 1.2 kW, outer gas flow rate of 12 L min^{-1}, and carrier gas flow rate of 0.85 L min^{-1}. Mass flow controllers (Brooks Models 5878/5850) were used to measure both flow rates. The detection was performed by means of an electron multiplier working in analog mode.

RESULTS

The effect of increasing glycerol concentration on some ion signals is summarized in Figure 1. It can be seen that the enhancement for Hg can reach 600% for a glycerol concentration of 1 mol L^{-1}. Similarly, As and Au showed enhancements of 240% and 325%, respectively. Other elements exhibiting the same effect were Se (250%) and Te (190%). This behavior was in contrast to other elements such as Bi, Co, Eu, Ho, I, In, La, Mo, Ni, Pb, Pt, Sn, Sr, Tl, and U where the change in the signal was between 90% and 110%. A similar effect on the ion signals was observed when working with glucose. At this stage, it was thought that the change in the signal was not due to any variation in the nebulizer efficiency but to a change in the ion formation in the plasma due to the presence of carbon. To confirm this assumption, a similar experiment was carried out with methane in the argon carrier gas. Concentrations of methane up to 6% (v/v) were added to the carrier gas flow. The variation in the responses for As, Se, Te, Eu, and Pb is shown in Figure 2. It can be seen that the enhancement was observed for the same elements as for the addition of glucose or glycerol. The effect is therefore linked to the presence of carbon in the matrix. Moreover, this effect seemed to be relatively independent of the concentration of the analyte because the calibration curves for As, for example (Figure 3), are linear for deionized water and for two concentrations of glycerol.

DISCUSSION

Additions of methane and propane have already been used in ICP atomic emission spectrometry (AES) (*5*, *6*) and atomic fluorescence spectrometry (AFS) (*7*, *8*). The purpose of the addition of these gases was to reduce the formation of the refractory oxide by producing CO, with the following proposed reaction:

$$MO + C \rightarrow M + CO$$

Alder and Mermet (*5*) used a 6-kW ICP. At this high power, no LaO emission was observed with pure argon and the addition of CH_4 did not modify the La signal. Long and Winefordner (*7*) used a torch configuration modified for AFS with an extended tail. They used a low power (500–700 W), so the results were very poor for elements forming refractory oxides or monohydroxides such as Mo and Ca, respectively. However, the addition of propane significantly enhanced the fluorescence signal of Ca and Mo. Demers (*8*) used the same torch configuration and found that a moderate addition of propane (10 mL min^{-1}) reduced the formation of oxides with a dissociation energy between 4 and 6 eV. A larger concentration of propane (50 mL min^{-1}) was needed for the dissociation of oxides with an energy greater than 6 eV. Elements such as Mo, Ta, Ti, and V could only be determined in the presence of propane. Walters et al. (*9*), using a saturated absorption method for measuring the spatial distribution of absorbing species, indicated that a change of the Sr population was observed at the edge of the central channel when propane was added. This was attributed to the reaction of carbon radicals with the Sr oxide. In a recent paper (*6*), Long and Bolton studied the effects of the addition of propane in ICPAES. They also found that the addition of propane reduced the formation of LaO. This reduction in oxide formation can also be applied to elements such as Al and Cr. However, they observed a different result for Ca, where the decrease in the possible formation of CaO or CaOH did not correspond to an increase in the Ca signal. This is in marked contrast to the results obtained in AFS. It should be noted that AES and AFS do not produce the same type of information, as AES deals with excited states and AFS with ground states.

It does not seem that the results mentioned above can be applied to those obtained in this work. Elements such as La, Eu, and Ho exhibit the most refractory oxides and should be strongly affected by the presence of methane, if the oxide reduction is the main process. In fact, the signals from these ions were not markedly modified. An alternative explanation of the depression observed for some elements, proposed by Long and Bolton (*6*), was the formation of stable metal carbides. However, no depression effects were observed for elements such as Mo. They also suggested that a change in the population of excited states was obtained by collisions with C or carbon radicals. However, this should not drastically affect the concentration of the ions in the ground state.

As it does not seem that the enhancement effect is linked to the chemical properties of the elements, we have investi-

0003-2700/91/0363-1497$02.50/0 © 1991 American Chemical Society

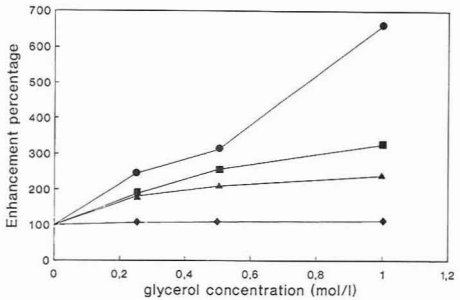

Figure 1. Enhancement percentage for selected elements as a function of the glycerol concentration: (●) Hg; (■) Au; (▲) As; (♦) La.

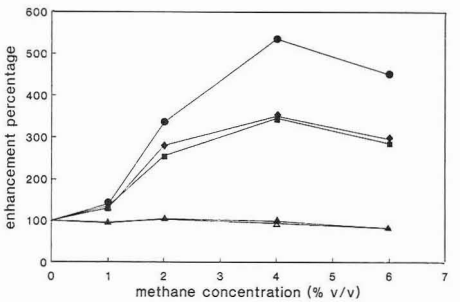

Figure 2. Enhancement percentage for selected elements as a function of the methane concentration in the carrier gas flow: (●) As; (♦) Te; (■) Se; (▲) Eu; (△) Pb.

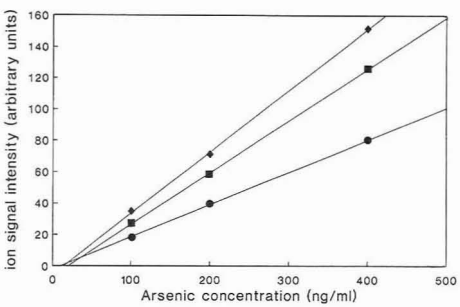

Figure 3. Calibration curves of As for several glycerol concentrations: (●) deionized water; (■) glycerol 0.25 mol L^{-1}; (♦) glycerol 0.5 mol L^{-1}.

gated the influence of the ionization energy. A plot of the enhancement percentage for glycerol at 1 mol L^{-1} as a function of the ionization energy for each element is given in Figure 4. There is obviously an effect between 9 and 11 eV. Iodine (10.44 eV) is the only noticeable exception in this range. It should be noted that Br (11.30 eV) also does not exhibit an enhancement effect. Clearly, the addition of organic compounds modifies the ionization equilibrium over a limited range of energy. It must be noted that the ionization energy of C (11.20 eV) is slightly above the upper limit.

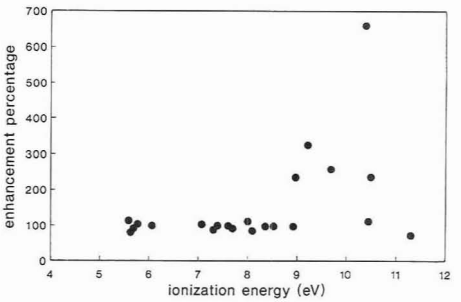

Figure 4. Enhancement percentage as a function of the ionization energy.

A consequence of this difference in response of each element, is the difficulty in selecting an internal standard. In previous work (*4*), Eu was selected as an internal standard. The use of Eu is adequate with most elements but not with those which exhibit an enhancement effect.

The use of MS as the detection method for an ICP allows access to information on the population of the ion ground state in contrast with AES, which concerns ion excited states. This probably explains why such a matrix effect has not been reported for ICPAES.

LITERATURE CITED

(1) Tan, S. H.; Horlick, G. *Appl. Spectrosc.* **1986**, *40*, 445–460.
(2) Vaughan, M. A.; Horlick, G. *Appl. Spectrosc.* **1986**, *40*, 434–445.
(3) Tan, S. H.; Horlick, G. J. *Anal. At. Spectrom.* **1987**, *2*, 765–772.
(4) Allain, P.; Mauras, Y.; Dougé, C.; Jaunault, L.; Delaporte, T.; Beaugrand, C. *Analyst* **1990**, *115*, 813–815.
(5) Alder, J. F.; Mermet, J. M. *Spectrochim. Acta, Part B* **1973**, *23*, 421–433.
(6) Long, G. L.; Bolton, J. S. *Spectrochim. Acta, Part B* **1987**, *42*, 581–589.
(7) Long, G. L.; Winefordner, J. D. *Appl. Spectrosc.* **1984**, *38*, 563–567.
(8) Demers, D. R. *Spectrochim. Acta, Part B* **1985**, *40*, 93–105.
(9) Walters, P. E.; Long, G. L.; Winefordner, J. D. *Spectrochim. Acta, Part B* **1984**, *39*, 69–76.

Pierre Allain*
Laurent Jaunault
Yves Mauras

Laboratoire de Pharmacologie
Centre Hospitalier Universitaire
49033 Angers Cedex, France

Jean-Michel Mermet

Laboratoire des Sciences Analytiques
Bat. 308, Université Claude Bernard-Lyon I
69622 Villeurbanne Cedex, France

Thierry Delaporte

Delsi-Nermag
98ter, Boulevard Heloise
95100 Argenteuil, France

RECEIVED for review November 21, 1990. Accepted March 12, 1991.

TECHNICAL NOTES

On-Detector Injector for Flow Injection Amperometric Measurements. The Wall-Jet/Thin-Layer Cell

Joseph Wang* and Liang Chen[1]

Department of Chemistry, New Mexico State University, Las Cruces, New Mexico 88003

INTRODUCTION

Because of its attractive features, flow injection analysis (FIA) has received considerable attention for high-speed analysis of discrete samples (*1*, *2*). The technique involves the injection of small sample volumes into a carrier stream that transports the sample zone toward a detector. The detector is normally placed at the end of the system (Figure 1A). However, with the growing trend toward miniaturization and the development of active detectors, several groups have recently demonstrated the advantages of placing the detector within the injection valve. Hence, on-valve optical monitoring of extraction processes (*3*) or amperometric biosensing of glucose (*4*) have been successfully accomplished. Other efforts have focused on the coupling of the separation and detection functions in FIA systems (*5*).

Reported here is a novel approach based on placing the sample injector directly within a common electrochemical detector. Electrochemical detectors account for one-third of the detectors used in FIA (*5*). Several cells, originally developed for liquid chromatography/electrochemistry (LC/EC), have been employed in FIA, with the thin-layer (*6*) and wall-jet (*7*) configurations representing the most popular ones. however, considering the different requirements and conditions of FIA and LC systems and the growing popularity of FIA, it is desirable to design new detectors that address the specific needs of FIA systems.

The injector/detector described in the present work separates the sample and carrier introduction functions within the detector body (Figure 1B). This is accomplished with the carrier stream flowing parallel to the working electrode while the sample striking its surface perpendicularly. For this purpose, a conventional (commercial) thin-layer cell is modified for accommodating the sample introduction opposite the working electrode (Figure 2). Samples are reproducibly injected, with a microsyringe, through a rubber septum placed in a cavity above a nozzle inlet. (Such gas chromatographic like injection is facilitated by the low pressures of FIA systems.) The resulting hybrid wall-jet/thin-layer injection/detector unit exhibits a very attractive FIA performance, the characteristics of which are explored and illustrated in the following sections.

EXPERIMENTAL SECTION

Apparatus. The wall-jet/thin-layer cell design is shown in Figure 2. A "homemade" upper block was made of Plexiglas to combine with a commercial lower block of a thin-layer detector (Model TL-5, Bioanalytical Systems (BAS)), containing the glassy carbon working electrode and the carrier solution inlet and outlet. A hole (3 mm narrowed to 0.5 mm) was drilled through the center of the Plexiglas body to accommodate the rubber-diaphragm injector and to serve as inlet nozzle through which samples impinge perpendicularly onto the working electrode. Teflon spacers maintained the channel width at 175 μm. The reference and auxiliary electordes were located in a downstream compartment (Model RC-2A, BAS). All potentials were reported versus the Ag/AgCl reference electrode (Model RE-1, BAS). Samples (usually 10 μL) were injected with a Hamilton microsyringe (Model 705). The carrier reservoir (a 400-mL Nalgene beaker) was connected to the cell through Teflon tubing. Flow of the carrier solution was maintained by gravity. The FIA system and thin-layer cell, used in comparison studies, consisted of carrier and sample reservoirs, interconnecting tubing, a Rheodyne Model 5020 injection valve, and a Model TL-5 (BAS) detector. The detector was placed 6 cm from the valve.

Electrochemical detection was performed in the amperometric mode with an EG&G PAR Model 173 potentiostat/galvanostat, the output of which was displayed on a Houston Omniscribe strip-chart recorder.

Reagents. All solutions were prepared with double-distilled water. The chemicals used were the following: caffeic acid, glucose (Sigma), and potassium ferrocyanide (Baker). Glucose oxidase (Type X-S, EC 1.1.3.4) was also purchased from Sigma. The poly(ester–sulfonic acid) polymer (Eastman AQ-55D) was obtained from Eastman Kodak Co. Supporting electrolytes were 0.05 M potassium nitrate and 0.05 M phosphate buffer (pH 6.5).

Procedure. In most experiments, the polished glassy carbon electrode was potentiostated at +0.5 V and transient currents were allowed to decay. Glucose measurements were carried out at +0.95 V. These measurements were performed after covering the surface with a 10-μL drop of the mixed polymer/glucose oxidase solution (1.4% polymer/1 mg/mL enzyme). The coatings were then dried for 15 min with a heat gun, held 40 cm above the surface.

RESULTS AND DISCUSSION

The attractive features of the hybrid wall-jet/thin-layer injector/detector are best illustrated when comparing its FIA response with that of a conventional thin-layer cell. Such comparison is shown in Figure 3, from the amperometric peaks for 20 μL ferrocyanide solutions; both operations employed the *same* working electrode under otherwise identical conditions. The negligible dispersion, associated with the short residence time of the sample in the wall-jet/thin-layer detector, results in a very fast response (b). The baseline peak widths are 6 and 4 s (at 0.6 (A) and 1.1 (B) mL/min, respectively), as compared to 21 and 14 s at the thin-layer cell (a). Even much shorter response times can be obtained by coupling smaller sample volumes with faster carrier flow rates. For example, with 5 μL and 1.9 mL/min, the baseline peak width is only 0.7 s (c). Such significantly short response times of the integrated unit correspond to extremely high injection rates of more than 3600 samples/h. The fast response indicates that injected samples are rapidly replenished (and "pushed") from the surface by the flow-by carrier solution. Note also that the sensitivity of the wall-jet/thin-layer detector compares favorable with that of the thin-layer one (ca. 45% higher). The latter is attributed to the convection "pulse" (associated with the injection action), which leads to further reduction of the diffusion-layer thickness.

The high speed and sensitivity of the wall-jet/thin-layer detector are coupled with excellent reproducibility and absence of carryover effects. These are illustrated from the series of

[1] Permanent address: Anhui University, Hefei, People's Republic of China.

0003-2700/91/0363-1499$02.50/0 © 1991 American Chemical Society

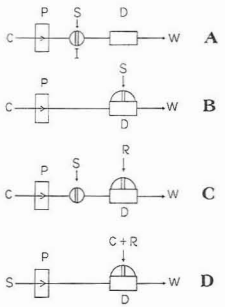

Figure 1. Configurations of different FIA systems. (A) Conventional FIA; (B) FIA with on-detector injector; (C) FIA with on-detector reagent introduction; (D) reversed FIA with on-detector carrier introduction.

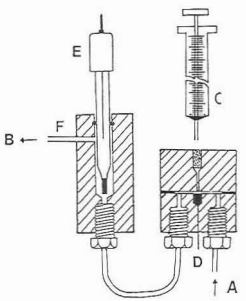

Figure 2. Wall-jet/thin-layer detector. (A) Carrier solution inlet; (B) solution outlet; (C) sample introduction; (D) working electrode; (E) reference electrode; (F) auxiliary electrode.

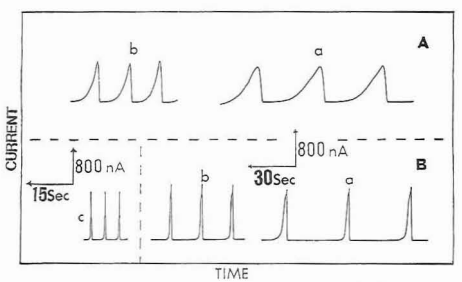

Figure 3. Flow injection current–time profiles for 3 × 10^{-4} M ferrocyanide at the thin-layer (A) and wall-jet/thin-layer (B) detectors: sample volume, 20 (a, b) and 5 (c) μL; operating potential, +0.5 V; flow rate, 0.6 (a), 1.1 (b), and 1.9 (c) mL/min; carrier and electrolyte, 0.05 M KNO_3.

sequential injections of caffeic acid solutions differing in concentration and from 54 repetitive measurements of a 3 × 10^{-4} M ferrocyanide solution (Figure 4, A and B, respectively). The former exhibits no observable carryover, while the later yields a relative standard deviation of 1.7%. Note (again) the extremely sharp response peaks. The high precision indicates that the microsyringe offers reproducible sample introduction. The reproducibility, and overall performance, may be further improved through automation.

Response characteristics resulting from the unique coupling of flow-by (carrier) and flow-onto (sample) have been examined. Figure 5 shows the effect of several experimental variables upon the response of the wall-jet/thin-layer cell. The

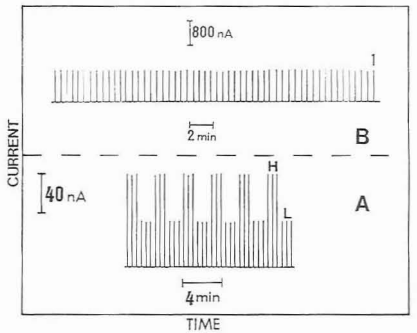

Figure 4. Repetitive injections with the wall-jet/thin-layer detector. (A) Carryover between sequential samples of 1 × 10^{-5} M (L) and 2 × 10^{-5} M (H) caffeic acid. (B) Precision for replicate injections of a 3 × 10^{-4} M ferrocyanide solution. Sample volume, 10 μL; other conditions, as in Figure 3B.

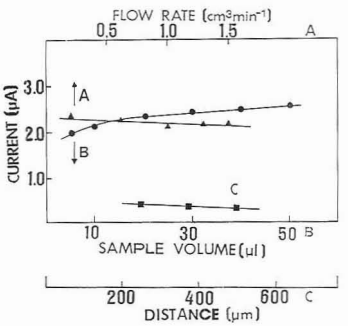

Figure 5. Dependence of the ferrocyanide peak current upon the carrier flow rate (A), sample volume (B), and inlet-electrode distance (C). Ferrocyanide concentration, 3 × 10^{-4} M (A, B), 2 × 10^{-5} M (C). Sample volume, 10 μL; flow rate, 1.5 (B) and 1.3 (C) mL/min. Other conditions as in Figure 3B.

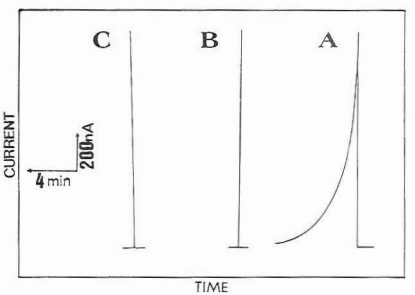

Figure 6. Flow injection peaks for 3 × 10^{-4} M ferrocyanide at carrier flow rates of 0 (A), 0.7 (B), and 1.5 (C) mL/min. Other conditions as in Figure 3B.

flow injection peaks are independent of the carrier flow rate (A), indicating that it is the jet emerging from the nozzle (i.e., the injection action) that governs the analyte flux at the surface. Such flow rate independence can be attractive to various FIA applications, as it minimizes the carrier consumption (without compromising the sensitivity) and offers high reproducibility (even when the flow rate fluctuates). The peak height increases slowly with increasing sample volume

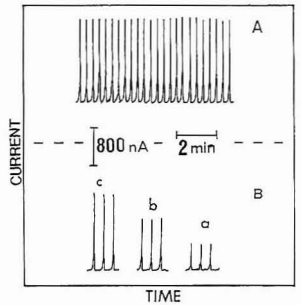

Figure 7. Flow injection peaks for glucose at the glucose oxidase wall-jet/thin-layer detector: (A) 6×10^{-3} M; (B) increasing concentrations (2–6) $\times 10^{-3}$ M (a–c). Sample volume, 10 μL; operating potential, +0.95 V; flow rate, 0.9 mL/min; carrier and electrolyte, 0.05 M phosphate buffer (pH 6.5).

(between 5 and 20 μL), after which it starts to level off (B). In addition, the peak decreases slowly as the inlet-electrode distance increases between 250 and 500 μm (C).

A unique situation occurs for a zero carrier flow rate (Figure 6). In accordance with the flow rate independence (reported in Figure 5), such a flow rate yields a peak current similar to that observed at higher flow rates (A versus B and C). However, in the absence of the carrier pushing action, the fast rise in the current is followed by a very slow decay (in a manner analogous to stopped-flow FIA experiments).

Repetitive injections of ferrocyanide solutions of increasing concentrations ($(1 - 6) \times 10^{-5}$ M) were used to estimate the linearity and detectability. The response was linear over the entire concentration range (slope, 2.61 μA/mM; intercept, 14 nA; correlation coefficient, 0.999 (not shown)). The signal-to-noise characteristics ($S/N = 3$) of the 1×10^{-5} M ferrocyanide peak indicated a detection limit of 7×10^{-7} M. Analogous measurements of caffeic acid (e.g., Figure 4A(L)) yielded a detection limit of 3×10^{-7} M.

The placement of the sample injector onto the detector is particularly attractive in connection with active detector surfaces. Highly specific enzyme electrodes, resulting from the judicious immobilization of biocatalysts onto the glassy carbon surface, represent such an opportunity. Figure 7 illustrates the performance of a glucose oxidase based wall-jet/thin-layer detector. The enzyme electrode responds rapidly and reproducibly to the dynamic changes in the glucose concentration. For the 24 repetitive injections (shown in B) the relative standard deviation is 1.2%. At least 240 glucose measurements can be made every hour at physiologically relevant concentrations. The enzyme immobilization was accompplished by incorporation within a Kodak-AQ poly(ester–sulfonic acid) film. Because of the additional (protection and permselective) functions offered by AQ polymers (*8*), such incorporation is extremely attractive for integrated injector/reactor/detector systems for FIA (which lack solution handling capability).

In conclusion, the on-detector injector has been demonstrated to be a very practical device, which addresses the trends toward integration and miniaturization of FIA systems. In addition to its ultrafast (flow-rate independent) response and high sensitivity, such a wall-jet/thin-layer configuration holds promise for performing other FIA procedures. In particular, the versatility and flexibility obtained by introducing the carrier and sample through different inlets (on the detector body) allows additional schemes. These may include on-detector reagent introduction (with minimum dispersion of the product, Figure 1C) or reversed FIA (with on-detector injection of the carrier into the flowing sample solution, Figure 1D). Such schemes should further minimize reagent consumption and enhance the sensitivity, in comparison to analogous FIA systems with separated injector and detector components (*1*, *9*). Stopped-flow, flow-reversal, and titrimetric procedures, performed at the surface, can also be envisioned. The separate control of the sample and carrier introduction should facilitate such schemes and may offer new FIA procedures. As such, the on-detector injection is much more versatile than on-valve detection. In addition, such modification of commercial flow cells offers greater convenience, simplicity, and reliability than the on-valve microelectrode detector (*4*). The concept of on-detector injector should be suitable for other (nonelectrochemical) detection schemes. A direct injection into a large optical (absorption) flow cell has already been reported (*10*).

Registry No. Eastman AQ-55D, 116326-12-6; glucose, 50-99-7.

LITERATURE CITED

(1) Ruzicka, J.; Hansen, H. E. *Flow Injection Analysis*; Wiley: New York, 1981.
(2) Christian, G.; Krull, I.; Tyson, J. *Anal. Chem.* **1990**, *62*, 455A.
(3) Canete, F.; Rios, A.; Luque de Castro, M. D.; Valcarcel, M. *Anal. Chem.* **1988**, *60*, 2354.
(4) Wang, J.; Li, R. *Anal. Chem.* **1990**, *62*, 2414.
(5) Valcarcel, M.; Luque de Castro, M. D. *Anal. Proc.* **1989**, *26*, 313.
(6) Kissinger, P. R. *J. Chem. Ed.* **1983**, *60*, 308.
(7) Fleet, B.; Little, C. J. *J. Chromatogr. Sci.* **1974**, *12*, 747.
(8) Wang, J.; Golden, T. *Anal. Chem.* **1989**, *61*, 1397.
(9) Johnson, K. S.; Petty, R. L. *Anal. Chem.* **1982**, *54*, 1185.
(10) Eswara Dutt, V. V. S.; Mottola, H. A. *Anal. Chem.* **1975**, *47*, 357.

RECEIVED for review December 18, 1990. Accepted April 8, 1991.

Application of Scanning Electrochemical Microscopy to Generation/Collection Experiments with High Collection Efficiency

Chongmok Lee, Juhyoun Kwak, and Fred C. Anson*

Arthur Amos Noyes Laboratories, Division of Chemistry and Chemical Engineering, California Institute of Technology, Pasadena, California 91125

The technique of scanning electrochemical microscopy (SECM) was introduced by Bard and co-workers (*1*) who have utilized it in a variety of experiments (*2*). The use of a microelectrode placed close to a substrate electrode to detect electroactive products generated at the latter, as described by Engstrom and co-workers (*3*, *4*), is one attractive application of the SECM technique (*1*). In previous studies, this type of generation/detection experiment has usually been carried out with the microelectrode used as the detector electrode (*1–5*). In the present study, a larger (100 μm diameter) substrate

* To whom correspondence should be addressed.

0003-2700/91/0363-1501$02.50/0 © 1991 American Chemical Society

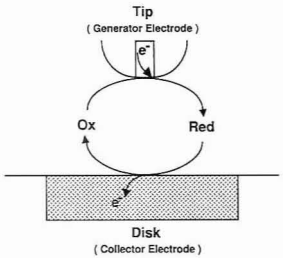

Figure 1. Schematic depiction of the electrode and mass-transfer processes occurring in generator/collector experiments with a microtip electrode positioned very close to a macrodisk electrode in a solution containing a redox couple, Ox/Red. In the experiments of this study, the tip and substrate electrode diameters were 11 and 100 μm, respectively. Both were mounted in glass shrouds.

electrode is used to detect and collect electrode reaction products generated at a microtip electrode positioned at various distances above the substrate electrode. The collection efficiency (in the sense employed for rotating ring–disk electrodes (*6*)) of such an arrangement is virtually 100% at easily achievable separation distances. The advantages of carrying out generation/collection experiments with the present apparatus are exemplified with some simple experimental systems. Comparisons with similar recent experiments in which arrays of microband electrodes are utilized (*7, 8*) are also provided.

EXPERIMENTAL SECTION

A carbon microtip electrode with a diameter of 11 μm and a platinum macrodisk electrode with a diameter of 100 μm were fabricated, mounted in glass, and polished according to previously described procedures (*1*). The carbon and platinum electrodes were employed as the tip and substrate, respectively, in SECM experiments. The miniature electrochemical cell and cell mounting were similar to those described in previous studies (*9*). The computer-controlled instrument employed in the SECM measurements was based on a previous design (*9*) with substitution of low-noise operational amplifiers in the bipotentiostat to increase the signal-to-noise ratio in the current measurements and a modification in the programs which control the x–y scanning of the tip electrode so that tip current–tip position data could be acquired and stored separately for scans in the forward or reverse direction across the substrate (*10*). The separation between the tip and substrate electrodes was determined by comparing the measured and calculated (*11*) tip current-separation distance data in solutions of $Ru(NH_3)_6^{3+}$ or $Fe(CN)_6^{3-}$.

RESULTS AND DISCUSSION

For experiments directed at maximizing the collection efficiency, i.e., the fraction of a reactant generated at a microtip electrode which diffuses to a nearby substrate electrode to be detected by electrochemical oxidation or reduction, one might expect the largest possible substrate electrode to be desirable. However, residual background currents increase with the area of the substrate electrode and substantial increases in signal-to-noise are obtained by limiting the size of the substrate electrode. We found a ratio of the diameters of the substrate to tip electrode of about 10 to provide both good collection efficiencies and acceptable signal-to-noise levels.

To carry out high collection efficiency experiments with substrate electrodes having diameters in the range of 100 μm, it is important to position the microtip electrode above the center of the substrate electrode, as depicted in Figure 1. The necessary positioning of the tip electrode is readily accomplished by employing the SECM instrument to scan the tip electrode across the substrate electrode in solutions containing a reversible, electroactive redox couple according to the protocols described by Kwak and Bard (*9*). In Figure 2 are shown results from some typical SECM scans in a solution of $Ru(NH_3)_6^{3+}$. The tip was held 11 μm above the plane containing the substrate electrode and scanned across a 200 μm by 200 μm region containing the substrate electrode. The potential of the tip electrode was held at −0.5 V vs SCE where the $Ru(NH_3)_6^{3+}$ was continuously reduced to $Ru(NH_3)_6^{2+}$, and the substrate electrode was maintained at 0.2 V so that any $Ru(NH_3)_6^{2+}$ reaching it was oxidized. Very similar behavior resulted when $Fe(CN)_6^{3-}$ was employed as the reactant with the tip and substrate potentials set at −0.2 and 0.5 V vs SCE, respectively.

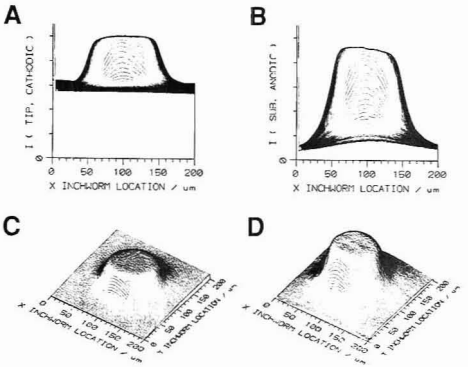

Figure 2. Images of the 100-μm platinum substrate electrode obtained by scanning the 11-μm carbon tip electrode at 10 μm s^{-1} over the substrate in a solution of 5 mM $Ru(NH_3)_6^{3+}$ in 0.1 M K_2SO_4. The distance between the substrate and the tip when it was centered over the substrate was 11 μm. The tip and substrate potentials were −0.5 and 0.2 V, respectively. The images in (A) and (C) were obtained from the tip current; those in (B) and (D), from the substrate current. (A) and (B) are cross-sectional views; (C) and (D) are three-dimensional views. The tip currents in (A) range from 5.4 to 10.0 nA. The substrate currents in (B) range from −0.7 to −9.4 nA. The tic marks on the vertical axis are separated by 2 nA. When the tip was retracted to a position far (>300 μm) from the substrate, the tip and substrate currents were 6.8 and ∼0 nA, respectively. (Evaporation of the solution during the course of the experiments (5 h) increased the final tip current to 8.1 nA.)

In Figure 2A the current at the tip electrode at each value of x is shown for various values of y with $Ru(NH_3)_6^{3+/2+}$ as the active redox couple. The same data are displayed in a three-dimensional format in Figure 2C. The position of the substrate electrode is clearly defined, and the values of x and y needed to position the tip above the center of the substrate are easily located. The image benefits from the combination of positive and negative feedback (*11, 12*), which enhances the tip currents when the tip is above the conducting substrate electrode and suppresses the tip current when the tip is above the insulating glass shroud (*11*).

The images of the substrate electrode can also be obtained by measuring the current at the substrate as the tip electrode is scanned. The results of this mode of operation are shown in Figure 2B,D. The substrate current is essentially zero until the tip approaches the substrate electrode, which means that the relative changes in the current at the substrate electrode as the tip passes over it are larger than those at the tip electrode where the reduction of $Ru(NH_3)_6^{3+}$ proceeds at all tip positions.

It proved important to limit the scanning rates employed in acquiring the images from substrate currents (Figure 2B,D) to values low enough for the currents measured to approach their steady-state values. For example, images obtained by monitoring substrate currents while the tip was scanned at

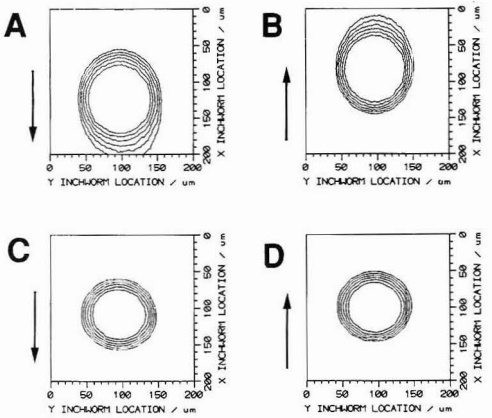

Figure 3. Current contour maps resulting from scans of the 100 μm diameter platinum-disk electrode by SECM. The experimental conditions were the same as those in Figure 2 except that the tip was positioned to be 30 μm above the center of the platinum disk and was scanned at 50 μm s^{-1}. (A, B) Scan in "forward" and "reverse" direction while recording the tip currents, which vary between ca. 6.8 and 7.0 nA, for the six contours shown; (C, D) Repeat of A and B while recording the disk currents, which vary between −4.5 and −5.7 nA, for the six contours shown.

50 μm s^{-1} portrayed an apparently inclined surface with the direction of the inclination depending on the direction of the scan. By contrast, the images in Figure 2A,C, obtained with a tip scanning rate of 10 μm s^{-1}, were independent of the scan direction and closely resembled the images obtained from tip current measurements at both scanning rates.

The current sensitivity and low noise level of the SECM instrument employed in this study permitted some subtle effects to be observed. For example, in Figure 3 are shown a set of isocurrent contours obtained for the tip and substrate electrodes during scans with a separation distance (30 μm) greater than that employed in Figure 2. The asymmetric shape of the pattern obtained for the tip currents (Figure 3A,B) allowed the direction in which the tip was scanned to be established by inspection. The increased separation between the isocurrent lines that results as the tip is moved from positions over the conducting substrate to positions over the insulating glass shroud results from the interplay between the rate of relaxation of the concentration gradients provoked by the crossing of the conductor/insulation interface and the rate at which the tip is scanned. The asymmetry is diminished as the scan rate or the separation distance is decreased, as was observed in a previous study (*12*). The absence of corresponding asymmetry in the isocurrent contours for the substrate electrode (Figure 3C,D) shows that the substrate currents relax more rapidly than do those at the tip electrode at the separation distance employed. The difference in relaxation times reflects the way in which the layer between the tip and substrate, which is depleted of reactant while the tip is above the insulating glass shroud, is repopulated with reactant as the tip crosses the glass/platinum boundary. Reactant generated at the substrate must diffuse to the vicinity of the tip to establish a new steady-state concentration profile, and this process proceeds less rapidly than the steady-state profile is generated at the substrate electrode.

In attempting to position a microtip electrode over the center of a small substrate electrode it is desirable to avoid conditions (i.e., large separation distances and high scan rates) that give rise to patterns such as those in Figure 3A,B in order to avoid misjudgements about the true center of the substrate.

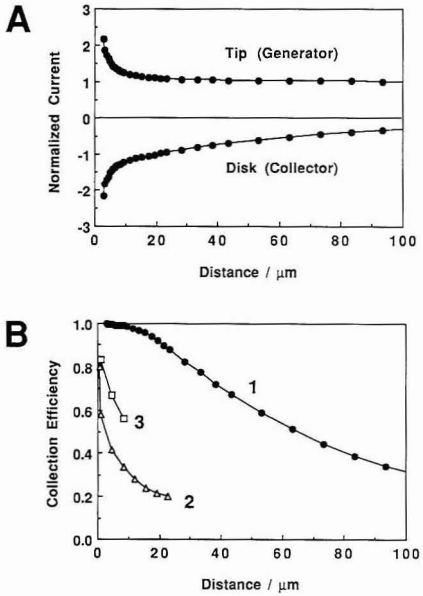

Figure 4. Generation/collection measurements with the 11 μm diameter carbon-fiber tip electrode positioned above the center of the 100-μm platinum-disk collector electrode. (A) Tip and disk currents as a function of the distance between the two electrodes. Both currents are normalized with respect to the tip current when the separation distance is large (>300 μm). Tip and disk potentials were −0.2 and 0.5 V vs SCE, respectively. The test solution was 5 mM $Fe(CN)_6^{3-}$ in 0.1 M KCl–0.005 M HCl. (B). Collection efficiencies (i.e., disk current/tip current) as a function of separation distance: (1) the system from (A); single (2) or a pair (3) of microband collector electrodes flanking a microband generator electrode (data taken from ref 8). For (2) and (3) the distance is the gap separating the band electrodes.

Positioning by means of the pattern of substrate current contours appears to be preferable in such circumstances. However, we found it difficult to obtain such clear images if much larger substrate electrodes (e.g., 1 mm diameter) were employed because of larger contributions to the substrate current from background or "leakage" currents. Fortunately, it was not necessary to employ larger substrate electrodes in order to obtain high collection efficiencies.

Collection Efficiency Measurements. Once the tip (generator) electrode was positioned over the center of the substrate (collector) electrode, it was of interest to determine how the collection efficiency (as measured by the ratio of substrate current to tip current) varied with the distance separating the tip and substrate. In Figure 4A are plotted the tip and substrate currents (normalized with respect to the tip current obtained when the separation distance is large enough to render the presence of the substrate electrode negligible) vs the distance between the two electrodes. The solution contained $Fe(CN)_6^{3-}$, and the potential of the tip was set at a value where the reduction to $Fe(CN)_6^{4-}$ proceeded at a diffusion-controlled rate while the substrate was held at a potential where the $Fe(CN)_6^{4-}$ was oxidized back to $Fe(CN)_6^{3-}$. The steady-state current at the tip increased significantly above the constant value obtained at large distances when the separation became less than ca. 10 μm. This behavior is the result of the electrochemical feedback process that has been elucidated in earlier reports (*11*). The current at the substrate electrode was essentially zero at sufficiently large separations

(not shown) and increased slowly as the separation decreased until the sharp rise resulting from the electrochemical feedback set in and the tip and substrate currents became nearly equal.

In Figure 4B are plotted collection efficiencies as a function of the tip-to-substrate separation for a solution of $Fe(CN)_6^{3-}$. Attractively high collection efficiencies are obtained. They exceed 0.9 for separations below 20 μm, and even at 100 μm the efficiency is 0.3. Thus, the closely spaced microtip–macrodisk system allows very efficient capture by the disk of species generated at the tip.

Geometrical differences between microband arrays and tip–substrate systems will, of course, produce behavioral differences, but it is of interest to compare these two methods of conducting generation/collection experiments with separation distances in the micron range. Curves 2 and 3 in Figure 4B give the collection efficiencies obtained in a recent study with interdigitated microband electrodes (*8*). Larger efficiencies were obtained from generator band electrodes that were flanked by two collector electrodes (curve 3) than from a side-by-side pair of microband electrodes (curve 2). The microtip–macrodisk system provides not only larger collection efficiencies but also a reasonable range of separations where the collection efficiency is close to unity and insensitive to small changes in the separation.

Preliminary results of a digital simulation study of the effect of tip geometry and substrate size on collection efficiencies (*10*) show that collection efficiencies greater than 0.9 are to be anticipated at separation distances comparable to the radius of the tip, even when the substrate and tip have similar radii, so long as the tip is perfectly disk-shaped.

CONCLUSIONS

The experimental system described in this study has several attractive features: Unusually large collection efficiencies are easily achievable, which would be valuable in the detection of short-lived intermediates generated at the tip or in measurements of the kinetics of reactions between species generated at the tip and other reactants present in the solution. Compared with rotating ring–disk or interdigitated microband electrode systems that can be employed for the same purposes, the present system allows a wider range of generator-to-collector distances to be examined by means of the continuously variable micropositioning apparatus. The other techniques would require that a series of electrodes with varying separations be constructed. The fabrication of a macrodisk electrode opposed to adjustable microtip electrode is somewhat simpler than is the construction of ring–disk or interdigitated microband electrode assemblies.

The ability to use substrate currents instead of tip currents to obtain images by means of the SECM technique is another advantage of the present system because it permits successful imaging at large separation distances where the changes in tip current are considerably smaller than the changes in substrate current.

The system described in this study was constructed with the intention of applying it to studies of ionic transport at the surfaces of electrodes coated with polymers and polyelectrolytes. The high collection efficiencies that have been demonstrated should prove useful in quantitative measurements of electroactive species ejected from such coatings when current is passed through them. The results of these experiments will be described in a forthcoming report.

LITERATURE CITED

(1) Bard, A. J.; Fan, F.-R.; Kwak, J.; Lev, O. *Anal. Chem.* **1989**, *61*, 132.
(2) Bard, A. J.; Denault, G.; Lee, C.; Mandler, D.; Wipf, D. O. *Acc. Chem. Res.* **1990**, *23*, 357 and references therein.
(3) Engstrom, R. C.; Weaver, M.; Wunder, D. J.; Burgess, R.; Winquist, S. *Anal. Chem.* *1986*, *58*, 844.
(4) Engstrom, R. C.; Meaney, T.; Tople, R.; Wightman, R. M. *Anal. Chem.* **1987**, *59*, 2005.
(5) Engstrom, R. C.; Pharr, C. M. *Anal. Chem.* **1989**, *61*, 1099A.
(6) Albery, W. J.; Hitchman, M. L. *Ring-Disc Electrodes*; Clarencon Press: Oxford, U.K., 1971.
(7) Bard, A. J.; Crayston, J. A.; Kittlesen, G. P.; Varco Shea, T.; Wrighton, M. S. *Anal. Chem.* **1986**, *58*, 2321.
(8) Bartelt, J. E.; Deakin, M. R.; Amatore, C.; Wightman, R. M. *Anal. Chem.* **1988**, *60*, 2167.
(9) Kwak, J.; Bard, A. J. *Anal. Chem.* **1989**, *61*, 1794.
(10) Kwak, J.; Anson, F. C. Unpublished work.
(11) Kwak, J.; Bard, A. J. *Anal. Chem.* **1989**, *61*, 1221.
(12) Kwak, J.; Lee, C.; Bard, A. J. *J. Electrochem. Soc.* **1990**, *137*, 1481.

RECEIVED for review January 14, 1991. Accepted April 18, 1991. This work was supported by the National Science Foundation. This is Contribution No. 8379 from the Division of Chemistry and Chemical Engineering.

For Over Six Decades...

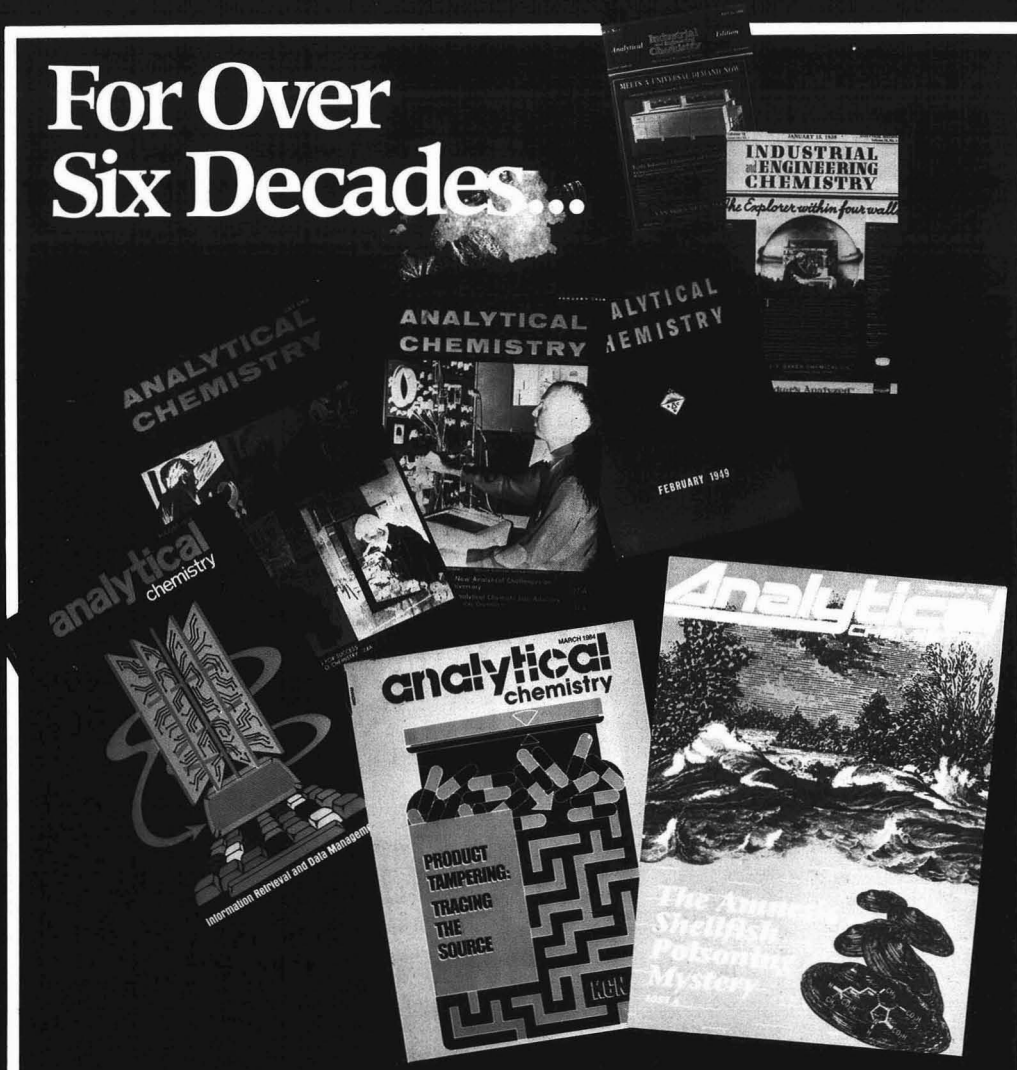

The Leader in the Field.

ANALYTICAL CHEMISTRY, the world's foremost publication in the vital field of measurement science, comes to you semi-monthly packed with *more* research articles, special features and application papers.

Keeping pace with the changes has continued to make *ANALYTICAL CHEMISTRY* the pinnacle of publications in the field . . . for over 6 decades.

For your personal subscription:

CALL TOLL FREE (800) 227-5558 (U.S. only)
Outside U.S. (202) 872-4363

Telex: 440159 UI
89 2582 ACSPUBS

American Chemical Society
1155 16th St., NW
Washington, DC 20036

NEW! Combined IR/MS

New research grade GC/LC/MS/DS gives you more than you'd expect...

1. MS Engine: *the* high performance, mid-priced quadrupole mass spectrometer. Its open structure keeps all your application options open.

2. Low picogram to low femtogram sensitivity, full-scan and SIM.

3. Research versatility with GC/MS, thermospray and particle beam LC/MS, EI, CI, NCI, DCI, DIP.

4. Autoswitching, programmable EI/CI source for ease of use.

5. Differential pumping for flexibility and optimum CI.

6. Optional 2000 amu mass range for high molecular weight analysis.

7. New thermospray source for higher sensitivity and increased fragmentation.

8. New higher sensitivity particle beam LC/MS for EI, CI and NCI spectra.

9. Multitasking MS ChemStation (HP-UX series) with X-Window System based software for efficient operation and easy networking.

10. GC/IR/MS system classifies and confirms unknowns in a single injection.

...for less than you'd expect.

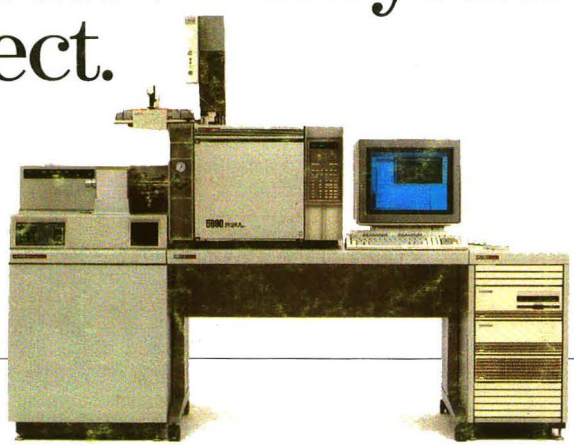

Our new MS Engine system brings you the highest performance in its class. At the lowest price in its class.* Along with the sensitivity, reproducibility, versatility and reliability you need for demanding research, methods development and service laboratory applications. Add to this HP's acclaimed quality, reliability and support, and the deal gets even better.

The MS platform for the 1990s, this flexible system combines HP's advanced GC, LC and FTIR technologies plus our multitasking MS ChemStation with X-Windows. For information, call **1 800 334-3110, Ext. 10246.**

HEWLETT PACKARD

* Under $130,000 (U.S. list price) for a complete standard GC/MS/DS system, including EI/CI source

© 1991 Hewlett Packard Company AG04006(R)

CIRCLE 60 ON READER SERVICE CARD